# Illuminating Innovations: Design and Synthesis of Maleimide Fluorophores Inspired by Luminescence Mechanisms and Structural Characteristics

by

**Yu Lu**

**Supervisor: Rachel K. O'Reilly**

A thesis submitted to the University of Birmingham for the degree of

DOCTOR OF PHILOSOPHY


UNIVERSITY OF BIRMINGHAM

School of Chemistry

College of Engineering and Physical Sciences

University of Birmingham

March 2025

# Table of Contents

# Abstract

Maleimide-type fluorophores have attracted significant attention over the years due to their various advantages. For instance, maleimide molecules are relatively small and possess multiple modification sites, facilitating the synthesis of fluorophores with different emission wavelengths. Additionally, the push-pull system and twisted intramolecular charge transfer emission mechanism endows maleimide-type fluorophores with features such as solvatochromism and sensitivity to microenvironmental changes. Therefore, based on the structural and luminescent characteristics of maleimide molecules, the main work of this thesis involves designing and synthesising different types of fluorescent compounds.

Dual state emission molecules represent a novel class of fluorophores that possess efficient luminescence capabilities in both solution and aggregated states. They hold great potential for applications in various fields such as bioimaging and information anti-counterfeiting. The work in Chapter 2 demonstrates a series of maleimide derivatives with dual-state emission properties. By attaching *para*-haloanilines and 4-n-butylaniline to the nitrogen atom of the imide ring and the double bond site, respectively, efficient luminescence in both solution and solid states was achieved (with quantum yields up to 41.9% in solution and 84.1% in the solid state). Further single-crystal structure analysis revealed the effect of substituent positions on the intramolecular torsion angles. Finally, theoretical calculations validated the experimental results and provided in-depth insights into the molecular luminescence mechanism. This study presents a universal design strategy for dual-state emission molecules, paving the way for the development of next-generation fluorescent materials.

The work in Chapter 3 demonstrates a series of maleimide derivatives with photochromic properties. Aiming at the research gap in functionalized maleimide derivatives, a strategy was proposed to prepare a series of fluorophores exhibiting photochromism via photoisomerization and photocycloaddition by attaching photoresponsive groups to the nitrogen atom site of the imide ring. First, fluorescence spectroscopic characterization of azobenzene-based maleimide molecules revealed their photochromic properties, followed by theoretical calculations to explore the photochromic mechanism. Furthermore, the successful photochromism achieved by connecting different photoresponsive groups to maleimide validated the universality of this molecular design strategy. This study presents a novel and simple design concept for photochromic molecules, contributing to the further development of photoresponsive materials.

The work in Chapter 4 investigates the room-temperature phosphorescence (RTP) properties of maleimide derivatives. In view of the absence of research reports on the RTP properties of maleimide molecules, this study first proposes the realization of RTP through a host-guest doping strategy. Initially, RTP characterization using benzophenone and 4-phenylmaleimide as small-molecule hosts failed to observe RTP; subsequently, RTP was achieved using PMMA polymer as the host. Theoretical calculations were further conducted to explore the phosphorescence mechanism of such molecules. This study demonstrates the potential of maleimide derivatives to achieve RTP, providing more molecular design options for the development of the room-temperature phosphorescence field.

# Acknowledgements

I would like to express my heartfelt gratitude to my parents, Mr. Bixin Lu (卢碧新) and Ms. Mei Li (李梅). During my doctoral studies, they provided me with endless support and were my firmest backing.

I also sincerely thank my girlfriend, Yuanjie Lu (鲁渊婕). She has always been by my side throughout my long academic journey, giving me warmth and encouragement.

I am honoured to join Rachel O'Reilly's research group. Here, I would like to extend my deep gratitude to my supervisor. Thank you for your meticulous guidance and help on my academic path. At the same time, I would also like to especially thank Calum Ferguson for your support and assistance.

I feel extremely happy and fortunate to work, have heated discussions, and make progress together with my Chinese colleagues in the group. Thank you, Laihui Xiao, Tianlai Xia, Jian Zhang, and Peng Sun. In particular, I would like to thank La Zhuo for her great help in the High-Resolution Mass Spectrometry tests. In addition, I would also like to express my gratitude to Dr. Yujie Xie for her assistance with my projects and for reviewing my thesis.

Finally, I would like to give myself credit for my perseverance and hard work during my doctoral career.

# Abbreviations

1. **AIEgens**: Aggregation-induced emission luminogens
2. **ACQ**: Aggregation-caused quenching
3. **D-A**: Donor-Acceptor
4. **DMSO**: Dimethyl sulfoxide
5. **DFT**: Density functional theory
6. **EDG**: Electron-donating group
7. **EAG**: Electron-accepting group
8. **ESP**: Electrostatic potential
9. **HOMO**: Highest occupied molecular orbital
10. **HRMS**: High-Resolution Mass Spectra
11. **LE**: Locally excited
12. **LUMO**: Lowest unoccupied molecular orbital
13. **NMR**: Nuclear magnetic resonance
14. **PCM**: Polarised continuum model
15. **RIM**: Restriction of intramolecular motions
16. **RIV**: Restriction of intramolecular vibrations
17. **$S_0$**: Ground state
18. **$S_1$**: First excited singlet state
19. **SMD**: Solvation model based on density
20. **TICT**: Twisted intramolecular charge transfer
21. **THF**: Tetrahydrofuran
22. **UV-vis**: Ultraviolet-visible
23. **VMD**: Visual Molecular Dynamics
24. **ADBN**: 6-Amino-2-benzylidene-3,4-dihydronaphthalen-1 (2H)-one
25. **BVA**: (E)-4-(2-(benzo [d] thiazol-2-yl) vinyl) aniline
26. **CIE**: Commission Internationale de l'Eclairage

27. **SMD**: Solvation Model Based on Density
28. **BP**: Benzophenone
29. **BPO**: Benzophenone-based
30. **NPA**: N-Phenylmaleimide
31. **PMMA**: Polymethyl methacrylate
32. **PS**: Polystyrene
33. **PVA**: Polyvinyl alcohol
34. **RTP**: Room-temperature phosphorescence
35. **SOC**: Spin-orbit coupling
36. **S1**: Excited singlet state
37. **T1**: Triplet state
38. **ISC**: Intersystem crossing
39. **LE**: Locally excited
40. **TICT**: Twisted intramolecular charge transfer
41. **Mn**: Number-average molecular weight

# Declaration of Authorship

This thesis is submitted to the University of Birmingham in support for the degree of Doctor of Philosophy. It has been composed by myself and has not been submitted in any previous application for any degree.

All project designs, experimental work, data analysis, and figure or table production in this thesis were independently completed by the author (Yu Lu). Except for the above, specific declarations regarding part of the collaborative work will be made as follows:

1. All theoretical calculations in this thesis were independently completed by the author but guided by Prof. Peng Sun from Beijing Institute of Technology.
2. The measurement of low-temperature (77K) delayed spectroscopy in Chapter 4 was assisted by Beijing Institute of Technology.

# Chapter 1 Introduction

## 1.1 Luminescence

### 1.1.1 Photophysical Processes

Luminescent materials are widely present in our daily lives, having a profound impact on human existence. This phenomenon involves a photophysical process, specifically the conversion of electrons from the ground state to an excited state, which can be elaborately explained through the Jablonski diagram (Fig 1.1). In this process, molecules at the ground state absorb photons, prompting electron excitation from the ground state ($S_0$) to higher excited states ($S_n$). These elevated energy states are inherently unstable, leading electrons to release their excess energy through various relaxation pathways. Initially, electrons transfer to the lowest excited state ($S_1$) via internal conversion and non-radiative relaxation. Subsequently, electrons on $S_1$ return to the $S_0$, a process often accompanied by the emission of photons, manifesting as the mechanism of dynamic electronic transitions within molecular fluorescence phenomena.[1]

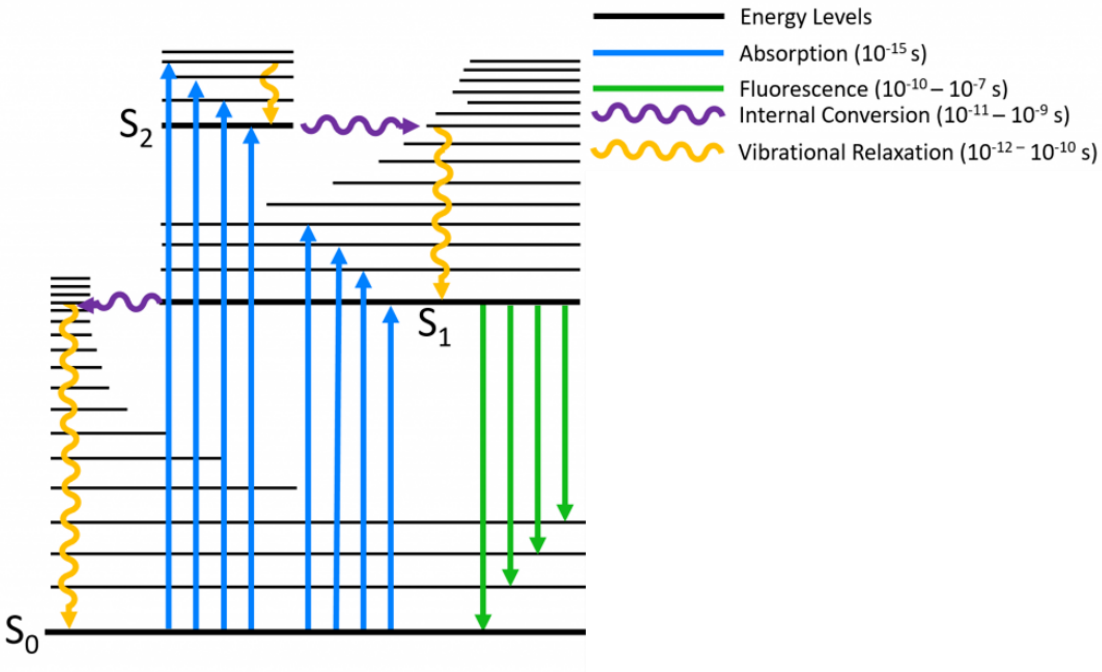


Figure 1.1 Simplified Jablonski diagram explaining the photophysical process between the absorption and emission of light.

According to Kasha's rule, molecules exhibit extreme instability and brief lifetimes upon

reaching high-energy excited states. They rapidly return to the lowest excited state, $S_1$, through internal conversion mechanisms, a process that takes a remarkably short time dimension, generally on the order of $10^{-12}$s.[2] The investigation into the photophysical and photochemical reactions that occur in the excited states during the fluorescence process is crucial for a comprehensive understanding of electron transfer dynamics. This research is not only pivotal for advancing the development of luminescent materials but also essential for elucidating the underlying mechanisms of various luminescent phenomena. It highlights key principles of energy conversion, underscoring its significance in the fields of physics and chemistry.[3-5]

The complexity of the physical deactivation process is evident in the transition of electrons from an excited state back to the ground state, which does not always occur through radiative means (such as light emission). Non-radiative transitions play a crucial role in this context, which predominantly involves the coupling between different electronic states within the molecule through vibrational-rotational energy levels, facilitating the non-radiative release of energy. Specifically, under this mechanism, the energy of an excited electron is converted into vibrational energy of a lower electronic state of the molecule via non-radiative process, rather than emitting light or other form of energy.[6,7] Internal conversion refers to the process where an electron transitions from a low vibrational energy level of a higher excited state to a high vibrational energy level of a lower electronic state (for example, from the lowest vibrational level of the $S_2$ state to a higher vibrational excited state of the $S_1$ state). The efficiency of internal conversion has profound implications for the photophysical properties of molecules, particularly in terms of fluorescence quantum yield, excited state lifetimes, temperature dependence, and spectral characteristics. Specifically, internal conversion competes with fluorescence, often resulting in a reduction of fluorescence quantum yield due to the non-radiative dissipation of energy. Additionally, the excited state lifetime can be significantly shortened when internal conversion is efficient, as the molecule quickly relaxes to a lower energy state without photon emission. The process is also temperature-dependent, with higher temperatures enhancing molecular vibrations and, consequently, the rate of internal conversion. Furthermore, the rapidity of internal conversion can influence the spectral properties of a molecule, potentially leading to the quenching of fluorescence and the absence of observable emission spectra.[8,9] Understanding these photophysical processes lays the foundation for quantifying fluorescence characteristics, which are governed by key parameters such as Stokes shift, quantum yield, and lifetime.

## 1.1.2 The Key Parameters of Fluorescence

### 1.1.2.1 Stokes Shift

Internal conversion and vibrational relaxation result in the loss of energy, leading to a difference between the absorbed and emitted energy. This disparity manifests as a shift in wavelength between the absorption and emission spectra, a phenomenon known as the Stokes shift. This shift is crucial for understanding molecular electronic transitions and is extensively utilized in spectroscopic techniques (Fig 1.2a).[10,11] The magnitude of the Stokes shift directly affects the overlap between the absorption and emission spectra: the greater the shift, the less the overlap, which reduces the efficiency of energy transfer and thus helps prevent a reduction in luminous efficiency caused by increased reabsorption, self-quenching, and energy loss through non-radiative decay.[12] This is crucial in applications like fluorescent bio-detection, where high luminous efficiency is essential for sensitive and accurate detection.[13-15] Steady-state and transient fluorescence spectrometers are fundamental instruments used in fluorescence spectroscopy. Their operating principle can be summarized as follows (Fig 1.2b): UV-visible light from the light source is spectrally divided by the excitation monochromator, and then irradiates the sample in the cell holder. These samples emit fluorescence upon irradiation with the excitation light, which is then spectrally divided by the emission monochromator, subsequently received by the photomultiplier tube, and converted into a corresponding electrical signal. This electrical signal is then amplified by an amplifier and sent to an A/D converter unit, ultimately converting the analogue signal into a digital signal. By analysing the data obtained from the fluorescence spectrometer, such as excitation wavelength, emission wavelength, and photoluminescent (PL) intensity, related fluorescence spectroscopy data can be gathered. It is noteworthy that PL intensity is influenced by various factors, including the concentration of the sample and the intensity of the test light source, etc., hence, PL intensity is not suitable as a quantitative parameter for assessing the capability of fluorescence emission intensity.

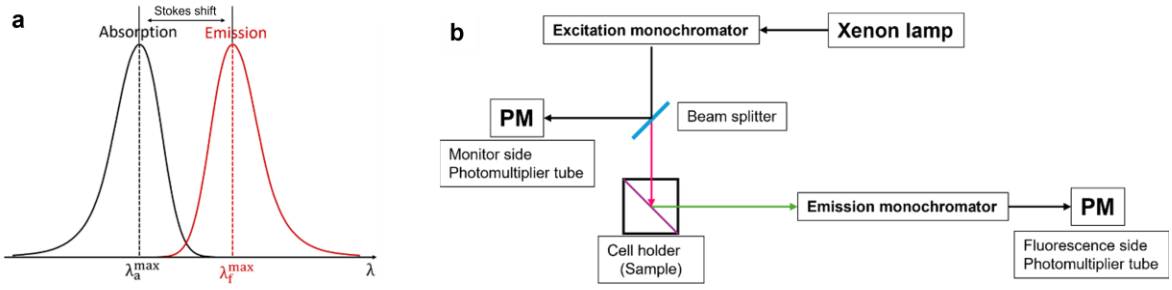


Figure 1.2 (a) The absorption and emission spectra explain the Stokes shift, (b) Simplified steady-state fluorescence spectrometer to explain the detection principles of the fluorescence spectrum.

### 1.1.2.2 Fluorescence Quantum Yield and Lifetime

To analyse and compare fluorescence characteristics more quantitively, quantum yield is evaluated as a core parameter for measuring the efficiency of the fluorescent process, typically defined as the ratio of the number of photons emitted to the number of photons absorbed.[16,17] When absorbing the same amount of energy, a molecule with a higher quantum yield is more efficient at converting the absorbed photon energy into the desired outcome (e.g., fluorescence). This efficiency is due to fewer or less effective non-radiative decay pathways, more efficient radiative decay, better stability, and/or more favourable interactions with its environment.[18,19] Specifically, the fluorescence quantum yield (φ) of a compound can be calculated using the formula (1):

$$\varphi = \frac{K_f}{K_f + \sum K'}, \quad (1)$$

where $K_f$ represents the rate constant of fluorescence emission, and ΣK' represents the sum of rate constants for all non-radiative transition processes. The quantum yield value represents the efficiency of the fluorescence emission process relative to the total energy used for excitation, accounting for both non-radiative transitions and radiative emissions. The measurement of fluorescence quantum yield is commonly carried out using an absolute method or a relative method.[17,20] The absolute quantum yield is determined by directly measuring the number of photons absorbed and emitted by a sample, eliminating the need for a reference standard. The sample, prepared in a suitable solvent at a low concentration to minimize reabsorption, has its absorbance at the excitation wavelength quantified using UV-vis spectroscopy. The fraction of photons absorbed ($f_{abs}$) is computed from the absorbance data. A calibrated light source excites the sample, and the total emitted photons are captured by a spectrofluorometer equipped with an integrating sphere, which ensures complete photon collection. The quantum yield is

calculated as the ratio of emitted to absorbed photons. Necessary corrections for refractive index and detector sensitivity are applied for accuracy. The absolute quantum yield is mathematically expressed as: $\varphi = \frac{N_{em}}{N_{abs}} \times C$, where $N_{em}$ represents the number of photons emitted, $N_{abs}$ represents the number of photons absorbed, and C represents the correction factor accounting for refractive index and detector sensitivity adjustments.[17,21,22]

The relative method involves comparing the diluted solutions of the unknown fluorescent substance with a standard sample with a known quantum yield under the same excitation conditions. This method measures the integrated fluorescence intensity (*i.e.*, the area included in the corrected emission spectrum) and the absorbance at a specific excitation wavelength of both solutions. The formula for calculating the quantum yield of the fluorescent sample is (2):

$$\varphi = \left(\frac{I_f}{I_{dye}}\right)\left(\frac{n_f}{n_{dye}}\right)^2\left(\frac{1-10^{-OD\,(dye)}}{1-10^{-OD\,(f)}}\right) \quad (2)$$

where I represent the integrated area of the fluorescence spectrum, n represents the refractive index of the solvent, and OD represents optical density. To ensure the accuracy of the measurement, the selected standard sample should be as similar as possible to the test sample in photophysical properties.[23-25]

Fluorescence lifetime is a critical parameter for characterizing the properties of fluorescent molecules. It is defined as the average time that excited electrons remain in the excited state before returning to the ground state via radiative transitions, emitting fluorescence. The fluorescence lifetime is defined by the time required for the fluorescence intensity to decay to 1/e of its initial value, represented by the formula (3)

$$I(t) = I_0 \cdot \exp^{(-t/\tau)} \quad (3)$$

where $I_0$ is the fluorescence intensity at time zero. Thus, the fluorescence lifetime is defined as the reciprocal of the total decay rate:

$$\tau = \frac{1}{K_f + K_{nf}} \quad (4)$$

where $K_f$ represents the rate constant for fluorescence emission and $K_{nf}$ represents the sum of rate constants for various non-radiative decay processes within the molecule. The fluorescence lifetime is influenced by the molecule's own structure and the microenvironment it is in (such as the polarity and viscosity of the solvent).[25-27]

### 1.1.3 Aggregation-Induced Emission

Traditional organic luminescent materials typically face a challenge termed Aggregation-Caused Quenching (ACQ), where the individual molecules are good emitters in their monomeric form but lose this ability when they aggregate. Molecules with ACQ properties typically tend to adopt a planar configuration, making them prone to intermolecular stacking in the aggregated state. This close stacking leads to the overlap of π-orbitals, which can promote non-radiative pathways (such as energy transfer or excimer formation) that compete with radiative decay (fluorescence or phosphorescence), thereby reducing the overall emission intensity.[28,29] For example, perylene emits strong luminescence in dilute tetrahydrofuran solution, but this luminescence vanishes as water, a poor solvent, is added, primarily due to intense π-π stacking interactions in the aggregated state. As shown in Figure 1.3(a), perylene's fluorescence intensity diminishes drastically at fw = 90% (fw refers to the weight fraction of water in the solvent mixture) due to π-π stacking-induced ACQ. In a sharp departure from ACQ, Aggregation-Induced Emission (AIE) is a concept where certain compounds, initially non-luminescent or weakly luminescent in dilute solutions, exhibit significantly enhanced luminescence upon aggregation. This groundbreaking concept was proposed by Professor Tang in 2001,[30] following his observation of hexaphenylsilole (HPS)'s increased luminescence in its aggregated state, as shown in Figure 1.3 (b), HPS exhibits a 10-fold emission enhancement under the same conditions, illustrating the AIE effect. The discovery of AIE has revolutionized traditional views on luminescent materials and opened new avenues in the development of novel luminescent materials, impacting fields like organic electronics and biological imaging.

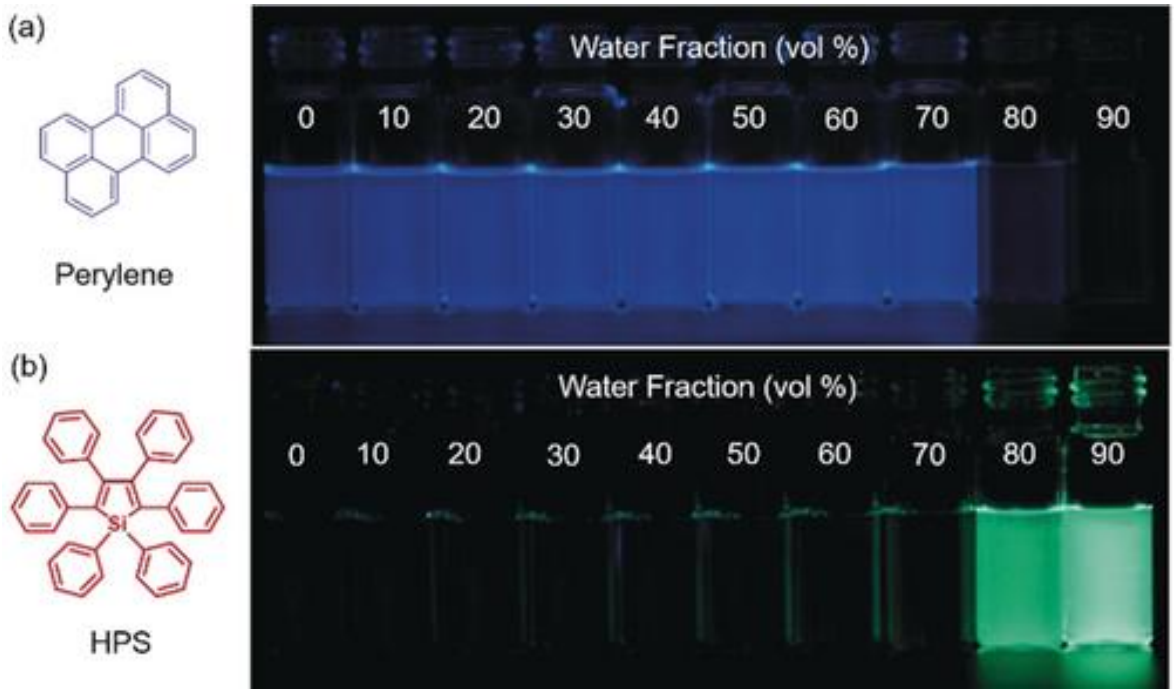


Figure 1.3 Images of fluorescence from solutions or suspensions showing (left) perylene (20 μM) and (right) hexaphenylsilole (HPS; 20 μM) in THF/water mixtures at varying water content (fw). In these images, perylene demonstrates the characteristic aggregation-caused quenching (ACQ) effect, while HPS exhibits aggregation-induced emission (AIE).[31]

### 1.1.3.1 Mechanism of Aggregation-Induced Luminescence

The currently accepted mechanism for AIE is the Restriction of Intramolecular Motion (RIM). The RIM mechanism comprises two distinct pathways: Restriction of Intramolecular Rotation (RIR) and Restriction of Intramolecular Vibration (RIV). RIR suppresses phenyl group rotations, while RIV minimizes vibrational energy dissipation. Taking tetraphenylethylene (TPE) as an example, in dilute solutions of tetrahydrofuran, the free rotation within TPE molecules leads to the excited state molecules predominantly returning to the ground state via non-radiative internal conversion (IC), a process that does not involve luminescence. However, in the aggregated state of TPE, the physical spatial constraints and the presence of intermolecular interactions significantly restrict the intramolecular motion. This restriction of motion impedes the non-radiative transition pathways, causing the excited state molecules to primarily decay to the ground state through radiative transition processes, thereby resulting in a significant enhancement of luminescence.[31] The propeller-shaped TPE in Figure 1.4 demonstrates how steric hindrance in aggregates restricts phenyl rotations (RIR), redirecting energy from non-radiative decay to radiative pathways.

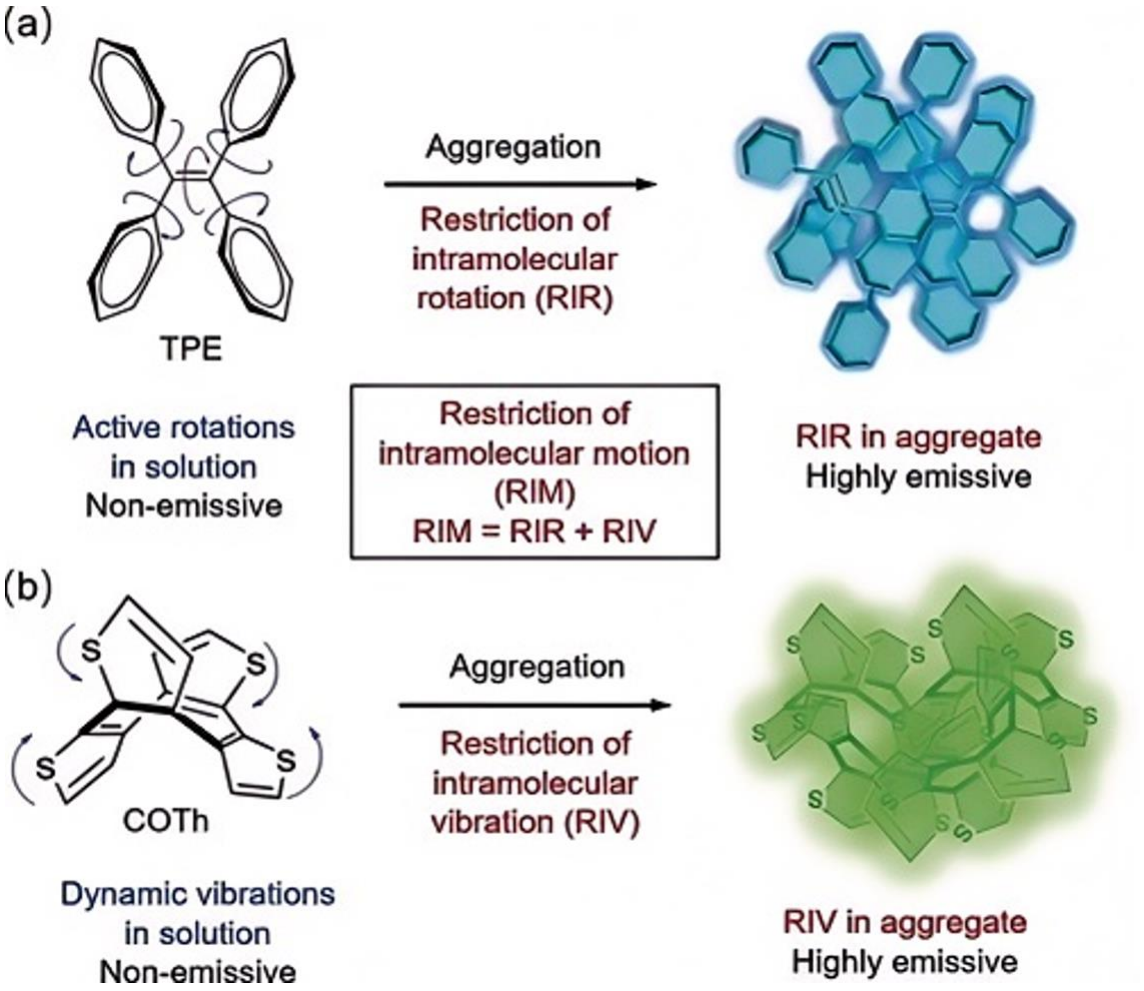


Figure 1.4 The tetraphenylethene (TPE) luminogen, with a propeller shape, does not emit light in a dilute solution; however, it becomes luminous upon aggregation, as this restricts the intramolecular rotation (RIR) of its phenyl rotors against the ethylene stator. Similarly, the shell-like luminogen of 10,10′,11,11′-tetrahydro-5,5′-bidibenzo[a,d][7]annulenylidene (THBA; 1) also becomes emissive in the aggregate state, where the intramolecular vibration (RIV) of its flexible vibrators is restricted.[32]

While AIE and ACQ represent opposing aggregation effects, Dual-State Emission bridges this dichotomy by integrating molecular flexibility and rigidity. This approach enables fluorescence in both solution and solid states, addressing the limitations of conventional systems.

### 1.1.4 Dual-State Emission (DSE)

As research progresses, an increasing variety of organic fluorophores with distinct photophysical properties have been reported. Among these, a particular class of fluorophores demonstrates the capability to exhibit fluorescence in both solution and solid states. This characteristic is referred to as dual-state emission. ACQ is linked to molecular rigidity, planarity,

high polarity, viscosity, and highly conjugated systems, all of which contribute to quenching effects. In contrast, AIE is favoured by reduced π-π interactions, and restricted intramolecular motion. DSE, which means that a fluorophore can exhibit photoluminescence in both solution and the solid state, plays a crucial role in balancing ACQ and AIE by introducing twisted molecular conformations, adding long chains or bulky peripheral groups, and employing donor-acceptor systems (Fig 1.5).[33]

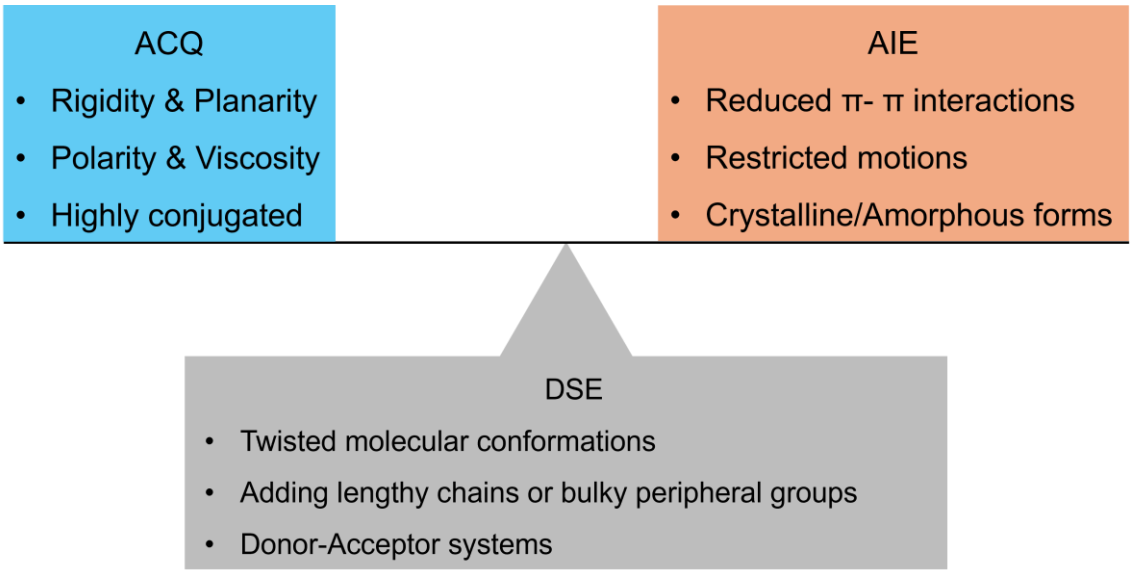


Figure 1.5 Characterization Comparison of AIE and ACQ and Key Parameters for DSE.

The construction of intramolecular twisted configurations proves crucial for developing fluorophores with DSE characteristics. This strategy aims to precisely regulate the intensity of intermolecular π-π stacking: excessive stacking induces ACQ effects via non-radiative transitions, while insufficient stacking leads to excited-state energy dissipation through free molecular rotation in solution. The intramolecular twisted configuration design effectively suppresses free molecular rotation in solution while simultaneously moderating intermolecular interactions in the aggregated state. For instance, Xu and colleagues designed a non-planar molecule that exhibited fluorescence in THF ($\Phi_F$ = 11.0%) and the solid state ($\Phi_F$ = 36.0%) (Fig 1.6a).[34] Additionally, Wu and collaborators developed a series of multisubstituted 1-aminoisoquinoline derivatives that showed strong emission in both solutions and the solid state, with quantum yields ranging from 40.3% to 98.1%, attributed to their twisted molecular structures (Fig 1.6b).[35] Furthermore, Dong and colleagues introduced a series of quinoline-based fluorophores, among which TPQ-TPA demonstrated high quantum yields in both solution (70%) and solid (48%) states (Fig 1.6c).[36]

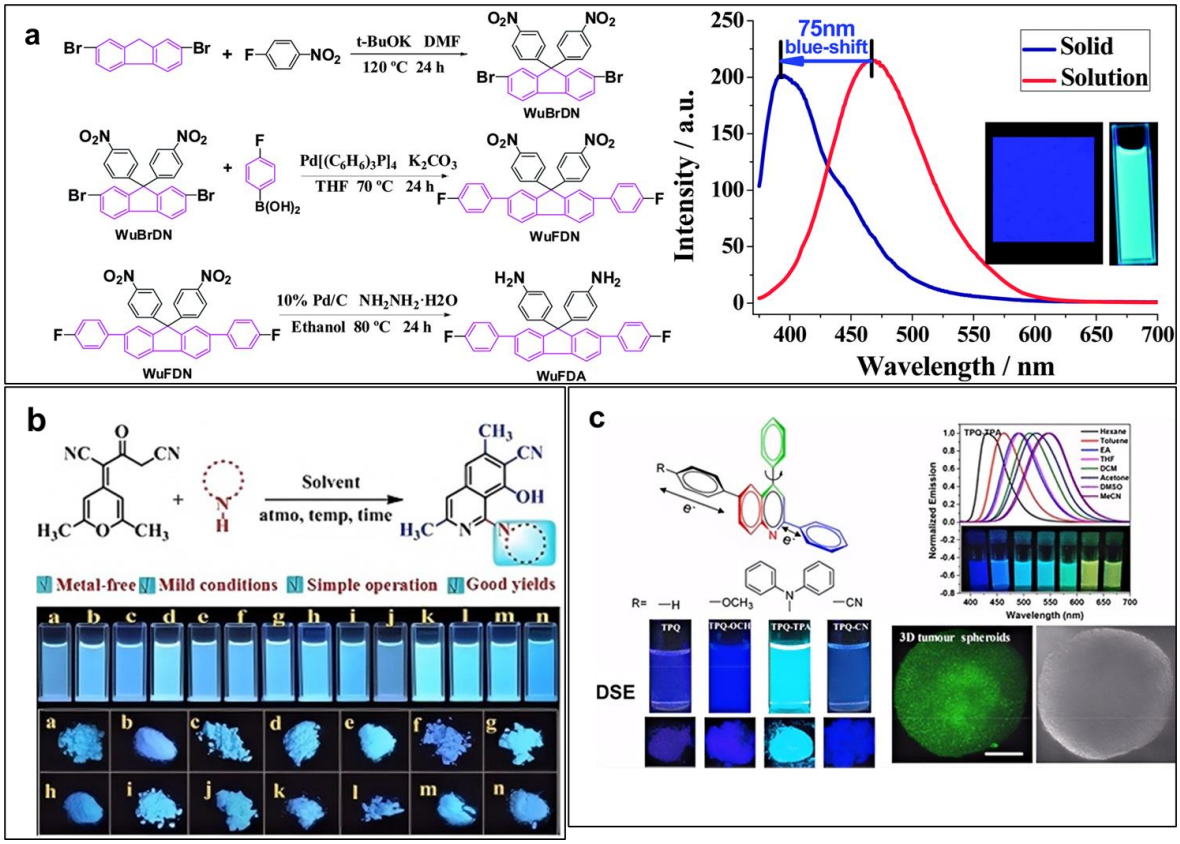


Figure 1.6 (a) Synthetic route and FL spectra in THF (1 × 10−5 M, Ex = 365nm) and solid state.[34] (b) synthetic route and chemical structures, emission picture in THF (1 × 10−5 M, Ex = 365nm), and solid state.[35] (c) chemical structures, FL spectra in various solvents, and emission pictures in various solvents and solid states.[36]

Introducing alkyl chains or doping with polymers to create a "self-isolated" effect is another effective strategy for achieving DSE properties. For instance, Zhao *et al*. devised a method that combines planar and distorted structures with long alkyl side chains, resulting in high quantum yields in both solution and solid states (Fig 1.7a).[37] Moreover, Meng *et al.* developed a strategy known as "self-isolated enhanced emission" (SIEE), which effectively reduces π–π stacking in solids, enabling DSE properties with an impressive quantum yield of 99.72% in solution and 77.46% in the solid state (Fig 1.7b).[38] This primarily stems from the steric hindrance effect generated by long alkyl chains combined with their "Z-shaped" arrangement. These dual mechanisms synergistically suppress excessive intermolecular stacking of π-conjugated systems in the aggregated state, thereby effectively mitigating the ACQ phenomenon commonly observed in conventional π-conjugated molecules.[39,40]

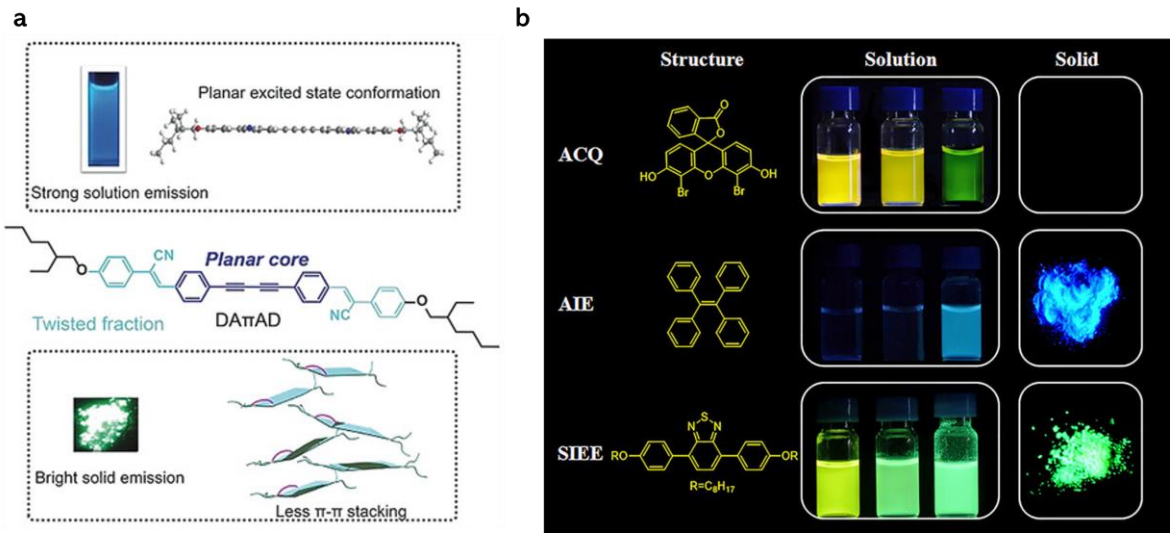


Figure 1.7 (a) chemical structure and emission pictures in solvent and solid state.[37] (b) chemical structure and emission pictures in solvent and solid state.[38]

Utilizing Donor-Acceptor (D–A) architectures is a potent method for creating strong dipoles, which has proven effective in achieving Dual-State Emission (DSE) properties. For instance, Lu and colleagues synthesized a series of triazolopyridine–thiophene donor-acceptor–donor (D–A–D) type conjugated molecules, which exhibited high quantum yields ($\Phi_F$) ranging from 80% to 89% in solution and up to 26% in the solid state (Fig 1.8a).[41] Additionally, Iyer and co-workers developed a series of monosubstituted dibenzofulvenes that displayed DSE properties with substantial quantum yields, attributed to the formation of J-type aggregates driven by the rigidity and planarization of the structure (Fig 1.8b).[42]

In summary, the introduction of twisted structures reduces aromatic stacking, and the intramolecular torsion can inhibit intermolecular interactions, thus achieving dual - state emission. On the other hand, long - chain alkyl groups or bulky groups are used to promote the "self - isolation" of fluorophores. Some compounds containing alkyl chains or bulky substituents can effectively reduce intermolecular interactions and further enhance the dual - state emission performance. In addition, constructing a donor - acceptor (D - A) structure is also an important means of regulating emission. By selecting appropriate molecular components, the emission characteristics of conjugated compounds can be changed. In the application field, DSE compounds show potential in many aspects. In optoelectronic devices, they can be used as colour - conversion materials in the lighting field or in organic light - emitting diodes (OLEDs) to improve the external quantum efficiency of OLEDs.[43] In the field of bioimaging, due to the fluorescence properties of DSE compounds in both solution and solid

state, the problems of traditional fluorophores during cell penetration and aggregation can be effectively avoided. Therefore, they can be used for cell staining, organelle detection, and disease diagnosis.[44] In the data encryption field, based on their fluorescence properties, DSE compounds can be used for the encryption and decryption of hidden information.[45] Although DSE compounds have broad development prospects, they still face many challenges at present. At the molecular design level, although the relationship between intramolecular rigidity, twisted conformation and luminescence behaviour is known, the quantitative relationship between the two has not been clarified, which makes it difficult to precisely design efficient DSE compounds. In practical applications, most of the existing DSE compounds emit at short wavelengths in the dual - state, and there are few compounds that emit in the near - infrared region, which limits their application in fields such as bioimaging that require a near - infrared window.[46]

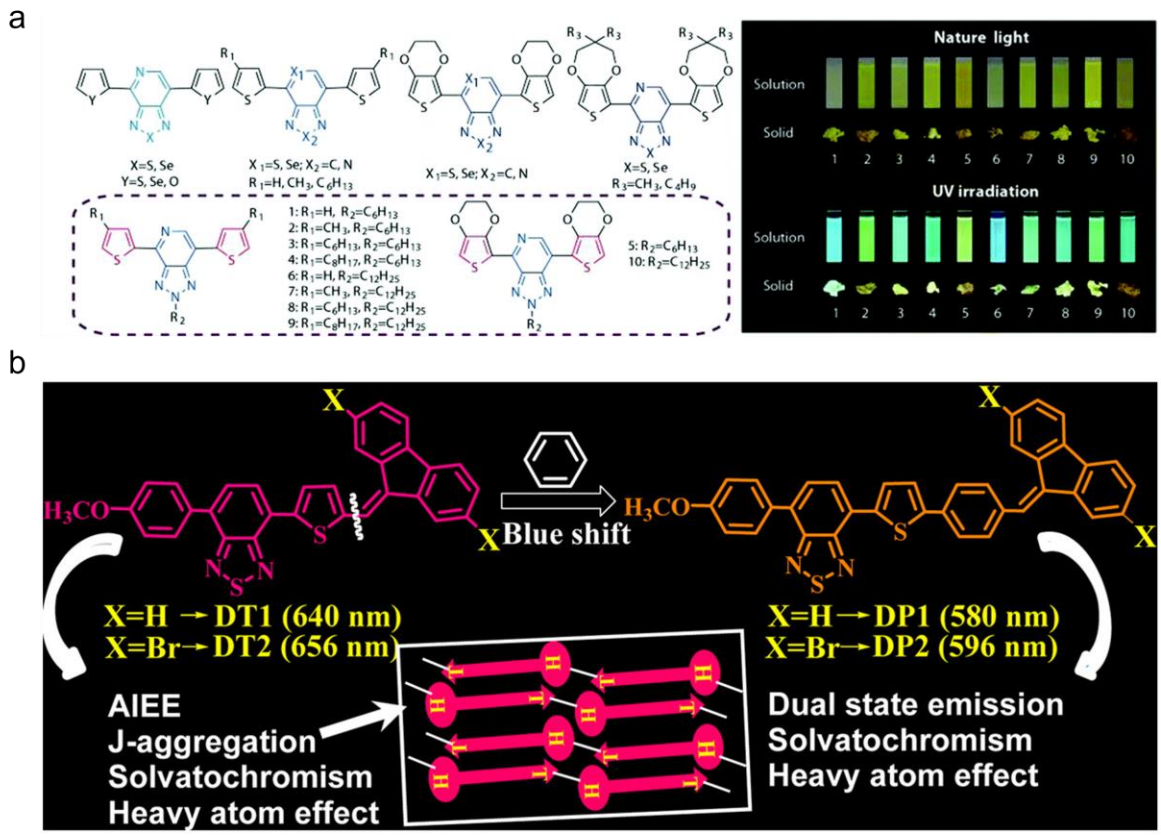


Figure 1.8 (a) Chemical structures of typical chalcogenodiazolo[3,4-c]pyridine derivative-based conjugated D–A–D type molecules reported in the literature and triazolopyridine–thiophene systems synthesized, and Photoluminescence of triazolopyridine–thiophene D–A–D type conjugated fluorophores (1–10) both in solution (DCM) and in the solid state.[41] (b) chemical structure and photophysical properties.[42]

## 1.2 Organic Photoresponsive Materials

In response to the escalating demand for advanced materials, smart materials have rapidly evolved and become integral in various sectors of daily life and industry. These materials, particularly stimulus-responsive or dynamic materials, possess the ability to detect and adapt to environmental changes.[42,47,48] Due to their capacity to respond to diverse external stimuli such as pressure, light, and heat, these materials can exhibit alterations in fluorescence, colour, shape, or conductivity. This adaptability has garnered significant scientific interest and led to widespread applications across fields such as sensing, biomedical imaging, and tissue engineering.[49-52] Particularly, light-responsive materials are at the forefront of research due to the fundamental role light plays in natural processes. The use of light as a stimulus offers several advantages, including its non-invasive nature, cleanliness as an energy source, and the capability for remote and precise control by adjusting light intensity and wavelength. This makes light-responsive materials highly promising for applications like artificial muscles and optical switches, where precise and reversible changes in material properties are essential.[53-55] Organic photochromic materials, whose optical properties change under specific wavelengths of light, represent a significant area of research. These materials were first discovered in 1867,[56,57] but systematic research did not begin until the 1950s.[57,58] Typically, they undergo structural changes upon light stimulation, resulting in colour shifts. However, due to the poor conjugation of these structures, the directly prepared solid-phase materials often lack significant fluorescence.[59,60] To fully utilise these molecules' photoresponsive characteristics, researchers have combined them with highly efficient fluorescent moieties to develop new types of photoresponsive luminescent materials, expanding their applications in data storage, anti-counterfeiting, and imaging.[54,61-63]

Photochromic molecules primarily achieve colour changes through two mechanisms: reversible photo-induced *cis-trans* isomerization and photo-cyclization reactions involving ring opening and closing.[64-66] Under the influence of light, these molecules undergo changes in their isomeric forms, affecting aspects such as conjugated structures, spatial conformation, and dipole moments. These alterations allow for the reversible modulation of the system's intrinsic effects and characteristics and can even introduce new functionalities. Figure 1.9 illustrates that common organic photochromic materials are categorized into three main classes based on their molecular structures: azobenzenes, diarylethenes, α-cyanodiarylethenes, and spiropyrans. In these materials, the reversible photo-isomerization between isomers leads to alterations in their electronic structures, subsequently affecting their ultraviolet absorption and fluorescence

emission properties.[67-69] Currently, utilizing photoisomerization molecules to achieve photochromism is a widely adopted approach.[70,71] *Cis-trans* isomerization (*Z/E*), as a type of stereoisomerism, significantly influences the properties of the isomers through the alteration of their spatial positions. Furthermore, introducing *cis-trans* isomerization into fluorescent molecules allows for the modulation of their luminescent properties by adjusting spatial positions. The simplicity and flexibility of light-induced *cis-trans* isomerization not only provides a unique method for studying the characteristics and interrelations of these materials but also hold significant importance for their future practical applications.[72-74]

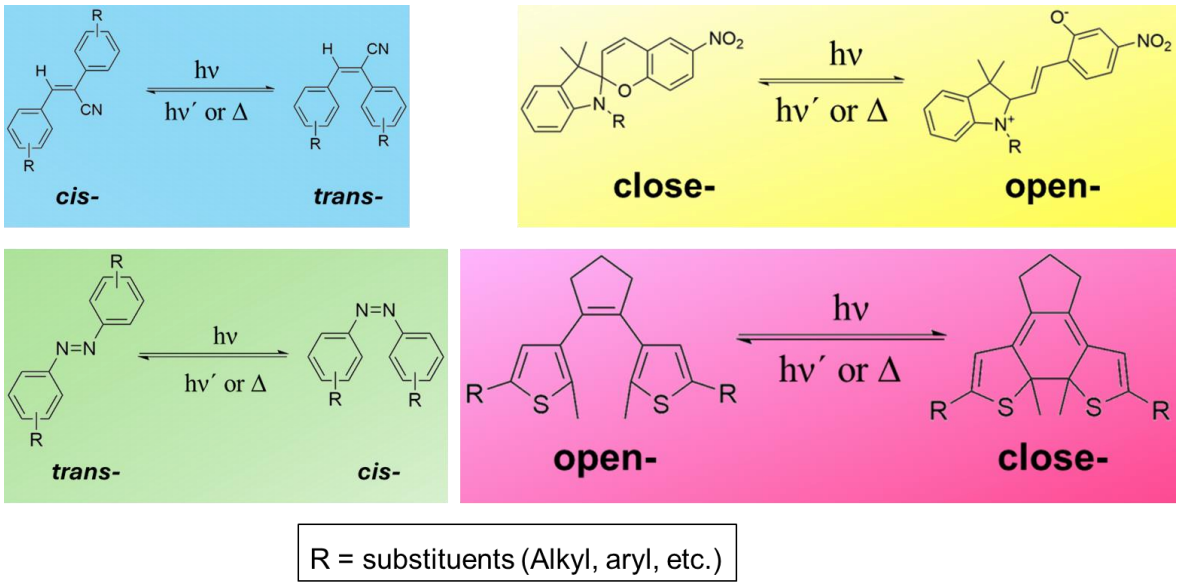


Figure 1.9 Typical examples of molecular structures of α-Cyanostilbene, spiropyran, azobenzene and dithienylethene and their photoisomerization process.

## 1.2.1 Cyanostyryl-based photoresponsive molecules

Based on their structural characteristics, photochromic cyanostyryl-based molecules can be categorized into three types: α-cyanostyrene, dicyanostilbene, and diaryl dicyanoethylene (Fig. 1.10). A common feature of these molecules is the substitution of cyano groups and the diverse configurations of aromatic groups. Notably, in these cyanostyrene molecules, hydrogen atoms are replaced by cyano groups, and the diaryl groups are evenly distributed on both sides of the carbon-carbon double bond. Recently, materials constructed from cyanostyrene molecules have garnered significant attention due to their unique responsiveness to various stimuli such as pressure, temperature, solvent vapours, pH levels, electric fields, and light.[75-78] The multifunctional nature of these materials makes them particularly suitable for application in optoelectronic device fields.[68]

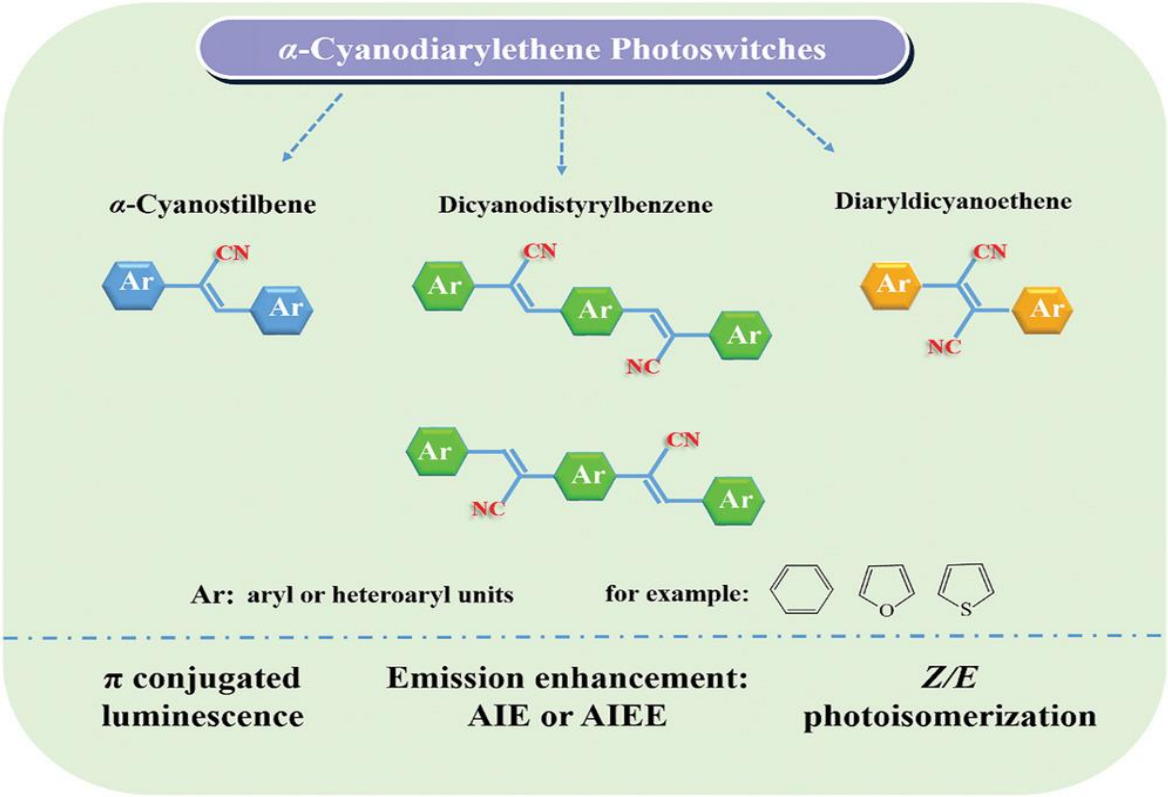


Figure 1.10 Types of fluorescent photochromic α-cyanodiarylethenes and their potential properties upon light irradiation.[79]

The primary advantage of cyanostyrene lies in its ease of synthesis and tunable structure. The strong electron-withdrawing nature of the cyano groups lowers the excitation energy, facilitating π-π stacking between molecules and leading to a redshift in the absorption and emission spectra. Furthermore, cyanostyrene molecules exhibit excellent luminescent properties in solid-state, assembled, and liquid crystalline states.[80-82] Some of these molecules display AIE or enhanced fluorescence (AIEE) in their aggregated state, a phenomenon attributed to the formation of flat π-conjugated frameworks and J-type aggregates.[83,84] It is noteworthy that during the photoisomerization process of α-cyanostilbene from its *trans* to *cis* form, the fluorescence intensity typically decreases due to the reduction in the π-conjugation length. Particularly, some *cis* isomers exhibit almost no light emission. However, there are exceptions where certain *cis* isomers of α-cyanostilbene demonstrate stronger emission characteristics compared to their *trans* counterparts. This enhanced emission is attributed to the planar configuration of the *cis* isomers, which inhibits the twisted intramolecular charge transfer (TICT) effect, thereby boosting their emissive properties.[85] In 2008, the research by Gulino (Fig 1.11a) revealed that α-cyanostilbene's molecular structure is particularly effective for reversible photoreactions.[86] They developed a derivative, (Z)-1-cyano-1-phenyl-2-[4′-(10-

undecenyloxy)phenyl]-ethylene, which forms a single-layer assembly on Si(100) surfaces. This layer is capable of reversible Z/E photoisomerization when exposed to UV light at 366 and 254 nm wavelengths in a solid-state environment, showcasing its potential for photonic applications. Park and coworkers (Fig 1.11b) investigated the behaviour of *cis-trans* isomeric molecules, noting that Z-form molecules exhibited strong cyan fluorescence, unlike E-forms.[87] These molecules, especially the rod-like (Z)-CN-MBE, showed a unique liquid crystal texture at specific temperatures. Upon UV irradiation, the compound shifted from an anisotropic to an isotropic state in liquid crystals, with the E-isomer causing a phase change due to altered molecular stacking. Cooling these irradiated samples led to a loss of their initial blue fluorescence. Park and his team (Fig 1.11c) extended their research beyond Z/E photoisomerization, discovering that certain asymmetric cyano-stilbene derivatives exhibit distinctive fluorescence switching properties under shear strain and UV light exposure.[88] These derivatives undergo a unique reversible [2+2] cycloaddition process in their π-dimer crystal form, highlighting a novel aspect of their molecular behaviour. Since the discovery of α-cyanostilbene-based molecular photoswitches, significant progress has been made in enhancing their emission properties through Z/E photoisomerization. In 2018, Tang and his team (Fig 1.11d) introduced a cyanostilbene-based molecule characterized by its Aggregation-Induced Emission (AIE) and capable of three distinct photoreactions: reversible Z/E isomerization, UV-induced photocyclization, and selective photodimerization in aqueous environments.[89] This breakthrough, combining multiple photoreactions in one molecule, has broadened its application in fields like optical materials, information storage, and nano-optoelectronics.[90,91]

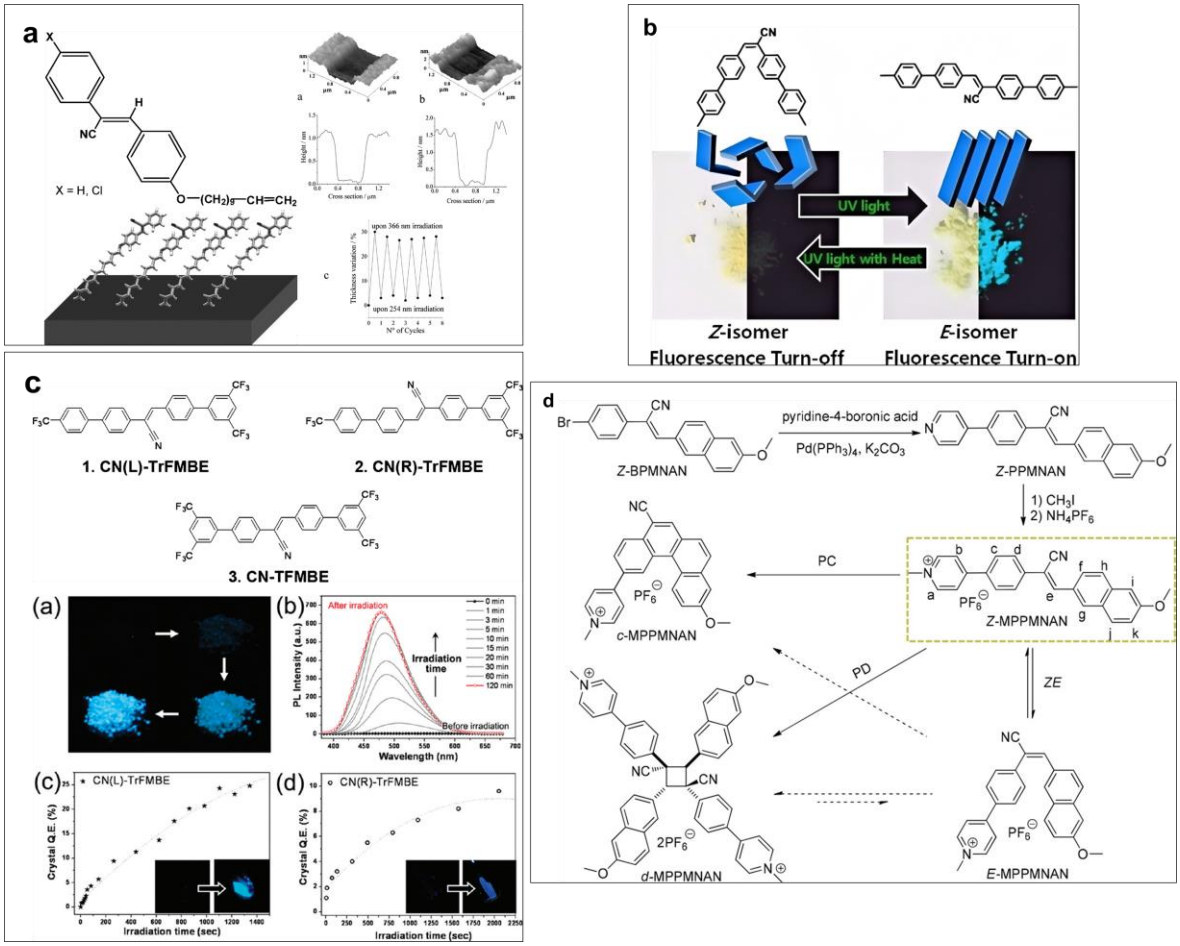


Figure 1.11 (a) Scheme representation of Si(100)-UCS-CAM for Z/E photoisomerization upon cycling irradiation.[86] (b) The photo/thermal Z/E isomerization of CN-MBE and corresponding LC-Iso phase transition.[87] (c) chemical structure and illustration of the photo-responsiveness process.[88] (d) MPPMNAN exhibits various and controllable light-responsive behaviors under different conditions, including "turn-on" and "turn-off" processes upon UV irradiation.[89]

## 1.2.2 Azobenzene-Based Photoresponsive Molecules

Azobenzene, initially used as an industrial dye, was discovered by Hartley in 1937 for its unique *cis-trans* photoisomerization ability.[92] This compound, featuring two phenyl rings connected by a nitrogen-nitrogen double bond, showcases photoisomeric and thermally reversible properties. The *trans*-isomer, typically more stable, can switch to the cis form either through visible light absorption or naturally in dark conditions. Azobenzene's isomers differ significantly in polarity, with the planar *trans*-isomer having a negligible dipole moment, in contrast to the twisted and polar cis-isomer.[93] Its UV-visible absorption spectrum, strongly influenced by various substituents, generally displays pronounced π-π* transitions in the UV range and weaker n-π* transitions in visible light.[94,95] The azobenzene photoisomerization

mechanism, though straightforward, remains unclear, with theories suggesting either an inversion or rotational process. The inversion mechanism, triggered by UV light, involves a low-energy n-π* electron transition, leading to the flipping of the bond between the nitrogen and carbon atoms in the aromatic ring via a planar transition state, culminating in isomerization. Conversely, the rotation mechanism under UV light involves a high-energy π-π* electron transition, which partially breaks the nitrogen-nitrogen double bond, temporarily giving it the properties of a single bond. This initiates a rotation through a non-planar transition state to complete the isomerization process (Fig 1.12).[72,96,97]

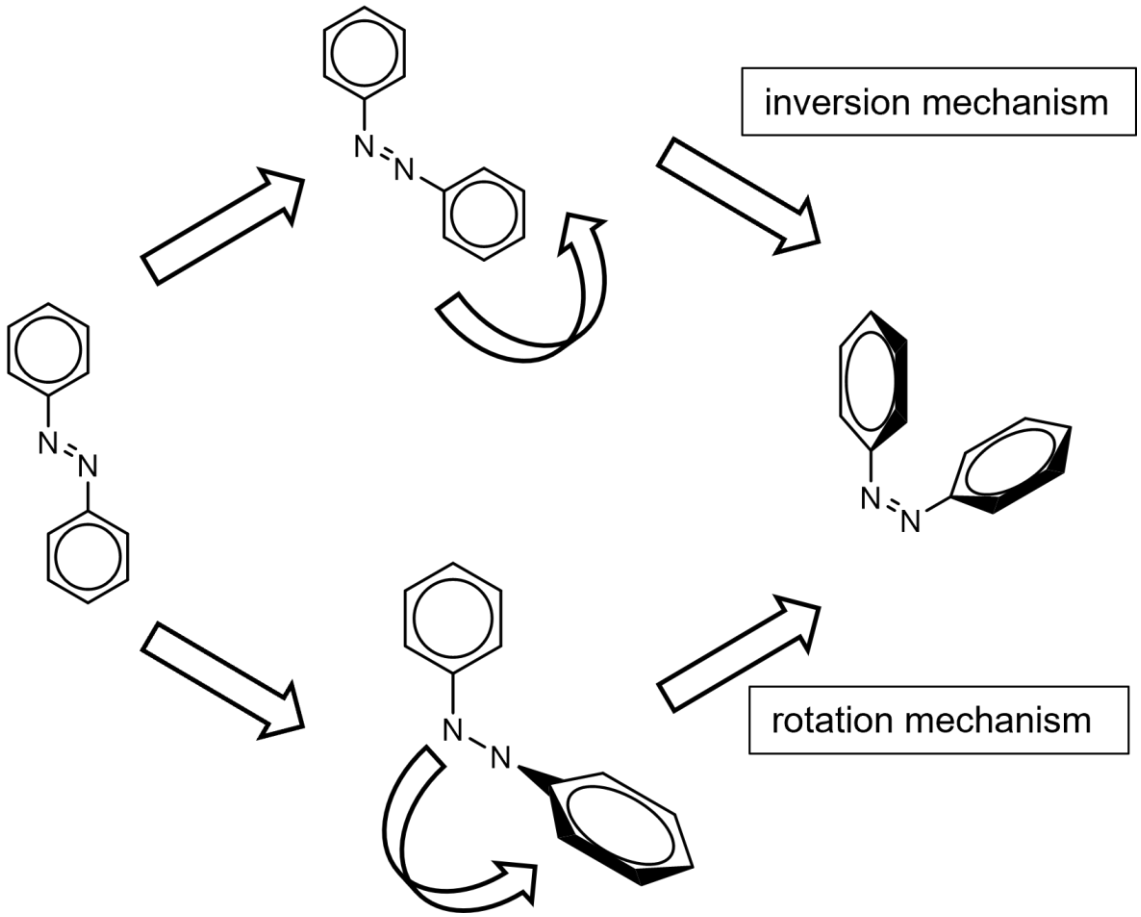


Figure 1.12 Illustration of the mechanism of the photoisomerization process of azobenzene.

Photo-responsive materials featuring azobenzene functional groups have been frequently reported in recent years. For example, azobenzene-based fluorophores have been developed for use in the field of biomedicine, particularly for biological imaging applications.[98] Recently, azobenzene has also been reported as a potential material for energy storage.[99]

### 1.2.3 Stilbene-Based Photoresponsive Molecules

The double bond in stilbene can undergo a *trans*-to-*cis* configurational change under UV

irradiation.[100,101] Derivatives of stilbene, such as stiff-stilbene, have garnered significant interest. For instance, Xu and colleagues designed and synthesized a series of *para*-formylated stiff-stilbenes that function as all-visible-light-driven P-type molecular switches.[102] Figure 1.13 illustrates the photoisomerization process of stilbene. The photoisomerization of stilbene can proceed through two pathways. In the first pathway, one phenyl ring remains fixed in the *trans* configuration, while the C=C-Ph single bond of the other phenyl ring rotates, resulting in the *cis* configuration. In the second pathway, both phenyl rings undergo rotation, but at different rates, ultimately leading to the formation of the cis configuration.[100,103]

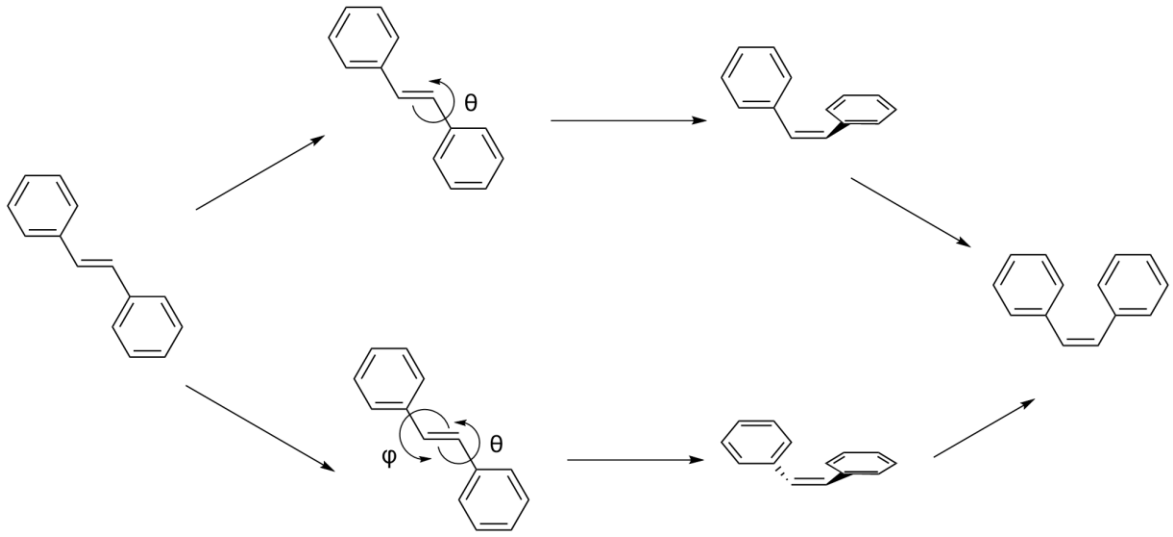


Figure 1.13 Illustration of the mechanism of the photoisomerization process of stilbene.

## 1.2.4 Anthracene-Based Photoresponsive Molecules

When anthracene absorbs UV light, it transitions from its ground state ($S_0$) to an excited singlet state ($S_1$), where an electron moves from the HOMO to the LUMO. In the $S_1$ state, anthracene molecules become highly reactive. When two excited anthracene molecules approach, their π orbitals overlap, forming a transient exciplex. This exciplex undergoes a [4πs+4πs] cycloaddition reaction, forming a cyclobutane ring and resulting in a dimer.[104,105] Since Fritzsche's discovery in 1866,[106,107] this photodimerization has been leveraged for developing photo-responsive molecules. For instance, Kristi et al. used it for cytocompatible PEG-based hydrogels in mechanobiology,[108] and Xinxing Zhang *et al*. developed photoswitchable and reversible fluorescent eutectogels for encryption and anti-counterfeiting applications.[109]

## 1.3 Room-Temperature Phosphorescence (RTP)

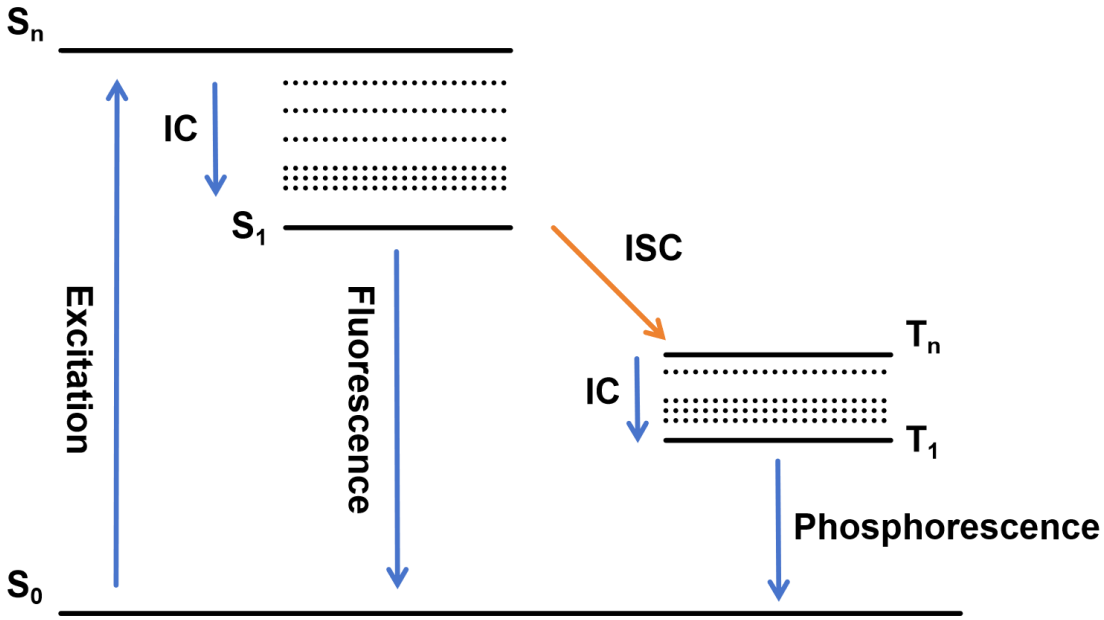


Figure 1.14 Illustration of the luminescence mechanism of phosphorescence.

According to the Pauli Exclusion Principle, electron pairs located in the same orbital will exist with opposite spins. Upon light excitation, a molecule transitions to a higher energy state, this process does not change the electrons' spin direction, maintaining their total spin quantum number at 1, thus forming what is known as a singlet excited state ($S_1$). However, this description is only applicable to idealized, static molecular models. In reality, molecules are constantly moving, and their molecular orbitals' overlap and symmetry adjust with dynamic changes. The activity of electrons within molecules can also generate magnetic fields and magnetic moments, thereby affecting the phase of electron spin, a phenomenon known as spin-orbit coupling. As a result, dynamic molecular motion and spin-orbit coupling can lead to a reversal in the direction of electron spin, at which point the total spin quantum number becomes 3, forming a triplet excited state, denoted as T state. The photons produced by the transition from the T state back to the ground state are called phosphorescence. According to a simplified Jablonski diagram, molecules with phosphorescent properties are excited to $S_1$ through a non-radiative transition via the internal conversion (IC) process; subsequently, a portion of the $S_1$ state excitons decays back to the $S_0$ ground state via fluorescence, while another portion is transformed into triplet state excitons through intersystem crossing (ISC); these triplet state excitons then transition to the $T_1$ state through the IC process without radiation, and finally decay back to the $S_0$ ground state through a radiative transition (Fig 1.14).[110-112]

## 1.3.1 The Key Parameters of Room Temperature Phosphorescence

### 1.3.1.1 Phosphorescence Lifetime

Phosphorescence lifetime, also known as $\tau_P$, describes the average duration a molecule remains in the triplet state before decaying back to the ground state $S_0$.[112] This duration can be calculated using the formula

$$\tau_P = \frac{1}{K_p + K_{nr} + K_q}$$

where $K_p$ and $K_{nr}$ represent the radiative and non-radiative transition rate constants from $T_1$ to $S_0$, respectively, while $K_q$ refers to the rate of triplet exciton quenching due to external factors such as oxygen, water, and temperature changes.[26,112] By fitting the time-resolved emission spectrum

$$I(t) = \sum_i A_i e^{-\frac{1}{\tau_i}}$$

with a multi-exponential decay function, this duration can be simulated, where $\tau_i$ represents the duration of each luminescent component, and $A_i$ is their relative proportion.

### 1.3.1.2 Phosphorescence Quantum Yield

Phosphorescence efficiency, $\Phi_P$, is defined as the ratio of phosphorescence-emitting excitons to absorbed excitons during the triplet-to-ground state transition.[17,112] Since room-temperature phosphorescence mainly originates from the internal conversion (ISC) process, $\Phi_P$ is directly proportional to $\Phi_{ISC}$, expressed as

$$\Phi_P = \Phi_{ISC} \frac{1}{K_p + K_{nr} + K_q} = \Phi_{ISC} k_p \tau_P.$$

In experimental operations, considering that most room-temperature phosphorescent molecules possess dual emission characteristics of fluorescence and phosphorescence, measuring $\Phi_P$ directly can be challenging, as only a portion of the photons contribute to phosphorescence. Thus, a method of fitting the steady-state spectrum into fluorescence and phosphorescence components to determine the phosphorescence to total luminescence ratio ($\eta_P$) and thereby calculate $\Phi_P$ value, is adopted, realized through the formula

$$\Phi_P = K_p \eta_p.$$

#### 1.3.1.3 Afterglow Duration

Afterglow duration is a key indicator for measuring room-temperature phosphorescence (RTP) systems with ultra-long lifetimes (exceeding 100 milliseconds).[113,114] This time period is defined as the duration required for the luminescence intensity of a sample, after being excited by a 1000±5% lx light source, to decrease to the lowest brightness recognizable by the naked eye (0.32 mcd/$m^2$), similar to the persistence of afterglow in inorganic RTP materials.

### 1.3.2 Strategies for Designing Molecules with Room Temperature Phosphorescence Characteristics

Based on the aforementioned discussion, facilitating the ISC process is essential for achieving RTP. This prerequisite underscores the importance of managing the ISC effectively to enable phosphorescent phenomena at ambient temperatures.[112,115] The ISC process, as an intrinsic property of molecules, is primarily influenced by the energy level difference ($\Delta_{EST}$) between singlet and triplet states, as well as their respective electronic configurations. According to the energy gap law, a smaller $\Delta_{EST}$ is particularly important for the ISC process. Therefore, when designing molecules with room-temperature phosphorescence characteristics, the main considerations include: firstly, enhancing the spin-flipping capability of excitons from the lowest excited singlet state $S_1$ to the excited triplet state $T_n$, that is, increasing the intersystem crossing (ISC) rate ($K_{ISC}$); secondly, minimizing the non-radiative transitions and quenching processes of triplet excitons, thereby reducing the non-radiative transition rate ($K_{nr}$) and quenching rate ($K_q$) (Fig 1.15). The introduction of heavy atoms (such as chlorine, bromine, iodine) or heteroatoms (such as nitrogen, oxygen, sulfur) can effectively enhance the spin-orbit coupling of organic phosphorescent molecules, thereby significantly improving the efficiency of ISC and promoting the formation of triplet excitons.[116,117] Moreover, crystalline materials can effectively inhibit the non-radiative relaxation of triplet excitons by restricting molecular motion and isolating water and oxygen from the environment, thus improving phosphorescence efficiency. Therefore, employing strategies such as crystal engineering,[118,119] host-guest doping,[120,121] polymerization,[113,122] and supramolecular self-assembly[123,124] to construct a rigid environment that not only restricts molecular motion but also isolates oxygen, is an effective means to enhance phosphorescence efficiency.

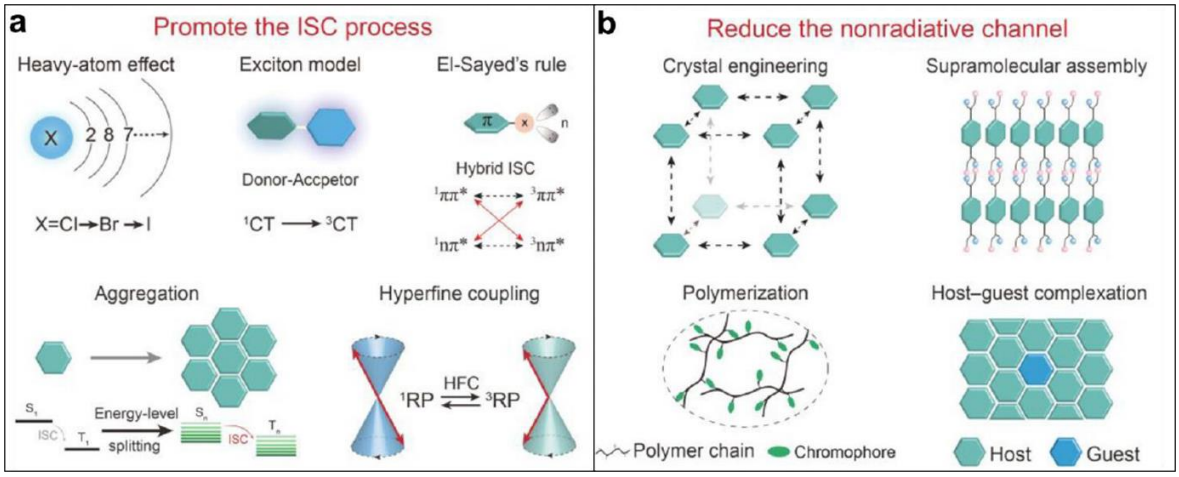


Figure 1.15 Demonstration of strategies to achieve room-temperature phosphorescence.

## 1.4 Substituted Maleimide Derivatives Fluorophores

Maleimide derivatives were initially and primarily used as bismaleimide resins. As a class of resin derived from the polyimide resin system, bismaleimide resin is a bifunctional compound with maleimide as the active end group. This resin shares similar plasticity and flow properties with epoxy resin but overcomes its disadvantage of low heat resistance, leading to its widespread application and rapid development.[125,126] Due to its outstanding heat resistance, wave transmission ability, flame retardancy, radiation resistance, and electrical insulation properties, bismaleimide resin is extensively applied in electronics, aviation, and machinery. It is used as a high-temperature insulating material in composite materials, as a resin matrix in advanced composites, and also as an adhesive.[125]

Maleimide derivatives are an important class of unsaturated cyclic amines and dienophiles. The strong electron-withdrawing nature of its double bond greatly reduces the energy of the lowest unoccupied molecular orbital, allowing for low-lying n-π* transitions that provide a non-radiative pathway for the decay of the excited state. This significantly reduces the emission of fluorescent groups. Therefore, unsubstituted maleimide has been widely reported as an effective fluorescence quencher through direct binding with fluorescent groups.[127]

The structurally rigid and inherently electron-deficient heterocyclic framework of substituted maleimides, characterized by three distinct modifiable positions, permits the strategic introduction of diverse substituents to fulfil specific macroscopic performance criteria. More precisely, the systematic incorporation of functional groups at the C3 and C4 positions of the maleimide core (Figure 1.16) enables precise modulation of both optical bandgap parameters and electron cloud distribution density. This site-specific functionalization strategy facilitates

controlled emission wavelength tuning across the visible spectrum, thereby achieving a comprehensive range of luminescent outputs spanning blue, green, yellow, orange, and red spectral regions.

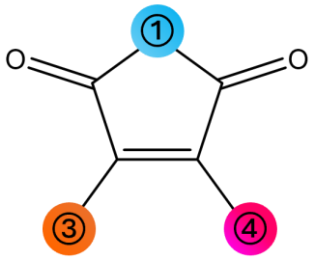


Figure 1.16 The structure of the maleimide derivatives.

The substituted maleimide chromophores, characterized by their small molecular weight, custom synthesis according to specific needs, and sensitivity to the microenvironment, have increasingly drawn the attention of numerous researchers. In 2003, Hsiu-Chih Yeh pioneered the synthesis of symmetrical 3,4-diaryl-substituted fluorescent maleimides using commercial aryl-substituted acetonitrile derivatives.[128] These maleimides stood out for their broad emission spectra, covering the entire visible range, marking a significant stride in fluorescence studies (Fig 1.17a). Fast forward to 2017, Hiroaki Imoto developed a straightforward approach to create 3,4-Diaminomaleimide dyes. [129] These dyes were remarkable for their red-shifted emission and enhanced efficiency in the solid state compared to the solution state, a notable advancement in the realm of luminescent dyes. This development furthered the practical use of organic dyes in diverse areas, including smart materials (Fig 1.17d). Our group has also been at the forefront of synthesizing various substituted maleimide fluorophores. For instance, in 2013, we introduced dithiomaleimides (DTMs), an innovative category of fluorescent molecules by addition-elimination reaction of halogenated maleimides with thiols.[130] These DTMs are known for their intense emission in different solvents and flexible functional thiol groups, which enables them to act both as conjugation sites and fluorescent labels. This dual feature is particularly valuable in biochemical applications such as PEGylation and fluorescent labelling of disulfide-containing proteins, without altering their molecular structure (Fig 1.17c). In 2015, our team achieved another milestone by developing aminomaleimide fluorophores.[131] These are distinguished by their large Stokes shifts and high quantum yields, resulting in robust emission. Intriguingly, these fluorophores exhibit varying emission characteristics in different solvent environments, including shifts in wavelength and intensity variations, making them versatile for various fluorescent probing applications (Fig 1.17b). Furthermore, we have

conducted systematic research in designing and synthesizing substituted maleimide dyes with adjustable fluorescence and solvafluorochromism (Fig 1.17e).[132] This study delves into the correlation between substitution patterns and the optical properties of these dyes, thereby deepening our understanding of their fluorescent behaviour. Such advancements hold immense potential for applications in biological labels, probes, and photoactive materials, paving the way for innovative uses in the field of fluorescence.[133]

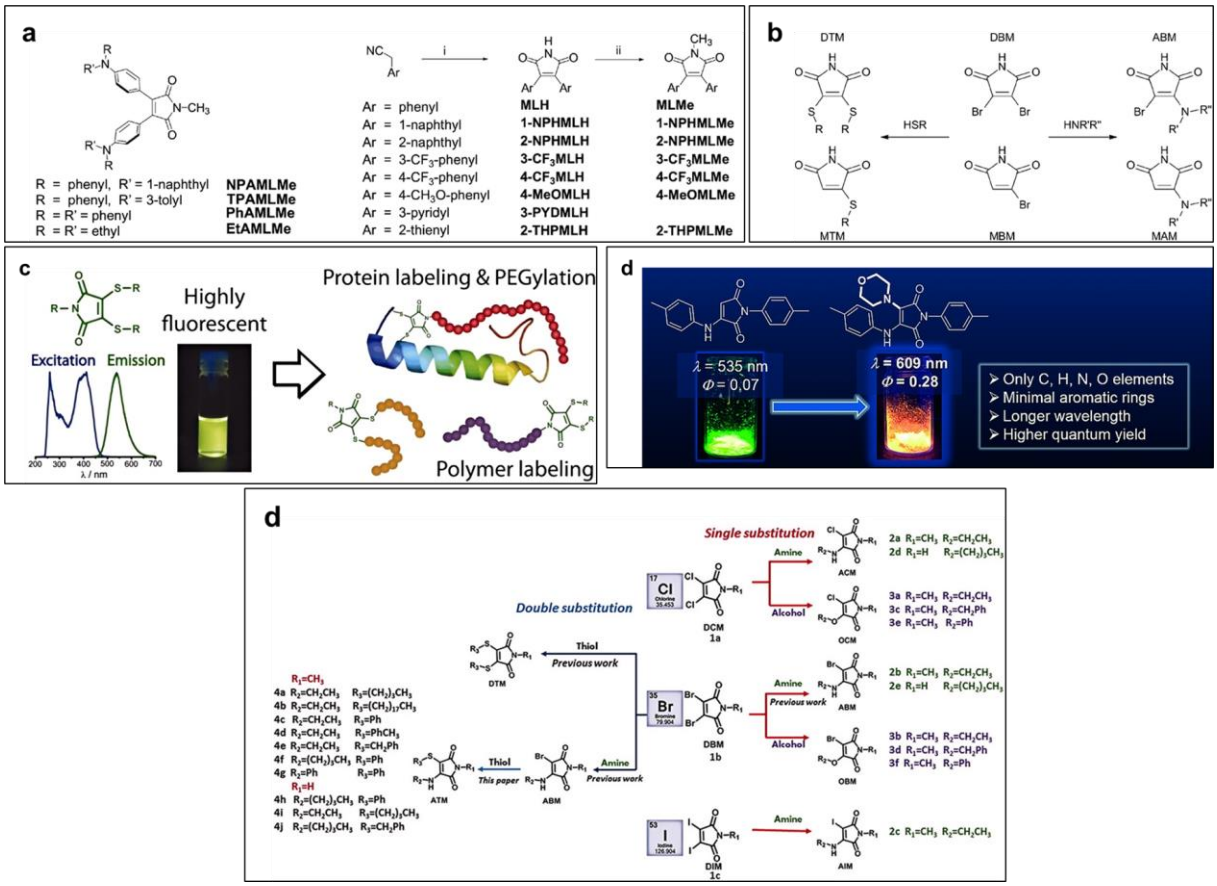


Figure 1.17 (a) Synthetic route and chemical structures.[128] (b) Synthetic route and chemical structures.[131] (c) chemical structure, excitation and emission spectra, and labelling.[130] (d) chemical structure and emission pictures in the solid state.[129] (e) synthetic route and each chemical structure synthesized in this literature.[132]

## 1.4.1 The Luminescence Mechanism of the Substituted Maleimide Fluorophore

Photo-induced electron transfer (PET) is an electron transfer process that occurs under light stimulation, involving the transition of electrons from one atom or molecule to another.[134,135] Depending on the target of electron transfer, this process can be divided into two types: intramolecular and intermolecular charge transfer.[136,137] In 1962, Lipper first reported an

unconventional fluorescence phenomenon based on 4-(dimethylamino)benzonitrile (DMABN), attributed to intramolecular charge transfer. [138,139] In solution, DMABN exhibits two types of excited states: a conventional molecular form and a polarized ionic form, each displaying distinct fluorescence peaks. Based on these observations, scientists have proposed various models, such as Twisted Intramolecular Charge Transfer (TICT), Planar Intramolecular Charge Transfer (PICT), and models involving the rehybridization of electron donors and acceptors (WICT and RICT), to explain these fluorescence phenomena.[140-144] Experimental and theoretical studies have shown that intramolecular charge transfer involves two fundamental components: the electron donor (D) and the electron acceptor (A). In this charger transfer state, the electron donor typically occupies the Highest Occupied Molecular Orbital (HOMO), while the electron acceptor resides in the Lowest Unoccupied Molecular Orbital (LUMO). Under light stimulation, electrons from the donor are first excited, transitioning from the HOMO to the LUMO, facilitating the transfer of electrons from the donor to the acceptor, thus forming the ICT state and leading to a redistribution of charge and electrostatic potential.[145]

TICT serves as one of the fundamental models to elucidate the intricacies of the ICT phenomenon. This model features an electron donor (D) and an electron acceptor (A) connected via a single bond, enabling their segments to rotate freely. When the molecule is photoexcited, it transitions into a charge transfer excited state, wherein electrostatic forces induce a 90° orthogonal twist in the configuration between D and A. This TICT state, characterized by a higher degree of charge separation, exhibits enhanced stability compared to the standard ICT state. The resulting 90° rotation between the donor and acceptor disrupts the HOMO-LUMO orbital alignment, causing electron decoupling and consequent fluorescence quenching, thus introducing TICT as an alternative non-radiative decay channel (Fig 1.18).[140,142]


Figure 1.18 Illustration of the TICT process.

In terms of classification, TICT compounds fall into two primary categories. The first, non-conjugated configuration, involves D and A linked by a single bond. Photoexcitation drives electron transfer from D to A, altering the molecular structure. Nonetheless, the proximity of D and A means electrons rapidly revert to D after excitation, leading to a less stable TICT structure. The second category encompasses conjugated system configurations, where D and A are connected via a π-bridge. This arrangement is advantageous as the π-bridge conjugated

system enhances electron transfer efficiency between D and A. Significantly, photoexcitation in these systems causes a marked change in dipole moments between the excited and ground states, particularly in polar solvents, thereby promoting the stability of the TICT structure.[142,146]

Recent studies on the solvatofluorochromic properties of substituted maleimide derivatives have revealed that these compounds can exhibit bright fluorescence and achieve high quantum yields in low or nonpolar solvents, such as cyclohexane. Conversely, in highly polar solvents, the quantum yield tends to decrease, leading to fluorescence quenching. A pivotal modification involves altering the C=C double bond by attaching electron-rich groups, like aniline. This modification creates a distinctive electronic push-pull structure between the newly attached group and the C=O group on the imide ring. Upon photoexcitation, electronic density shifts from the electron-donor group to the electron-acceptor group, initiating an intramolecular charge transfer (ICT) effect. Additionally, the rotation around the single bond of the modified C=C moiety can induce a twisted intramolecular charge transfer (TICT) effect (Fig 1.19).[132,147]

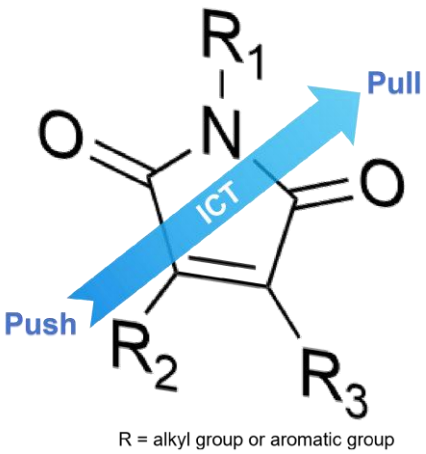


Figure 1.19 Illustration of the luminescent mechanism of maleimide-based fluorophores based on the ICT state.

## 1.4.2 Synthetic Methods of Substituted Maleimide Derivatives

Substituted maleimide derivatives, characterized by their five-member heterocyclic structure, are typically synthesized through a mediated approach involving the ammonolysis of maleic anhydrides. An example of this process is the condensation of glyoxylate esters with acetamides. However, a notable challenge in this method is the limited commercial availability of relevant glyoxylate esters, necessitating additional synthesis steps.[128,148] An alternative and more sophisticated approach has been developed: a one-step method utilizing aryl-substituted

acetonitrile as the starting material. This method offers significant advantages, primarily because aryl-substituted acetonitrile is both commercially available and easily prepared. This streamlined approach simplifies the synthesis process, making it more accessible and efficient for producing substituted maleimide derivatives (Fig 1.20).[149-152]

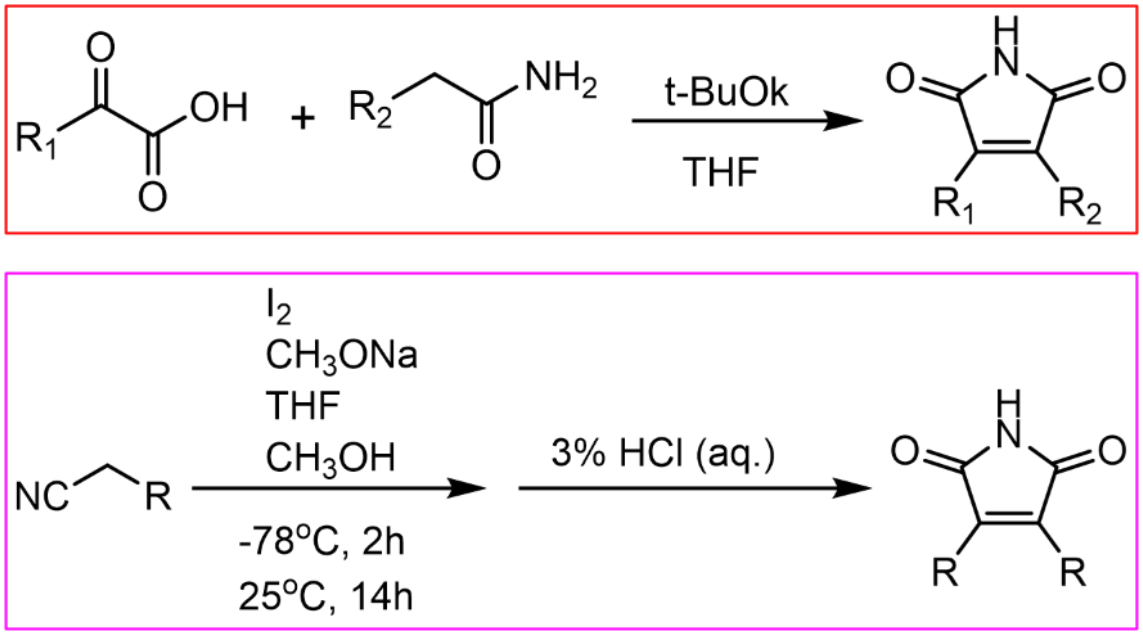


Figure 1.20 Synthetic route of maleimide derivatives.

To synthesize multi-functional substituted maleimide derivatives, a widely used approach is the two-step method. This method typically commences with either bromomaleic anhydride or 2,3-Dichloromaleic anhydride as the starting material. These anhydrides are then reacted with alkylamine or arylamine in an acetic acid medium. Subsequently, through a strategic addition-elimination reaction or Suzuki Coupling, chlorine or bromine atoms are replaced to form the desired substituted maleimide derivatives.[153-155] This two-step method is particularly effective for creating a variety of maleimide fluorophores. By carefully selecting and manipulating the starting materials and reaction conditions, researchers can produce maleimide derivatives with specific functional groups and properties.[156,157] This flexibility and versatility are key to the synthesis of maleimide fluorophores that meet diverse application needs in fields like biochemistry and material science. The method's reliability and efficiency in producing various substituted maleimides underscore its significance in the field of organic synthesis (Fig 1.21).

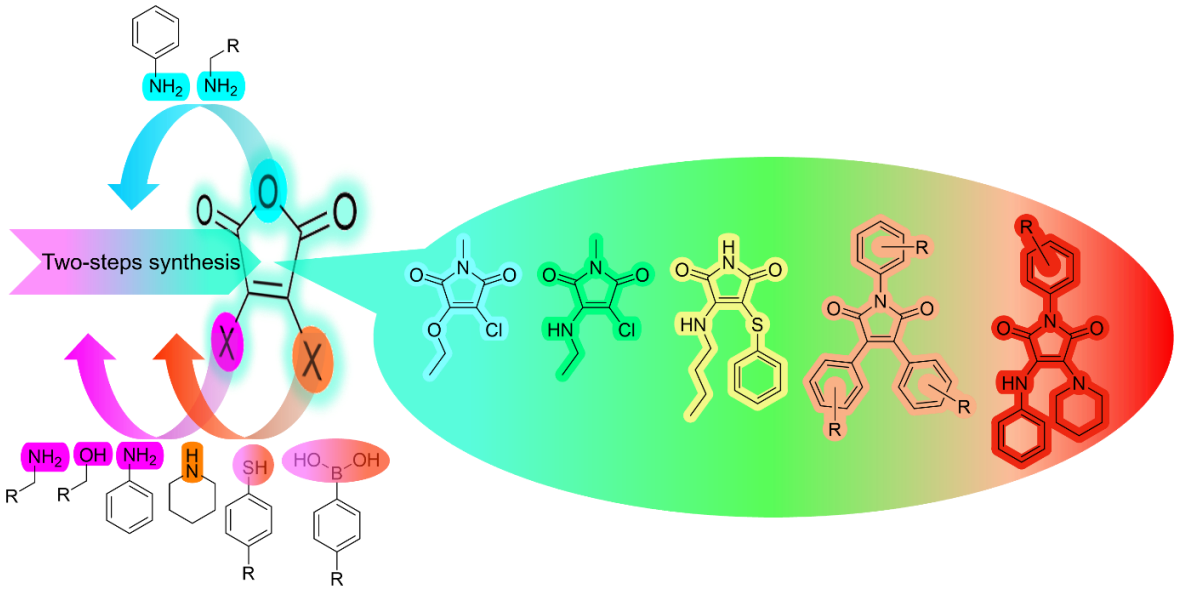


Figure 1.21 Illustration of the synthetic strategies of dual substitution maleimide derivatives.

## 1.5 The Aim of This Thesis

In summary, maleimide derivatives demonstrate multifunctional structural and photophysical advantages in developing novel fluorescent compounds. Structurally: (1) The three modifiable sites on their rigid backbone allow tailored substituent introduction, enabling molecular design flexibility; (2) The intramolecular torsional effect between substituents and the imide ring establishes unique structure-property relationships for dual-state emission systems; (3) Heteroatoms (nitrogen/ oxygen) within the framework significantly enhance ISC efficiency, providing a foundation for RTP materials. Photophysically: (1) Synergistic effects between TICT states and push-pull electronic configurations enable precise dual-emission wavelength modulation; (2) Dynamic coupling between electronic effects and photophysical properties offers controllable regulatory mechanisms for designing stimuli-responsive molecular systems.

Building on these merits, this work systematically engineered three functional material platforms: Chapter 2: design and synthesis of 2, 3-diamine-substituted maleimide derivatives with dual state emission properties; Chapter 3: Photochromic maleimide derivatives exhibiting reversible isomerization-triggered conjugation switching were synthesized, leveraging light-induced structural reconfiguration; Chapter 4: Small molecule-polymer doped RTP systems were constructed by exploiting heteroatom-mediated ISC enhancement, achieving efficient phosphorescence under ambient conditions.

# Chapter 2 Rational Design and Synthesis of Maleimide Fluorophores Exhibiting Dual-State Emission Characteristics

## 2.1 Design philosophy of this work

In the domain of luminescent materials, dual-state emission (DSE), where organic molecules emit brightly in both dilute solution and solid states, has attracted significant attention. Unlike traditional (aggregation caused quench) ACQ materials that are emissive in solution but quenched in the solid state, and AIE materials that emit only upon aggregation, DSE materials combine the merits of both states, enabling versatile applications.[33,46] For instance, in bioimaging, they can overcome the concentration-related issues of single-state emissive molecules, facilitating more accurate cell imaging.[158] The design of DSE molecules involves multiple strategies. Twisted molecular conformations reduce π-π aromatic stacking, contributing to emission in both states. The inclusion of alkyl chains or bulky groups promotes self-isolation of fluorophores, suppressing intermolecular interactions and enhancing emission. Additionally, donor-acceptor (D-A) architectures allow for emission tuning by controlling HOMO and LUMO energy levels.[38,46,159] DSE materials are of great importance and find applications in diverse fields. In optoelectronics, they can serve as colour-converting materials or active layers in OLEDs.[160,161] In bioimaging, they are promising fluorescent probes for cell and tissue staining and disease diagnosis.[162] They also function well in sensors for analyte detection and in data encryption for message deciphering.[163] However, DSE materials face several scientific challenges. Synthetic strategies are still in the early stage, and the quantitative relationship between structural factors and DSE properties remains unclear. Moreover, the number of DSE Luminogens (DSEgens) emitting beyond 700 nm is limited, restricting their use in NIR-related applications. The small range of emission colour change also restricts their application in dynamic bioimaging. Addressing these challenges is essential for the further development and wide-spread use of DSE materials.[33]

Based on the design strategy of DSE molecules and combined with the structural characteristics of maleimide-type derivatives, it is evident that maleimide-type derivatives hold great potential for the design and development of fluorophores with DSE properties. From the structure of maleimide-type derivatives, it can be observed that after substitution at the nitrogen atom and

the double-bond position of the imide ring, rotation around the single bond can effectively prevent non-radiative transition decay caused by molecular planarity and interactions, thereby promoting the emission efficiency of the molecules in the solid state. Moreover, the C=O carbonyl group in the imide ring, acting as a strong hydrogen-bond acceptor, can form intermolecular hydrogen-bond interactions with the C-H within the molecule or an additionally introduced hydrogen-bond donor. This not only enhances the probability of radiative transition of the molecule in the solid state but also effectively suppresses the non-radiative transition decay pathways resulting from the free rotation of the molecule in solution. Additionally, the luminescence mechanism of the electronic push-pull effect of maleimide-type fluorophores well meet the design requirements of DSE molecules. However, despite the promising development prospects of maleimide-type derivatives, reports on this type of derivatives with DSE properties are currently scarce. Tang et al. reported a series of Aminomaleimides. Nevertheless, only 2-butylamino-N-butylmaleimide (2But) and 2-oleylamino-N-oleylmaleimide (2Ol) exhibit high fluorescence emission efficiency in both the monomer and aggregate states, while the remaining molecules display ACQ.[164] Furthermore, Lin et al. reported a series of diphenylmaleimide derivatives that achieve DSE properties by regulating the electronic effects of substituents. The quantum yields of these molecules can reach up to 88.2% in solution and approach 100% in the solid state.[165] However, for the 3,4-diamine-substituted maleimide derivatives reported by Naka et al., they only emit light in the solid state, with the highest quantum yield reaching 28%. In solution, the quantum yields of all molecules are nearly zero.[129] Furthermore, our group has also reported maleimide-type derivatives with various substituents, such as alkylamino substitution and mercapto substitution. However, the fluorophores reported in these studies do not possess DSE properties.[132] Only by introducing trifluoroethyl groups to reduce the electronic cloud density of the imide ring have successfully achieved DSE properties.[166] This indicates that although maleimide-type derivatives have the potential to develop DSE properties, rational molecular design is still required. Based on the speculation derived from the currently reported maleimide-type fluorophores with DSE properties, it is postulated that regulating the electronegativity of the imide ring through the electronegativity of halogens can enhance the luminescence efficiency in both the solvent and solid states. Additionally, intermolecular hydrogen bonds can boost the luminescence efficiency in the solid state by promoting the radiative transition pathway. Furthermore, a certain degree of intramolecular torsion is required to reduce the non-radiative transition decay pathways caused by overly strong intermolecular forces. In light of these understandings, with the aim of further exploring and developing novel maleimide-type fluorophores with DSE

properties, in this work, a series of diamine-substituted maleimide-type derivatives were designed and synthesized. By varying the positions of 4-haloanilines (Cl, Br, I) and 4-butylaniline at the nitrogen atom and the double-bond position of the imide ring, regulating the electronic cloud density and torsion angles, and leveraging interactions such as C=O···N-H intermolecular hydrogen bonds, high quantum yields in both the solid and solvent states have been achieved.

## 2.2 Results and Discussion

### 2.2.1 Synthesis and Characterisation

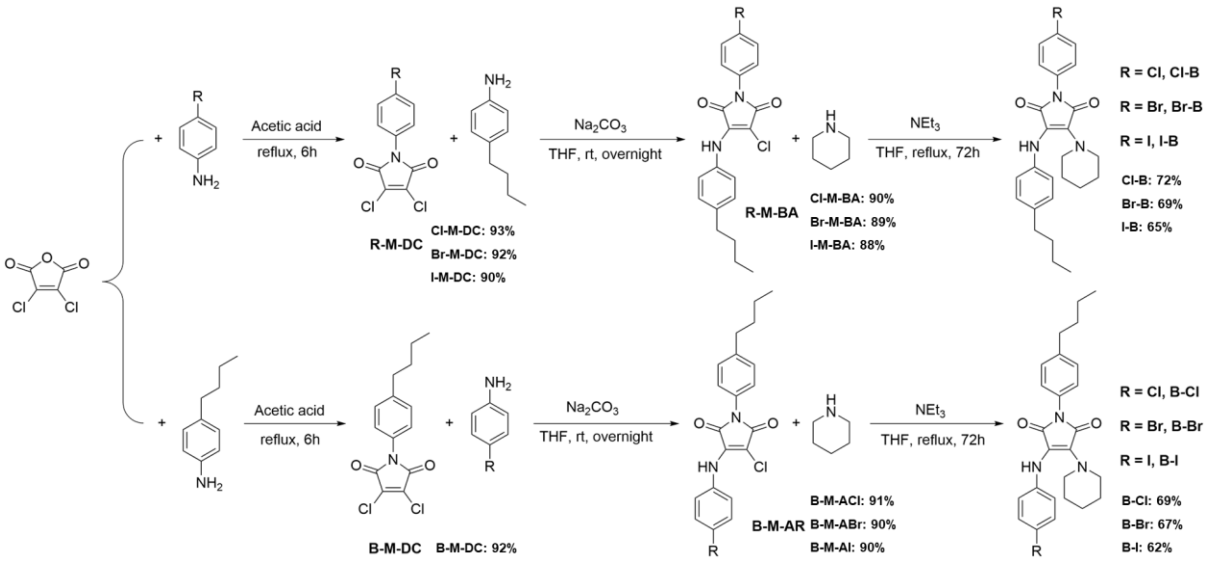


Figure 2.1 The synthetic route of each compound (B-Cl, B-Br, B-I, Cl-B, Br-B, I-B).

All target compounds were successfully prepared via a simple synthesis method (Fig. 2.1). Due to the similarity of the synthetic strategies, the synthesis procedure of B-Cl is taken as an example to illustrate the synthetic process here: Firstly, commercially available dichloromaleic anhydride and 4-butylaniline were refluxed in acetic acid. The first intermediate B-M-DC was obtained through ring-opening dehydration condensation. Subsequently, this intermediate was stirred overnight at room temperature with 4-chloroaniline in tetrahydrofuran (THF) using sodium carbonate as a catalyst. The second intermediate B-M-ACl was obtained via an addition-elimination reaction. Finally, this intermediate was refluxed with piperidine in THF for 3 days using triethylamine as a catalyst. The final product B-Cl was obtained through another addition-elimination reaction. All the obtained compounds were characterized by $^{1}H$ NMR, $^{13}C$ NMR, high-resolution mass spectrometry, and single-crystal X-ray diffraction (supporting information).

## 2.2.2 Investigation of photophysical properties

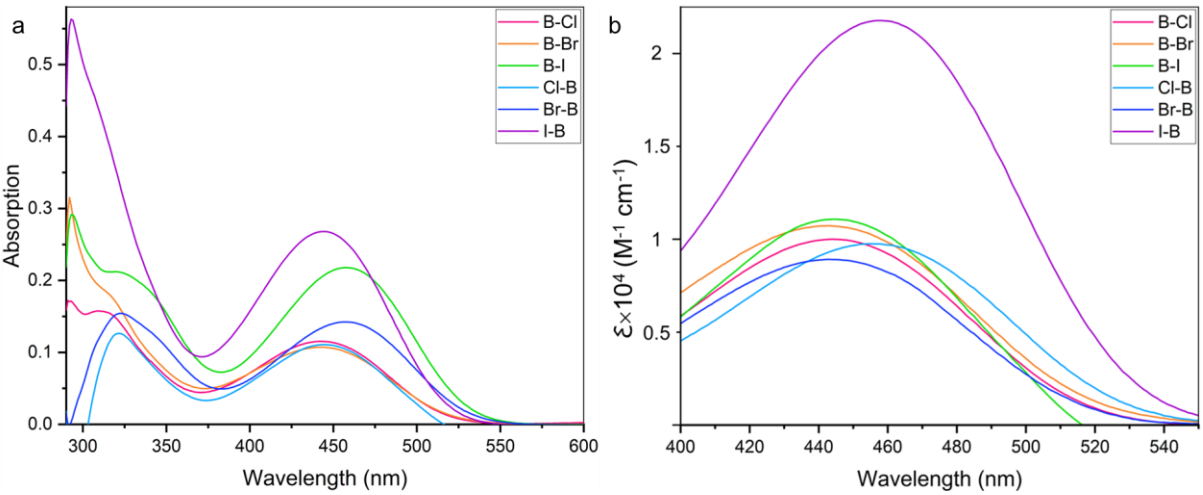


Figure 2.2 (a) UV-vis of each molecule in THF ([c] = 0.01mg/ml); (b) Molar Extinction Coefficient (Ɛ) of each molecule in THF.

First, the absorption spectra of each molecule were measured. Figure 2.2 (a) shows that all molecules exhibit two absorption peaks. One relatively intense peak is located at around 300 nm, followed by a broad peak at approximately 450 nm. The peak at 300 nm can be attributed to the π→π* transition of the benzene ring and the imide ring. The peak at 450 nm is ascribable to the red-shift resulting from the intramolecular charge-transfer (ICT) state formed after substitution at the double bond of the imide ring.[165] As can be observed from Figure 2.2 (a), the intensities of the absorption peaks of different molecules at 450 nm vary, indicating that different molecules are affected differently by the ICT effect. Therefore, to further explore the underlying mechanism, the molar extinction coefficients of each molecule were characterized. Figure 2.2 (b) presents the molar extinction coefficients of all molecules. The molar extinction coefficients of all molecules are around $10^4$, suggesting that all molecules have a relatively good probability of electron transition. Among them, the I-B molecule has the highest molar extinction coefficient value of $2.31\times10^4$ $M^{-1}$ $cm^{-1}$, followed by the B-I molecule, Ɛ is $1.07\times10^4$ $M^{-1}$ $cm^{-1}$. This is consistent with the intensity of the absorption peak at 450 nm in Figure 2.1 (a), while the molar extinction coefficients of the remaining molecules are relatively close. To further investigate the underlying principle, two aspects were considered. Firstly, since all molecules are influenced by the ICT effect, generally, the greater the influence of the ICT effect, the larger the transition dipole moment of the molecule. Furthermore, the ICT process enhances the molecule's ability to absorb light at specific wavelengths, which increases the molar extinction coefficient.[167-169] Thus, combining the results shown in Figure 2.2 (a) that the I-B

molecule exhibits the strongest characteristic absorption of the ICT state at 450 nm and the results shown in Figure 2.2 (b) that this molecule has the largest molar extinction coefficient, it is speculated that the I-B molecule is most significantly affected by the ICT effect.

To further verify this conjecture, theoretical calculations were carried out to compute the oscillator strengths of each molecule in THF. From the formula $f = \frac{2}{3} E_{nm} \cdot |\mu_{nm}|^2$ (where $f$ represents the oscillator strength, $E_{nm}$ denotes the transition energy, and $\mu_{nm}$ represents the dipole moment), it can be seen that the oscillator strength is proportional to the dipole moment. Moreover, from the formula $\varepsilon_{max} \approx \frac{9.78\times10^3 \cdot f}{\Delta\nu_{1/2}}$ ($\varepsilon_{max}$ represents the maximum value of the molar extinction coefficient, and $\Delta\upsilon_{1/2}$ represents the full-width at half-maximum of the absorption peak), substituting the oscillator strength formula into the equation for the maximum molar extinction coefficient, we can obtain $\varepsilon_{max} \propto \frac{E_{nm}\cdot|\mu_{nm}|^2}{\Delta\nu_{1/2}}$, indicating that the molar extinction coefficient is proportional to the dipole moment. Therefore, to explore the photophysical properties in more depth, the oscillator strengths and dipole moments of each molecule in the first excited state ($S_1$) were calculated. Firstly, each molecule was optimized using the density-functional theory (DFT) with the cam-B3LYP functional and the 6-31G*(d, p) basis set. Subsequently, the oscillator strengths and dipole moments at $S_1$ were calculated using Multiwfn.[170-172]

Table 2.1 The oscillator strengths ($f$) and dipole moment at $S_1$ of each molecule.

| Molecule | oscillator strengths | dipole moment |
|---|---|---|
| B-Cl | 0.1271 | 12.1D |
| B-Br | 0.1284 | 11.5D |
| B-I | 0.1357 | 14.3D |
| Cl-B | 0.1255 | 13.2D |
| Br-B | 0.1249 | 12.7D |
| I-B | 0.1513 | 15.7D |

Table 2.1 presents the oscillator strengths and transition dipole moments of various molecules. Among them, the I-B molecule exhibits the largest oscillator strength, indicating that this molecule has the highest probability of electron transition and the strongest light-absorption ability. In addition, the B-I molecule ranks second in both oscillator strength and transition

dipole moment values, while the numerical differences among other molecules are relatively small. This result is consistent with that shown by the molar extinction coefficients in Figure 2.1 (b). Furthermore, the I-B molecule possesses the largest transition dipole moment, which is 15.7 D, followed by B-I molecule ranks second with a value of 14.3 D, the values of the remaining molecules are relatively close, approximately in the range of 11 to 13. From the perspective of molecular structure analysis, it is hypothesized that the I-B and B-I molecules possess a high degree of molecular planarity. Meanwhile, the through-space conjugation effect involving iodine atoms enhances the overall conjugation degree of the molecules, thereby increasing the transition dipole moment.[173-175]

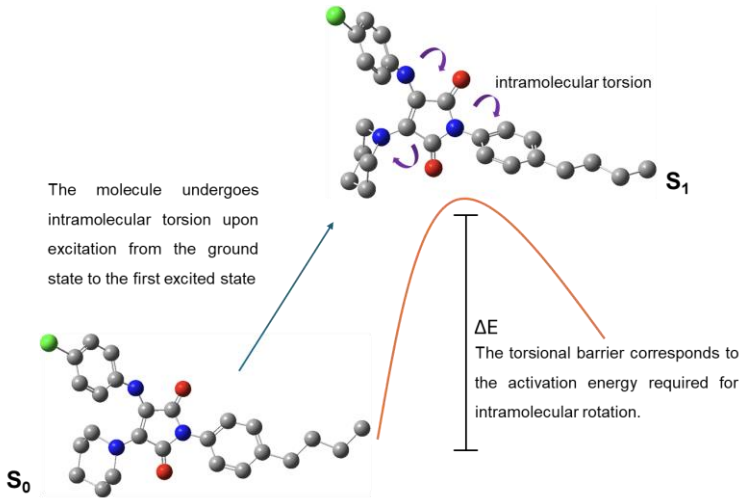


Figure 2.3 Illustration of the calculation of the twisted potential energy in the excited state.

Regarding the speculation of this result, it is likely that when 4-iodoaniline is connected to the N atom of the imide ring, the through-space conjugation effect formed between the lone electron pair of the iodine atom and the imide ring effectively enhances the ICT state. Consequently, this increases the intramolecular transition dipole moment, leading to an enhancement of the molar extinction coefficient. On the other hand, the planarity of the molecule also affects the molar extinction coefficient. Specifically, the higher the degree of molecular planarity, the greater the degree of conjugation, thereby effectively enhancing the light-absorption ability. For the I-B and B-I molecules, it is possible that due to the heavy-atom effect of the iodine atom, the free-rotation ability of the molecules in THF is restricted. As a result, these molecules exhibit better planarity. In contrast, the remaining molecules have a greater free-rotation ability in the solution, thus resulting in a decrease in intramolecular planarity. To verify this conjecture, the free-rotation potential energies of all molecules in THF

were calculated through theoretical calculations. Taking the B-Cl molecule shown in Figure 2.3 as an example, the calculation process is as follows: In DFT, using the same functional and basis set as mentioned above, the ground-state molecule of B-Cl in THF solution (with the solvent effect corrected by the polarized continuum model (PCM)) was optimized. Subsequently, the torsional potential energy difference of the molecule from the ground state ($S_0$) to the first excited state ($S_1$) was calculated through a dynamic potential energy surface scan by TD-DFT at the same level. Generally, the larger the torsional potential energy difference, the more difficult it is for the molecule to undergo torsion, which means it is more conducive to maintaining planarity.

Table 2.2 Potential energy surface (PES) difference of each molecule

| Name | PES difference ΔE (kJ/mol) |
|---|---|
| B-Cl | 107.31 |
| B-Br | 109.79 |
| B-I | 142.58 |
| Cl-B | 112.17 |
| Br-B | 114.83 |
| I-B | 188.74 |

Table 2.2 presents the torsional potential energy (ΔE) of each molecule during the transition from the ground state to the first excited state. Among them, the I-B molecule has the largest ΔE value, indicating that upon photo-excitation, the degree of intramolecular torsion of this molecule is minimal. The B-I molecule follows, while the ΔE values of the remaining molecules are relatively close. This computational result validates the above-mentioned conjecture. Due to their relatively large torsional potential energies, the I-B and B-I molecules appear to exhibit a higher degree of planarity.

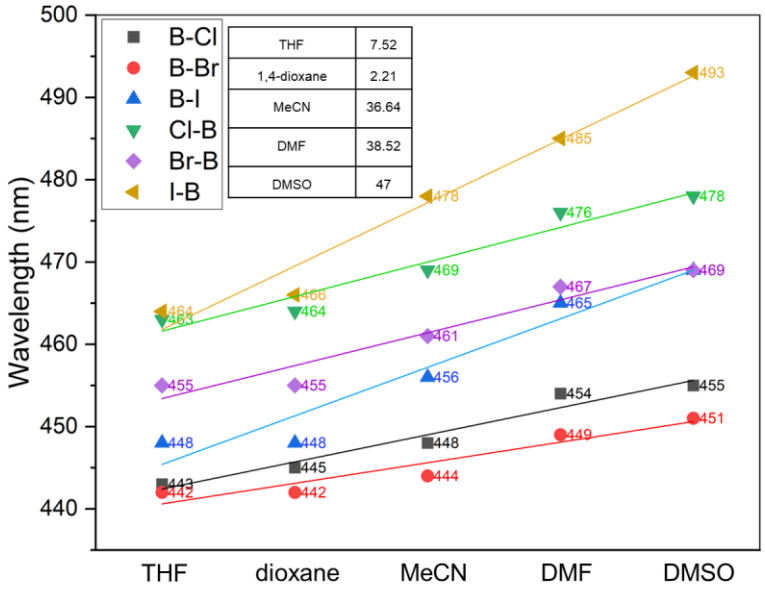


Figure 2.4 The maximum excitation wavelengths of each molecule in different solvents. The table in the lower-right corner of the figure presents the dielectric constants of various solvents to indicate the magnitude of solvent polarity. The dielectric constants are provided by the "*CRC Handbook of Chemistry and Physics*".[176]

Considering that the polarity differences among different solvents can influence the electronic cloud distribution and energy-level differences of molecules upon photoexcitation, to further explore the photophysical properties of each molecule, the excitation wavelengths of various molecules in solvents with different polarities were determined.[177-179] Figure 2.4 shows the maximum excitation wavelengths ($\lambda_{EX}$) of each molecule in THF, dioxane, acetonitrile, N, N-dimethylformamide (DMF), and dimethyl sulfoxide (DMSO), respectively. The $\lambda_{EX}$ of all molecules exhibits a correlation with the solvent polarity. Specifically, as the solvent polarity increases, $\lambda_{EX}$ gradually undergoes a red shift. Generally, the solvent polarity stabilizes the energies of the ground state and the excited state, and the greater the solvent polarity, the more the ground-state energy decreases, thereby causing the excitation wavelength to red shift. As shown in Figure 2.4, the $\lambda_{EX}$ of I-B is most significantly affected by the solvent polarity. Its $\lambda_{EX}$ in THF is 464 nm, and in DMSO, it is red shifted by 29 nm compared to that in THF. According to the above discussion, due to the high planarity and conjugation degree of I-B, it has the strongest interaction with solvent molecules, resulting in the greatest decrease in the ground-state energy level. In addition, the magnitude of the red-shift for B-I molecule is the second most significant, with its $\lambda_{EX}$ exhibiting a 21 nm redshift in DMSO relative to THF. The red shift ranges of the remaining molecules are all approximately around 15 nm. Furthermore, it is noted that the Cl-B molecule exhibits the second-largest $\lambda_{EX}$ across all solvents. It is

speculated that this may be because the chlorine atom has the highest electronegativity, making the Cl-B molecule possess the strongest electron-withdrawing group. Consequently, this molecule has the most pronounced donor-acceptor system or the maximum electronic push-pull ability. Thus, the $\lambda_{EX}$ of this molecule is significantly affected by the ICT effect. Moreover, the $\lambda_{EX}$ of the B-Br molecule is the lowest in all solvents, and its red-shift degree is also the lowest. Specifically, the $\lambda_{EX}$ in DMSO is only red shifted by 9 nm compared to that in THF, indicating that this molecule is least affected by the ICT effect. It is hypothesized that this result may be due to the relatively low electronegativity of the bromine atom, which endows the B-Br molecule with the weakest intramolecular electronic push-pull ability. Furthermore, when considering that the B-Br molecule in Table 2.1 has the smallest transition dipole moment, it can be inferred that this molecule is the least affected by solvent polarity. As a result, it exhibits the smallest degree of redshift.

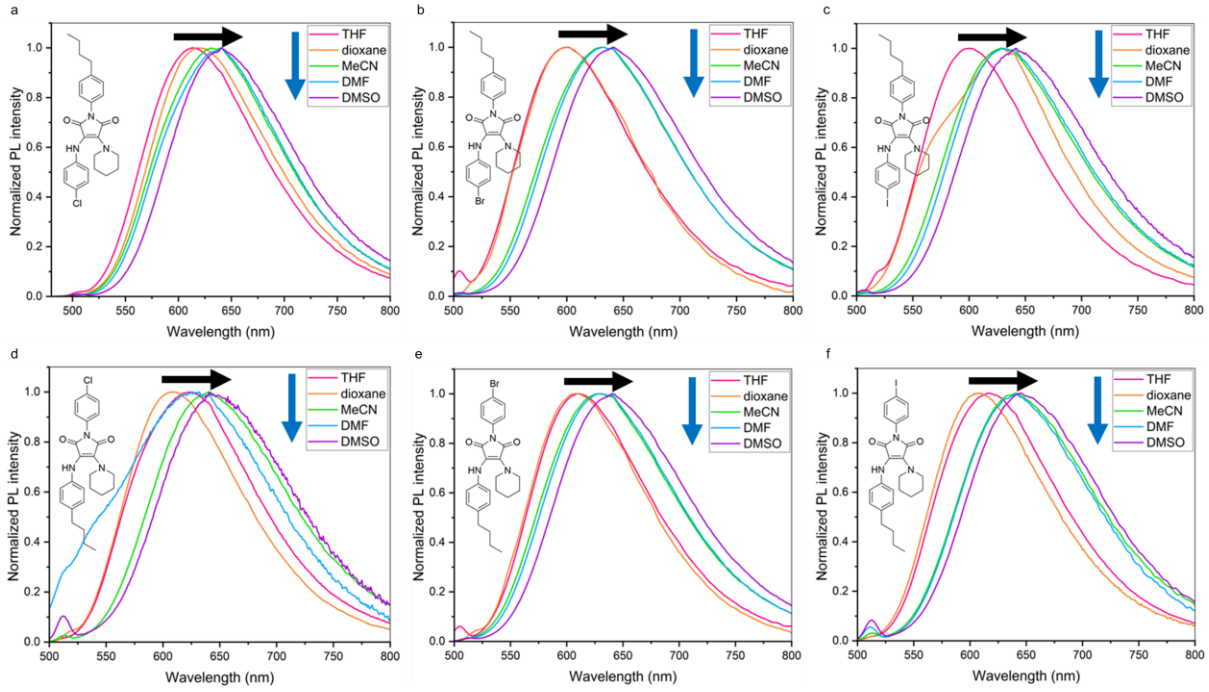


Figure 2.5 Fluorescent (FL) spectra of each molecule in the different solvents (a: B-Cl; b: B-Br; c: B-I; d: Cl-B; e: Br-B; f: I-B); the black arrow indicates the red shift of emission wavelength; the blue arrow indicates the increase of the polarity of the solvent. All FL spectra were recorded at 1 μg/ml, Ex = 450nm.

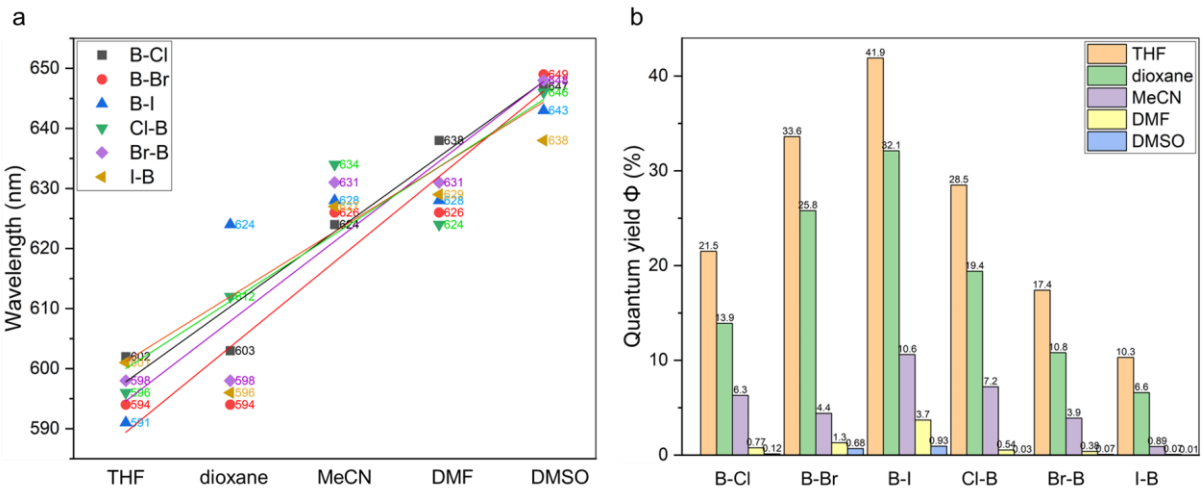


Figure 2.6 (a) the summary of the maximum emission wavelength ($\lambda_{em}$) of each molecule in different solvents; (b) the quantum yield ($\Phi_{solvent}$ (%)) of each molecule in different solvents. Rhodamine B in ethanol as the reference ($\lambda_{ex}$ = 495nm, $\Phi$ = 0.89) for measuring the quantum yield in each solvent.[180,181]

The photophysical properties of maleimide-type fluorophores exhibit pronounced solvent polarity dependence. Notably, their emission wavelengths are regulated by the TICT effect upon photoexcitation, typically manifesting redshift phenomena.[132,164] To systematically investigate solvent effects, the emission profiles of each molecule in solvents of varying polarity were characterized. As shown in Figure 2.5, all compounds demonstrate solvent polarity-dependent emission redshift: the emission wavelength ($\lambda_{em}$) progressively shifts bathochromically with increasing solvent polarity. Taking B-Cl as an example, $\lambda_{em}$ measures 602 nm in low-polarity THF, redshifts to 624 nm ($\Delta\lambda$=22 nm) in MeCN, and further to 647 nm (45 nm redshift from THF) in strongly polar DMSO. This observation confirms the significant regulatory role of the TICT effect on excited states: enhanced solvent polarity promotes molecular twisting, increasing the dipole moment to stabilize excited states through energy level reduction, thereby inducing redshift. Remarkable differentiation in TICT response was observed among halogenated derivatives. Figure 2.6 (a) reveals in THF the $\lambda_{em}$ values follow Cl>Br>I trend (602, 594, 591 nm for B-Cl, B-Br, B-I respectively). This blue-shift sequence may originate from chlorine's higher electronegativity: when strong electron-withdrawing groups occupy the double-bond position of the imide ring, charge separation in the excited state is suppressed, reducing energy gap and consequent redshift with the increase in the electronegativity of halogen atoms. Solvent polarity impacts derivatives differently: Cl-B shows maximum redshift in MeCN ($\Delta\lambda$=38 nm, $\lambda_{em}$=634 nm), whereas B-Cl exhibits minimal

shift (Δλ=12 nm). In DMSO, B-Br demonstrates maximum redshift (Δλ=55 nm, $\lambda_{em}$=649 nm), while I-B shows the lowest shift (Δλ=37 nm, $\lambda_{em}$=638 nm). From the perspective of the TICT effect, it is indicated that the B-Br molecule is most significantly affected by the TICT effect. That is, when the solvent polarity increases from the low-polarity THF to the high-polarity DMSO, the B-Br molecule experiences the greatest degree of intramolecular torsion in the excited state, while the I-B molecule experiences the least. Additionally, from the aspect of electronic effects, iodine's lower electronegativity at the imide nitrogen attenuates electron-withdrawing capacity, weakening intramolecular charge transfer and solvent effect susceptibility. Fluorescence quantum yield (Φ) analysis in Figure 2.6 (b) reveals halogen position critically modulates emission efficiency. In THF, double-bond-substituted B-I achieves the highest Φ (41.9%), while nitrogen-substituted I-B shows the lowest (17.4%). Notably, double-bond derivatives follow B-I>B-Br>B-Cl Φ order, suggesting enhanced electron-donating effects promote quantum yield by elevating HOMO levels and narrowing energy gaps to favor radiative transitions. Conversely, nitrogen-substituted derivatives exhibit Cl-B>Br-B>I-B trend, where stronger electronic withdrawing capacity suppresses nonradiative pathways. Solvent polarity dramatically reduces Φ values for all compounds. For instance, B-Cl's Φ decreases from 21.5% in THF to 6.3% in MeCN and 0.12% in DMSO, with nitrogen-substituted derivatives being nearly quenched (Φ≈0) in DMSO. This validates TICT formation mechanism: enhanced dipole-dipole interactions in polar solvents facilitate TICT state generation, substantially increasing nonradiative transition probability.

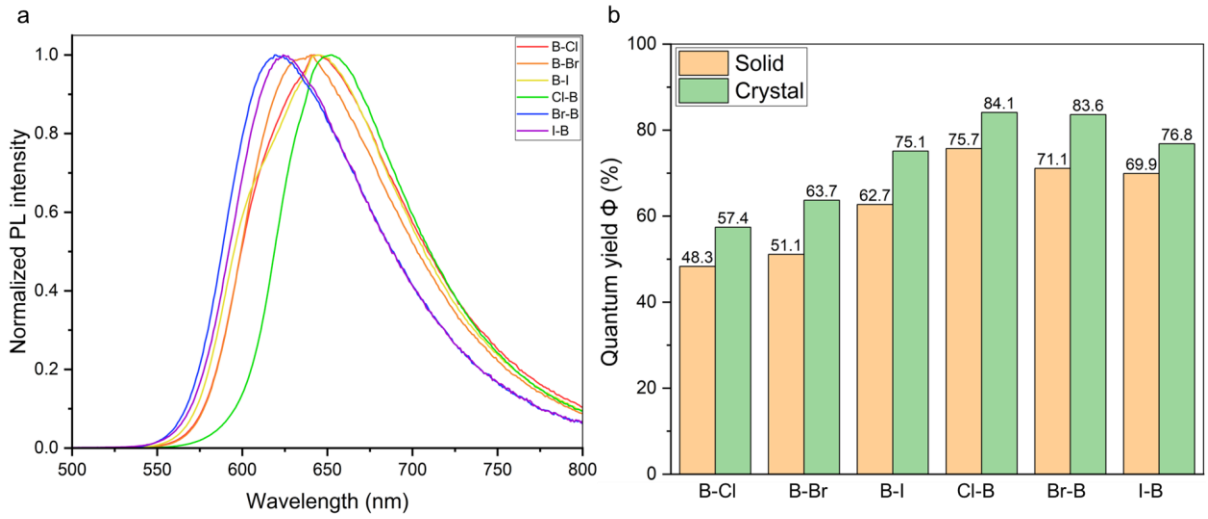


Figure 2.7 (a) FL spectra of each molecule in the solid state; (b) Quantum yield of each molecule in the solid and crystal state. integrating sphere of Edinburgh FLS900 was used to measure the quantum yield in the solid state.

The photoluminescence spectra in solid state and quantum yields (Φ) in both solid and crystal states were systematically characterized for all target molecules. The preparation of solid (or amorphous) samples involves dissolving the pure solid obtained after recrystallization in THF first. Subsequently, the solution is removed by rotary evaporation, and the resulting solid is dried in a vacuum oven at room temperature for 24 hours. For the preparation of crystalline samples, the solid obtained after multiple recrystallizations is used. As shown in Figure 2.7(a), the Cl-B exhibited the longest emission wavelength ($\lambda_{em}$=648 nm) in solid state, whereas B-I, B-Cl, and B-Br displayed blue-shifted emission maxima at 636, 635, and 631 nm with hypsochromic shifts of 12, 13, and 17 nm, respectively. Notably, I-B and Br-B molecules showed significantly blue-shifted emissions at 608 and 602 nm. These spectral variations strongly suggest distinct molecular packing patterns and intermolecular interactions modulated by different halogen substitutions. From theoretical perspective, stronger intermolecular interactions (e.g., π-π stacking or hydrogen bonding) could facilitate tight molecular packing to suppress non-radiative decay pathways arising from molecular vibrations, thereby stabilizing excited states and enhancing quantum yields.[12,182,183] The observed bathochromic shift of Cl-B implies its potentially optimized molecular packing density compared to the more disordered arrangements in I-B and Br-B. Figure 2.7 (b) presents comparative quantum yield between solid and crystal states. The Cl-B demonstrated the highest Φ values of 75.7% (solid) and 84.1% (crystal), confirming its superior radiative transition efficiency that correlates with strong intermolecular interactions. Intriguingly, when halogens occupied the imide nitrogen position (Br-B and I-B), substantial Φ values of 71.1% and 69.9% were recorded in solid state, indicating favorable molecular packing geometry. In contrast, halogen substitution at the double-bond position (B-I, B-Br, B-Cl) resulted in significantly reduced Φ values of 62.7%, 51.1%, and 48.3%, respectively, suggesting compromised intermolecular interactions. Remarkably, crystalline states universally enhanced Φ values through tighter molecular packing, taking B-Cl as an example, the Φ in the crystal state is 9.1% higher than that in the solid state. In addition, B-Br showing the largest increment (ΔΦ=12.6%), possibly due to newly formed strong intermolecular interaction that effectively suppressed non-radiative decay. Comparatively, I-B exhibited the smallest Φ improvement (ΔΦ=6.9%).

### 2.2.3 Analysis of single-crystal structures

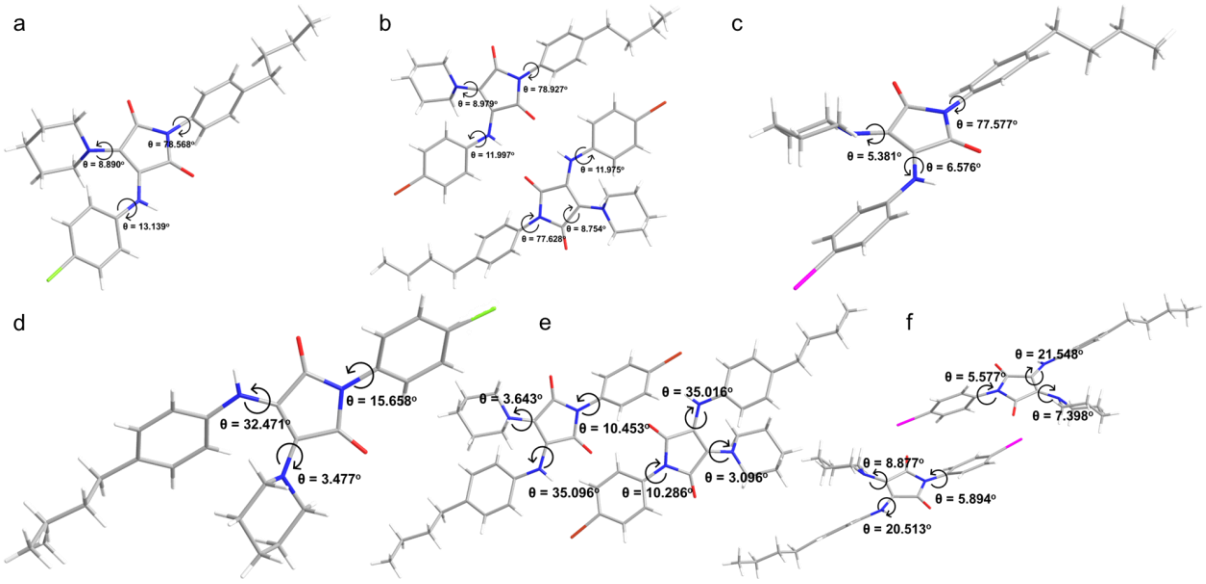


Figure 2.8 Single-crystal structure of each molecule. (a) B-Cl; (b) B-Br; (c) B-I; (d) Cl-B; (e) Br-B; (f) I-B.

The results of the fluorescence spectra and quantum yields of the above-mentioned molecules in the solid and crystalline states indicate that the intermolecular packing modes and intermolecular forces of different molecules in the aggregated state vary, and the position of the substituents also affects the intermolecular packing modes. Therefore, to delve deeper into the luminescence mechanism of the obtained molecules, the single-crystal structures of all molecules were analysed. Through slow evaporation in dichloromethane and n-hexane, the single-crystal structures of all molecules were successfully obtained. Figure 2.8 presents the single-crystal structures of all molecules. Among them, B-Br (b), Br-B (e), and I-B (f) all exhibit two different single-crystal structures with distinct configurations within a unit lattice. This phenomenon is known as polymorphism, where a single compound can have two or more single-crystal structures.[184,185] In addition, as shown in Figure 2.8, the torsion angles of different molecules vary. When the 4-butylphenyl group is connected to the nitrogen atom of the imide ring, there is a relatively large torsion angle between the benzene ring and the imide ring plane. As depicted in Figure 2.8 (a, b, c), the torsion angle in the B-Cl molecule is 77.5°, in the B-Br molecule it is 78.9° and 77.6° respectively, and in the B-I molecule it is 78.5°. Such a large torsion angle indicates a significant degree of distortion in this part. This may be due to the large steric hindrance of the butyl group, resulting in substantial van der Waals repulsive forces. Thus, a large torsion angle is required to reduce the intramolecular energy and achieve

a thermodynamically stable state. Moreover, the electron-donating property of the 4-butyl group increases the electronic cloud density of the benzene ring, leading to significant charge repulsion. Consequently, a large torsion angle is needed to relieve this repulsion and lower the energy. Furthermore, the torsion angles between the piperidinyl group and the halo-aniline group at the double bond of the imide ring and the imide ring are relatively small. The torsion angle between the halo-aniline group and the imide ring is approximately 10°, while that between the piperidinyl group and the imide ring is around 8°. Further, as shown in Figure 2.8 (d, e, f), when the halo-aniline is connected to the nitrogen atom of the imide ring, the torsion angle of this part is small. Specifically, for Cl-B it is 15.6°, for Br-B it is 10.4° and 10.2° respectively, and for I-B it is 5.5° and 5.9° respectively. This indicates that the connection of the halo-aniline to the nitrogen atom of the imide ring is conducive to reducing intramolecular distortion and enhancing the molecular planarity. This may be because the electronegativity of the halogen atom reduces the electronic cloud density of the benzene ring, thereby decreasing the charge repulsion in this part. Additionally, halogen atoms usually participate in intermolecular arrangements through weak interactions such as van der Waals induction forces, which is beneficial for reducing the torsion angle. The larger the radius of the halogen atom, the more pronounced this effect is, resulting in a smaller torsion angle. Moreover, due to the steric hindrance of the butyl group and the charge repulsion of the benzene ring, the torsion angle between the 4 - butylaniline group and the imide ring is relatively large. For Cl-B, it is 32.4°, for Br-B it is 35° and 35° respectively, and for I-B it is 20.5° and 21.5° respectively. In contrast, the torsion angle between the piperidinyl group and the imide ring is small, only around 3-5°. From the perspective of the single-crystal structure, when the halo-aniline is connected to the nitrogen atom of the imide ring, the overall torsion angle of the molecule is small, which improves the overall planarity of the molecule. Therefore, in the loose solid state, Cl-B, Br-B, and I-B molecules are more likely to form tight intermolecular packing, effectively suppressing the non-radiative transition decay pathways caused by intermolecular torsion. This explains why the quantum yields of Cl-B, Br-B, and I-B molecules in the solid state are higher than those of B-Cl, B-Br, and B-I molecules.

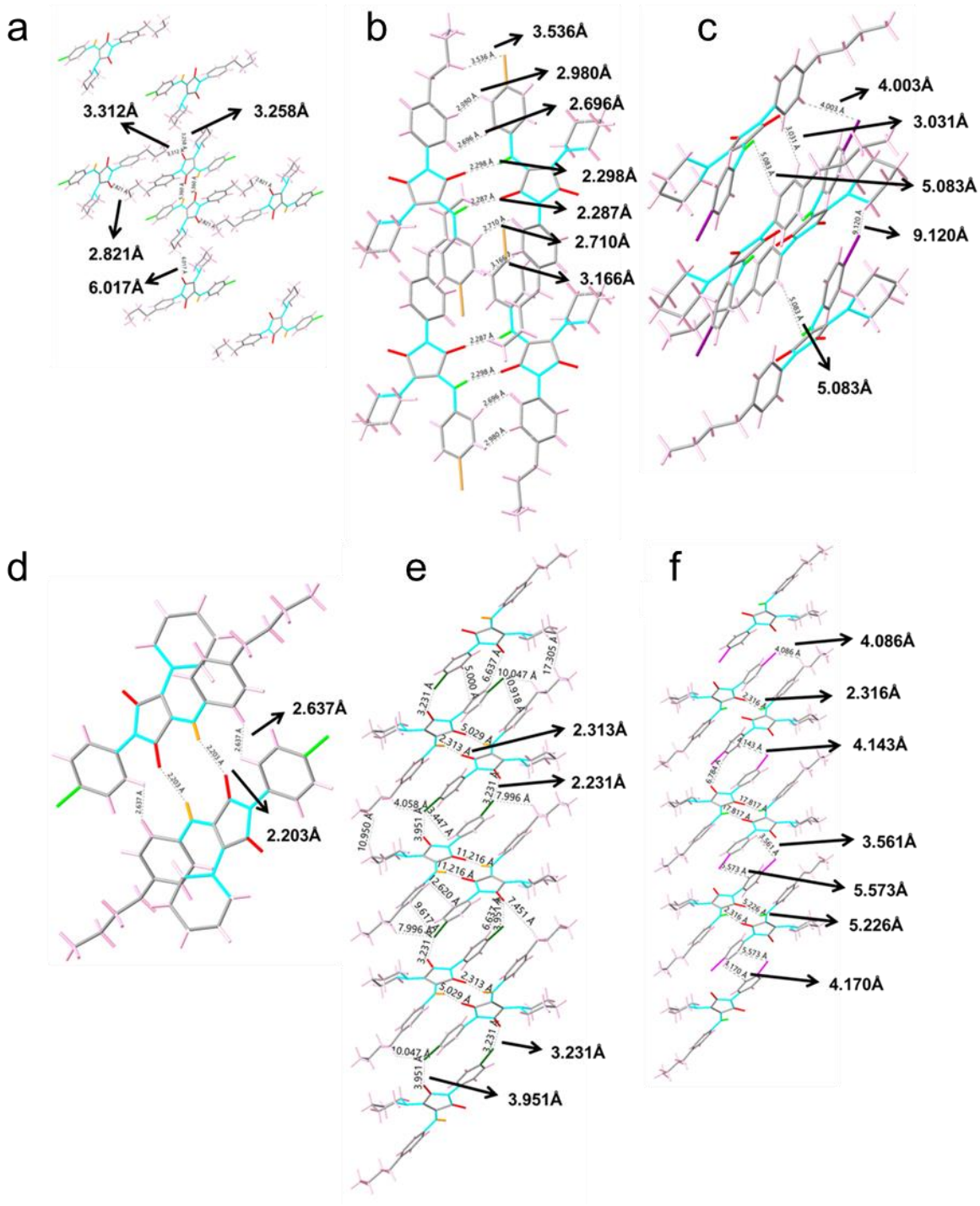


Figure 2.9 Single-crystal packing pattern of each molecule. (a) B-Cl; (b) B-Br; (c) B-I; (d) Cl-B; (e) Br-B; (f) I-B.

The quantum yields of all molecules in the crystalline state are higher than those in the solid state, indicating that as the intermolecular packing becomes gradually closer, intermolecular interactions such as interactions or intermolecular hydrogen bonds emerge. Therefore, to explore the underlying principle, the molecular single-crystal packing pattern of all molecules

were analysed. As shown in Figure 2.9, all molecules are arranged in a head-to-tail arrangement. Such an arrangement is conducive to suppressing molecular vibration and rotation. Simultaneously, it reduces the energy-transfer losses between molecules, thereby enhancing the quantum yield of molecules in the aggregated state.[186,187] In addition, all molecules exhibit varying degrees of weak interactions in the crystalline state. For B-Cl, there are intermolecular hydrogen bonds of C=O···H-C (2.821 Å, 3.312 Å) and C-H···H-C (3.258 Å). In the case of B-Br, there are weak van der Waals forces between halogen and hydrogen atoms of C-Br···H-C (3.536 Å), as well as intermolecular hydrogen bonds of C-H···H-C (2.696 Å, 2.710 Å, 2.980 Å), C=O···H-N (2.298 Å), and C=O···H-C (2.287 Å). For B-I, there is only an extremely weak van der Waals force between halogen and hydrogen atoms of C-I···H-C (4.003 Å), and no other intermolecular forces. Cl-B has intermolecular hydrogen bonds of C-H···H-C (2.637 Å) and C=O···H-C (2.203 Å). Br-B has a strong intermolecular hydrogen bond of C=O···H-N (2.313 Å) and van der Waals induction forces between bromine atoms and carbonyl groups of C=O···Br-C (2.231 Å, 2.951 Å). I-B has a strong intermolecular hydrogen bond of C=O···H - N (2.316 Å) and weak van der Waals forces between iodine atoms and hydrogen atoms of C-I···H-C (3.561 Å). These intermolecular interactions suggest that in the crystalline state, due to the formation of intermolecular hydrogen bonds and weak van der Waals forces, the non-radiative transition decay pathways are suppressed by effectively restricting molecular motion, stabilizing the excited state, and promoting electron delocalization.[188,189] As a result, the quantum yields of molecules in the crystalline state are higher than those in the solid state. In addition, the B-Br molecule forms the largest number of intermolecular interactions in the crystalline state, which also explains why the quantum yield of B-Br increases the most in the crystalline state compared to that in the solid state.

Table 2.3 Molecular orbitals and HOMO–LUMO distributions of each molecule; energy level in the HOMO and LUMO and energy gap in different solvents.

| Name | Distribution of electronic density | | Energy | THF | dioxane | MeCN | DMF | DMSO |
|---|---|---|---|---|---|---|---|---|
| B-Cl | LUMO | 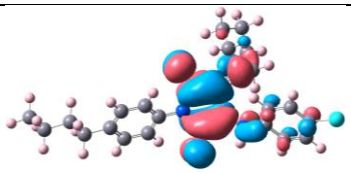 | $E_{LUMO}$ | -2.75 | -2.77 | -2.92 | -3.11 | -3.24 |
| | | | ΔE | 2.60 | 2.58 | 2.48 | 2.33 | 2.25 |
| | HOMO |  | $E_{HOMO}$ | -5.35 | -5.35 | -5.40 | -5.44 | -5.49 |
| B-Br | LUMO | 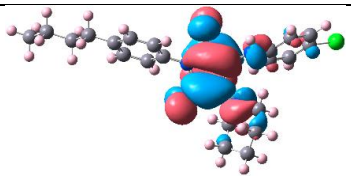 | $E_{LUMO}$ | -2.73 | -2.75 | -2.86 | -3.08 | -3.21 |
| | | | ΔE | 2.58 | 2.55 | 2.46 | 2.32 | 2.23 |
| | HOMO |  | $E_{HOMO}$ | -5.31 | -5.30 | -5.35 | -5.40 | -5.44 |
| B-I | LUMO | 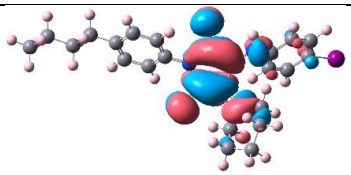 | $E_{LUMO}$ | -2.75 | -2.79 | -2.94 | -3.13 | -3.28 |
| | | | ΔE | 2.55 | 2.52 | 2.45 | 2.30 | 2.20 |
| | HOMO | 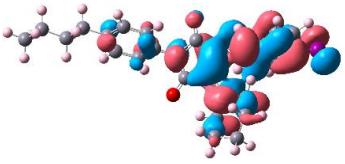 | $E_{HOMO}$ | -5.30 | -5.31 | -5.39 | -5.43 | -5.48 |

| | | | | | | | | |
|---|---|---|---|---|---|---|---|---|
| Cl-B | LUMO | 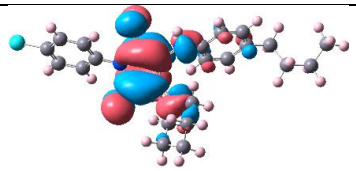 | $E_{LUMO}$ | -2.65 | -2.51 | -2.66 | -2.70 | -2.73 |
| | | | ΔE | 2.63 | 2.61 | 2.55 | 2.48 | 2.41 |
| | HOMO | 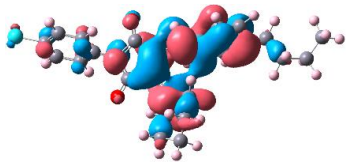 | $E_{HOMO}$ | -5.28 | -5.25 | -5.21 | -5.18 | -5.14 |
| Br-B | LUMO | 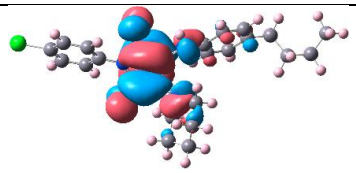 | $E_{LUMO}$ | -2.64 | -2.64 | -2.64 | -2.63 | -2.84 |
| | | | ΔE | 2.66 | 2.64 | 2.60 | 2.55 | 2.51 |
| | HOMO |  | $E_{HOMO}$ | -5.30 | -5.28 | -5.24 | -5.18 | -5.15 |
| I-B | LUMO | 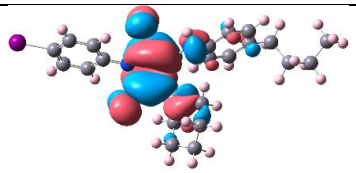 | $E_{LUMO}$ | -2.57 | -2.58 | -2.57 | -2.56 | -2.55 |
| | | | ΔE | 2.68 | 2.64 | 2.61 | 2.56 | 2.52 |
| | HOMO | 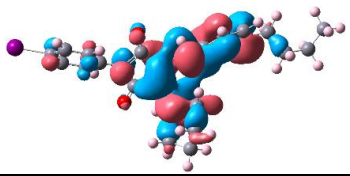 | $E_{HOMO}$ | -5.25 | -5.22 | -5.18 | -5.12 | -5.07 |

To gain a better understanding of the emission mechanism and photophysical properties of the fluorophores, each molecule was optimized by using density functional theory with the cam-B3LYP functional and 6-31G* (d, p) basis set and calculated the frontier molecular orbital energies using time-dependent density functional theory with the same basis set. As indicated by the frontier orbital distributions in Table 2.3, for all molecules, the electronic cloud density in the HOMO state is mainly delocalized over the double bond of the imide ring, the aniline group, and the piperidine ring. This indicates that this part serves as the electronic donating region of the system. Meanwhile, there is also a partial delocalized electronic cloud on the benzene ring connected to the nitrogen atom of the imide ring, suggesting that in the HOMO state, the electronic cloud density is mainly delocalized in the π-orbitals. In the LUMO state, the electronic cloud density is delocalized to the C=O carbonyl group of the imide ring,

indicating that this part is the electronic withdrawing region of the system. This delocalization of the electronic cloud between the HOMO and LUMO implies that the transition mode is a π→π* transition, and an obvious charge-separation phenomenon is presented, indicating the existence of the ICT state. This is also consistent with the above-mentioned characterization of the absorption spectra. In addition, the calculation results of the HOMO and LUMO energy levels in different solvents show that the HOMO energy levels of all molecules decrease as the solvent polarity increases. Taking B-Cl as an example, it is -5.35eV in THF and decreases to -5.49eV in DMSO. This may be due to the electrostatic interaction between the solvent and the molecule, which reduces the electron dipole moment in the HOMO state, thereby stabilizing the HOMO state. This is also consistent with the red shift of the excitation wavelength as the solvent polarity increases as described above. Furthermore, when the 4-butylaniline group is located at the double bond position of the imide ring, serving as the electron-donating moiety, the HOMO energy level is higher than that when it is a 4-haloaniline group. For example, the HOMO energy of the Cl-B molecule is -5.28eV, while that of the B-Cl molecule decreases to -5.35eV. This indicates that the electronic donating property of the 4-butyl group increases the electronic cloud density of the molecule in the HOMO state, thereby raising the HOMO energy. Moreover, the higher the HOMO energy, the easier it is for electrons to undergo transitions, leading to a redshift of the excitation wavelength. As shown in Table 2.3, taking the situation in THF as an example, the HOMO energy levels of the Cl-B, Br-B, and I-B molecules are -5.28eV, -5.30eV, and -5.25eV respectively, which are higher than those of the B-Cl, B-Br, and B-I molecules (-5.35eV, -5.31eV, and -5.30eV respectively). This is consistent with the results in Figure 2.4, that is, the excitation wavelengths of the Cl-B, Br-B, and I-B molecules are longer than those of the B-Cl, B-Br, and B-I molecules. Furthermore, the energy gap between the HOMO and LUMO shows that as the solvent polarity increases, the energy gap gradually decreases. Taking the B-Cl molecule as an example, the energy gap in THF is 2.60 eV, and it decreases to 2.25 eV in DMSO. This indicates that as the solvent polarity increases, the emission wavelength gradually redshifts, which is also in line with the above-mentioned spectral characterization results.

## 2.3 Conclusions

In this work, a series of maleimide-type fluorophores were designed and synthesized. The characterization of the absorption spectra indicated that all molecules possess relatively high molar extinction coefficients. Among them, the I-B molecule exhibits the highest molar extinction coefficient, reaching $2.31\times10^4$ $M^{-1}$ $cm^{-1}$. Additionally, the characterization of the

fluorescence spectra of all molecules revealed that the emission wavelength undergoes a red shift with the increase of solvent polarity due to the TICT effect. Analysis of the quantum yields in solvents demonstrated that all molecules exhibit relatively high quantum yields in THF. The B-I molecule has the highest quantum yield, amounting to 41.9%. Moreover, the position of the substituents was found to influence the quantum yield. Furthermore, the quantum yields of all molecules in the aggregated state were characterized. The results indicated that they all possess high quantum yields in the solid state, and the quantum yields in the crystalline state are higher than those in the solid state. Additionally, the position of the substituents also affects the quantum yield. For instance, the quantum yield of the Cl-B molecule is 75.7%, while that of the B-Cl molecule decreases to 48.3%. The analysis of the single-crystal structures of all molecules suggested that the position of the substituents can affect the quantum yield of molecules through different torsion angles. Moreover, in the crystalline state, the intermolecular interaction enhances the quantum yield. Consequently, this work has successfully achieved the preparation of maleimide-based fluorescent derivatives with dual state emission properties.

## 2.4 Supplementary information

### 2.4.1 Materials

2,3-Dichloromaleic anhydride (97%), 4-butylaniline (97%), 4-chloroaniline (98%), 4-bromoaniline (97%), 4-iodoaniline (98%), Piperidine (99%) were purchased from Merck (UK) and utilized as received without further purification. All solvents were purchased from Merck (UK) or Thermo Fisher Scientific (UK) and utilized as received without further purification. Dimethyl sulfoxide-d6 (DMSO-d6), used for nuclear magnetic resonance (NMR) measurement, was purchased from Thermo Fisher Scientific (UK).

### 2.4.2 Instrumentation

1. NMR spectroscopy: NMR spectra were recorded on a Bruker Avance 300, a Bruker Avance III HD 400 or a Bruker Avance III HD 500 spectrometer at 298K and 300, 400 and 500 MHz, respectively. Shifts are quoted in δ in parts per million and quoted relative to the internal standard trimethylsilane (TMS).

2. High-Resolution Mass Spectra (HR-MS) were obtained by using Bruker UHR-Q-ToF MaXis spectrometer with electrospray ionization.

3. UV-vis spectroscopy was performed on Evolution 350 UV-Vis spectrophotometer equipped with Xenon Flash Lamp light source and Dual Matched Silicon Photodiodes detector. Quartz cells (170 – 2000 nm) from Hellma with two polished sides were used for examining the absorption spectral data by using Thermo INSIGHT-2 v.10.0.30319.1 software.

4. Fluorescence spectral data in various solvents and solid state were obtained with an Edinburgh Instruments FS5 Spectrofluorometer. Quartz cells with four polished sides (Starna) were used for fluorescence measurements.

5. X-ray analysis data were collected on Agilent Technologies SuperNova single crystal X-ray diffractometer with dual wavelength microfocus X-ray sources (Mo and Cu) and an Atlas detector. The system is complemented by an Oxford Cryosystems Cryostream to collect data at temperatures as low as 100 K. The structures were solved by direct methods and refined anisotropically by the least-squares procedure implemented in the SHELX program system.

### 2.4.3 Computational details

The geometries of all compounds in the ground state were optimised using the density functional theory (DFT) method at the cam-B3LYP/6-31G* (d, p) level, The excited-state geometries were optimized using the time-dependent DFT method at the same level of theory. To investigate the solvent effect on the energy level and the distribution of electron density of each compound, the solvation model based on the density model of SMD and self-consistent reaction field was considered in the calculations. All the above calculations were carried out using the Gaussian 16 program.

### 2.4.4 The method of measuring the relative quantum yield

Rhodamine B in ethanol as the reference (λex = 495nm, Φ = 0.89), all recorded absorbance (both samples and reference) were measured while keeping a maximum absorbance value of 0.1. Measurements were made in quartz cuvettes with a total sample volume of 3 ml. The quantum yield in the solid state was obtained with an Edinburgh Instruments FLS1000 Spectrofluorometer fitted with an integrating sphere.

### 2.4.5 Synthetic methods

1. Synthesis of $R_1$-aniline-Maleimide Substitution

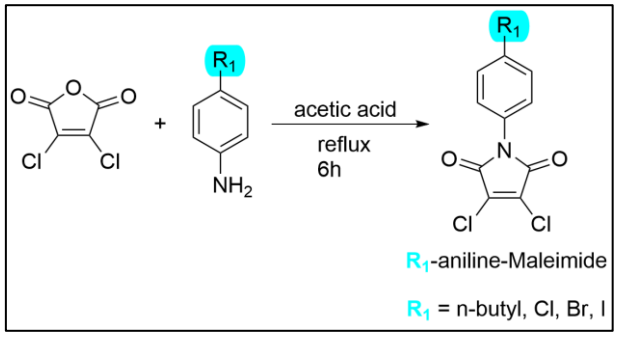


Scheme 1 Synthesis of $R_1$-aniline-Maleimide.

In a one-neck round-bottom flask, 2,3-dichloromaleic anhydride (1 eq.) was dissolved in acetic acid, followed by the addition of 4-butylaniline (or alternatively, 4-chloroaniline, 4-bromoaniline, or 4-iodoaniline) (1 eq.). The resulting mixture was refluxed for 6 hours. Upon completion of the reaction, the solution was cooled to room temperature, inducing the precipitation of the product. The precipitate was then filtered and washed with methanol, yielding a light yellow solid. The yield of each compound was approximately 95%.

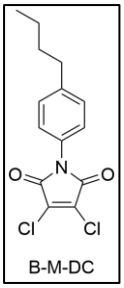


**$^{1}$H NMR (400 MHz, DMSO-d6, 25°C, TMS) δ (ppm)**: 7.34 (d, J = 8.4 Hz, 2H), 7.28 (d, J = 8.4 Hz, 2H), 2.63 (t, J = 7.7 Hz, 2H), 1.65 – 1.52 (m, J = 7.3Hz, 2H), 1.33 (h, J = 7.3 Hz, 2H), 0.92 (t, J = 7.4 Hz, 3H).

**$^{13}$C NMR (101 MHz, CDCl3, 25°C, TMS) δ (ppm)**: 162.4, 133.27, 132.63, 130.79, 129.43, 121.99.

**HRMS**: m/z: calculated for $[C_{14}H_{13}Cl_2NO_2]^-$: 297.0323, found: 297.0321.

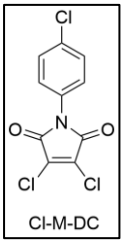


**$^{1}$H NMR (400 MHz, DMSO-d6, 25°C, TMS) δ (ppm)**: 7.61 (d, J = 8.9 Hz, 2H), 7.43 (d, J = 8.9 Hz, 2H).

**$^{13}$C NMR (101 MHz, CDCl3, 25°C, TMS) δ (ppm)**: 162.45, 133.52, 133.26, 130.35, 129.67, 129.17.

**HRMS**: m/z: calculated for $[C_{10}H_4Cl_3NO_2]^-$: 274.9308, found: 274.9312.

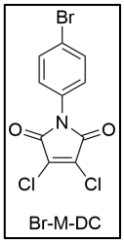


**$^{1}$H NMR (400 MHz, DMSO-d6, 25°C, TMS) δ (ppm)**: 7.75 (d, J = 8.8 Hz, 2H), 7.36 (d, J =8.8 Hz, 2H).

**$^{13}$C NMR (101 MHz, CDCl3, 25°C, TMS) δ (ppm)**: 162.40, 133.27, 132.63, 130.79, 129.43, 121.99.

**HRMS**: m/z: calculated for $[C_{10}H_4BrCl_2NO_2]^-$: 318.8802, found: 318.8803.

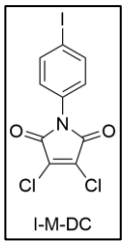


**$^{1}$H NMR (400 MHz, DMSO-d6, 25°C, TMS) δ (ppm)**: 7.90 (d, J = 8.9 Hz, 2H), 7.20 (d, J = 8.9 Hz, 2H).

**$^{13}$C NMR (101 MHz, CDCl3, 25°C, TMS) δ (ppm)**: 162.38, 138.48, 133.26, 131.26, 129.42, 95.10.

**HRMS**: m/z: calculated for $[C_{10}H_4Cl_2INO_2]^-$: 366.8664, found: 366.8661.

2. Synthesis of single substitution amino maleimide derivatives

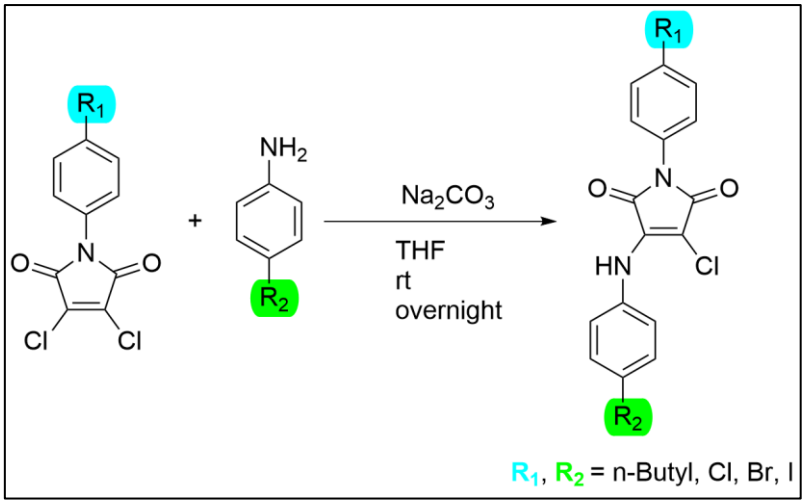


Scheme 2 Synthesis of single substitution amino maleimide derivatives.

The reactants (B-M-DC, Cl-M-DC, Br-M-DC, I-M-DC) (1 eq.) were dissolved in THF, followed by the addition of anhydrous sodium carbonate ($Na_2CO_3$) (2.5 eq.). Subsequently, 4-butylaniline (or alternatively, 4-chloroaniline, 4-bromoaniline, or 4-iodoaniline) (1.5 eq.) was added into the mixture. The mixture was then stirred at room temperature overnight. Upon completion of the reaction, the solids were filtered out, and the solution was evaporated under reduced pressure. The residual solid was washed with methanol, yielding the final yellow products, each with an approximate yield of 90%.

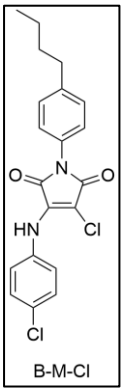


**$^1$H NMR (400 MHz, DMSO-d6, 25°C, TMS) δ (ppm)**: 9.99 (s, 1H), 7.45 (d, J = 8.6 Hz, 2H), 7.31 (dd, J = 14.1, 14.1 Hz, 4H), 7.24 (d, J = 8.7 Hz, 2H), 2.63 (t, J = 5,4 Hz, 2H), 1.65 – 1.53 (m, 2H), 1.35 – 1.22 (m, 2H), 0.92 (t, J = 7.3 Hz, 3H).

**$^{13}$C NMR (101 MHz, CDCl3, 25°C, TMS) δ (ppm)**: 166.70, 164.99, 142.62, 138.55, 136.36, 133.09, 129.61, 129.54, 129.35, 129.18, 128.68, 127.35, 127.10, 125.84, 93.83, 34.91, 33.52, 22.22, 14.23.

**HRMS**: m/z: calculated for $[C_{20}H_{18}Cl_2N_2O_2]^-$: 388.0745, found: 388.0746.

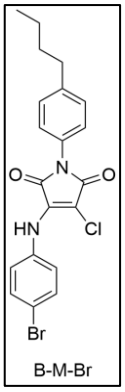


**$^{1}$H NMR (400 MHz, DMSO-d6, 25°C, TMS) δ (ppm)**: 9.98 (s, 1H), 7.57 (d, J = 8.9Hz, 2H), 7.32 (d, J = 8.9 Hz, 2H), 7.28 (d, J = 7.9 Hz, 8.2H), 7.18 (d, J = 7.9Hz, 2H), 2.63 (t, J = 5.4 Hz, 2H), 1.58 (m, 2H), 1.33 (m, 2H), 0.92 (td, J = 7.3Hz, 3H).

**$^{13}$C NMR (101 MHz, CDCl3, 25°C, TMS) δ (ppm)**: 166.96, 165.00, 162.77, 143.44, 142.63, 138.47, 136.81, 133.09, 131.60, 129.61, 129.35, 129.19, 127.36, 127.11, 126.14, 117.67, 94.02, 34.90, 33.52, 33.45, 22.22, 14.23.

**HRMS**: m/z: calculated for $[C_{20}H_{18}BrClN_2O_2]^-$: 432.0240, found: 432.0242.

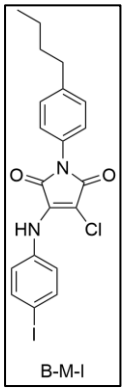


**$^{1}$H NMR (400 MHz, DMSO-d6, 25°C, TMS) δ (ppm)**: 9.97 (s, 1H), 7.72 (d, J = 8.4 Hz, 2H), 7.30 (dd, J = 7.7, 7.7 Hz, 4H), 7.04 (d, J = 8.4Hz, 2H), 2.63 (t, J = 5.4 Hz, 2H), 1.59 (m, 2H), 1.33 (m, 2H), 0.92 (td, J = 7.3Hz 3H).

**$^{13}$C NMR (101 MHz, CDCl3, 25°C, TMS) δ (ppm)**: 166.68, 165.01, 162.77, 143.43, 142.62, 138.36, 137.41, 137.26, 133.09, 129.61, 129.35, 129.18, 129.05, 127.36, 127.12, 126.27, 94.07, 89.87, 34.90, 33.52, 33.46, 22.21, 14.23.

**HRMS**: m/z: calculated for $[C_{20}H_{18}ICIN_2O_2]^-$: 480.0102, found: 488.0104.

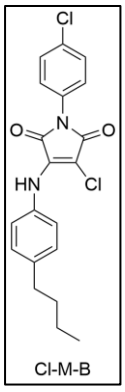


**$^{1}$H NMR (400 MHz, DMSO-d6, 25°C, TMS) δ (ppm)**: 9.94 (s, 1H), 7.71 (d, J = 8.7 Hz, 1H), 7.57 (d, J = 8.8Hz 1H), 7.45 (d, J = 8.8 Hz, 1H), 7.39 (d, J = 8.7 Hz, 1H), 7.21 (d, J = 8.5 Hz, 2H), 7.14 (d, J = 8.4 Hz, 2H), 2.59 (m, J = 7.8 Hz, 2H), 1.56 (m, J = 7.8Hz, 2H), 1.32 (m, J = 7.8 Hz, 2H), 0.91 (t, J = 7.3 Hz, 3H).

**$^{13}$C NMR (101 MHz, CDCl3, 25°C, TMS) δ (ppm)**: 166.50, 166.45, 164.70, 164.64, 140.02, 139.11, 134.69, 132.51, 132.31, 131.49, 131.05, 129.37, 129.06, 128.78, 128.51, 124.56, 120.92, 91.97, 34.77, 33.56, 22.22, 14.26.

**HRMS**: m/z: calculated for $[C_{20}H_{18}Cl_2N_2O_2]^-$: 388.0745, found: 388.0741.

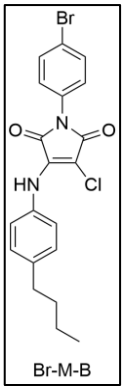


**$^{1}$H NMR (400 MHz, DMSO-d6, 25°C, TMS) δ (ppm)**: 9.93 (s, 1H), 7.71 (d, J = 8.7 Hz, 2H), 7.39 (d, J = 8.8 Hz, 2H), 7.21 (d, J = 8.7 Hz, 2H), 7.14 (d, J = 8.4 Hz, 2H), 2.58 (t, J = 5.4 Hz 2H), 1.57 (m, 2H), 1.32 (m, 2H), 0.91 (t, J = 7.3 Hz 3H).

**$^{13}$C NMR (101 MHz, CDCl3, 25°C, TMS) δ (ppm)**: 166.45, 164.64, 140.02, 139.12, 134.69, 132.31, 131.49, 129.07, 128.51, 124.56, 120.92, 91.97, 34.77, 33.56, 22.22, 14.26.

**HRMS**: m/z: calculated for $[C_{20}H_{18}BrClN_2O_2]^-$: 432.0240, found: 432.0243.

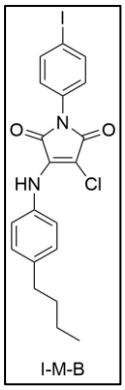


**$^{1}$H NMR (400 MHz, DMSO-d6, 25°C, TMS) δ (ppm)**: 9.93 (s, 1H), 7.86 (d, J = 8.4 Hz, 2H), 7.22 (d, J = 8.6 Hz, 4H), 7.14 (d, J = 8.6 Hz 2H), 2.58 (t, J = 5.4 Hz 2H), 1.56 (m, 2H), 1.32 (m, 2H), 0.91 (t, J = 7.3 Hz 3H).

**$^{13}$C NMR (101 MHz, CDCl3, 25°C, TMS) δ (ppm)**: 166.43, 164.62, 140.02, 139.11, 138.17, 134.69, 131.95, 129.10, 128.50, 124.56, 93.83, 91.97, 34.77, 33.56, 22.22, 14.26.

**HRMS**: m/z: calculated for $[C_{20}H_{18}ICIN_2O_2]^-$: 480.0102, found: 480.0104.

3. Synthesis of dual amino substitution maleimide derivations

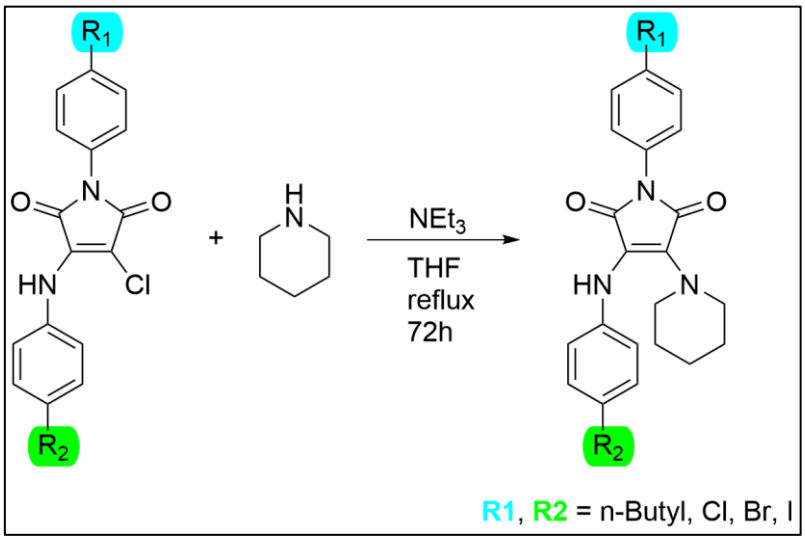


Scheme 3 Synthesis of dual amino substitution maleimide derivations.

The reactant from Step 2 (1 eq.) was dissolved in THF, followed by sequential additions of piperidine (5 eq.) and triethylamine ($NEt_3$) (5 eq.). This mixture was refluxed for 72 hours. Upon the reaction's completion, the solution was cooled and then filtered. The filtrate was evaporated under reduced pressure, leaving a solid residue. This residue was washed with methanol, resulting in the isolation of the final product, which was either orange or red, with each compound yielding approximately 70%.

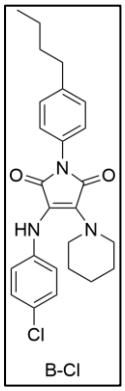


**$^{1}$H NMR (400 MHz, DMSO-d6, 25°C, TMS) δ (ppm)**: 7.83 (s, 1H), 7.27 (d, J = 8.6 Hz 2H), 7.23-7.20 (dd, J = 8.7, 8.7 Hz, 4H), 6.79 (d, J = 8.4 Hz, 2H), 3.47 (t, J = 5.3 Hz, 4H), 2.61 (t, J = 7.7 Hz, 2H), 1.64 – 1.26 (m, 10H), 0.91 (t, J = 7.3 Hz, 3H).

**$^{13}$C NMR (101 MHz, CDCl3, 25°C, TMS) δ (ppm)**: 168.47, 166.73, 143.92, 141.83, 134.66, 130.01, 128.96, 128.91, 127.03, 122.33, 117.10, 108.81, 48.56, 34.87, 33.55, 26.23, 24.01, 22.22, 14.24.

**HRMS**: m/z: calculated for $[C_{25}H_{28}ClN_3O_2]^-$: 437.1870, found: 437.1873.

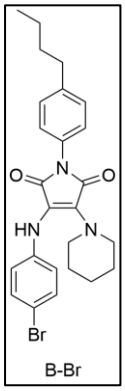


**$^{1}$H NMR (400 MHz, DMSO-d6, 25°C, TMS) δ (ppm)**: 7.82 (s, 1H), 7.32-7.22 (d, J=8.7Hz, 6H), 6.74 (d, J=8.2Hz, 2H), 3.49 (t, J = 5.1 Hz, 4H), 2.61 (t, J = 7.7 Hz, 2H), 1.64 – 1.39 (m, 10H), 0.91 (t, J = 7.3 Hz, 3H).

**$^{13}$C NMR (101 MHz, CDCl3, 25°C, TMS) δ (ppm)**: 168.45, 166.67, 144.49, 141.84, 135.08, 131.76, 130.01, 128.96, 127.03, 117.52, 109.86, 108.39, 48.55, 34.87, 33.55, 26.25, 24.01, 22.22, 14.24.

**HRMS**: m/z: calculated for $[C_{25}H_{28}BrN_3O_2]^-$: 481.1365, found: 481.1361.

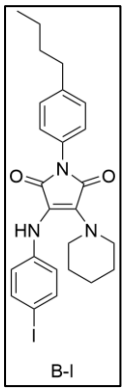


**$^{1}$H NMR (400 MHz, DMSO-d6, 25°C, TMS) δ (ppm)**: 7.78 (s, 1H), 7.47 (d, J=8.7Hz, 2H), 7.27 (d, J=8.5Hz, 2H), 7.21 (d, J=,8.5Hz 2H), 6.63 (d, J=8.7Hz, 2H), 3.48 (t, J = 5.2 Hz, 4H), 2.61 (t, J = 7.7 Hz, 2H), 1.64 – 1.26 (m, 10H), 0.91 (t, J = 7.3 Hz, 3H).

**$^{13}$C NMR (101 MHz, CDCl3, 25°C, TMS) δ (ppm)**: 168.45, 166.63, 145.13, 141.84, 137.54, 135.45, 130.00, 128.96, 127.03, 118.02, 108.02, 80.32, 48.55, 34.87, 33.54, 26.27, 24.02, 22.22, 14.24.

**HRMS**: m/z: calculated for $[C_{25}H_{28}IN_3O_2]^-$: 529.1226, found: 529.1223.

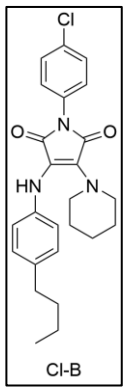


**$^{1}$H NMR (400 MHz, DMSO-d6, 25°C, TMS) δ (ppm)**: 7.79 (s, 1H), 7.66-7.36 (dd, J = 7.9, 7.9 Hz, 4H), 7.02 (d, J = 7.8Hz 2H), 6.74 (d, J = 7.8Hz 2H), 3.34 (t, J = 5.4 Hz, 4H), 2.48 (m, 2H), 1.54-1.24 (m, 10H), 0.88 (t, J = 7.3Hz, 3H).

**$^{13}$C NMR (101 MHz, CDCl3, 25°C, TMS) δ (ppm)**: 168.06, 168.00, 166.86, 166.80, 141.27, 133.43, 132.06, 131.87, 131.63, 131.43, 130.87, 129.12, 128.78, 128.74, 128.46, 119.98, 116.85,112.78, 116.76, 48.78, 34.57, 33.97, 25.97, 24.05, 22.06, 14.27.

**HRMS**: m/z: calculated for $[C_{25}H_{28}ClN_3O_2]^-$: 437.1870, found: 437.1873.

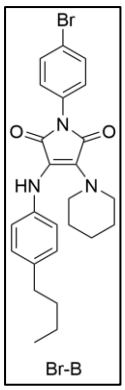


**$^{1}$H NMR (400 MHz, DMSO-d6, 25°C, TMS) δ (ppm)**: 7.79 (s, 1H), 7.66 (d, J = 8.0Hz 2H), 7.33 (d, J = 8.0Hz 2H), 7.02 (d, J = 7.9Hz 2H), 6,74 (d, J = 7.9Hz, 2H), 3.35 (t, J = 5.4 Hz, 4H), 2.48 (m, 2H), 1.54-1.24 (m, 10H), 0.88 (t, J = 7.3Hz, 3H).

**$^{13}$C NMR (101 MHz, CDCl3, 25°C, TMS) δ (ppm)**: 168.01, 166.80, 141.27, 133.42, 132.07, 131.87, 130.93, 128.78, 128.76, 199.99, 116.84, 112.73, 48.78, 34.56, 33.96, 25.97, 24.05, 22.06, 14.28.

**HRMS**: m/z: calculated for $[C_{25}H_{28}BrN_3O_2]^-$: 481.1365, found: 481.1364.

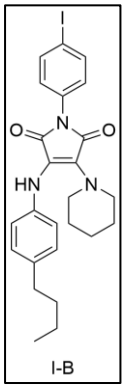


**$^{1}$H NMR (400 MHz, DMSO-d6, 25°C, TMS) δ (ppm)**: 7.80 (m, 3H), 7.18 (d, J = 7.8Hz, 2H), 7.02 (d, J = 7.8Hz 2H), 6.74 (d, J = 7.8Hz 2H), 3.35 (t, J = 5.4 Hz, 4H), 2.48 (m, 2H), 1.54-1.24 (m, 10H), 0.89 (t, J = 7.3Hz, 3H).

**$^{13}$C NMR (101 MHz, CDCl3, 25°C, TMS) δ (ppm)**: 167.99, 166.77, 141.29, 137.93, 133.41, 132.33, 131.00, 128.87, 128.79, 116.82, 112.70, 92.76, 48.77, 34.55, 33.96, 25.97, 24.05, 22.05, 14.28.

**HRMS**: m/z: calculated for $[C_{25}H_{28}IN_3O_2]^-$: 529.1226, found: 529.1217.

## 2.4.6 Nuclear Magnetic Resonance (NMR) Spectra

### B-M-DC

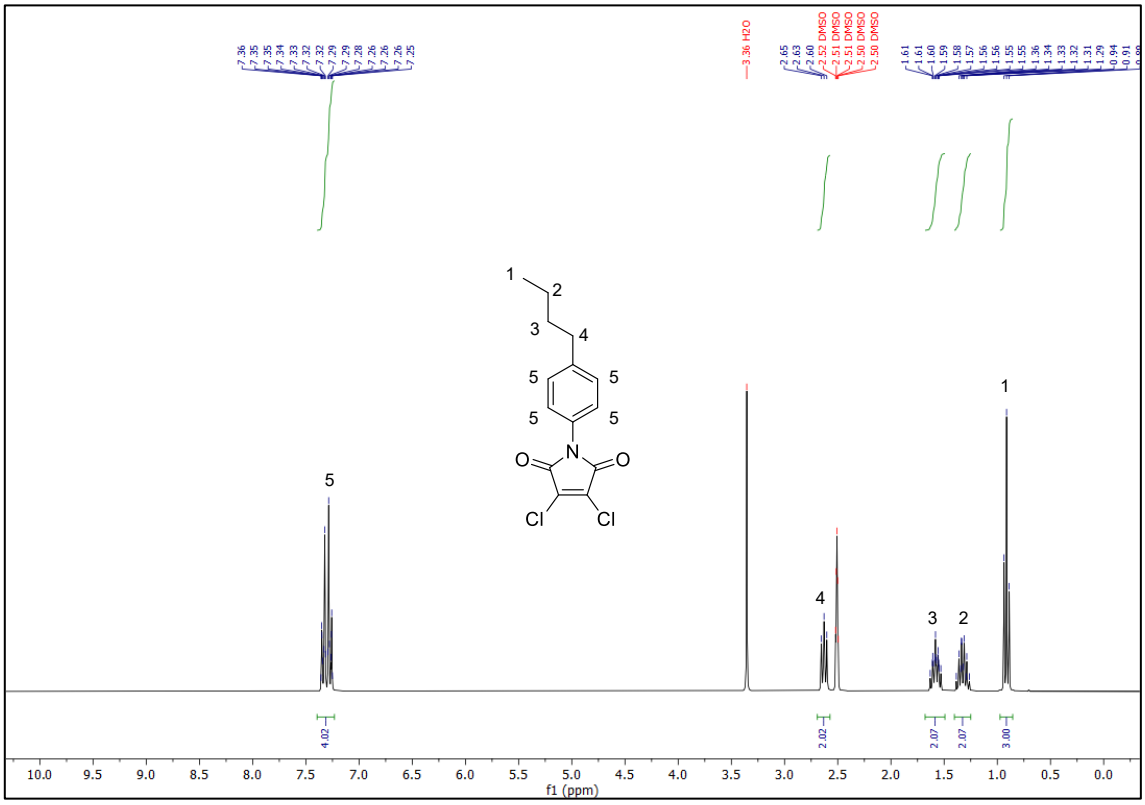


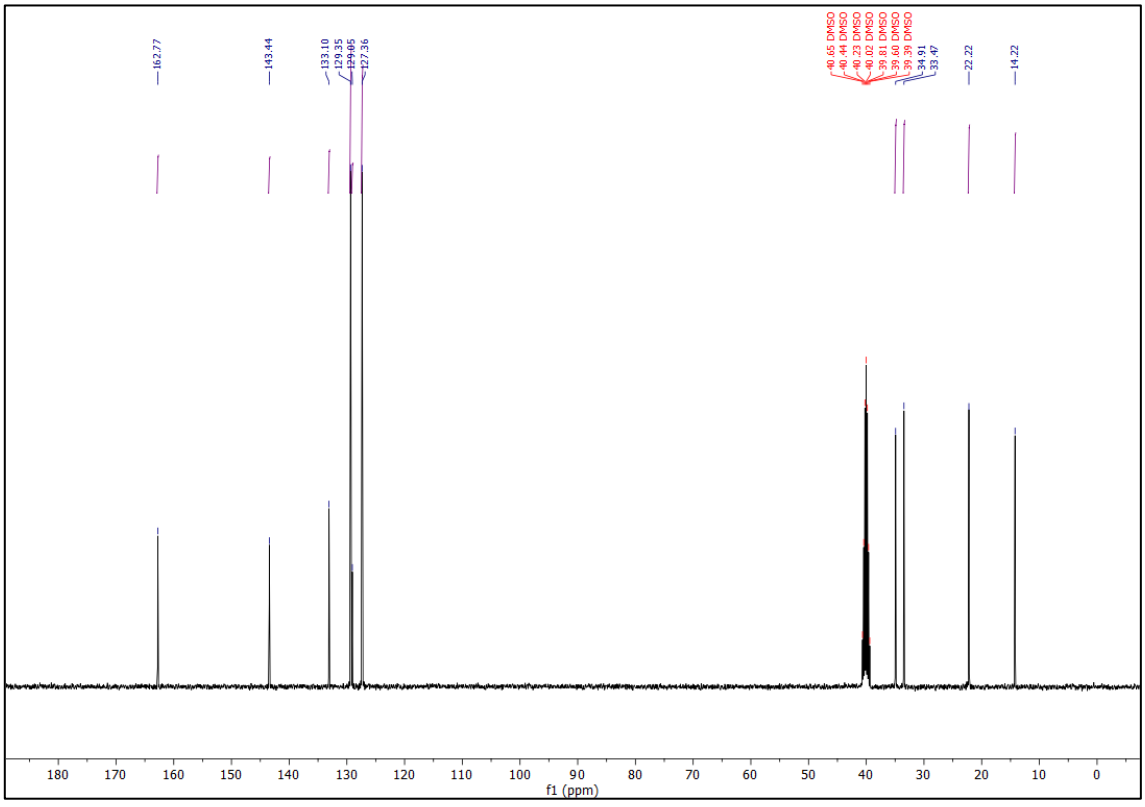

Figure 1 (a) $^{1}H$ and (b) $^{13}C$ NMR spectra of B-M-DC in DMSO-d6.

**Cl-M-DC**

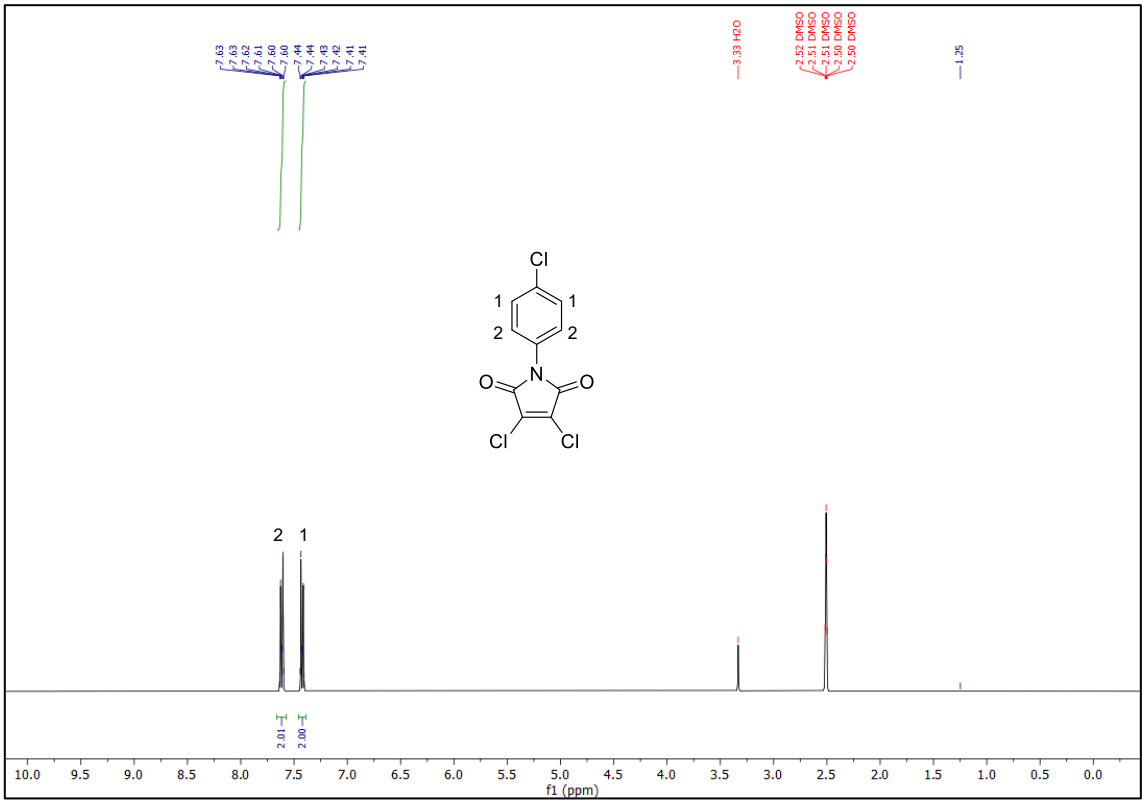


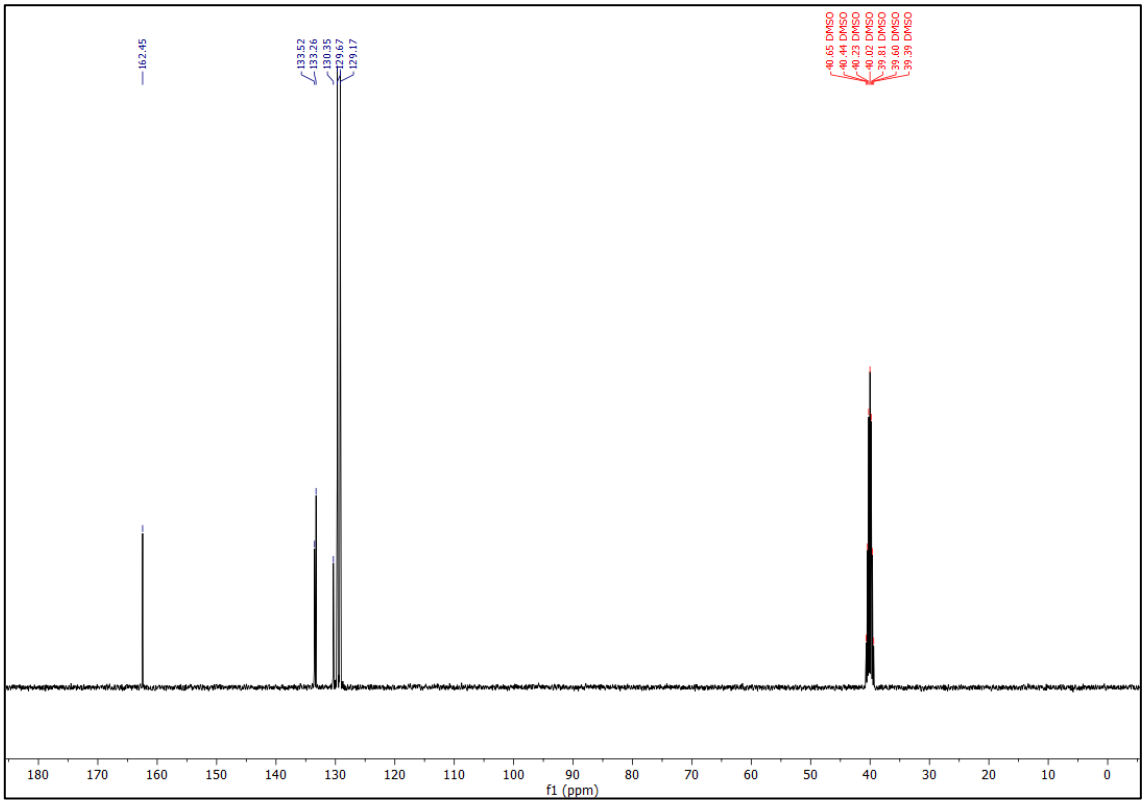

Figure 2 (a) $^{1}H$ and (b) $^{13}C$ NMR spectra of Cl-M-DC in DMSO-d6.

**Br-M-DC**

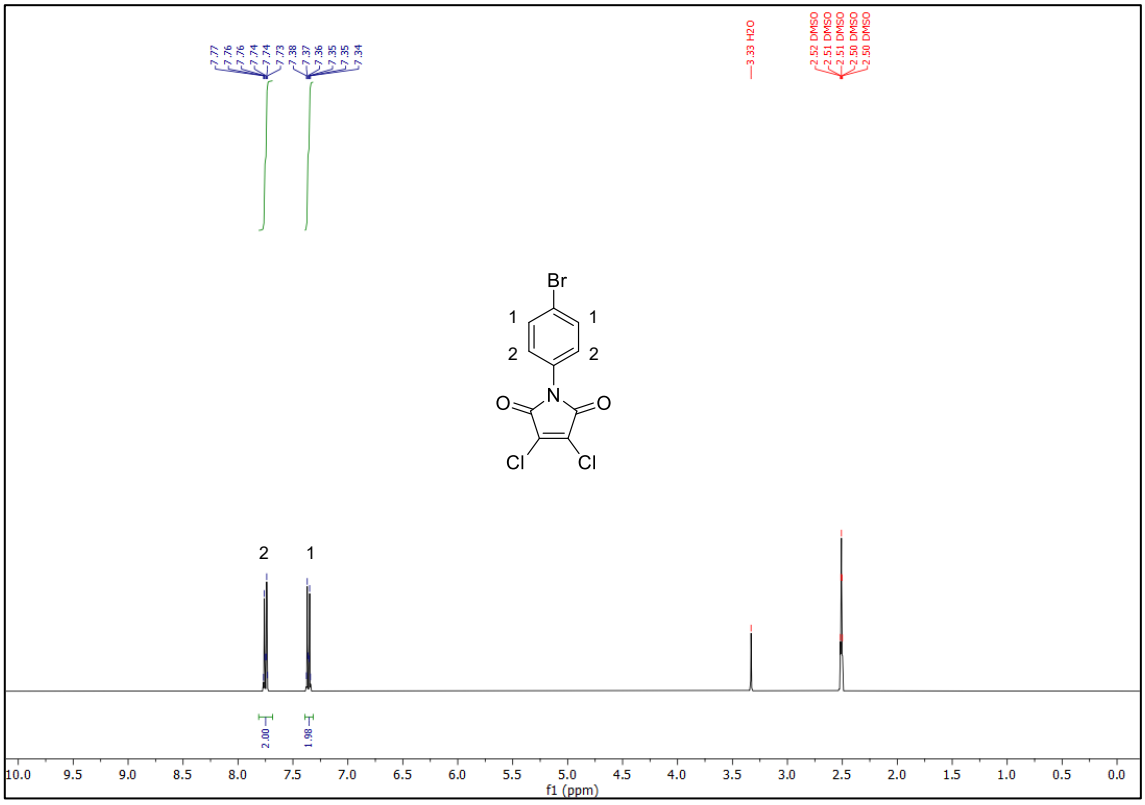


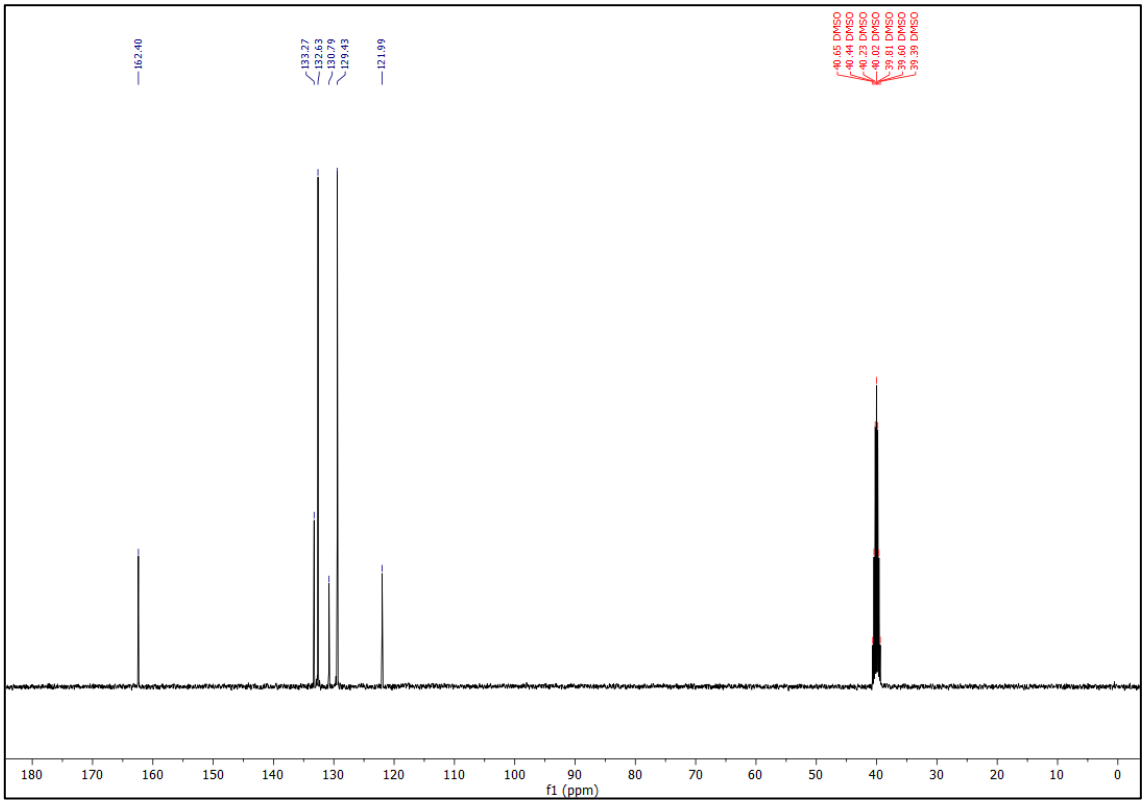

Figure 3 (a) $^{1}H$ and (b) $^{13}C$ NMR spectra of Br-M-DC in DMSO-d6.

**I-M-DC**

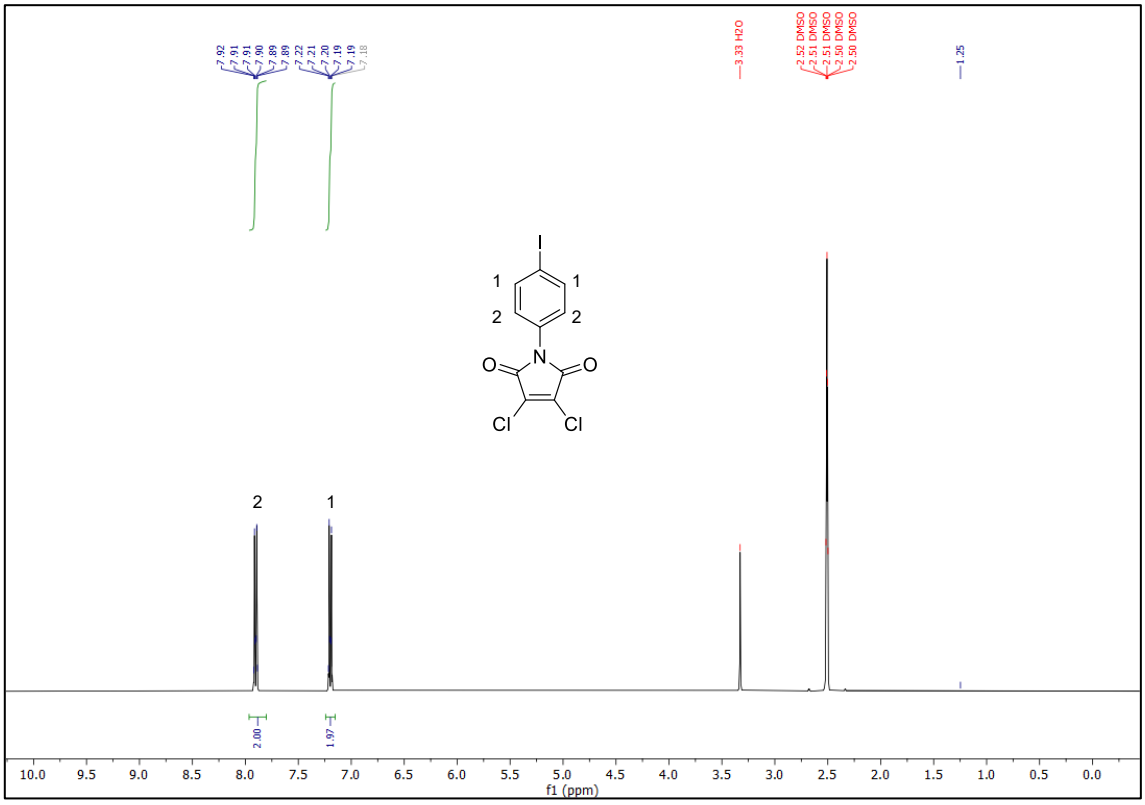


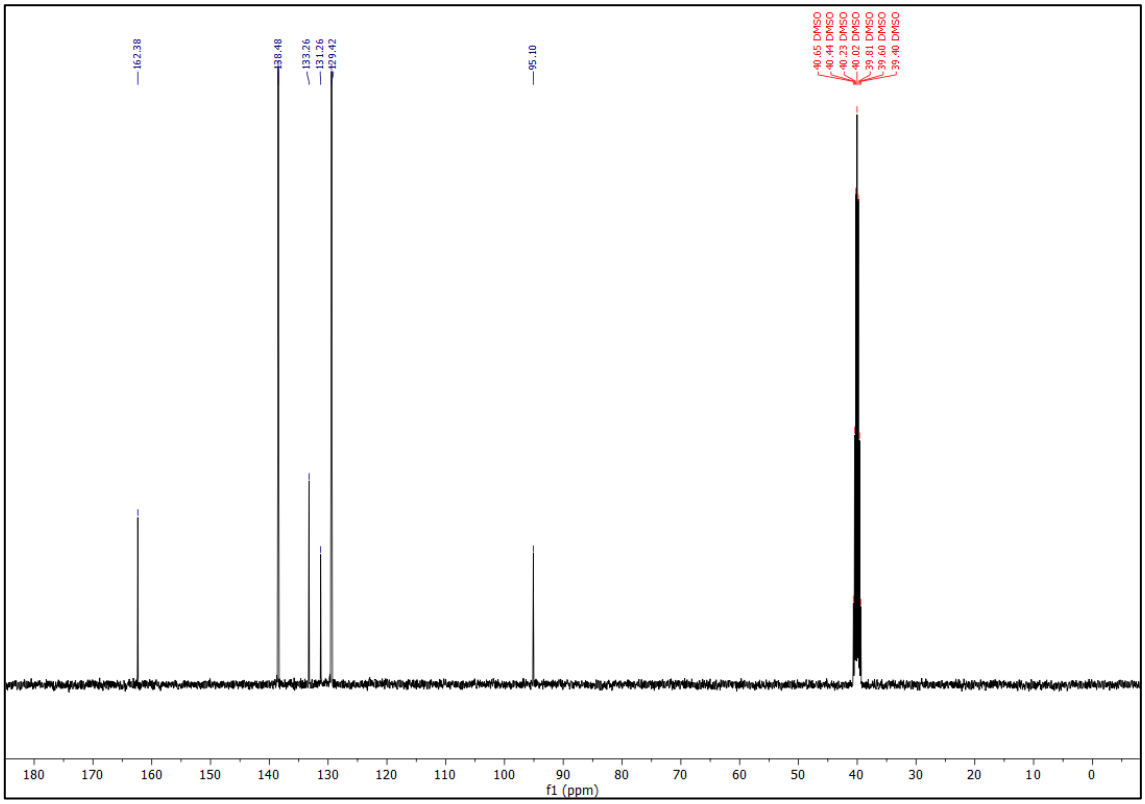

Figure 4 (a) $^{1}H$ and (b) $^{13}C$ NMR spectra of I-M-DC in DMSO-d6.

**B-M-Cl**

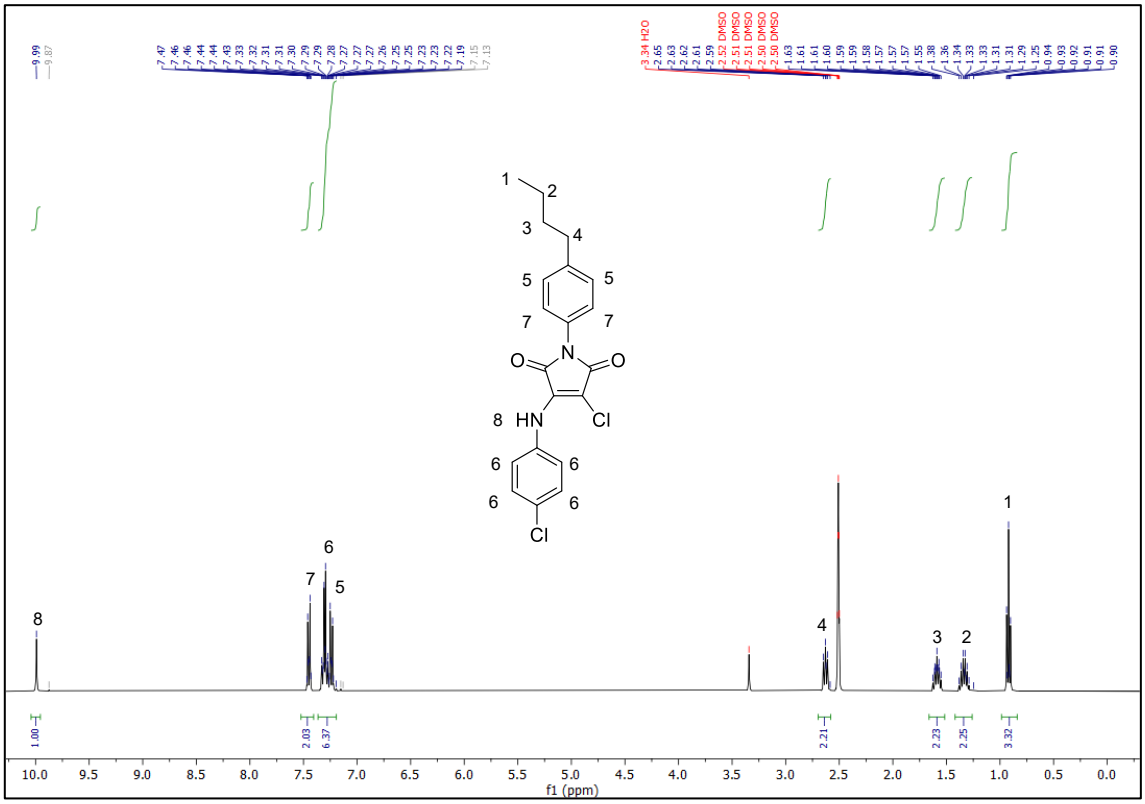


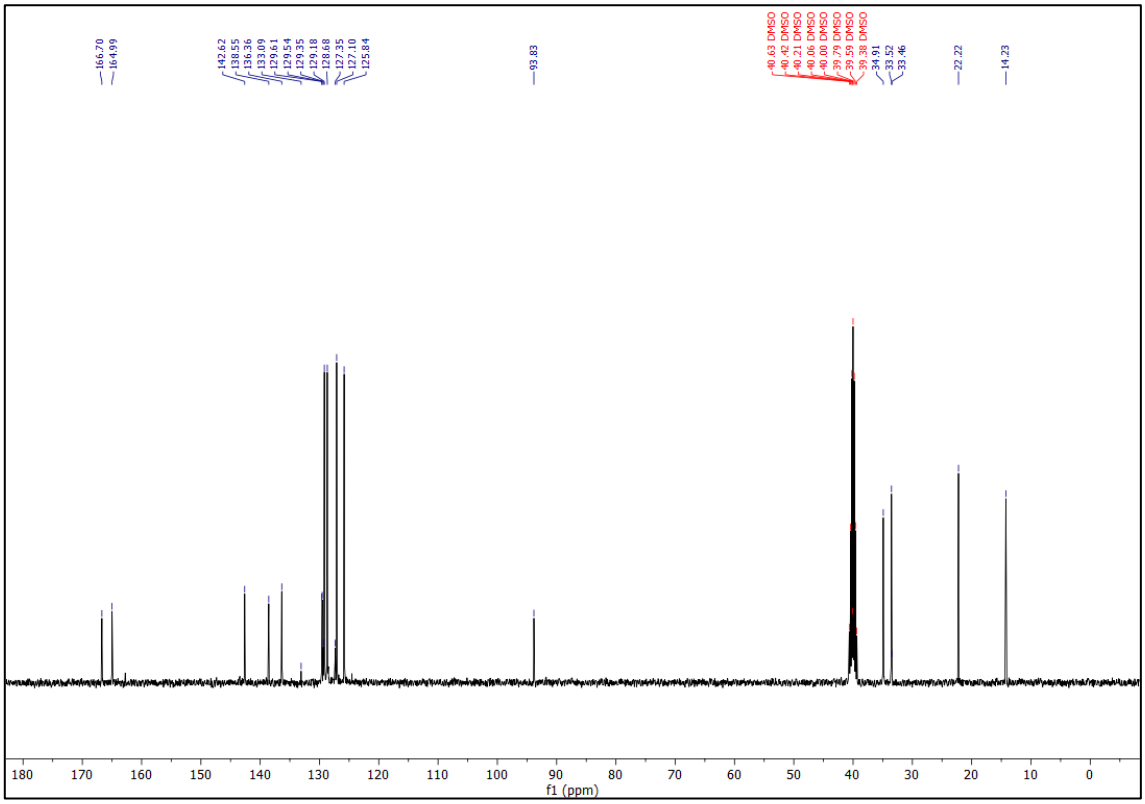

Figure 5 (a) $^{1}H$ and (b) $^{13}C$ NMR spectra of B-M-Cl in DMSO-d6.

**B-M-Br**

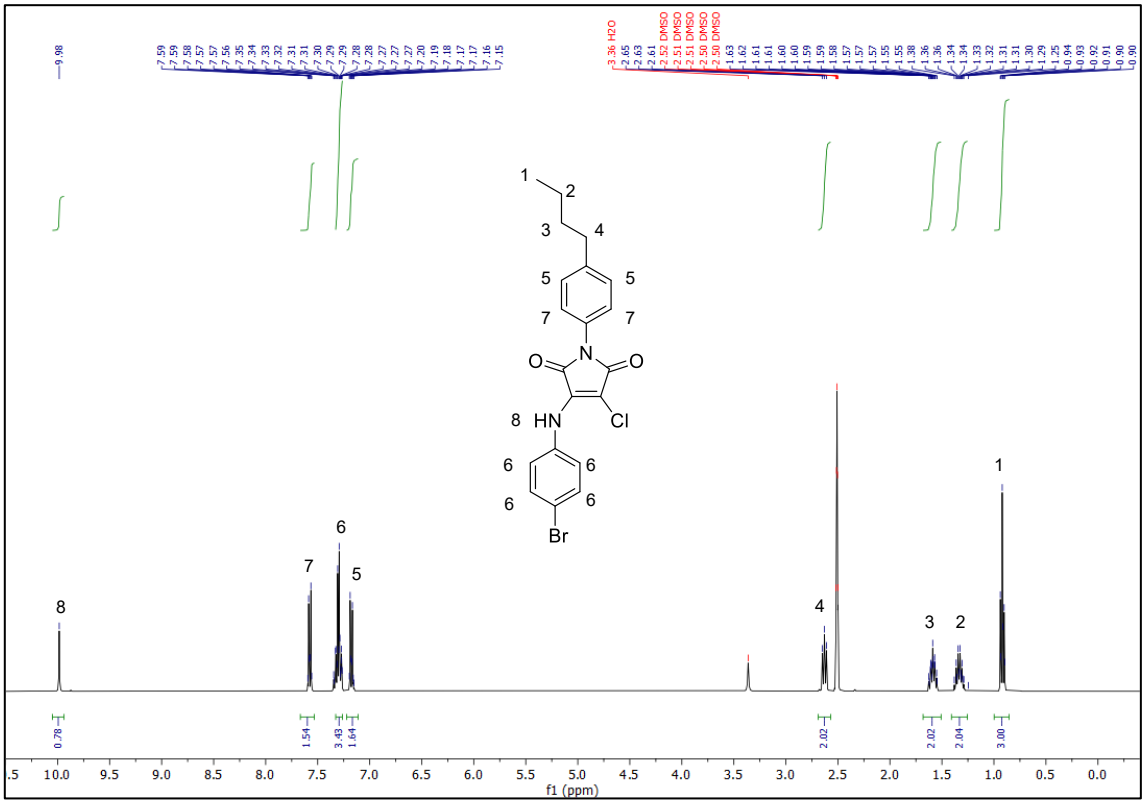


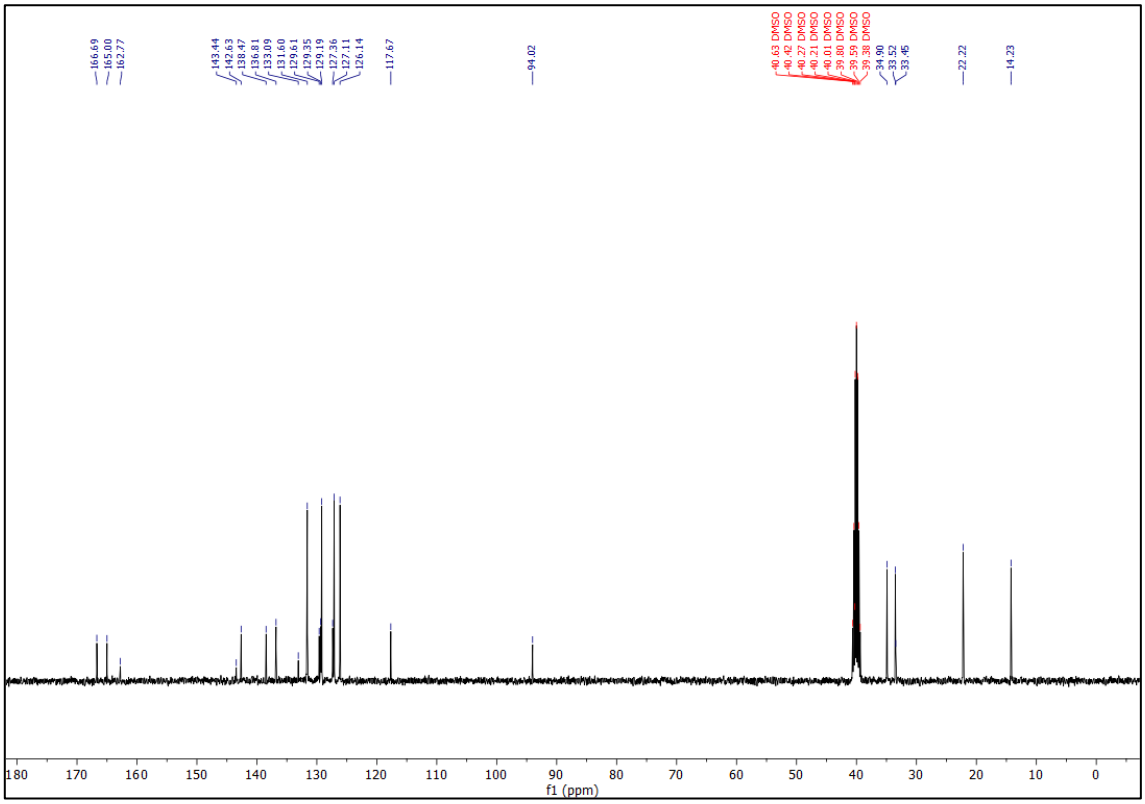

Figure 6 (a) $^{1}H$ and (b) $^{13}C$ NMR spectra of B-M-Br in DMSO-d6.

**B-M-I**

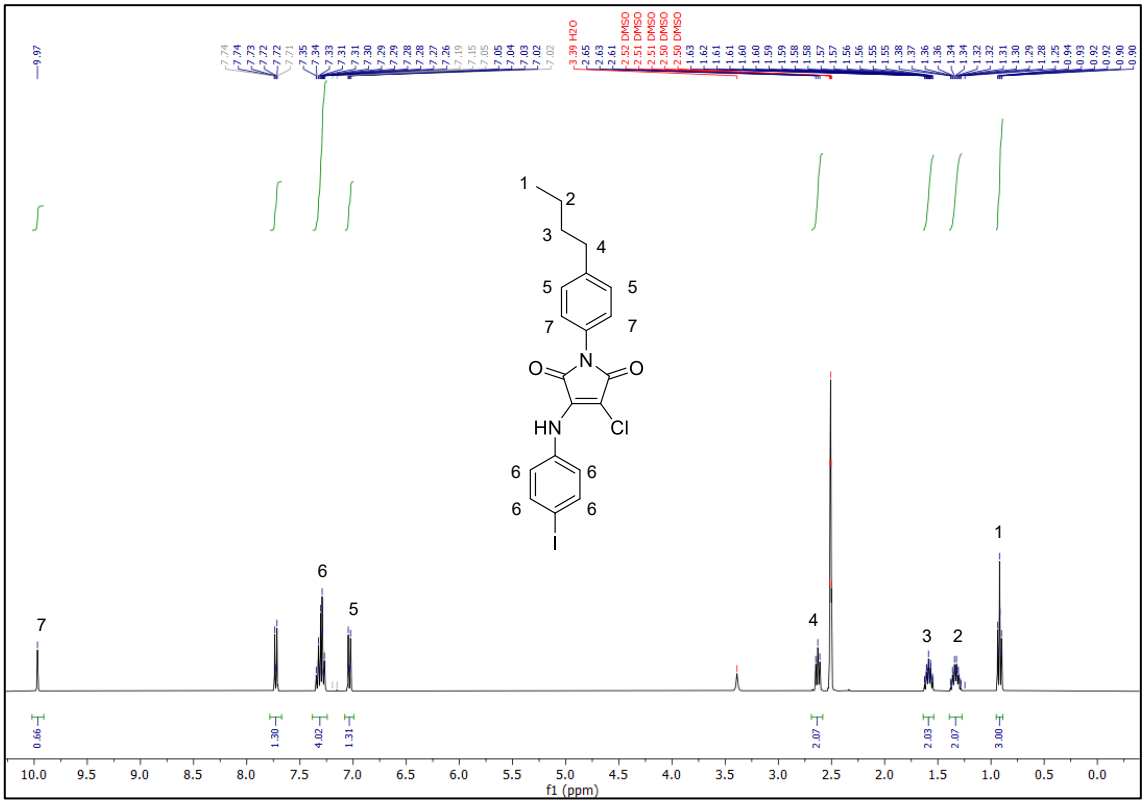


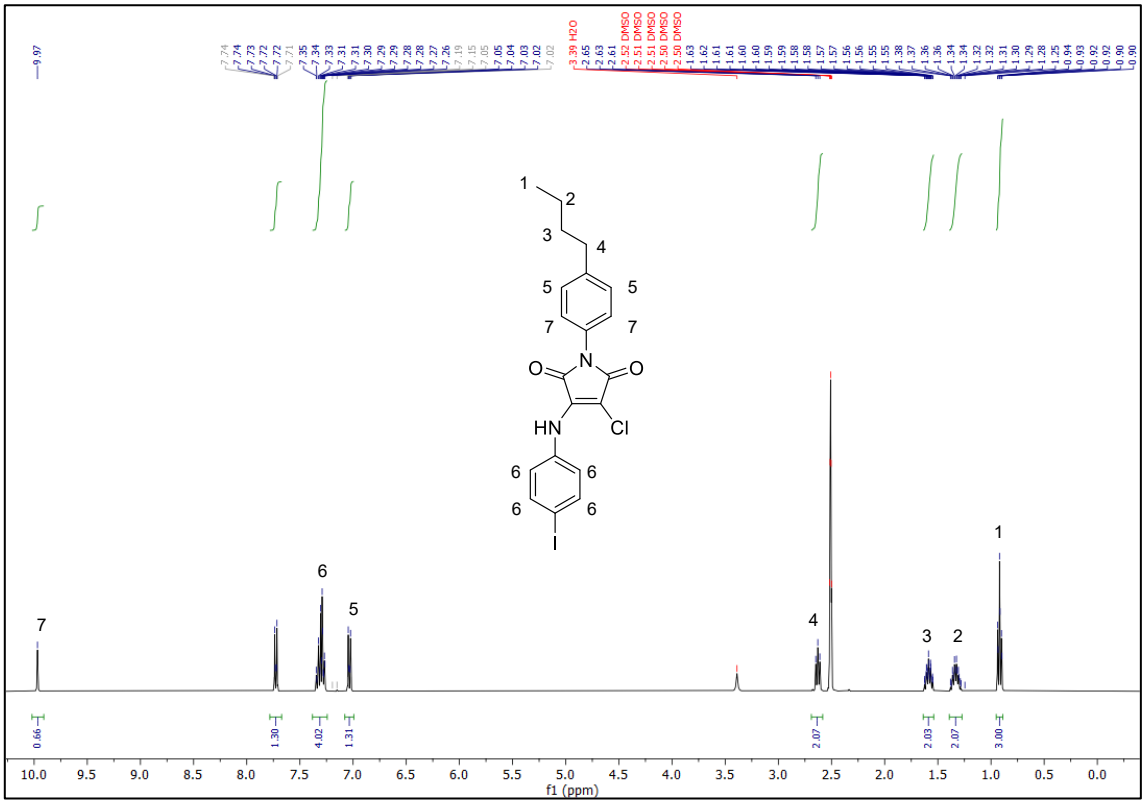

Figure 7 (a) $^{1}H$ and (b) $^{13}C$ NMR spectra of B-M-I in DMSO-d6.

**Cl-M-B**

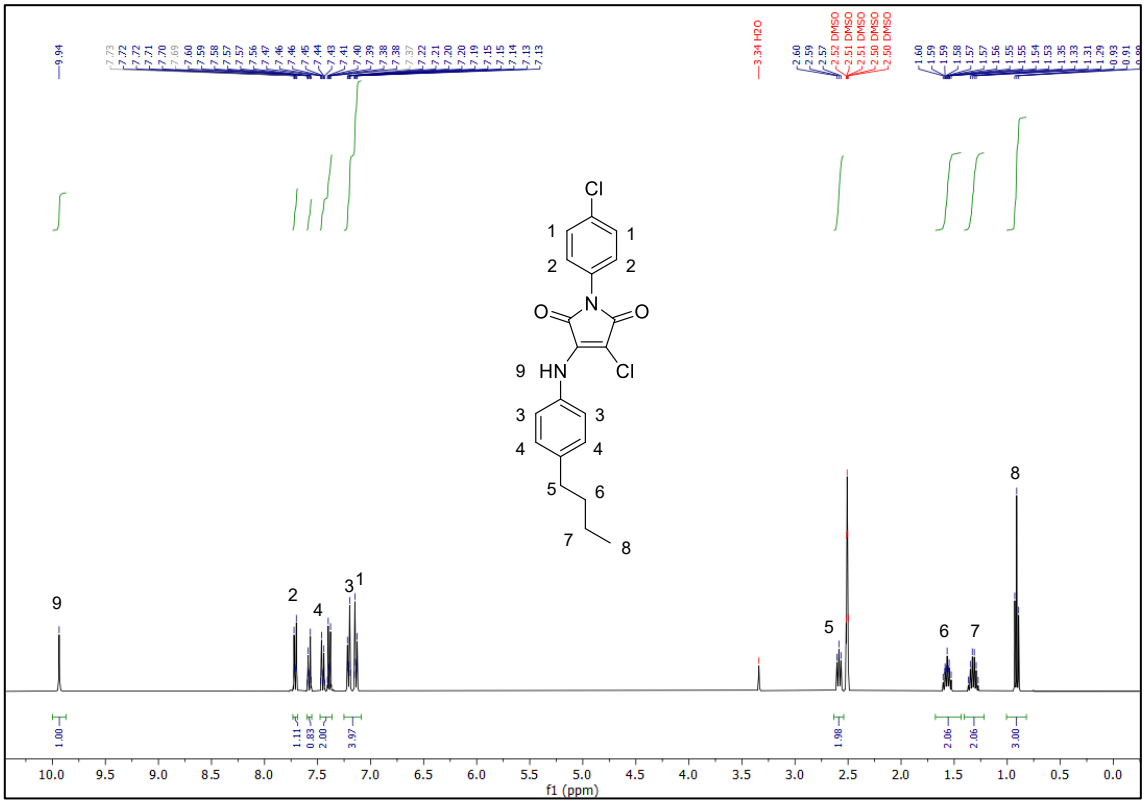


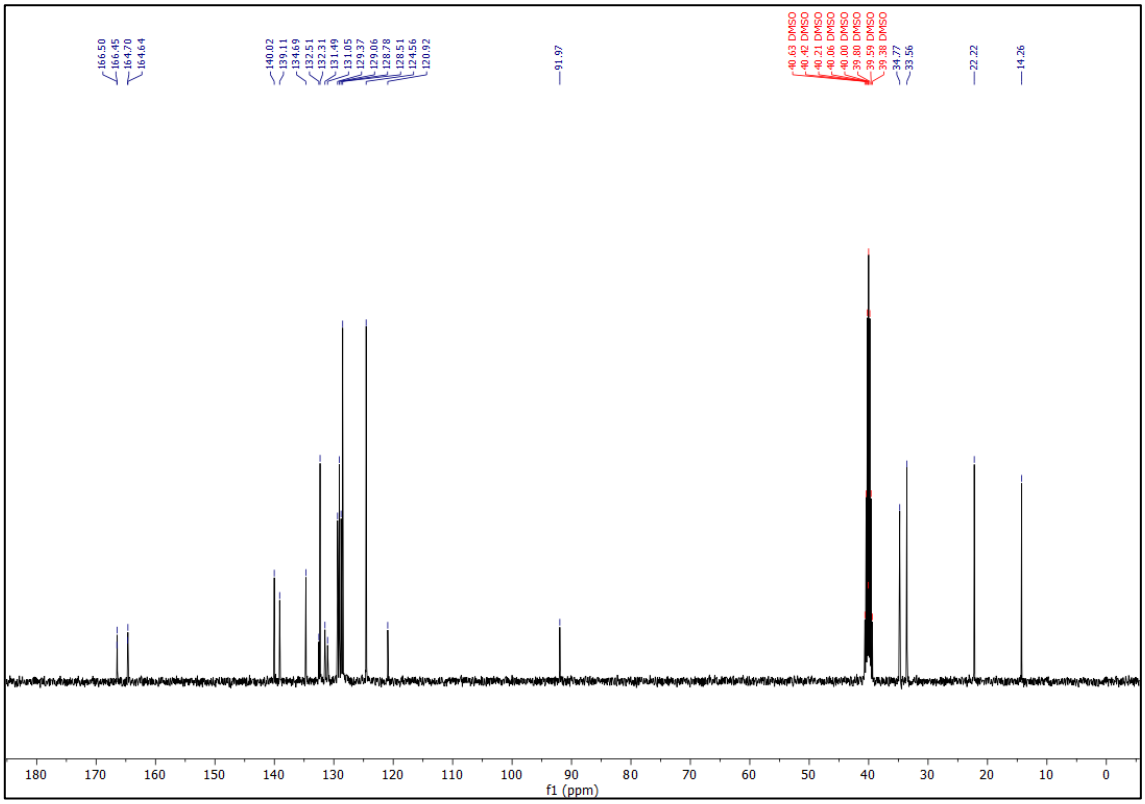

Figure 8 (a) $^{1}H$ and (b) $^{13}C$ NMR spectra of Cl-M-B in DMSO-d6.

**Br-M-B**

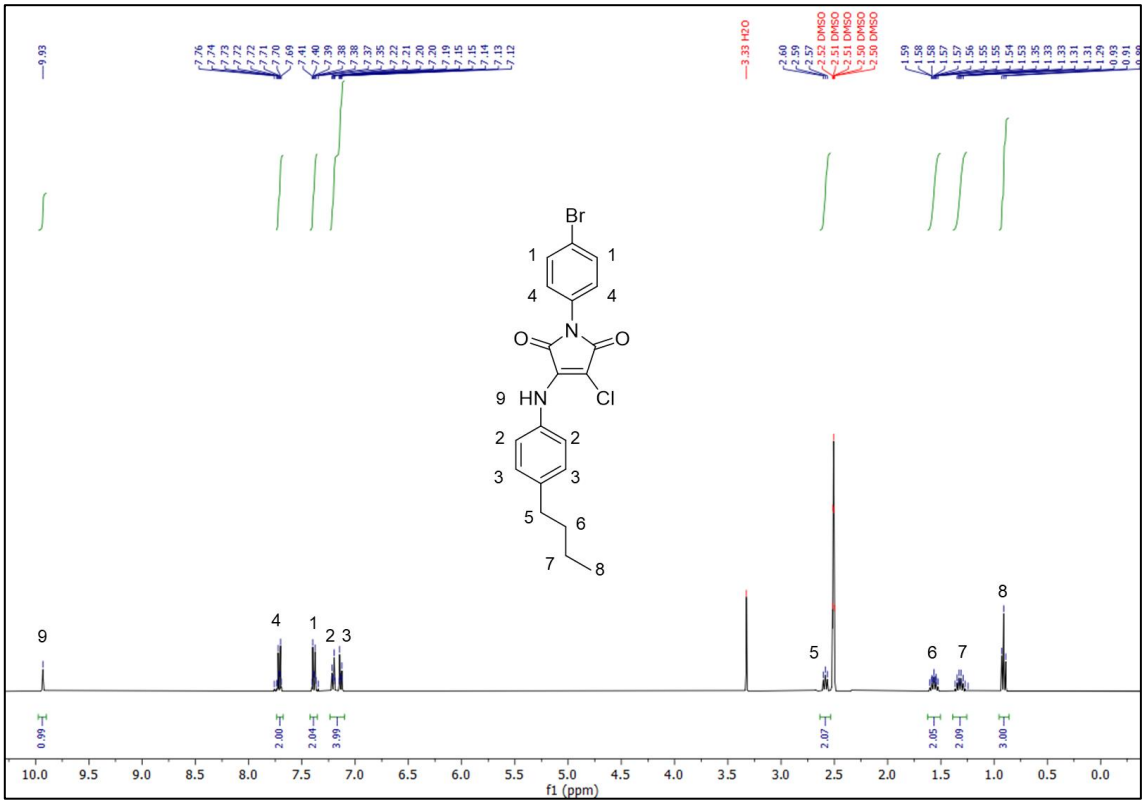


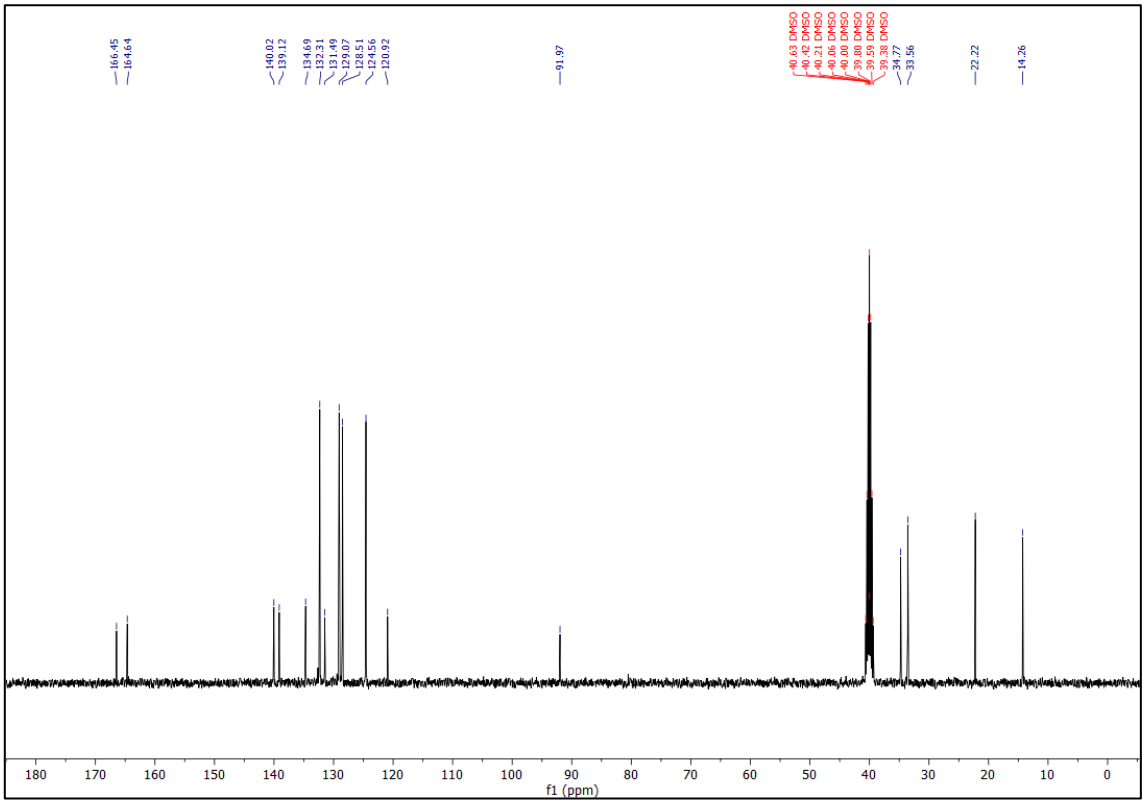

Figure 9 (a) $^{1}H$ and (b) $^{13}C$ NMR spectra of Br-M-B in DMSO-d6.

**I-M-B**

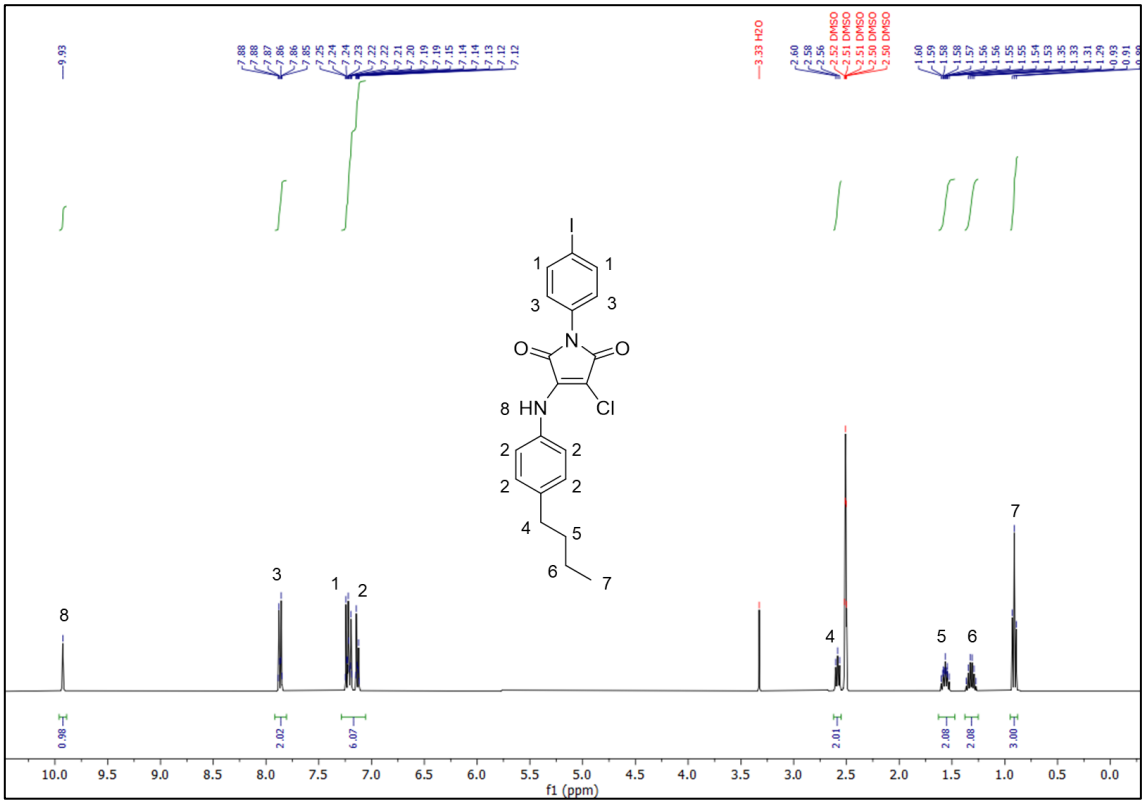


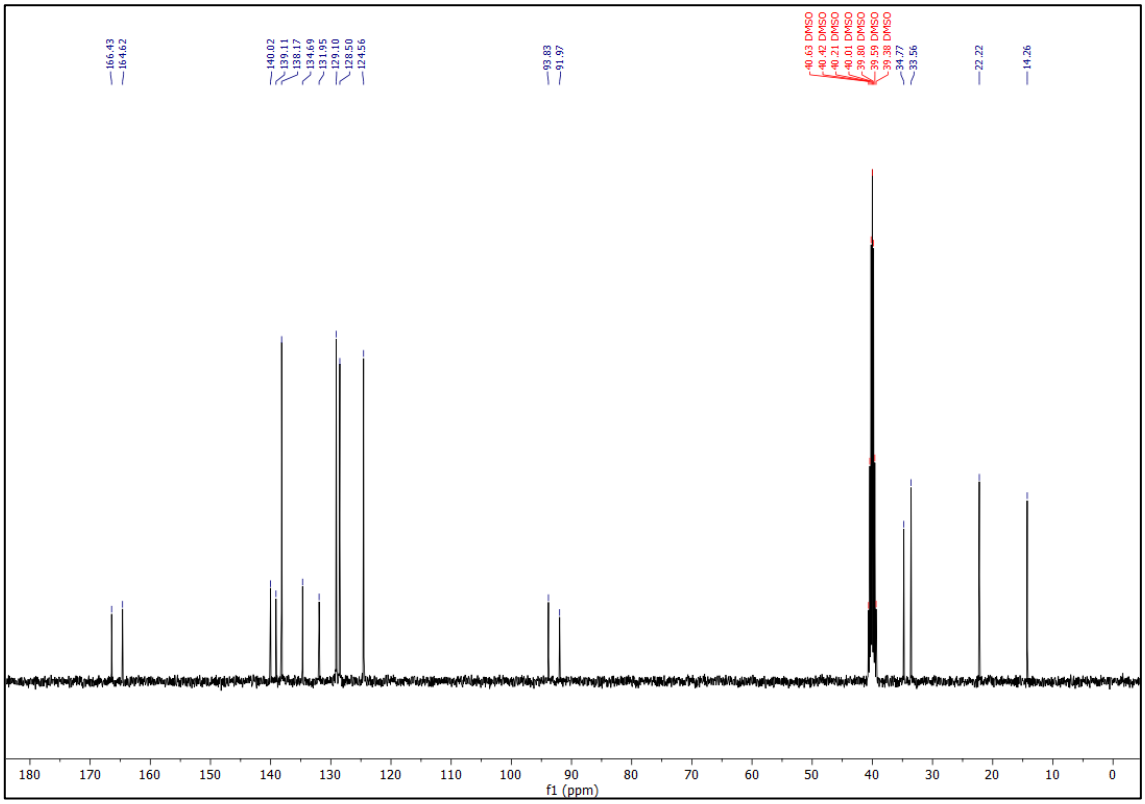

Figure 10 (a) $^{1}H$ and (b) $^{13}C$ NMR spectra of I-M-B in DMSO-d6.

**B-Cl**

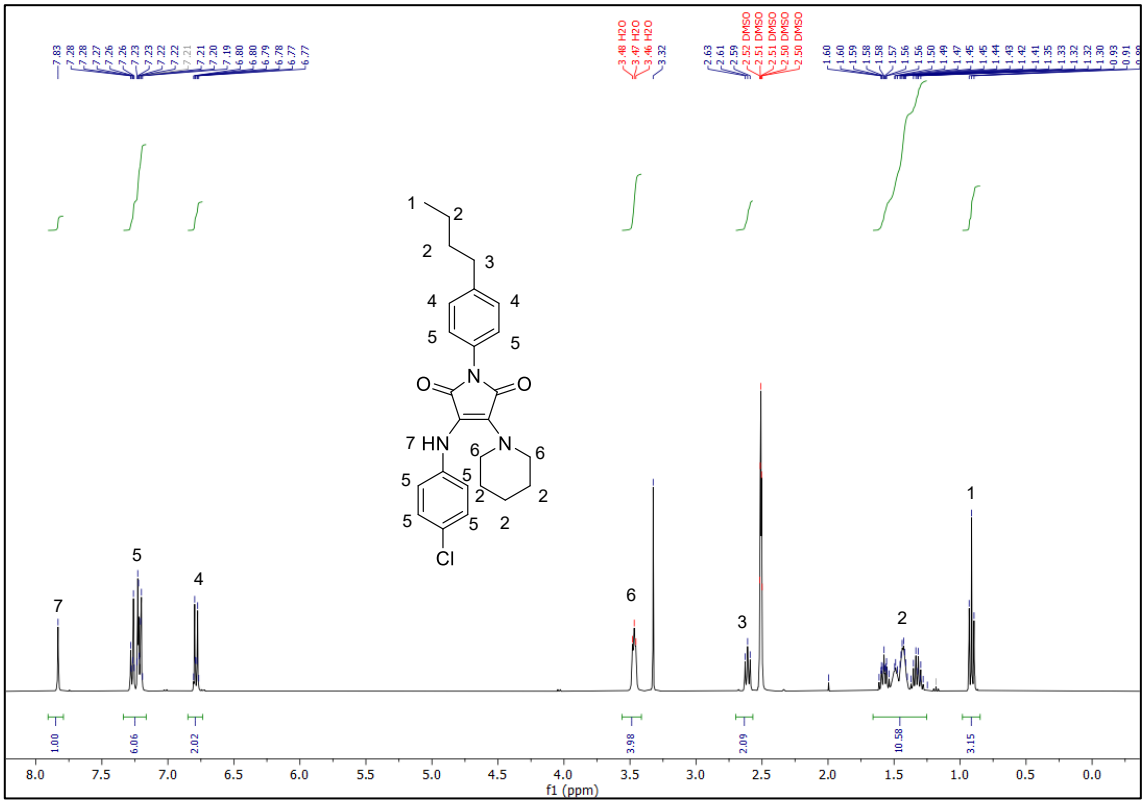


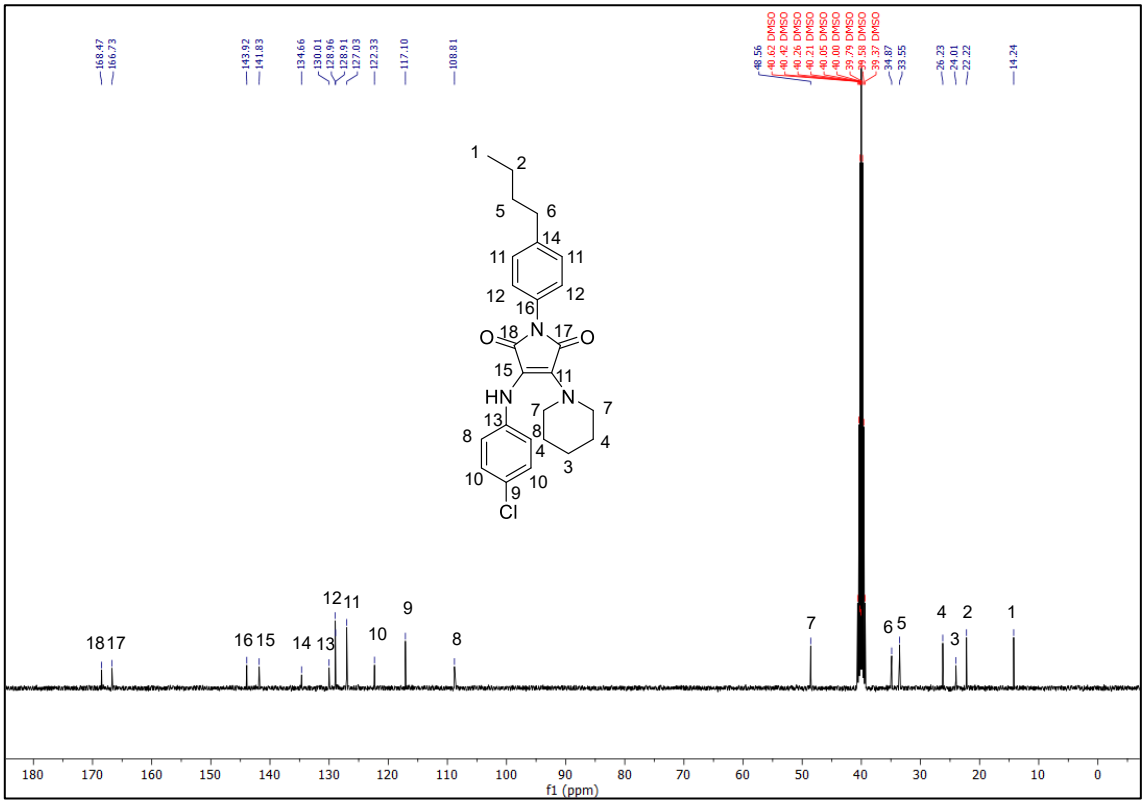

Figure 11 (a) $^{1}H$ and (b) $^{13}C$ NMR spectra of B-Cl in DMSO-d6.

**B-Br**

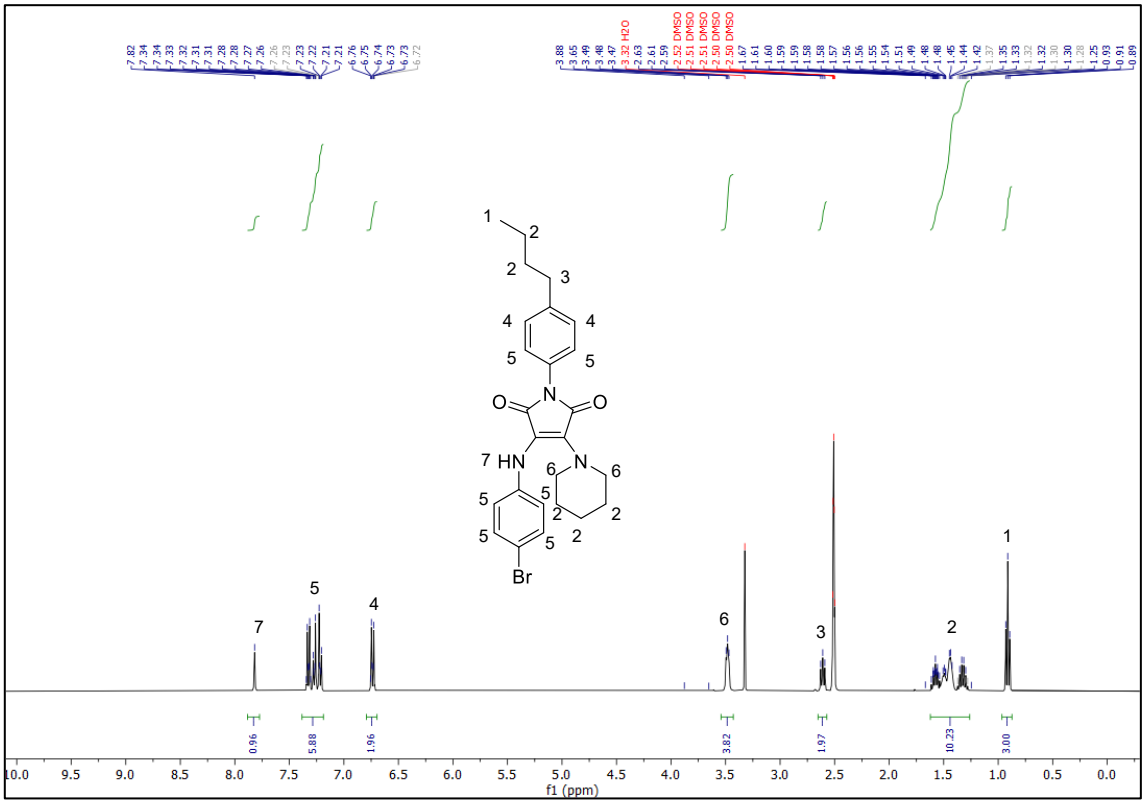


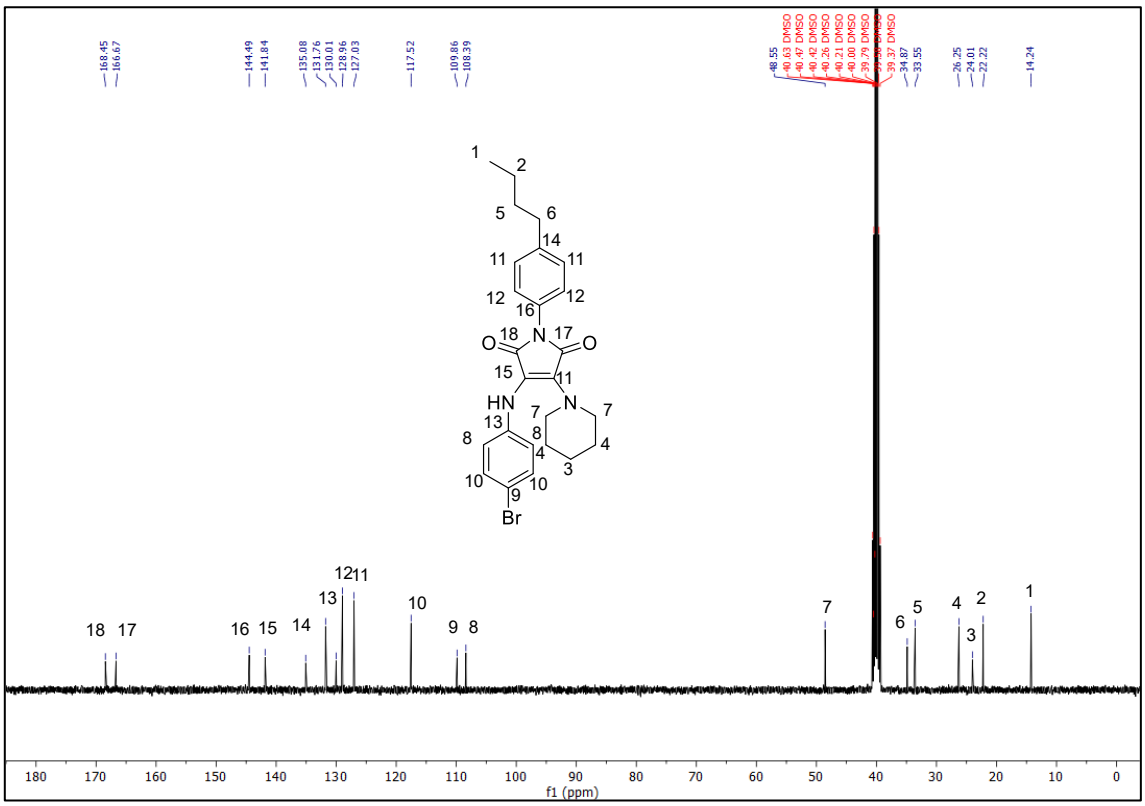

Figure 12 (a) $^{1}H$ and (b) $^{13}C$ NMR spectra of B-Br in DMSO-d6.

**B-I**

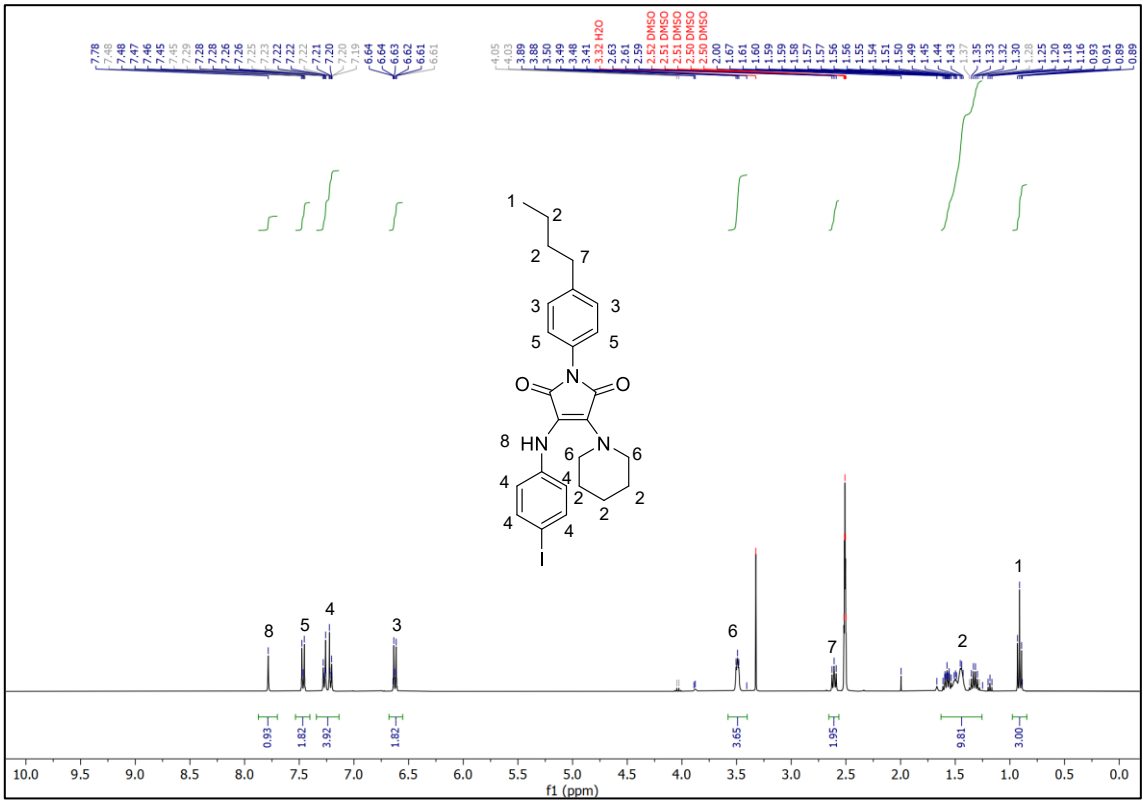


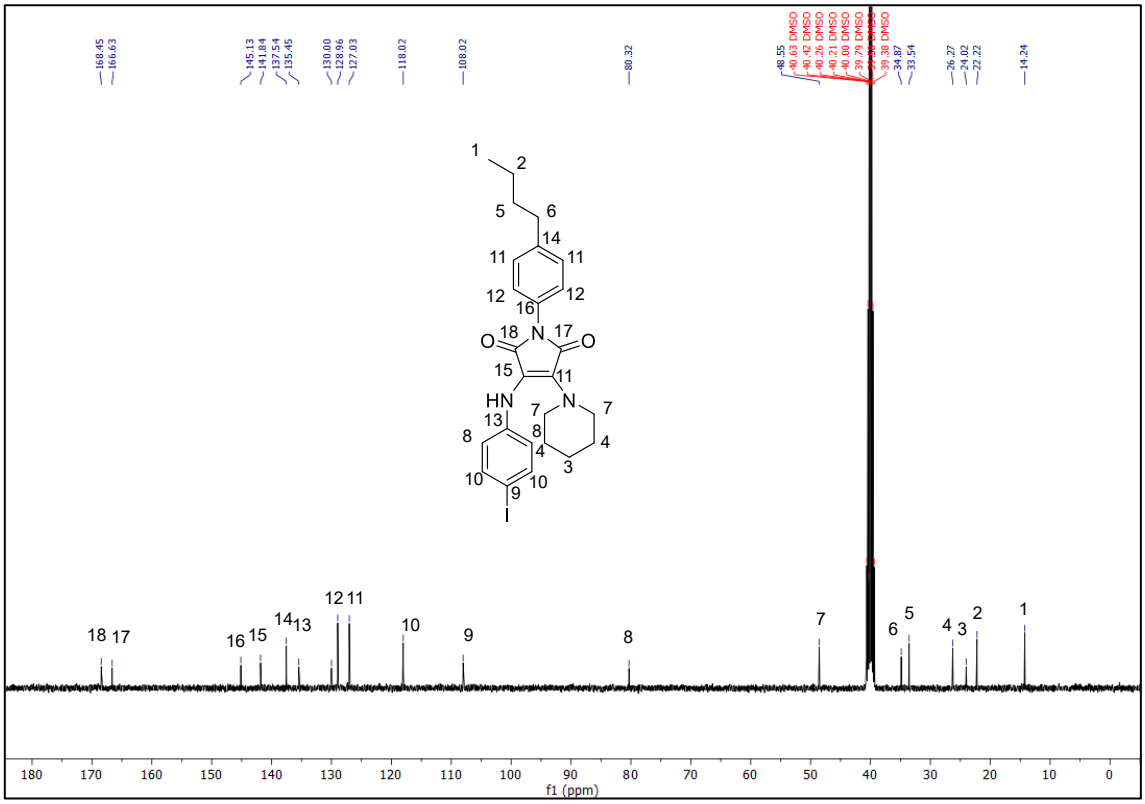

Figure 13 (a) $^{1}H$ and (b) $^{13}C$ NMR spectra of B-I in DMSO-d6.

**Cl-B**

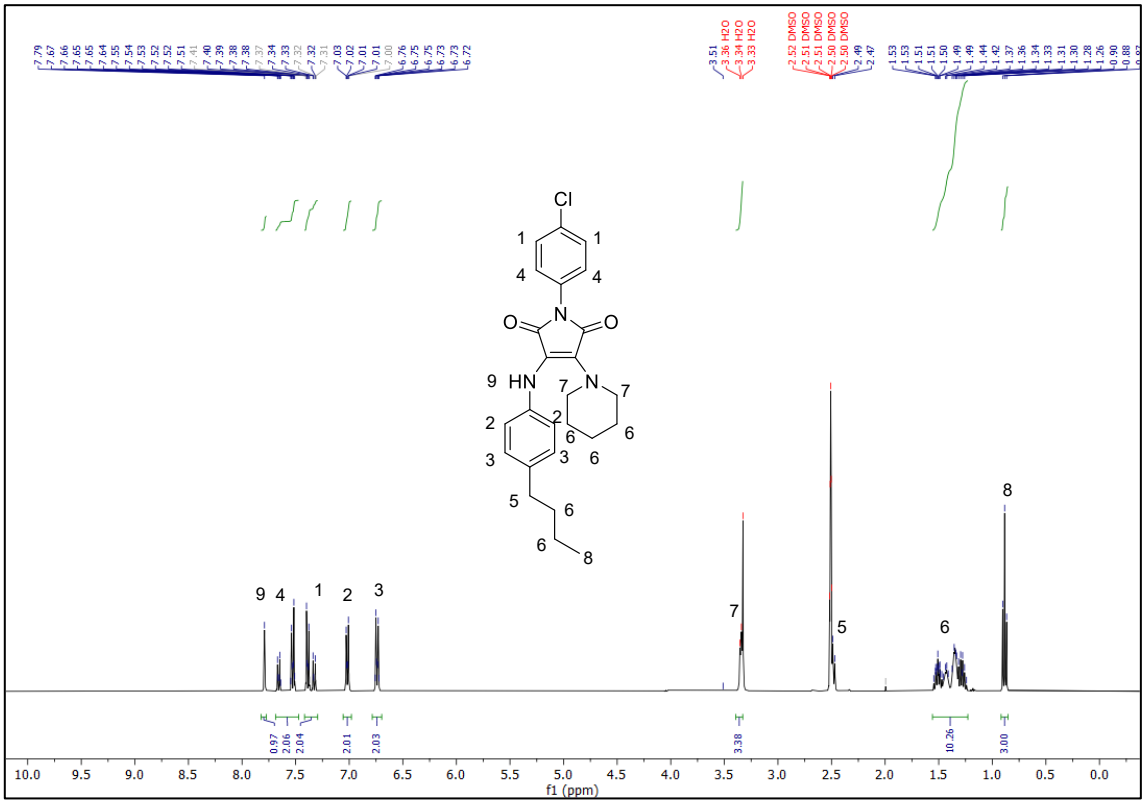


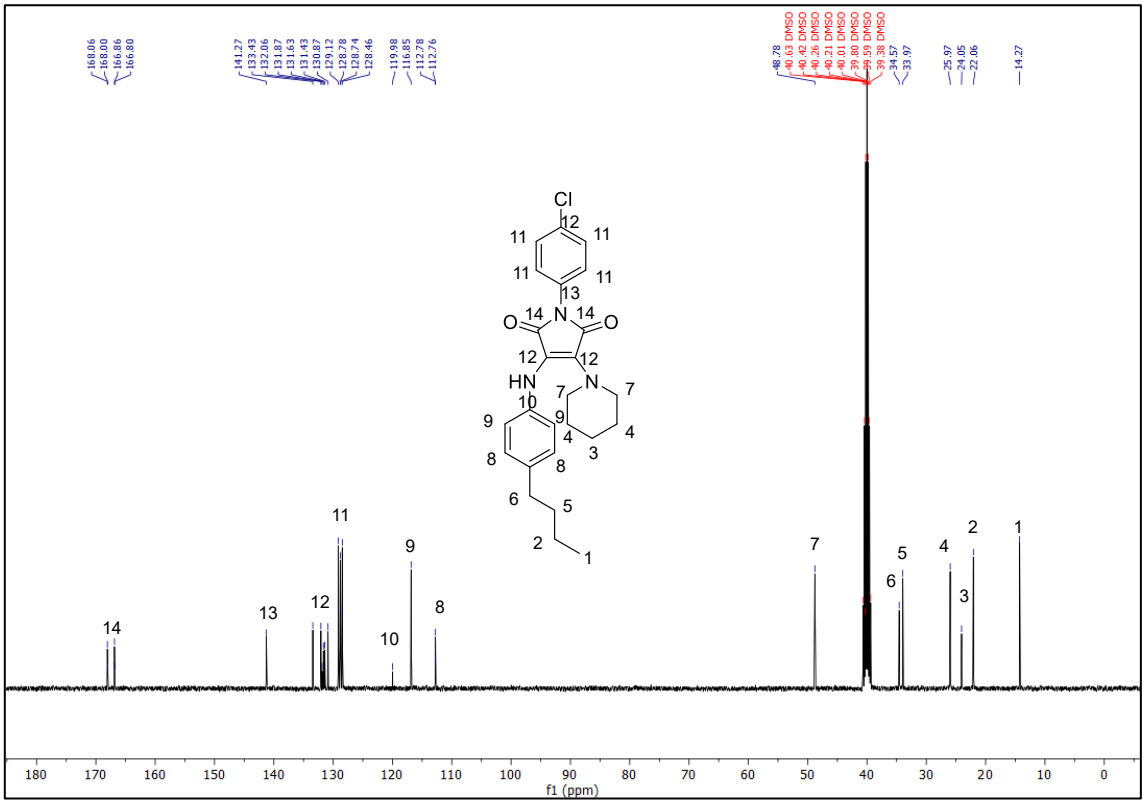

Figure 14 (a) $^{1}H$ and (b) $^{13}C$ NMR spectra of Cl-B in DMSO-d6.

**Br-B**

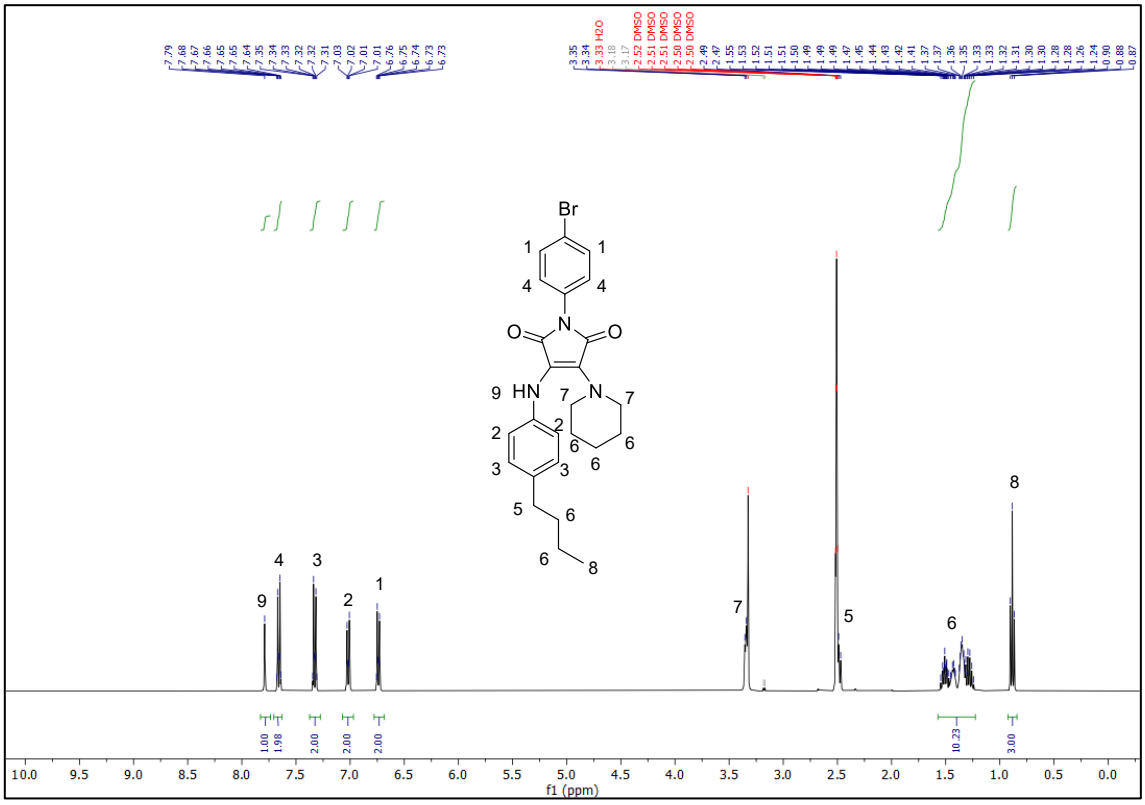


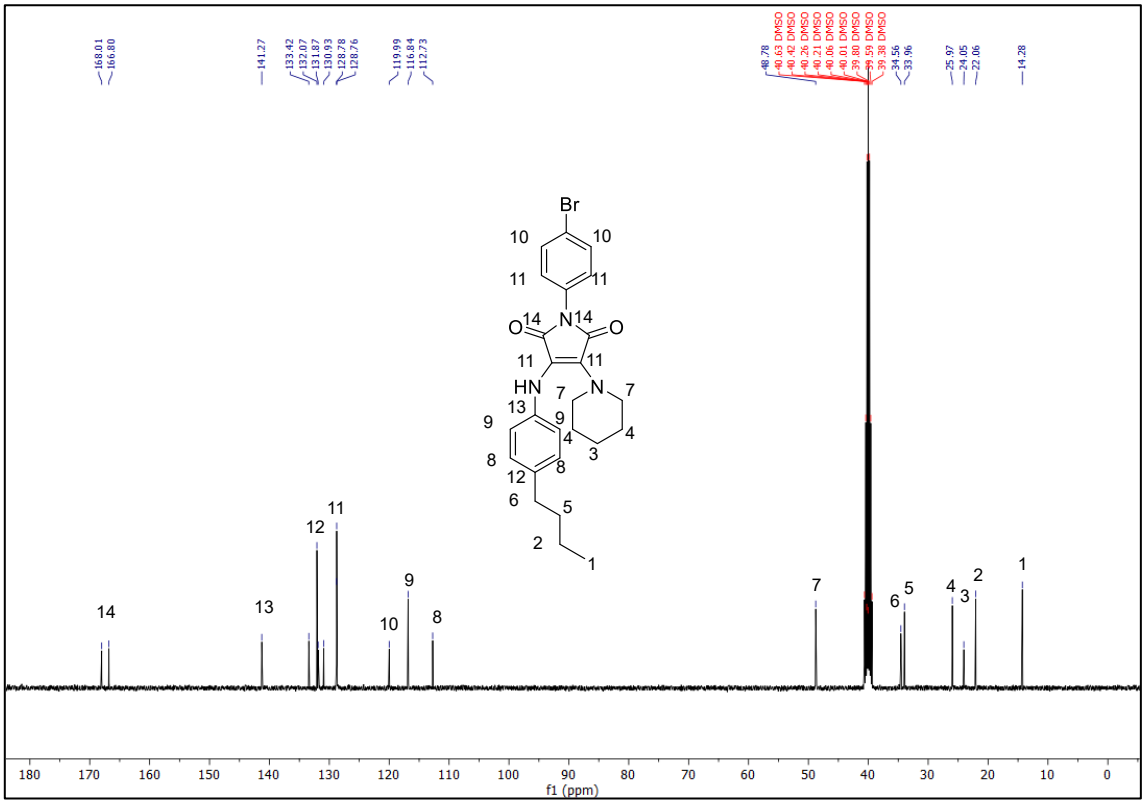

Figure 15 (a) $^{1}H$ and (b) $^{13}C$ NMR spectra of Br-B in DMSO-d6.

**I-B**

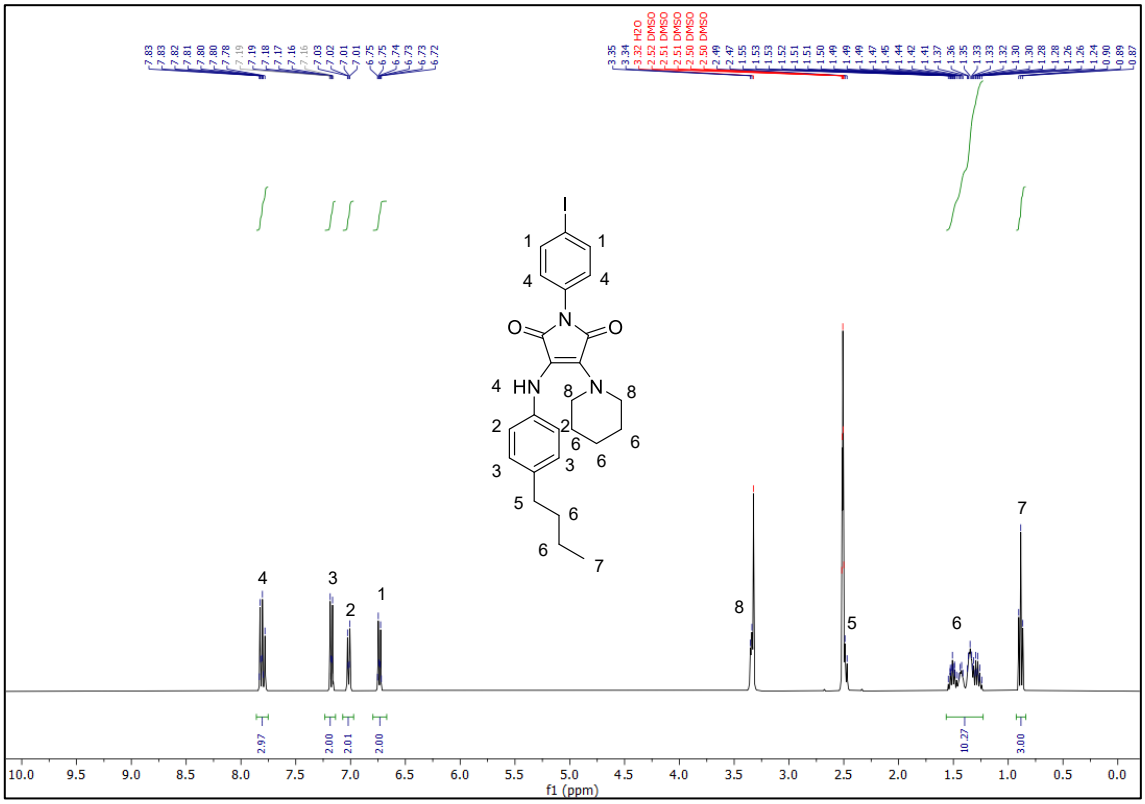


Figure 15 (a) $^{1}H$ and (b) $^{13}C$ NMR spectra of I-B in DMSO-d6.

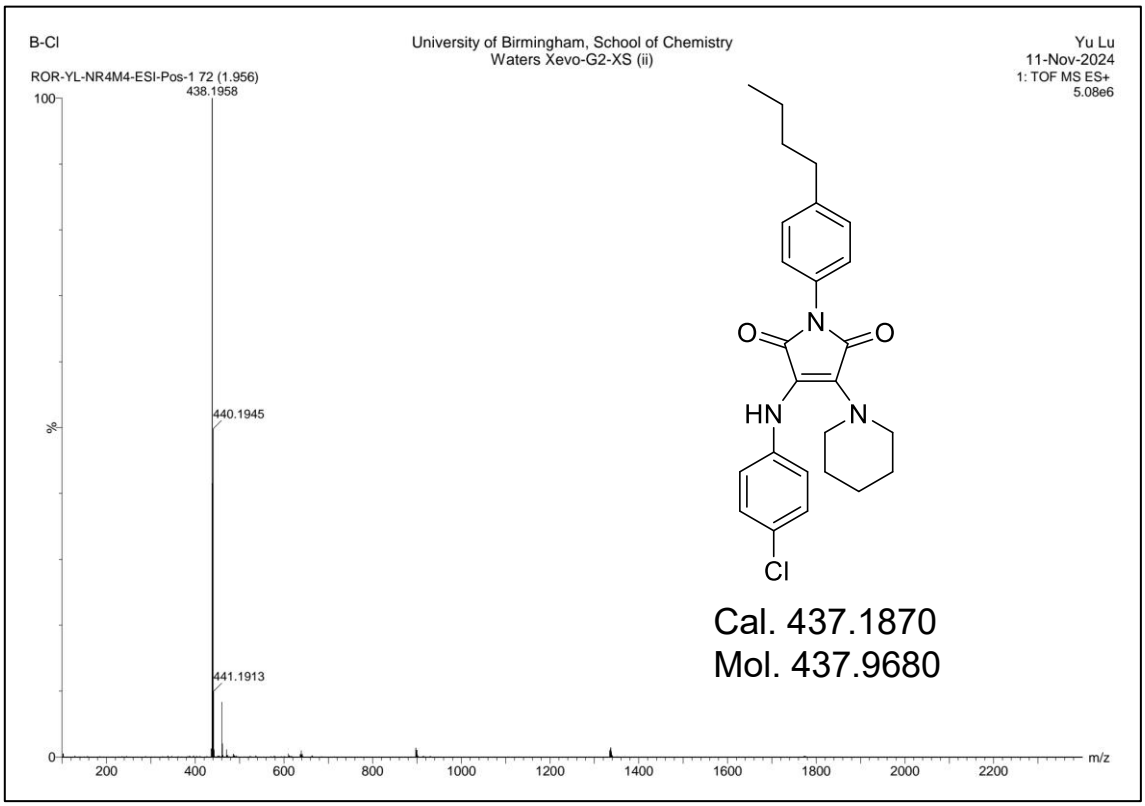


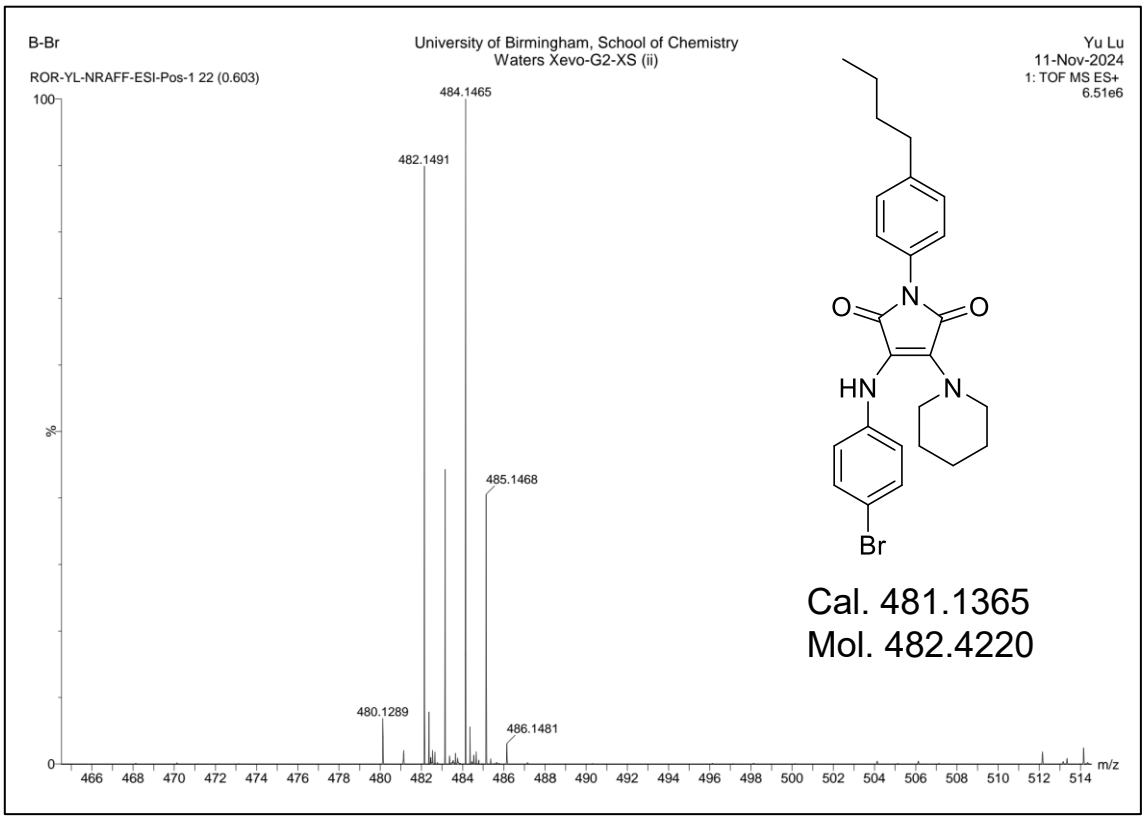

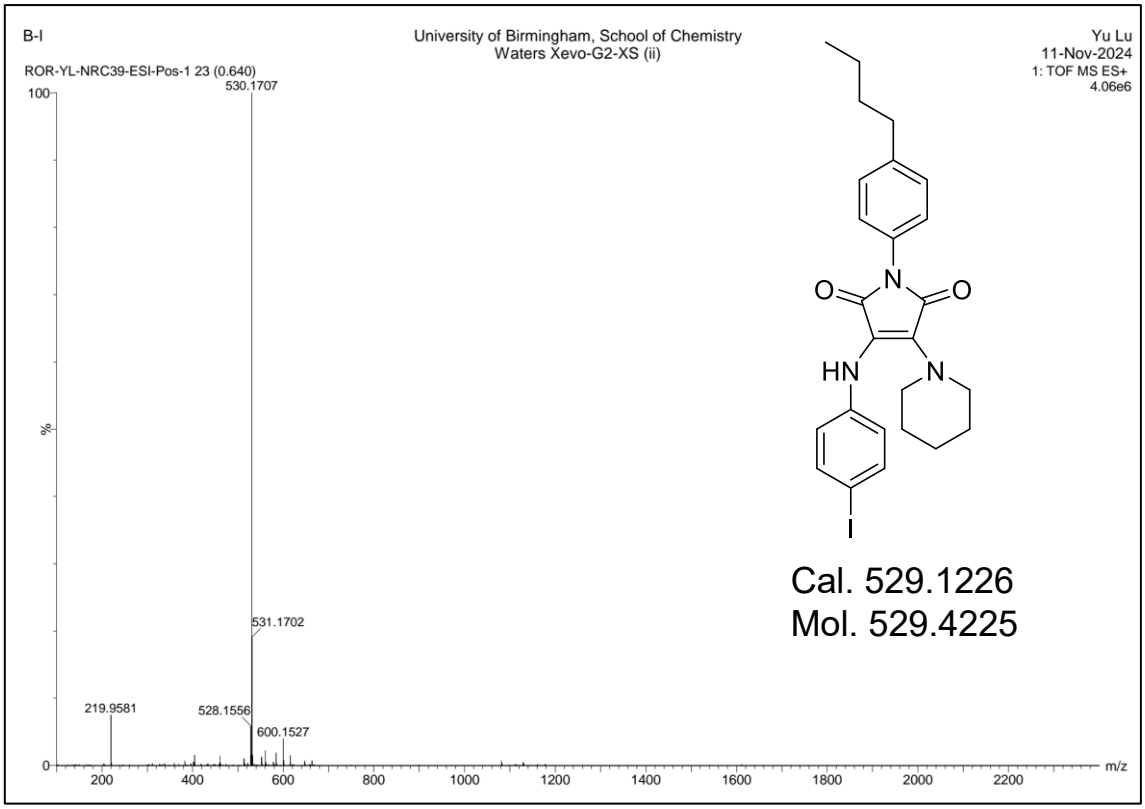
B-I
University of Birmingham, School of Chemistry
Waters Xevo-G2-XS (ii)
Yu Lu
11-Nov-2024
1: TOF MS ES+
4.06e6
ROR-YL-NRC39-ESI-Pos-1 23 (0.640)
530.1707
531.1702
219.9581
528.1556
600.1527
%
m/z
Cal. 529.1226
Mol. 529.4225

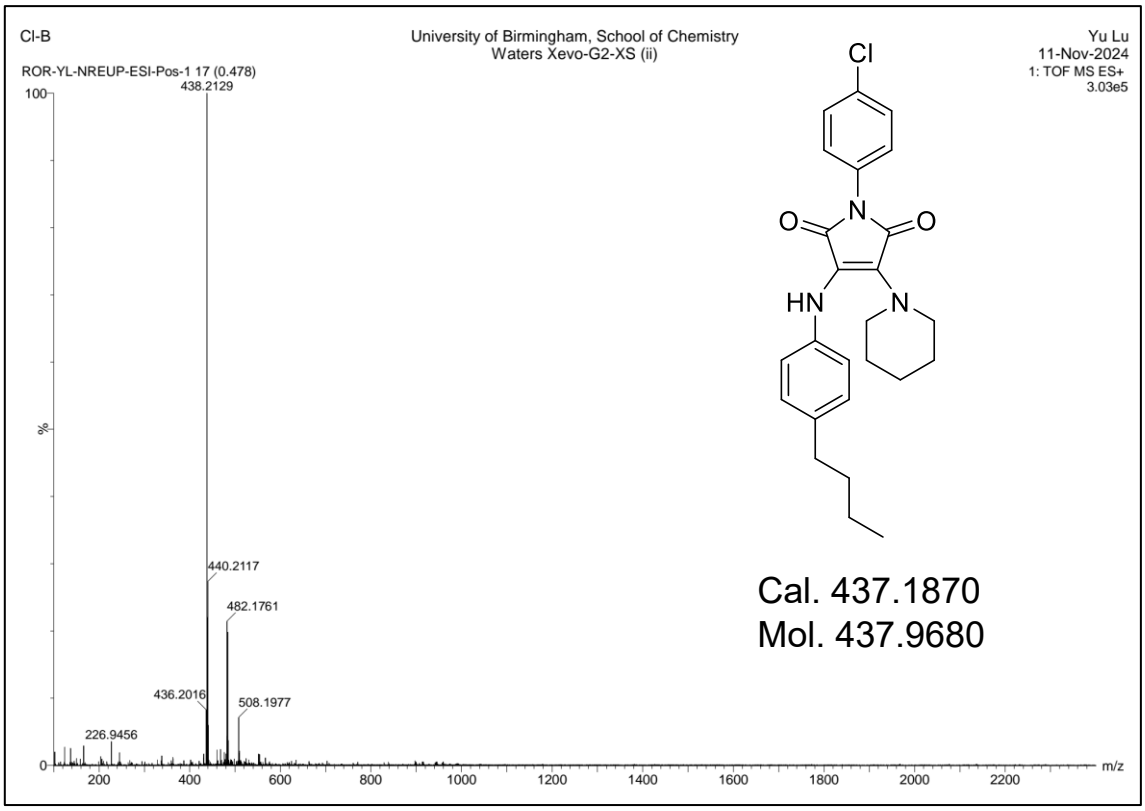
Cl-B
University of Birmingham, School of Chemistry
Waters Xevo-G2-XS (ii)
Yu Lu
11-Nov-2024
1: TOF MS ES+
3.03e5
ROR-YL-NREUP-ESI-Pos-1 17 (0.478)
438.2129
440.2117
482.1761
436.2016
508.1977
226.9456
%
m/z
Cal. 437.1870
Mol. 437.9680

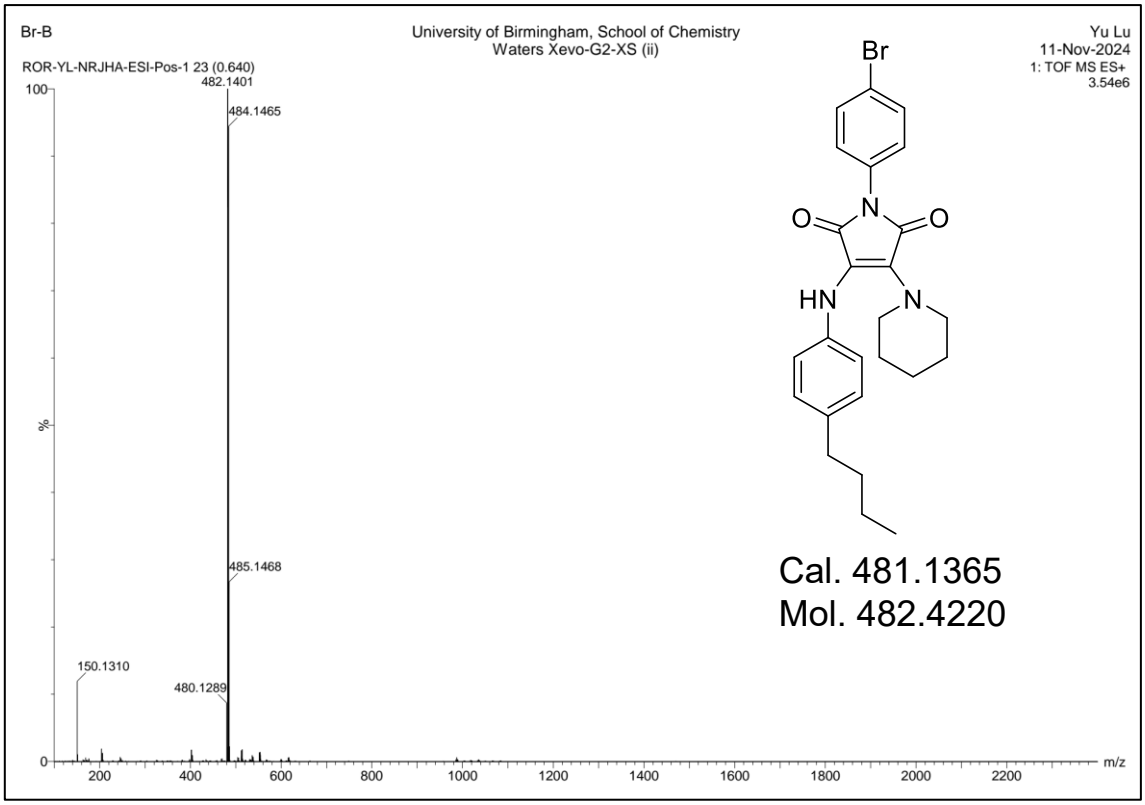
Br-B
University of Birmingham, School of Chemistry
Waters Xevo-G2-XS (ii)
Yu Lu
11-Nov-2024
1: TOF MS ES+
3.54e6
ROR-YL-NRJHA-ESI-Pos-1 23 (0.640)
482.1401
484.1465
485.1468
150.1310
480.1289
100
%
0
200
400
600
800
1000
1200
1400
1600
1800
2000
2200
m/z
Br
O
N
O
HN
N
Cal. 481.1365
Mol. 482.4220

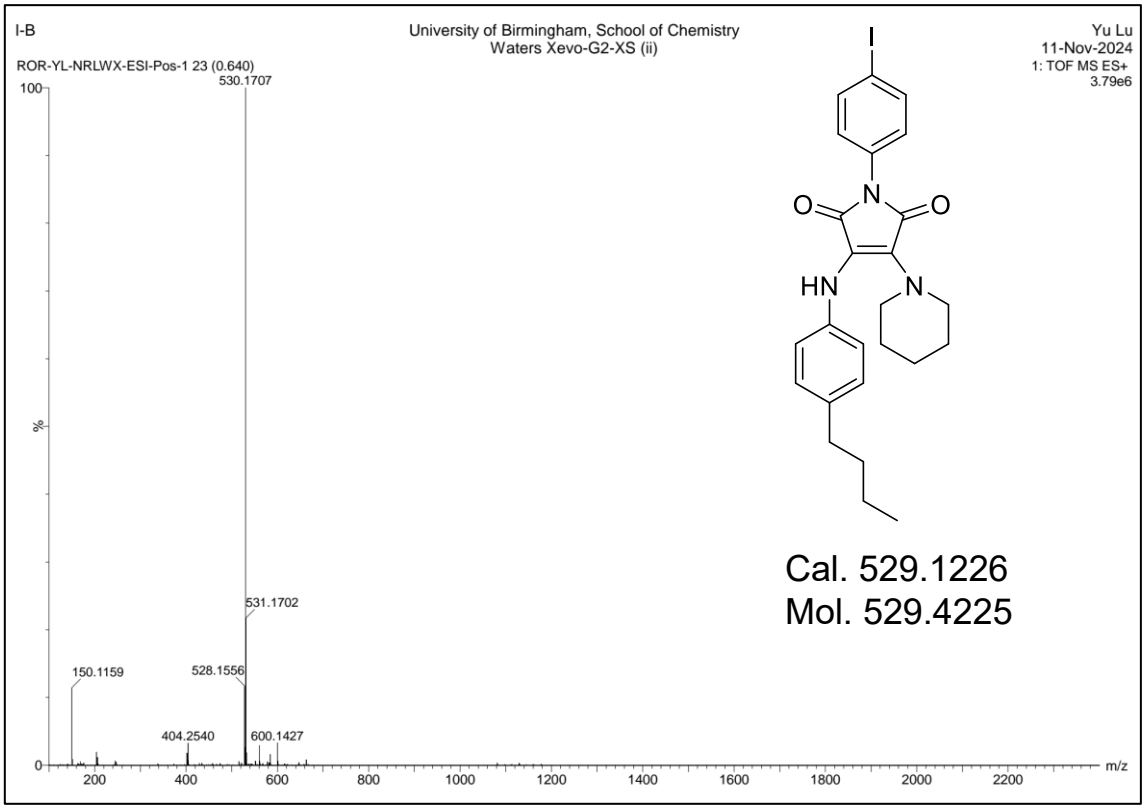
I-B
University of Birmingham, School of Chemistry
Waters Xevo-G2-XS (ii)
Yu Lu
11-Nov-2024
1: TOF MS ES+
3.79e6
ROR-YL-NRLWX-ESI-Pos-1 23 (0.640)
530.1707
531.1702
150.1159
528.1556
404.2540
600.1427
100
%
0
200
400
600
800
1000
1200
1400
1600
1800
2000
2200
m/z
I
O
N
O
HN
N
Cal. 529.1226
Mol. 529.4225

## 2.4.7 Characterization of photophysical properties

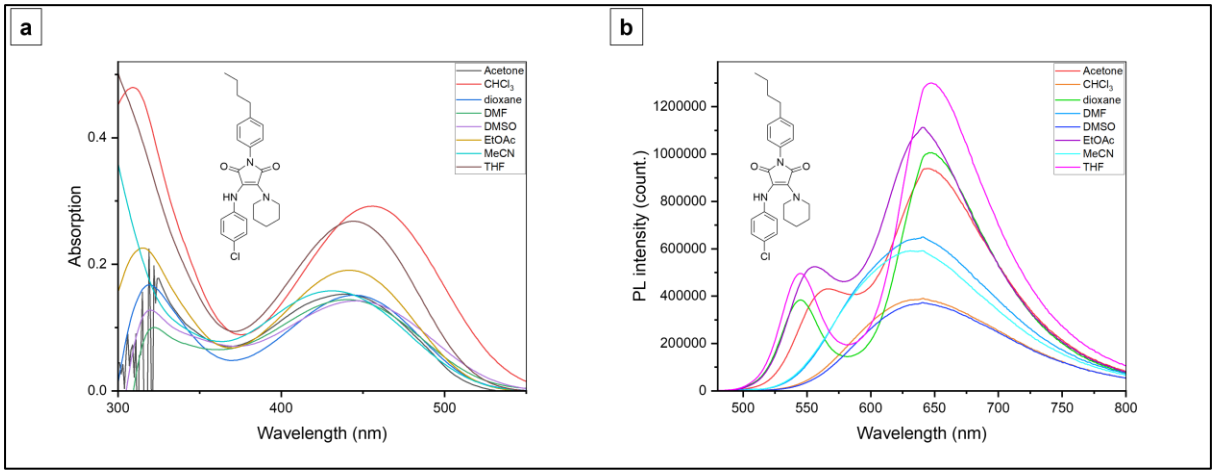


Figure 16 UV absorption (a) and FL spectra (b) in different solvents.

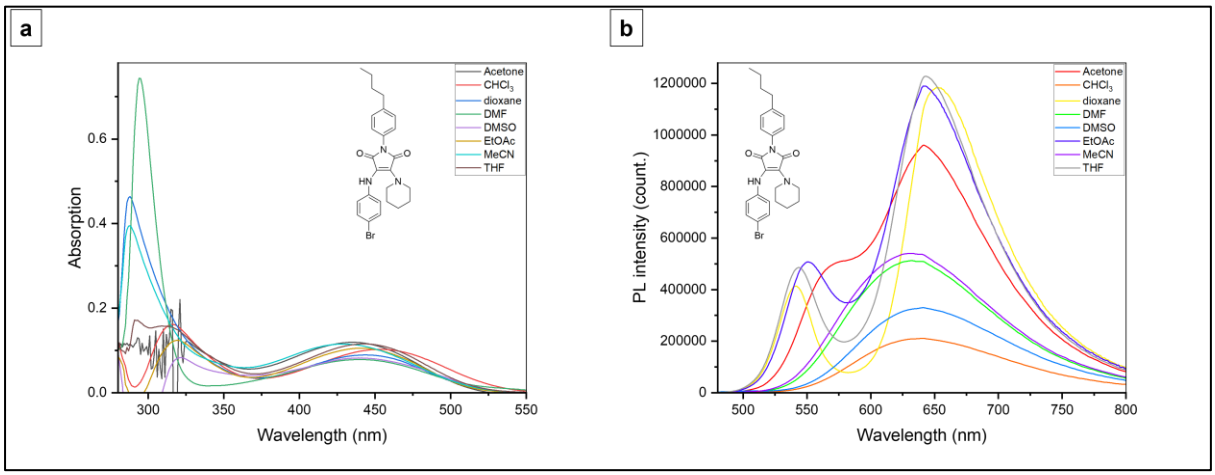


Figure 17 UV absorption (a) and FL spectra (b) in different solvents.

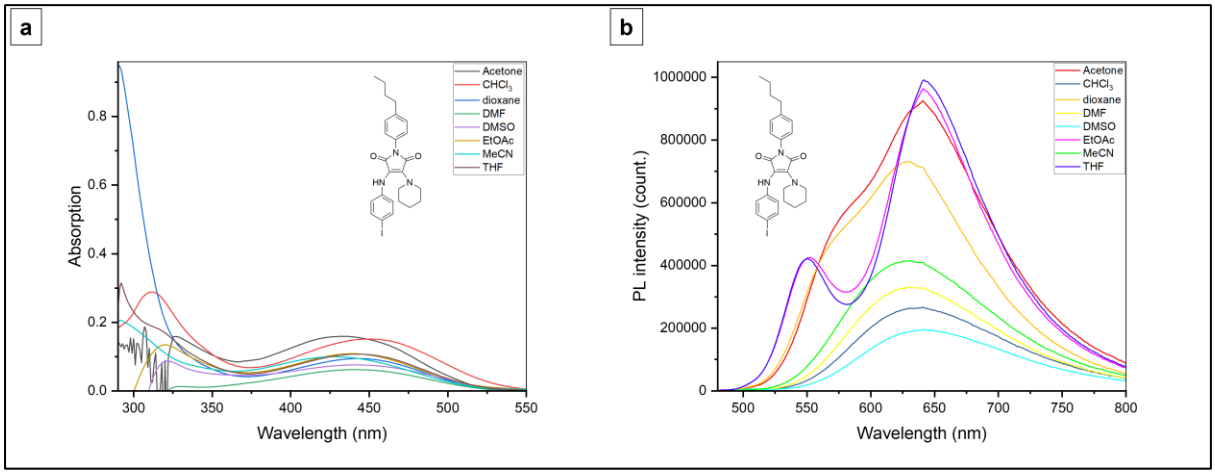


Figure 18 UV absorption (a) and FL spectra (b) in different solvents.

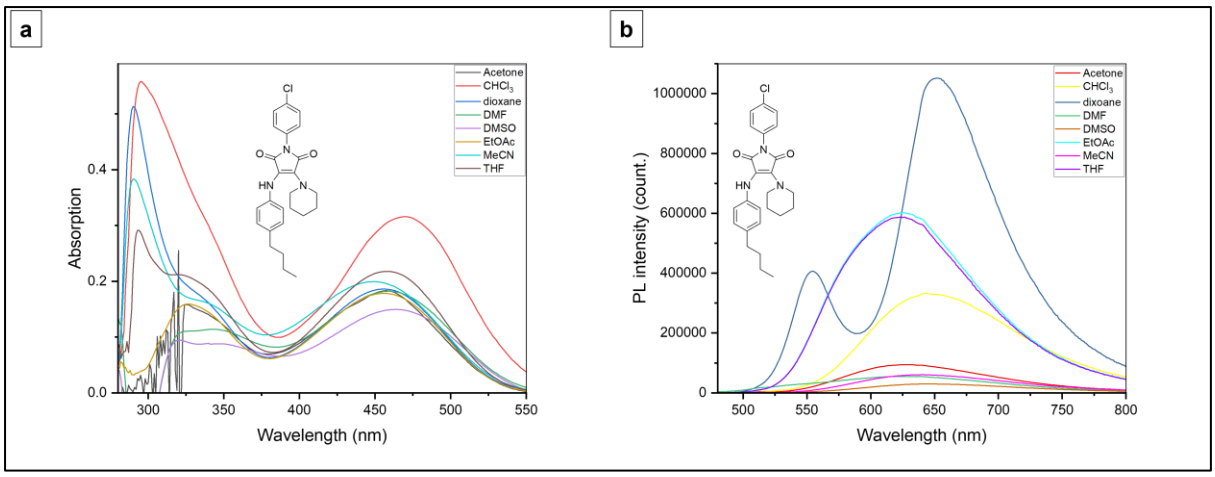


Figure 19 UV absorption (a) and FL spectra (b) in different solvents.

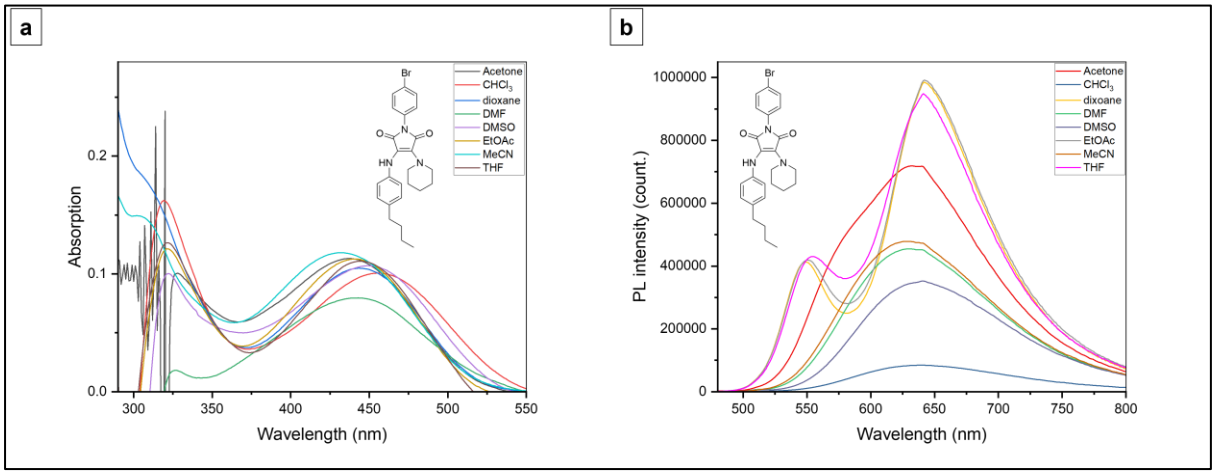


Figure 20 UV absorption (a) and FL spectra (b) in different solvents.

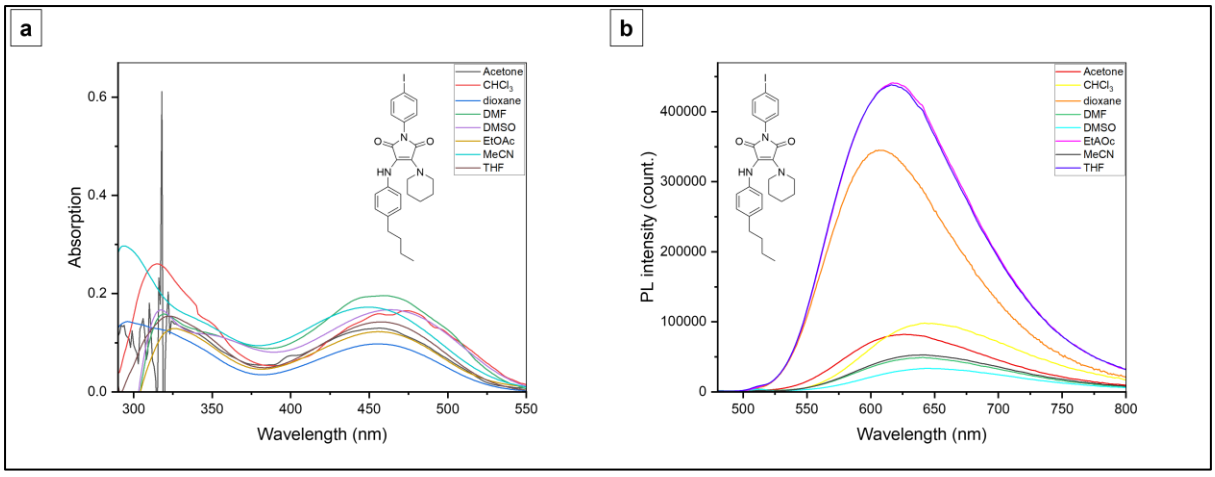


Figure 21 UV absorption (a) and FL spectra (b) in different solvents.

## 2.4.9 Frontier molecular orbitals

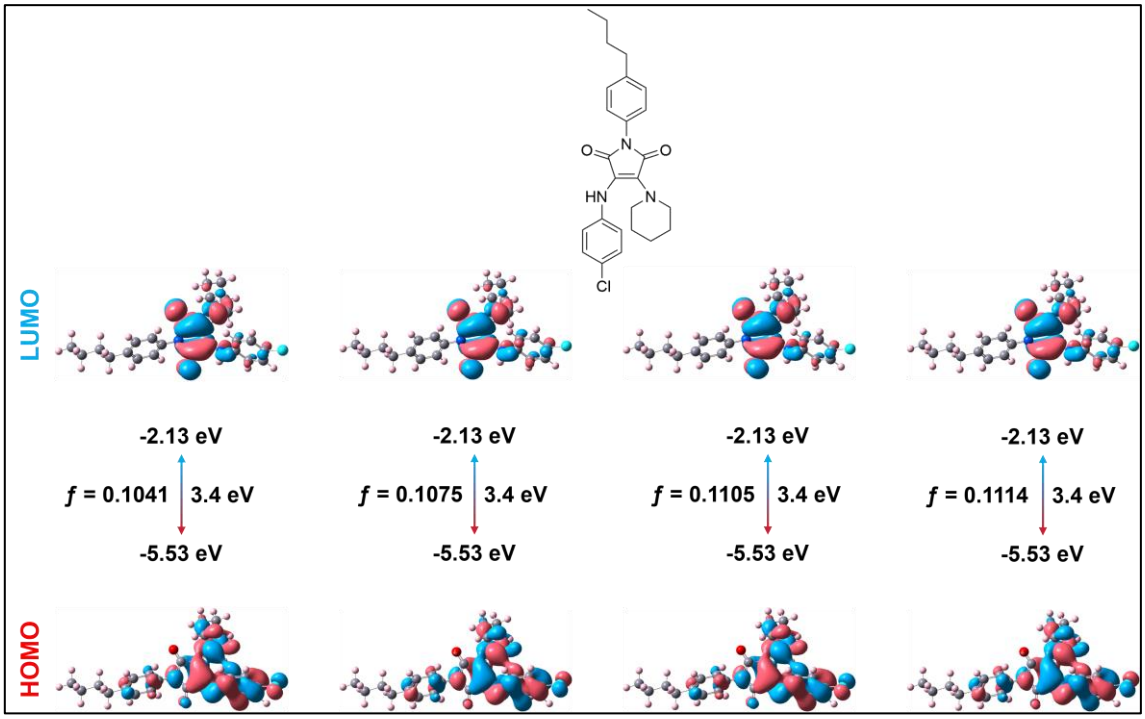


Figure 22 Frontier molecular orbitals and oscillator strength (*f*) in different solvents (from left to right is $CHCl_3$, dioxane, THF).

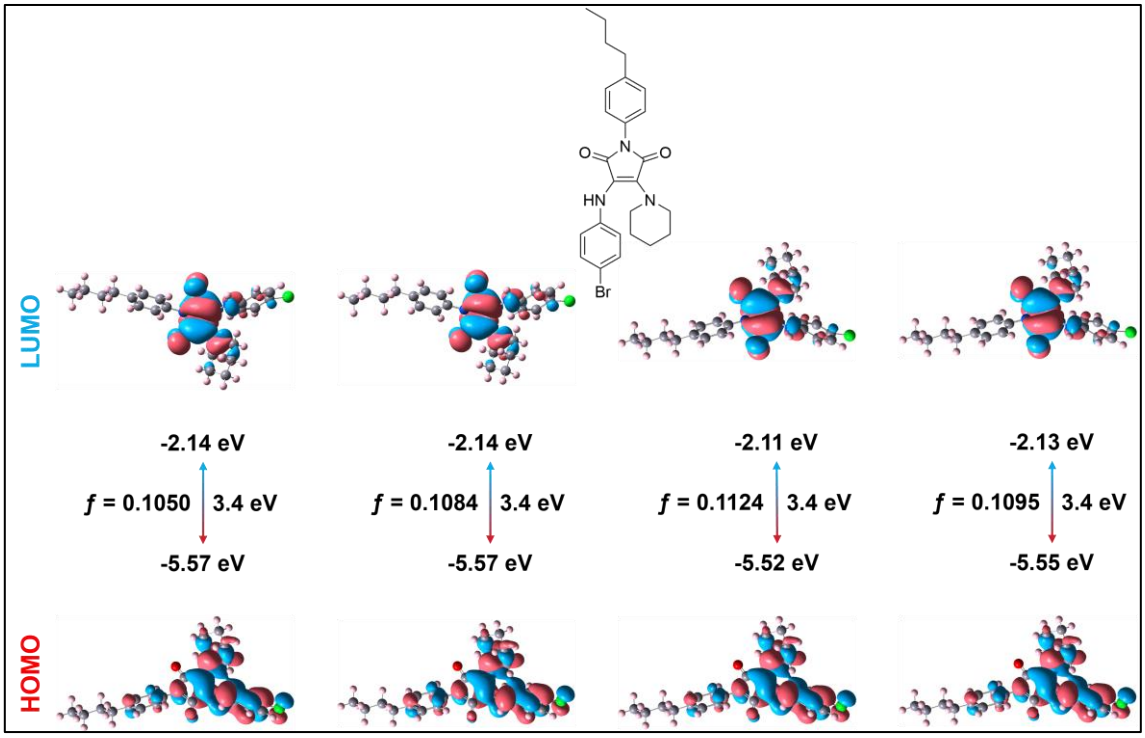


Figure 23 Frontier molecular orbitals and oscillator strength (*f*) in different solvents (from left to right is $CHCl_3$, dioxane, THF).

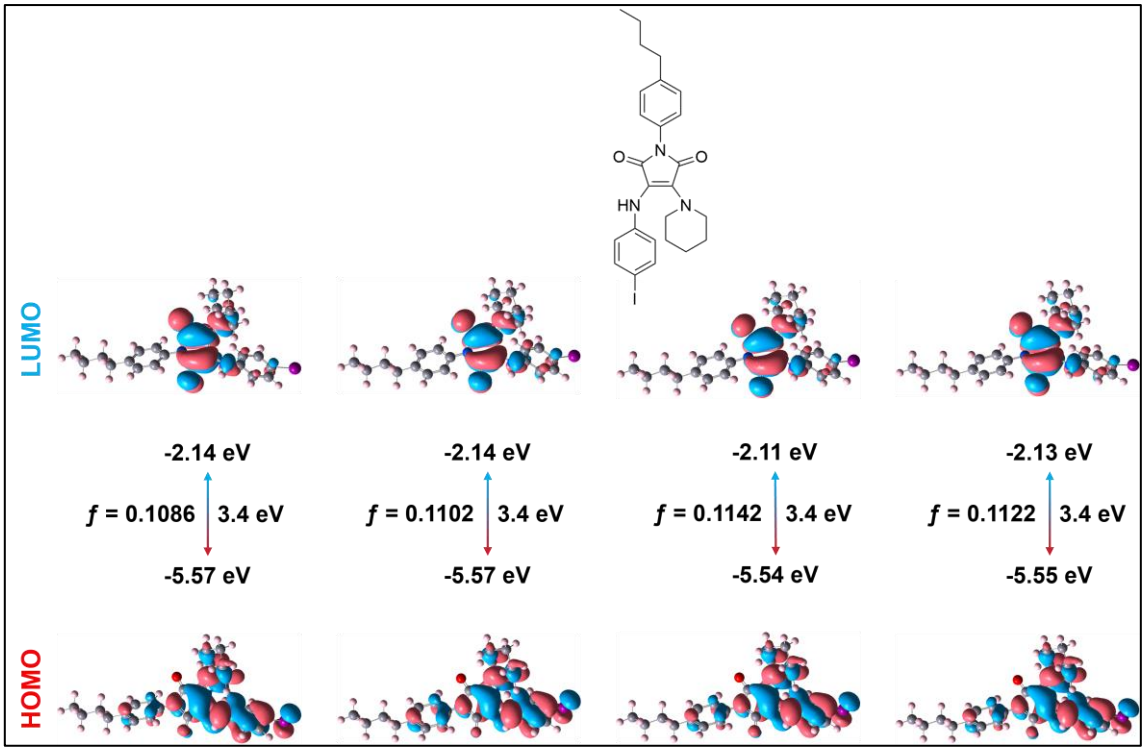


Figure 24 Frontier molecular orbitals and oscillator strength (*f*) in different solvents (from left to right is $CHCl_3$, dioxane, THF).

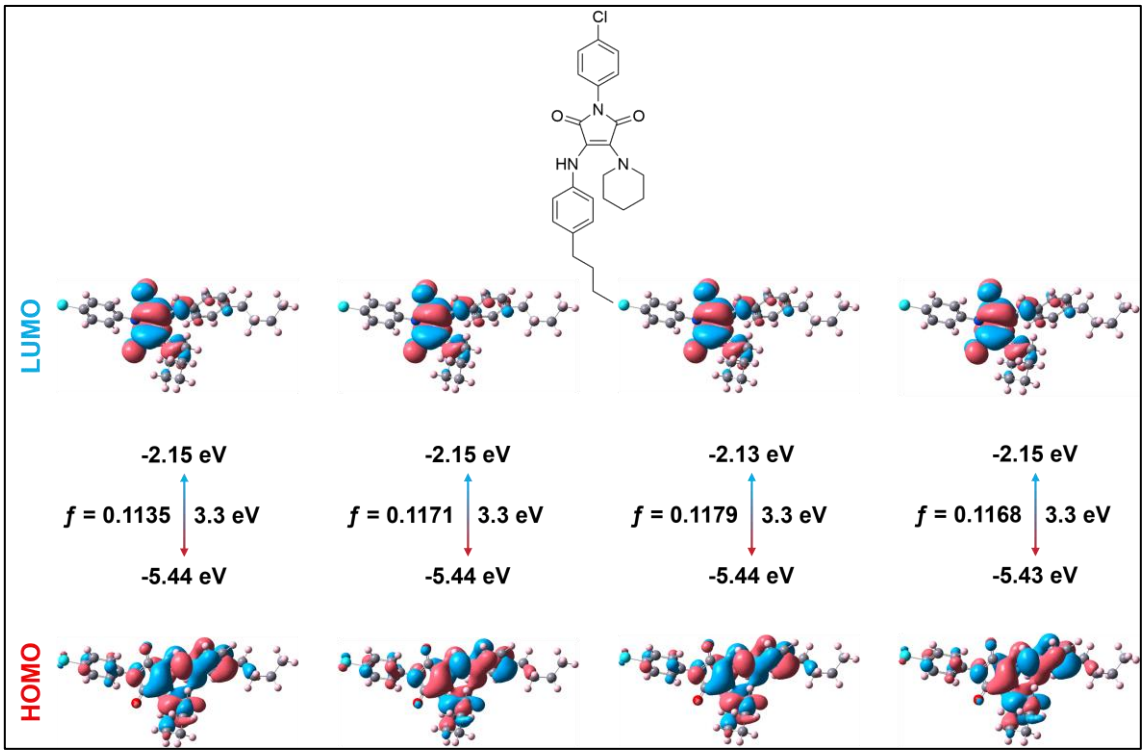


Figure 25 Frontier molecular orbitals and oscillator strength (*f*) in different solvents (from left to right is $CHCl_3$, dioxane, THF).

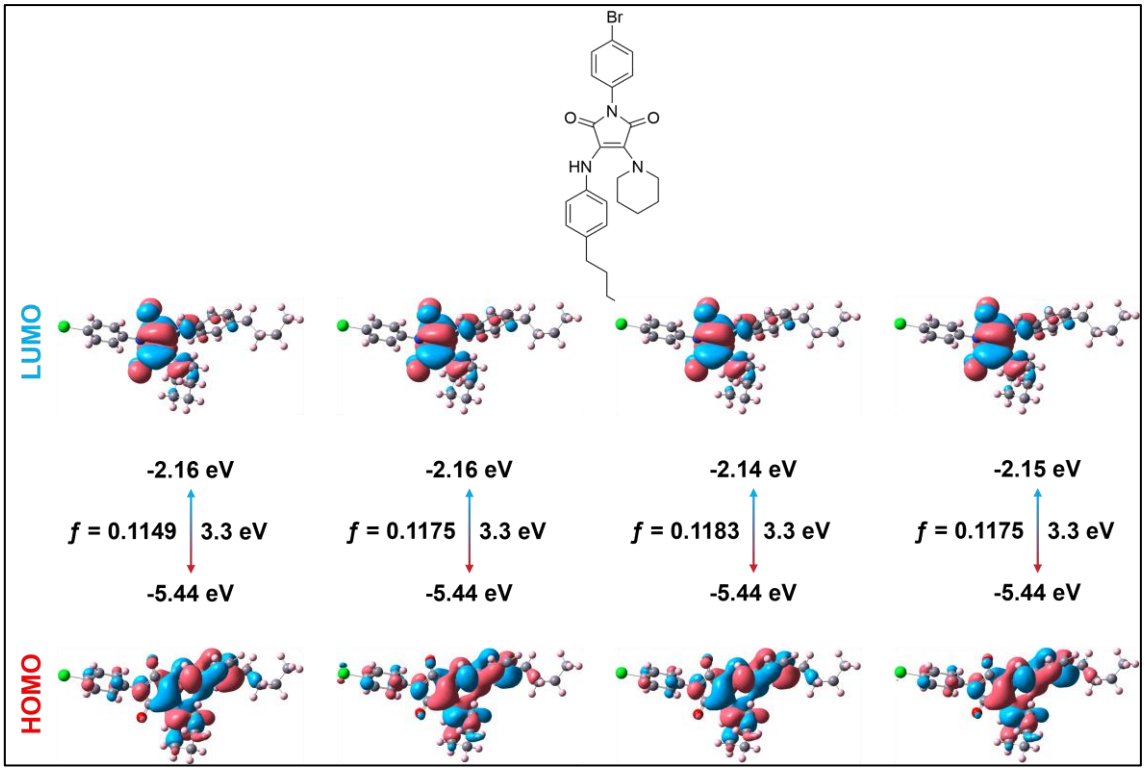


Figure 26 Frontier molecular orbitals and oscillator strength (*f*) in different solvents (from left to right is $CHCl_3$, dioxane, THF).

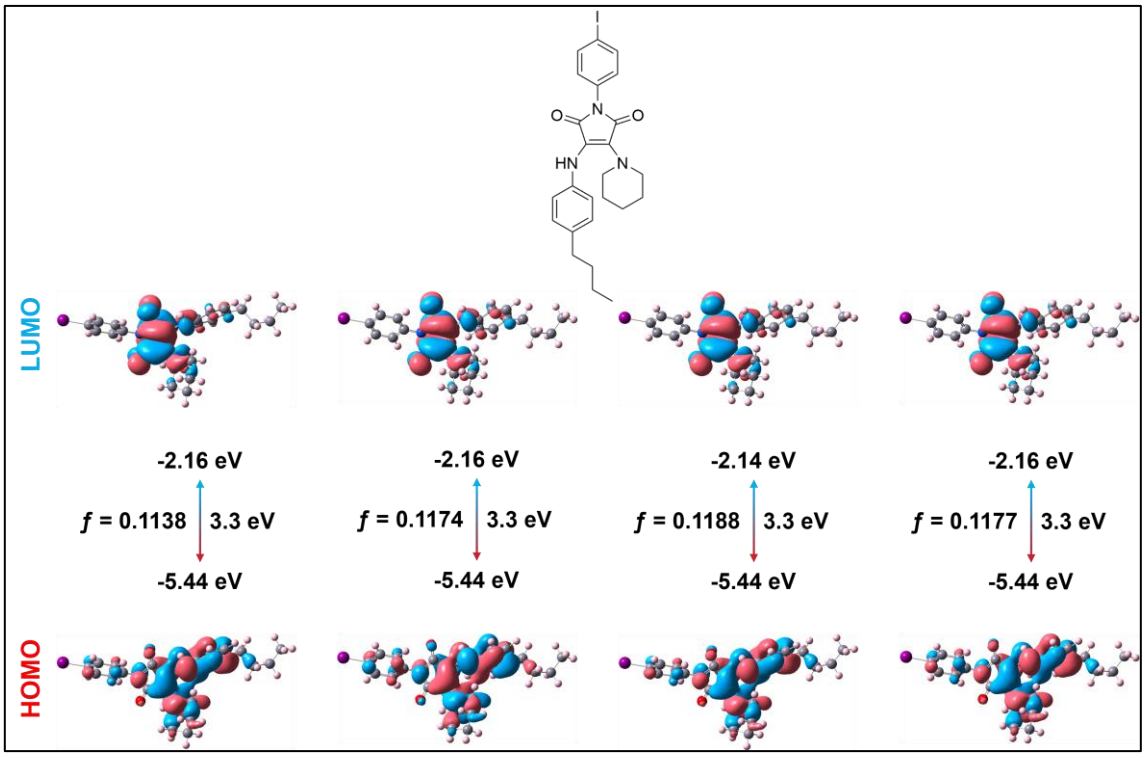


Figure 27 Frontier molecular orbitals and oscillator strength (*f*) in different solvents (from left to right is $CHCl_3$, dioxane, THF).

## 2.4.10 Single-crystal data

**B-Cl**

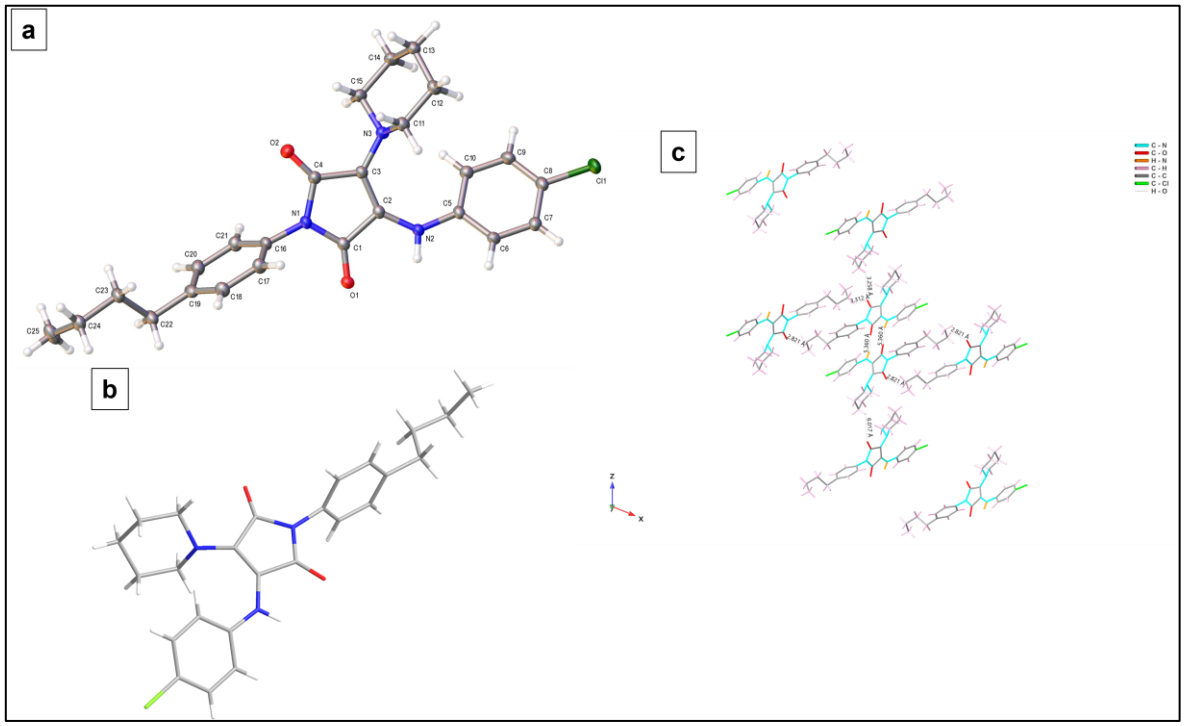


Figure 28 (a) single-crystal structure with atom number; (b) single-crystal structure; (c) molecular packing pattern.

Crystal data and structure refinement for B-Cl.

| | |
|---|---|
| Identification code | B-Cl |
| Empirical formula | C25H28N3O2Cl |
| Formula weight | 437.95 |
| Temperature/K | 100.00(10) |
| Crystal system | monoclinic |
| Space group | I2/a |
| a/Å | 23.8032(4) |
| b/Å | 6.18880(10) |
| c/Å | 31.3891(6) |
| α/° | 90 |

β/° 111.831(2)

γ/° 90

Volume/Å3 4292.42(14)

Z 8

ρcalcg/cm3 1.355

μ/mm-1 1.795

F(000) 1856.0

Crystal size/mm3 0.152 × 0.061 × 0.042

Radiation Cu Kα (λ = 1.54184)

2Θ range for data collection/° 6.066 to 157.912

Index ranges -29 ≤ h ≤ 30, -6 ≤ k ≤ 7, -36 ≤ l ≤ 39

Reflections collected 32416

Independent reflections 4563 [Rint = 0.0672, Rsigma = 0.0388]

Data/restraints/parameters 4563/0/285

Goodness-of-fit on F2 1.087

Final R indexes [I>=2σ (I)] R1 = 0.0405, wR2 = 0.0993

Final R indexes [all data] R1 = 0.0509, wR2 = 0.1054

Largest diff. peak/hole / e Å-3 0.21/-0.36

**B-Br**

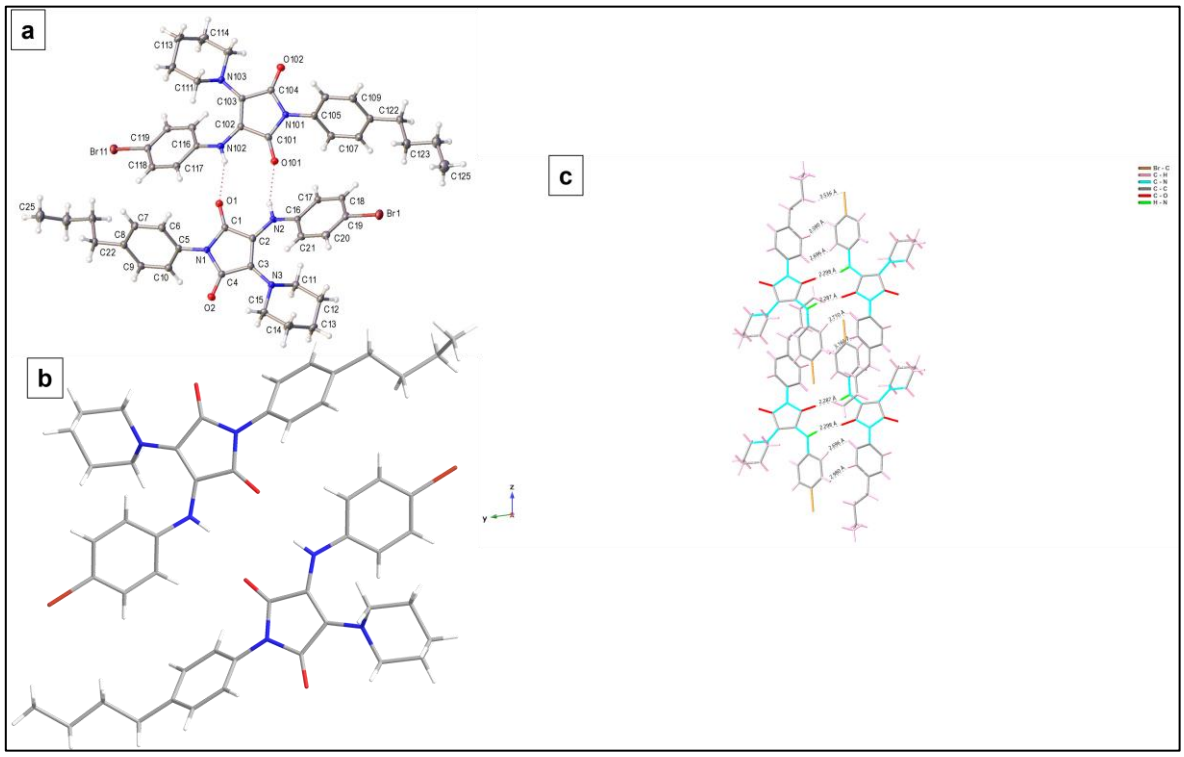


Figure 29 (a) single-crystal structure with atom number; (b) single-crystal structure; (c) molecular packing pattern.

Crystal data and structure refinement for B-Br.

| | |
|---|---|
| Identification code | B-Br |
| Empirical formula | C25H28N3O2Br |
| Formula weight | 482.41 |
| Temperature/K | 100.00(10) |
| Crystal system | triclinic |
| Space group | P-1 |
| a/Å | 9.18320(10) |
| b/Å | 12.35360(10) |
| c/Å | 20.14360(10) |
| α/° | 96.0940(10) |

β/° 95.5450(10)

γ/° 102.6060(10)

Volume/Å3 2200.55(3)

Z 4

ρcalcg/cm3 1.456

μ/mm-1 2.762

F(000) 1000.0

Crystal size/mm3 0.141 × 0.095 × 0.057

Radiation Cu Kα (λ = 1.54184)

2Θ range for data collection/° 4.446 to 156.654

Index ranges -11 ⩽ h ⩽ 11, -15 ⩽ k ⩽ 14, -25 ⩽ l ⩽ 23

Reflections collected 42074

Independent reflections 8917 [Rint = 0.0294, Rsigma = 0.0215]

Data/restraints/parameters 8917/0/569

Goodness-of-fit on F2 1.123

Final R indexes [I>=2σ (I)] R1 = 0.0291, wR2 = 0.0801

Final R indexes [all data] R1 = 0.0323, wR2 = 0.0820

Largest diff. peak/hole / e Å-3 0.55/-0.36

**B-I**

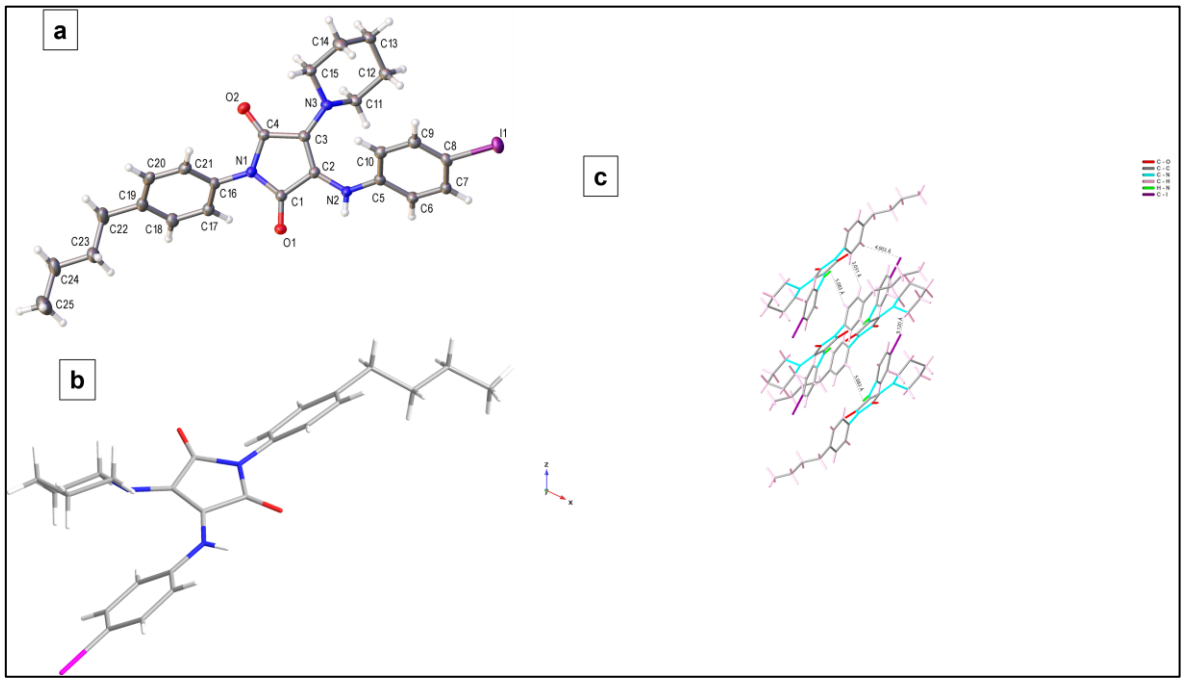


Figure 30 (a) single-crystal structure with atom number; (b) single-crystal structure; (c) molecular packing pattern.

Crystal data and structure refinement for B-I.

| | |
|---|---|
| Identification code | B-I |
| Empirical formula | C25H28N3O2I |
| Formula weight | 529.40 |
| Temperature/K | 99.99(10) |
| Crystal system | monoclinic |
| Space group | P21/c |
| a/Å | 14.0406(2) |
| b/Å | 15.0922(2) |
| c/Å | 12.0645(2) |
| α/° | 90 |
| β/° | 114.840(2) |

γ/° 90

Volume/Å3 2319.99(7)

Z 4

ρcalcg/cm3 1.516

μ/mm-1 11.051

F(000) 1072.0

Crystal size/mm3 0.098 × 0.069 × 0.042

Radiation Cu Kα (λ = 1.54184)

2Θ range for data collection/° 6.938 to 157.666

Index ranges -16 ⩽ h ⩽ 17, -19 ⩽ k ⩽ 17, -15 ⩽ l ⩽ 15

Reflections collected 22341

Independent reflections 4895 [Rint = 0.0432, Rsigma = 0.0265]

Data/restraints/parameters 4895/0/285

Goodness-of-fit on F2 1.106

Final R indexes [I>=2σ (I)] R1 = 0.0307, wR2 = 0.0793

Final R indexes [all data] R1 = 0.0327, wR2 = 0.0805

Largest diff. peak/hole / e Å-3 0.57/-0.69

**Br-B**

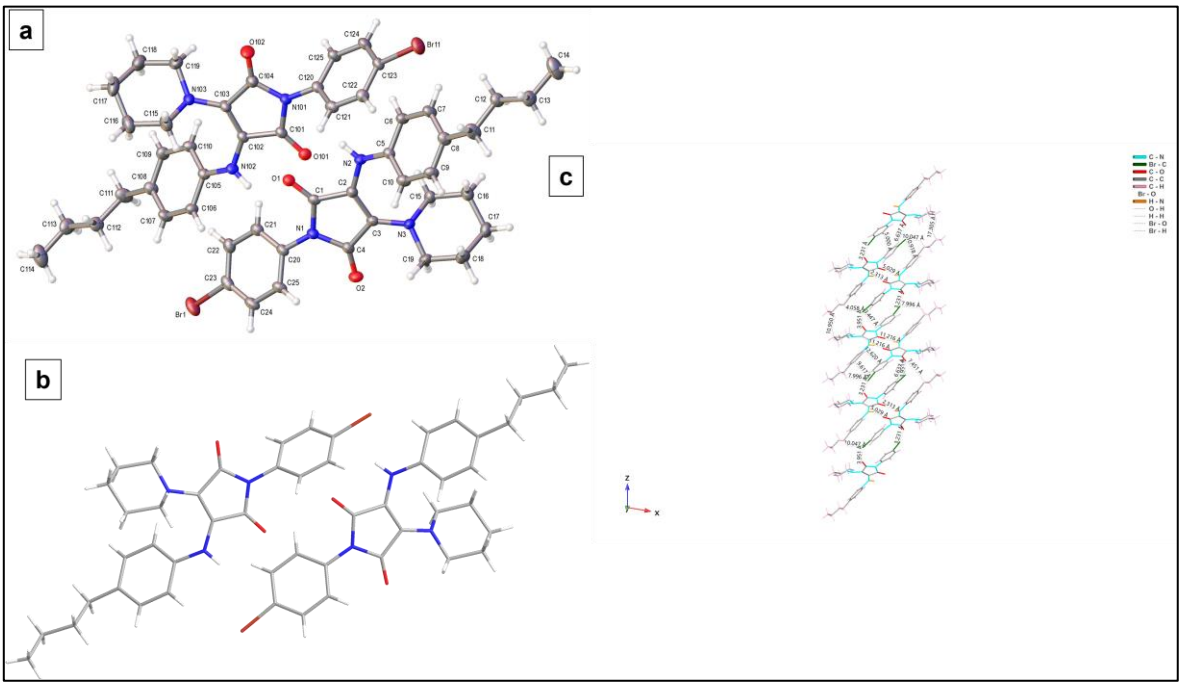


Figure 31 (a) single-crystal structure with atom number; (b) single-crystal structure; (c) molecular packing pattern.

Crystal data and structure refinement for Br-B.

| | |
|---|---|
| Identification code | Br-B |
| Empirical formula | C25H28N3O2Br |
| Formula weight | 482.41 |
| Temperature/K | 150.00(10) |
| Crystal system | monoclinic |
| Space group | P21/c |
| a/Å | 17.7107(7) |
| b/Å | 6.4169(3) |
| c/Å | 40.1057(13) |
| α/° | 90 |
| β/° | 99.326(3) |

γ/° 90

Volume/Å3 4497.7(3)

Z 8

ρcalcg/cm3 1.425

μ/mm-1 2.702

F(000) 2000.0

Crystal size/mm3 0.25 × 0.06 × 0.04

Radiation Cu Kα (λ = 1.54184)

2Θ range for data collection/° 7.27 to 154.076

Index ranges -22 ⩽ h ⩽ 20, -8 ⩽ k ⩽ 7, -31 ⩽ l ⩽ 50

Reflections collected 24767

Independent reflections 9319 [Rint = 0.0537, Rsigma = 0.0583]

Data/restraints/parameters 9319/1/568

Goodness-of-fit on F2 1.042

Final R indexes [I>=2σ (I)] R1 = 0.0498, wR2 = 0.1181

Final R indexes [all data] R1 = 0.0709, wR2 = 0.1312

Largest diff. peak/hole / e Å-3 0.61/-0.69

**I-B**

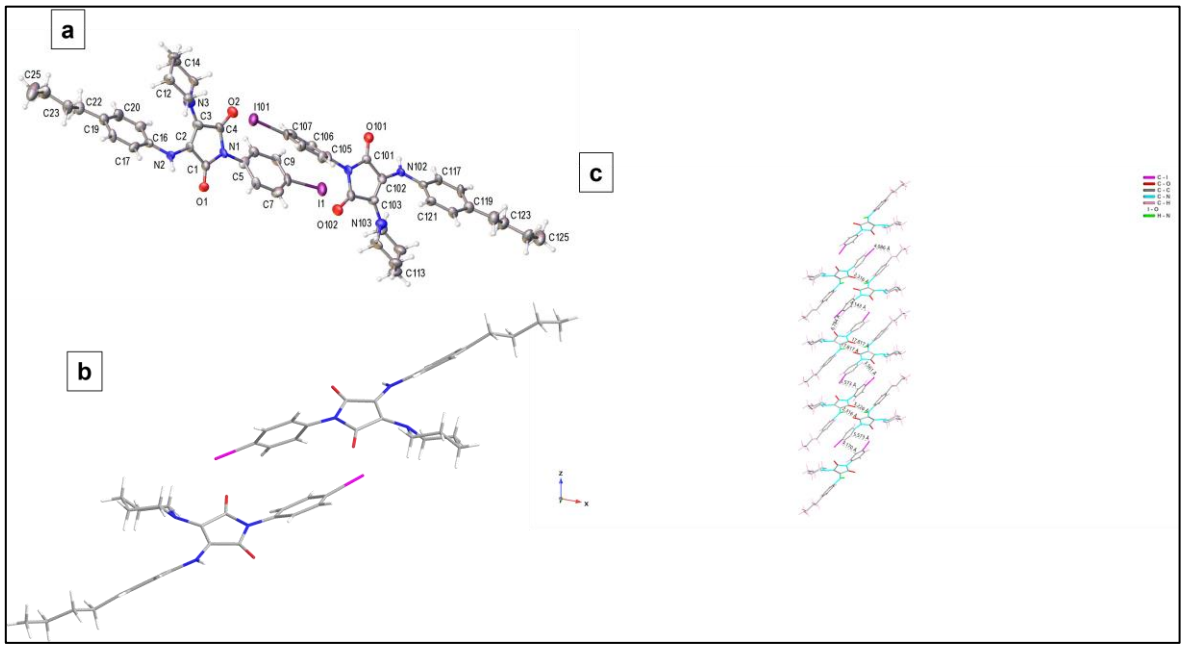


Figure 32 (a) single-crystal structure with atom number; (b) single-crystal structure; (c) molecular packing pattern.

Crystal data and structure refinement for I-B.

| | |
|---|---|
| Identification code | I-B |
| Empirical formula | C25H28N3O2I |
| Formula weight | 529.40 |
| Temperature/K | 149.99(10) |
| Crystal system | monoclinic |
| Space group | P21/c |
| a/Å | 17.6222(6) |
| b/Å | 6.4081(2) |
| c/Å | 41.3056(12) |
| α/° | 90 |
| β/° | 99.763(3) |
| γ/° | 90 |

Volume/Å3 4596.9(3)

Z 8

ρcalcg/cm3 1.530

μ/mm-1 11.154

F(000) 2144.0

Crystal size/mm3 0.25 × 0.032 × 0.017

Radiation Cu Kα (λ = 1.54184)

2Θ range for data collection/° 5.088 to 140.142

Index ranges -21 ⩽ h ⩽ 19, -4 ⩽ k ⩽ 7, -50 ⩽ l ⩽ 46

Reflections collected 26765

Independent reflections 8511 [Rint = 0.0630, Rsigma = 0.0549]

Data/restraints/parameters 8511/0/561

Goodness-of-fit on F2 1.606

Final R indexes [I>=2σ (I)] R1 = 0.1362, wR2 = 0.3690

Final R indexes [all data] R1 = 0.1549, wR2 = 0.3840

Largest diff. peak/hole / e Å-3 7.12/-2.35

# Chapter 3 Innovative Coupling of Photoresponsive Moieties with Maleimide Groups for Multichromatic Photochromism

## 3.1 Design philosophy of this work

Photoisomerizable molecules, such as azobenzene, undergo significant spatial configuration changes during the transition from the *trans* to the *cis* configuration. This is because the *trans* configuration tends to be planar, and during the transition to the *cis* configuration, the molecule undergoes a "flipping" process, leading to a reduction in conjugation.[93,190] Therefore, the change in conjugation degree caused by spatial configuration changes is a key feature of photoisomerizable molecules, which can typically be observed in UV absorption spectra.[191,192]

Currently, the general design strategy for photoresponsive fluorescent compounds involves using known photoresponsive molecules (e.g., azobenzene) as the basic framework, with donor and acceptor groups introduced at the para-positions to construct D-π-A systems. The introduction of donor-acceptor (D-A) systems can induce intramolecular charge transfer effects and increase molecular polarization, thereby influencing the degree of charge separation between the ground and excited states, which in turn affects photophysical properties. For example, Filip et al. introduced a donor-acceptor system into stilbene derivatives, utilizing the differences between the cis and trans configurations during photoisomerization to create photochromic compounds.[193] Similarly, Jaung et al. used dithienylethene as a framework to construct a D-π-A system and successfully synthesized photochromic compounds.[194] From these D-π-A system designs, it can be observed that, in the absence of a photoresponse, the electron cloud is delocalized over the donor and acceptor regions in the ground and excited states, respectively. However, upon photoresponse, the chemical structure or spatial configuration of the photoresponsive molecule changes, leading to significant alterations in the overall charge transfer effect and intramolecular polarization, which in turn affects the degree of intramolecular charge separation and, consequently, the photophysical properties.

Inspired by the approach of constructing D-A systems to develop photo-responsive molecules, we

hypothesize that maleimide can serve as a backbone for synthesizing photo-responsive fluorophores. The luminescence mechanism of maleimide-based fluorophores relies on the intramolecular electron push-pull effect, similar to D-A systems. By introducing substituents with different electronic effects at the nitrogen atom and double bond of maleimide, the intramolecular push-pull strength can be modulated, resulting in fluorophores with varying emission wavelengths.[132,165] Therefore, changes in intramolecular electronic effects are critical in influencing the photophysical properties of maleimide-based fluorophores. Photo-responsive molecules, such as azobenzene, undergo configurational changes upon photoisomerization, altering the spatial conjugation, which subsequently affects the polarization and electronic effects within the molecule. If a photo-responsive molecule is connected to maleimide, a series of effects will inevitably alter the fluorophore's photophysical properties upon photoresponse. Currently, there are no reports on photo-responsive maleimide-based compounds. Therefore, in this work, we propose for the first time the integration of photo-responsive molecules with maleimide to develop photo-responsive maleimide-based fluorophores.

The design strategy is as follows: (1) To better reflect the changes brought by conjugation differences during photoisomerization, combine photoisomerizable molecules (such as azobenzene) with the nitrogen atom of maleimide to achieve maximum conjugation; (2) Introduce p-n-butylaniline and piperidine at the double bonds of maleimide. This design is considered from the following perspectives: firstly, from a synthetic viewpoint, the addition-substitution reactions of introducing p-n-butylaniline and piperidine are relatively straightforward, and the n-butyl group can enhance the solubility of the molecule. Secondly, from the perspective of photophysical properties, the introduction of diamino substituents can achieve a red shift in emission wavelength and improve the fluorescence intensity of the compound in solution (Scheme 3.1).

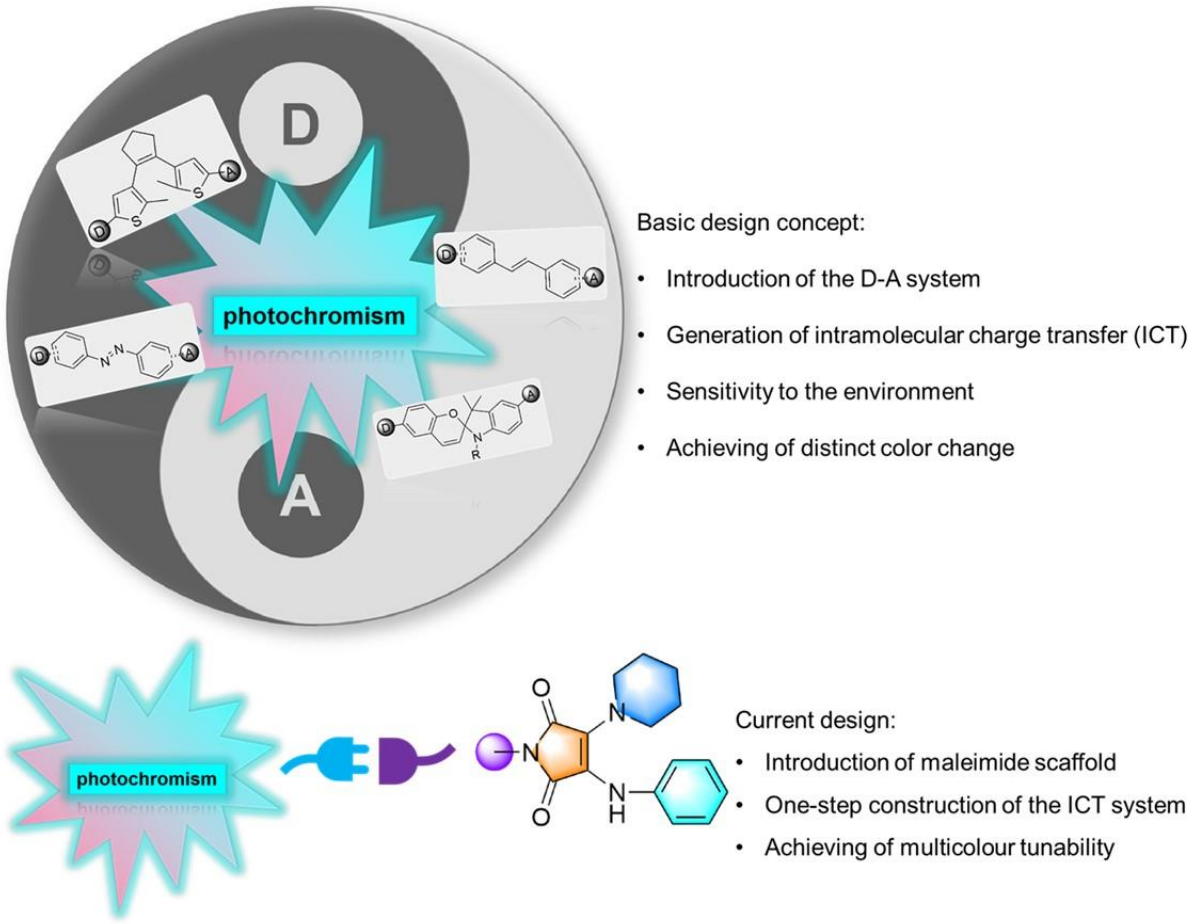


Scheme 3.1 design concept in this work.

## 3.2 Synthesis of azobenzene-based maleimide fluorophore

Firstly, aniline is diazotized in an alkaline aqueous solution of sodium nitrite, followed by coupling in a hydrochloric acid aqueous solution to prepare 4-aminoazobenzene (named as azo-$NH_2$). Next, 4-aminoazobenzene is reacted with commercial 2,3-dichloromaleic anhydride in glacial acetic acid under reflux conditions to synthesize 2,3-dichloroazobenzene maleimide through a ring-opening dehydration condensation reaction. Finally, through an addition-elimination reaction, p-n-butylaniline and piperidine are attached to the double bonds of maleimide, resulting in the final azobenzene-based maleimide fluorophore (named as azo-M) (Figure 3.1). The obtained compound was characterized by $^{1}H$ NMR, $^{13}C$ NMR, high-resolution mass spectrometry, and single-crystal X-ray diffraction (supporting information).

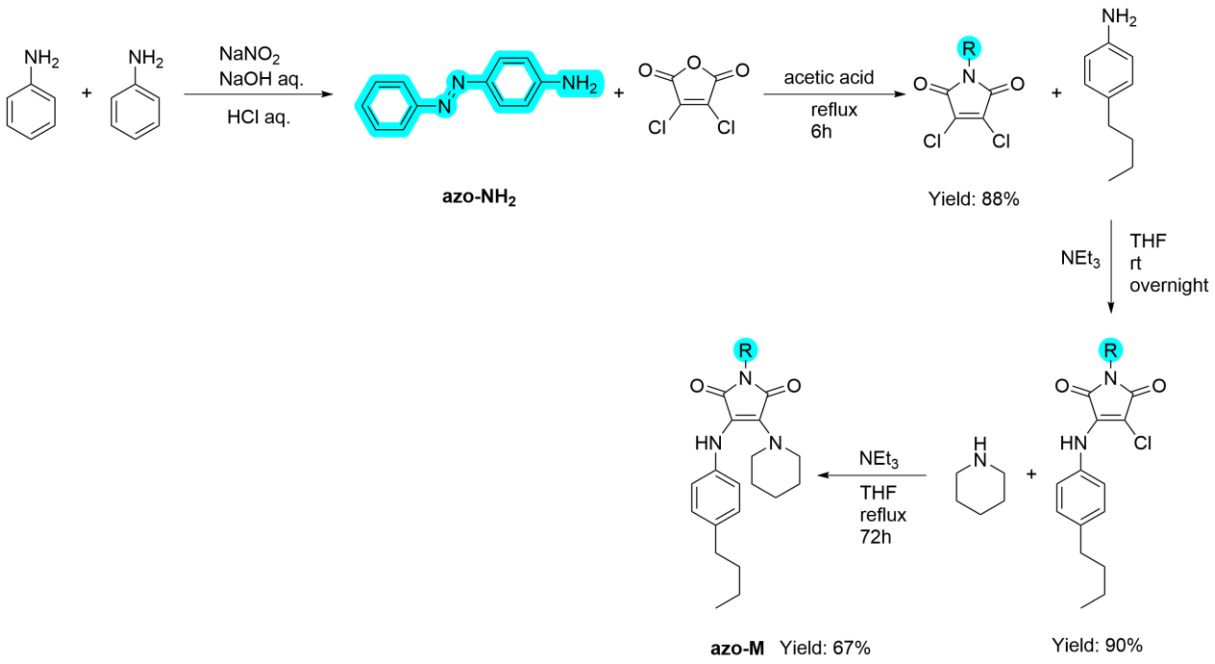


Figure 3.1 The synthetic route of the azobenzene-based maleimide fluorophore.

## 3.2.1 Results and Discussion

## Investigation of photophysical properties

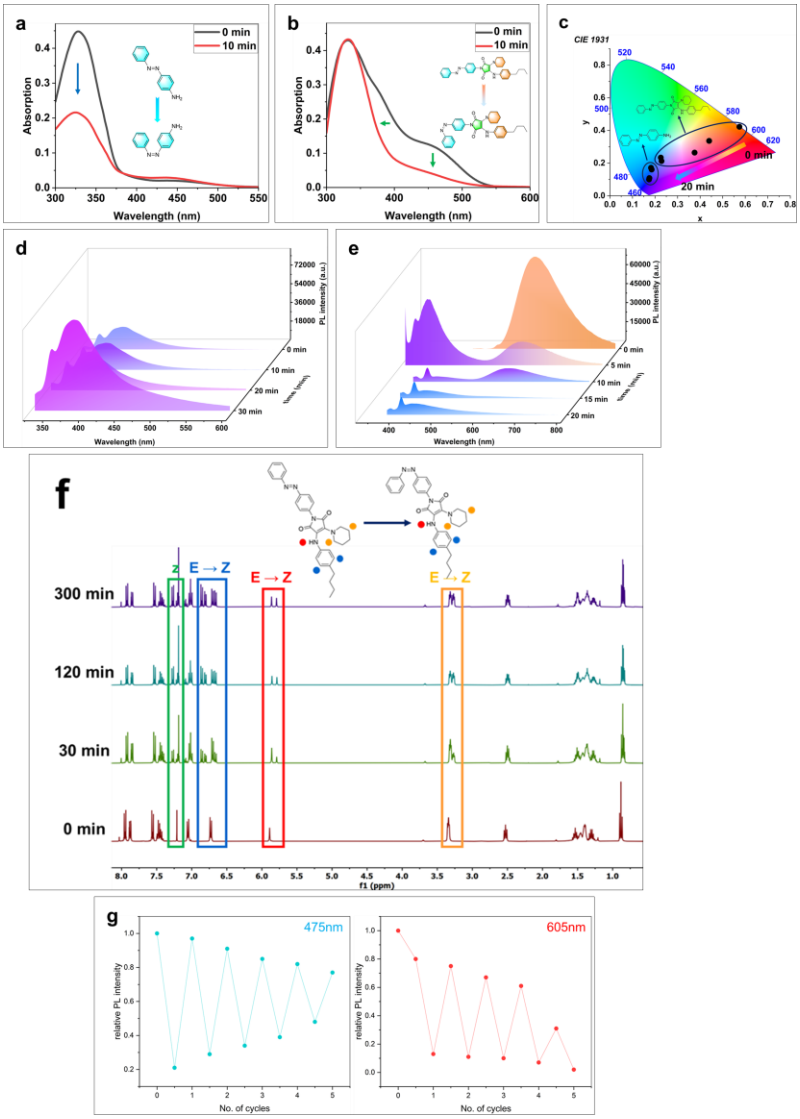


Figure 3.2 The UV-vis and fluorescent (FL) spectra of azo-$NH_2$ and azo-M were recorded in dioxane, 0.01mg/ml, Ex = 365nm. (a) UV-vis spectra of azo-$NH_2$ at 0 min and after UV (365nm) irradiation for 10 min; (b) UV-vis spectra of azo-M at 0 min and after UV irradiation for 10 min; (c) CIE diagram of azo-$NH_2$ and azo-M during various UV irradiation periods; (d) FL spectra of azo-$NH_2$ during various UV irradiation periods, the each data was recorded every 10 minutes; (e) FL spectra of azo-M during various UV irradiation periods, the each data was recorded every 5 minutes; (f) NMR spectra of azo-M during various UV irradiation periods, the data was recorded at 0, 30, 120 and 300 min, respectively. Each NMR sample was in $CDCl_3$, 10mg/ml. (g) Cycle at 475 nm under UV irradiation for 5 minutes; (h) Cycle at 605 nm under UV irradiation for 5 minutes.

The study of photoisomerization of azo-$NH_2$ has been reported multiple times.[195,196] In this work, we first characterized the photoisomerization of azo-$NH_2$ using UV and fluorescence spectroscopy. Figure 3.2 (a) shows that azo-$NH_2$ exhibits two UV absorption peaks, one around 330 nm attributed to the $\pi \rightarrow \pi^*$ transition due to azobenzene conjugation, and another around 430 nm attributed to the $n \rightarrow \pi^*$ transition of aniline. After 10 minutes of UV light irradiation, the absorption peak at 330 nm significantly decreased, due to the reduction in conjugation as azo-$NH_2$ transitions from *trans* to *cis* configuration. However, the absorption intensity at 430 nm slightly increased, due to the stronger overlap between n and π orbitals in the cis configuration compared to the *trans* configuration. Figure 3.2 (d) shows that under continuous UV irradiation, the emission peak position of azo-$NH_2$ did not shift significantly, indicating that azo-$NH_2$ did not exhibit photochromic properties during the photoisomerization process. The intensity of the emission peak gradually increases with the continuous irradiation of UV light. It is hypothesized that due to the high symmetry of the *trans* configuration, strong intermolecular π - π interactions enhance the non - radiative transition pathways. However, for the cis configuration, the decreased symmetry effectively suppresses the non - radiative transition pathways resulting from intermolecular π - π interactions, thereby enhancing the emission efficiency.[68]

Next, we characterized azo-M using the same methods. Figure 3.2 (b) shows that azo-M has two UV absorption peaks: the peak around 330 nm is attributed to the $\pi \rightarrow \pi^*$ transition of the conjugated azobenzene and maleimide, while the peak around 450 nm is due to the increased conjugation from diamine substitution and the resulting intramolecular charge transfer leading to a $\pi \rightarrow \pi^*$ transition. Figure 3.2 (e) shows that the emission wavelength of azo-M exhibits a significant red shift compared to azo-$NH_2$, which is attributed to the increased conjugation degree after diamine substitution and the reduced energy gap in the excited state caused by the introduction of the ICT effect.[140] Furthermore, the fluorescence spectrum of azo-M changes significantly under continuous UV irradiation. As depicted in Figure 3.2 (b), under continuous irradiation with 365nm UV light, the intensity of the absorption peak originally at 450 nm decreases, indicating a weakening of the ICT effect during the isomerization process from the *trans* configuration to the *cis* configuration. Additionally, the overall width of the absorption peak demonstrates a noticeable narrowing phenomenon. This observation can potentially be attributed to the decreased conjugation degree existing within the *cis* configuration. Specifically, the intramolecular distortion induced by such configuration changes weakens the vibrational coupling

between molecular components. As a direct consequence of this weakened interaction, the spectral linewidth of the absorption peak undergoes a significant narrowing process. In addition, Figure 3.2 (e) shows that the initial emission wavelength of azo-M is around 630 nm. With continued UV irradiation, the intensity of the initial emission peak decreases, indicating a reduction in the *trans* configuration content, while a new emission peak appears around 450 nm, attributed to the formation of the *cis* configuration. Compared to the *trans* configuration, the *cis* configuration has reduced conjugation, weakening the interaction between π-π* orbitals and increasing the HOMO-LUMO energy gap; additionally, increased twisting in the *cis* configuration typically reduces the degree of excited-state charge transfer, thereby increasing the energy gap. Therefore, the introduction of maleimide allows the molecule to exhibit photochromic properties induced by photoisomerization. Figure 3.2 (c) visually demonstrates the differences in photochromism between azo-$NH_2$ and azo-M. Under continuous UV irradiation, the fluorescence colour of azo-$NH_2$ did not change significantly, remaining in the blue region. However, for azo-M, the fluorescence colour gradually shifts from orange to blue, indicating that maleimide-based fluorophores can visually express the differences generated during photoisomerization. This characteristic is due to the sensitivity of the intramolecular push-pull electronic system to the electronic effects generated by the transition from *trans* to *cis* configuration. Figure 3.2 (f) shows the NMR spectrum, which macroscopically records the structural changes of azo-M during the photoisomerization process. As photoisomerization proceeds, the initial peak intensity gradually decreases, and new peaks appear. For example, the hydrogen atom at the aniline position (marked by the red dot in the figure) initially appears as a singlet at 5.86 ppm. During photoisomerization, a new singlet appears at 5.79 ppm, and its intensity gradually increases. According to the integration ratio calculations at different times, the proportion of the cis configuration increases before 120 minutes, but at 120 and 300 minutes, the integration ratios of the *trans* and *cis* configurations are 0.88:1.12, indicating that a photostationary state is reached after 120 minutes. Dynamic photostability constitutes a critical parameter for evaluating photo-responsive molecular performance. Systematic characterization of azo-M's dynamic photostability was conducted through the following protocol: The *trans*-isomer sample was first irradiated with 365 nm UV light for 5 minutes, followed by 24-hour dark storage to monitor spontaneous recovery. No significant intensity variations were observed at the 475 nm and 605 nm emission bands during dark incubation. To investigate photoinduced isomerization reversibility, subsequent green light

irradiation (500-550 nm, 5 minutes) induced distinct spectral changes: a marked intensity decreases at 475 nm accompanied by enhancement at 605 nm (Figure 3.2g, h). Notably, during five consecutive UV-green light cycling tests, characteristic peak intensity variations displayed progressive attenuation. The 475 nm fluorescence intensity exhibited cumulative enhancement with cycling, while the 605 nm intensity demonstrated continuous decline, culminating in the complete disappearance of the 605 nm peak after the fifth cycle. These observations reveal that the photo-isomerization reversibility of azo-M progressively deteriorates with irradiation cycles, ultimately stabilizing in the *cis*-configuration as the final state.

**Investigation of solvatochromism effect**

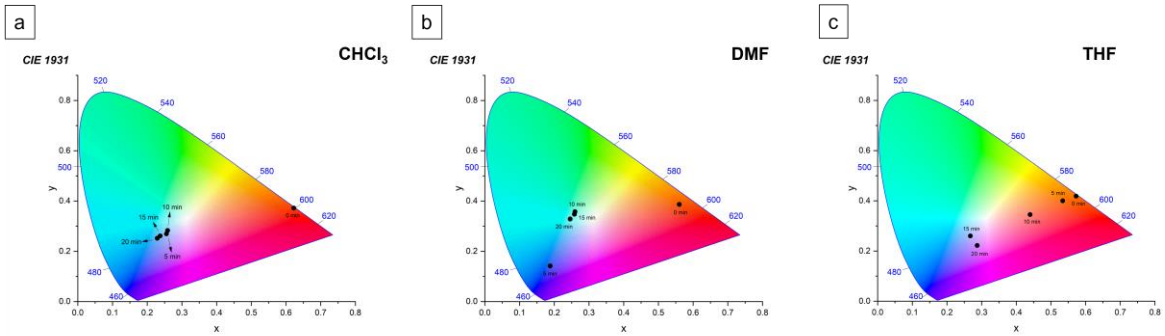


Figure 3.3 the CIE diagram of azo-M in different solvents during the different times of UV irradiation, the data was recorded each 5 mins from 0 to 20 mins. 0.01mg/ml, Ex = 365nm. (a) CHCl3; (b) DMF; (c) THF

Solvatochromism is a notable characteristic of maleimide-based fluorophores, where the fluorophores exhibit different fluorescence colours in solvents of varying polarities. This phenomenon arises from the interaction between solvent molecules and the fluorophores, affecting the intramolecular electron push-pull effect. Additionally, the intramolecular twisted charge transfer (TICT) effect under solvation also influences their photophysical properties.[197] Therefore, we further investigated the photoisomerization behaviour of azo-M in different solvents. Figure 3.3 shows that azo-M exhibits different solvent effects in solvents of varying polarities. In $CHCl_3$, the initial emission wavelength is 600 nm, while in DMF, THF, and dioxane, the initial emission wavelengths are around 630 nm. The shortest emission wavelength in $CHCl_3$ may be attributed to the best solubility of azo-M in $CHCl_3$, resulting in the weakest π-π intermolecular interactions and a relative blue shift in the emission wavelength. In DMF, THF, and dioxane, the initial emission

wavelengths did not exhibit significant solvatochromic effects, possibly due to the poor solubility of azo-M in these solvents, resulting in strong π-π intermolecular interactions that restrict intramolecular twisting, thus preventing the TICT effect from manifesting differently in solvents of varying polarities.

With continued UV irradiation, the photoisomerization behaviour of azo-M varied in different solvents. In $CHCl_3$, the fluorescence colour of azo-M completely changed to blue within just 5 minutes and remained stable thereafter, indicating a very rapid isomerization in $CHCl_3$. This is consistent with the previous hypothesis that azo-M has the best solubility and weakest intermolecular interactions in $CHCl_3$, allowing it to exist as monomers, minimizing resistance during isomerization. In DMF, the fluorescence colour also turned blue within 5 minutes, indicating good solubility. However, over time, the fluorescence colour gradually red-shifted. This may be due to the increasing intramolecular twisting force during the transition from *trans* to *cis* configuration, disrupting the π-π stacking and weakening intermolecular interactions. As the intermolecular interactions weakened, solute-solvent interactions and solvation effects gradually strengthened. Concurrently, the TICT effect in DMF became more pronounced with increasing solvation, causing a red shift in the emission wavelength after 5 minutes. In THF, the trend of fluorescence colour change indicated that the isomerization speed of azo-M was the slowest, suggesting that azo-M had the poorest solubility or the strongest intermolecular interactions in THF, resulting in an aggregated form and the greatest resistance during isomerization.

**Analysis of single-crystal structure**

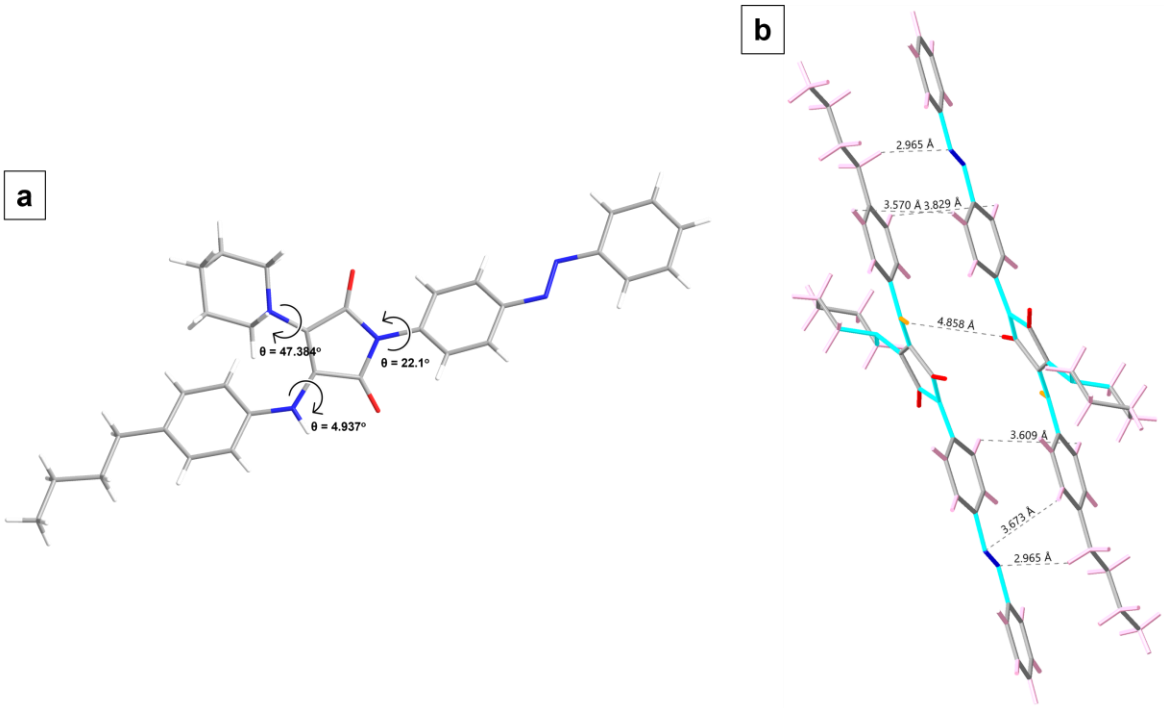


Figure 3.4 (a) single-crystal structure; (b) molecular packing pattern.

Using solvent diffusion in chloroform and n-hexane, we successfully obtained the single-crystal structure of azo-M. Figure 3.4 (a) shows that the torsional angle between the azobenzene group and the maleimide ring is 22.1°, likely due to the repulsive interactions between the nitrogen atom and surrounding atoms, requiring a degree of twisting to reduce this repulsion and stabilize the molecule. Additionally, this torsional angle helps alleviate close molecular packing, enabling the molecule to undergo photoisomerization even in high-concentration solutions. Furthermore, the relatively small torsional angle enhances the conjugation between the azobenzene group and the maleimide ring, thereby increasing the contribution of azobenzene to the photophysical properties. The torsional angle between the piperidine group and the maleimide ring is 47.384°, which could be attributed to reduced steric hindrance in this region, allowing for greater freedom of rotation of the piperidine group. The torsional angle between the p-n-butylphenyl group and the maleimide ring is only 4.937°, likely due to the increased rigidity imparted by the n-butyl group, restricting the rotation of the phenyl ring. Figure 3.4 (b) shows that various intermolecular hydrogen bonds exist, such as C-H···N at 2.965 Å and C-H···H-C hydrogen bonds ranging from 3.5 to 4 Å. These weak interactions effectively limit intermolecular motion, reducing non-radiative decay pathways

and thus enhancing the luminescence of the molecule in solution. Additionally, the piperidine group does not participate in intermolecular packing and exhibits no significant intermolecular interactions, which also explains the larger torsional angle between the piperidine group and the maleimide ring.

**Theoretical analysis**

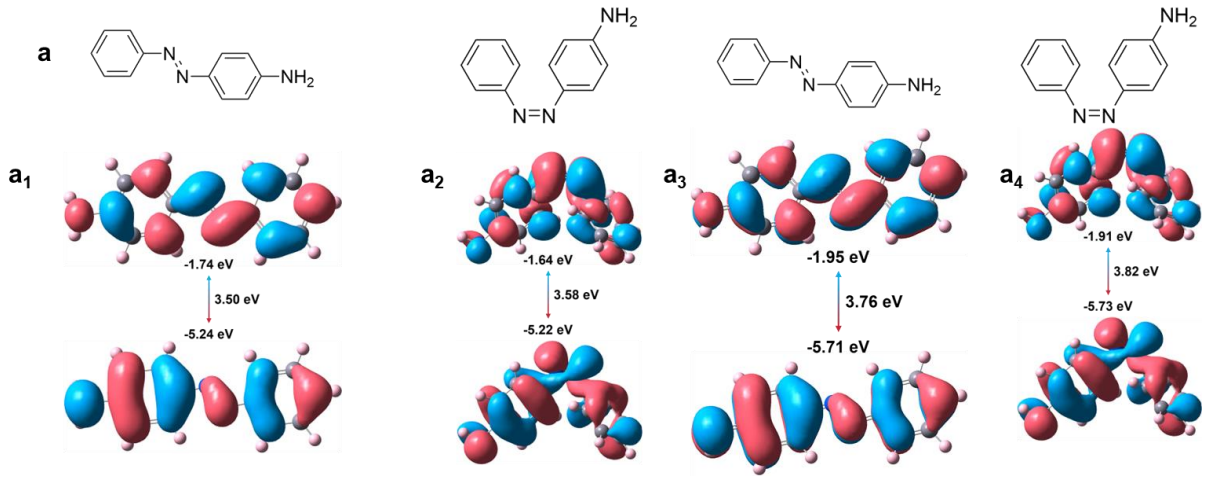


Figure 3.5 Distribution of electronic cloud of the *trans* and *cis* configuration of azo-$NH_2$ and energy gap in vacuum and dioxane. (a) chemical structures of *trans* and *cis* configuration; ($a_1$, $a_2$) in vacuum; ($a_3$, $a_4$) in dioxane.

From the analysis of the photophysical properties, it is evident that the introduction of the maleimide group effectively induces changes in the emission wavelength during the photoisomerization process. To further explore this difference, we conducted theoretical calculations on both the precursors and the final products. The geometries of all compounds in the ground state were optimized using the density functional theory (DFT) method at the PBE1PBE/def2SVP level, The excited-state geometries were optimized using the time-dependent DFT method at the same level of theory.

Figure 3.5 ($a_1$, $a_2$, $a_3$, $a_4$) shows the delocalized electronic cloud density distributions of the *cis*- and *trans*-configurations of the azo-$NH_2$ molecule in vacuum and dioxane, respectively. According to Figure 3.5 ($a_1$), for the *trans*-configuration in the vacuum state, in the HOMO state, the electronic cloud density is delocalized over the π-orbitals of the benzene ring, the π-orbital of the N=N double bond, and the n-orbital of the -$NH_2$ group. In the LUMO state, there is no obvious

charge-separation phenomenon in the delocalized electronic cloud density distribution, and it is still delocalized over the benzene ring, the -C-N=N-C- region, and the -$NH_2$ group, mainly in the form of π* and n* orbitals. Therefore, the transition modes of the *trans*-configuration of the azo-$NH_2$ molecule include π→π* transition, n→n* transition, and n→π* transition, which is consistent with the UV-vis spectrum shown in Figure 3.2 (a). In addition, the absence of obvious charge separation in HOMO→LUMO is due to the lack of a distinct donor - acceptor system in the azo-$NH_2$ molecule. Moreover, for the *cis*-configuration, in the HOMO state, the electronic cloud density is also mainly delocalized over the π - orbitals of the benzene ring, the π-orbital of the N=N double bond, and the n-orbital of the -$NH_2$ group. In the LUMO state, the electronic cloud density is mainly delocalized over the benzene ring, the -C-N=N-C- region, and the -$NH_2$ group, and the transition modes are also π→π* transition, n→n* transition, and n→π* transition. Therefore, the delocalization of electronic cloud density in the HOMO and LUMO states and the charge separation in HOMO→LUMO are the same for the *trans*- and *cis*- configurations. In addition, the energy-level differences (ΔE) of the two are similar. The ΔE of the *trans*-configuration is 3.50 eV, and the ΔE of the *cis* configuration is 3.58 eV, with a difference of only 0.08 eV. This indicates that the emission wavelengths of the *trans*- and *cis*- configurations are relatively close without significant displacement, which is also consistent with the fluorescence spectrum results in Figure 3.2 (d). The situation in dioxane is similar to that in the vacuum state and will not be described in detail.

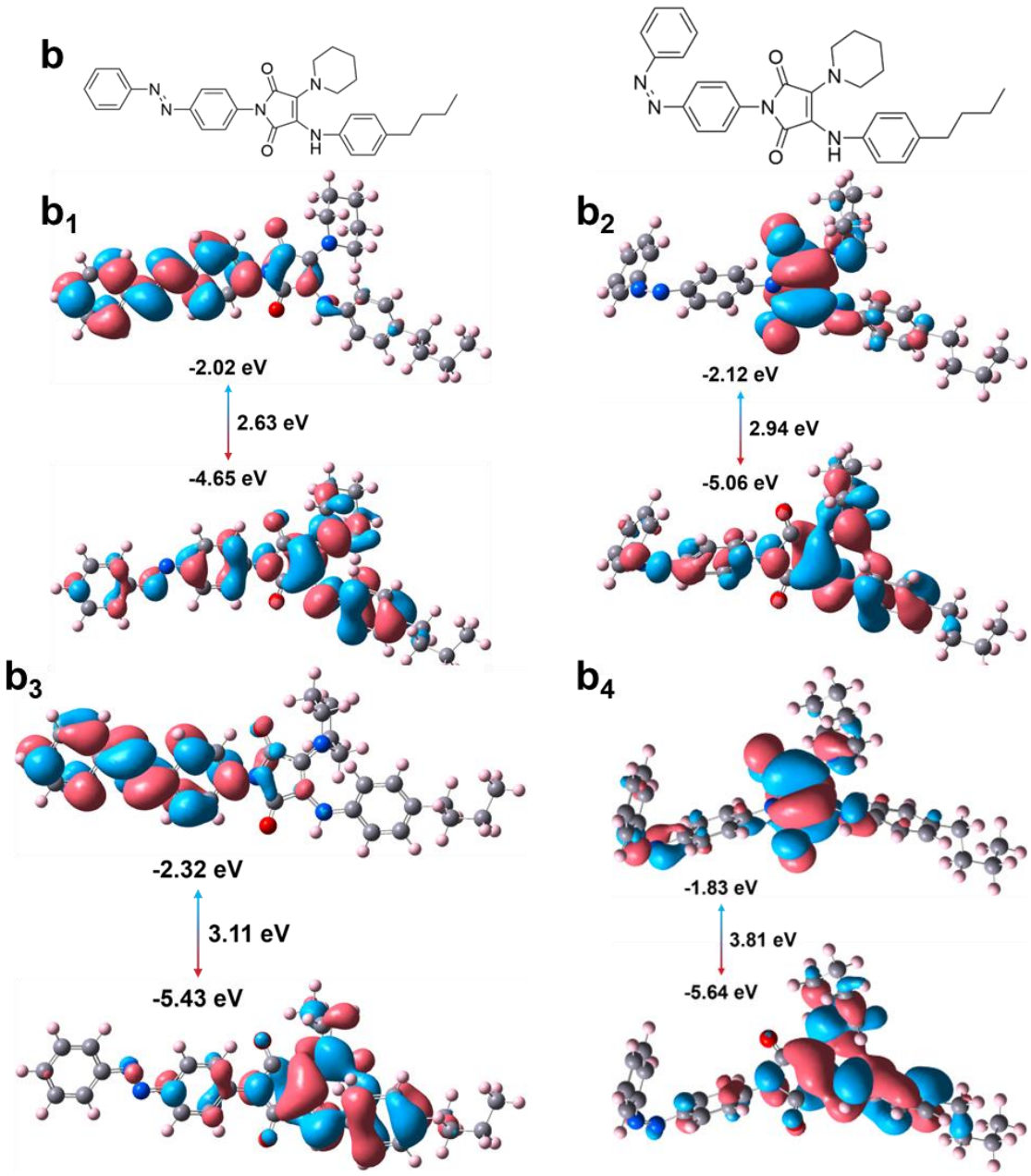


Figure 3.6 Distribution of electronic cloud of *trans* and *cis* configuration of azo-M and energy gap in vacuum and dioxane. (b) chemical structures of *trans* and *cis* configuration; ($b_1$, $b_2$) in vacuum; ($b_3$, $b_4$) in dioxane.

As can be observed from the fluorescence spectra in Figure 3.2, under continuous ultraviolet light irradiation, the photophysical properties of azo-M exhibit significant changes. This indicates that there are substantial differences in the electronic cloud distributions of the *trans* and *cis* structures in the HOMO and LUMO states and also differences in the energy-level differences between the

HOMO and LUMO. Therefore, to explore the luminescence mechanisms of the *cis*-*trans* structures, theoretical calculations were carried out for the *trans* and *cis* structures at the same level respectively. As shown in Figure 3.6 ($b_1$, $b_2$), in the vacuum state, the electronic cloud distributions of the *trans* and *cis* configurations in the HOMO state are similar. The electronic cloud density is mainly delocalized over the double bond of the imide ring, the aniline part of the 4-butylaniline group, and the piperidinyl group. In addition, there is also delocalization on the benzene ring where the azobenzene group is connected to the nitrogen atom of the imide ring, indicating that in the HOMO state, the electronic cloud is mainly delocalized in the form of π-orbitals. In the LUMO state, the *trans* and *cis* configurations show differences. According to Figure 3.6 ($b_1$), in the LUMO state, the electronic cloud density migrates to the azobenzene group and is mainly delocalized in the form of the π*-orbitals of the benzene ring. Therefore, the *trans* configuration mainly undergoes π→π* transitions, which is consistent with the above-mentioned analysis. However, in the *cis* configuration, the electronic cloud density only migrates to the double bond of the imide ring, and there is no delocalization of the electronic cloud density on the azobenzene group. It is mainly delocalized in the form of the π*-orbitals of the carbonyl C = O. Thus, the *cis* configuration also mainly undergoes π→π* transitions. This result indicates that the degree of electronic cloud density delocalization in the *cis* configuration is less than that in the *trans* configuration. This may be due to the decreased conjugation degree of the azobenzene group in the *cis* configuration, which reduces the coplanarity between the azobenzene group and the imide ring, weakens the overlap degree of the π-orbitals, and consequently, in the LUMO state of the *cis* configuration, the electronic cloud density cannot be delocalized to the azobenzene group and can only transition to the imide ring. In addition, the smaller the difference in electronic cloud distribution, the larger the energy-level difference is often. This is because when the difference in electronic cloud distribution is small, the overlap degree of the HOMO and LUMO orbitals is relatively high. In this case, the electrons are more strongly bound during the transition and need to overcome a larger energy barrier to achieve the transition, so the energy-level difference is large. Therefore, the energy-level difference between the HOMO and LUMO shows that it is 2.63eV in the *trans* configuration and 2.94eV in the *cis* configuration, indicating that the emission wavelength of the *cis* configuration is blue-shifted compared to that of the *trans* configuration, which is also consistent with the experimental results. Furthermore, the calculation results in the dioxane state shown in Figure 3.6 ($b_3$, $b_4$) are similar to those in the vacuum state.

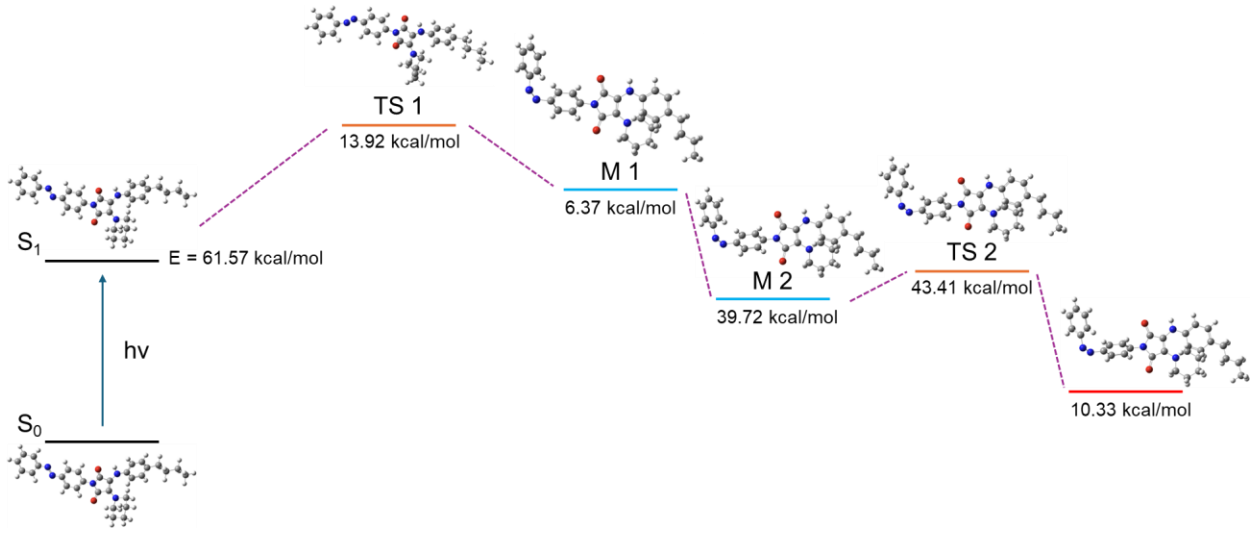


Figure 3.7 The illustration of the photoisomerization process of azo-M.

Based on the above analysis, significant differences in photophysical properties and molecular conformations were observed between the *trans* and *cis* configurations of azo-M. To gain deeper insights into the *cis-trans* isomerization process and conformational evolution, systematic theoretical calculations were conducted. Geometry optimizations of all structures were performed using the M06-2X functional with the 6-31+G (d, p) basis set. Frequency calculations were carried out to obtain Gibbs free energy corrections at 298.15 K, and single-point calculations were performed with the 6-311+G (d, p) basis set. The SMD implicit solvation model was employed for all calculations with 1,4-dioxane as the solvent. Figure 3.7 illustrates the photoinduced isomerization pathway of azo-M in dioxane solution. Initially, the ground-state ($S_0$) molecule is excited to the first excited state ($S_1$) with a vertical excitation energy of 61.57 kcal/mol. The $\pi \rightarrow \pi^*$ transition of the N=N double bond weakens the π-bonding, enabling the torsion of the Ph-N=N-C moiety. The bond length of N=N increases from 1.27 Å (double bond) to 1.48 Å (single bond), and the dihedral angle between the two benzene rings attached to the nitrogen atoms reaches 85.657° (nearly perpendicular), corresponding to the first transition state (TS1). The Gibbs free energy barrier $\Delta G‡ = G(TS1) - G(S_1)$ is 13.92 kcal/mol. Subsequent relaxation along the potential energy surface leads to the formation of the first intermediate M1 with $\Delta G‡ = G(M1) - G(S_1)$ of 6.37 kcal/mol. At this stage, the N=N double bond reforms, and the dihedral angle between the imide ring and azobenzene unit increases from 25.153° ($S_1$) to 53.771°, reflecting a torsional amplitude of 28.618°. This conformational change is attributed to the TICT effect, where the molecule reduces its dipole moment through intramolecular torsion in the excited state. M1 further

relaxes to the second intermediate M2 via intramolecular torsion, with $\Delta G‡ = G(M2) - G(S_0)$ of 39.72 kcal/mol. Although no N-N bond rotation occurs, the dihedral angle increases to 65.278°, indicating continued energy minimization through torsion. Upon continued excitation, M2 undergoes a second isomerization to reach the second transition state (TS2), with $\Delta G‡ = G(TS2) - G(S_0)$ of 43.41 kcal/mol. In TS2, the dihedral angle of the azobenzene moiety reaches 143.58°, signifying complete cis isomerization, while the dihedral angle between the imide ring and azobenzene increases to 69.437°. Finally, the cis isomer is formed with a Gibbs free energy difference of 10.33 kcal/mol relative to the ground state, stabilized by a dihedral angle of 73.594°. The reduced conjugation between the azobenzene and imide ring in the cis configuration is accompanied by continuous torsion to minimize the potential energy barrier. In summary, the photo-isomerization of azo-M involves a synergistic process of photo-induced isomerization and intramolecular torsion. The conjugation disruption and increased dihedral angles in the *cis* configuration not only rationalize the experimental observation of attenuated UV absorption peaks but also align with the frontier orbital calculations showing inefficient electron delocalization onto the azobenzene moiety.

**Exploration of the Universality of This Design Concept**

Based on the above work, we successfully utilized the intramolecular push-pull electron effect of maleimide to prepare azobenzene-based maleimide fluorophores with photochromic characteristics. To explore the universality of this design concept, we further selected classic photoisomerizable molecules, such as cyanostilbene and stilbene derivatives, as precursors. Using similar methods, we linked these photoisomerizable molecules to maleimide and studied each precursor and the corresponding maleimide fluorophores.

## 3.3 Synthesis of cyanostilbene-based maleimide fluorophores

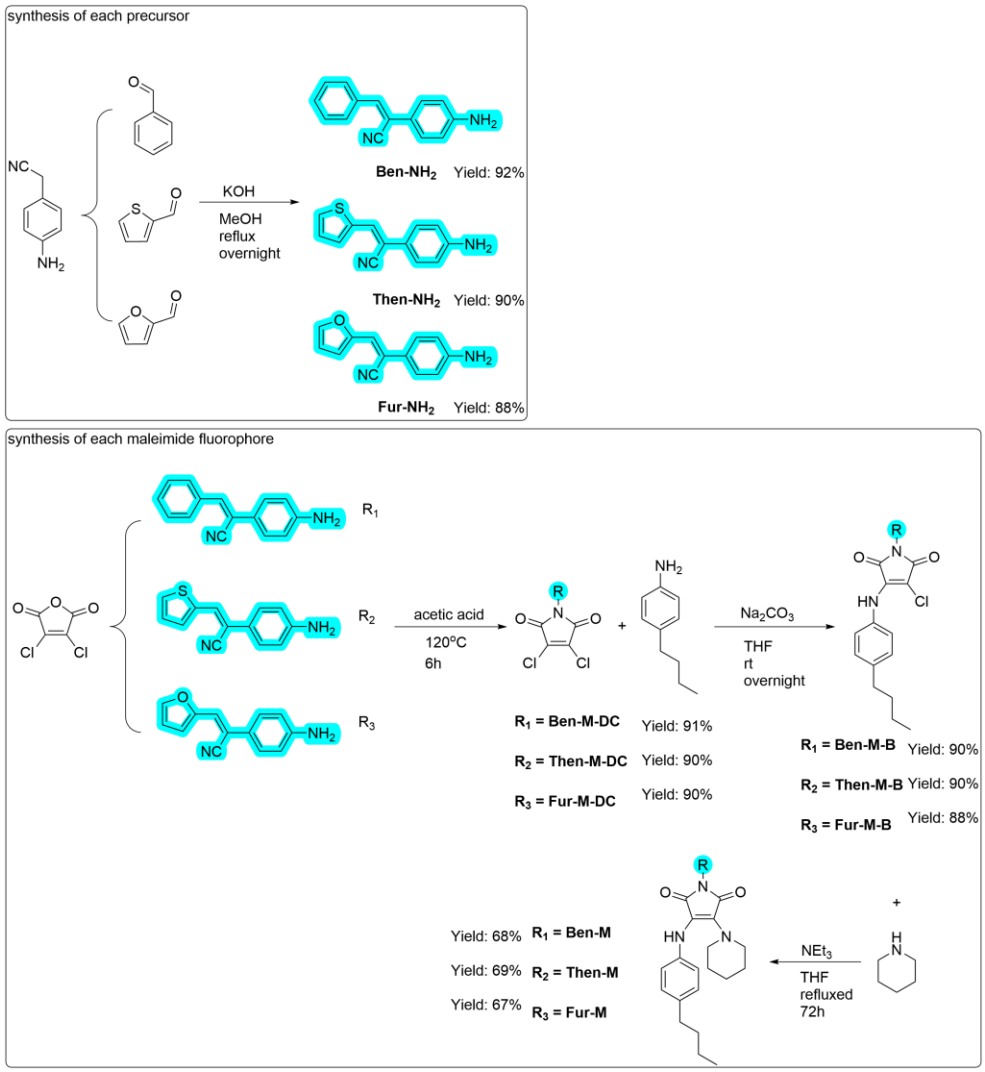


Figure 3.8 Synthetic route of each cyanostilbene derivative and maleimide fluorophore.

The photoisomerization mechanism of cyanostilbene is similar to that of azobenzene, and there are increasing reports on the use of cyanostilbene to prepare photoresponsive fluorophores. The basic strategy involves using cyanostilbene as a bridge to introduce donor-acceptor systems. Building on the results of the previous work, in this section, we first prepared three widely used cyanostilbene derivatives through the Knoevenagel condensation reaction, named Ben-$NH_2$, Then-$NH_2$, and Fur-$NH_2$. Subsequently, we synthesized three maleimide-based fluorophores derived from these cyanostilbene derivatives, named Ben-M, Then-M, and Fur-M, respectively (Fig 3.8).

## 3.3.1 Results and Discussion

### Investigation of photophysical properties

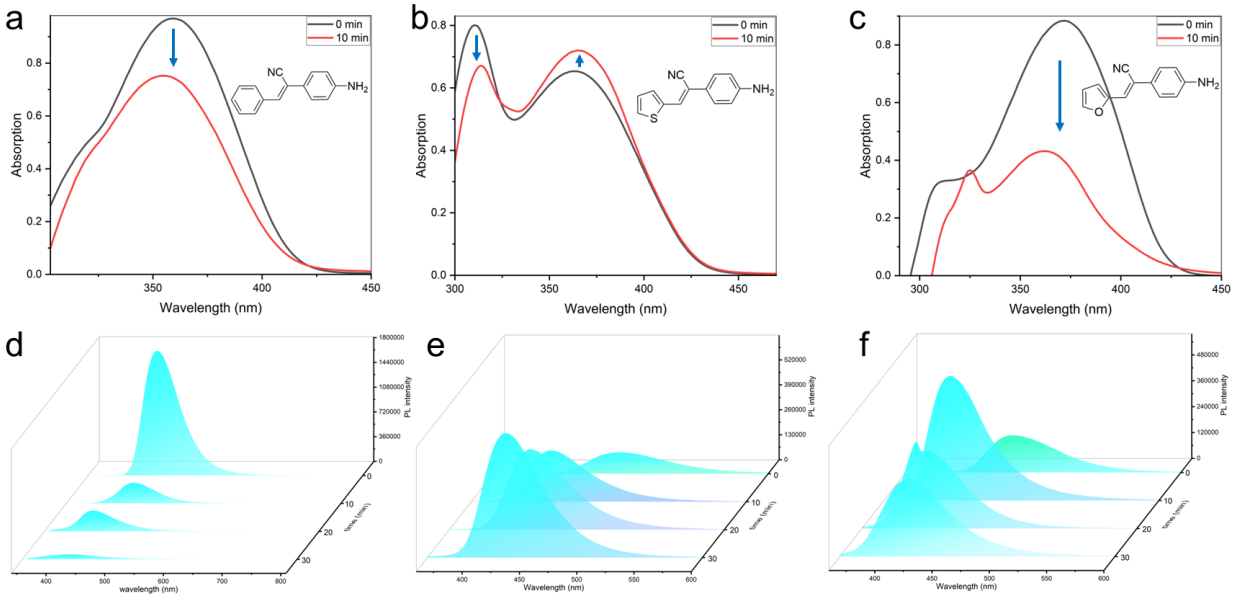


Figure 3.9 All samples were measured in dioxane, 0.01mg/ml, Ex = 365nm. The UV-vis spectra were recorded at 0 min and after UV irradiation for 10 min, the FL spectra was recorded every 10 min from 0 to 30 mins. (a) UV-vis spectra of Ben-$NH_2$; (b) UV-vis spectra of Then-$NH_2$; (c) UV-vis spectra of Fur-$NH_2$; (d) FL spectra of Ben-$NH_2$; (e) FL spectra of Then-$NH_2$; (f) FL spectra of Fur-$NH_2$.

First, the photophysical properties of each precursor were measured. Figure 3.9 shows that the intensity of the UV absorption peaks and fluorescence spectra of each precursor varies under UV irradiation, similar to the results observed in previous studies on azobenzene-based maleimide fluorophore. Figure 3.9 (a) shows that the initial UV absorption peak of Ben-$NH_2$ is around 350 nm, primarily corresponding to the $\pi \rightarrow \pi^*$ transition of the conjugated system. Furthermore, the absorption peak exhibits a relatively broad shape, which may be attributed to the overlap between the $n \rightarrow \pi^*$ orbitals involving the -$NH_2$ group and the $\pi \rightarrow \pi^*$ orbitals. Subsequently, after 10 minutes of UV light irradiation, the intensity of the absorption peak decreases, and meanwhile, the peak shape becomes narrower. This indicates that the molecule undergoes a transformation process from the *trans* configuration to the *cis* configuration. That is, the conjugation degree of the *trans*-configuration molecule decreases, and the degree of intramolecular distortion becomes greater.

Additionally, Figure 3.9 (d) indicates that the emission wavelength of Ben-$NH_2$ did not shift significantly with continued UV irradiation, but the emission intensity decreased, which is also attributed to the reduction in conjugation during photoisomerization. Figure 3.9 (b) shows that Then-$NH_2$ has two absorption peaks, at approximately 320 nm and 360 nm. The 320 nm peak arises from the $\pi \rightarrow \pi^*$ transition of the benzene ring, while the 360 nm peak may result from the $n \rightarrow \pi^*$ transition involving the lone electron pairs of the thiophene ring. After UV irradiation, the intensity of the 320 nm peak decreases due to the reduced conjugation caused by isomerization, leading to a decrease in the electron cloud density on the benzene ring and consequently weakening the $\pi \rightarrow \pi^*$ transition. The slight increase in the 360 nm peak intensity may be due to during the transition from the *trans* conformation to the *cis* conformation, the molecular symmetry decreases. As a result, the symmetry - forbidden transition is lifted, and the transition dipole moment increases. Consequently, the transition ability of $n \rightarrow \pi^*$ is enhanced. Furthermore, Figure 3.9 (e) shows that while the emission peak position did not shift significantly with continued UV irradiation, the intensity gradually increased. This could be due to the more linear structure of the *trans* configuration, which promotes π-π stacking and increases non-radiative transition pathways; in contrast, the reduced symmetry of the *cis* configuration diminishes π-π stacking, weakening non-radiative transitions. The behaviour of Fur-$NH_2$, as shown in Figures 3.9 (c, f), is similar to that of Then-$NH_2$.

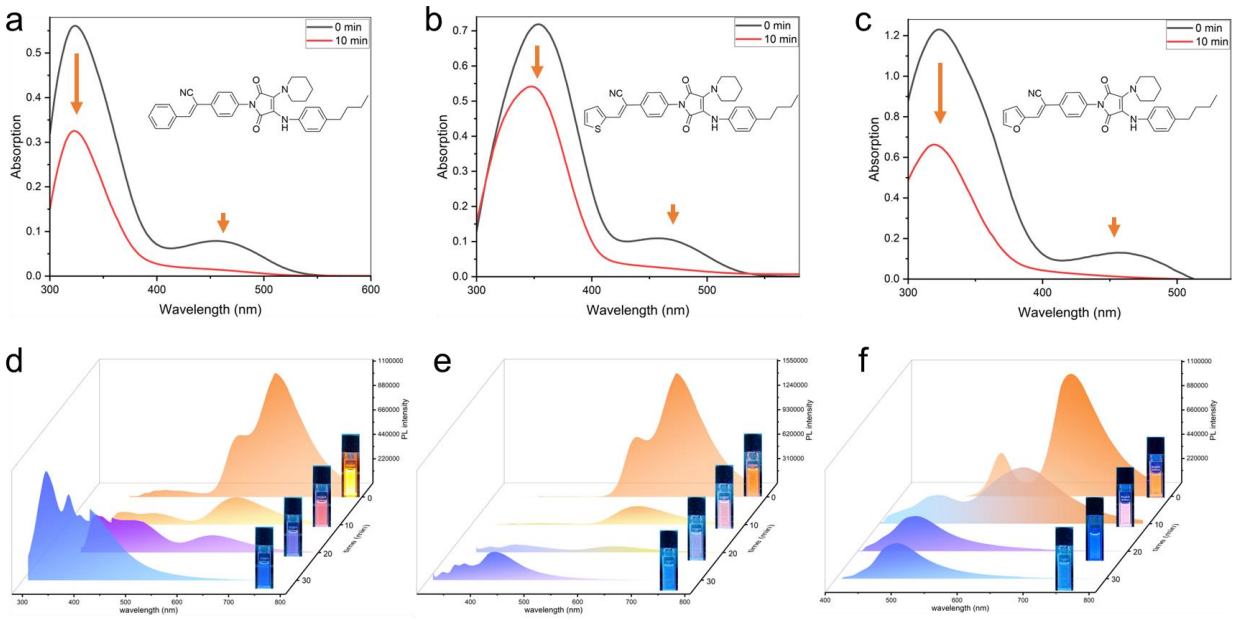


Figure 3.10 UV-vis spectra and FL spectra in dioxane, 0.01mg/ml, Ex = 365nm. The UV-vis spectra were recorded at 0 min and after UV irradiation for 10 min, the FL spectra was recorded every 10 min from 0 to 30 mins. (a) UV-vis spectra of Ben-M; (b) UV-vis spectra of Then-M; (c) UV-vis spectra of Fur-M; (d) FL spectra of Ben-M; (e) FL spectra of Then-M; (f) FL spectra of Fur-M.

Figure 3.10 (a, b, c) shows that all fluorophores exhibit two initial absorption peaks, located around 330 nm and 450 nm. The absorption peak at 330 nm primarily corresponds to the π→π* transition resulting from the conjugation between the maleimide ring and the benzene ring, while the 450 nm peak is mainly due to the extended conjugation induced by the diamine groups, consistent with the experimental results of azo-M mentioned earlier. Upon continuous UV (365nm) light irradiation, the absorption peak changes of all molecules are similar to those of the azo-M molecule. Specifically, the intensity of the absorption peak at 450 nm decreases, indicating a weakening of the ICT effect during the isomerization process from the *trans* configuration to the *cis* conformation. Moreover, the intensity of the absorption peak at 330 nm also decreases, and simultaneously, the width of the absorption peak narrows, suggesting a decrease in the conjugation degree due to intramolecular distortion during the isomerization process. Figure 3.10 (d, e, f) shows that the initial emission wavelengths of all fluorophores are around 620 nm, similar to the case of azo-M. With prolonged UV irradiation, the emission wavelengths of all fluorophores undergo significant changes. The initial emission peak intensity gradually decreases, while a new emission peak emerges around 450 nm, with its intensity steadily increasing. This change is similar

to what was observed for azo-M, where the higher conjugation and symmetry of the *trans* configuration compared to the *cis* configuration reduce the electron delocalization effect in the *cis* form, leading to the observed shifts in the fluorescence spectrum.

**Investigation of the photodynamic stability**

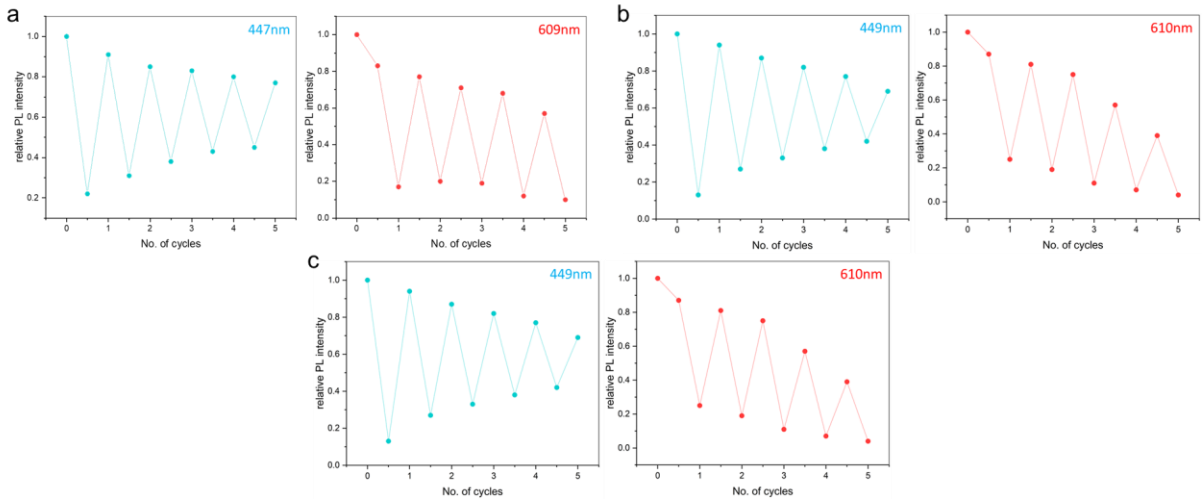


Figure 3.11 The number of cycles under UV irradiation for 5 minutes. (a) Ben-M; (b) Then-M; (c) Fur-M.

To explore the number of *cis-trans* isomerization cycles and evaluate the photostability of the molecules, the dynamic photostability of each molecule was characterized. Starting from the point where, after irradiating the *trans*-configuration with 365nm ultraviolet light for 10 minutes, two emission peaks emerged. The irradiated sample was then placed in a darkroom. However, after 24 hours of continuous storage, no changes were observed in the spectral characterization. Therefore, based on the experience with the azo-M molecule, the same green light was used for irradiation. As shown in Figure 3.11, all molecules can undergo cycling between 365nm ultraviolet light and green light. Taking the Ben-M molecule as an example, after 10-minute irradiation with continuous green light, the peak intensity at 447 nm, which represents the emission wavelength of the *cis*-configuration, decreases, while the peak intensity at 609 nm, representing the *trans*-configuration, increases. Subsequently, when irradiated with 365nm ultraviolet light, the peak intensity at 447 nm increases, and the peak intensity at 609 nm decreases, achieving one cycle. In addition, under green-light irradiation, the *cis*-configuration does not completely convert to the *trans*-configuration, and the peak intensity of the *trans*-configuration gradually decreases after each

cycle. After the fifth cycle, the cycling can no longer occur. It is speculated that at this time, the *trans*-configuration may have undergone photobleaching, or the *cis* configuration in the system can no longer return to the trans configuration.

**Investigation of the isomerization behaviour in the high concentration solvent.**

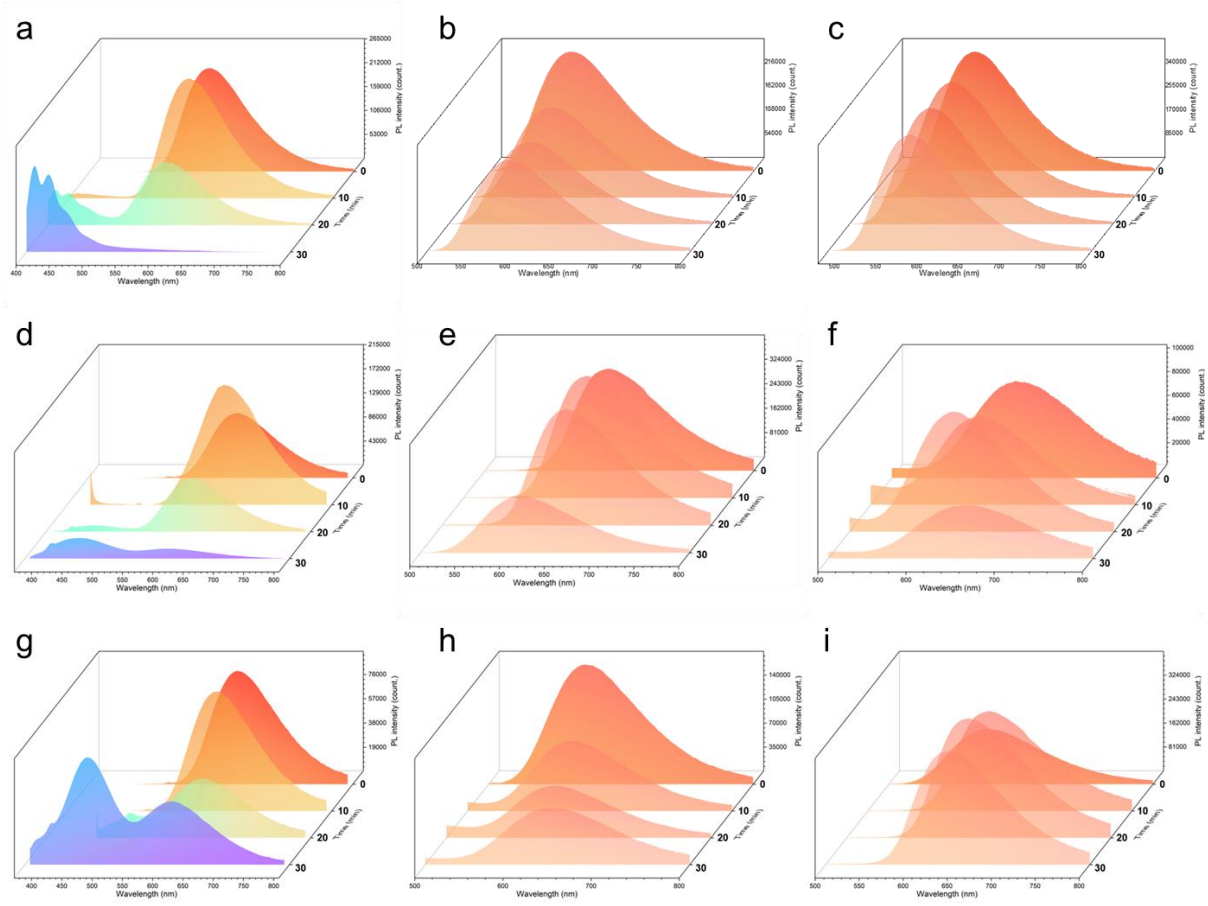


Figure 3.12 FL spectra of each molecule during the 365nm UV irradiation for 30min. (Ex = 365nm). (a, b, c) Ben-M; (d, e, f) Then-M; (g, h, i) Fur-M. All samples were prepared in mixed solutions of dioxane and n-hexane, with the volume ratios of dioxane to n-hexane being 1:0.5 for Figures a, d, g; 1:1 for Figures b, e, h; and 1:2 for Figures c, f, i. The concentration of all mixed solutions was 1 μg/mL.

When attempting to characterize the isomerization process by $^{1}$H NMR, it was found that even after 24-hour continuous ultraviolet light irradiation, there were no changes in the NMR spectra. At this point, it was noted that the sample concentration in the photophysical property characterization was 1 μg/ml, while the concentration in the NMR sample preparation was 10

mg/ml. It is speculated that after the concentration is increased, the enhancement of intermolecular forces may hinder the occurrence of isomerization behaviour. Therefore, to verify this hypothesis, a 1 mg/ml dioxane solution was first prepared. Then, 3 μl of this solution was taken and added to a 3 ml mixed solution of dioxane and the poor solvent n-hexane to prepare a 1 μg/ml mixed solution sample, where the volume ratios of $V_{dioxane}$: $V_{n\text{-}Hexane}$ in the mixed solution were 1:0.5, 1:1, and 1:2, respectively. Figure 3.12 shows the fluorescence spectra of Ben-M (the first row a, b, c), Then-M (the second row d, e, f), and Fur-M (the third row g, h, i) at different volume ratios (from left to right, the volume ratio of n-hexane gradually increases). As shown in this figure, with the increase in the proportion of n-hexane, the intermolecular forces gradually increase, effectively inhibiting the isomerization behaviour. Taking the Ben-M molecule as an example, as shown in Figure 3.11 (a), when the volume ratio of n-hexane is 0.5, after 10-minute ultraviolet light irradiation, no obvious changes occur in the fluorescence spectrum. However, in a pure dioxane solution, under the same irradiation time, the emission peak of the *cis* configuration has already emerged. A new emission peak appears at around 450 nm only after 20-minute continuous irradiation, indicating that the isomerization rate has decreased at this time. After 30-minute continuous irradiation, the peak at around 600 nm disappears, and only the peak at 450 nm remains. In addition, as shown in Figure 3.11 (b, c), when the volume ratio of n-hexane increases to 1 and 2, the fluorescence spectrum no longer shows changes in the peak position under continuous ultraviolet light irradiation. This indicates that with the enhancement of intermolecular interactions, the isomerization process is hindered, and the Then-M and Fur-M molecules exhibit the same behaviour. This result explains why the NMR spectra of the 10 mg/ml samples do not change with ultraviolet light irradiation.

Subsequently, we performed TD-DFT theoretical calculations for all the fluorophores. The results were consistent with those of azo-M, showing significant differences in charge separation and energy gap between the trans and cis configurations. Therefore, we will not repeat the descriptions and explanations here; all data (TD-DFT, single-crystal structure and NMR spectra) can be found in the Supporting information (SI).

## 3.4 Synthesis of stilbene-based maleimide fluorophores

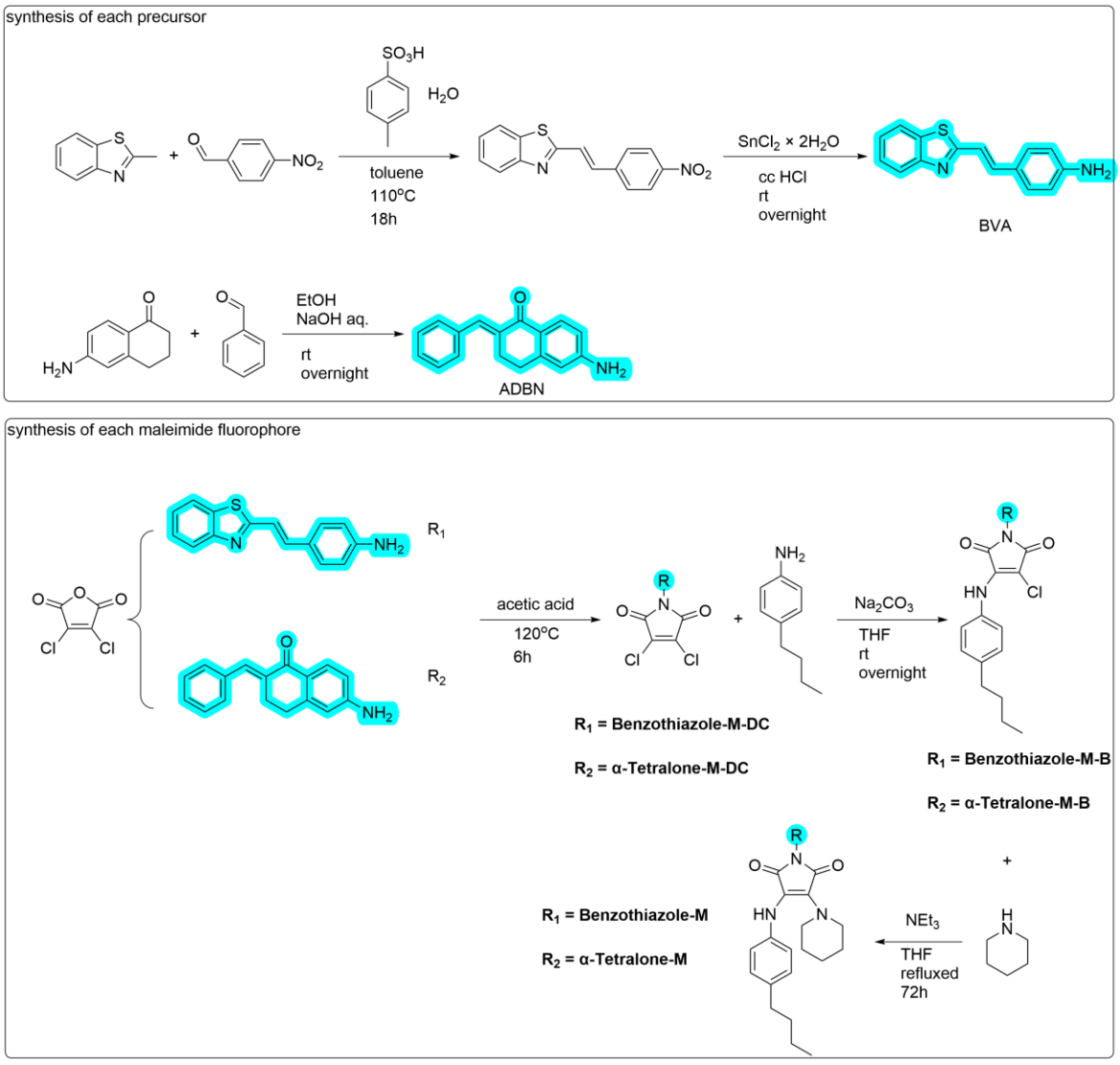


Figure 3.13 Synthetic route of each stilbene derivative and maleimide fluorophore.

Furthermore, we synthesized two known photoisomerizable stilbene derivatives as precursors, named BVA and ADBN, respectively.[70,198] Subsequently, following a design strategy similar to that described earlier, we prepared two maleimide-based fluorophores, named Benzothiazole-M and α-Tetralone-M (Fig 3.13).

## 3.4.1 Results and Discussion

### Investigation of photophysical properties

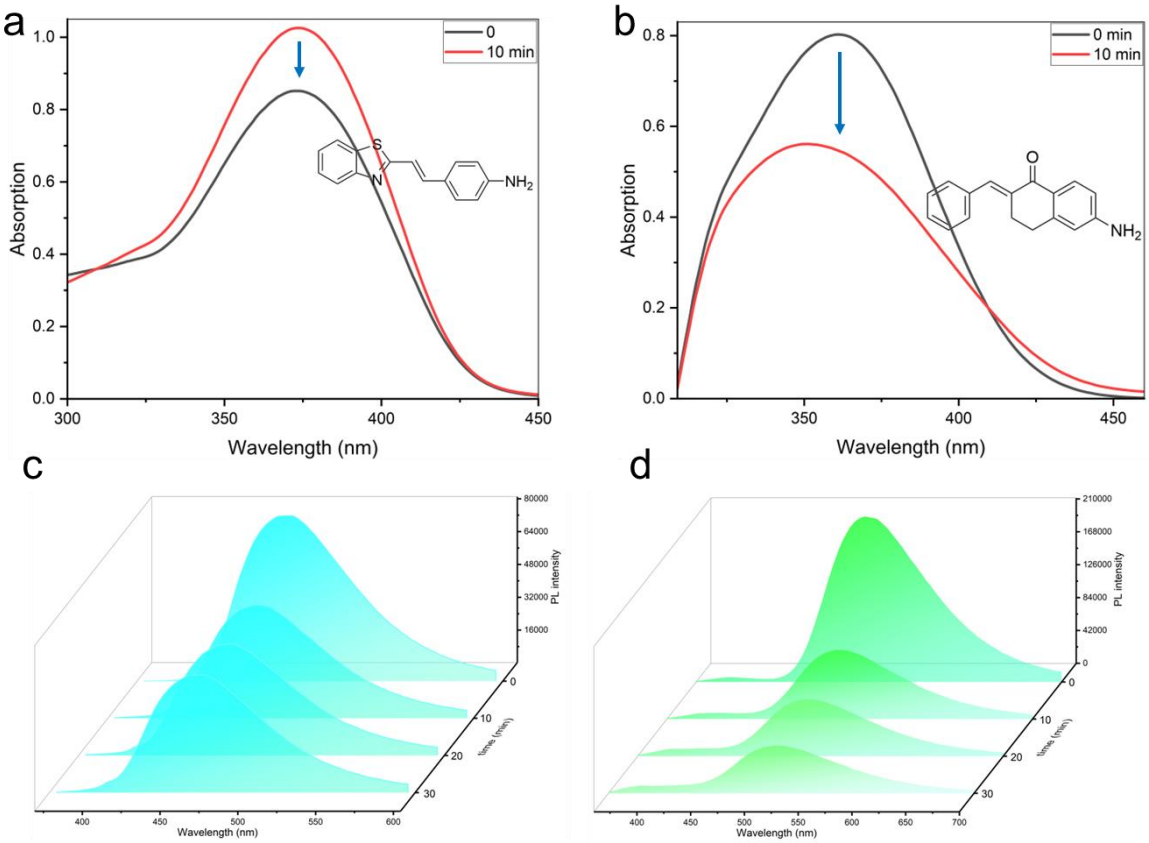


Figure 3.14 UV-vis spectra and FL spectra of BVA and ADBN in dioxane, 0.01mg/ml, Ex = 365nm. (a) UV-vis spectra of BVA; (b) UV-vis spectra of ADBN; (c) FL spectra of BVA; (d) FL spectra of ADBN.

Figure 3.14 (a) shows that the initial absorption peak of BVA is around 360 nm, with a relatively broad absorption range. Given the presence of multiple heteroatoms in the molecule, the absorption is likely due to the overlapping of π→π* transitions of the benzene rings and n→π* transitions involving the heteroatoms.[199] After UV irradiation, the intensity of the BVA absorption peak decreases, which is attributed to the reduced conjugation resulting from photoisomerization. Similarly, Figure 3.14 (c) shows that the initial emission peak of BVA is around 480 nm. Although the peak position did not shift significantly with continuous UV irradiation, the peak intensity decreased markedly, again due to the reduction in conjugation caused by photoisomerization.[103]

Figures 3.14 (b) and (d) show similar changes for ADBN under UV irradiation, with the underlying reasons being the same as discussed above, so they will not be elaborated further here.[200,201]

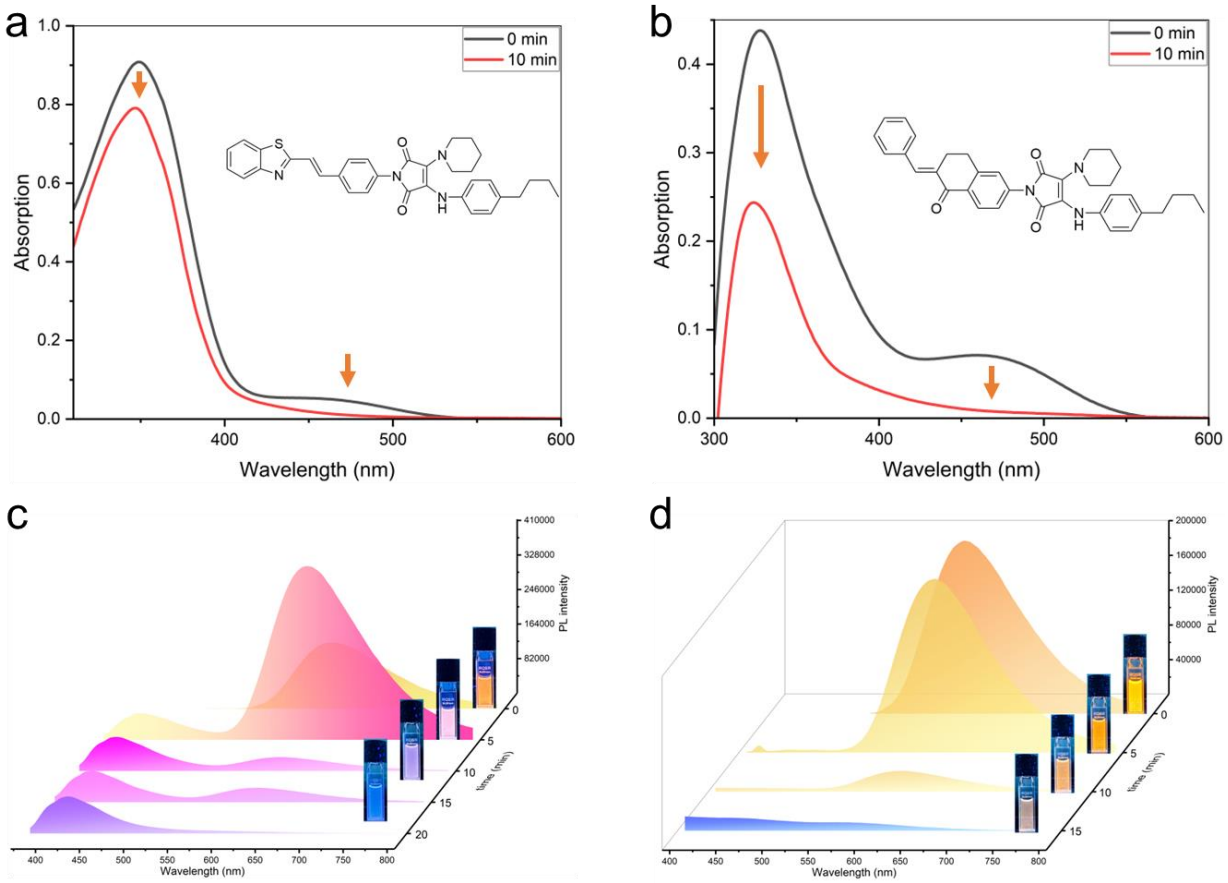


Figure 3.15 UV-vis spectra and FL spectra of Benzothiazole-M and α-Tetralone-M in dioxane, 0.01mg/ml, Ex = 365nm. (a) UV-vis spectra of Benzothiazole-M; (b) UV-vis spectra of α-Tetralone-M; (c) FL spectra of Benzothiazole-M; (d) FL spectra of α-Tetralone-M.

Figures 3.15 (a, b) show that Benzothiazole-M and α-Tetralone-M both exhibit two absorption peaks, located around 350 nm and 450 nm, respectively. Similar to the previously discussed molecules, the absorption peak at 350 nm is attributed to the π→π* transition resulting from the conjugation between the benzene ring and the maleimide ring, while the absorption peak at 450 nm is due to the π→π* transition induced by the extended conjugation from diamine substitution. Similar to the aforementioned results, under UV light irradiation, the intensities of the absorption peaks at 450 nm and 350 nm both decreases. This respectively indicates the weakening of the ICT effect during the photoisomerization process and the reduction of the conjugation degree in the *cis*

configuration. Additionally, Figures 3.15 (c, d) show that the initial emission peaks of Benzothiazole-M and α-Tetralone-M are both located around 600 nm. This is attributed to the extended conjugation induced by diamine substitution and the redshift caused by the introduction of the ICT effect. With continued UV irradiation, Benzothiazole-M's emission wavelength undergoes significant changes. Figure 3.15 (c) shows that after 5 minutes of UV irradiation, the emission peak intensity of benzothiazole-M increased by nearly threefold compared to the initial state. We speculate that this could be due to the planarisation of the *trans* configuration, which enhances π-π stacking between molecules, thereby increasing non-radiative transition pathways and reducing emission intensity. However, as isomerization occurs, intramolecular twisting disrupts this stacking, reducing non-radiative transitions and enhancing emission intensity. Additionally, a new emission peak emerges at 450 nm, likely due to the formation of the *cis* configuration. The reduced conjugation in the *cis* configuration decreases electron delocalization, leading to a blue shift in the emission wavelength. With continued UV irradiation, the intensity at 600 nm gradually decreases, while the intensity at 20 minutes increased by nearly 1.5-fold compared to that at 5 minutes. Based on the changes in Benzothiazole-M's fluorescence spectrum, we conclude that the molecule undergoes isomerization under UV irradiation, which disrupts intermolecular interactions, and that the *cis* configuration has a lower degree of conjugation compared to the *trans* configuration. Figure 3.15 (d) shows that during the first 10 minutes of UV irradiation, the emission peak position of α-Tetralone-M does not shift, but the intensity decreased by nearly 8-fold. We speculate that the *trans* configuration content of α-Tetralone-M decreases with UV exposure. Additionally, the *cis* configuration is more planar than the *trans* configuration, possibly leading to intermolecular energy transfer and the absence of fluorescence in the solution.[68] After 15 minutes of UV irradiation, the emission peak at 600 nm disappears, and a weaker emission peak appears around 400 nm, possibly indicating the occurrence of photobleaching.[69,101] During the isomerization of stilbene derivatives from the *trans* to the *cis* configuration, fluorescence intensity decreases or is even quenched. This is primarily due to the reduction in conjugation and the increase in non-radiative decay pathways caused by changes in molecular conformation. In the *trans* configuration, the molecule exhibits strong conjugation, which promotes fluorescence emission. However, in the *cis* configuration, the conjugation between phenyl rings is weakened, leading to a decrease in fluorescence quantum yield. Additionally, the *cis* configuration increases molecular flexibility and non-radiative decay pathways, making it easier for the excited-state

energy to dissipate through non-radiative processes, further reducing fluorescence intensity or causing quenching.[202,203]

The results of the TD-DFT theoretical calculations further confirm the feasibility of this design strategy. Since the results are consistent with previous findings, detailed discussions are omitted here. All data (TD-DFT, single-crystal structure and NMR spectra) can be found in the Supporting Information (SI).

## 3.5 Synthesis of anthracene-based maleimide fluorophore

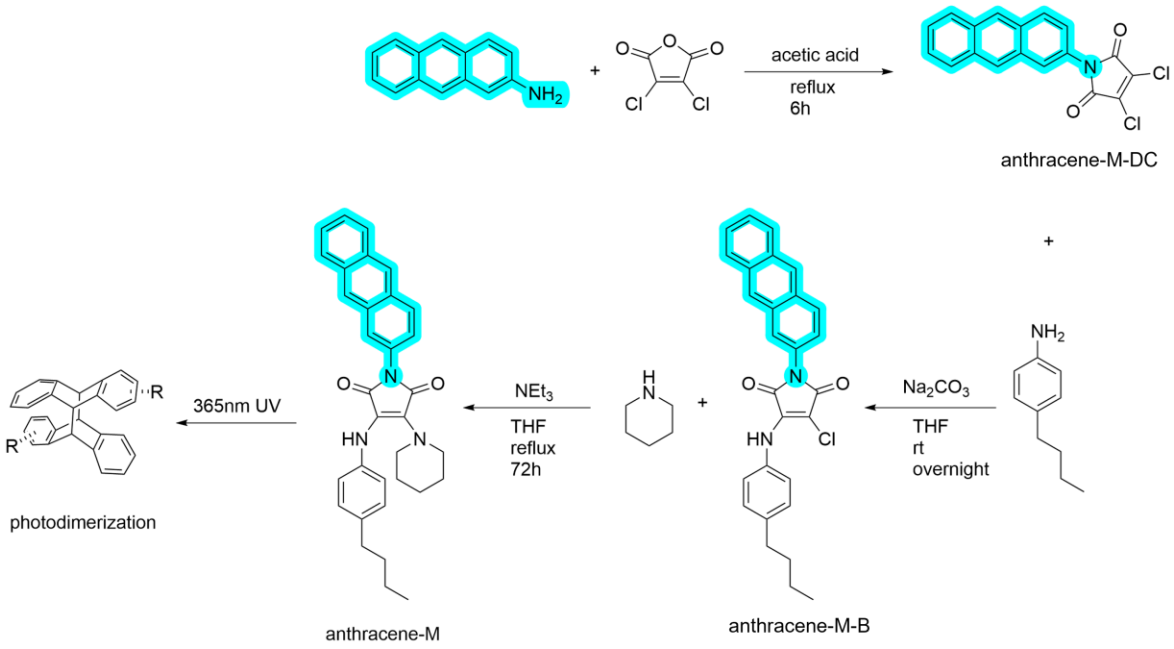


Figure 3.16 Synthetic route of anthracene-based maleimide fluorophore.

The above experimental results indicate that changes in intramolecular conjugation can significantly influence the charge separation in both the ground and excited states of maleimide fluorophores, thereby altering their emission wavelengths. Based on this, we hypothesize that combining molecules capable of light-induced conjugation changes with maleimide could lead to the development of photochromic fluorophores. anthracene emerges as an ideal candidate for this approach. Under 365 nm UV irradiation, anthracene undergoes a 4π+4π photocycloaddition reaction, forming a dimer with significantly different conjugation compared to anthracene itself, as evident in their UV absorption spectra.[104,204] Consequently, we designed and synthesized an anthracene-based maleimide fluorophore, named anthracene-M, aiming to utilize the

photocycloaddition properties of anthracene to develop novel photoresponsive maleimide fluorophores (Fig 3.16).

## 3.5.1 Result and Discussion

### Investigation of photophysical properties

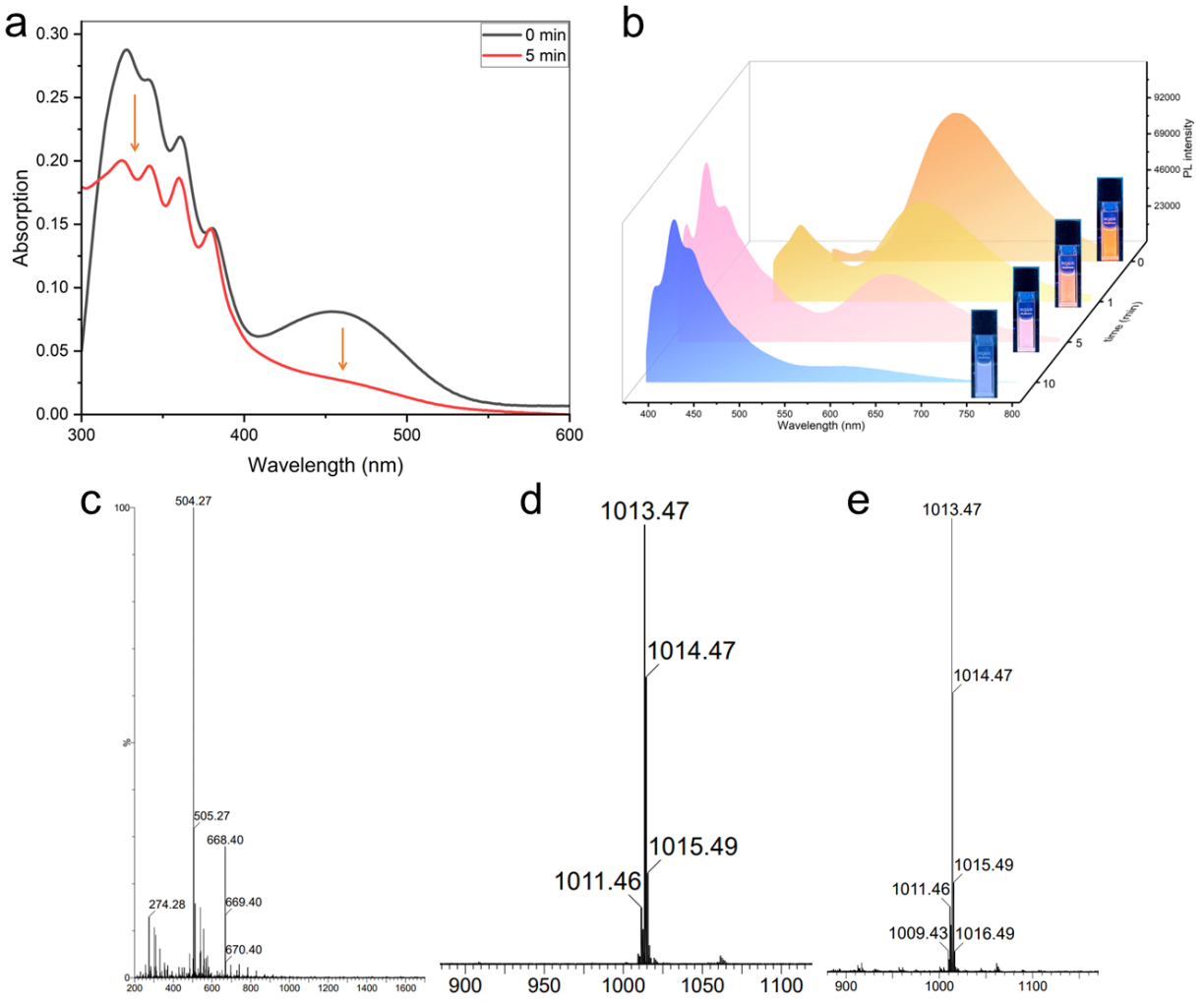


Figure 3.17 UV-vis and FL spectra in dioxane, 0.01mg/ml, Ex = 365nm. (a) UV-vis spectra of anthracene-M; (b) FL spectra of anthracene-M; (c) mass spectra (MS, $ES^+$) of anthracene-M at 0 min; (d) MS ($ES^+$) of anthracene-M after UV irradiation for 5 min; (e) MS ($ES^+$) of anthracene-M after UV irradiation for 10 min.

Figure 3.17 (a, b) illustrates the changes in the UV absorption and fluorescence spectra of anthracene-M under continuous UV irradiation. Figure 3.17 (a) shows that anthracene-M exhibits

two UV absorption peaks, located around 320 nm and 450 nm. The peak at 320 nm is attributed to the π→π* transition resulting from the conjugation between the anthracene and maleimide rings, while the peak at 450 nm is due to the extended conjugation induced by diamine substitution and the resulting intramolecular charge transfer, consistent with earlier observations. After 5 minutes of UV irradiation, the intensity of the UV absorption peaks decreases significantly. The decrease in the 320 nm peak suggests that the anthracene undergoes a 4π+4π photocycloaddition reaction.[104] Additionally, the decline in the 450 nm peak intensity may be due to the reduced conjugation of anthracene after cycloaddition, which affects the degree of intramolecular charge separation and transfer, leading to a decrease in the peak intensity. Figure 3.17 (b) shows that the initial emission wavelength of anthracene-M is around 600 nm, which represents a significant red shift compared to the 300 nm emission wavelength of anthracene.[104] This observation is consistent with previous findings and is attributed to the increased conjugation and enhanced intramolecular charge transfer effect introduced by the diamine-substituted maleimide, causing the initial emission wavelength of anthracene-M to redshift. With continued UV irradiation, the fluorescence spectrum undergoes notable changes. The intensity of the peak at 600 nm gradually decreases, indicating a reduction in the concentration of the initial compound, anthracene-M. Additionally, a new emission peak appears around 420 nm, and its intensity increases with UV exposure, indicating the formation of new molecules. Based on the photocycloaddition properties of anthracene, we infer that the emission peak at 420 nm corresponds to the dimeric form (dimer-anthracene-M). The reduced conjugation in the dimer weakens the molecule's UV absorption and π→π* transition capabilities, and decreases the intramolecular charge transfer effect, resulting in a blue shift of the emission wavelength in the dimer. Furthermore, we used high-resolution mass spectrometry to monitor the photoinduced cycloaddition process. Figures 3.17 (c, d, e) show the mass spectra of anthracene-M from the initial monomeric state to after various durations of UV irradiation (details in SI). In the absence of UV irradiation, the initial monomeric state exhibits an m/z of 504.27, with no peaks observed at m/z > 1000. However, with continued UV exposure, a new mass spectral peak appears at m/z 1013.47. Although this value is greater than twice the molecular weight of anthracene-M, we hypothesize that the peak may result from an oxidation reaction between the dimer and oxygen in the solution during ionization.[205,206] Therefore, combined with the PL spectra, we conclude that the newly observed peak at m/z 1013.47 is attributed to the (4π+4π) photoinduced cycloaddition of anthracene-M under UV irradiation.

**Analysis of single-crystal structure**

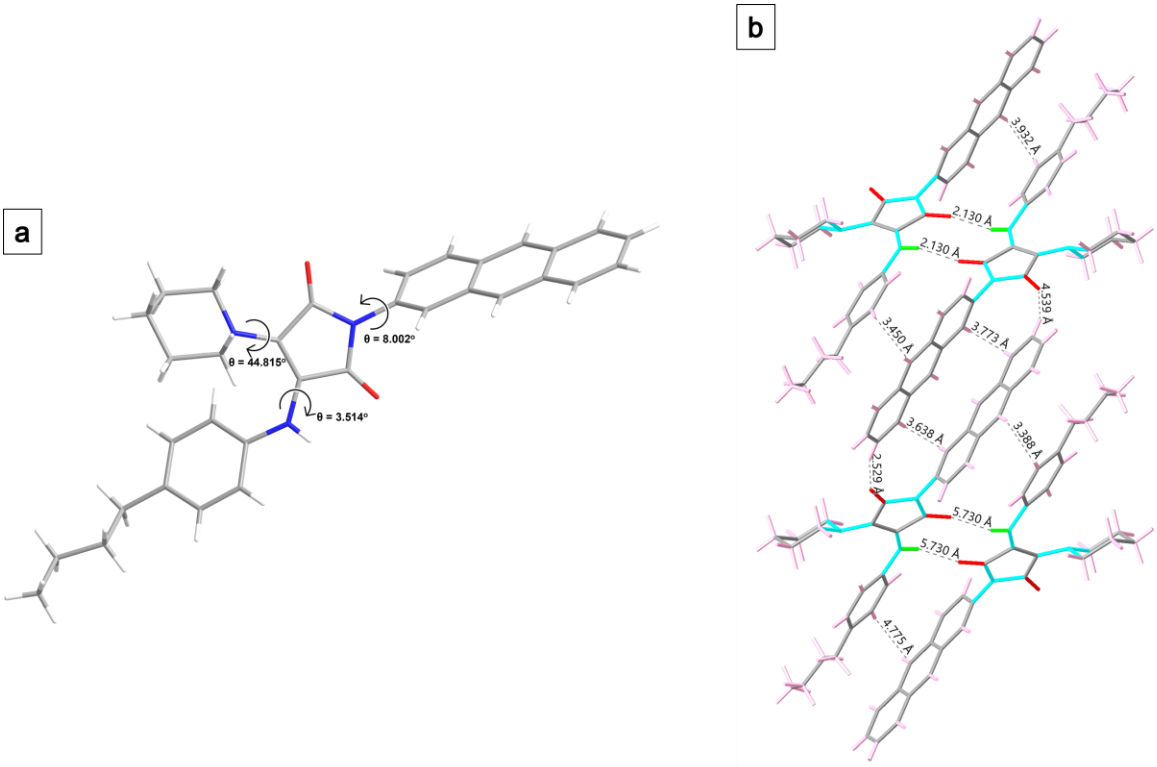


Figure 3.18 (a) single-crystal structure; (b) molecular packing pattern.

Figure 3.18 (a) shows that the torsional angle between the anthracene group and the maleimide ring is only 8.002°. This small torsional angle is likely due to the strong electron-withdrawing nature of the maleimide, which reduces the electron cloud density of the anthracene group, thereby diminishing the electrostatic repulsion between anthracene units. As a result, a large torsional angle is not required to achieve a stable energy state between the anthracene group and the maleimide ring. Additionally, the coplanarity of the anthracene group contributes to significant steric hindrance in this region, and the increased rigidity further limits torsion. The torsional angle between the piperidine group and the maleimide ring is 44.815°, which may be attributed to the relatively loose packing in this region, allowing for greater freedom of rotation. The torsional angle between the p-n-butylphenyl group and the maleimide ring is only 3.514°, likely due to the increased rigidity of the phenyl ring imposed by the n-butyl group, which restricts torsion. Figure 3.18 (b) shows that the molecule exhibits various intermolecular hydrogen bonds of different strengths, such as the stronger N-H···O=C hydrogen bond (2.130 Å) and the C-H···O=C hydrogen bond (2.529 Å). Additionally, there are weaker C-H···H-C hydrogen bonds, primarily occurring

between anthracene groups or between anthracene and p-n-butylphenyl groups, with distances ranging from 3 to 5 Å. These weak interactions effectively limit intramolecular motion, thereby suppressing non-radiative decay pathways and enhancing the emission efficiency of the molecule in solution. Furthermore, the molecular packing pattern reveals that the piperidine group does not participate in intermolecular stacking and exhibits no significant intermolecular interactions, which facilitates its free rotation and explains the large torsional angle between the piperidine group and the maleimide ring.

## 3.6 Conclusion

In conclusion, this study successfully demonstrated the design, synthesis, and photophysical characterization of maleimide-based fluorophores incorporating photoisomerizable molecules, such as azobenzene, cyanostilbene, stilbene, and anthracene derivatives. By leveraging the intramolecular push-pull electron effect of maleimide and the unique properties of photoisomerizable units, the resulting fluorophores exhibit multichromatic photochromism. This work highlights the versatility of maleimide as a bridging moiety in creating donor-acceptor systems that significantly influence the photophysical properties of the synthesized compounds Furthermore, the solvent-dependent photochromic behaviour observed in the experiments suggests a complementary relationship between isomerization and the dipole moment changes induced by solvent polarization, underscoring the ingenuity of this design strategy. The theoretical analyses, supported by TD-DFT calculations, provided deeper insight into the electronic structure changes during the trans-cis isomerization, further validating the experimental findings. This comprehensive approach to designing photoresponsive materials paves the way for the development of novel functional materials with tunable optical properties, suitable for applications in sensing, imaging, and data storage.

## 3.7 Supplementary information

### 3.7.1 Materials

4-Aminophenylacetonitrile (99%), Benzaldehyde (99%), Thenaldehyde (98%), Furfural (99%), 6-Amino-1-tetralone (97%), 2,3-Dichloromaleic anhydride (97%), 4-butylaniline (97%), Piperidine (99%) were purchased from Merck (UK) and utilized as received without further purification. All solvents were purchased from Merck (UK) or Thermo Fisher Scientific (UK) and utilized as received without further purification. Dimethyl sulfoxide-d6 (DMSO-d6), Chloroform-d used for nuclear magnetic resonance (NMR) measurement, was purchased from Thermo Fisher Scientific (UK).

### 3.7.2 Instrumentation

1. NMR spectroscopy: NMR spectra were recorded on a Bruker Avance 300, a Bruker Avance III HD 400 or a Bruker Avance III HD 500 spectrometer at 298K and 300, 400 and 500 MHz, respectively. Shifts are quoted in δ in parts per million and quoted relative to the internal standard trimethylsilane (TMS).

2. High-Resolution Mass Spectra (HR-MS) were obtained by using Bruker UHR-Q-ToF MaXis

spectrometer with electrospray ionization.

3. UV-vis spectroscopy was performed on Evolution 350 UV-Vis spectrophotometer equipped with Xenon Flash Lamp light source and Dual Matched Silicon Photodiodes detector. Quartz cells (170 - 2000 nm) from Hellma with two polished sides were used for examining the absorption spectral data by using Thermo INSIGHT-2 v.10.0.30319.1 software.

4. Fluorescence spectral data were obtained with an Edinburgh Instruments FS5 Spectrofluorometer. Quartz cells with four polished sides (Starna) were used for fluorescence measurements.

5. X-ray analysis data were collected on Agilent Technologies SuperNova single crystal X-ray diffractometer with dual wavelength microfocus X-ray sources (Mo and Cu) and an Atlas detector. The system is complemented by an Oxford Cryosystems Cryostream to collect data at temperatures as low as 100 K. The structures were solved by direct methods and refined anisotropically by the

least-squares procedure implemented in the SHELX program system.

### 3.7.3 Computational details

The geometries of all compounds in the ground state were optimised using the density functional theory (DFT) method at the PBE1PBE/def2SVP level, The excited-state geometries were optimized using the time-dependent DFT method at the same level of theory. To investigate the solvent effect on the energy level and the distribution of electron density of each compound, the solvation model based on the density model of SMD and self-consistent reaction field was considered in the calculations. All the above calculations were carried out using the Gaussian 16 program.

### 3.7.4 Synthetic methods

1. synthesis of α-Cyanostilbene-Based derivatives

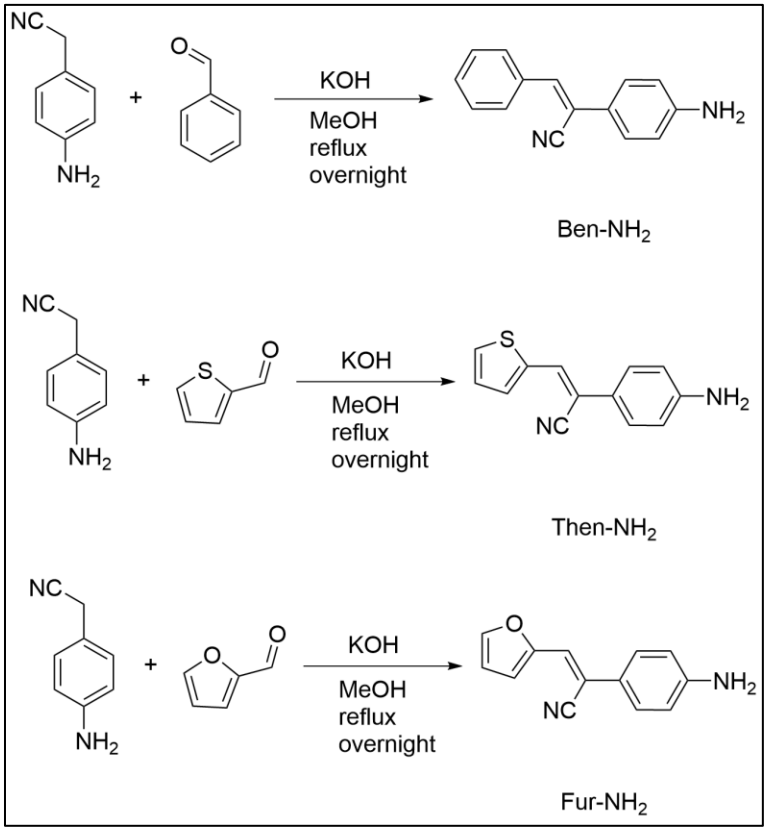


Scheme 1 Synthesis of α-Cyanostilbene-Based derivatives.

The synthesis of Ben-NH2 serves as an example: In a one-neck round-bottom flask, 4-

Aminophenylacetonitrile (1g, 7.58 mmol, 1.5 eq.) was dissolved in methanol. Subsequently, potassium hydroxide (0.57g, 2 eq.) was also dissolved in methanol and added to the mixture. Benzaldehyde (0.54g, 5.06 mmol, 1 eq.) was then introduced. The solution was refluxed overnight. Upon completion of the reaction, the solvent was removed under reduced pressure, and the residue was recrystallized from ethanol to yield a yellow solid (90% yield).

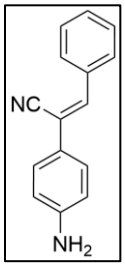


**$^{1}$H NMR (400 MHz, DMSO-d6, 25°C, TMS) δ (ppm)**: 7.86 (m, J = 7.4Hz, 2H), 7.70 (s, 1H), 7.49-7.43 (m, 5H), 6.66 (m, J = 7.4Hz, 2H), 5.63 (s, 2H).

**$^{13}$C NMR (101 MHz, CDCl3, 25°C, TMS) δ (ppm)**: 150.64, 149.24, 148.62, 137.07, 136.62, 134.95, 129.95, 129.70, 129.49, 129.28, 129.16, 129.04, 128.98, 128.51, 128.20, 127.29, 121.20, 120.27, 120.08, 118.78, 117.82, 114.58, 114.52, 114.34, 114.08, 111.44, 53.66, 40.63, 40.42, 40.21, 40.00, 39.79, 39.58, 39.49, 39.37, 22.00.

**HRMS**: m/z: calculated for $[C_{15}H_{12}N_2]^-$: 220.1000, found: 220.1014.

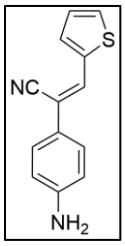


**$^{1}$H NMR (400 MHz, DMSO-d6, 25°C, TMS) δ (ppm)**: 7.93 (s, 1H), 7.77 (dd, J = 7.4Hz, 1H), 7.62 (dt, J = 3.6, 1.0Hz, 1H), 7.41 (m, J = 7.8Hz, 2H), 7.20 (dd, J = 5.1, 3.7Hz, 1H), 6.64 (m, J = 7.7Hz, 2H), 5.60 (s, 2H).

**$^{13}$C NMR (101 MHz, CDCl3, 25°C, TMS) δ (ppm)**: 150.41, 138.77, 132.77, 130.22, 129.93, 129.16, 128.25, 127.01, 120.75, 118.86, 114.57, 114.42, 107.75, 40.63, 40.42, 40.21, 40.00, 39.79, 39.59, 39.37, 22.00.

**HRMS**: m/z: calculated for $[C_{13}H_{10}N_2S]^-$: 226.0565, found: 226.0538.

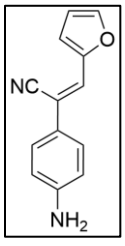


**$^{1}$H NMR (400 MHz, DMSO-d6, 25°C, TMS) δ (ppm)**: 7.89 (d, J = 7.9Hz 1H), 7.51 (s, 1H), 7.40 (dd, J = 5.0Hz, 2.1Hz, 2H), 7.00 (d, J = 3.5Hz, 1H), 6.70 (dd, J = 7.7Hz 1H), 6.63 (d, J = 8.7Hz, 2H), 5.62 (s, 2H).

**$^{13}$C NMR (101 MHz, CDCl3, 25°C, TMS) δ (ppm)**: 150.75, 150.51, 145.34, 129.16, 127.00, 123.31, 120.66, 118.45, 114.57, 114.39, 113.27, 107.36, 40.63, 40.42, 40.21, 40.00, 39.79, 39.58, 39.37.

**HRMS**: m/z: calculated for $[C_{13}H_{10}N_2O]^-$: 210.0793, found: 210.0789.

2. synthesis of $R_1$-maleimide derivatives ($R_1$ = Ben-$NH_2$, Then-$NH_2$, Fur-$NH_2$)

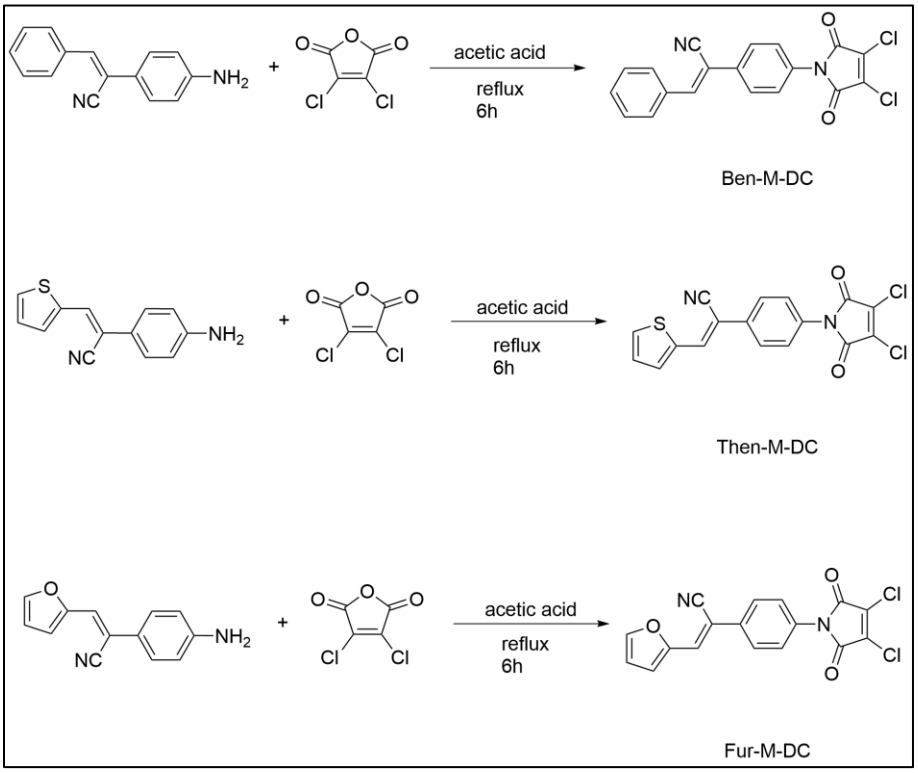


Scheme 2 synthesis of $R_1$-maleimide derivatives.

2,3-Dichloromaleic anhydride (1 eq.) was dissolved in acetic acid. Ben-NH2 (alternatively, Then-NH2 or Fur-NH2) (1 eq.) was then added to the mixture. The solution was refluxed for 6 hours. After the reaction concluded, the solution was allowed to cool and then filtered. The residue was washed with methanol to yield a dark red solid (93% yield).

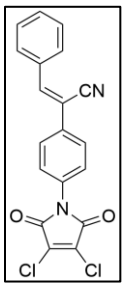

**$^1$H NMR (400 MHz, DMSO-d6, 25°C, TMS) δ (ppm)**: 8.13 (s, 1H), 7.95 (dd, J = 1.4, 4.7 Hz, 5H), 7.58-7.55 (m, 4H).

**$^{13}$C NMR (101 MHz, CDCl3, 25°C, TMS) δ (ppm)**: 162.51, 144.49, 134.30, 133.31, 132.12, 131.37, 129.71, 129.52, 127.84, 127.06, 109.92, 40.64, 40.43, 40.22, 40.01, 39.80, 39.59, 39.38.

**HRMS**: m/z: calculated for $[C_{19}H_{10}Cl_2N_2O_2]^-$: 368.0119, found: 368.0121.

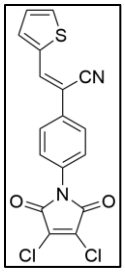

**$^{1}$H NMR (400 MHz, DMSO-d6, 25°C, TMS) δ (ppm)**: 8.38 (s, 1H), 7.97 (d, J = 1.1 Hz, 1H), 7.87 (d, J = 8.7 Hz, 2H), 7.80 (dt, J = 3.6, 1.1 Hz, 1H), 7.53 (d, J = 8.7 Hz, 2H), 7.30 (dd, J = 5.1, 3.7 Hz, 1H).

**$^{13}$C NMR (101 MHz, CDCl3, 25°C, TMS) δ (ppm)**: 162.51, 137.89, 137.12, 135.49, 133.93, 133.29, 132.55, 131.74, 128.63, 127.85, 126.63, 118.32, 105.71, 40.63, 40.42, 40.22, 40.01, 39.80, 39.59, 39.38.

**HRMS**: m/z: calculated for $[C_{17}H_8Cl_2N_2O_2S]^-$: 373.9684, found: 373.9681.

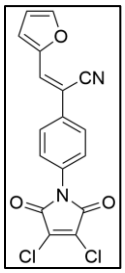

**$^{1}$H NMR (400 MHz, DMSO-d6, 25°C, TMS) δ (ppm)**: 8.05 (dd, J = 1.8, 0.7 Hz, 1H), 7.95 (s, 1H), 7.87 (m, 2H), 7.51 (d, J = 6.7 Hz, 2H), 7.20 (dt, J = 3.5, 0.6 Hz, 1H), 6.79 (dd, J = 3.5, 1.8 Hz, 1H).

**$^{13}$C NMR (101 MHz, CDCl3, 25°C, TMS) δ (ppm)**: 162.50, 150.03, 147.12, 133.84, 133.29, 131.80, 129.80, 127.83, 126.60, 118.12, 117.92, 113.79, 105.21, 40.63, 40.42, 40.21, 40.00, 39.80, 39.59, 39.38.

**HRMS**: m/z: calculated for $[C_{17}H_8Cl_2N_2O_3]^-$: 357.9912, found: 357.9915.

3. synthesis of $R_2$-M-aniline ($R_2$ = Ben-M-DC, Then-M-DC, Fur-M-DC)

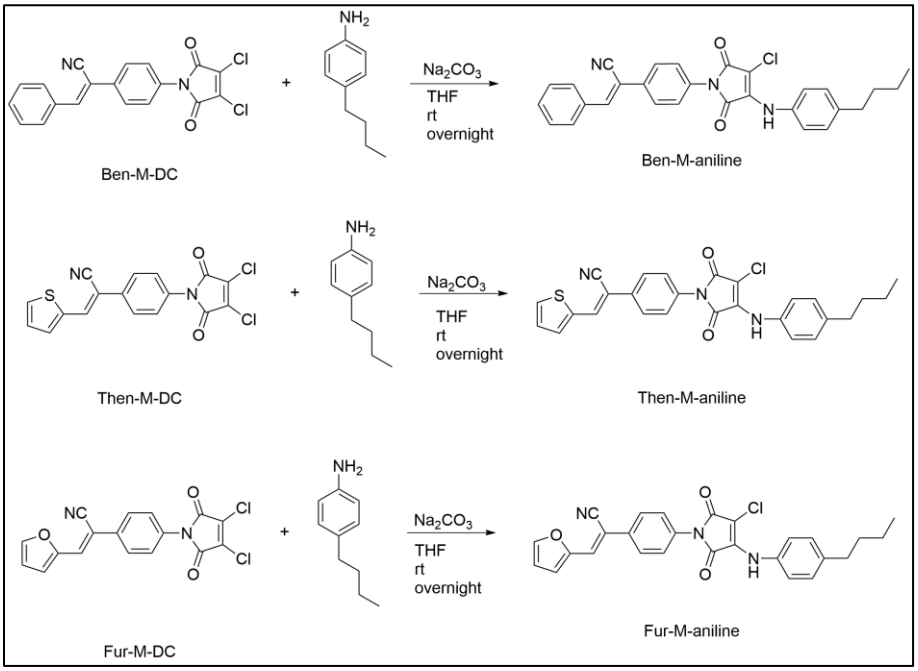


Scheme 3 Synthesis of $R_2$-M-aniline.

Ben-M-DC (Then-M-DC, Fur-M-DC) (1 eq.) was dissolved in THF, and Sodium carbonate (2.5 eq.) was then added to the mixture. 4-Butylaniline (1.5 eq.) was added to the mixture. The solution was stirred at room temperature overnight. After the reaction concluded, the solvent was filtered and removed under pressure. The residue was washed with methanol to obtain a yellow solid (90% yield).

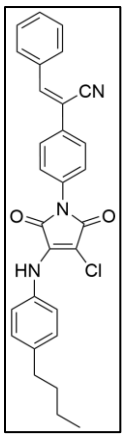


**$^{1}$H NMR (400 MHz, DMSO-d6, 25°C, TMS) δ (ppm)**: 9.96 (s, 1H), 8.12 (s, 1H), 7.97 (d, J = 7.2 Hz, 2H), 7.90 (d, J = 7.5 Hz, 2H), 7.58-7.54 (m, 5H), 7.19 (dd, J = 17.1 Hz, 4H), 2.13 (t, J = 7.7 Hz, 2H), 1.57 (m, J = 7.3 Hz, 2H), 1.33 (m, J = 7.3 Hz, 2H), 0.91 (t, J = 7.3 Hz, 3H).

**$^{13}$C NMR (101 MHz, CDCl3, 25°C, TMS) δ (ppm)**: 166.54, 164.75, 144.01, 140.05, 139.13, 134.70, 134.13, 133.35, 132.88, 131.27, 129.67, 129.50, 128.52, 127.39, 126.80, 124.59, 118.25, 110.06, 92.04, 40.63, 40.42, 40.21, 40.01, 39.80, 39.59, 39.38, 34.79, 33.58, 25.60, 22.24, 14.27.

**HRMS**: m/z: calculated for $[C_{19}H_{24}ClN_3O_2]^-$: 481.1557, found: 481.1548.

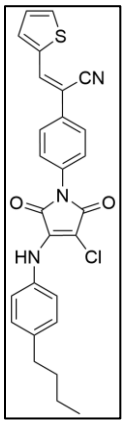


**$^{1}$H NMR (400 MHz, DMSO-d6, 25°C, TMS) δ (ppm)**: 9.95 (s, 1H), 8.36 (s, 1H), 7.96 (d, J = 5.2 Hz, 1H), 7.85 (d, J = 8.7 Hz, 2H), 7.79 (d, J = 2.5 Hz, 1H), 7.56 (d, J = 6.5 Hz, 2H), 7.29 (dd, J = 5.1, 3.7 Hz, 1H), 7.22 (d, J = 7.4 Hz, 2H), 7.15 (d, J = 8.5 Hz, 2H), 2.59 (t, J = 7.7 Hz, 2H), 1.57 (m, J = 7.3 Hz, 2H), 1.32 (m, J = 7.3 Hz, 2H), 0.91 (t, J = 7.3 Hz, 3H).

**$^{13}$C NMR (101 MHz, CDCl3, 25°C, TMS) δ (ppm)**: 166.55, 164.75, 140.04, 139.12, 137.96, 136.69, 135.31, 134.70, 132.99, 132.51, 132.37, 128.60, 128.52, 127.44, 126.40, 124.58, 118.37, 105.91, 92.02, 67.49, 40.63, 40.42, 40.22, 40.01, 39.80, 39.59, 39.38, 34.78, 33.57, 22.23, 14.26.

**HRMS**: m/z: calculated for $[C_{27}H_{22}ClN_3O_2S]^-$: 487.1121, found: 487.1124.

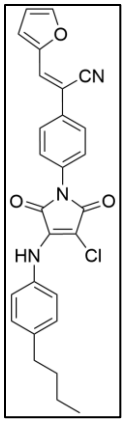

**$^{1}$H NMR (400 MHz, DMSO-d6, 25°C, TMS) δ (ppm)**: 9.96 (s, 1H), 8.05 (dd, J = 1.8, 0.7 Hz, 1H), 7.95 (s, 1H), 7.84 (d, J = 6.52 Hz, 2H), 7.54 (d, J = 1.9, 2.0 Hz, 2H), 7.20 (d, J = 8.1 Hz, 3H), 7.14 (d, J = 8.2 Hz, 2H), 6.79 (dd, J = 3.5, 1.8 Hz, 1H), 2.58 (t, J = 7.7 Hz, 2H), 1.55 (m, J = 7.4 Hz, 2H), 1.32 (m, J = 7.4 Hz, 2H), 0.91 (t, J = 7.3 Hz, 3H).

**$^{13}$C NMR (101 MHz, CDCl3, 25°C, TMS) δ (ppm)**: 166.54, 164.74, 150.09, 146.99, 140.04, 139.12, 134.69, 132.89, 132.58, 129.40, 128.51, 127.40, 126.37, 124.58, 117.97, 117.86, 113.75, 105.42, 92.02, 40.63, 40.42, 40.21, 40.00, 39.80, 39.59, 39.38, 34.78, 33.57, 22.23, 14.26.

**HRMS**: m/z: calculated for $[C_{27}H_{12}ClN_3O_3]^-$: 471.1350, found: 471.1346.

3. synthesis of maleimide fluorophores

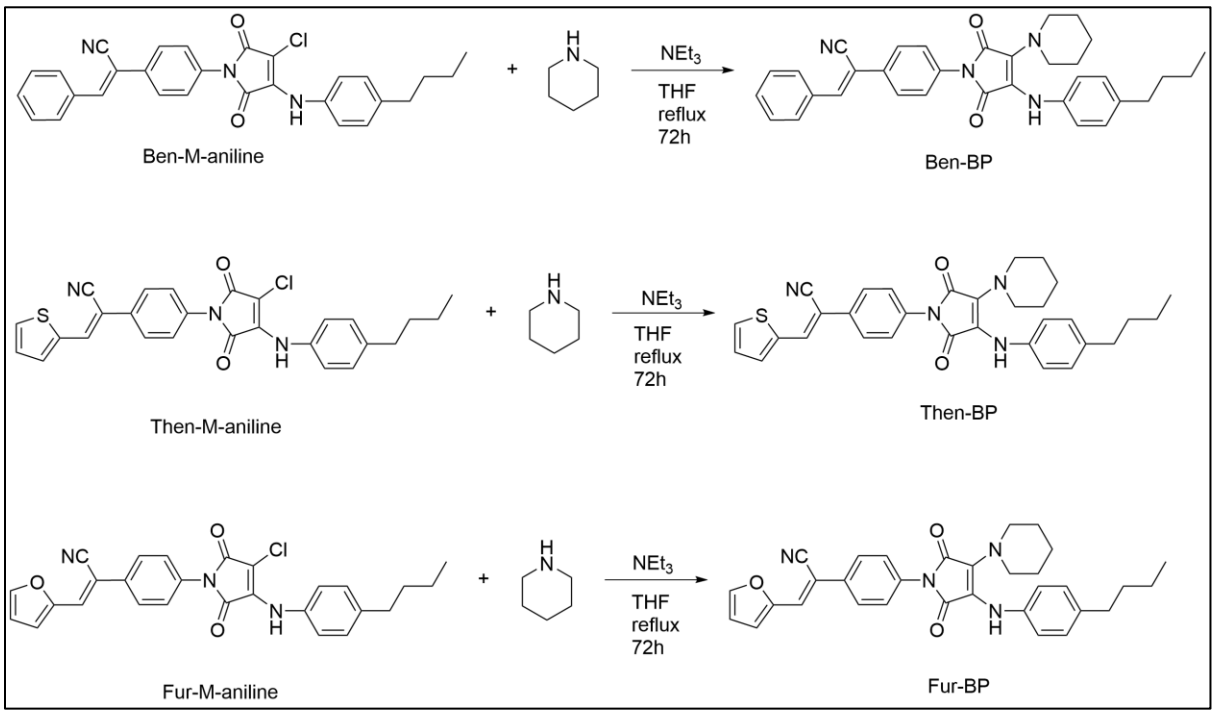


Scheme 4 Synthesis of maleimide fluorophores.

Ben-M-aniline (Then-M-aniline, Fur-M-aniline) (1 eq.) was dissolved in THF, and triethylamine (5 eq.) was then added to the mixture. Subsequently, piperidine (5 eq.) was added to the mixture. The solution was refluxed for 72h. After the reaction concluded, the solution was filtrated and removed under pressure. The residue was washed with methanol to obtain an orange solid (75% yield).

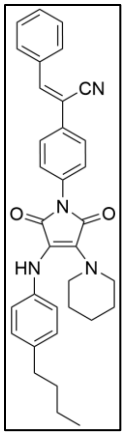

**$^1$H NMR (400 MHz, DMSO-d6, 25°C, TMS) δ (ppm)**: 8.10 (s, 1H), 7.96 (d, J = 8.1 Hz, 2H), 7.85 (m, 3H), 7.53 (m, 5H), 7.03 (d, J = 8.2 Hz, 2H), 6.76 (d, J = 8.1 Hz, 2H), 3.36 (t, J = 5.4 Hz, 4H), 2.47 (m, 2H), 1.50-1.30 (m, 10H), 0.89 (t, J = 7.3Hz, 3H).

**$^{13}$C NMR (101 MHz, CDCl3, 25°C, TMS) δ (ppm)**: 168.09, 166.89, 143.57, 141.26, 134.18, 133.48, 133.32, 132.48, 131.17, 130.91, 129.63, 129.47, 128.81, 127.06, 126.58, 118.28, 116.89, 112.86, 110.16, 67.49, 48.80, 40.63, 40.42, 40.26, 40.21, 40.00, 39.79, 39.58, 39.37, 34.57, 33.97, 25.98, 25.60, 24.06, 22.06, 14.28.

**HRMS**: m/z: calculated for $[C_{34}H_{34}N_4O_2]^-$: 530.2682, found: 530.2677.

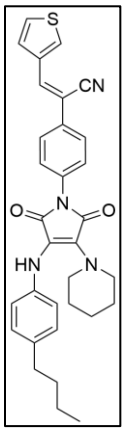

**$^1$H NMR (400 MHz, DMSO-d6, 25°C, TMS) δ (ppm)**: 8.34 (s, 1H), 7.94 (dd, J = 5.1, 0.9 Hz, 1H), 7.80 (m, 4H), 7.50 (d, J = 7.9 Hz, 2H), 7.28 (dd, J = 5.0, 3.7 Hz, 2H), 7.03 (d, J = 7.7Hz, 2H), 6.76 (d, J = 7.7Hz, 2H), 3.36 (t, J = 5.4 Hz, 4H), 2.48 (m, 2H), 1.51-1.33 (m, 10H), 0.89 (t, J = 7.3Hz, 3H).

**$^{13}$C NMR (101 MHz, CDCl3, 25°C, TMS) δ (ppm)**: 168.10, 166.89, 141.27, 138.02, 136.28, 135.15, 133.46, 132.96, 132.20, 132.12, 130.92, 128.80, 128.56, 127.12, 126.19, 118.40, 116.88, 112.83, 106.02, 48.80, 40.64, 40.43, 40.22, 40.01, 39.80, 39.59, 39.38, 34.56, 33.96, 25.98, 24.06, 22.06, 14.28.

**HRMS**: m/z: calculated for $[C_{32}H_{32}N_4O_2S]^-$: 536.2246, found: 536.2241.

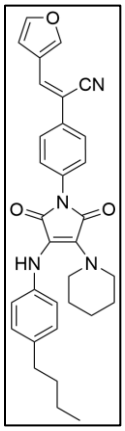

**$^1$H NMR (400 MHz, DMSO-d6, 25°C, TMS) δ (ppm)**: 8.09 (s, 1H), 7.95 (d, J = 7.9 Hz, 2H), 7.84 (m, 3H), 7.56-7.52 (m, 5H), 7.03 (d, J = 7.6 Hz, 2H), 6.75 (d, J = 7.6 Hz, 2H), 3.35 (t, J = 5.4 Hz 4H), 2.47 (m, 2H), 1.51-1.27 (m, 10H), 0.88 (t, J = 7.3Hz, 3H).

**$^{13}$C NMR (101 MHz, CDCl3, 25°C, TMS) δ (ppm)**: 168.14, 167.12, 142.36, 139.22, 135.94, 133.67, 132.89, 132.70, 130.64, 129.34, 129.00, 128.86, 127.07, 126.45, 125.80, 117.84, 117.61, 113.59, 111.01, 77.37, 77.06, 76.74, 48.98, 34.89, 33.87, 26.02, 24.06, 22.27, 13.99.

**HRMS**: m/z: calculated for $[C_{32}H_{32}N_4O_3]^-$: 520.2474, found: 520.2475.

5. synthesis of benzothiazole-M-DC

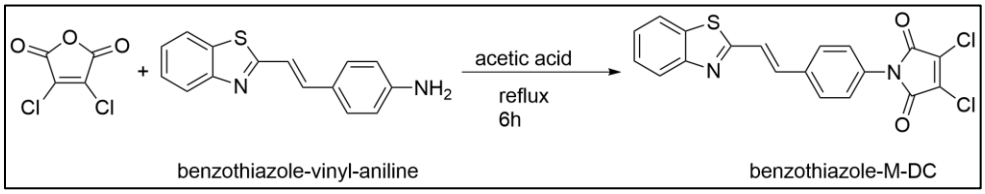


Scheme 5 Synthesis of benzothiazole-M-DC.

2,3-Dichloromaleic anhydride (0.66g, 4mmol, 1 eq.) was dissolved in acetic acid. Benzothiazole-vinyl-aniline (1g, 4mmol, 1 eq.) was then added to the mixture. The solution was refluxed for 6 hours. After the reaction concluded, the solution was allowed to cool and then filtered. The residue was washed with methanol to yield a brown solid (91% yield).

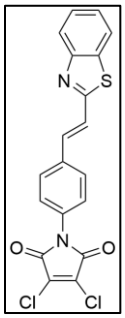

**$^{1}$H NMR (400 MHz, DMSO-d6, 25°C, TMS) δ (ppm)**: 8.12 (td, J = 1.0, 0.6, Hz, 1H), 8.00 (dd, J = 1.2, 1.2 Hz, 1H), 7.94 (d, J = 7.9 Hz, 2H), 7.71 (d, J = 3.5Hz, 2H), 7.49 (m, 4H).

The solubility of the compound is too poor to measure the $^{13}$C NMR spectra.

**HRMS**: m/z: calculated for $[C_{19}H_{10}Cl_2N_2O_2S]^-$: 399.9840, found: 399.9831.

6. synthesis of benzothiazole-M-aniline

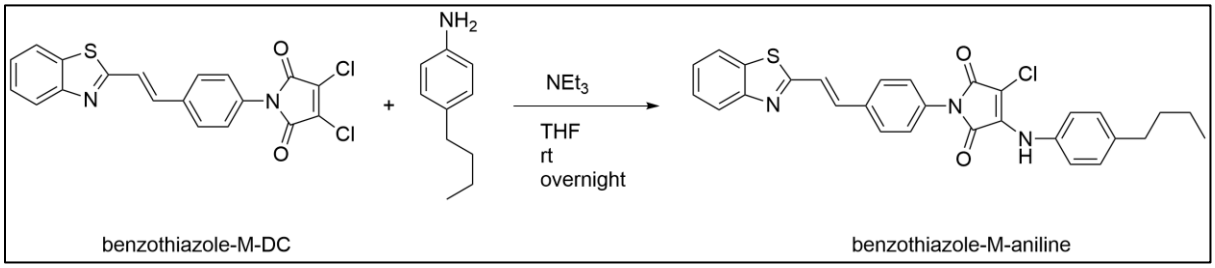


Scheme 6 Synthesis of benzothiazole-M-aniline.

benzothiazole-M-DC (1g, 2,49mmol, 1 eq.) was dissolved in THF, and Sodium carbonate (0.66g, 6.23mmol, 2.5 eq.) was then added to the mixture. 4-Butylaniline (0.6ml, 3.74mmol, 1.5 eq.) was added to the mixture. The solution was stirred at room temperature overnight. After the reaction concluded, the solvent was filtered and removed under pressure. The residue was washed with methanol to obtain a yellow solid (90% yield).

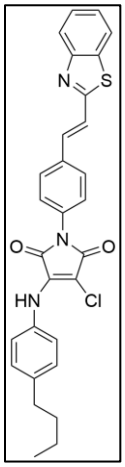

**$^{1}$H NMR (400 MHz, DMSO-d6, 25°C, TMS) δ (ppm)**: 9.94 (s, 1H), 8.12 (ddd, J = 8.0, 1.3, 0.7 Hz, 1H), 7.99 (ddd, J = 8.2, 1.3, 0.7 Hz, 1H), 7.96 (d, J = 7.9 Hz, 2H), 7.70 (d, J = 7.9 Hz, 2H), 7.54-7.45 (m, 4H), 7.21 (dd, J = 1.9, 1.8Hz, 2H), 7.15 (dd, J = 1.9, 1.8Hz, 2H). 2.58 (m, J = 7.7 Hz, 2H), 1.56 (dq, J = 14.6, 7.4 Hz, 2H), 1.32 (dq, J = 14.6, 7.4 Hz, 2H), 0.91 (t, J = 7.3Hz, 3H).

**$^{13}$C NMR (101 MHz, CDCl3, 25°C, TMS) δ (ppm)**: 166.75, 166.58, 164.76, 153.93, 140.03, 139.10, 136.95, 134.79, 134.71, 134.58, 132.93, 128.71, 128.54, 128.52, 127.53, 127.12, 127.05, 126.01, 124.58, 123.07, 122.94, 122.70, 92.02, 67.49, 40.64, 40.44, 40.23, 40.02, 39.81, 39.60, 39.39, 34.78, 33.57, 22.23, 14.26.

**HRMS**: m/z: calculated for $[C_{29}H_{24}ClN_3O_2S]^-$: 513.1278, found: 513.1273.

7. synthesis of benzothiazole-maleimide fluorophore

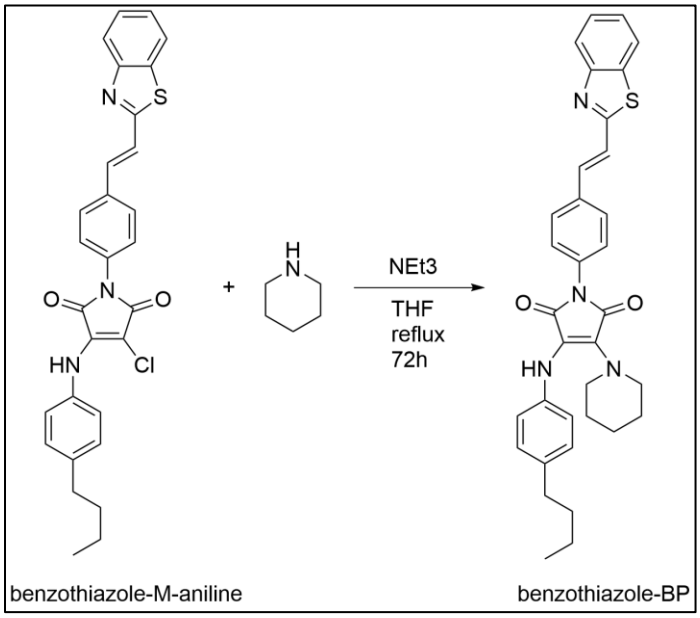


Scheme Synthesis of benzothiazole-maleimide fluorophore.

benzothiazole-M-aniline (1g, 1.95 mmol, 1 eq.) was dissolved in THF, and triethylamine (1.35ml, 9.73mmol, 5 eq.) was then added to the mixture. Subsequently, piperidine (0.96ml, 9.73mmol, 5 eq.) was added to the mixture. The solution was refluxed for 72h. After the reaction concluded, the solution was filtrated and removed under pressure. The residue was washed with methanol to obtain an orange solid (72% yield).

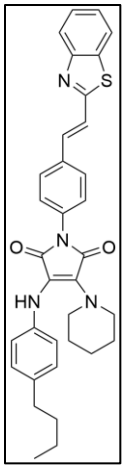

**$^{1}$H NMR (400 MHz, $CDCl_3$, 25°C, TMS) δ (ppm)**: 7.93 (dt, J = 8.2, 1.2, 0.6 Hz, 1H), 7.80 (dt, J = 7.9, 1.3, 0.6 Hz, 1H), 7.75 (d, J = 8.6 Hz, 2H), 7.46-7.32 (d, J = 8.4 Hz, 8H), 7.02 (d, J = 8.4 Hz, 2H), 5.84 (s, 1H), 3.31 (t, J = 5.3 Hz, 4H), 2.50 (t, *J* = 7.9 Hz, 2H), 1.50-1.28 (m, 10H), 0.86 (t, J = 7.3 Hz, 3H).

**$^{13}$C NMR (101 MHz, $CDCl_3$, 25°C, TMS) δ (ppm)**: 168.17, 167.20, 166.84, 153.88, 139.22, 136.77, 135.92, 134.41, 133.75, 132.90, 128.85, 128.00, 127.80, 126.95, 126.37, 126.24, 125.69, 125.40, 123.87, 123.00, 122.39, 121.54, 117.62, 113.65, 77.35, 77.03, 76.72, 49.84, 48.98, 34.88, 33.85, 26.79, 26.02, 24.06, 22.26, 13.97.

**HRMS**: m/z: calculated for $[C_{34}H_{34}N_4O_2S]^-$: 562.2402, found: 562.2414.

8. synthesis of α-Tetralone-M-DC

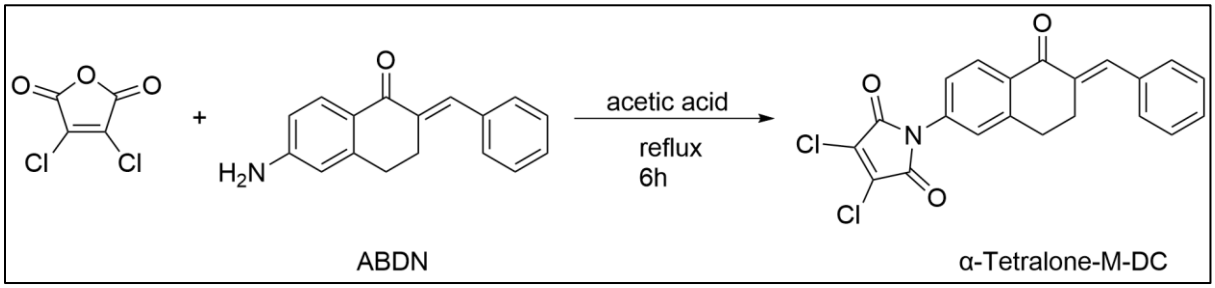


Scheme 8 Synthesis of α-Tetralone-M-DC.

2,3-Dichloromaleic anhydride (0.67g, 4.02 mmol, 1 eq.) was dissolved in acetic acid. ABDN (1g, 4.02 mmol, 1 eq.) was then added to the mixture. The solution was refluxed for 6 hours. After the reaction concluded, the solution was allowed to cool and then filtered. The residue was washed with methanol to yield a brown-red solid (90% yield).

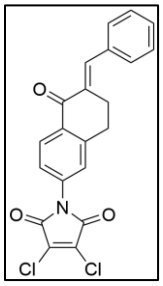

**$^{1}$H NMR (400 MHz, DMSO-d6, 25°C, TMS) δ (ppm)**: 8.10 (d, J = 8.3 Hz, 1H), 7.75 (d, J = 1.9Hz,1H), 7.56 (dd, J = 1.8, 4.3Hz, 2H), 7.45 (m, 5H), 3.14 (td, J = 6.9, 5.5, 1.9 Hz, 2H), 2.99 (dd, J = 7.6, 5.3 Hz, 2H).

**$^{13}$C NMR (101 MHz, DMSO-d6, 25°C, TMS) δ (ppm)**: 186.44, 162.32, 144.75, 136.58, 135.59, 133.41, 132.76, 130.45, 129.39, 129.09, 128.96, 126.46, 125.42, 40.64, 40.43, 40.23, 40.02, 39.81, 39.60, 39.39, 28.31, 26.98, 21.52.

**HRMS**: m/z: calculated for $[C_{21}H_{13}Cl_2NO_3]^-$: 397.0272, found: 397.0268.

9. synthesis of α-Tetralone-M-aniline

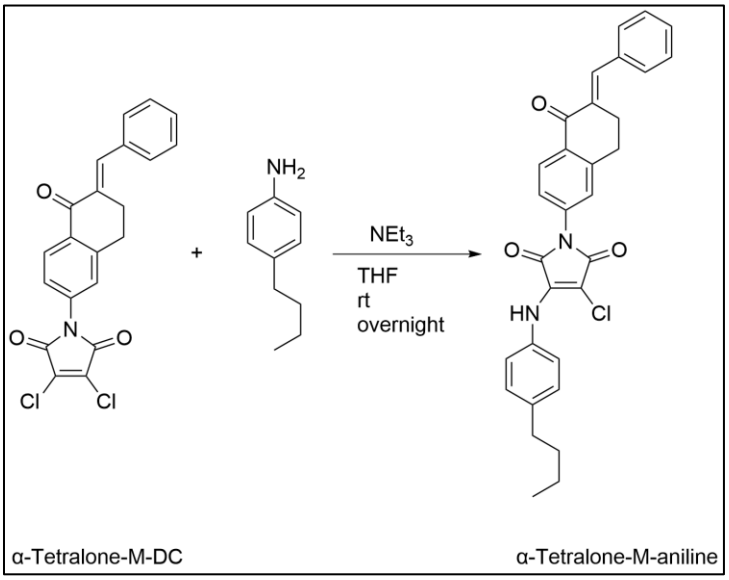


Scheme 9 Synthesis of α-Tetralone-M-aniline.

α-Tetralone-M-DC (1g, 2,51mmol, 1 eq.) was dissolved in THF, and Sodium carbonate (0.67g, 6.28mmol, 2.5 eq.) was then added to the mixture. 4-Butylaniline (0.6ml, 3.77mmol, 1.5 eq.) was added to the mixture. The solution was stirred at room temperature overnight. After the reaction concluded, the solvent was filtered and removed under pressure. The residue was washed with methanol to obtain a yellow solid (90% yield).

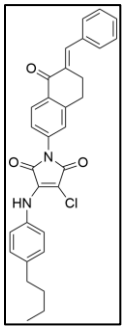

**$^{1}$H NMR (400 MHz, DMSO-d6, 25°C, TMS) δ (ppm)**: 9.98 (s, 1H), 8.07 (d, J = 8.3 Hz, 1H), 7.75 (d, J = 1.8 Hz, 1H), 7.49 (m, 7H), 7.21 (d, J = 8.5Hz, 2H), 7.14 (d, J = 8.5Hz, 2H), 3.14 (td, J = 7.9, 3.0 Hz, 2H), 2.99 (dd, J = 7.6, 5.2 Hz, 2H), 2.58 (t, J = 8.7, 2H), 1.56 (tt, J = 8.7, 7.3 Hz, 2H), 1.34 (tt, J = 8.7, 7.3 Hz, 2H), 0.90 (t, J = 7.3Hz, 3H).

**$^{13}$C NMR (101 MHz, DMSO-d6, 25°C, TMS) δ (ppm)**: 186.44, 166.30, 164.54, 144.54, 140.11, 139.22, 136.39, 135.71, 135.65, 134.66, 131.95, 130.43, 129.34, 129.08, 128.74, 128.52, 125.87, 124.95, 124.65, 92.26, 40.64, 40.43, 40.23, 40.02, 39.81, 39.60, 39.39, 34.78, 33.56, 28.41, 27.05, 22.23, 14.26.

**HRMS**: m/z: calculated for $[C_{31}H_{27}ClN_2O_3]^-$: 510.1710, found: 510.1724.

10. synthesis of α-Tetralone-maleimide fluorophore

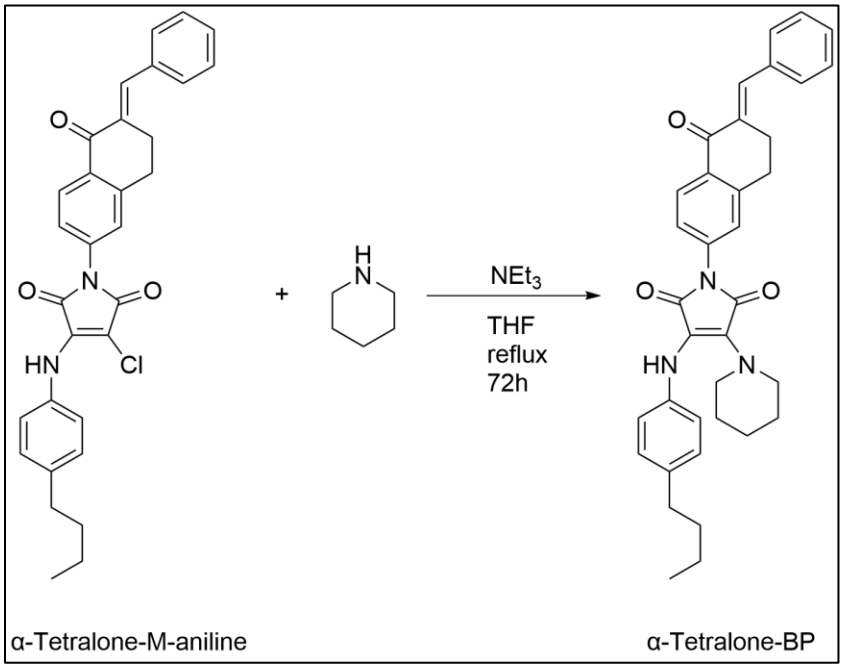


Scheme 10 Synthesis of α-Tetralone-maleimide fluorophore.

α-Tetralone-M-aniline (1g, 2mmol, 1 eq.) was dissolved in THF, and triethylamine (1.36ml, 9.78mmol, 5 eq.) was then added to the mixture. Subsequently, piperidine (0.96ml, 9.78mmol, 5 eq.) was added to the mixture. The solution was refluxed for 72h. After the reaction concluded, the solution was filtrated and removed under pressure. The residue was washed with methanol to obtain an orange solid (75% yield).

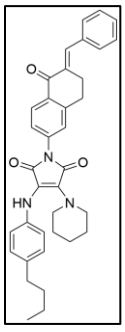

**$^{1}$H NMR (400 MHz, $CDCl_3$, 25°C, TMS) δ (ppm)**: 8.13 (d, J = 8.5 Hz, 1H), 7.81 (d, J = 1.7 Hz, 1H), 7.36 (m, 7H), 7.03 (d, J = 8.4 Hz, 2H), 6.69 (d, J = 8.4 Hz, 2H), 5.85 (s, 1H), 3.30 (t, J = 5.2 Hz, 4H), 3.07 (ddd, J = 6.8, 5.6, 1.8 Hz, 2H), 2.90 (dd, J = 7.6, 5.2 Hz, 2H), 2.50 (t, J = 7.6 Hz, 2H), 1.50-1.23 (m, 10H), 0.85 (t, J = 7.3Hz, 3H).

**$^{13}$C NMR (101 MHz, $CDCl_3$, 25°C, TMS) δ (ppm)**: 187.09, 167.95, 167.01, 144.01, 139.06, 136.80, 136.32, 136.06, 135.85, 135.33, 131.47, 129.91, 129.15, 128.87, 128.58, 128.46, 127.83, 126.90, 124.12, 123.56, 117.70, 113.84, 77.36, 77.04, 76.72, 49.01, 34.88, 33.85, 29.00, 27.12, 26.01, 24.04, 22.25, 13.97.

**HRMS**: m/z: calculated for $[C_{36}H_{37}N_3O_3]^-$: 559.2835, found: 559.2832.

11. synthesis of azobenzene-M-DC

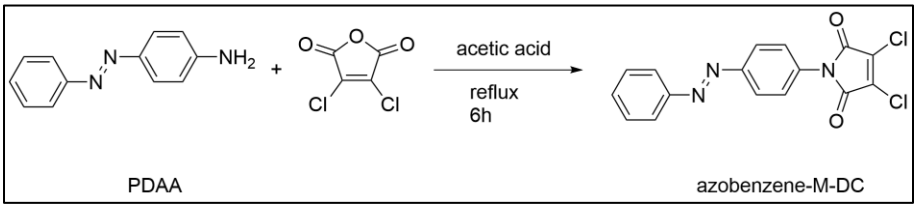


Scheme 11 Synthesis of azobenzene-M-DC.

2,3-Dichloromaleic anhydride (0.85g, 5.08mmol, 1 eq.) was dissolved in acetic acid. ABDN (1g, 5.08mmol, 1 eq.) was then added to the mixture. The solution was refluxed for 6 hours. After the reaction concluded, the solution was allowed to cool and then filtered. The residue was washed with methanol to yield a brown solid (86% yield).

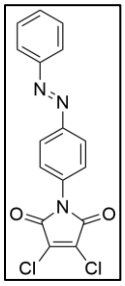

**$^{1}$H NMR (400 MHz, DMSO-d6, 25°C, TMS) δ (ppm)**: 8.04 (m, 2H), 7.92 (m, 2H), 7.63-7.57 (m, 5H).

**$^{13}$C NMR (101 MHz, DMSO-d6, 25°C, TMS) δ (ppm)**: 162.68, 162.47, 152.34, 151.53, 133.91, 133.37, 133.14, 132.38, 131.50, 130.02, 129.56, 129.02, 128.06, 127.51, 123.62, 123.17, 40.64, 40.44, 40.23, 40.02, 39.81, 39.60, 39.39.

**HRMS**: m/z: calculated for $[C_{16}H_9Cl_2N_3O_2]^-$: 345.0072, found: 345.0068.

12. synthesis of azobenzene-M-aniline

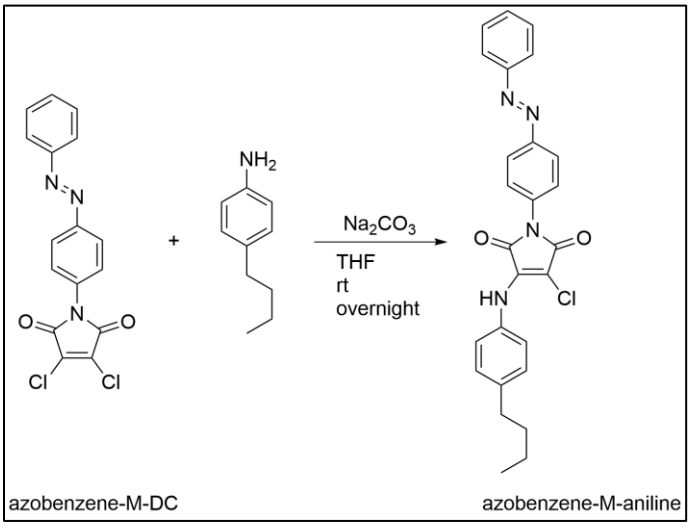


Scheme 12 Synthesis of azobenzene-M-aniline.

azobenzene-M-DC (1g, 2.9mmol, 1 eq.) was dissolved in THF, and Sodium carbonate (0.77g, 7.25mmol, 2.5 eq.) was then added to the mixture. 4-Butylaniline (0.68ml, 4.33mmol, 1.5 eq.) was added to the mixture. The solution was stirred at room temperature overnight. After the reaction concluded, the solvent was filtered and removed under pressure. The residue was washed with methanol to obtain a dark yellow solid (90% yield).

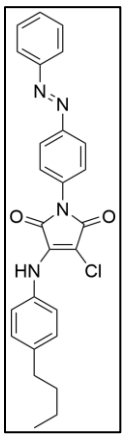

**$^{1}$H NMR (400 MHz, DMSO-d6, 25°C, TMS) δ (ppm)**: 9.97 (s, 1H), 8.02 (d, J = 8.8 Hz, 2H), 7.93 (d, J = 1.4 Hz, 2H), 7.64 (m, 5H), 7.21 (d,  = 8.5Hz, 2H), 7.16 (d, J = 8.4 Hz, 2H), 2.59 (t, J = 7.7 Hz, 2H), 1,56 (tdd, J = 10.4, 7.9, 4.4 Hz, 2H), 1.32 (dd, J = 7.3 Hz, 2H), 0.91 (t, J = 7.3Hz, 3H).

**$^{13}$C NMR (101 MHz, DMSO-d6, 25°C, TMS) δ (ppm)**: 166.44, 164.68, 152.38, 150.87, 140.06, 139.18, 134.74, 134.68, 132.16, 129.95, 129.31, 128.49, 127.40, 127.17, 124.60, 124.53, 123.43, 123.11, 92.21, 79.76, 79.44, 79.10, 40.66, 40.45, 40.24, 40.03, 39.82, 39.62, 39.41, 34.81, 33.58, 22.24, 14.26.

**HRMS**: m/z: calculated for $[C_{26}H_{23}ClN_4O_2]^-$: 458.1510, found: 458.1513.

13. synthesis of azobenzene-maleimide fluorophore

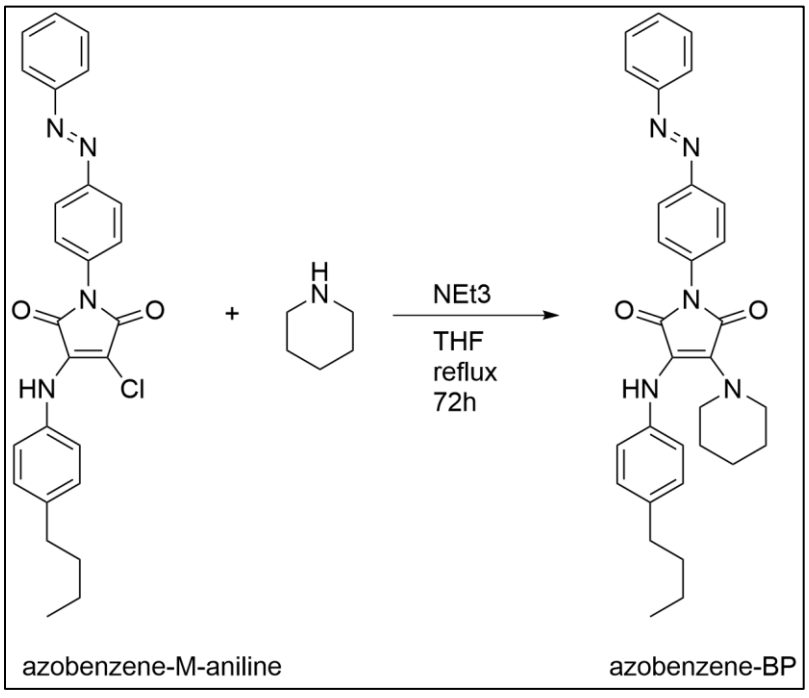


Scheme 13 Synthesis of azobenzene-maleimide fluorophore.

azobenzene-M-aniline (1g, 2.18mmol, 1 eq.) was dissolved in THF, and triethylamine (1.52ml, 10.9mmol, 5 eq.) was then added to the mixture. Subsequently, piperidine (1.07ml, 10.9mmol, 5 eq.) was added to the mixture. The solution was refluxed for 72h. After the reaction concluded, the solution was filtrated and removed under pressure. The residue was washed with methanol to obtain an orange solid (73% yield).

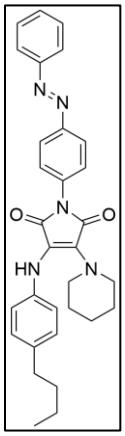

**$^{1}$H NMR (400 MHz, $CHCl_3$, 25°C, TMS) δ (ppm)**: 7.92 (dd, J = 2.0, 2.0Hz 2H), 7.85 (dd, J = 1.7, 1.8Hz, 2H), 7.53 (d, J = 8.7Hz, 2H), 7.46 (m, 3H), 7.03 (d, J = 8.4Hz, 2H), 6.70 (d, J = 8.4Hz, 2H), 5.86 (s, 1H), 3.31 (t, J = 5.3 Hz, 4H), 2.50 (t, J = 7.7 Hz, 2H), 1.49-1.28 (m, 10H), 0.85 (t, J = 7.4 Hz, 3H).

**$^{13}$C NMR (101 MHz, $CHCl_3$, 25°C, TMS) δ (ppm)**: 168.14, 167.16, 152.68, 150.59, 139.19, 135.96, 134.38, 131.03, 129.10, 128.86, 126.97, 125.70, 123.37, 122.90, 117.66, 113.75, 77.35, 77.03, 76.71, 49.00, 34.89, 33.86, 26.02, 24.07, 22.26, 13.98.

**HRMS**: m/z: calculated for $[C_{31}H_{33}N_5O_2]^-$: 507.2634, found: 507.2627.

14. synthesis of Anthracene-M-DC

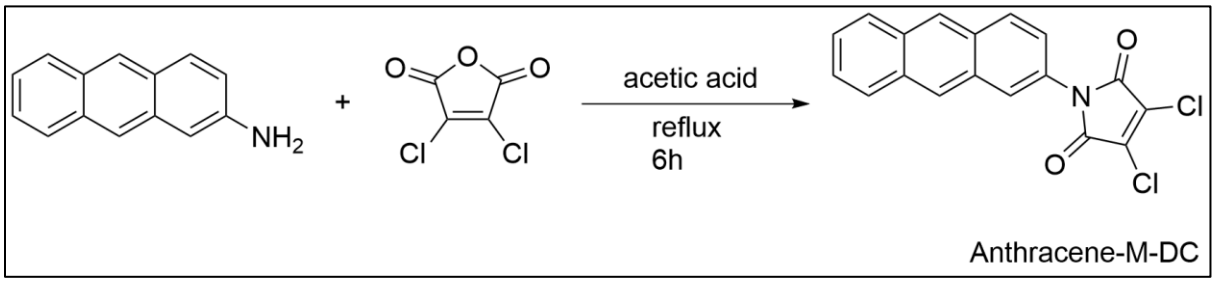


Scheme 14 Synthesis of Anthracene-M-DC.

2,3-Dichloromaleic anhydride (0.87g, 5.18mmol, 1 eq.) was dissolved in acetic acid. 2-Aminoanthracene (1g, 5.18mmol, 1 eq.) was then added to the mixture. The solution was refluxed for 6 hours. After the reaction concluded, the solution was allowed to cool and then filtered. The residue was washed with methanol to yield a brown-grey solid (86% yield).

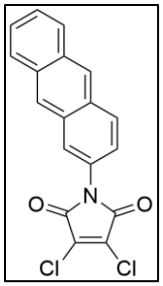

**$^{1}$H NMR (400 MHz, DMSO-d6, 25°C, TMS) δ (ppm)**: 8.43 (t, J = 1.7Hz, 2H), 8.00-7.93 (m, 4H), 7.38 (m, 3H).

The solubility of the compound is too poor to measure the $^{13}$C NMR spectra.

**HRMS**: m/z: calculated for $[C_{18}H_9Cl_2NO_2]^-$: 341.0010, found: 341.0013.

15. synthesis of Anthracene-M-aniline

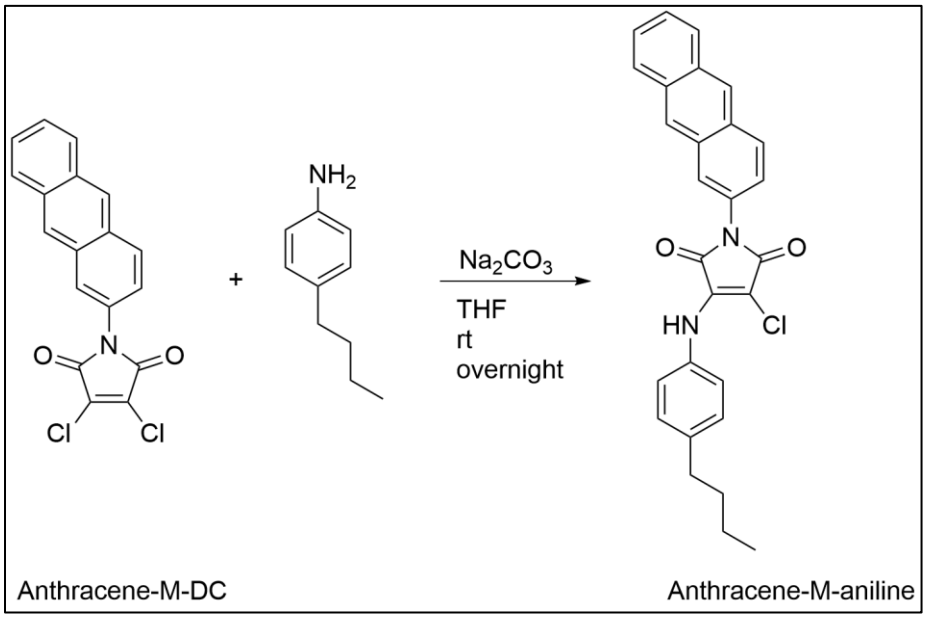


Scheme 15 Synthesis of Anthracene-M-aniline.

Anthracene-M-DC (1g, 3mmol, 1 eq.) was dissolved in THF, and Sodium carbonate (0.77g, 7.25mmol, 2.5 eq.) was then added to the mixture. 4-Butylaniline (0.68ml, 4.33mmol, 1.5 eq.) was added to the mixture. The solution was stirred at room temperature overnight. After the reaction concluded, the solvent was filtered and removed under pressure. The residue was washed with methanol to obtain a dark yellow solid (90% yield).

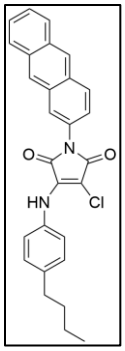

**$^{1}$H NMR (400 MHz, DMSO-d6, 25°C, TMS) δ (ppm)**: 9.98 (s, 1H), 8.65 (s, 1H), 8.20-8.13 (m, 4H), 7.56 (m, 3H), 7.18 (m, 4H), 2.59 (t, J = 5.7Hz, 2H), 1.57 (td, J = 14.7, 8.3, 6.2 Hz, 2H), 1.34 (td, J = 14.7, 8.3, 6.2 Hz 2H), 0.91 (t, J = 7.3Hz, 3H).

**$^{13}$C NMR (101 MHz, DMSO-d6, 25°C, TMS) δ (ppm)**: 166.89, 165.08, 140.03, 139.15, 134.76, 132.00, 131.02, 130.32, 129.38, 129.25, 128.61, 128.54, 128.50, 126.88, 126.67, 126.50, 126.43, 125.58, 125.04, 124.61, 91.99, 40.63, 40.42, 40.26, 40.21, 40.00, 39.79, 39.58, 39.37, 34.79, 33.59, 22.24, 14.27.

**HRMS**: m/z: calculated for $[C_{28}H_{23}ClN_2O_2]^-$: 454.1448, found: 454.1436.

16. synthesis of Anthracene-maleimide fluorophore

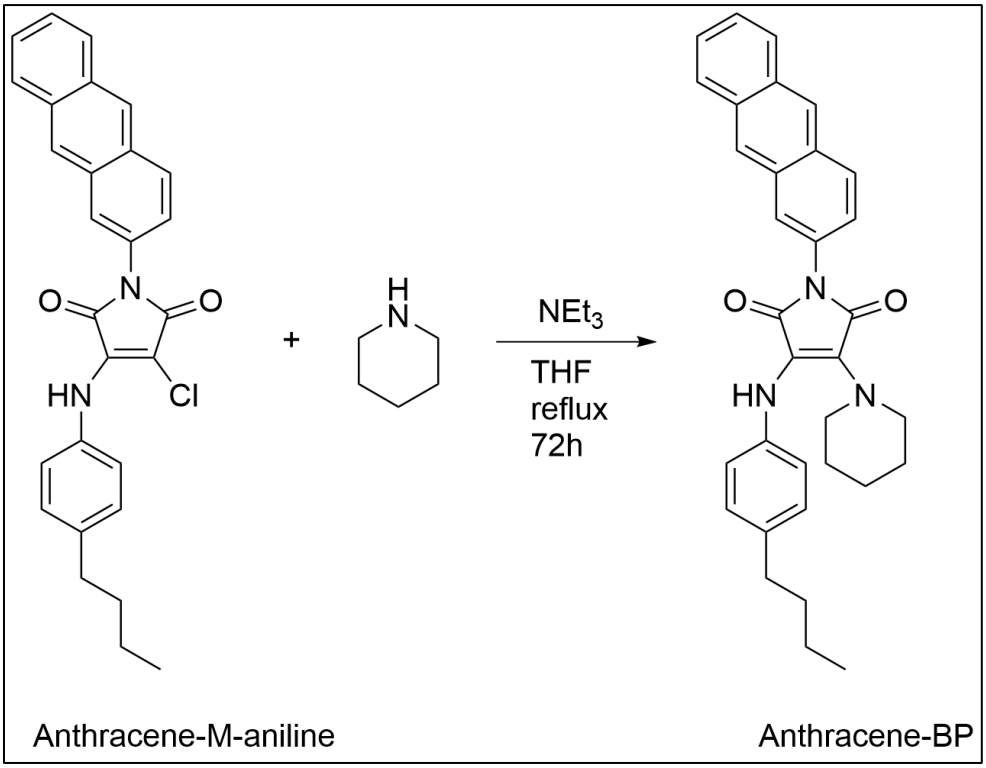


Scheme 16 Synthesis of Anthracene-maleimide fluorophore.

Anthracene-M-aniline (1g, 2.2mmol, 1 eq.) was dissolved in THF, and triethylamine (1.5ml, 11mmol, 5 eq.) was then added to the mixture. Subsequently, piperidine (1.08ml, 11mmol, 5 eq.) was added to the mixture. The solution was refluxed for 72h. After the reaction concluded, the solution was filtrated and removed under pressure. The residue was washed with methanol to obtain an orange solid (70% yield).

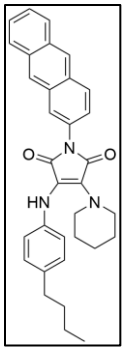

**$^{1}$H NMR (400 MHz, $CDCl_3$, 25°C, TMS) δ (ppm)**: 8.35 (s, 2H), 7.93 (m, 4H), 7.41 (m, 3H), 7.03 (d, J = 8.1Hz, 2H), 6.72 (d, J = 7.9Hz, 2H), 5.88 (s, 1H), 3.34 (t, J = 5.1 Hz, 4H), 2.50 (t, J = 7.7 Hz, 2H), 1.52-1.28 (m, 10H), 0.86 (t, J = 7.4Hz, 3H).

The solubility of the compound is too poor to measure the $^{13}$C NMR spectra.

**HRMS**: m/z: calculated for $[C_{33}H_{33}N_3O_2]^-$: 503.2573, found: 503.2575.

## 3.7.5 Nuclear Magnetic Resonance (NMR) Spectra

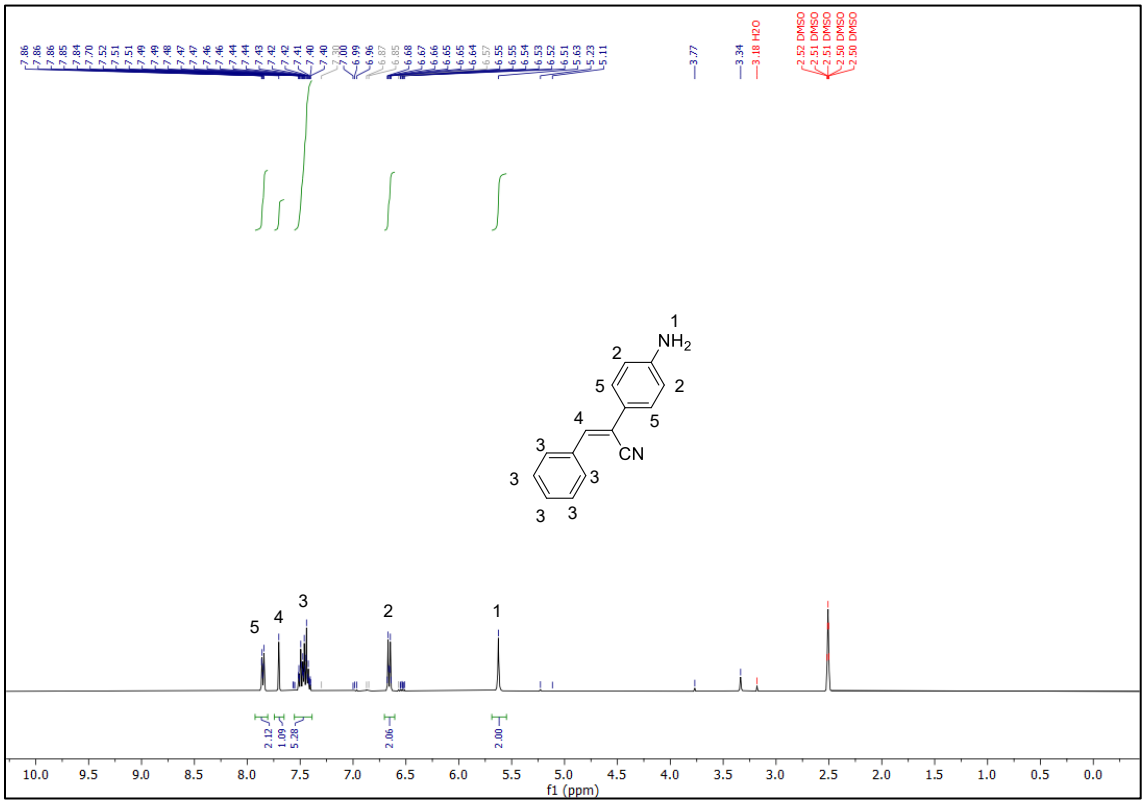

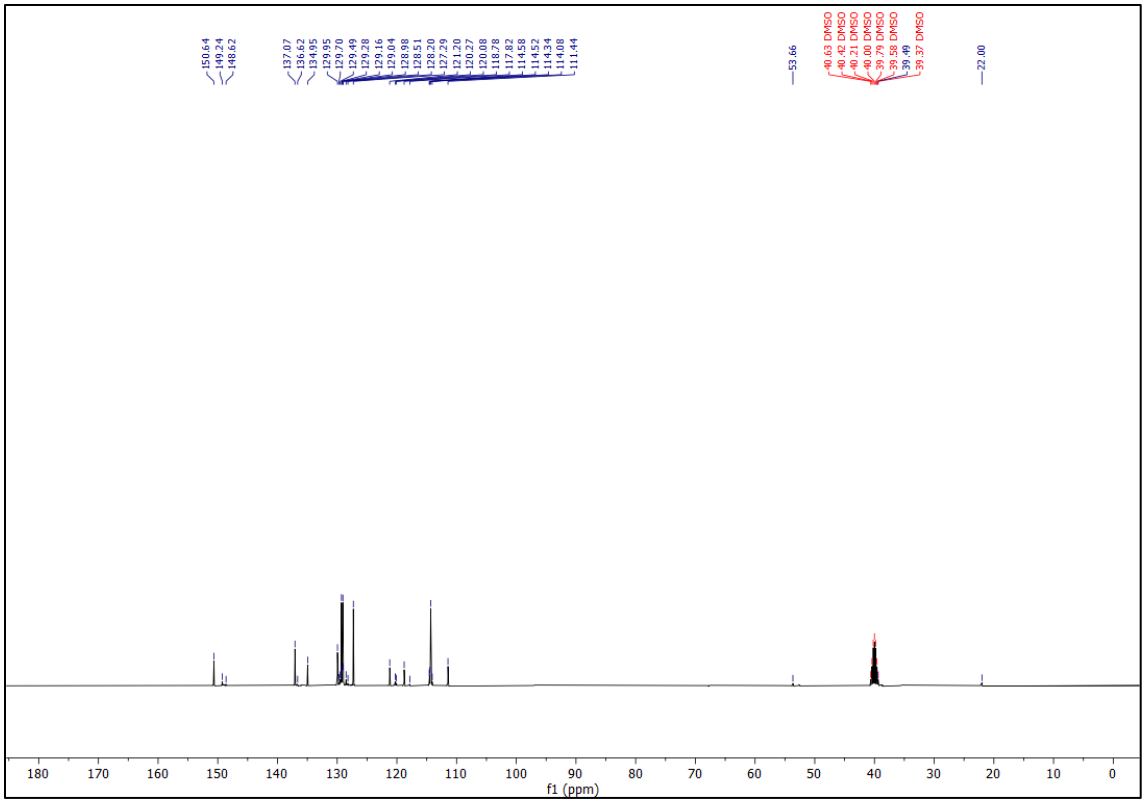


Figure 1 $^{1}H$ and $^{13}C$ NMR spectra of Ben-$NH_2$ in DMSO-d6.

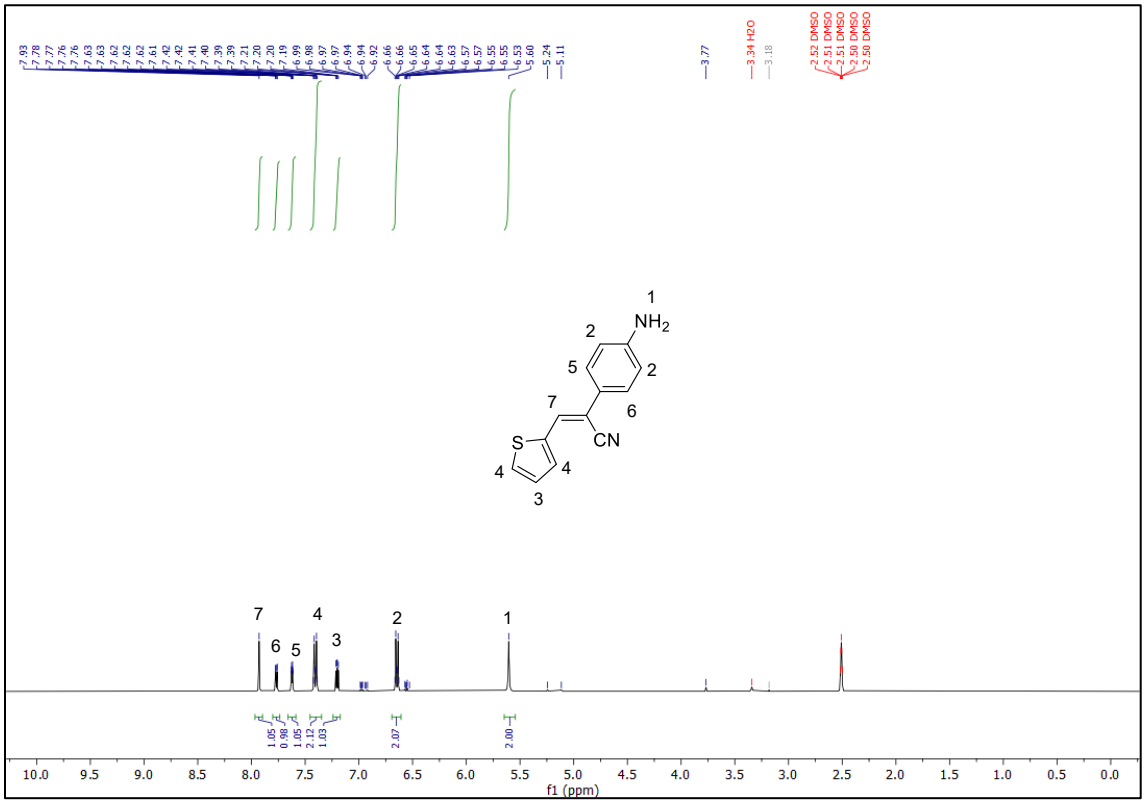

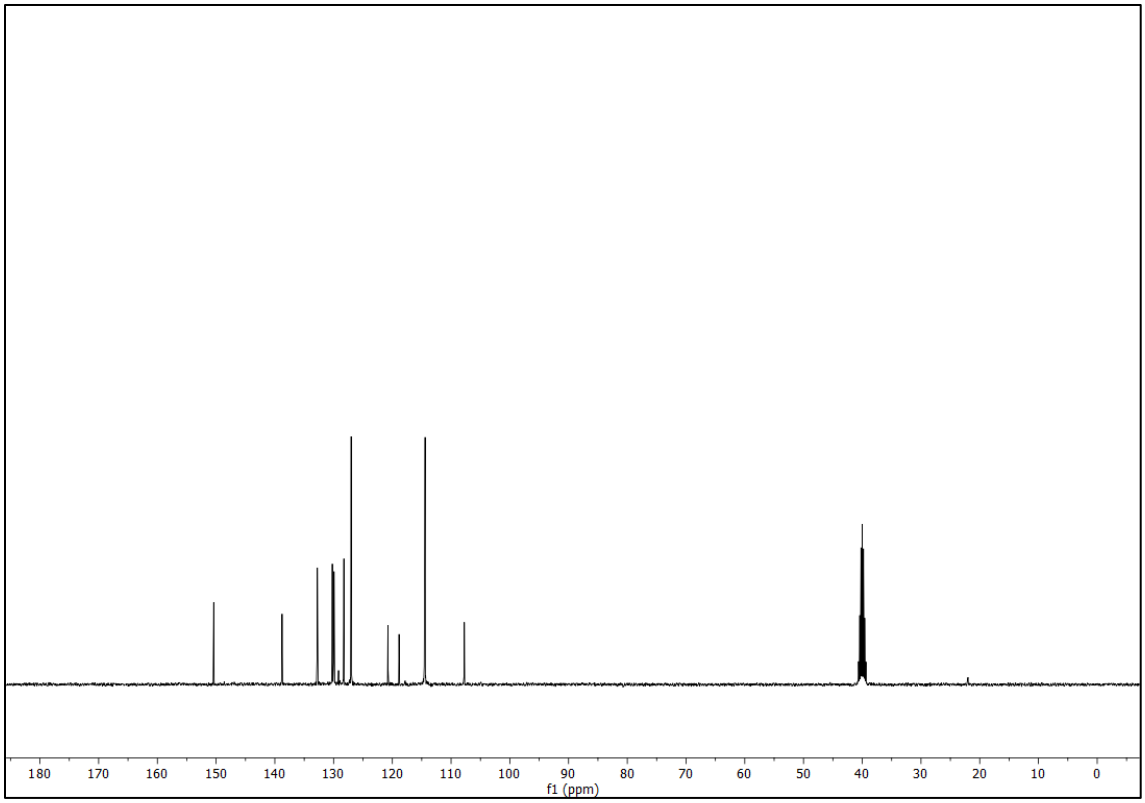


Figure 2 $^{1}H$ and $^{13}C$ NMR spectra of Then-$NH_2$ in DMSO-d6.

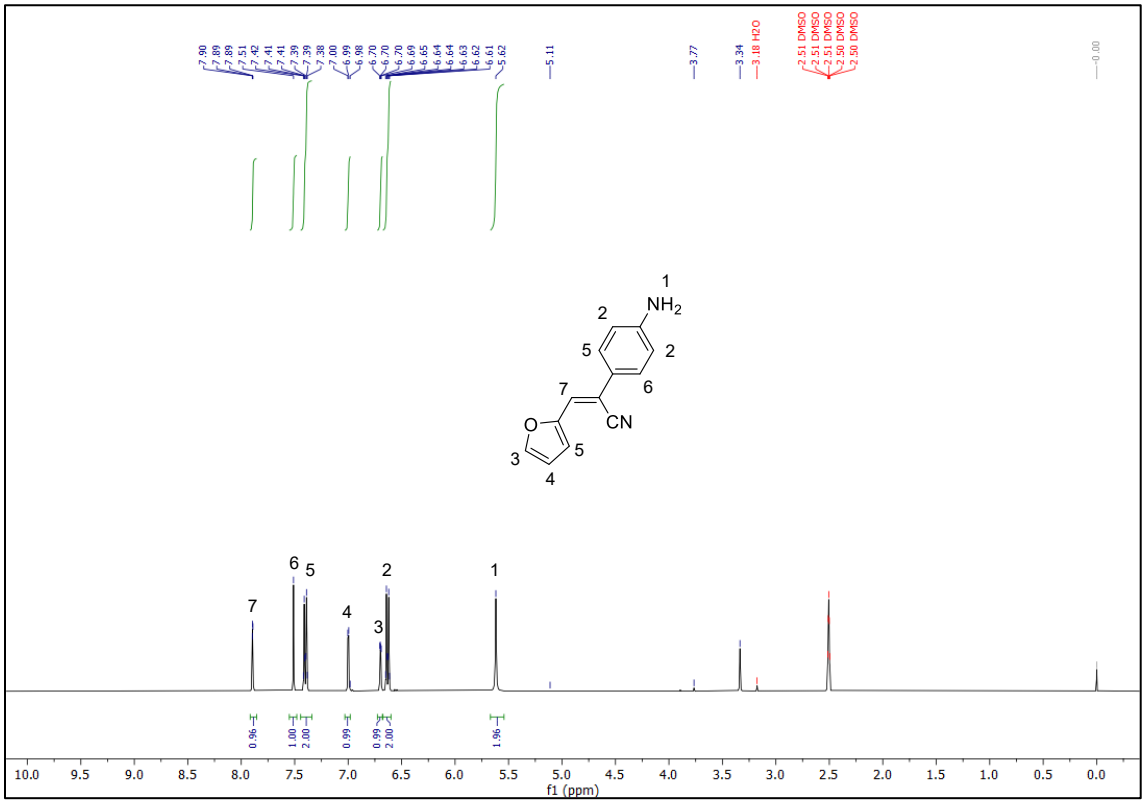

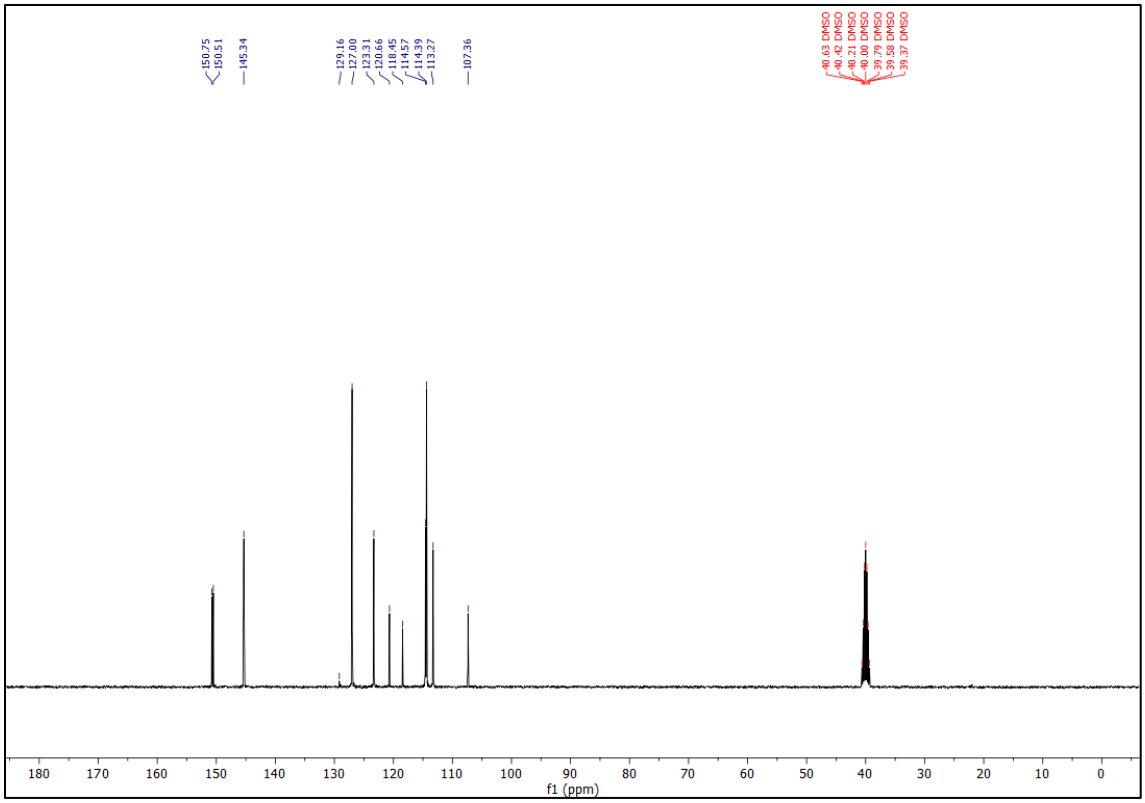


Figure 3 $^{1}H$ and $^{13}C$ NMR spectra of Fur-$NH_2$ in DMSO-d6.

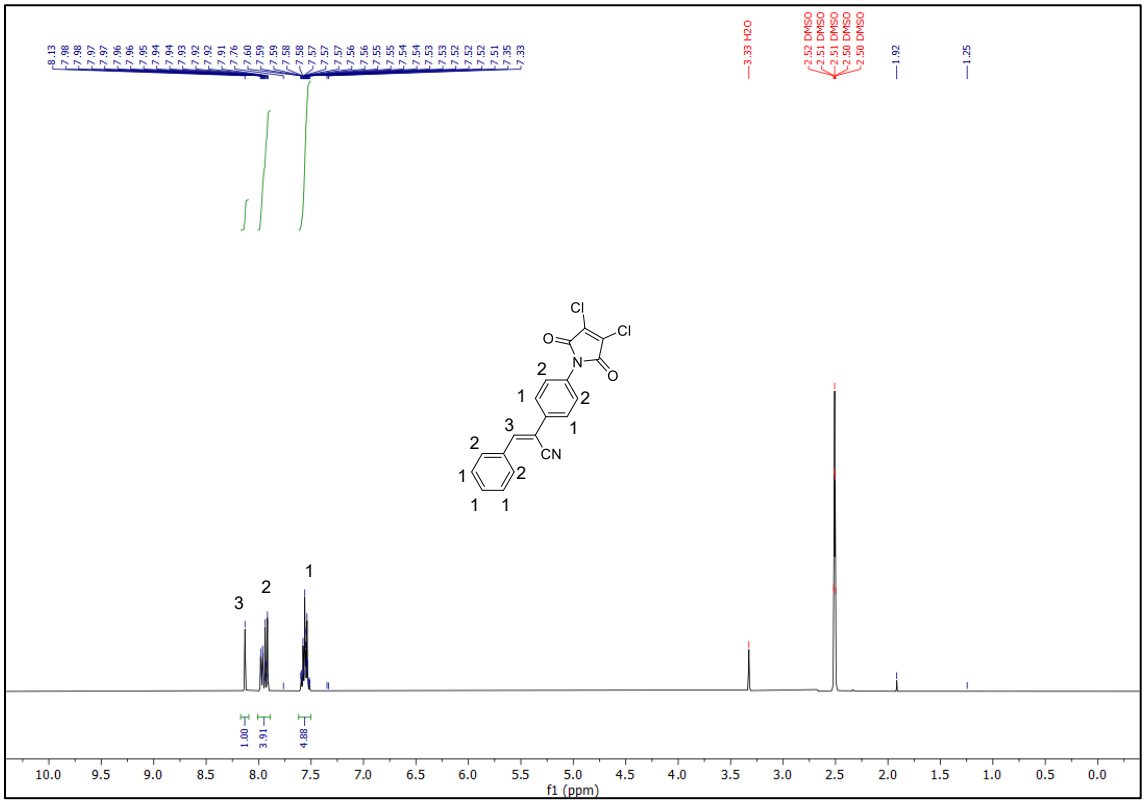

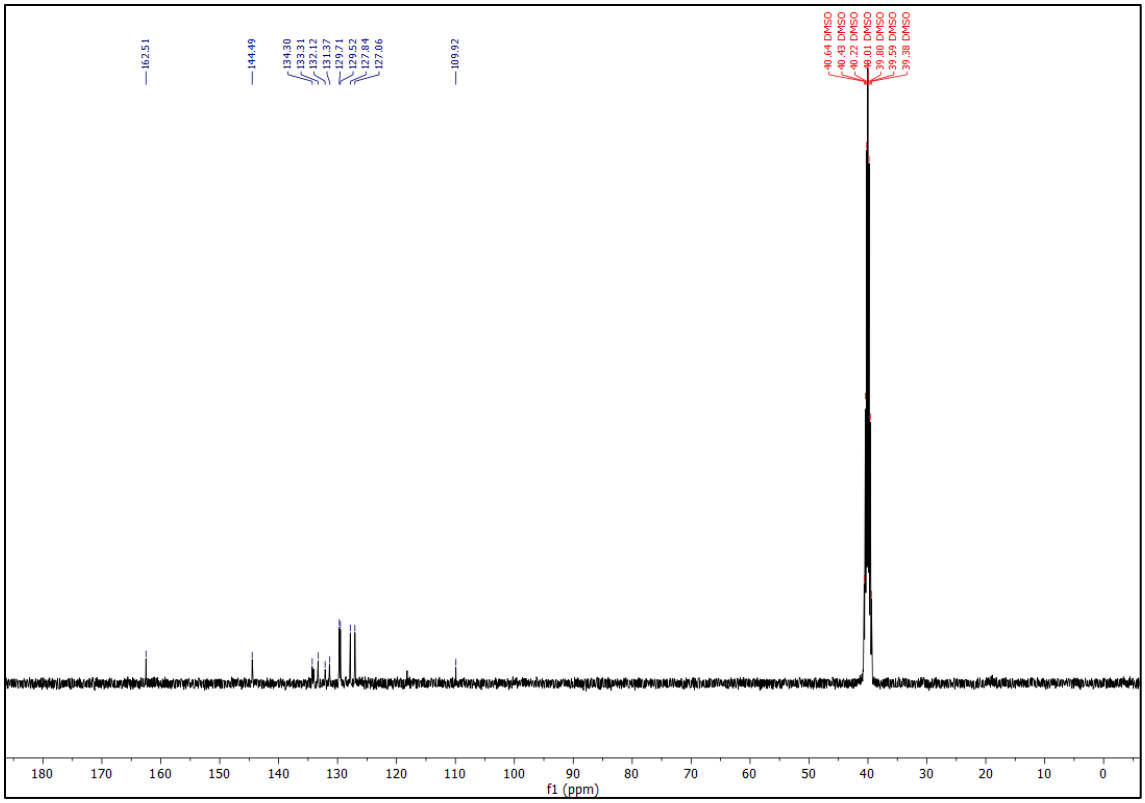


Figure 4 $^{1}H$ and $^{13}C$ NMR spectra of Ben-M-DC in DMSO-d6.

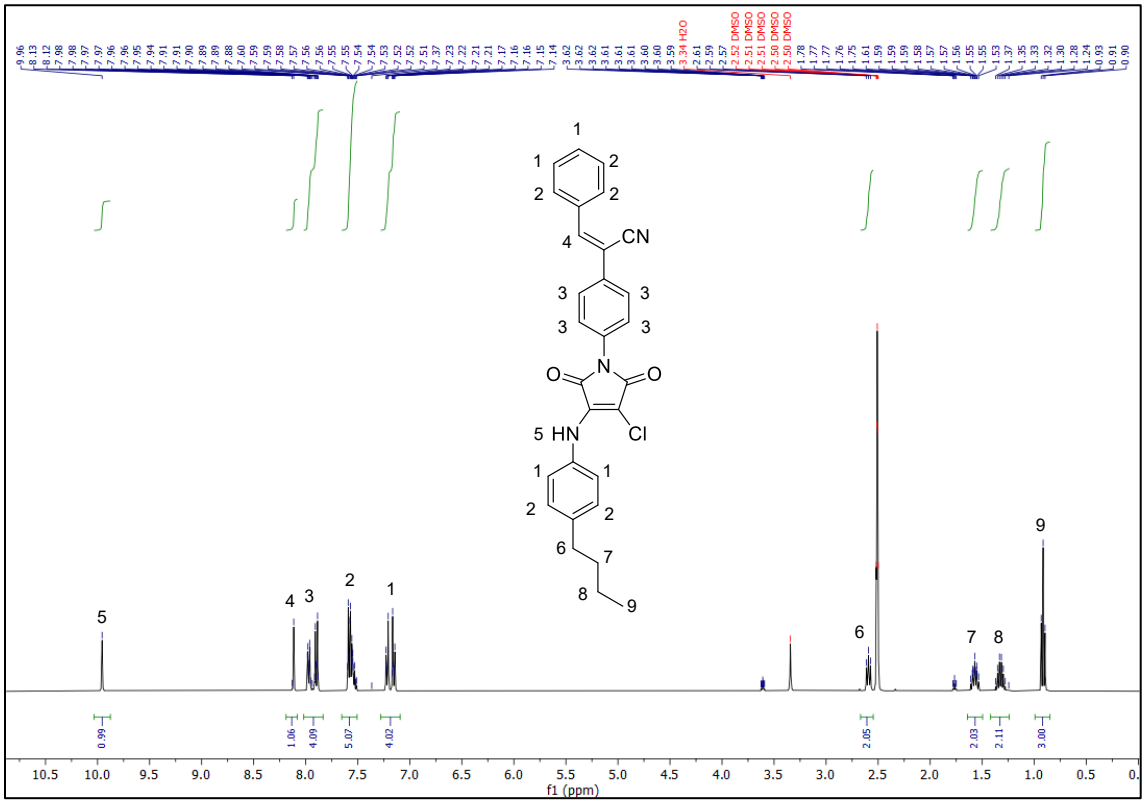

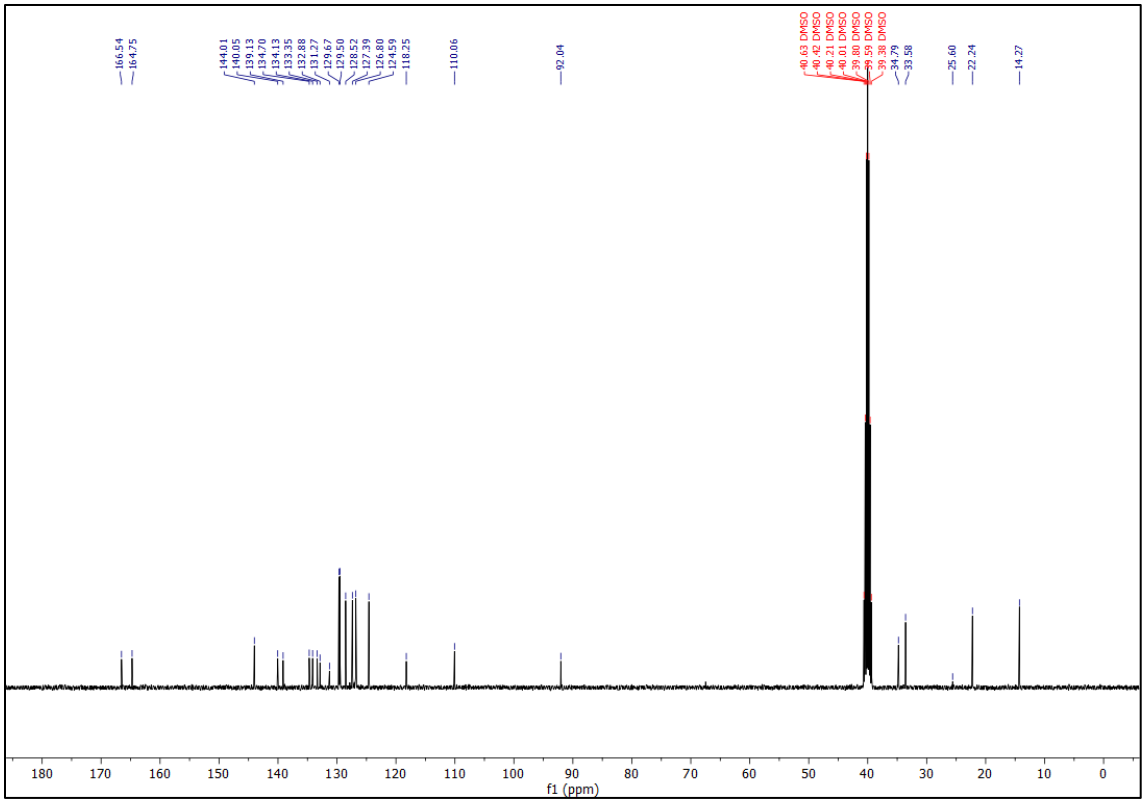


Figure 5 $^{1}H$ and $^{13}C$ NMR spectra of Ben-M-aniline in DMSO-d6.

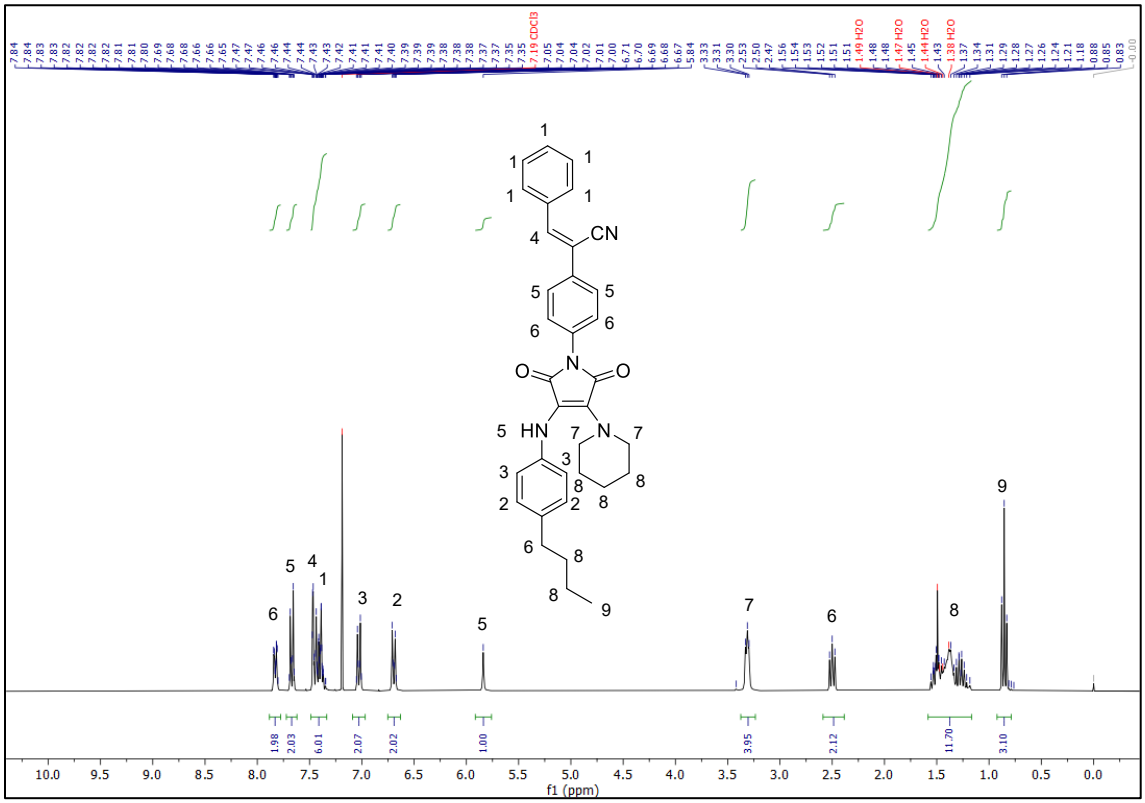

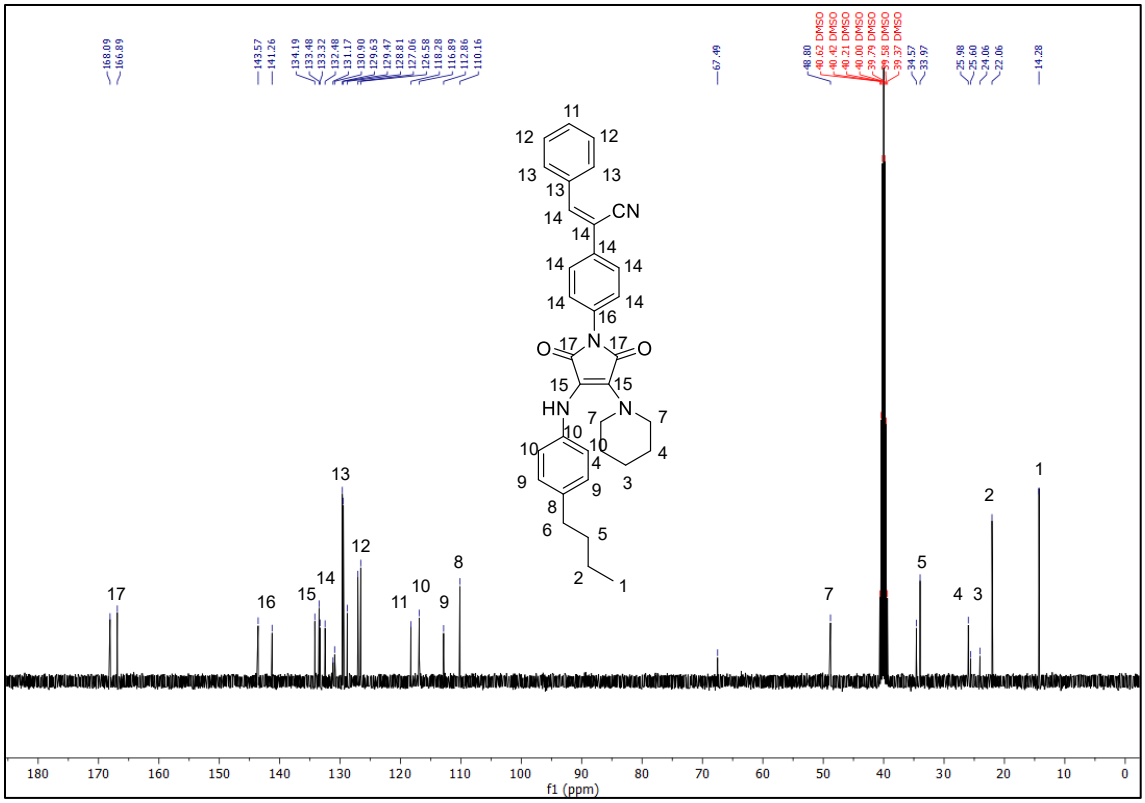


Figure 6 $^{1}$H and $^{13}$C NMR spectra of Ben-BP in DMSO-d6.

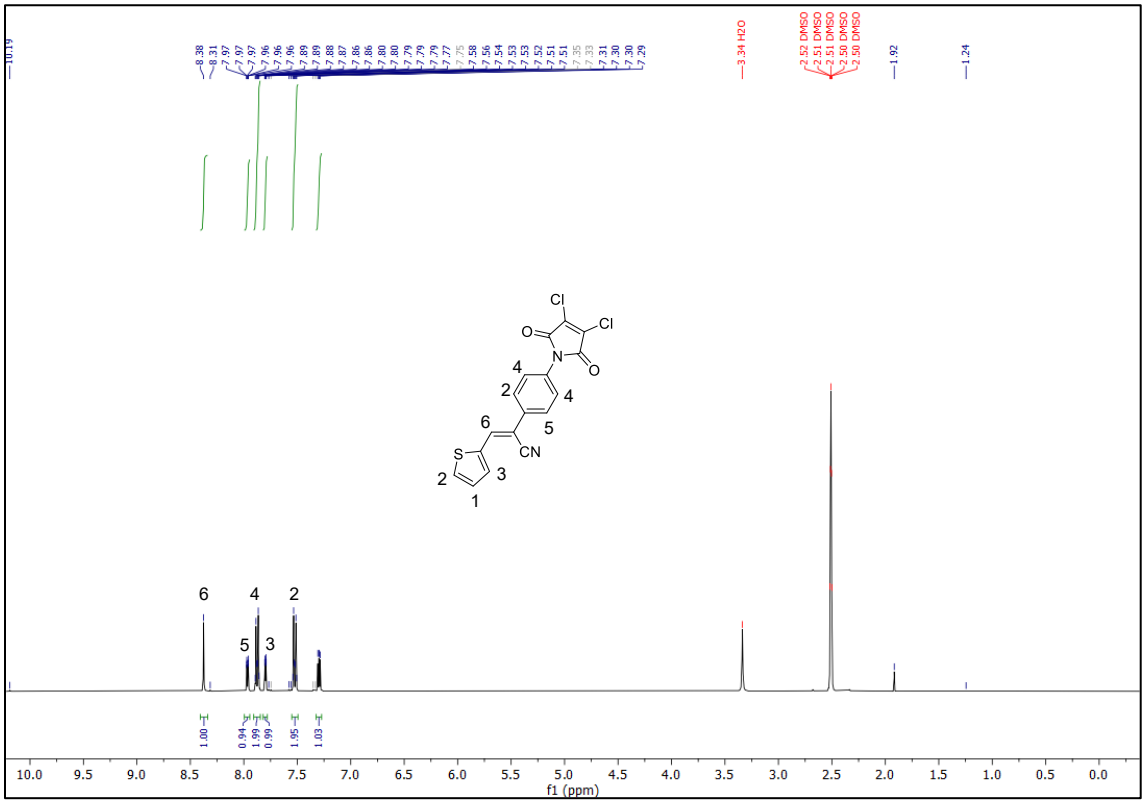

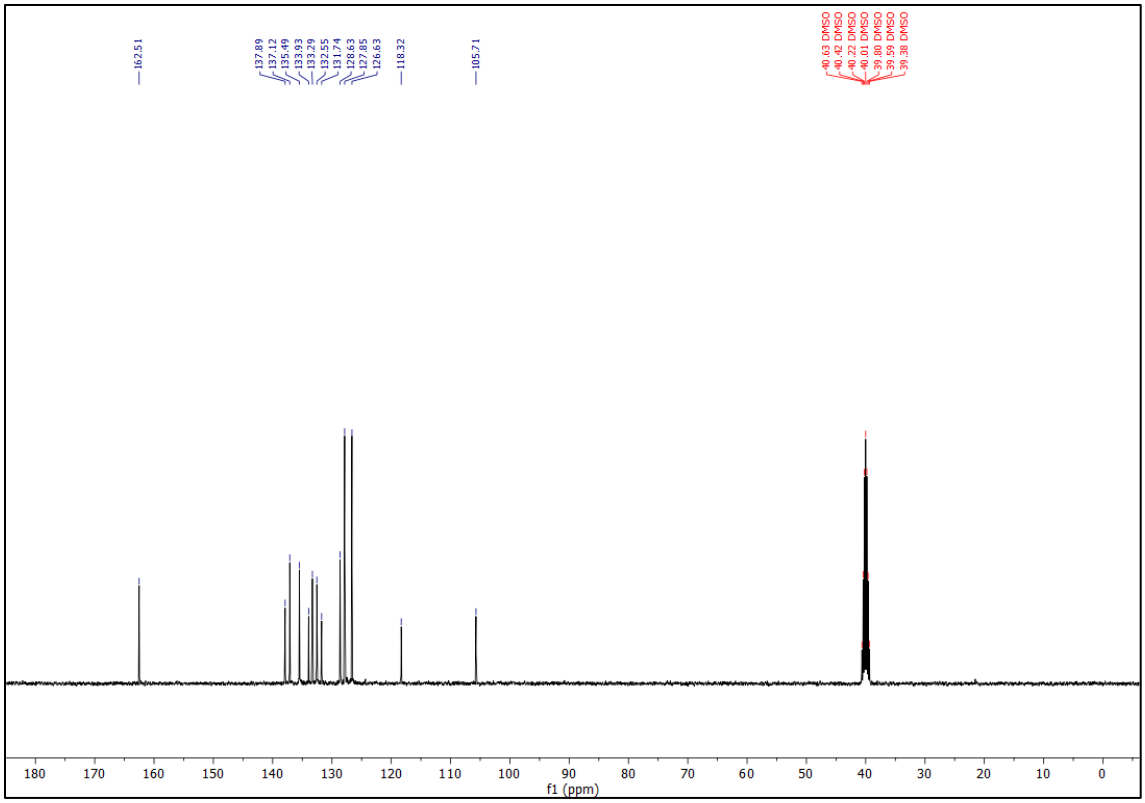


Figure 7 $^{1}H$ and $^{13}C$ NMR spectra of Then-M-DC in DMSO-d6.

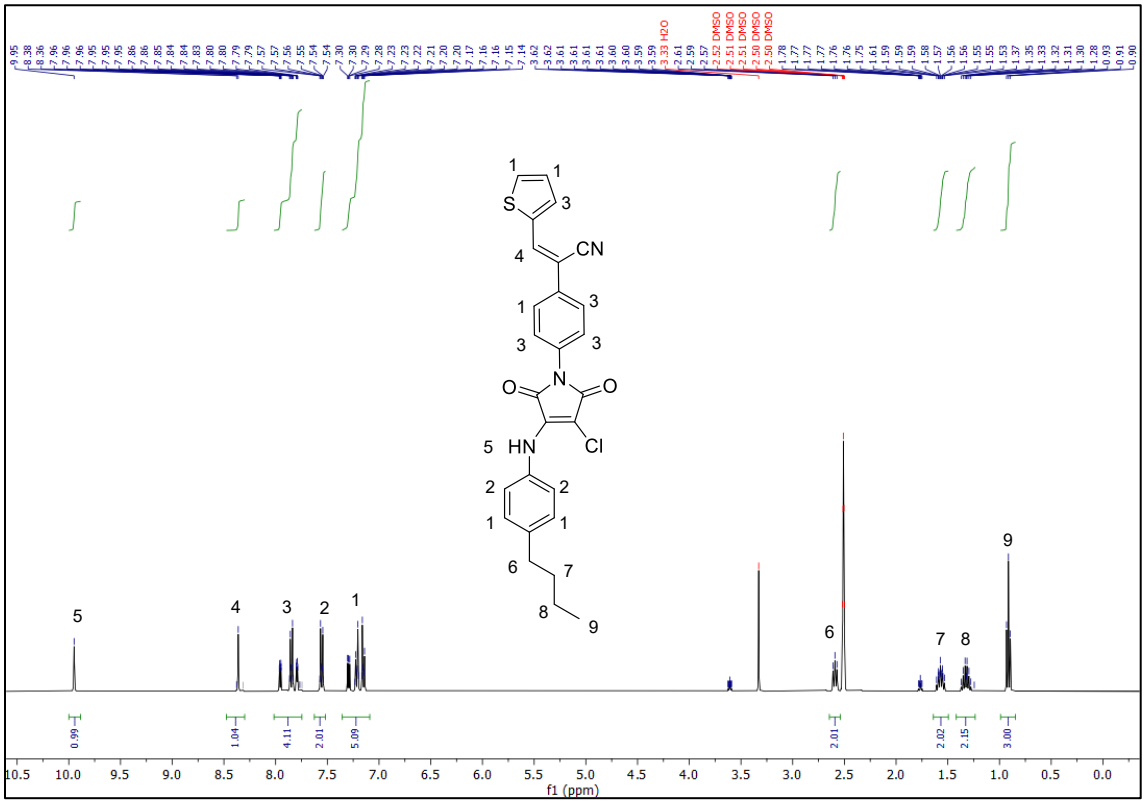

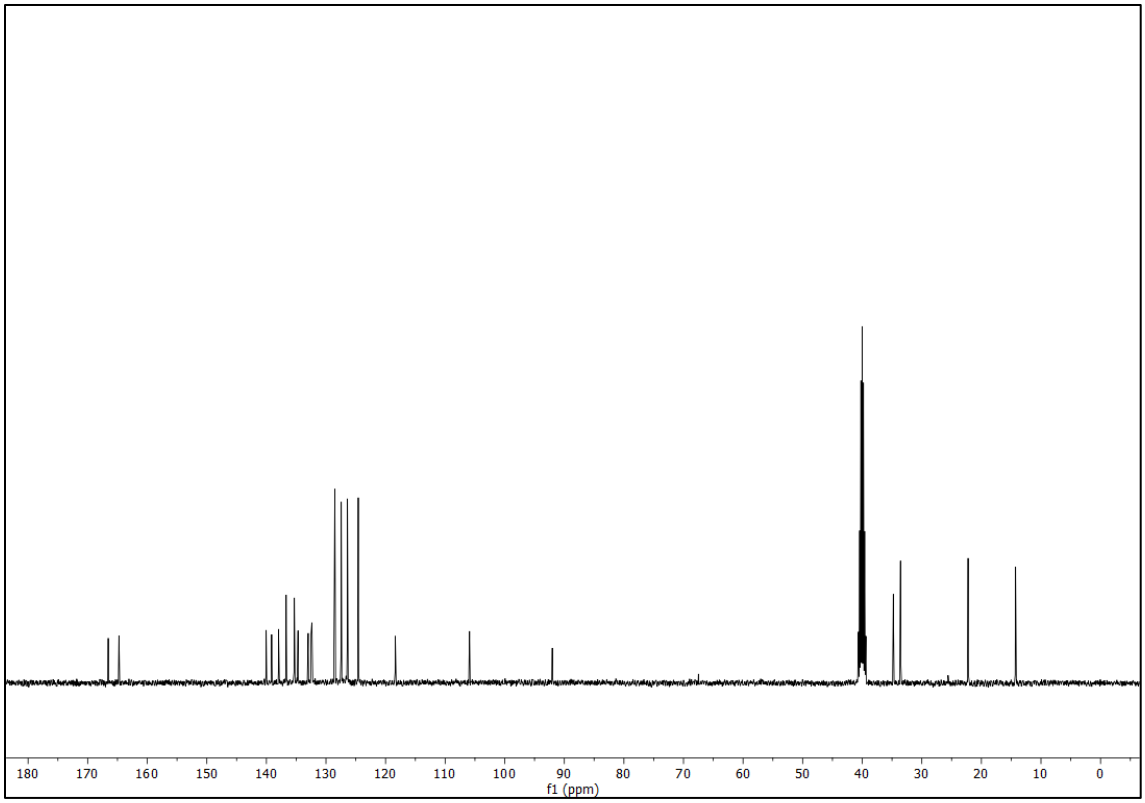


Figure 8 $^{1}H$ and $^{13}C$ NMR spectra of Then-M-aniline in DMSO-d6.

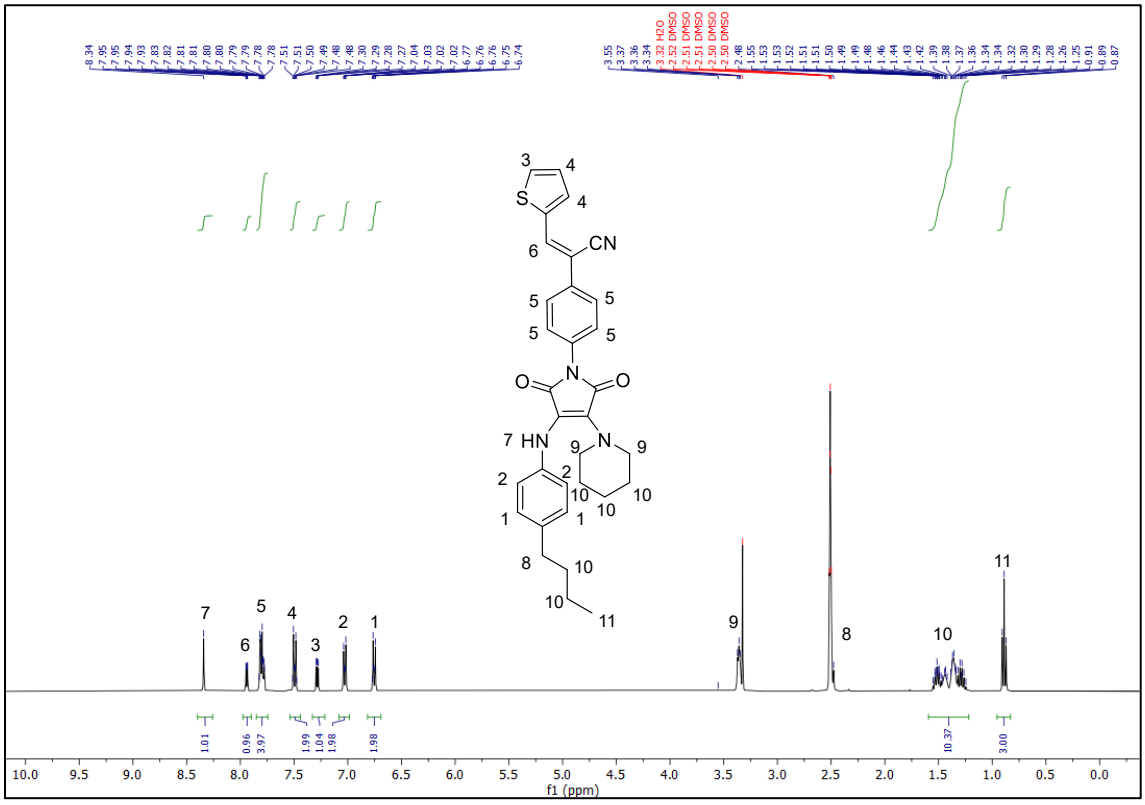

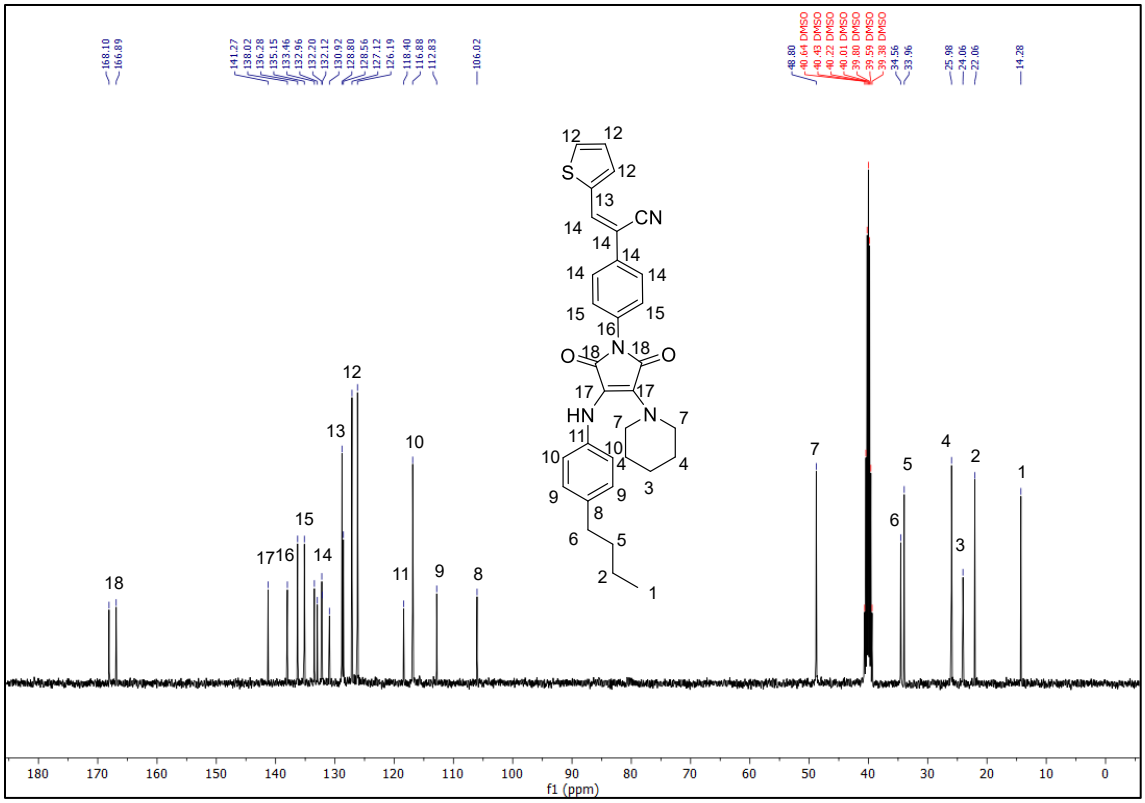


Figure 9 $^{1}H$ and $^{13}C$ NMR spectra of Then-BP in DMSO-d6.

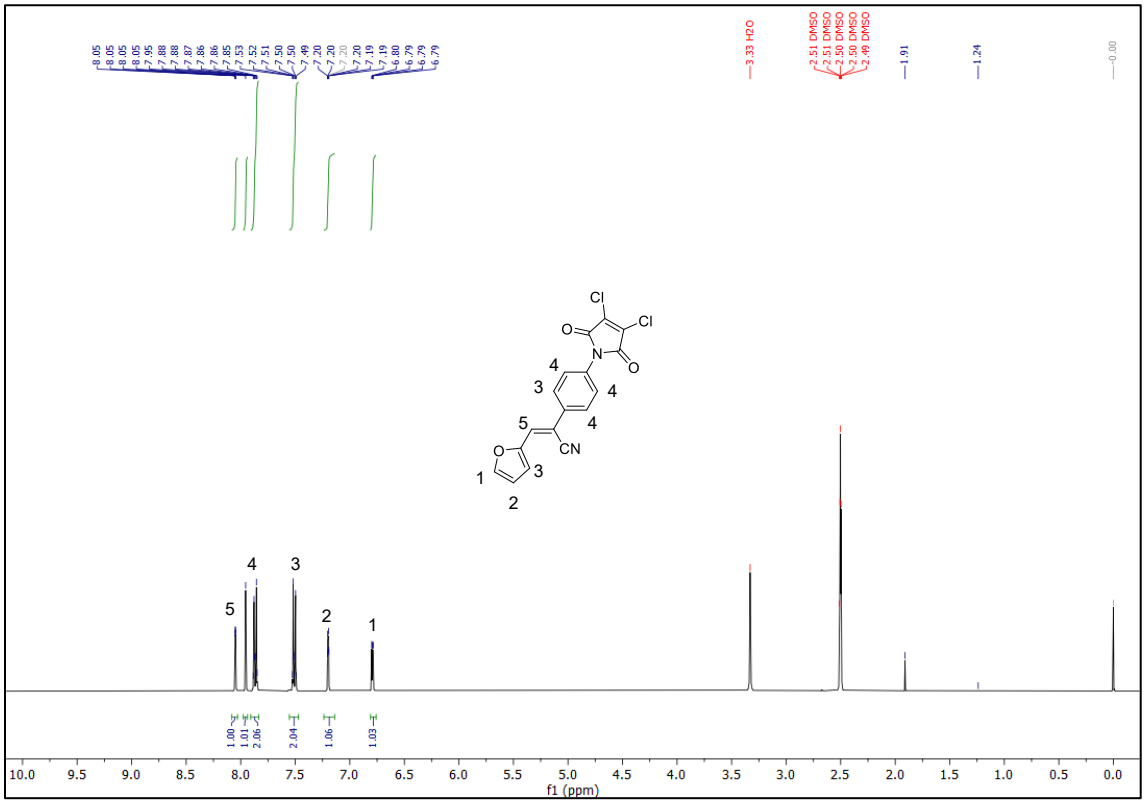

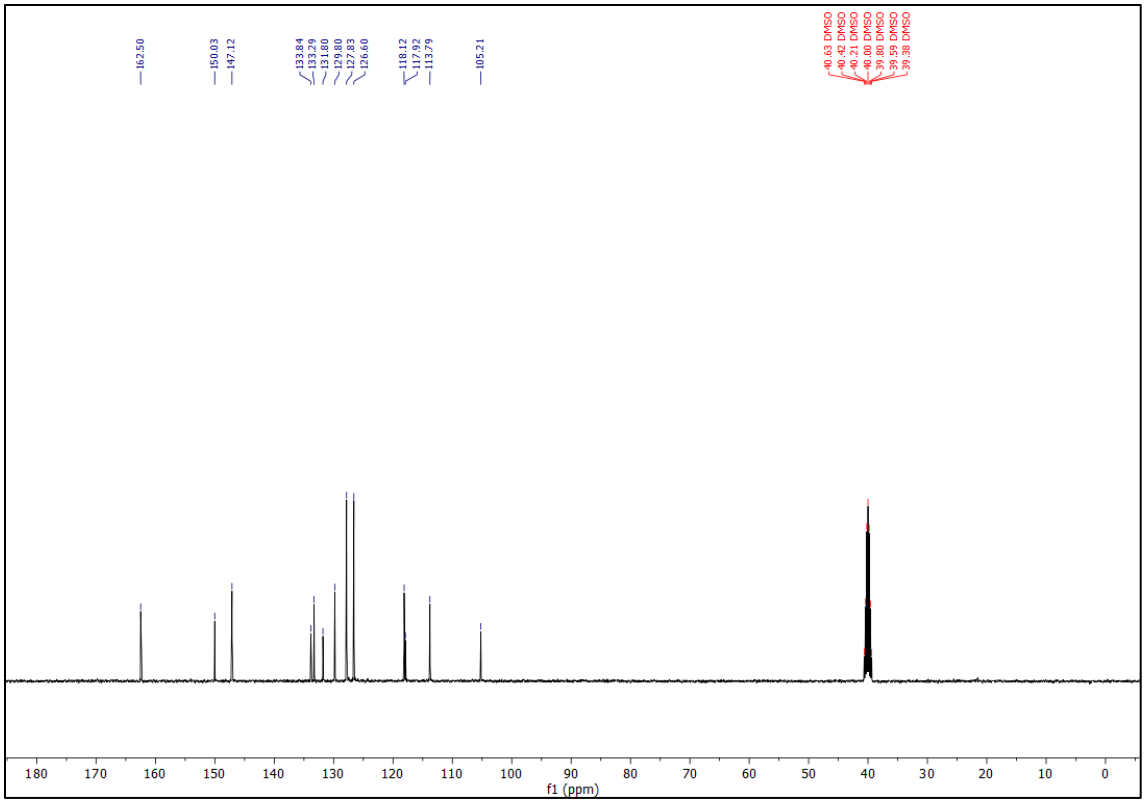


Figure 10 $^{1}H$ and $^{13}C$ NMR spectra of Fur-M-DC in DMSO-d6.

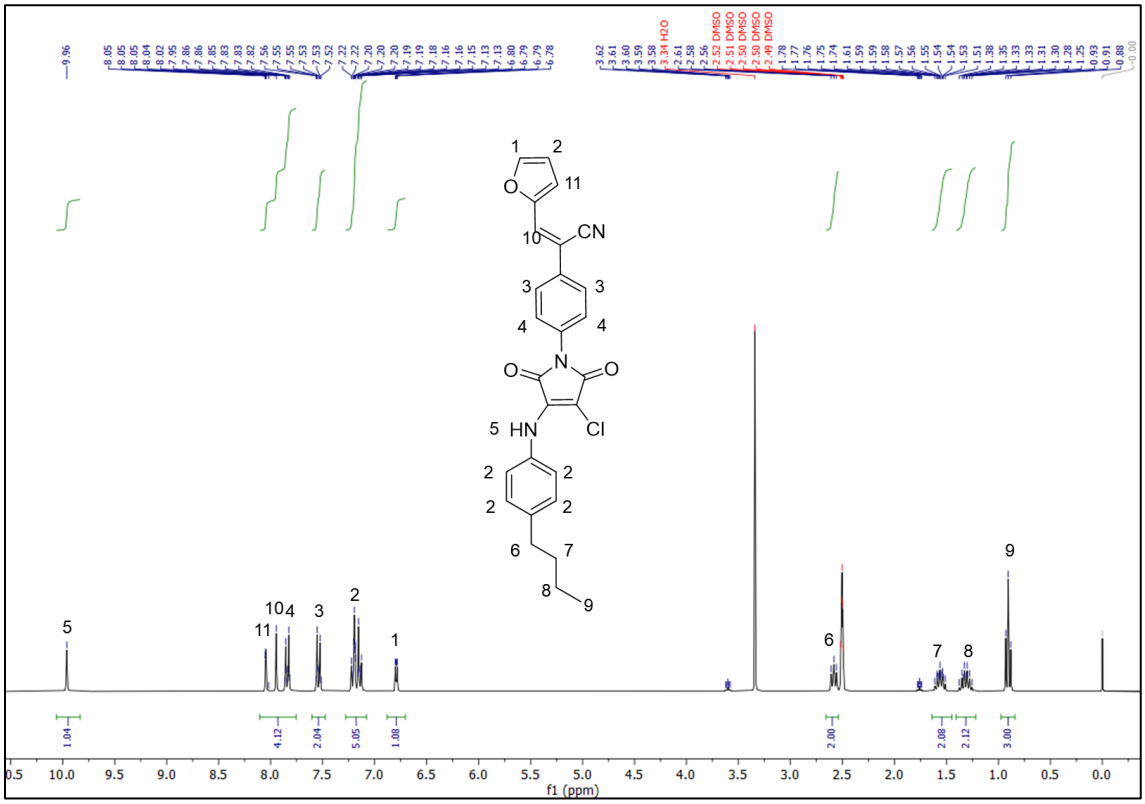

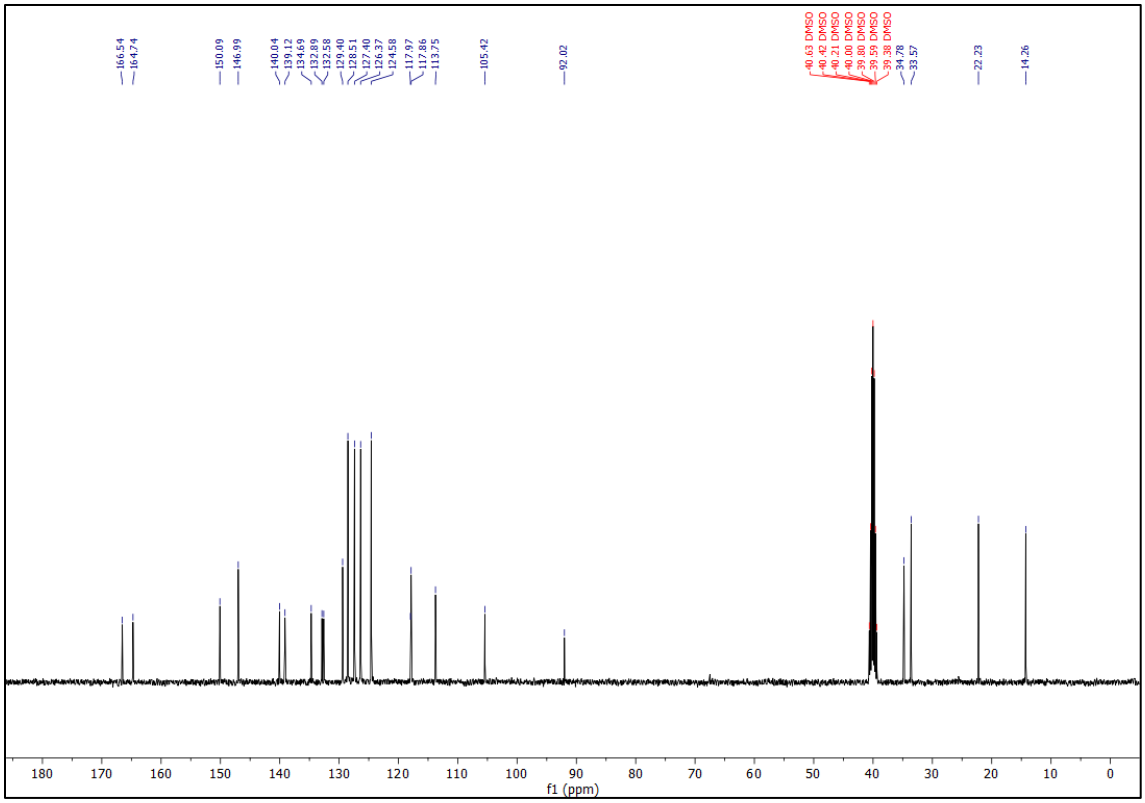


Figure 11 $^{1}H$ and $^{13}C$ NMR spectra of Fur-M-aniline in DMSO-d6.

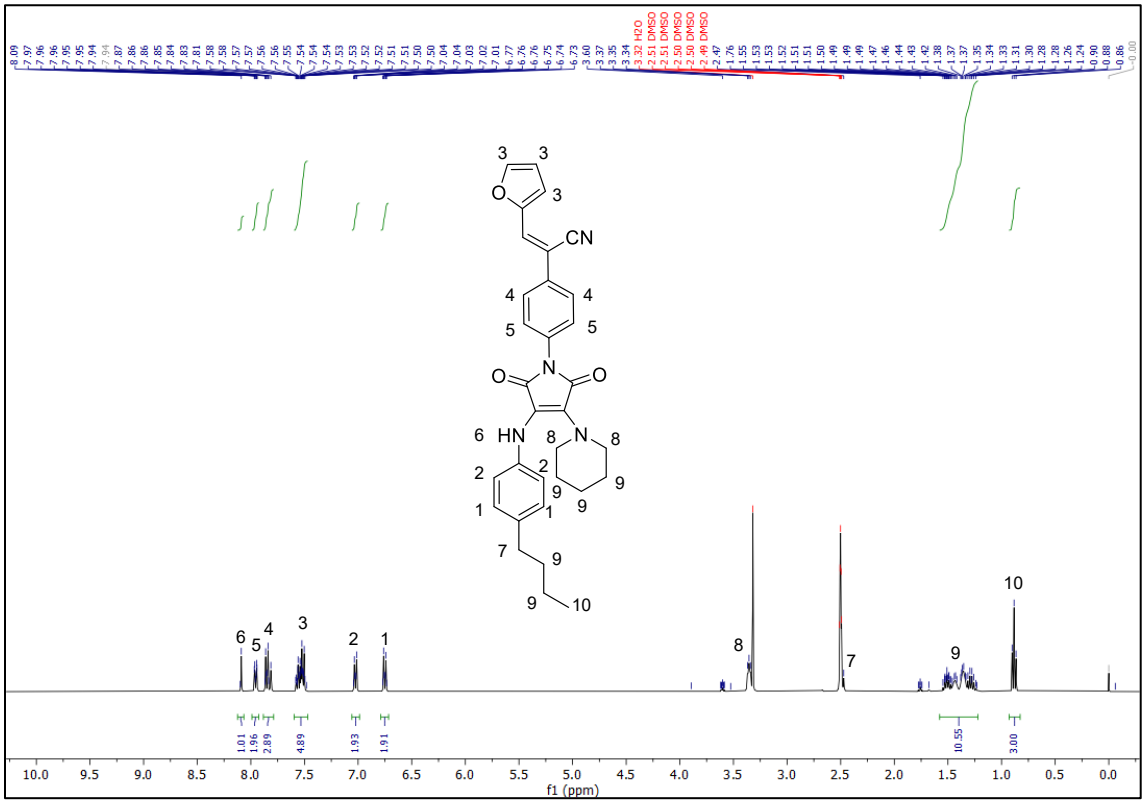

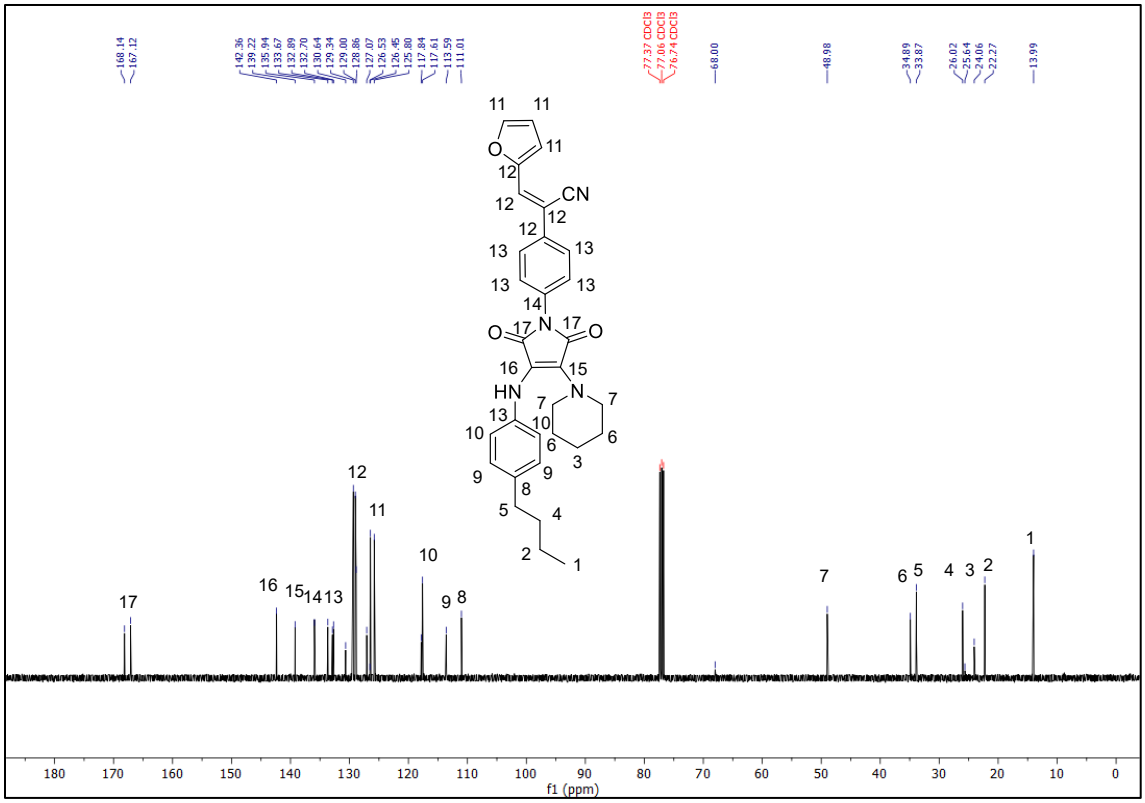


Figure 12 $^{1}$H and $^{13}$C NMR spectra of Fur-BP in DMSO-d6.

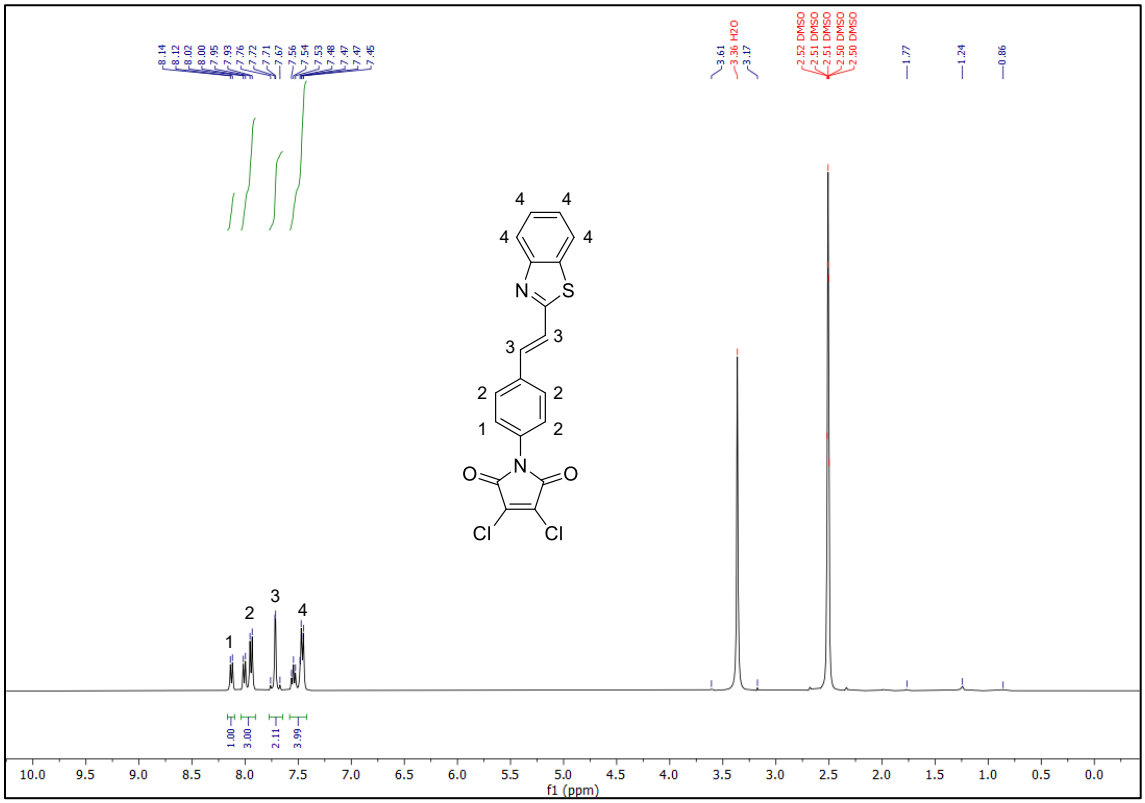

Figure 13 [1]H NMR spectra of benzothiazole-M-DC in DMSO-d6.

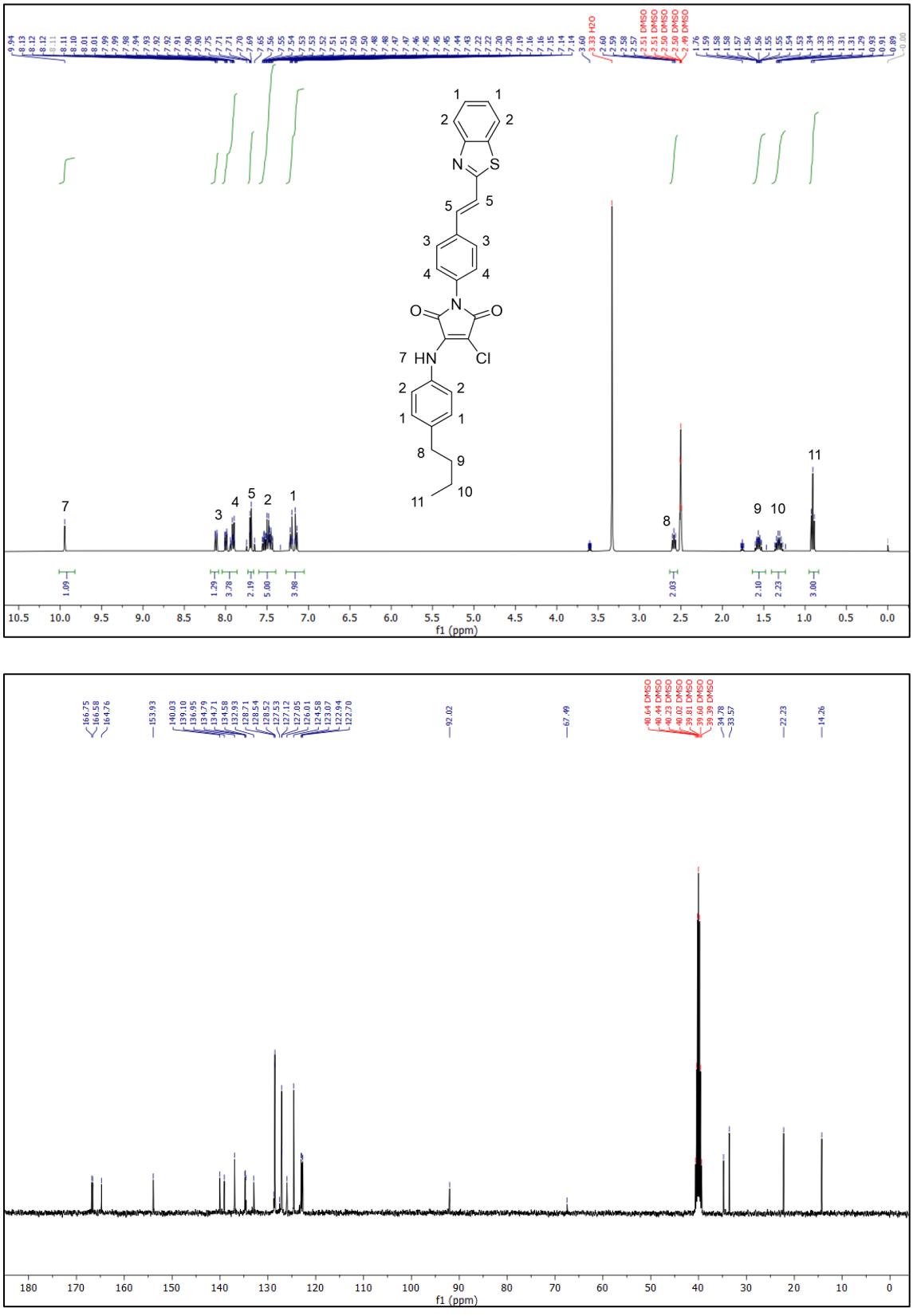

Figure 13 $^{1}H$ and $^{13}C$ NMR spectra of benzothiazole-M-aniline in DMSO-d6.

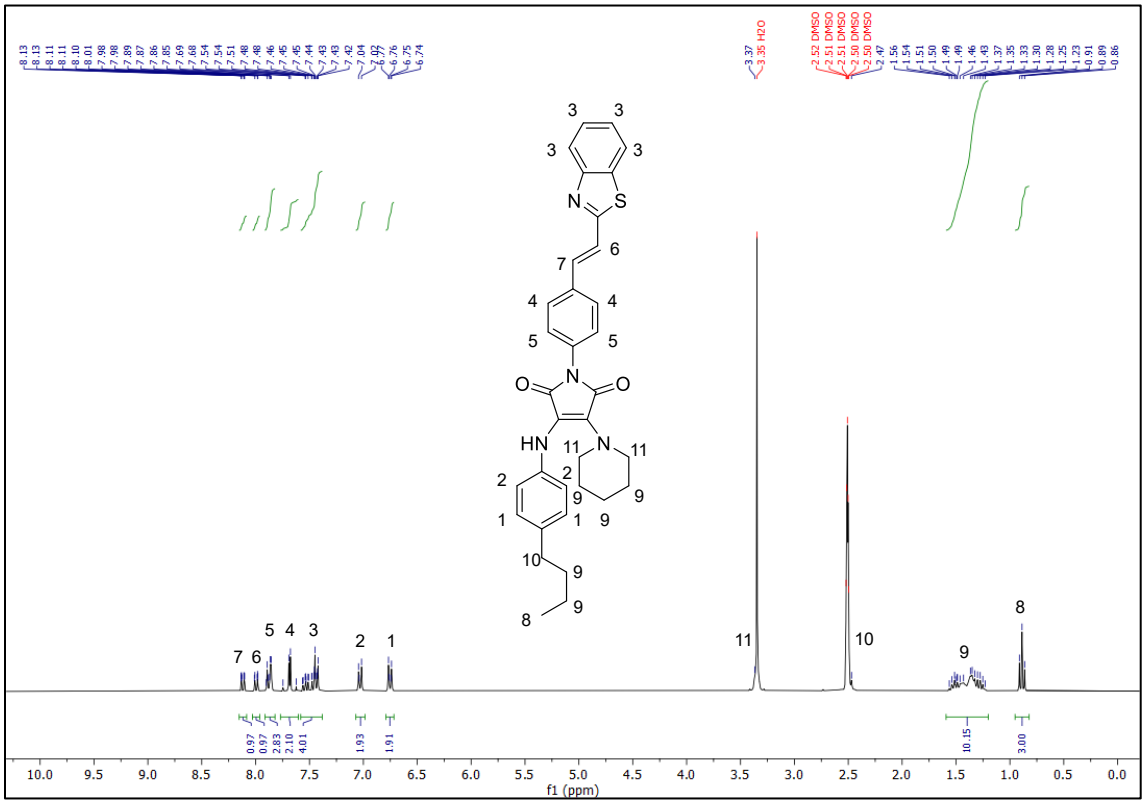


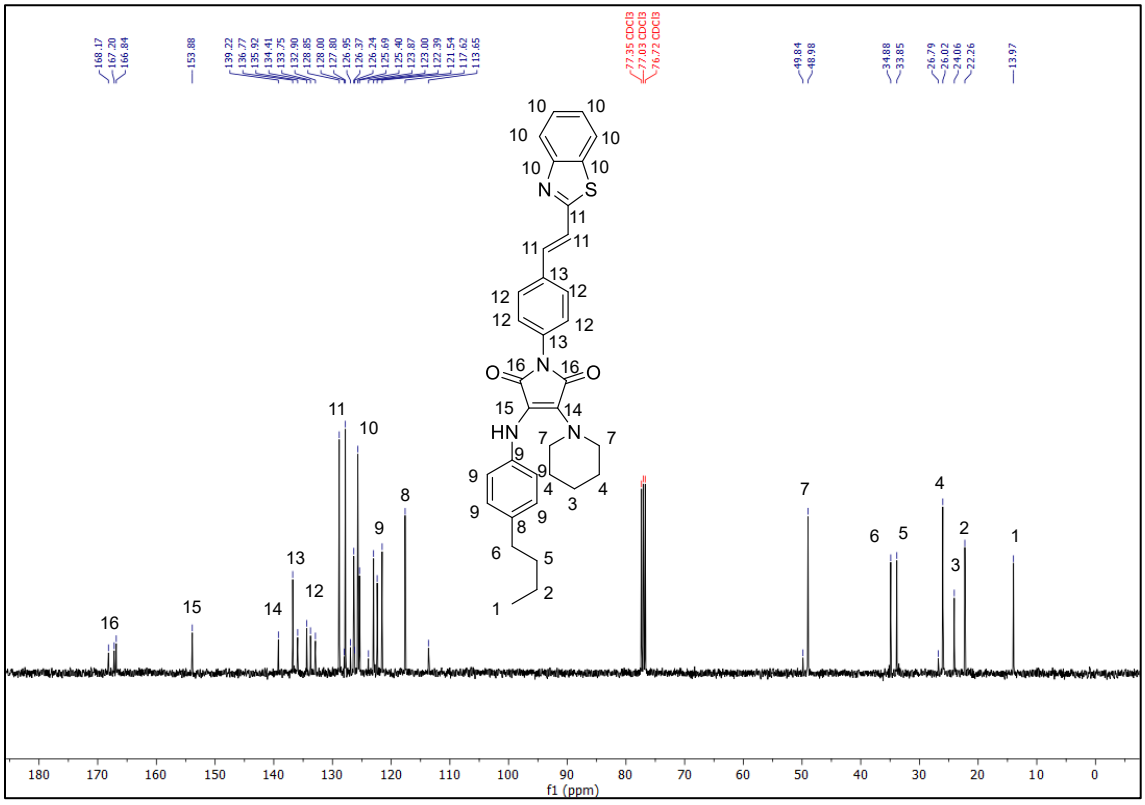

Figure 14 $^{1}H$ and $^{13}C$ NMR spectra of benzothiazole-BP in $CDCl_3$.

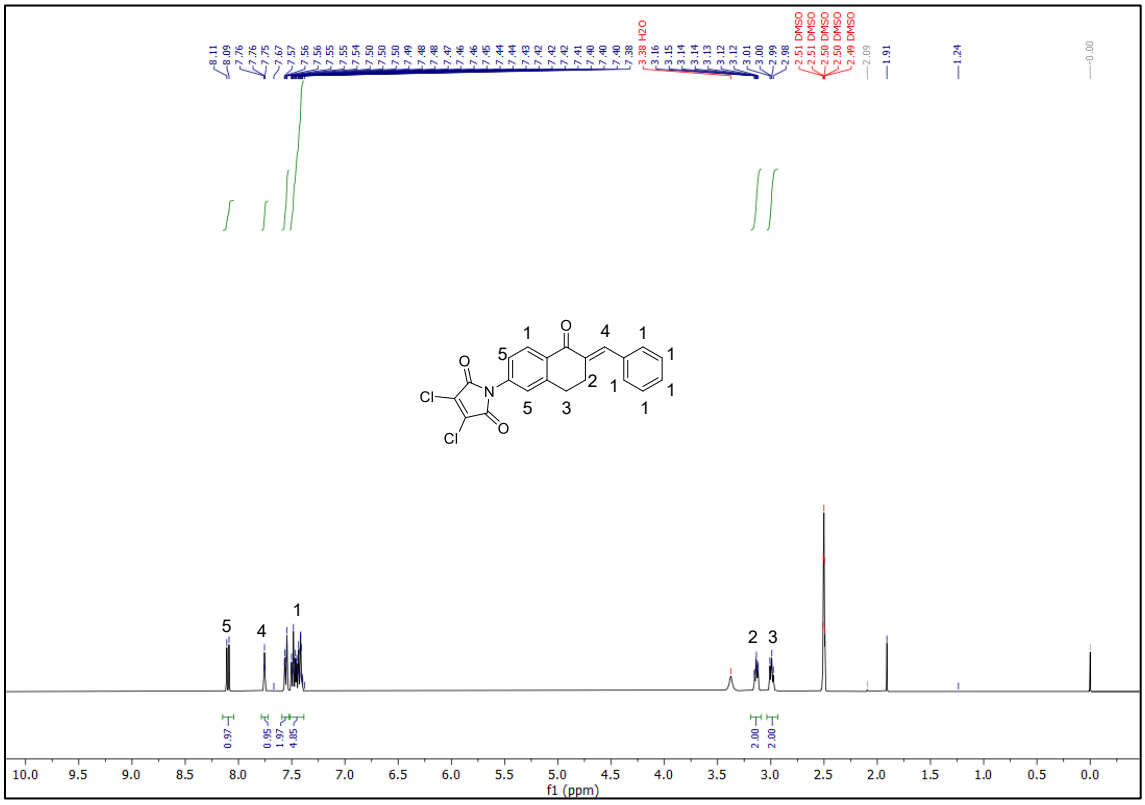


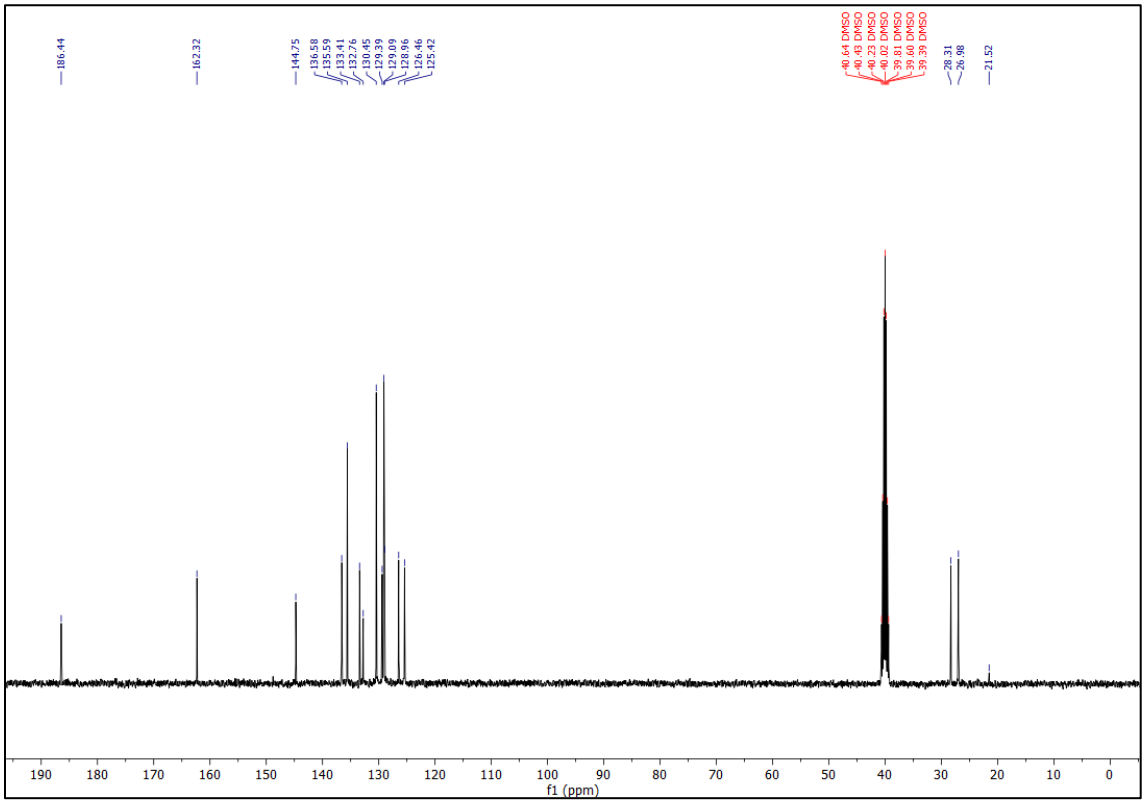

Figure 15 $^{1}H$ and $^{13}C$ NMR spectra of α-Tetralone-M-DC in DMSO-d6.

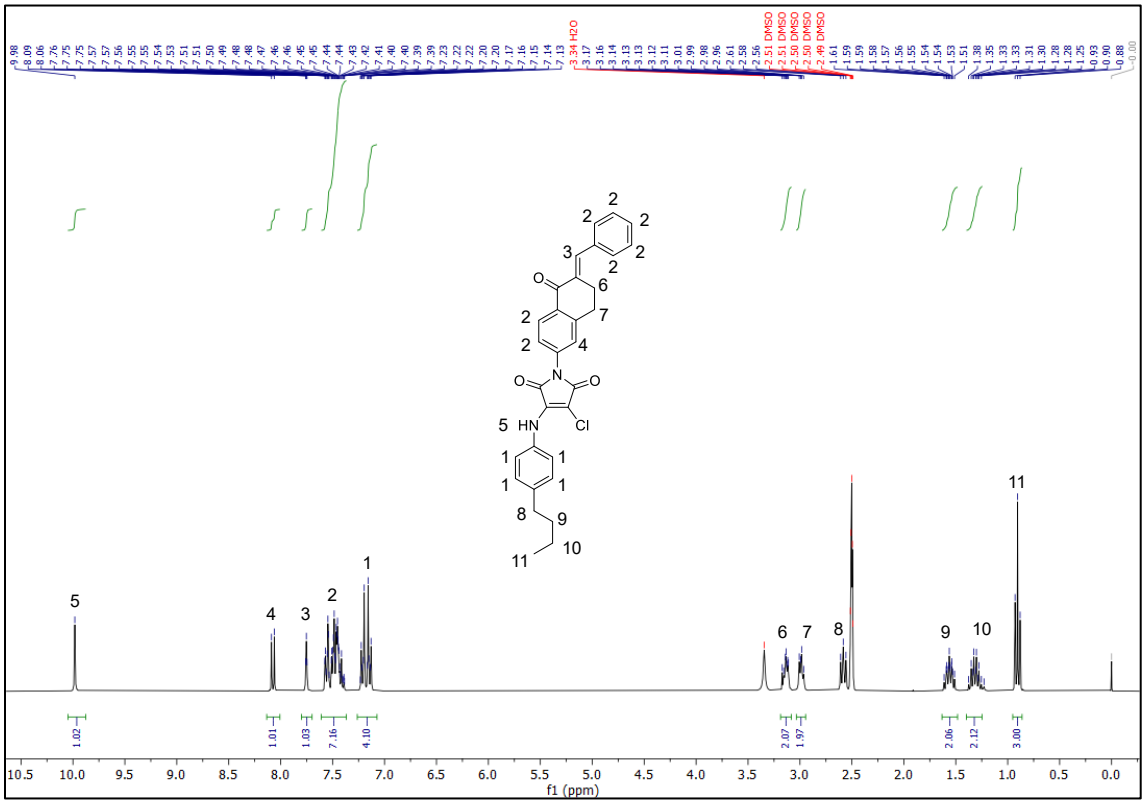


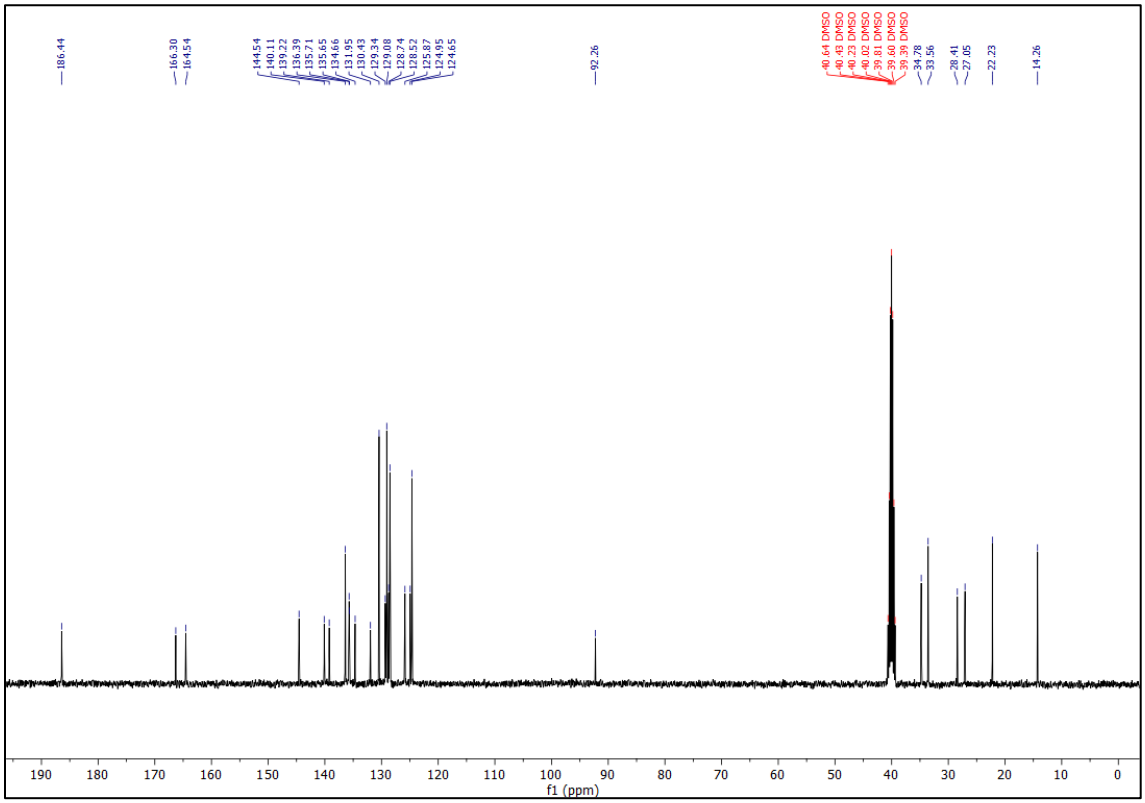

Figure 16 $^{1}H$ and $^{13}C$ NMR spectra of α-Tetralone-M-aniline in DMSO-d6.

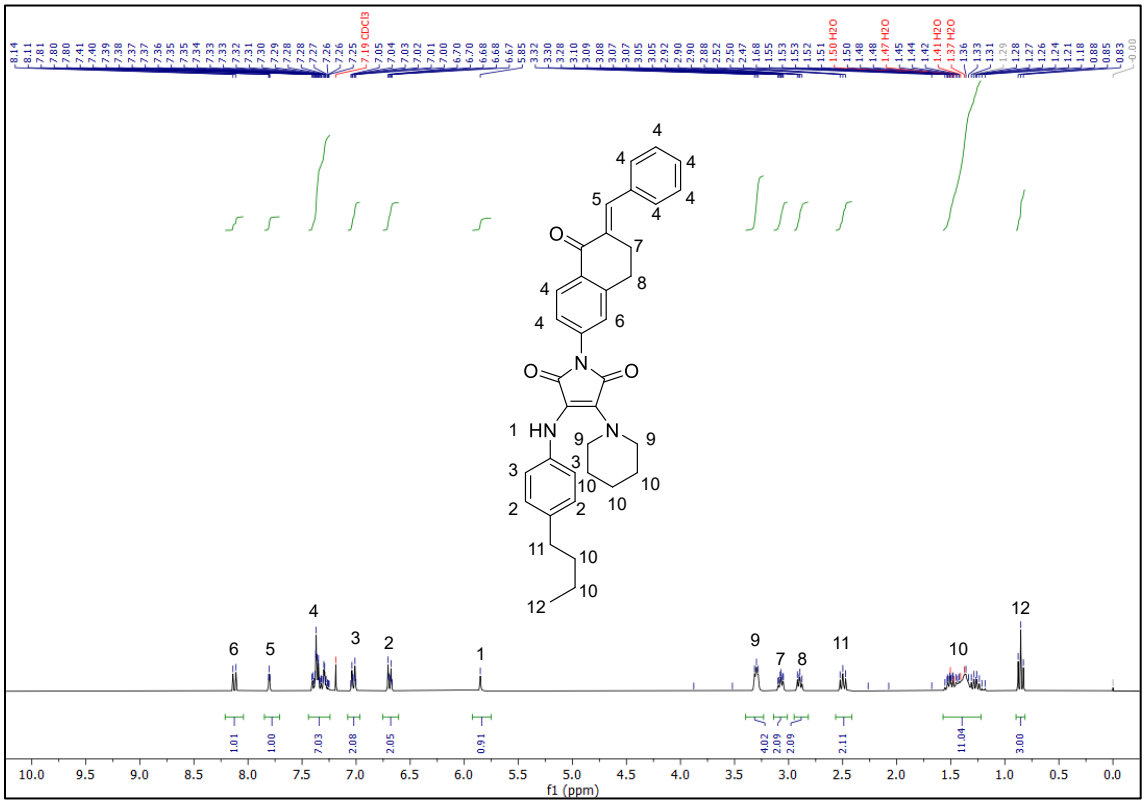


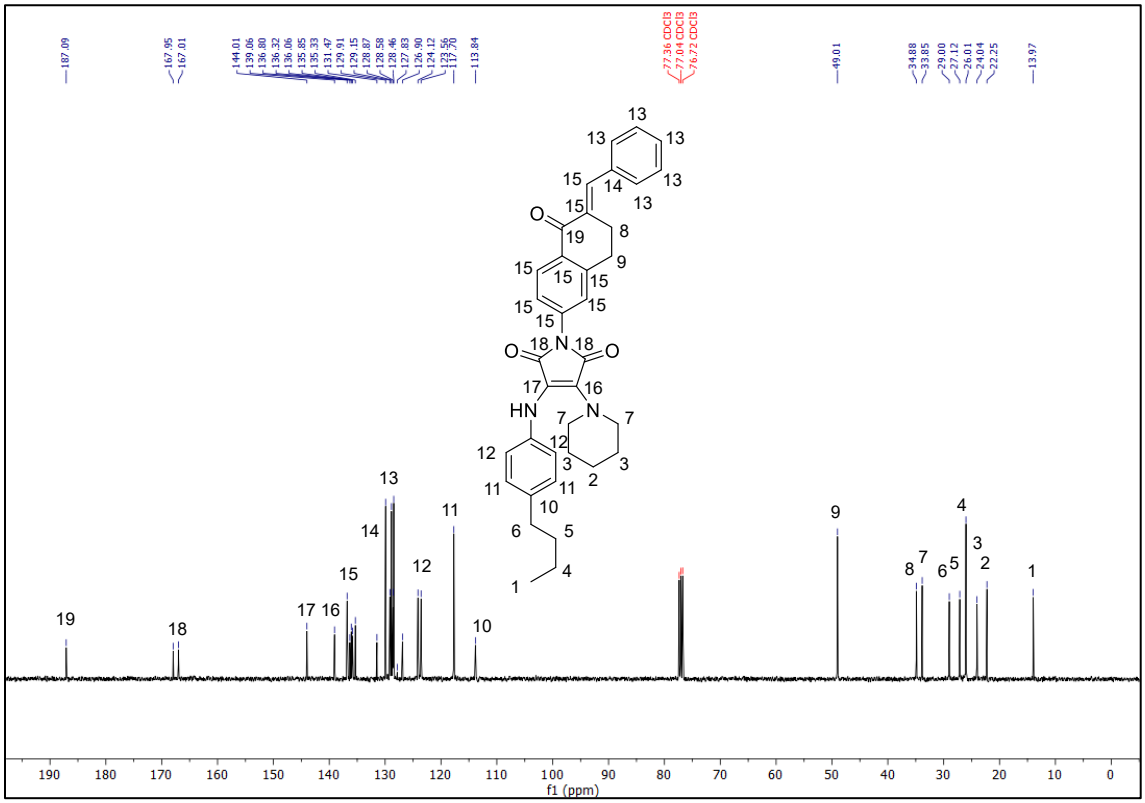

Figure 17 $^{1}H$ and $^{13}C$ NMR spectra of α-Tetralone-M in $CDCl_3$.

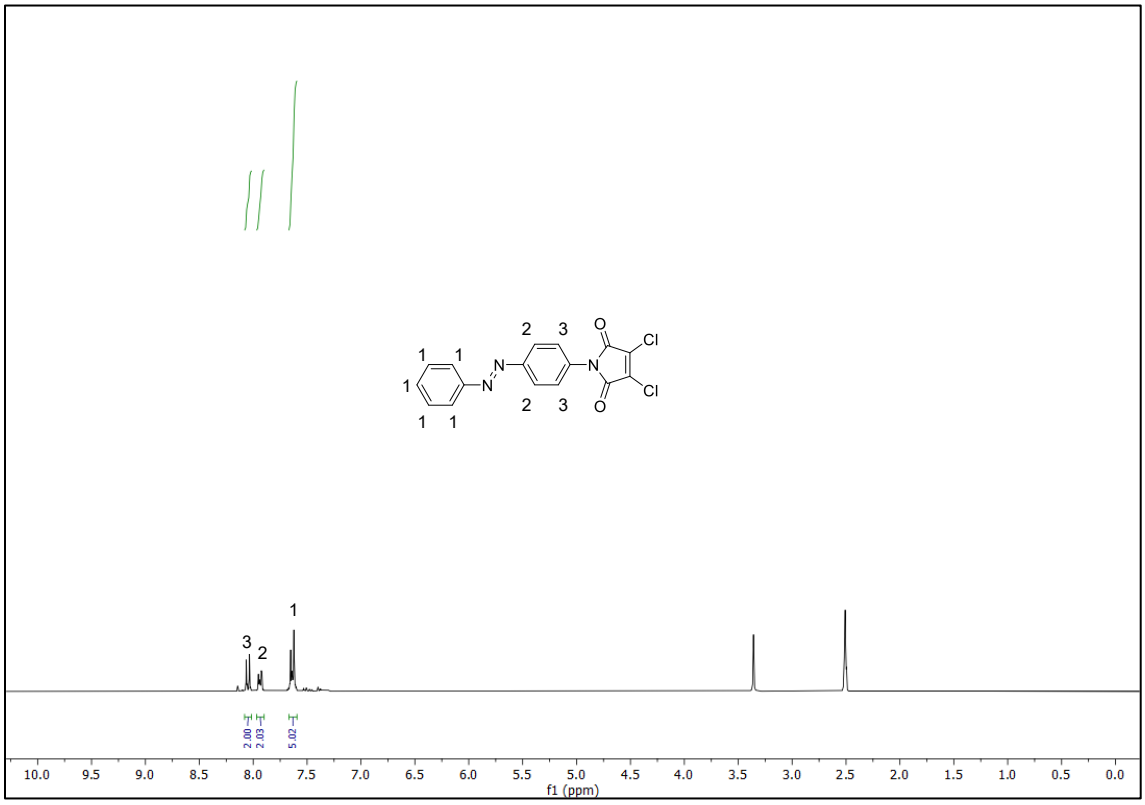


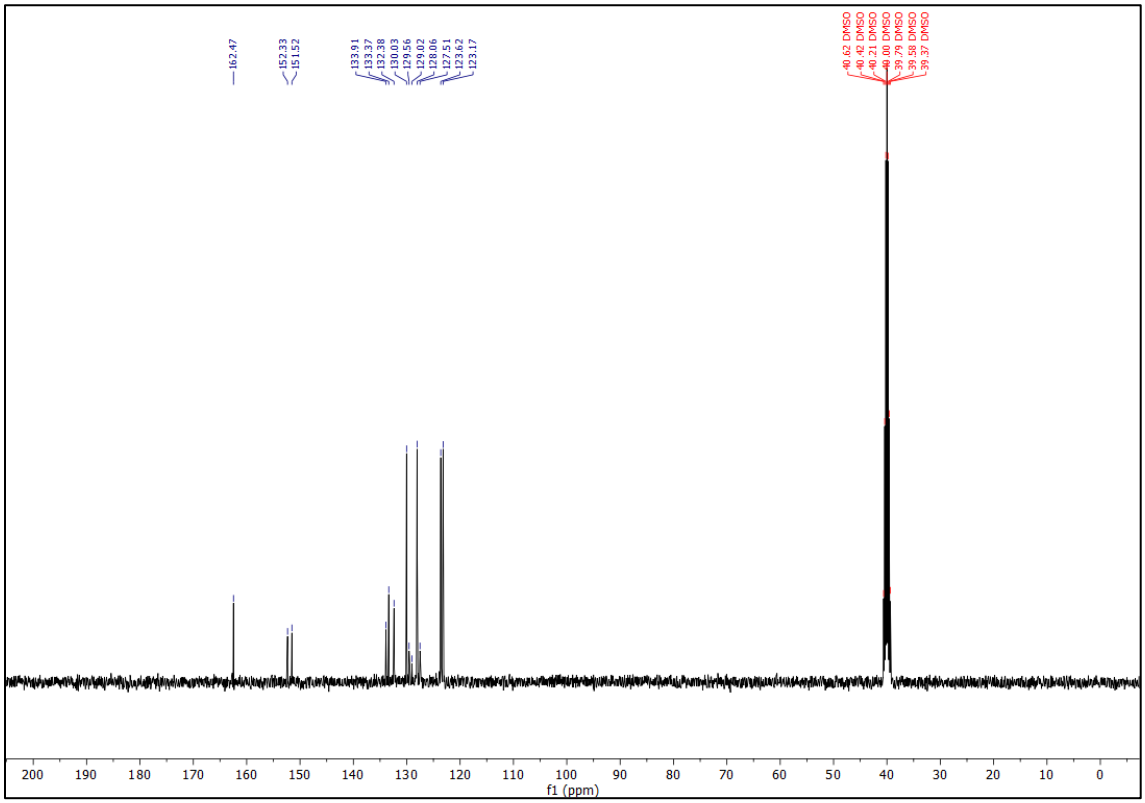

Figure 18 $^{1}H$ and $^{13}C$ NMR spectra of azobenzene-M-DC in DMSO-d6.

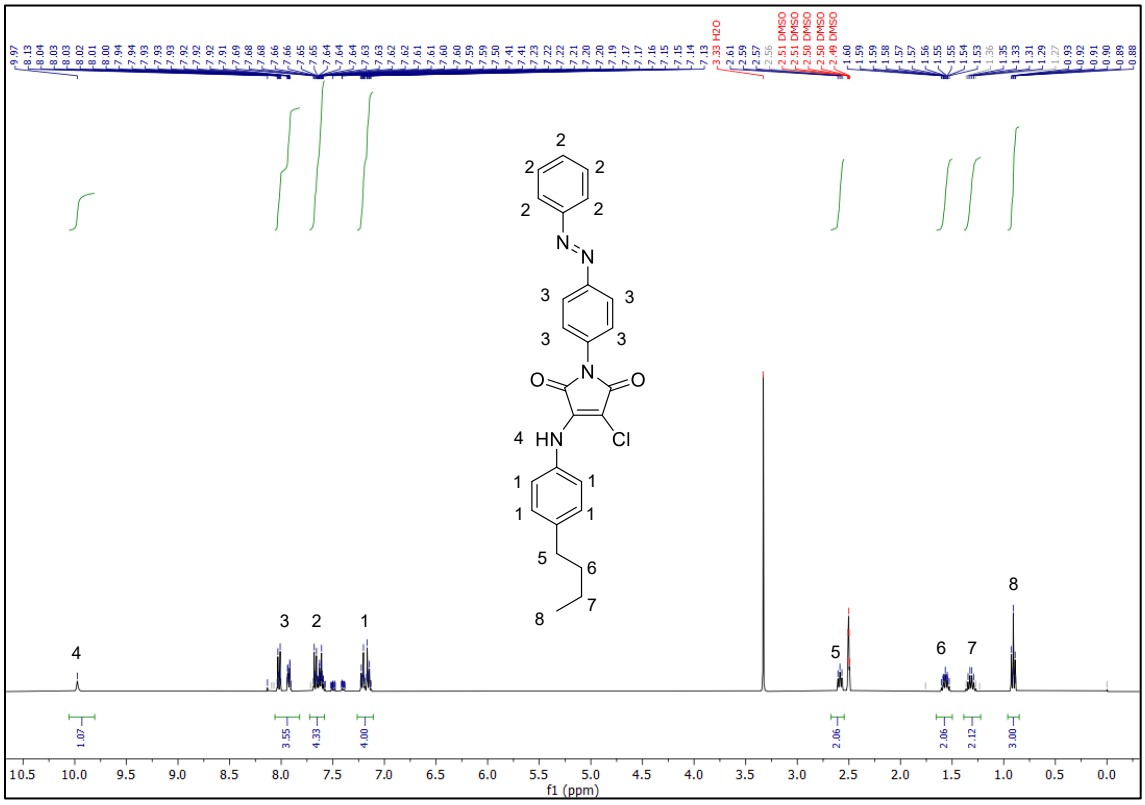


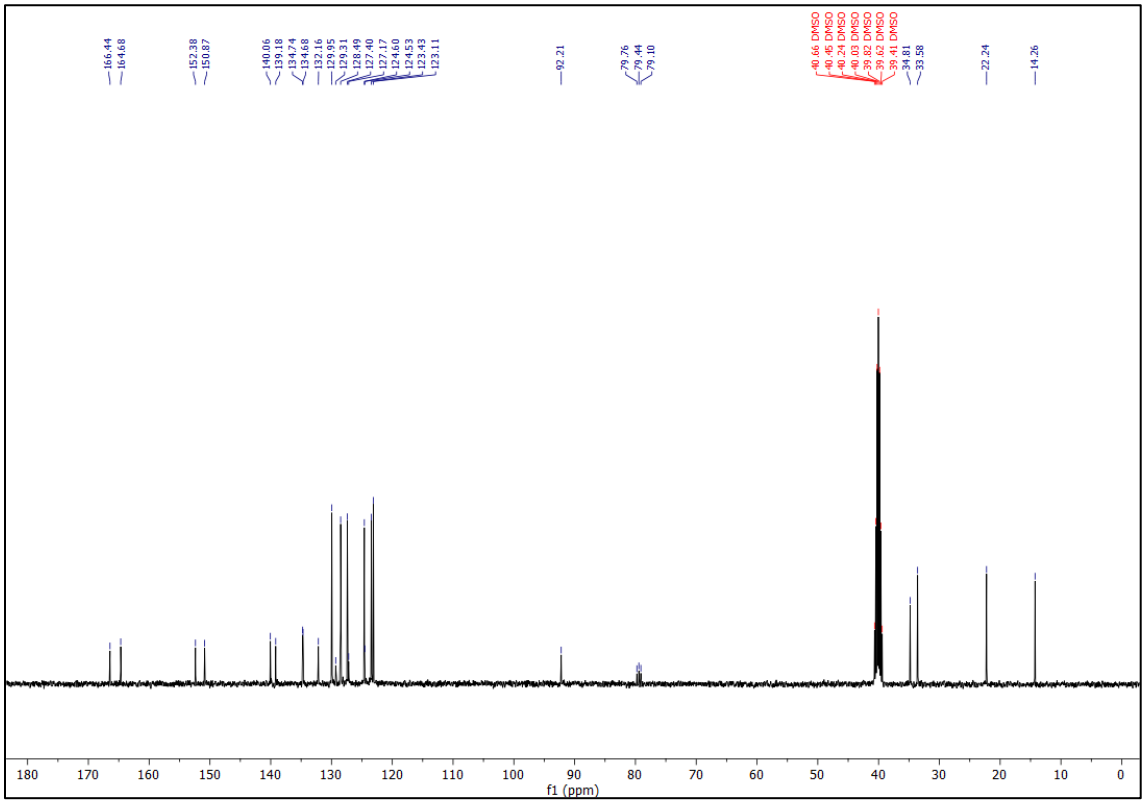

Figure 19 $^{1}H$ and $^{13}C$ NMR spectra of azobenzene-M-aniline in DMSO-d6.

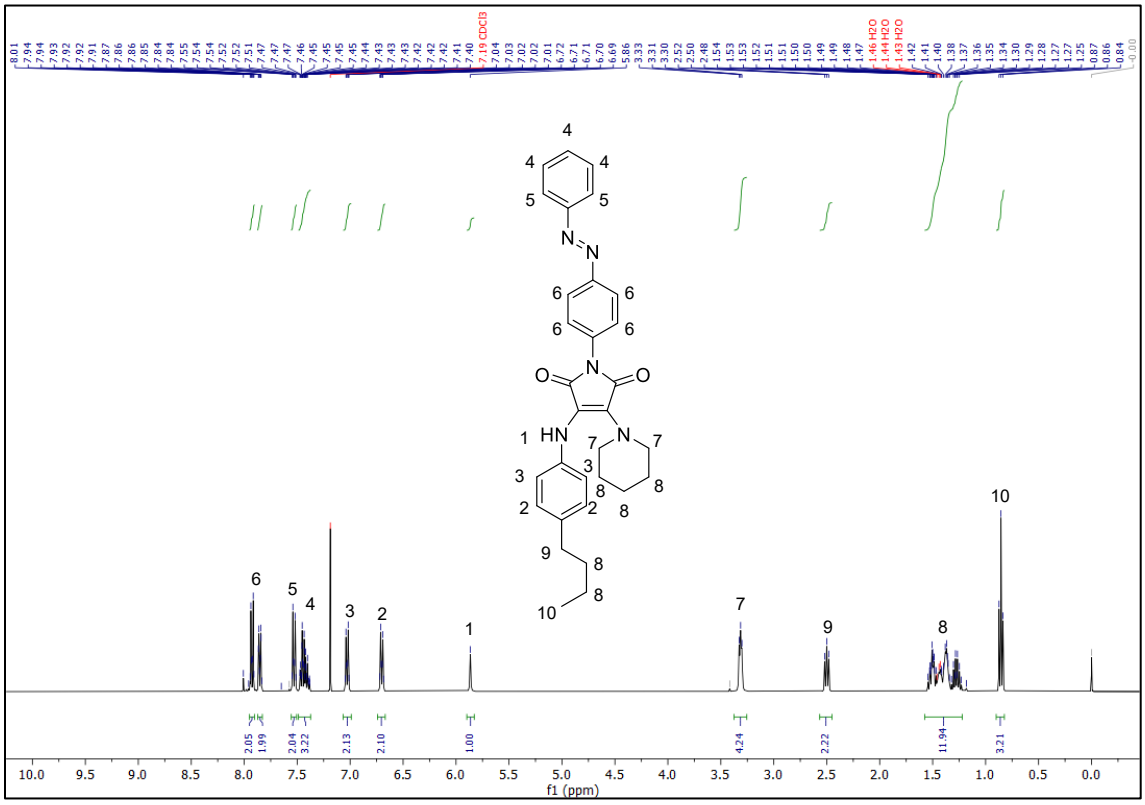


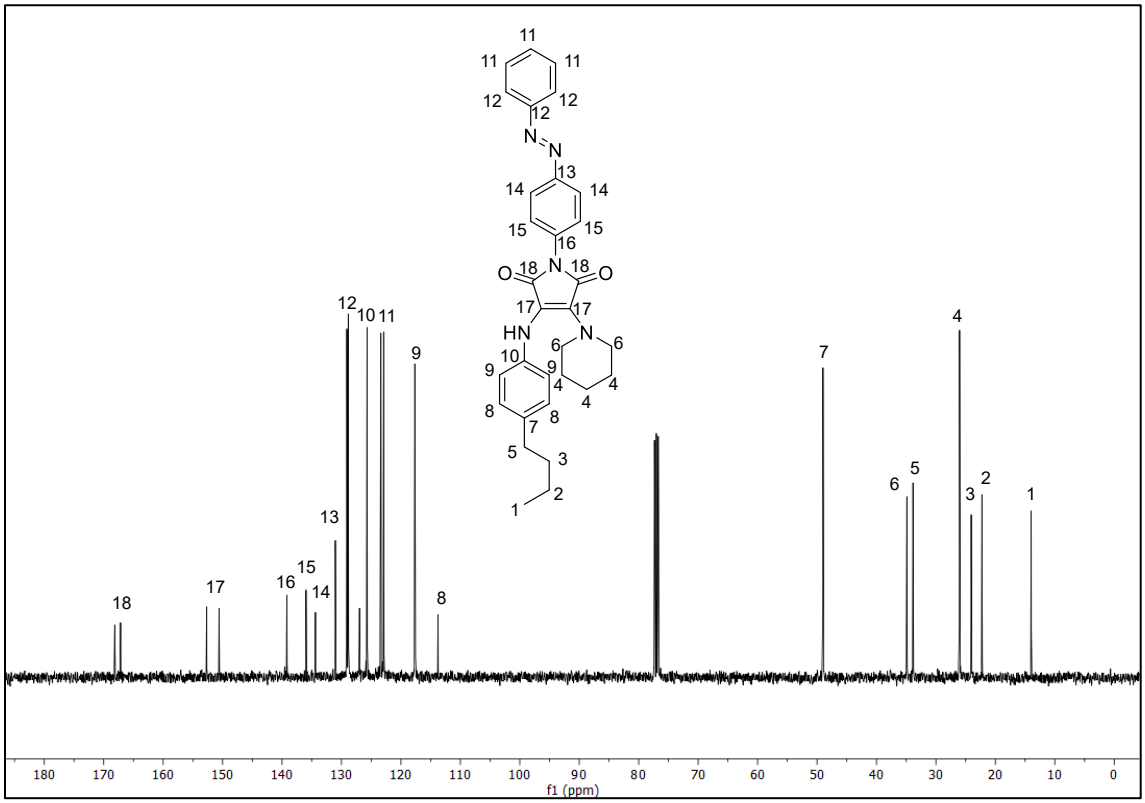

Figure 20 $^{1}H$ and $^{13}C$ NMR spectra of azobenzene-M in $CHCl_3$.

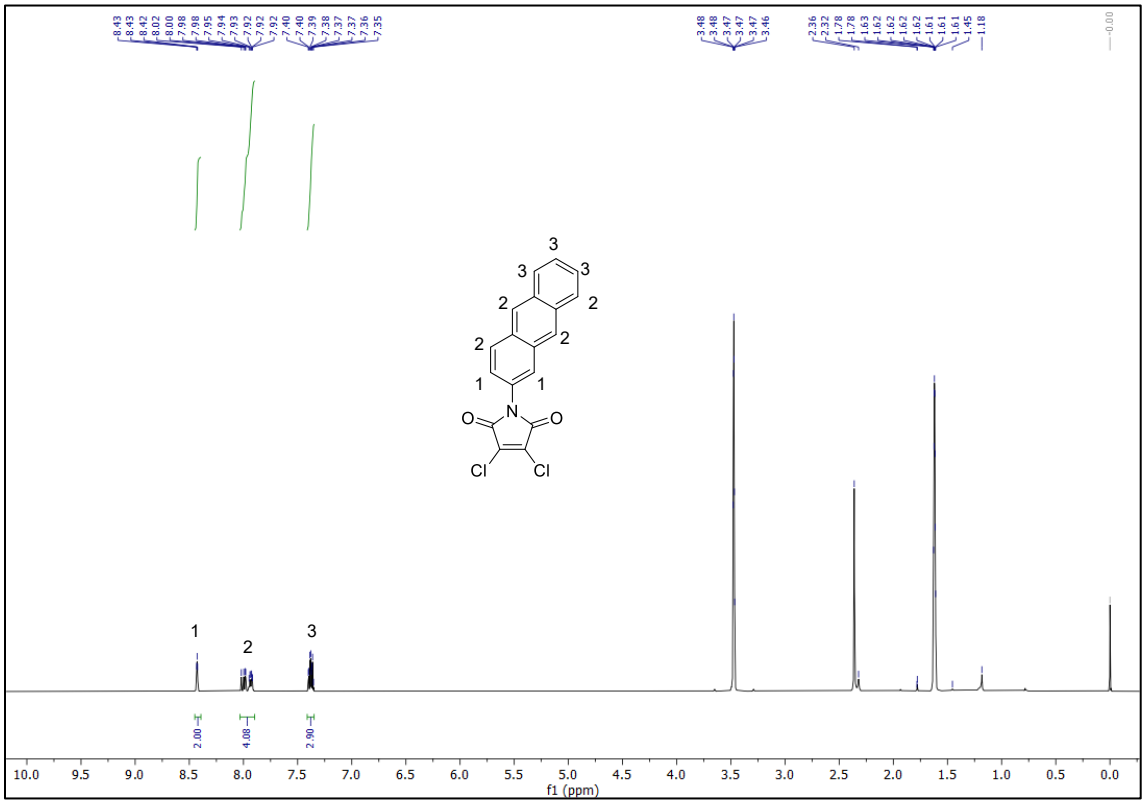


Figure 21 $^{1}H$ NMR spectra of Anthracene-M-DC in DMSO-d6.

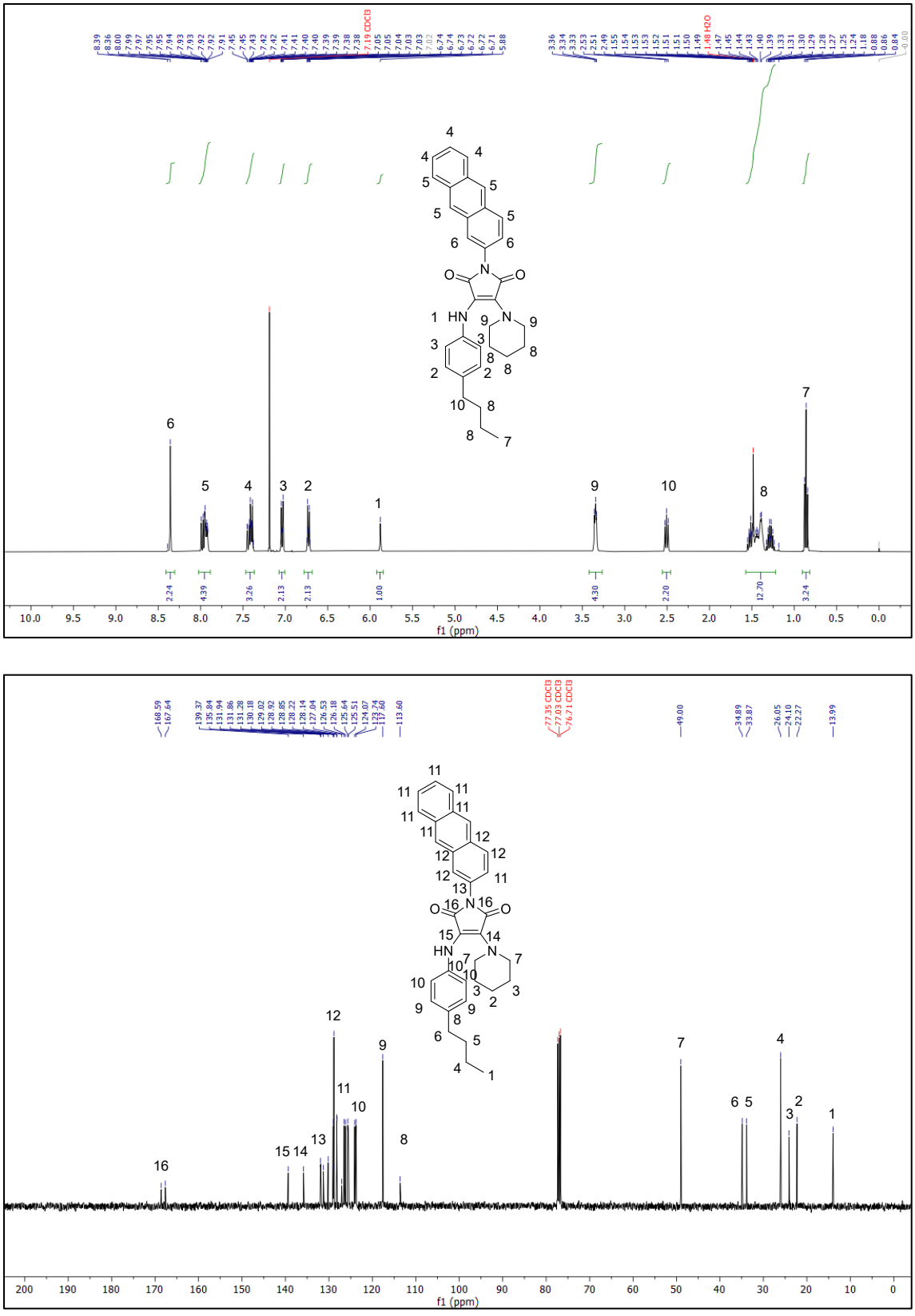

Figure 23 $^{1}$H NMR spectra of Anthracene-M in $CHCl_3$.

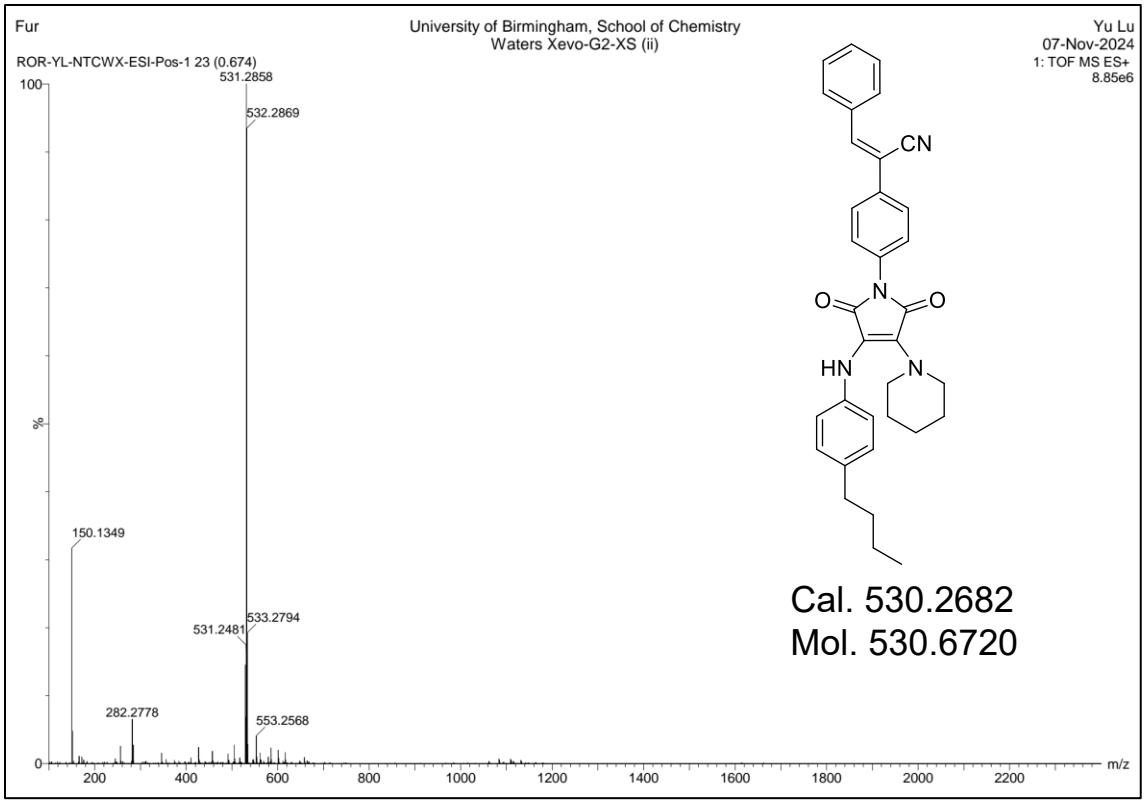
Fur
University of Birmingham, School of Chemistry
Waters Xevo-G2-XS (ii)
Yu Lu
07-Nov-2024
1: TOF MS ES+
8.85e6
ROR-YL-NTCWX-ESI-Pos-1 23 (0.674)
531.2858
532.2869
150.1349
533.2794
531.2481
282.2778
553.2568
CN
O
N
O
HN
N
Cal. 530.2682
Mol. 530.6720
%
m/z

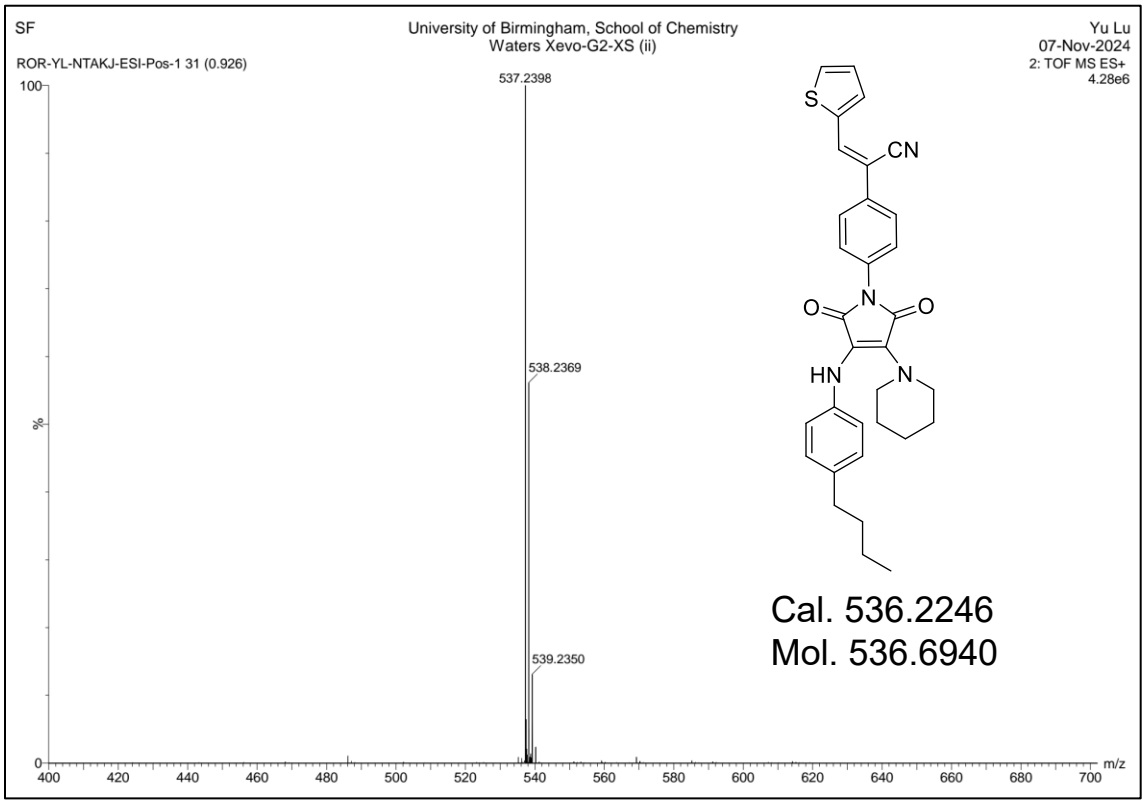
SF
University of Birmingham, School of Chemistry
Waters Xevo-G2-XS (ii)
Yu Lu
07-Nov-2024
2: TOF MS ES+
4.28e6
ROR-YL-NTAKJ-ESI-Pos-1 31 (0.926)
537.2398
538.2369
539.2350
S
CN
O
N
O
HN
N
Cal. 536.2246
Mol. 536.6940
%
m/z

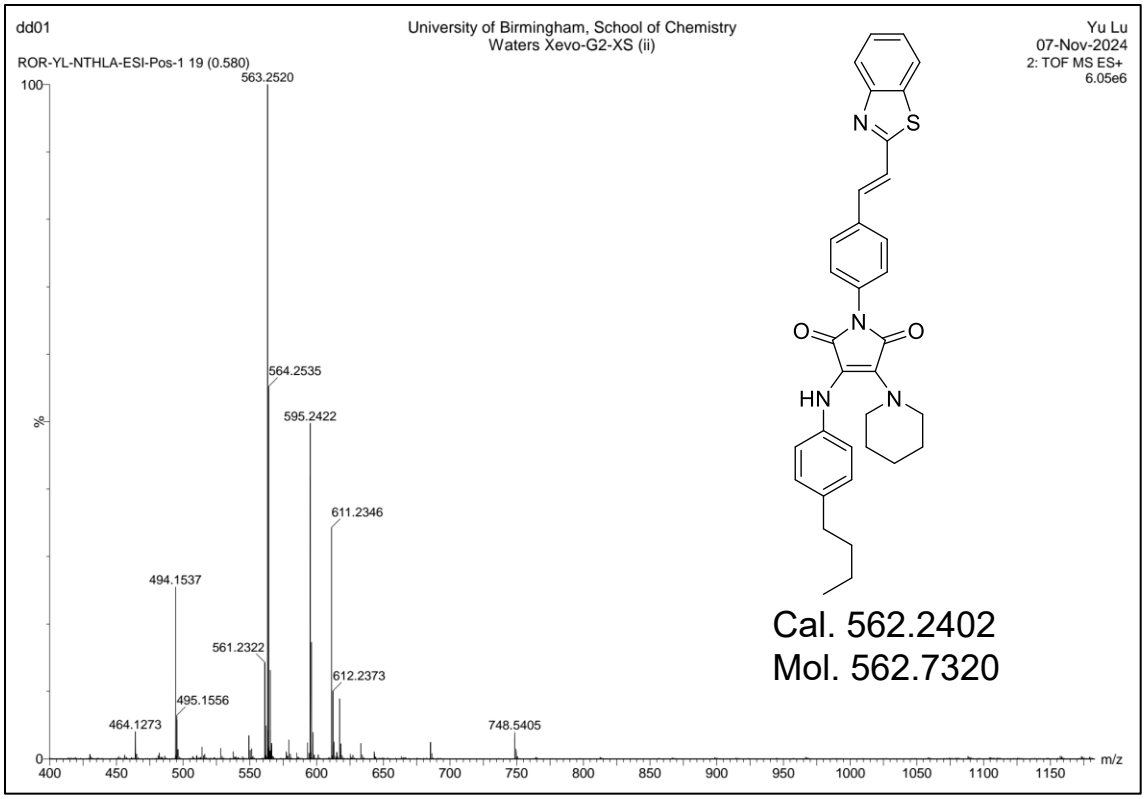
dd01
University of Birmingham, School of Chemistry
Waters Xevo-G2-XS (ii)
Yu Lu
07-Nov-2024
2: TOF MS ES+
6.05e6
ROR-YL-NTHLA-ESI-Pos-1 19 (0.580)
563.2520
564.2535
595.2422
611.2346
494.1537
561.2322
612.2373
495.1556
464.1273
748.5405
Cal. 562.2402
Mol. 562.7320

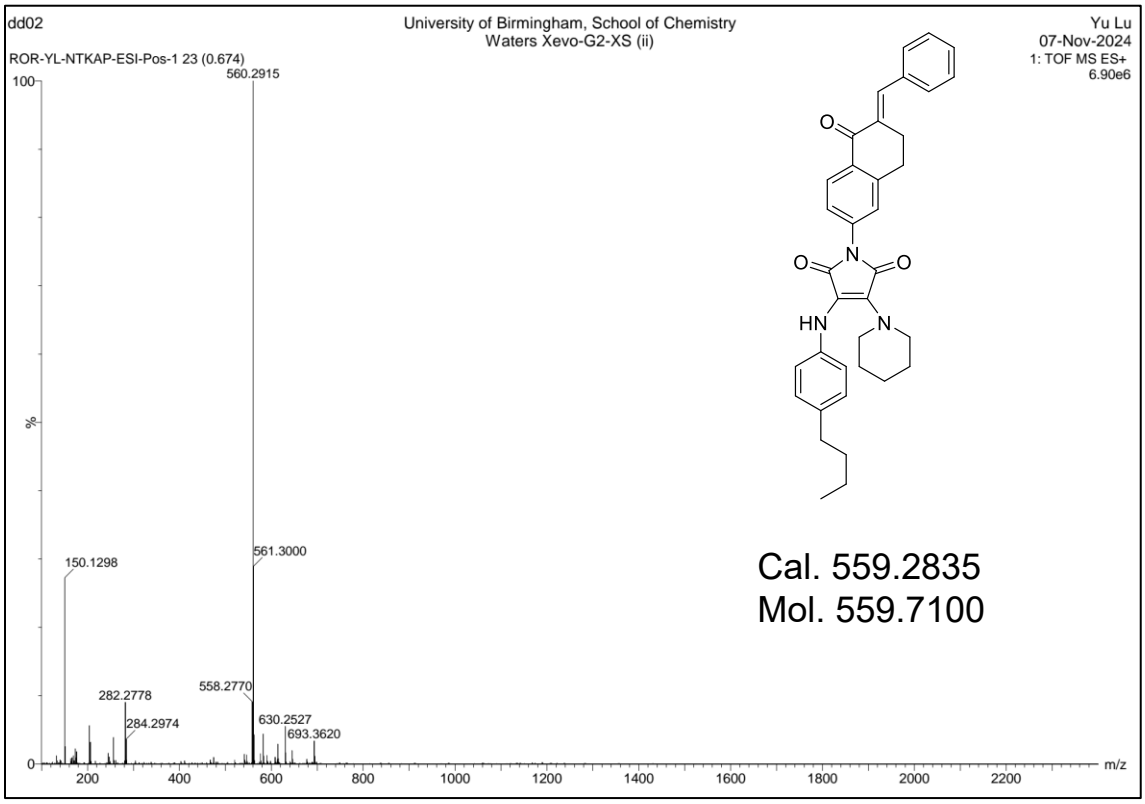
dd02
University of Birmingham, School of Chemistry
Waters Xevo-G2-XS (ii)
Yu Lu
07-Nov-2024
1: TOF MS ES+
6.90e6
ROR-YL-NTKAP-ESI-Pos-1 23 (0.674)
560.2915
561.3000
150.1298
558.2770
282.2778
284.2974
630.2527
693.3620
Cal. 559.2835
Mol. 559.7100

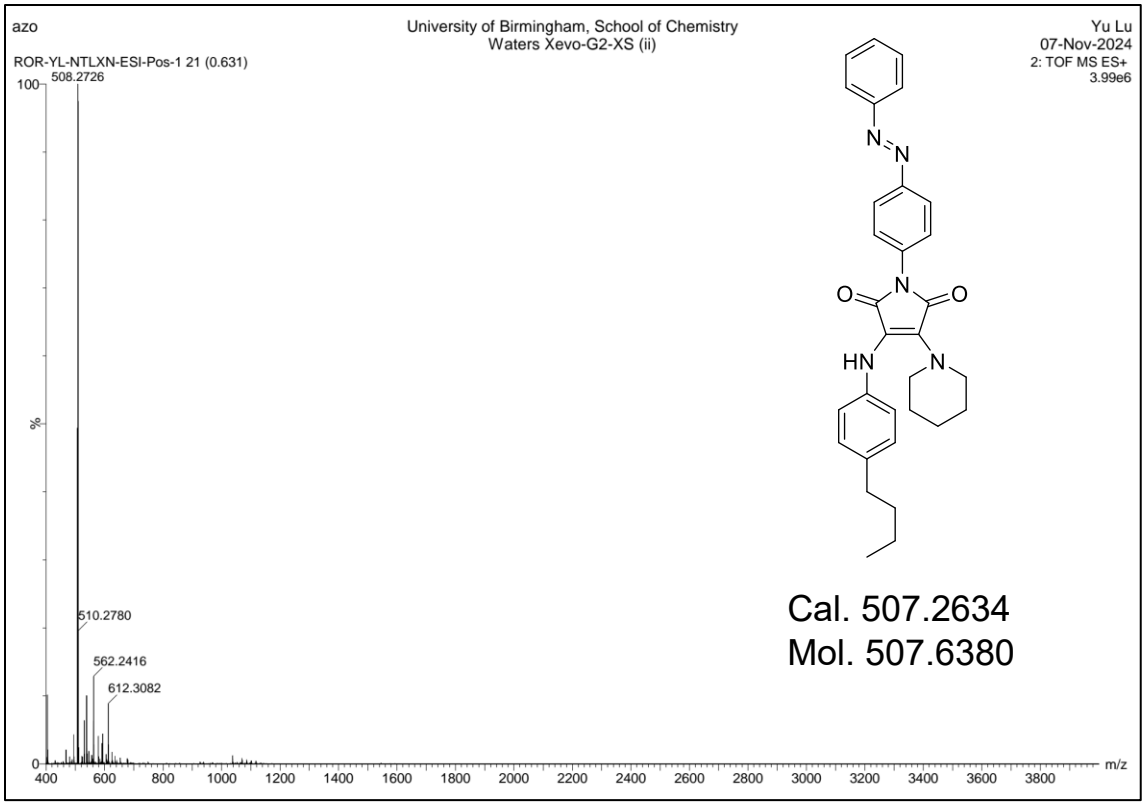
azo
University of Birmingham, School of Chemistry
Waters Xevo-G2-XS (ii)
Yu Lu
07-Nov-2024
2: TOF MS ES+
3.99e6
ROR-YL-NTLXN-ESI-Pos-1 21 (0.631)
508.2726
510.2780
562.2416
612.3082
%
m/z
Cal. 507.2634
Mol. 507.6380

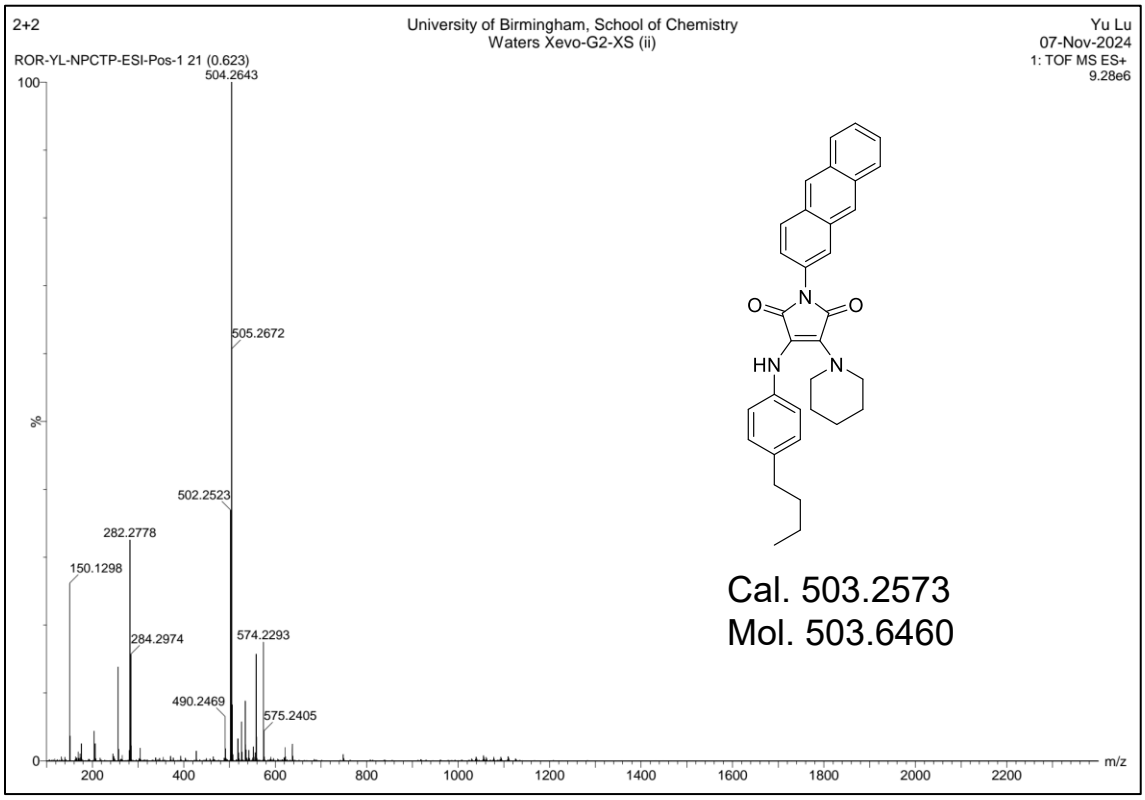
2+2
University of Birmingham, School of Chemistry
Waters Xevo-G2-XS (ii)
Yu Lu
07-Nov-2024
1: TOF MS ES+
9.28e6
ROR-YL-NPCTP-ESI-Pos-1 21 (0.623)
504.2643
505.2672
502.2523
282.2778
150.1298
284.2974
574.2293
490.2469
575.2405
%
m/z
Cal. 503.2573
Mol. 503.6460

### 3.7.6 Characterization of photophysical properties

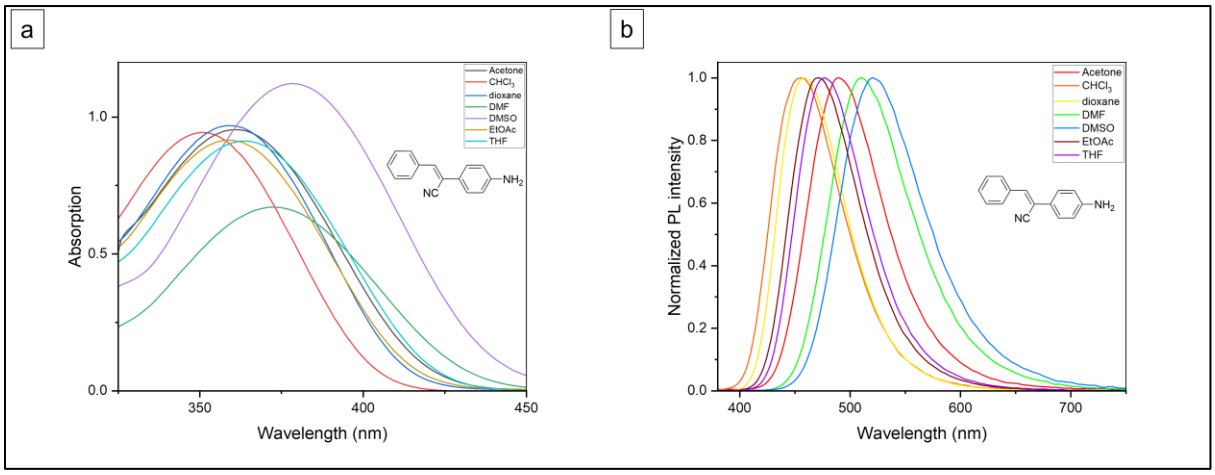


Figure 24 UV absorption (a) and normalized fluorescent spectra (b) in different solvents.

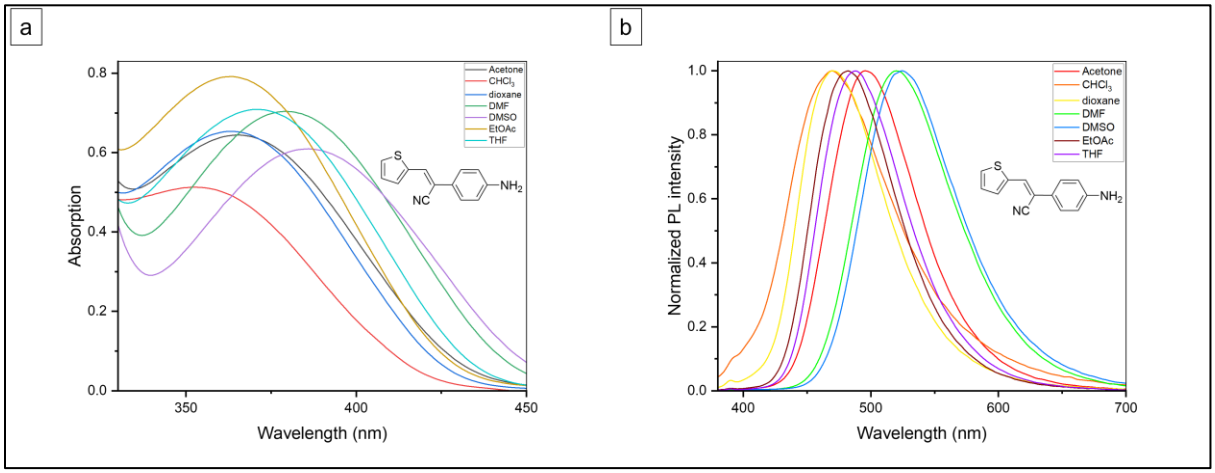


Figure 25 UV absorption (a) and normalized fluorescent spectra (b) in different solvents.

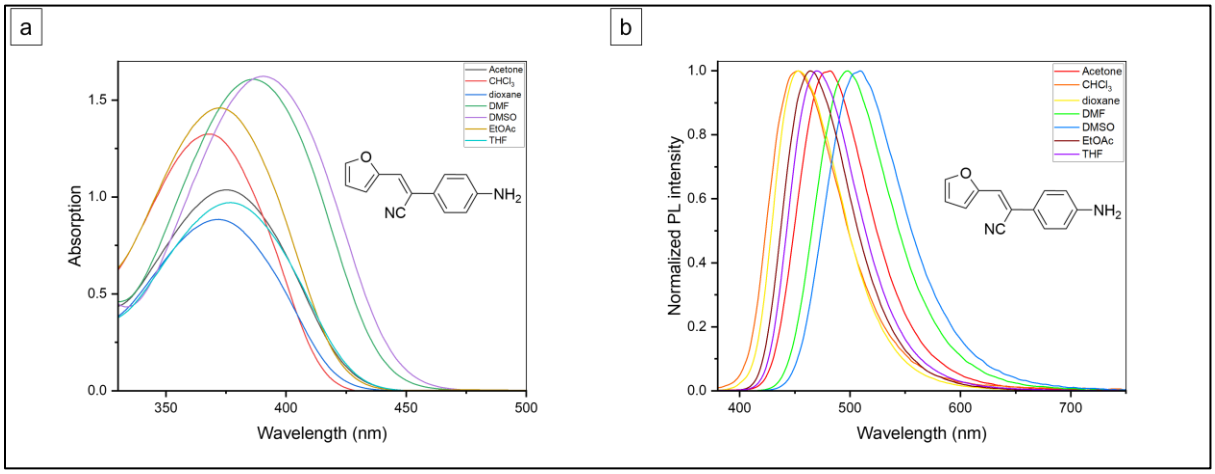

Figure 26 UV absorption (a) and normalized fluorescent spectra (b) in different solvents.

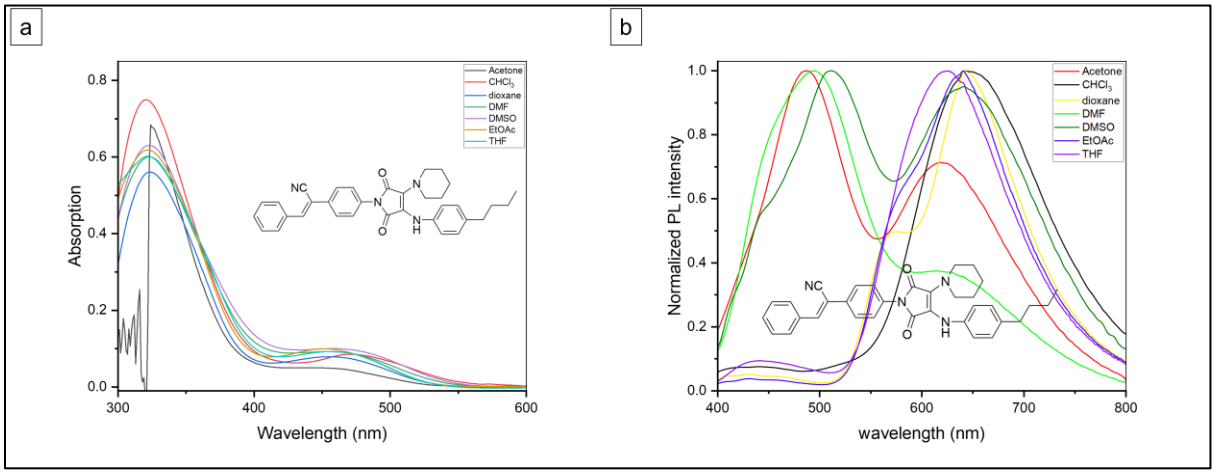


Figure 27 UV absorption (a) and normalized fluorescent spectra (b) in different solvents.

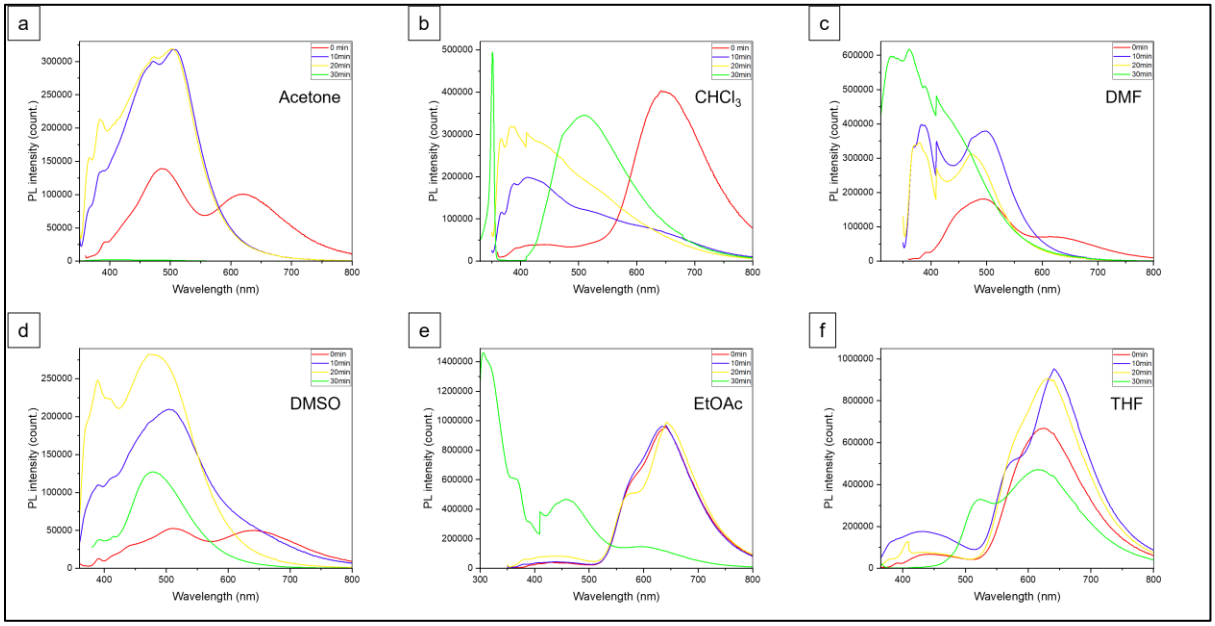


Figure 28 The FL spectra of Ben-BP in various solvents under different durations of UV irradiation.

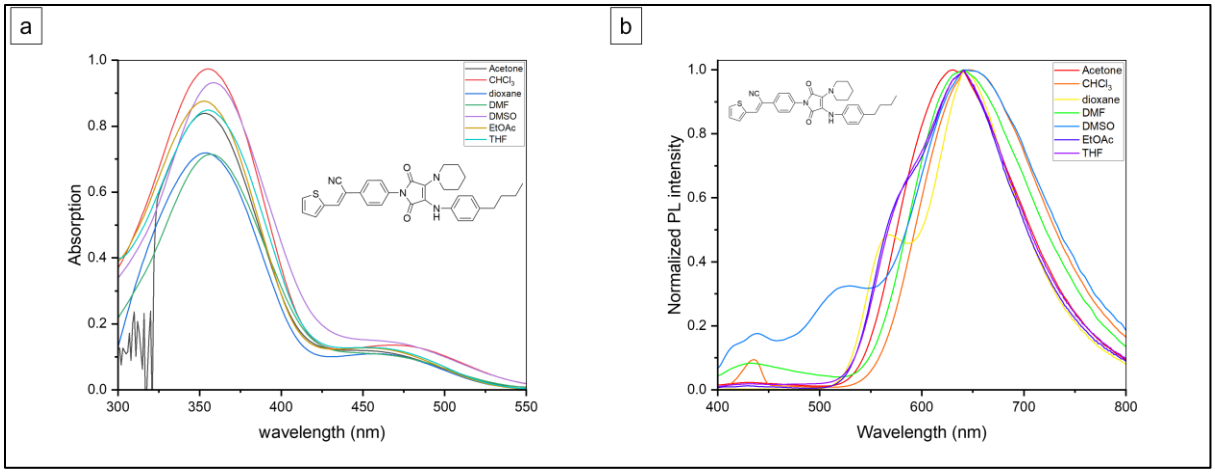


Figure 29 UV absorption (a) and normalized fluorescent spectra (b) in different solvents.

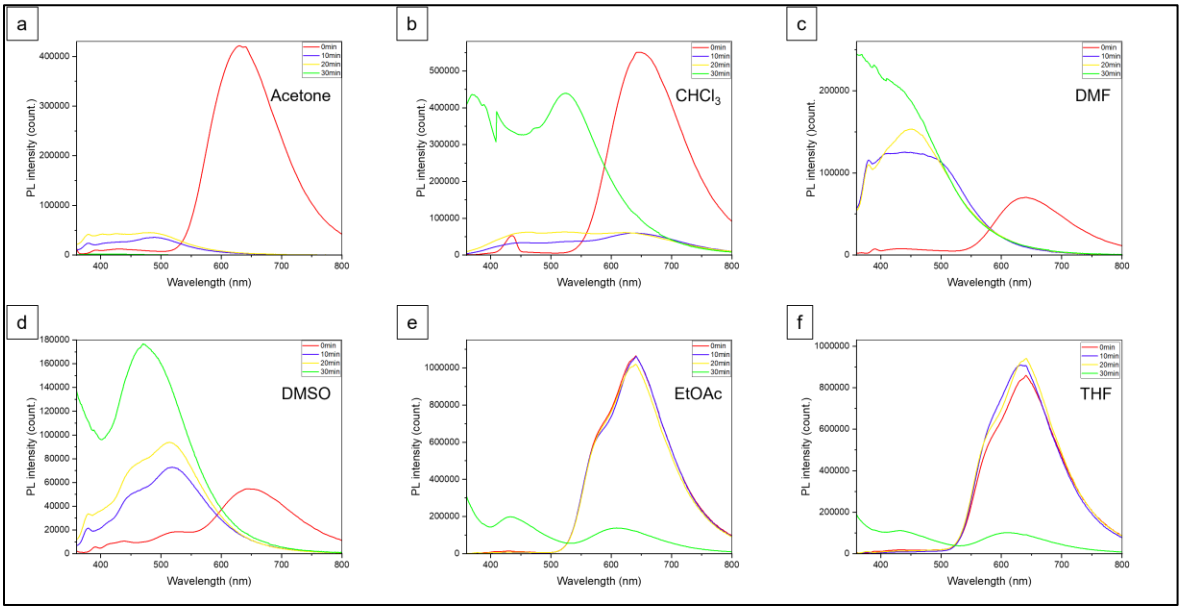


Figure 30 The FL spectra of Then-BP in various solvents under different durations of UV irradiation.

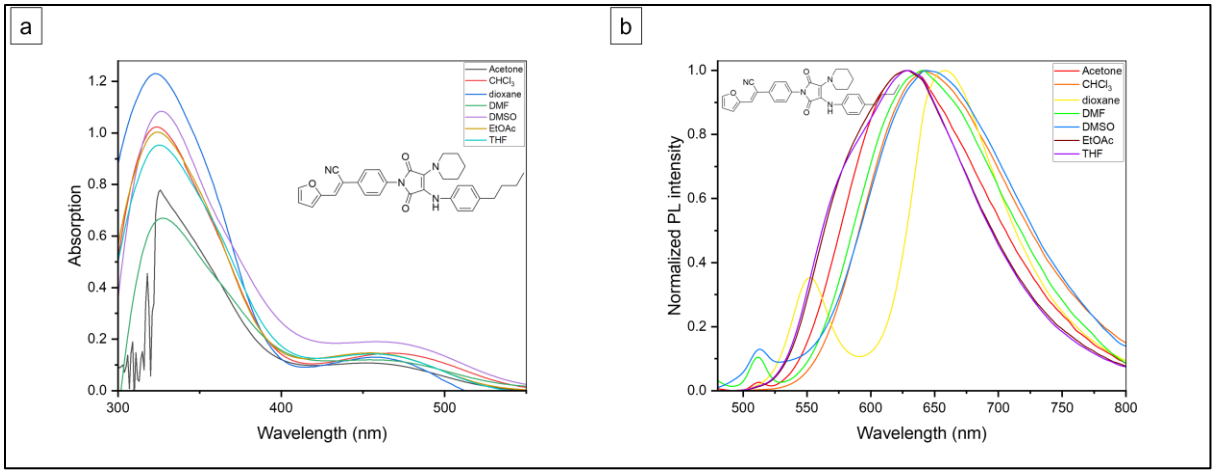


Figure 31 UV absorption (a) and normalized fluorescent spectra (b) in different solvents.

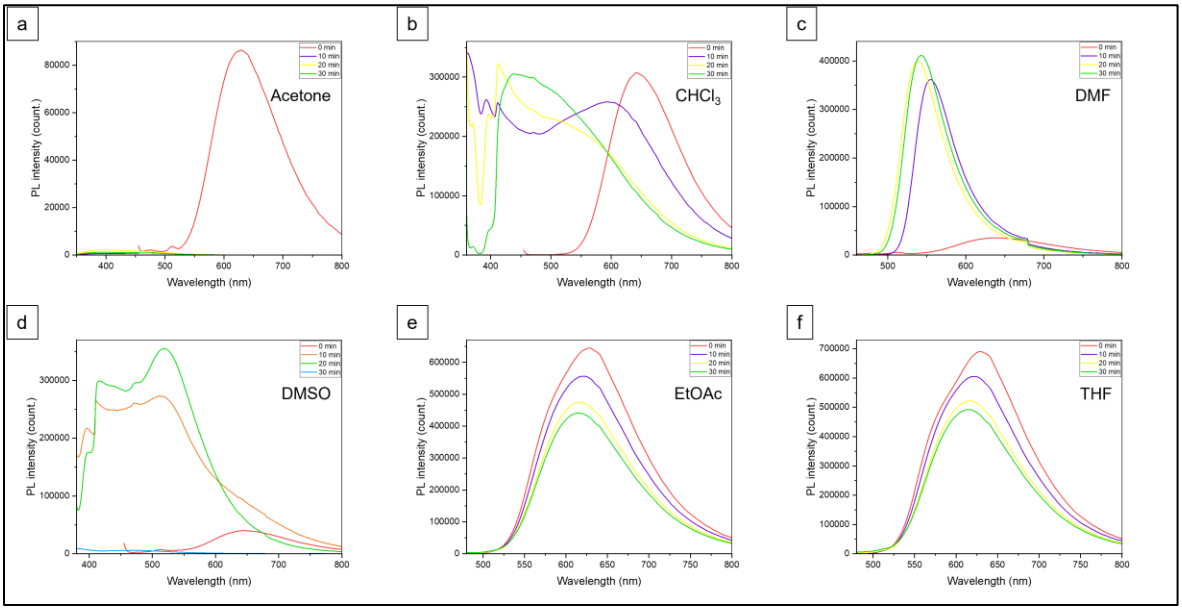


Figure 32 The FL spectra of Fur-BP in various solvents under different durations of UV irradiation.

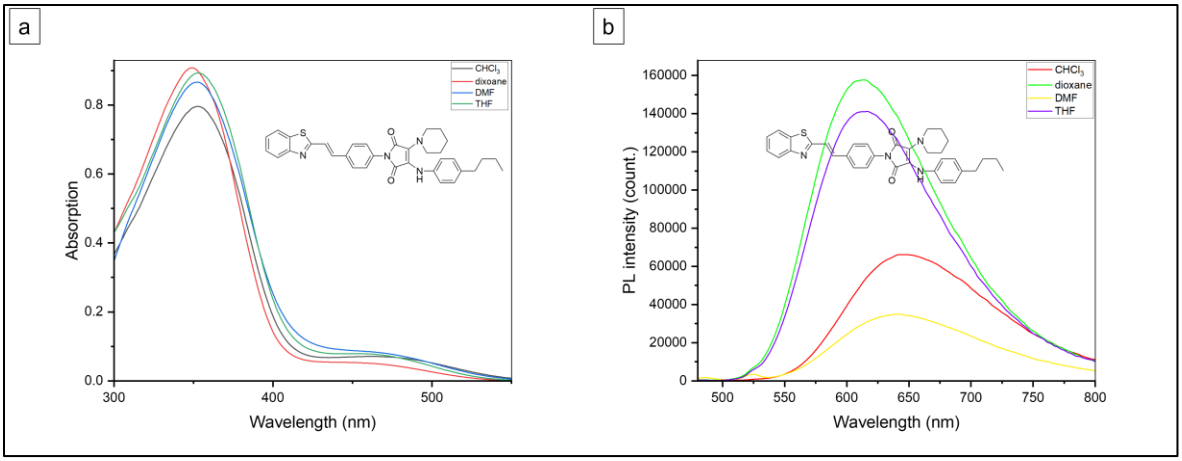


Figure 33 UV absorption (a) and fluorescent spectra (b) in different solvents.

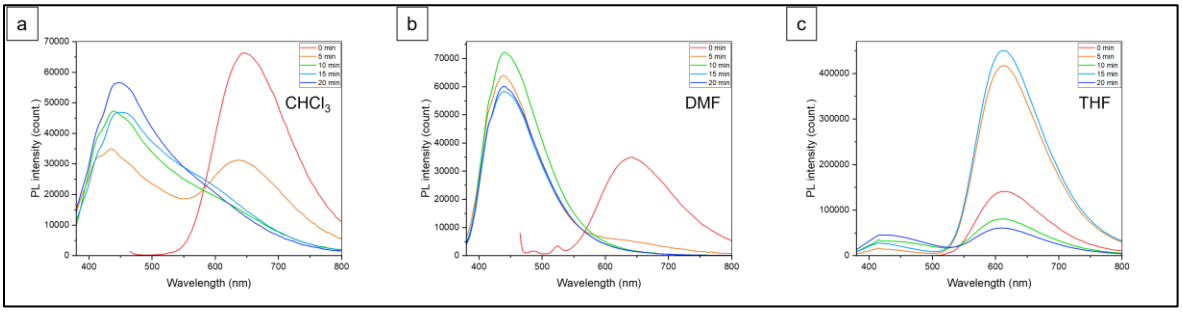


Figure 34 The FL spectra of benzothiazole-BP in various solvents under different durations of UV irradiation.

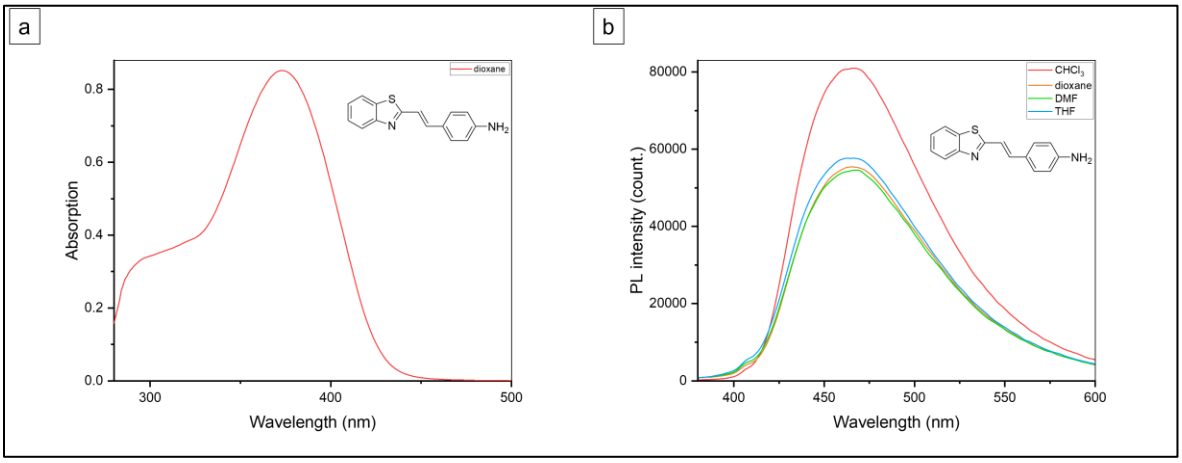


Figure 35 UV absorption (a) and fluorescent spectra (b) in different solvents.

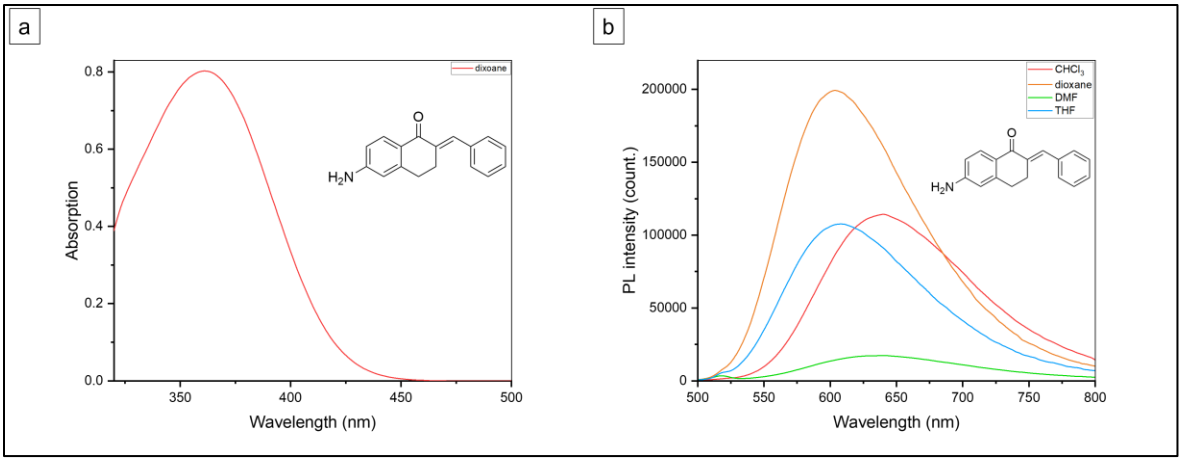


Figure 36 UV absorption (a) and fluorescent spectra (b) in different solvents.

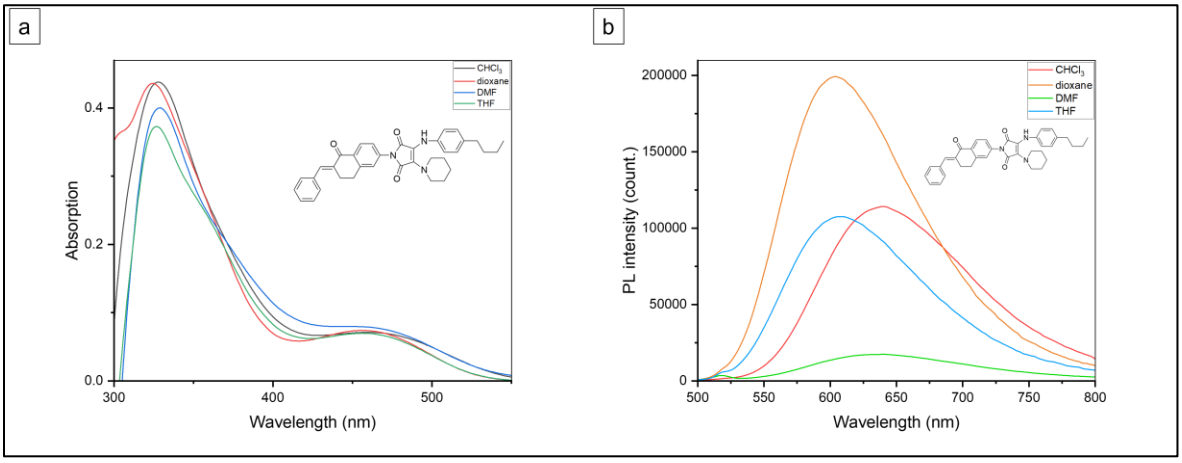


Figure 37 UV absorption (a) and fluorescent spectra (b) in different solvents.

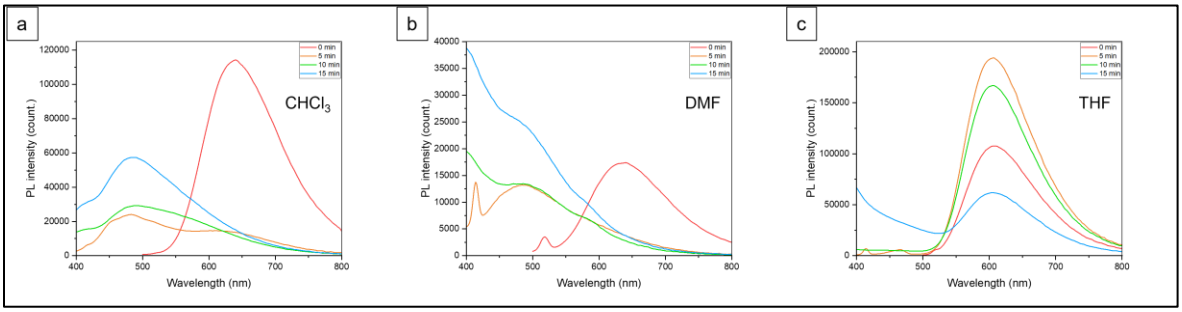


Figure 38 The FL spectra of α-Tetralone-BP in various solvents under different durations of UV irradiation.

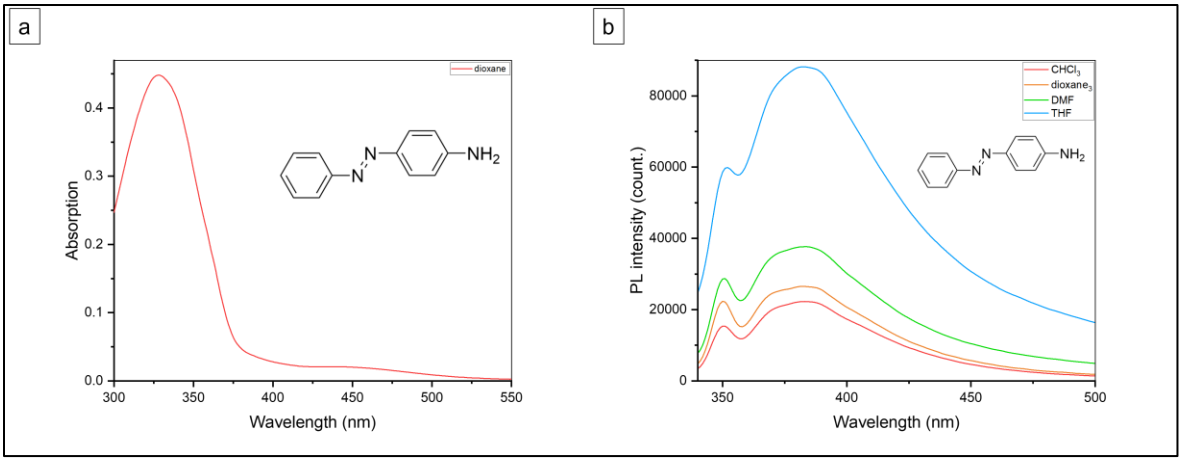


Figure 39 UV absorption (a) in dixoane and fluorescent spectra (b) in different solvents.

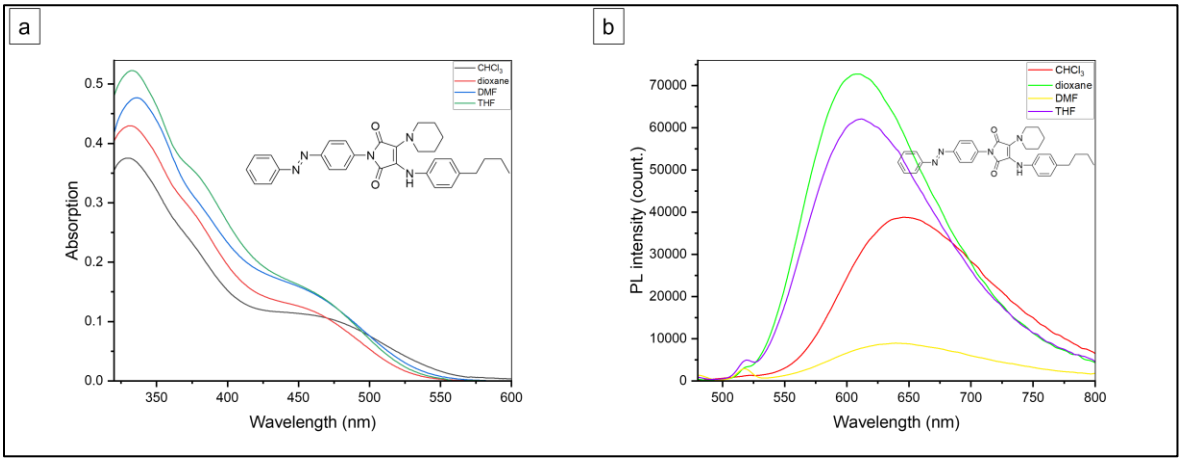


Figure 40 UV absorption (a) and fluorescent spectra (b) in different solvents.

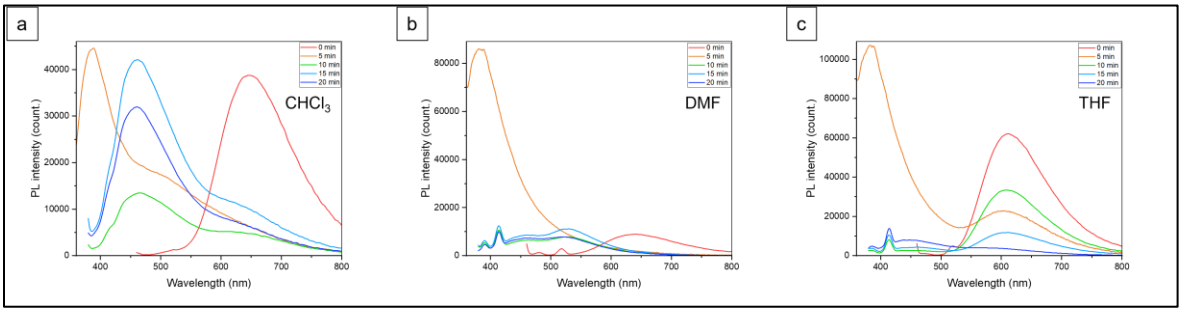


Figure 41 The FL spectra of azobenzene-BP in various solvents under different durations of UV irradiation.

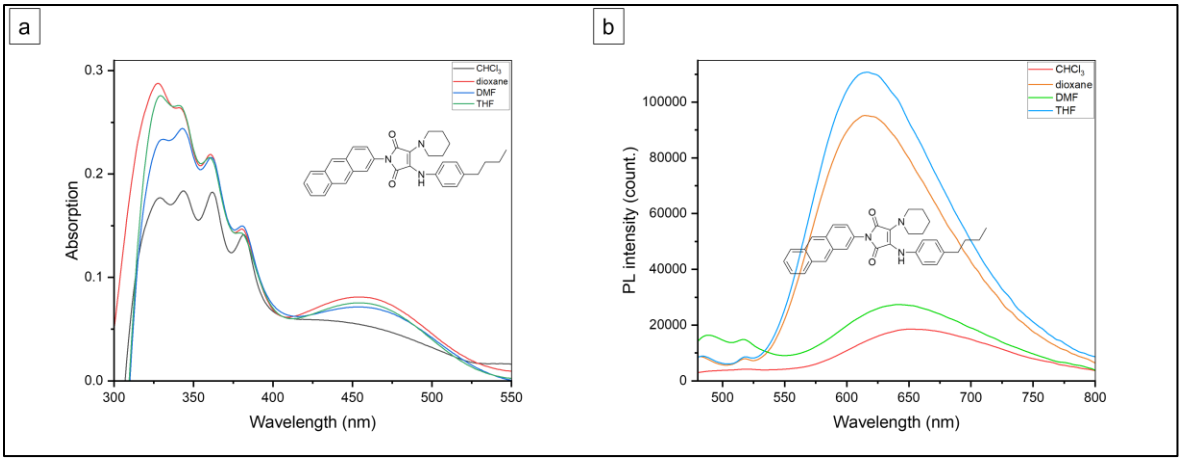


Figure 42 UV absorption (a) and fluorescent spectra (b) in different solvents.

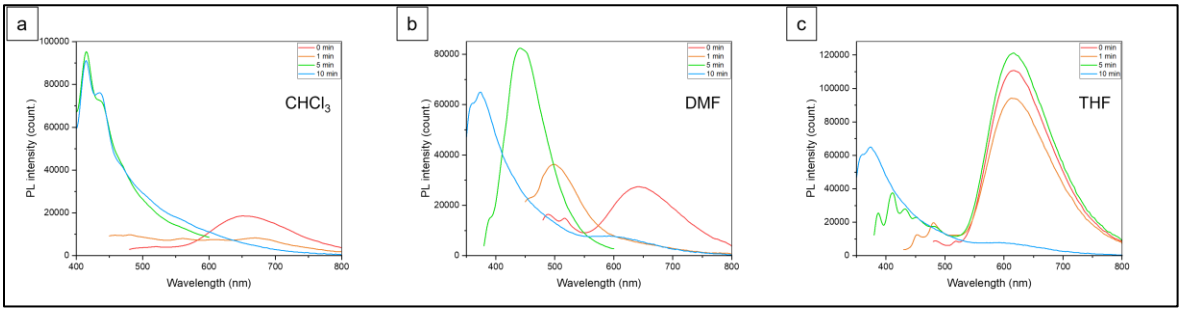


Figure 43 The FL spectra of anthracene-BP in various solvents under different durations of UV irradiation.

### 3.7.7 Frontier molecular orbitals

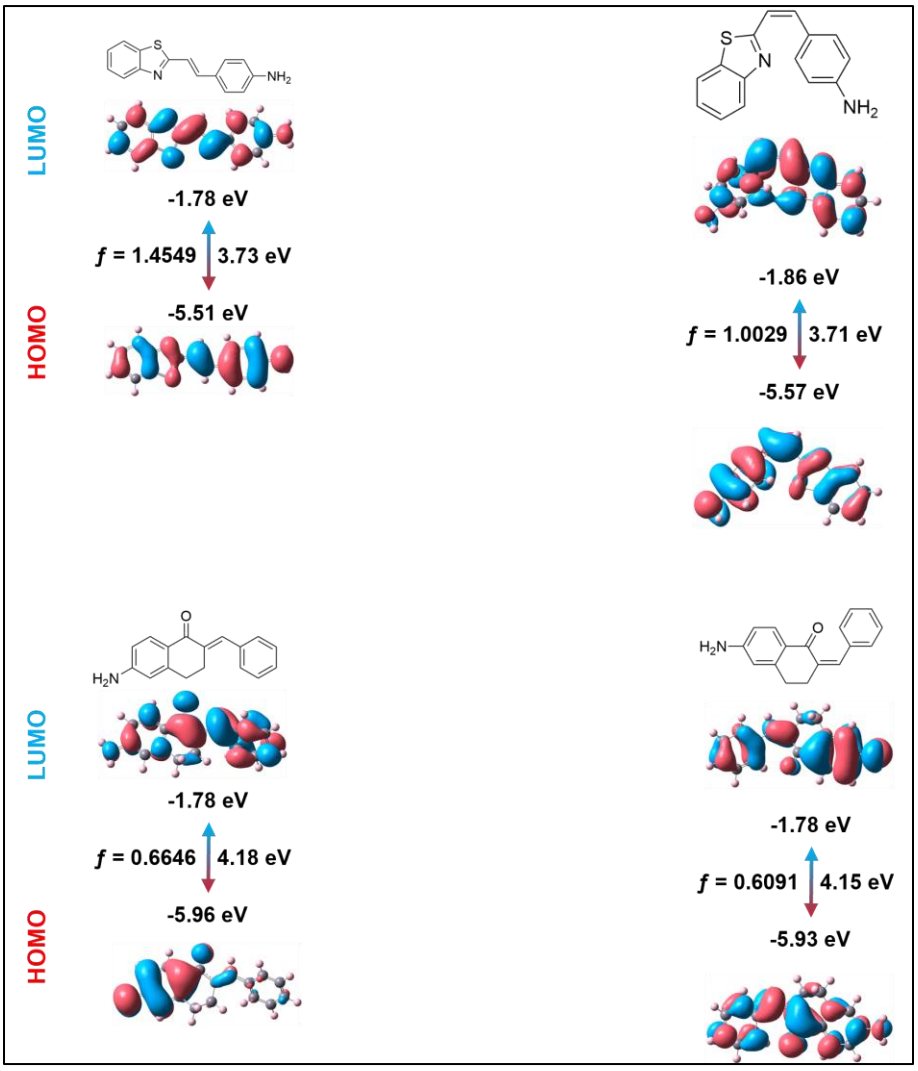


Figure 44 Frontier molecular orbitals and oscillator strength ($f$) in dioxane.

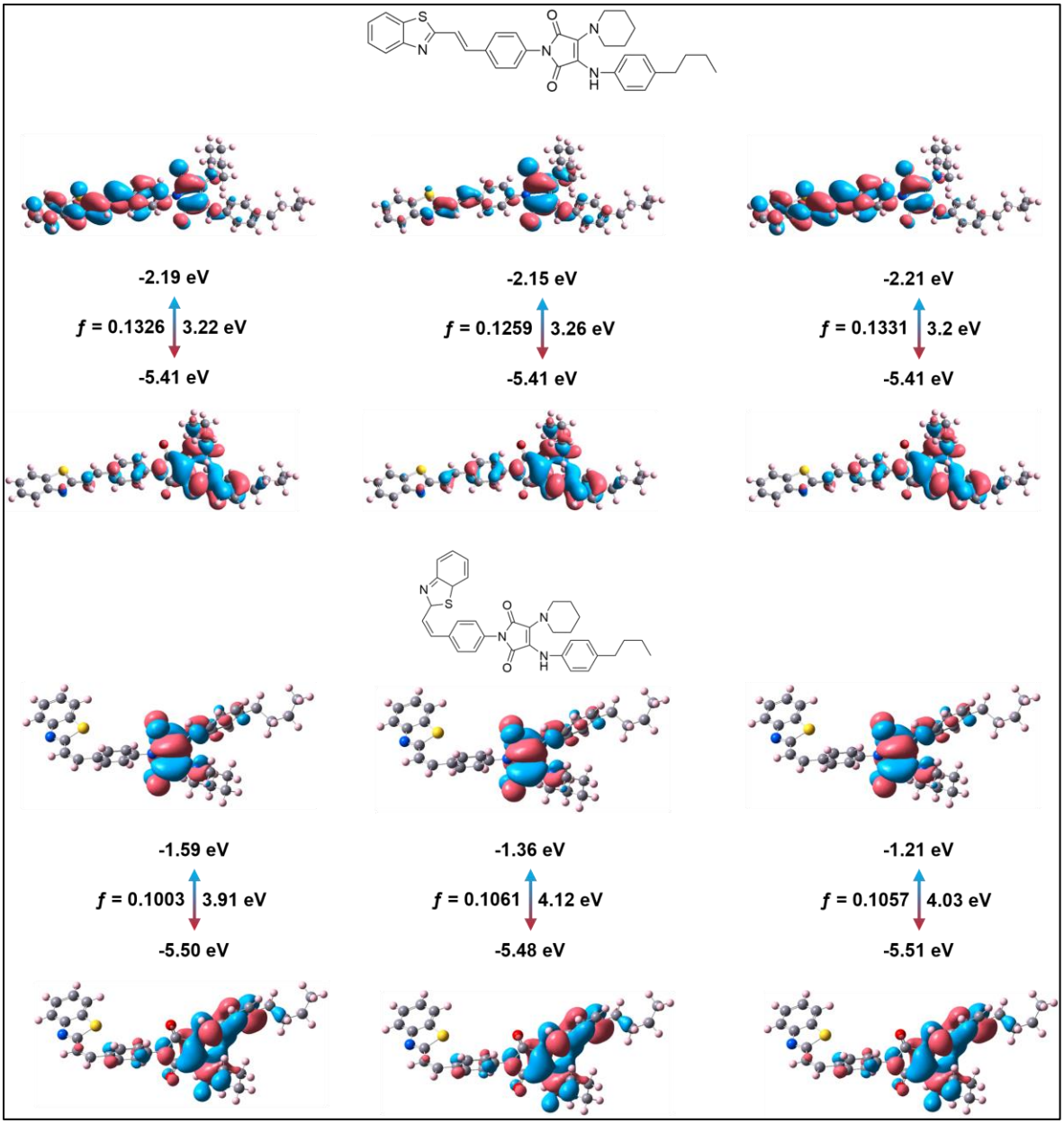


Figure 45 Frontier molecular orbitals and oscillator strength ($f$) in different solvents (from left to right is $CHCl_3$, dioxane, THF).

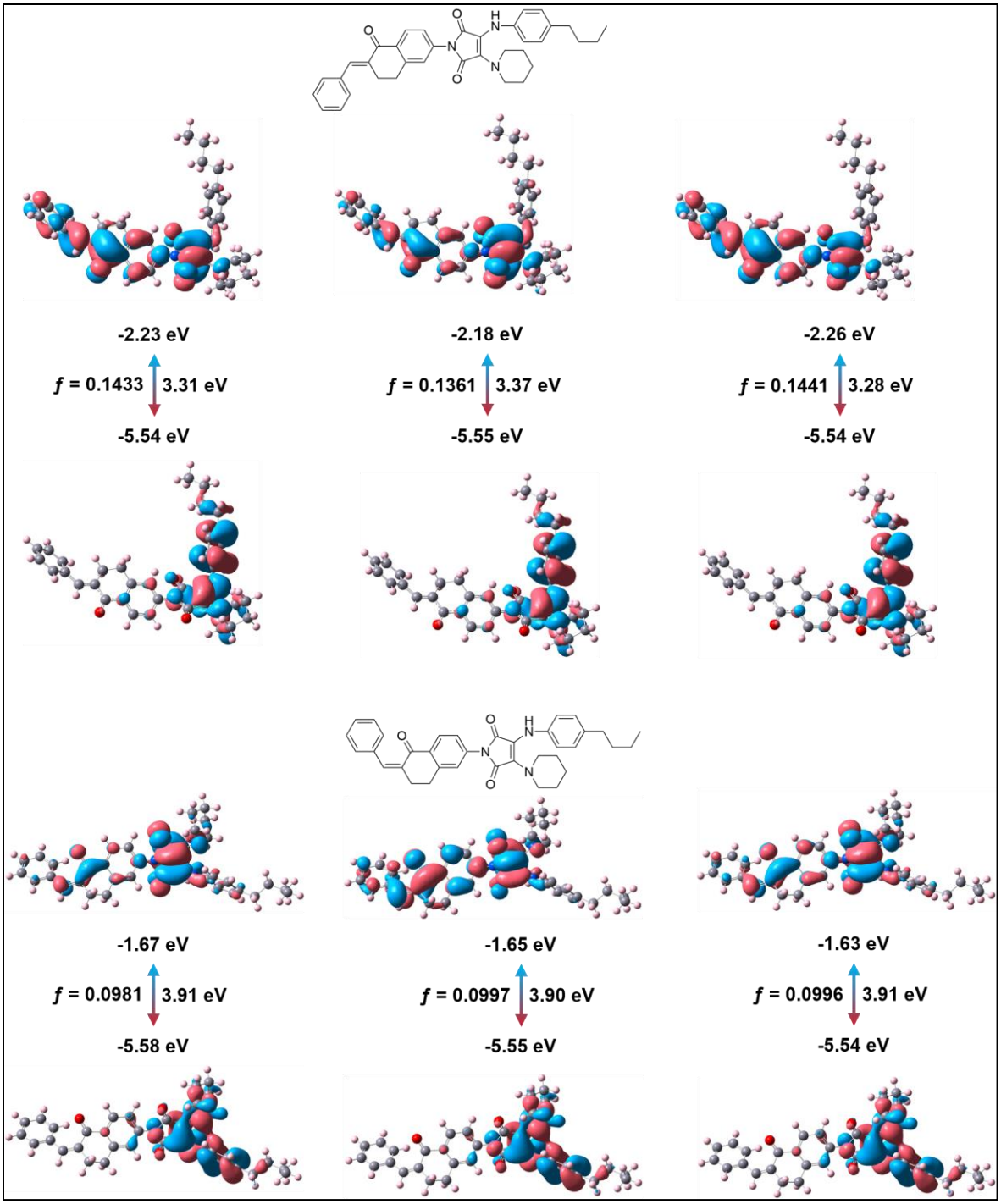


Figure 46 Frontier molecular orbitals and oscillator strength ($f$) in different solvents (from left to right is $CHCl_3$, dioxane, THF).

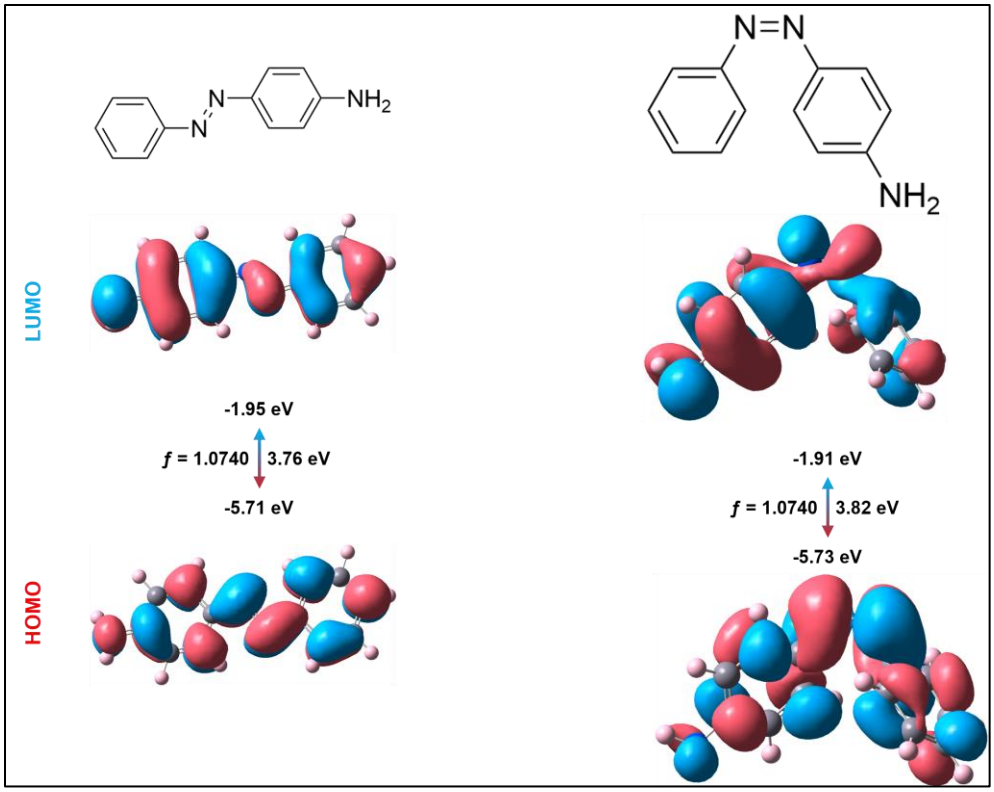


Figure 47 Frontier molecular orbitals and oscillator strength ($f$) in dioxane.

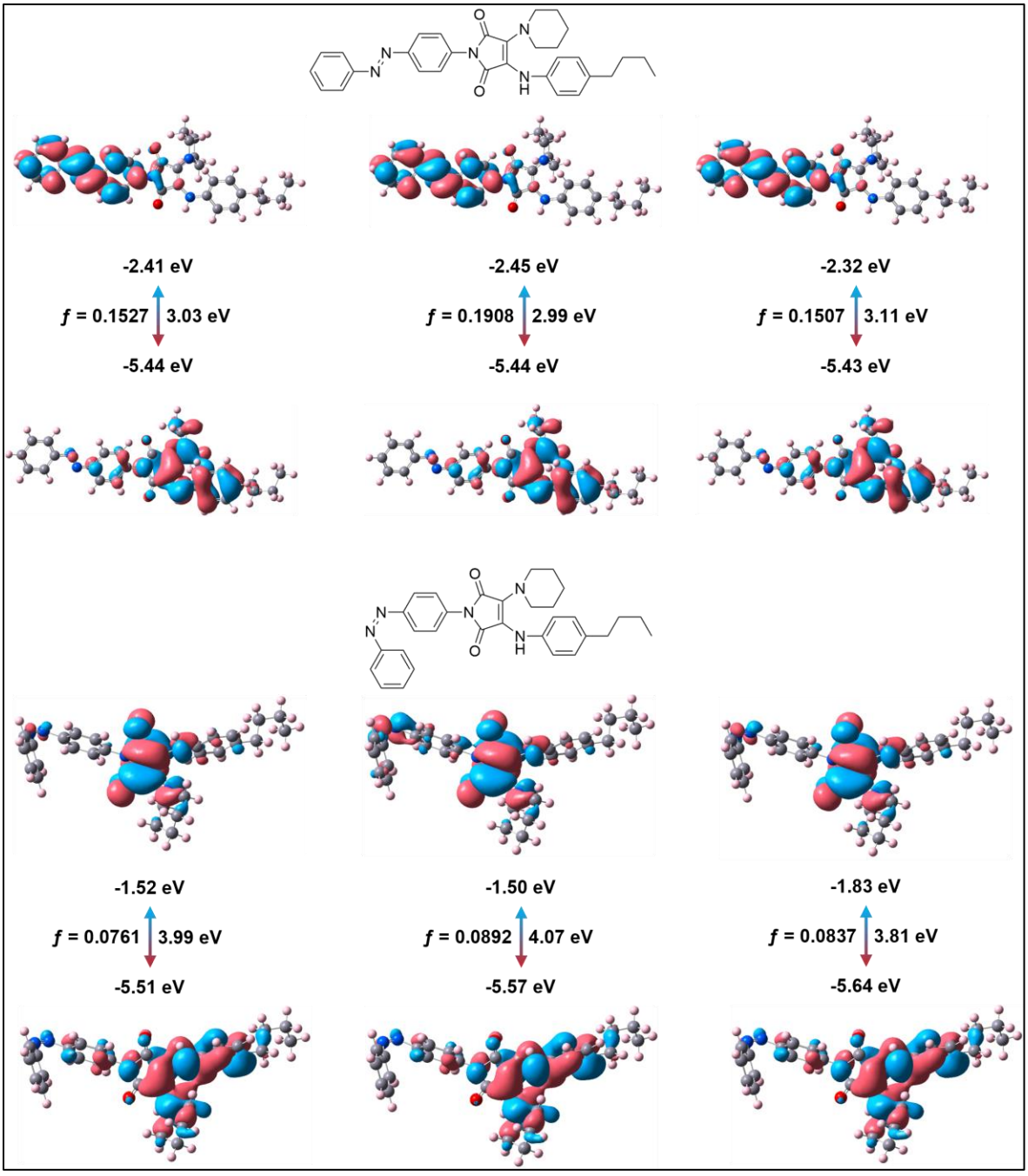


Figure 48 Frontier molecular orbitals and oscillator strength ($f$) in different solvents (from left to right is $CHCl_3$, dioxane, THF).

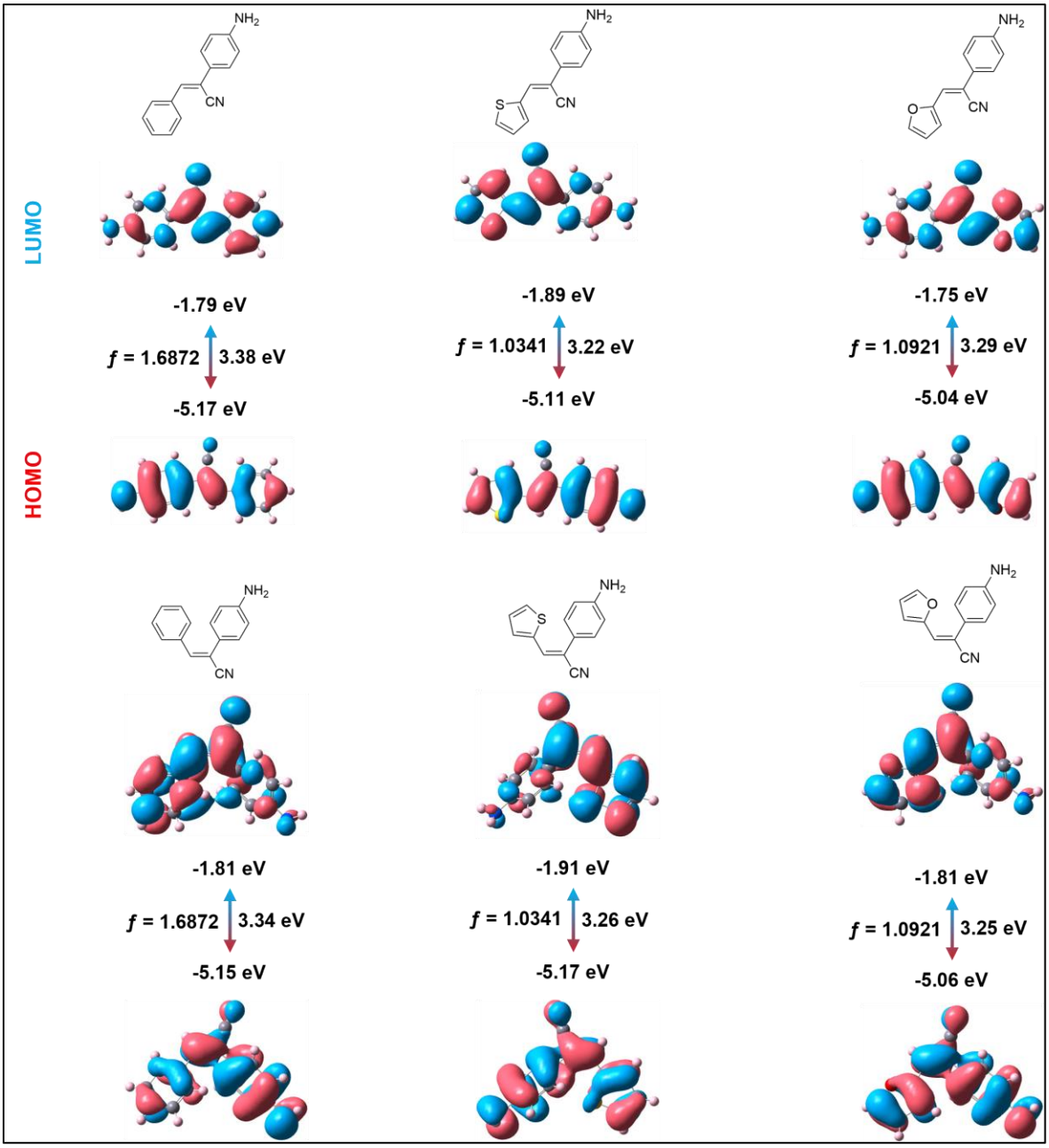


Figure 49 Frontier molecular orbitals and oscillator strength ($f$) in dioxane.

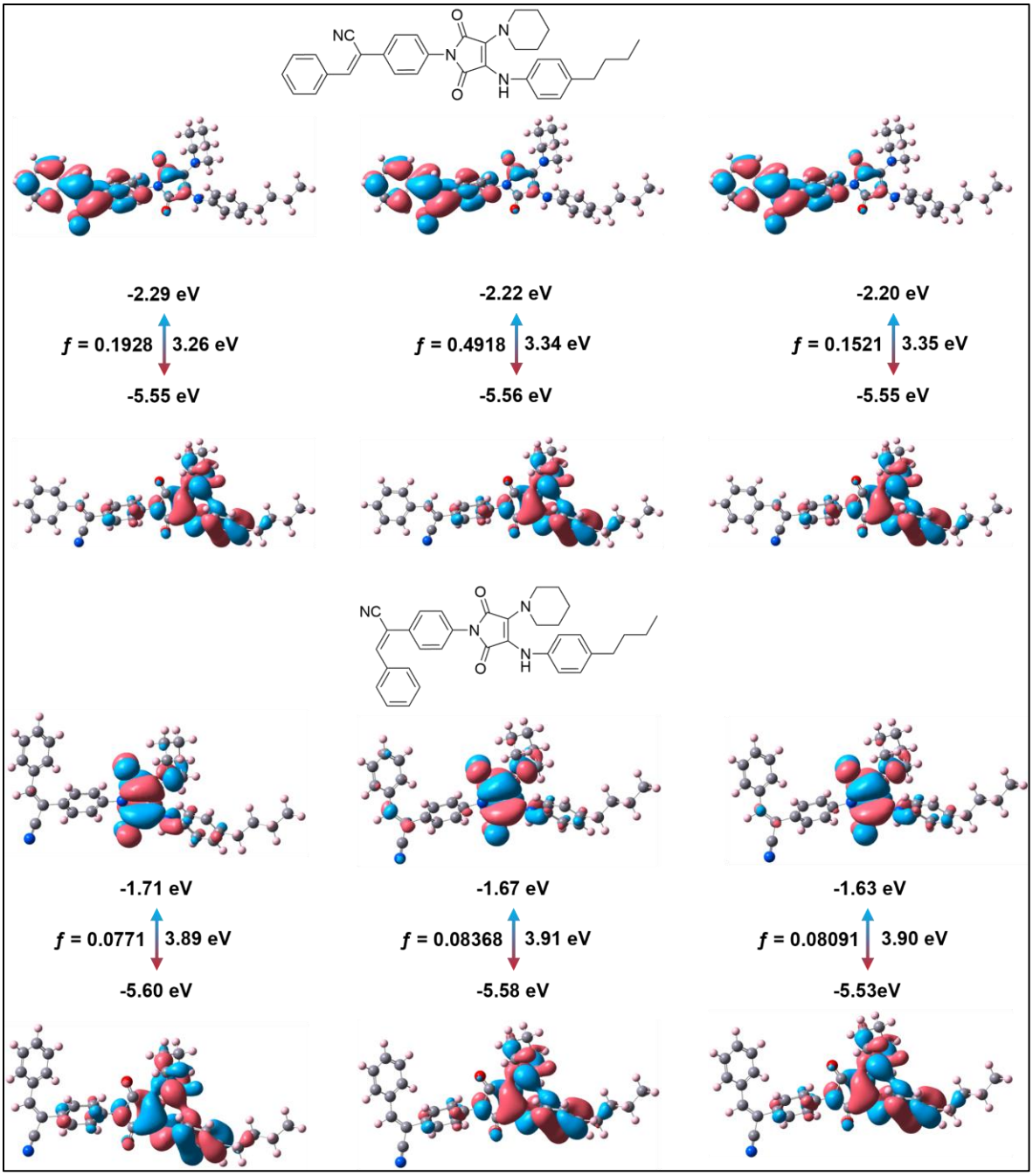


Figure 50 Frontier molecular orbitals and oscillator strength ($f$) in different solvents (from left to right is $CHCl_3$, dioxane, THF).

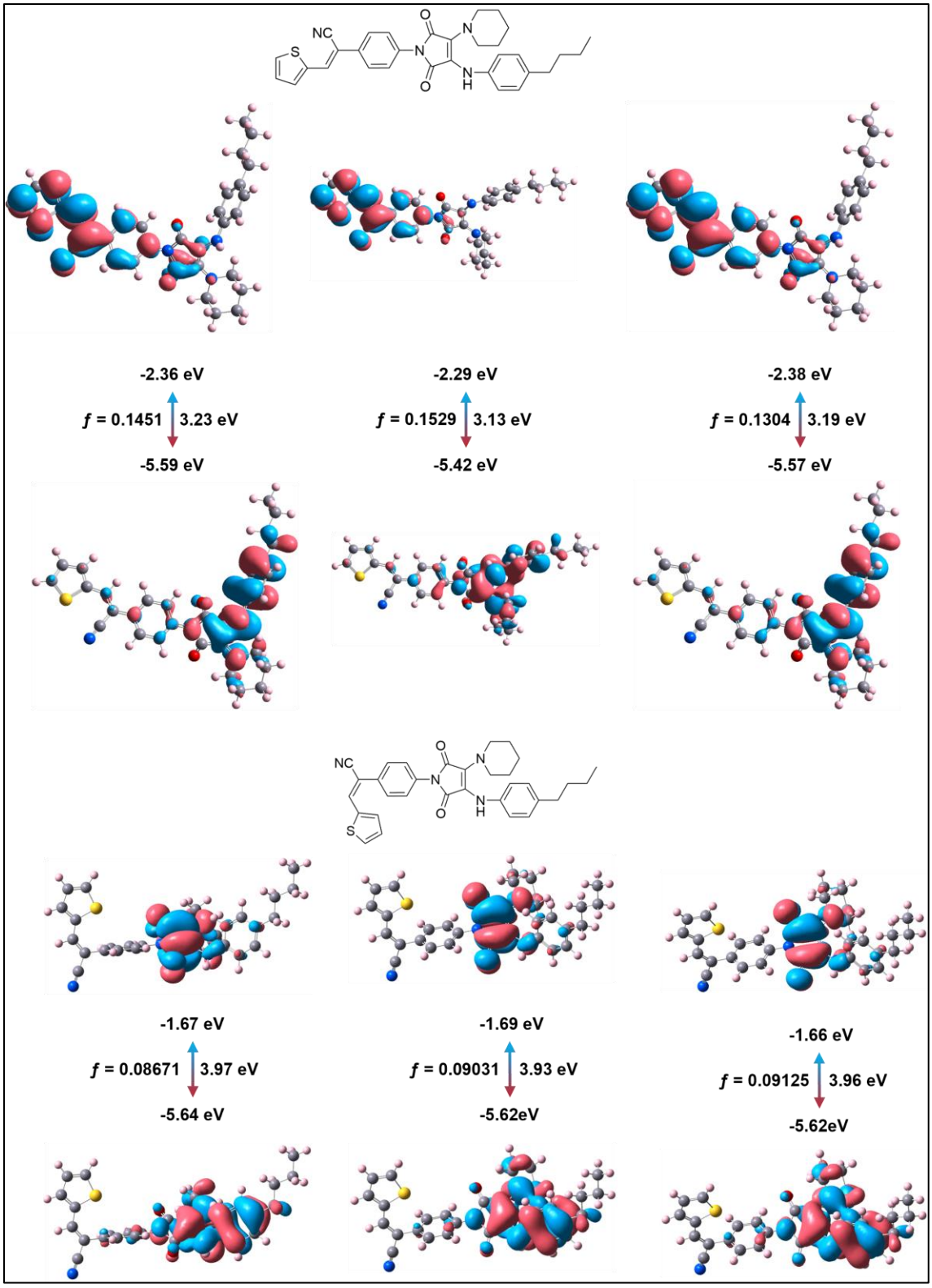


Figure 51 Frontier molecular orbitals and oscillator strength ($f$) in different solvents (from left to right is $CHCl_3$, dioxane, THF).

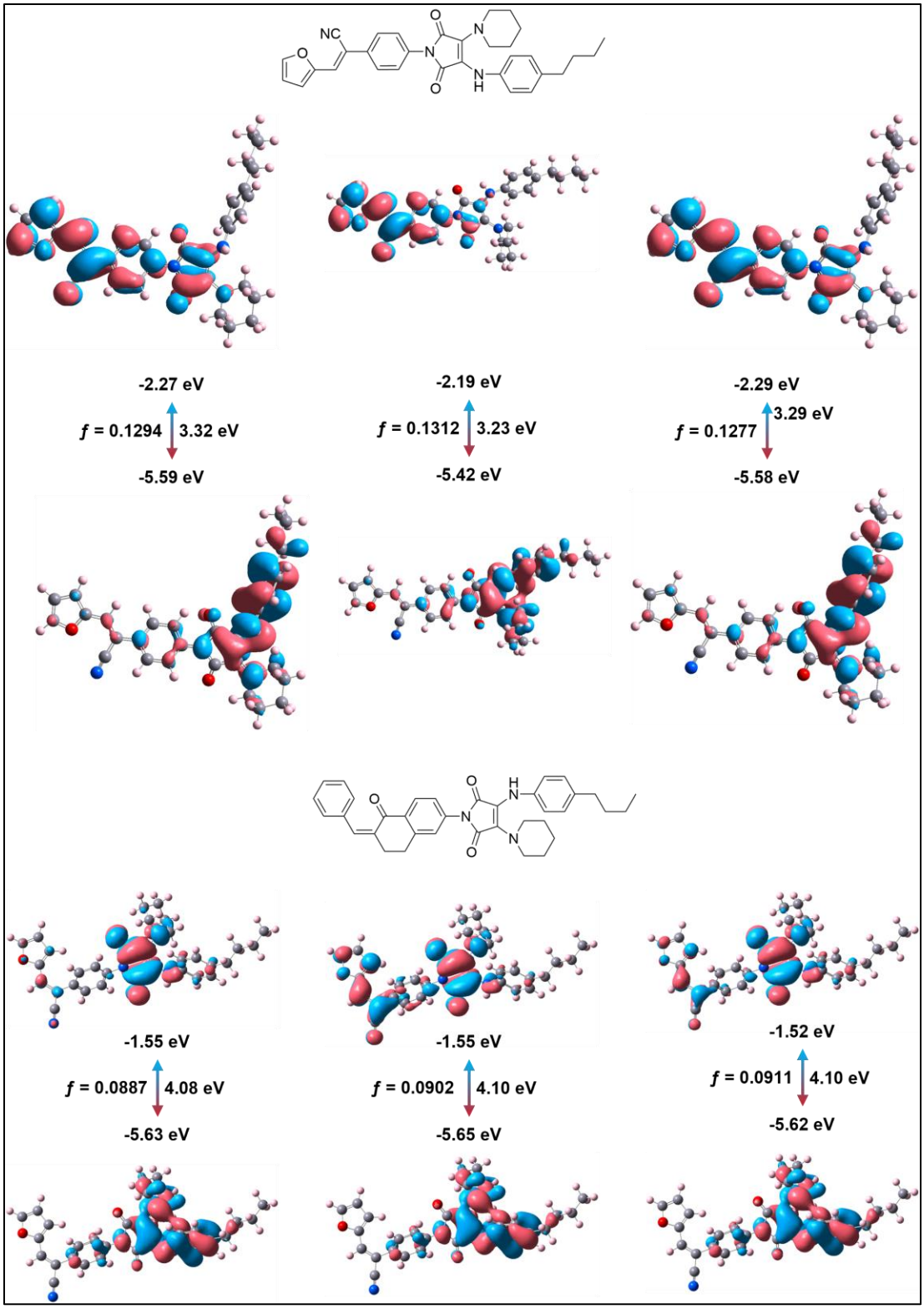


Figure 52 Frontier molecular orbitals and oscillator strength ($f$) in different solvents (from left to right is $CHCl_3$, dioxane, THF).

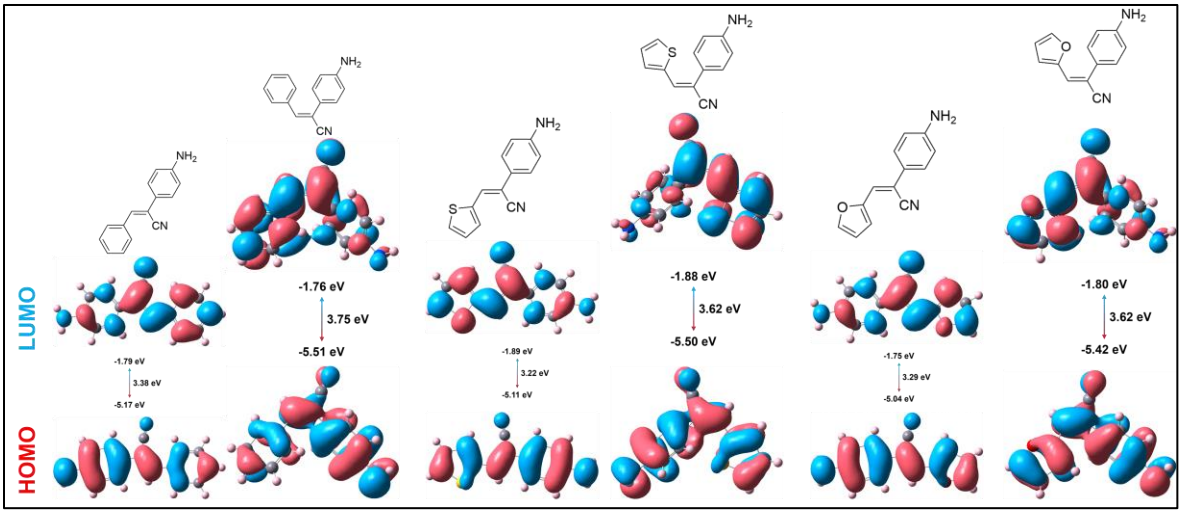


Figure 53 Frontier molecular orbitals in the vacuum state.

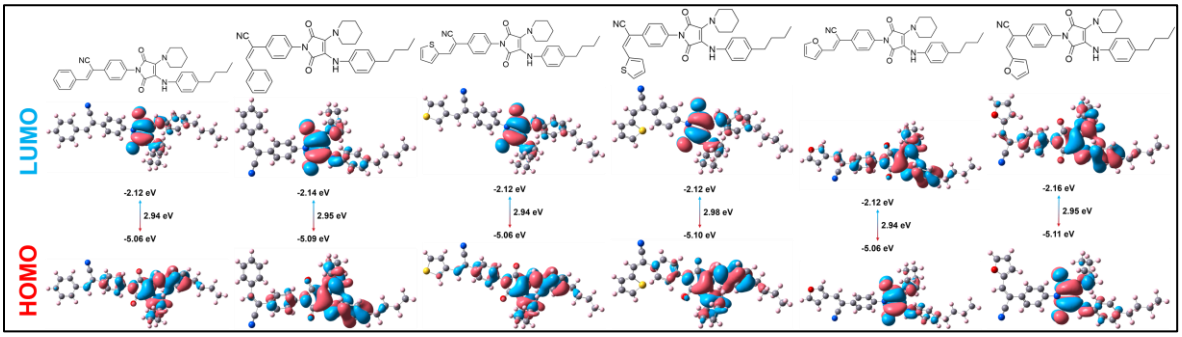


Figure 54 Frontier molecular orbitals in the vacuum state.

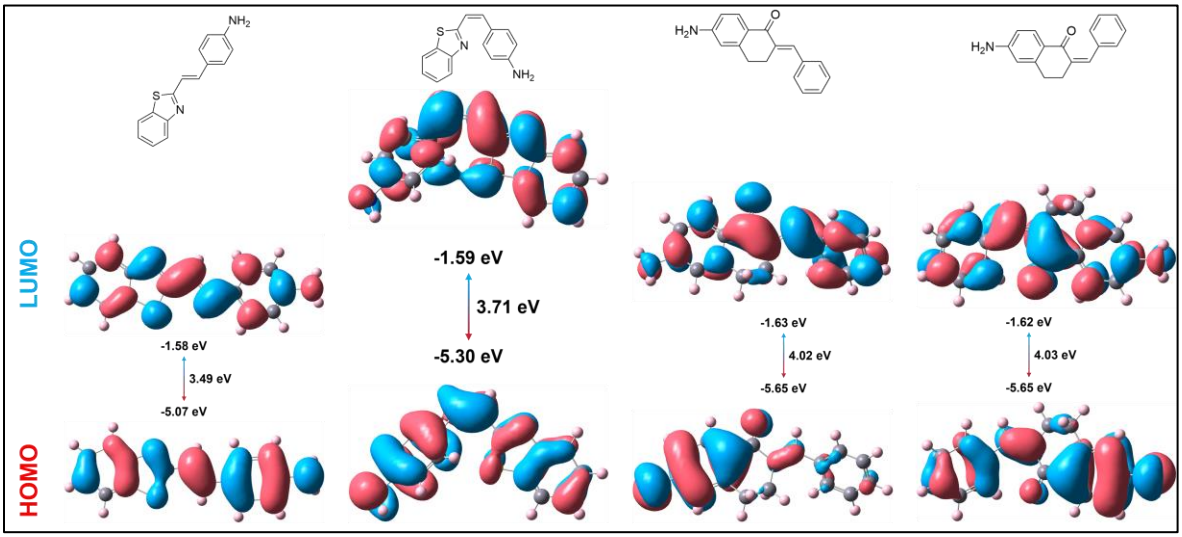


Figure 55 Frontier molecular orbitals in the vacuum state.

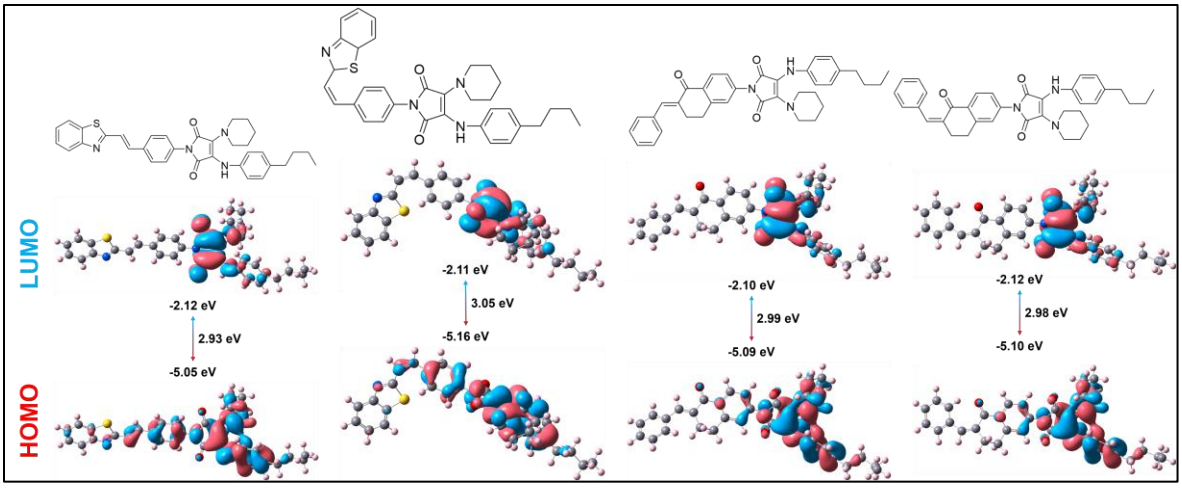


Figure 55 Frontier molecular orbitals in the vacuum state.

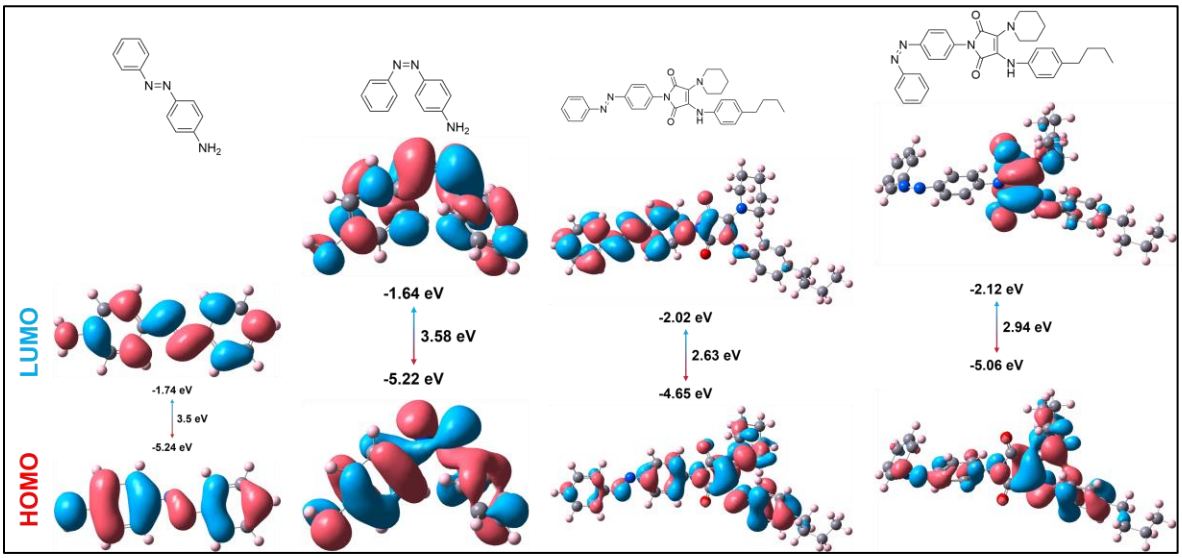


Figure 56 Frontier molecular orbitals in the vacuum state.

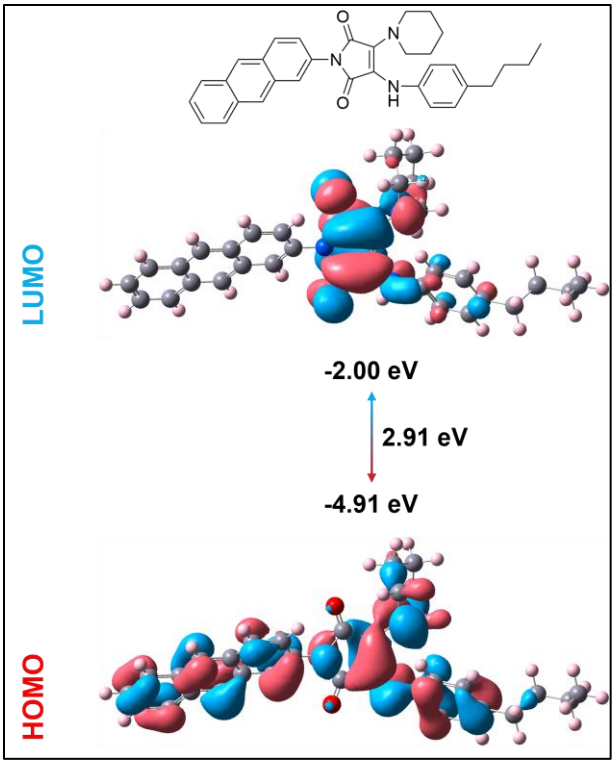


Figure 57 Frontier molecular orbitals in the vacuum state.

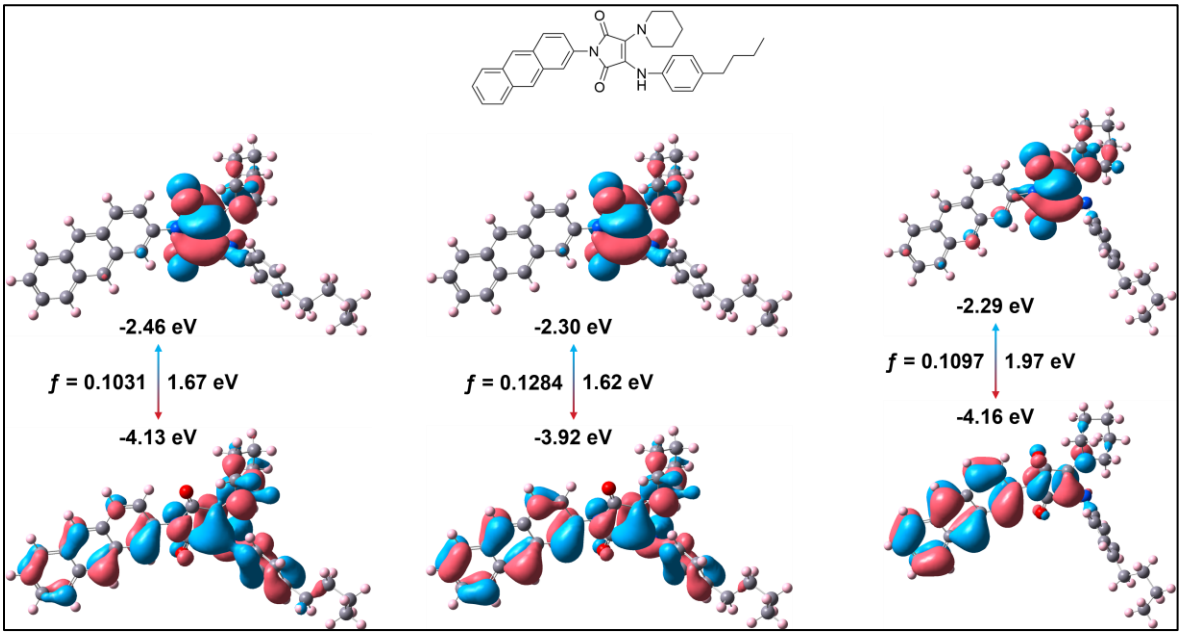


Figure 58 Frontier molecular orbitals and oscillator strength ($f$) in different solvents (from left to right is $CHCl_3$, dioxane, THF).

### 3.7.8 NMR spectroscopy during the different times of UV irradiation

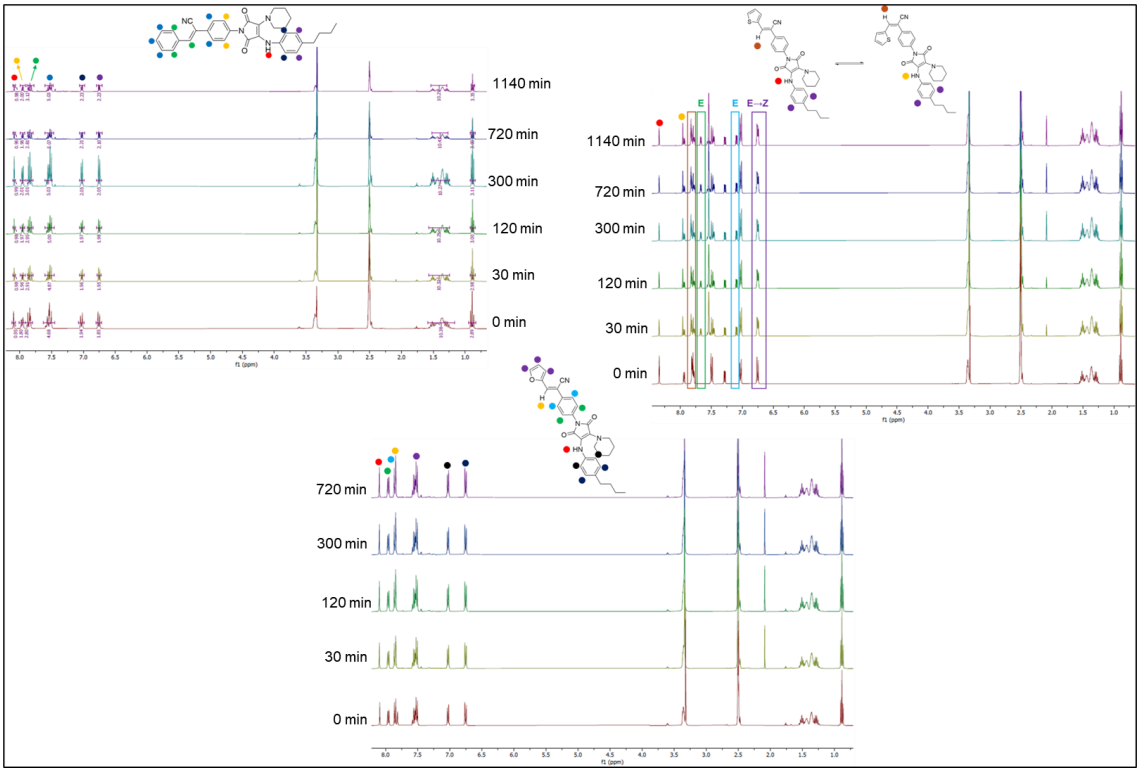


Figure 59 NMR spectroscopy of each molecule during the different times of UV irradiation (from bottom to top is 0 min, 30 min, 120 min, 300 min, 720 min, 1140 min).

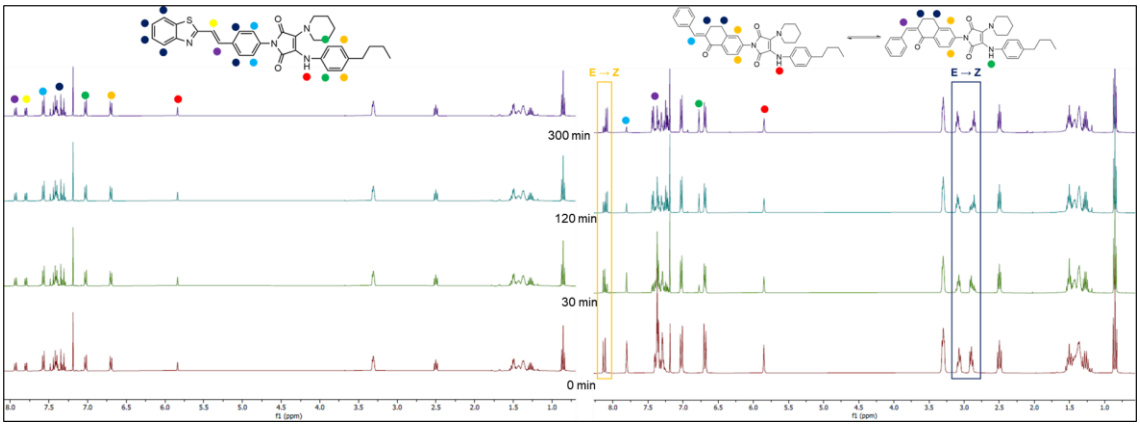


Figure 60 NMR spectroscopy of each molecule during the different times of UV irradiation (from bottom to top is 0 min, 30 min, 120 min, 300 min).

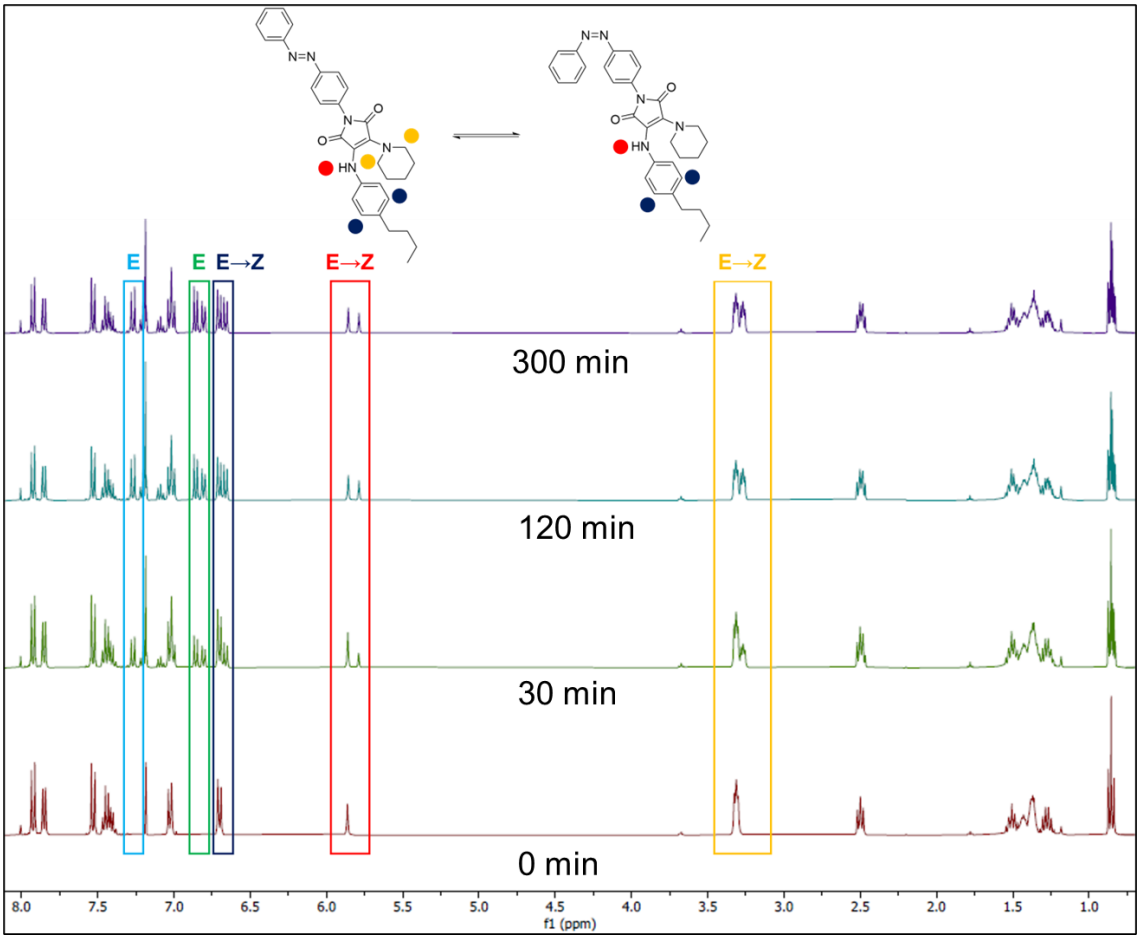


Figure 61 NMR spectroscopy of each molecule during the different times of UV irradiation (from bottom to top is 0 min, 30 min, 120 min, 300 min).

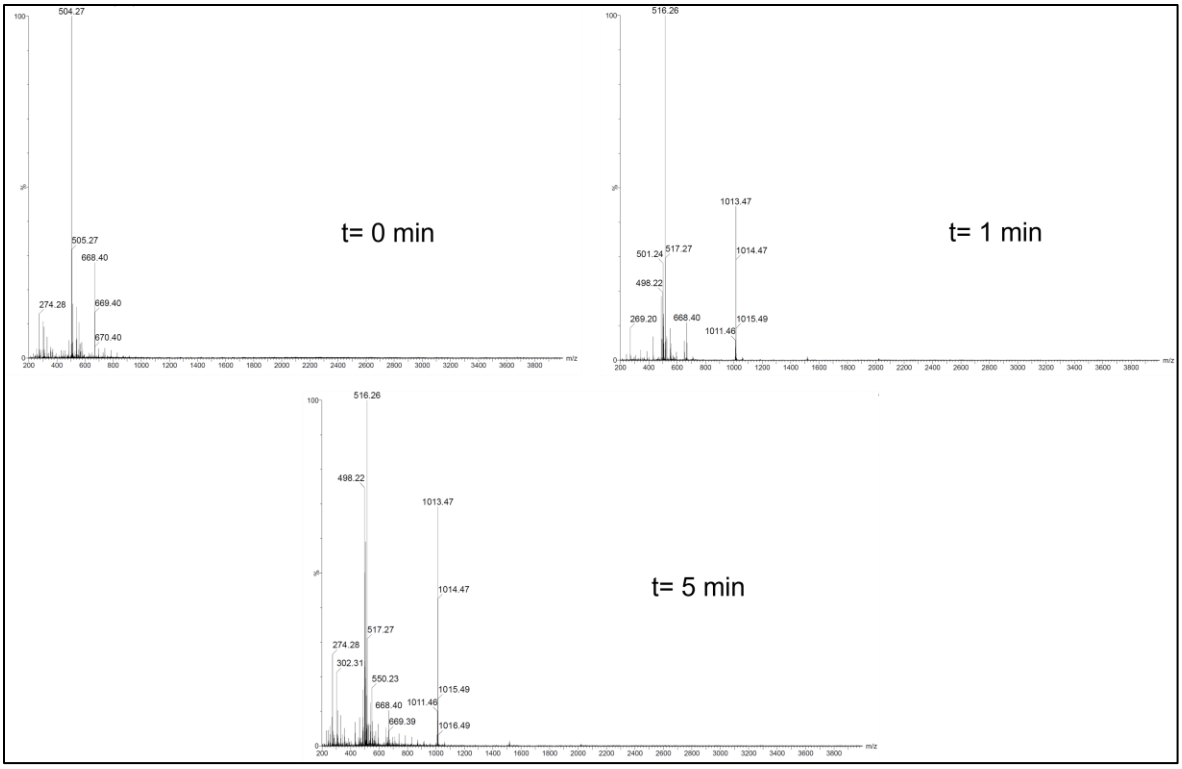


Figure 62 HRMS ($ES^+$) of Anthracene-M after the UV irradiation during different times.

## 3.7.9 Single-crystal data

**Ben-M**

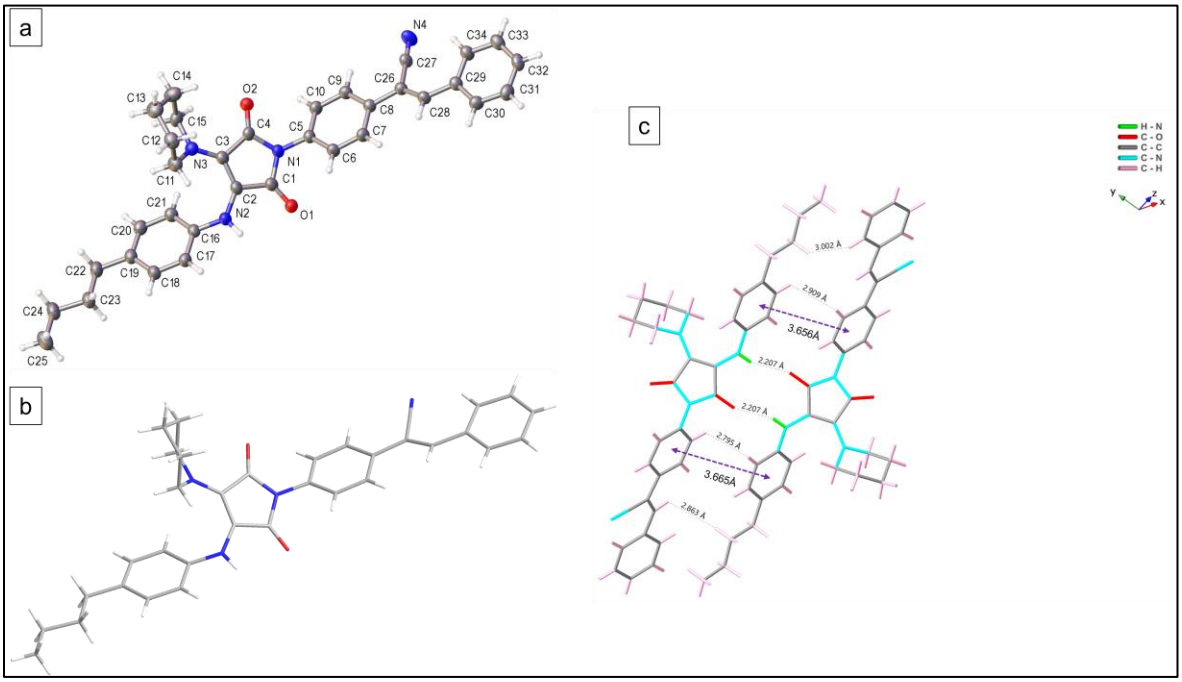


Figure 63 (a) single-crystal structure with atom number; (b) single-crystal structure of Ben-BP; (c) molecular packing pattern.

Crystal data and structure refinement for Ben-M.

| | |
|---|---|
| Identification code | Cyan-AIE |
| Empirical formula | C34H34N4O2 |
| Formula weight | 530.65 |
| Temperature/K | 149.99(10) |
| Crystal system | triclinic |
| Space group | P-1 |
| a/Å | 6.6758(2) |
| b/Å | 14.4265(6) |
| c/Å | 15.3740(5) |

α/° 108.946(4)

β/° 92.796(3)

γ/° 100.070(3)

Volume/Å3 1369.97(9)

Z 2

ρcalcg/cm3 1.286

μ/mm-1 0.639

F(000) 564.0

Crystal size/mm3 0.254 × 0.057 × 0.036

Radiation Cu Kα (λ = 1.54184)

2Θ range for data collection/° 6.118 to 157.258

Index ranges -8 ⩽ h ⩽ 7, -17 ⩽ k ⩽ 18, -17 ⩽ l ⩽ 19

Reflections collected 12777

Independent reflections 5234 [Rint = 0.0438, Rsigma = 0.0421]

Data/restraints/parameters 5234/0/366

Goodness-of-fit on F2 1.075

Final R indexes [I>=2σ (I)] R1 = 0.0627, wR2 = 0.1811

Final R indexes [all data] R1 = 0.0732, wR2 = 0.1913

Largest diff. peak/hole / e Å-3 0.34/-0.24

**Then-M**

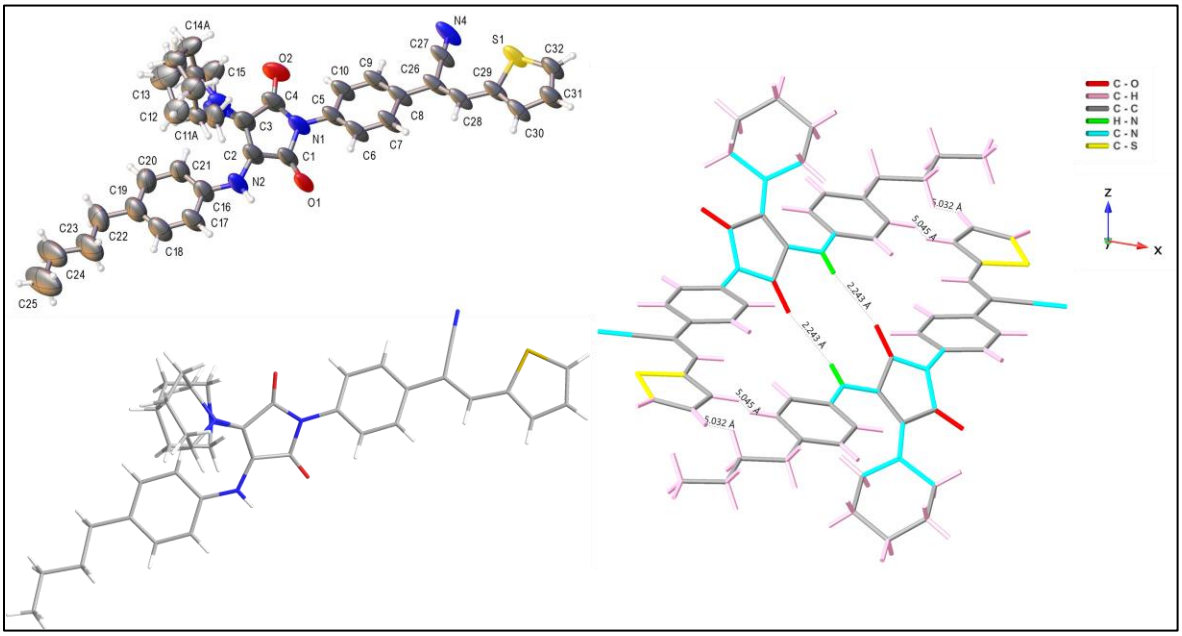


Figure 64 (a) single-crystal structure with atom number; (b) single-crystal structure of Then-BP; (c) molecular packing pattern.

Crystal data and structure refinement for Then-M.

| | |
|---|---|
| Identification code | SF |
| Empirical formula | C32H32N4O2S |
| Formula weight | 536.67 |
| Temperature/K | 99.98(11) |
| Crystal system | triclinic |
| Space group | P-1 |
| a/Å | 6.6456(2) |
| b/Å | 14.3016(6) |
| c/Å | 14.6895(7) |
| α/° | 102.809(4) |

β/° 98.158(3)

γ/° 94.038(3)

Volume/Å3 1340.08(10)

Z 2

ρcalcg/cm3 1.330

μ/mm-1 1.368

F(000) 568.0

Crystal size/mm3 0.25 × 0.1 × 0.05

Radiation Cu Kα (λ = 1.54184)

2Θ range for data collection/° 6.252 to 157.794

Index ranges -5 ⩽ h ⩽ 8, -18 ⩽ k ⩽ 18, -17 ⩽ l ⩽ 17

Reflections collected 16154

Independent reflections 5255 [Rint = 0.0348, Rsigma = 0.0355]

Data/restraints/parameters 5255/191/411

Goodness-of-fit on F2 1.062

Final R indexes [I>=2σ (I)] R1 = 0.0820, wR2 = 0.2198

Final R indexes [all data] R1 = 0.1106, wR2 = 0.2457

Largest diff. peak/hole / e Å-3 0.29/-0.50

**α-Tetralone-M**

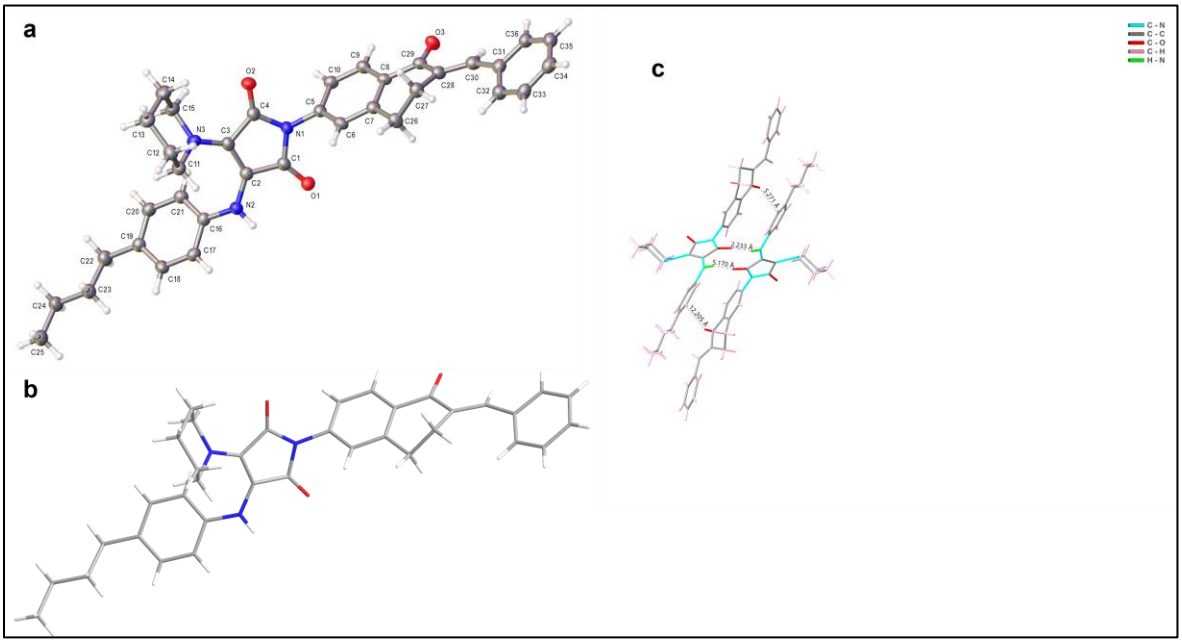


Figure 65 (a) single-crystal structure with atom number; (b) single-crystal structure of α-Tetralone-M; (c) molecular packing pattern.

Crystal data and structure refinement for α-Tetralone-M.

| | |
|---|---|
| Identification code | dd02 |
| Empirical formula | C36H37N3O3 |
| Formula weight | 559.68 |
| Temperature/K | 99.99(10) |
| Crystal system | monoclinic |
| Space group | P21 |
| a/Å | 15.0584(5) |
| b/Å | 6.4620(2) |
| c/Å | 15.6802(6) |
| α/° | 90 |

β/° 111.368(4)

γ/° 90

Volume/Å3 1420.91(9)

Z 2

ρcalcg/cm3 1.308

μ/mm-1 0.660

F(000) 596.0

Crystal size/mm3 0.153 × 0.05 × 0.034

Radiation Cu Kα (λ = 1.54184)

2Θ range for data collection/° 6.052 to 157.908

Index ranges -19 ⩽ h ⩽ 17, -5 ⩽ k ⩽ 8, -19 ⩽ l ⩽ 19

Reflections collected 10727

Independent reflections 4651 [Rint = 0.0582, Rsigma = 0.0751]

Data/restraints/parameters 4651/2/384

Goodness-of-fit on F2 1.064

Final R indexes [I>=2σ (I)] R1 = 0.0488, wR2 = 0.1210

Final R indexes [all data] R1 = 0.0582, wR2 = 0.1278

Largest diff. peak/hole / e Å-3 0.23/-0.30

Flack parameter 0.4(3)

**Azo-M**

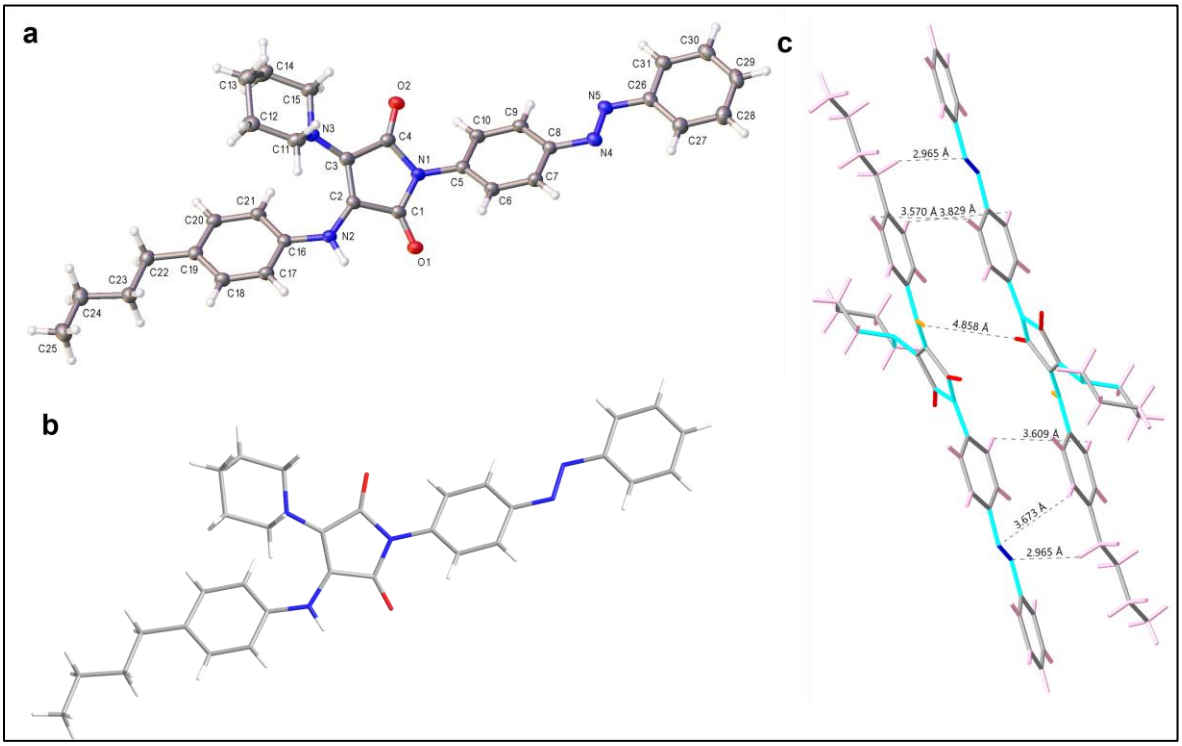


Figure 66 (a) single-crystal structure with atom number; (b) single-crystal structure of azo-M; (c) molecular packing pattern.

Crystal data and structure refinement for azo-M.

| | |
|---|---|
| Identification code | azo |
| Empirical formula | C31H33N5O2 |
| Formula weight | 507.62 |
| Temperature/K | 100.00(10) |
| Crystal system | triclinic |
| Space group | P-1 |
| a/Å | 6.3373(3) |
| b/Å | 14.3358(8) |
| c/Å | 14.8146(7) |

α/° 99.271(4)

β/° 96.490(4)

γ/° 100.572(5)

Volume/Å3 1291.60(12)

Z 2

ρcalcg/cm3 1.305

μ/mm-1 0.663

F(000) 540.0

Crystal size/mm3 0.29 × 0.067 × 0.033

Radiation Cu Kα (λ = 1.54184)

2Θ range for data collection/° 7.976 to 144.244

Index ranges -7 ⩽ h ⩽ 7, -17 ⩽ k ⩽ 17, -18 ⩽ l ⩽ 18

Reflections collected 25406

Independent reflections 5076 [Rint = 0.0657, Rsigma = 0.0467]

Data/restraints/parameters 5076/0/348

Goodness-of-fit on F2 1.048

Final R indexes [I>=2σ (I)] R1 = 0.0506, wR2 = 0.1251

Final R indexes [all data] R1 = 0.0730, wR2 = 0.1435

Largest diff. peak/hole / e Å-3 0.32/-0.27

**Anthracene-M**

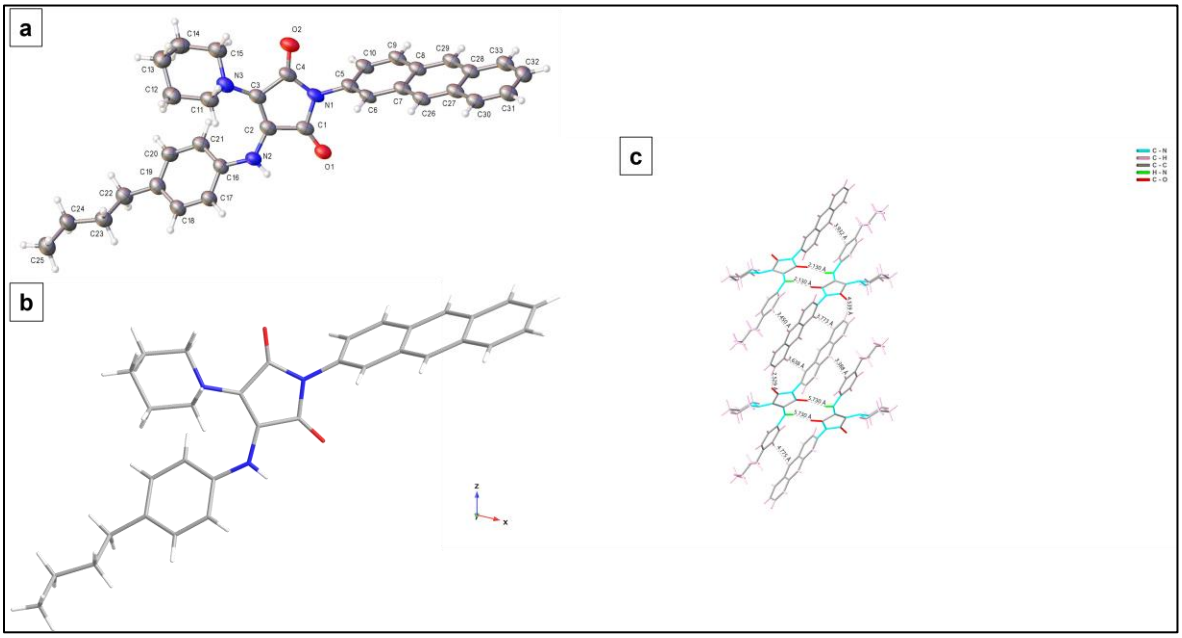


Figure 67 (a) single-crystal structure with atom number; (b) single-crystal structure of Anthracene -M; (c) molecular packing pattern.

Crystal data and structure refinement for Anthracene -M.

| | |
|---|---|
| Identification code | 2+2 |
| Empirical formula | C33H33N3O2 |
| Formula weight | 503.62 |
| Temperature/K | 100.00(11) |
| Crystal system | monoclinic |
| Space group | P21/c |
| a/Å | 15.7794(13) |
| b/Å | 6.5040(4) |
| c/Å | 25.915(2) |
| α/° | 90 |

β/° 102.883(8)

γ/° 90

Volume/Å3 2592.7(3)

Z 4

ρcalcg/cm3 1.290

μ/mm-1 0.635

F(000) 1072.0

Crystal size/mm3 0.303 × 0.289 × 0.033

Radiation Cu Kα (λ = 1.54184)

2Θ range for data collection/° 8.006 to 153.978

Index ranges -19 ⩽ h ⩽ 19, -3 ⩽ k ⩽ 8, -31 ⩽ l ⩽ 32

Reflections collected 10919

Independent reflections 5229 [Rint = 0.0535, Rsigma = 0.0709]

Data/restraints/parameters 5229/0/348

Goodness-of-fit on F2 1.020

Final R indexes [I>=2σ (I)] R1 = 0.0879, wR2 = 0.2297

Final R indexes [all data] R1 = 0.1252, wR2 = 0.2644

Largest diff. peak/hole / e Å-3 0.41/-0.30

# Chapter 4 Construction of room-temperature phosphorescence in maleimide-based derivatives via host-guest doping

## 4.1 Design philosophy of this work

When a phosphorescent chromophore with room-temperature phosphorescence (RTP) absorbs light energy, electrons first transition to the excited singlet state ($S_1$). Subsequently, some electrons undergo intersystem crossing (ISC) from the singlet state to the triplet state ($T_1$). In the triplet state, the electron spin orientation is opposite to that of the singlet state, making the transition from the triplet state back to the ground state a "forbidden transition". This results in a longer phosphorescence emission time. Due to this spin-forbidden transition characteristic, electrons remain in the triplet state for an extended period before returning to the ground state, releasing energy in the form of light as phosphorescence, which delays the emission process.[112,207] The primary approaches for achieving room-temperature phosphorescence involve molecular engineering and crystal engineering. In molecular engineering, RTP is mainly realized through the incorporation of halogen and heteroatoms. Halogen atoms (such as iodine, bromine, and chlorine) have high atomic numbers, significantly enhancing spin-orbit coupling (SOC) within the molecule. This coupling effect increases the transition probability between the $T_1$ and the $S_0$, thereby enhancing non-radiative transitions from the triplet state and promoting phosphorescence. Additionally, the incorporation of halogen atoms increases the molecular rigidity, reducing intramolecular rotations and vibrations, which helps to suppress non-radiative relaxation processes. This rigidity contributes to the stability of the triplet state, further enhancing the phosphorescence lifetime and efficiency.[116,208,209] On the other hand, heteroatoms (such as nitrogen, oxygen, and sulfur) can modulate the electron density distribution of the molecule, affecting its excited-state properties. For instance, the lone pairs of nitrogen atoms can influence the HOMO-LUMO energy gap of the molecule, adjusting the position and energy of the triplet state, thereby affecting RTP efficiency. Moreover, heteroatoms often contain lone pairs that can form hydrogen bonds or other non-covalent interactions with other molecules, enhancing molecular packing stability and reducing the likelihood of triplet state quenching by the external environment.[112,210,211] Furthermore, the simultaneous incorporation of both heteroatoms and halogen atoms into the molecule can

create a synergistic effect, further enhancing spin-orbit coupling within the molecule. This cooperative interaction significantly increases the transition probability between the triplet and singlet states, thereby boosting phosphorescence emission.[212,213] Crystal engineering represents another effective strategy for achieving RTP. The realization of RTP through host-guest doping primarily relies on the precise interactions between the host and guest materials, enhancing the stability of the excited state and phosphorescence efficiency. Host materials typically consist of inorganic or organic compounds, such as sodium chloride crystal or triphenylamine with high rigidity and low vibrational energy, while the guest molecules are phosphorescent chromophores. Through energy level matching, host-guest doping facilitates the transfer of the excited state from the guest molecule to the host-guest system, forming the excited state necessary for phosphorescence emission. The rigid structure of the host material effectively restricts the rotation and vibration of guest molecules, significantly reducing the probabilities of non-radiative transitions such as internal conversion and intersystem crossing, thereby stabilizing the guest molecules and minimizing energy loss from the excited state, ultimately enhancing phosphorescence efficiency. Moreover, the introduction of heavy atoms (such as iodine and bromine) within the host-guest system can increase the intersystem crossing rate, accelerating the transfer of excited electrons to the triplet state and markedly boosting RTP emission efficiency. Additionally, the rigidity of the host material and its encapsulation of the guest molecules effectively shield the excited state from quenching agents such as oxygen, extending the triplet state lifetime and making phosphorescence more stable and persistent at room temperature. Molecular interactions such as hydrogen bonding, π-π stacking, and van der Waals forces further stabilize the conformation of the excited state, reduce molecular vibration and rotation, and effectively block non-radiative transition pathways, ultimately enhancing phosphorescence intensity. In summary, the host-guest doping strategy, through the synergistic effects of multiple mechanisms, achieves efficient and stable phosphorescence emission at room temperature.[120,214,215] RTP materials have significant applications in various fields, including biomedical imaging, anti-counterfeiting and security labelling, optoelectronic devices, information storage and encryption, catalysis, and sensing.[216-219]

Based on the above analysis, incorporating halogen or heteroatoms into molecules and employing host-guest doping are excellent strategies to achieve RTP, and maleimide molecules are promising candidates. Maleimide derivatives contain oxygen and nitrogen heteroatoms, which can facilitate RTP. However, current methods for achieving RTP in maleimide compounds mainly rely on crystallization-driven room-temperature phosphorescence, where

RTP is realized only in the crystalline state. For example, Tianwen Zhu et al. reported near-infrared, long-lived RTP in crystalline halogenated maleimide rings.[220] However, the difficulty in preparing crystalline states significantly hinders their practical application. To develop RTP-capable molecules, we propose the following design strategy:

1. **Molecular Engineering**: We design halogen-containing diamine-substituted maleimide derivatives based on the maleimide scaffold, ensuring the presence of nitrogen, oxygen, and halogen atoms along with intermolecular weak interactions. This aims to maximize the probability of intersystem crossing to the triplet state.

2. **Crystal Engineering**: Host-guest doping is an effective method for RTP realization. We propose using benzophenone as the host molecule, a known effective host, and synthesize a series of maleimide derivatives containing benzophenone groups to enhance the compatibility between host and guest molecules, ensuring maximum integration of guest molecules into the host crystal lattice.[221-223] Additionally, we attempt to use N-phenylmaleimide as the host and halogenated phenyl-substituted maleimide derivatives as the guest for the first time. By leveraging the structural similarity of the molecules, the guest molecules are embedded into the host based on the principle of like-dissolves-like.

# 4.2 Synthesis

## 4.2.1 Synthesis of Benzophenone-based maleimide derivatives

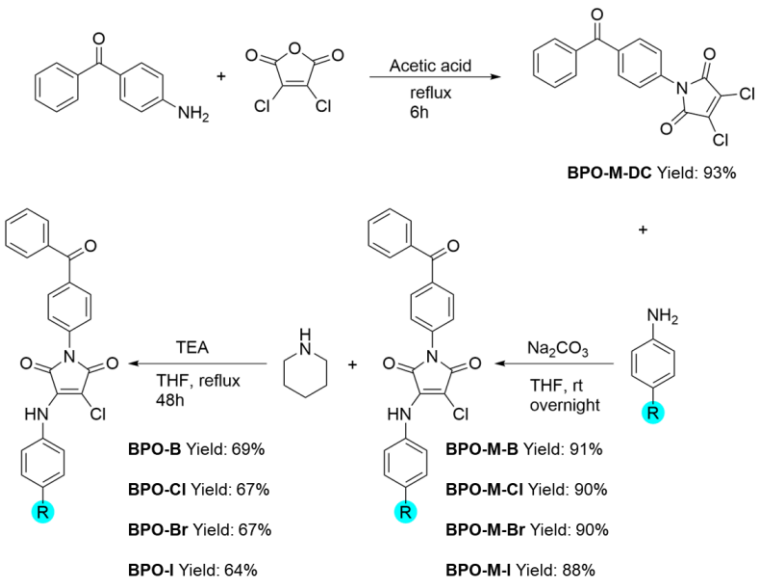


Scheme 4.1 Synthesis of Benzophenone-based maleimide derivatives (R = Cl, Br, I)

As discussed, our molecular design strategy encompasses two components. First, we synthesized a benzophenone-based maleimide derivative by attaching benzophenone to the nitrogen atom of maleimide. This design aims for the derivative to mimic the crystalline form of benzophenone, allowing it to function effectively as a guest molecule. Secondly, we use halogenated aniline to boost the probability of intersystem crossing. The inclusion of halogen atoms in the structure is intended to facilitate this process (Figure 4.1). All the obtained compounds were characterized by $^{1}H$ NMR, $^{13}C$ NMR, high-resolution mass spectrometry, and single-crystal X-ray diffraction (supporting information).

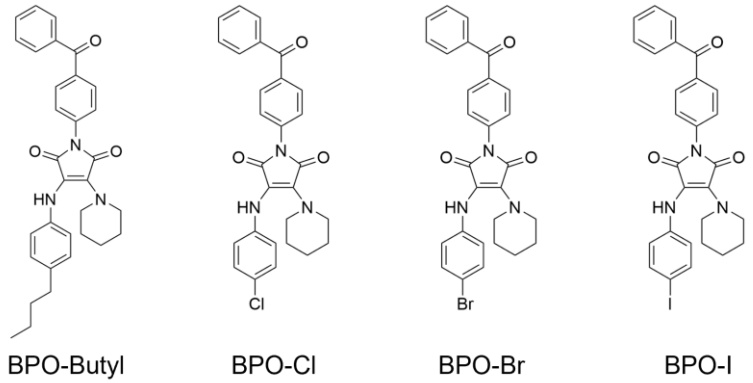


Figure 4.1 Each chemical structure synthesized in this Chapter.

## 4.2.2 Synthesis of Halo-phenyl-based maleimide derivatives

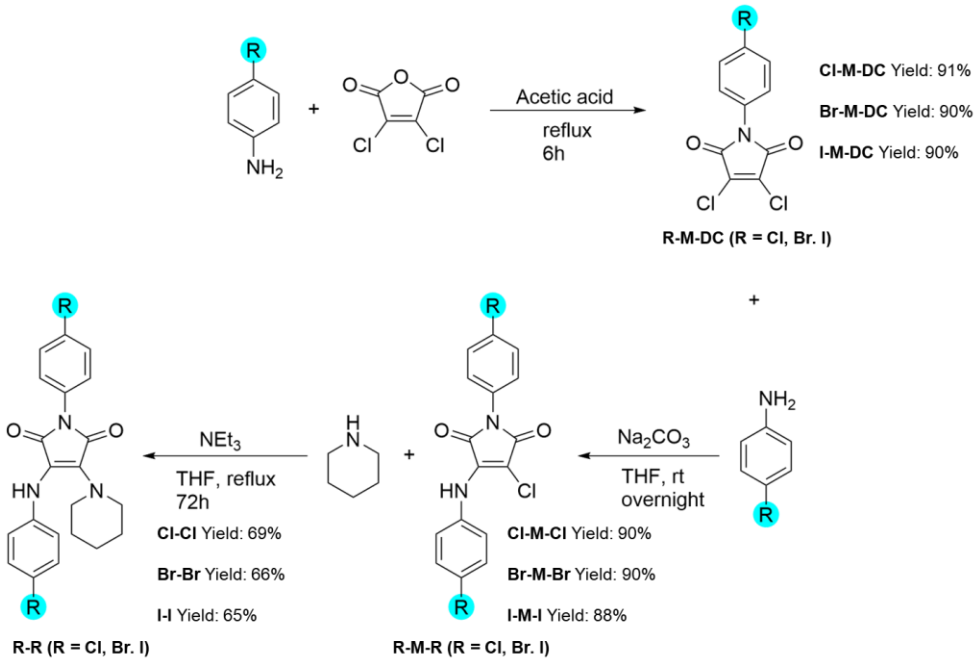


Scheme 4.2 Synthesis of Halo-phenyl maleimide derivatives (R = Cl, Br, I)

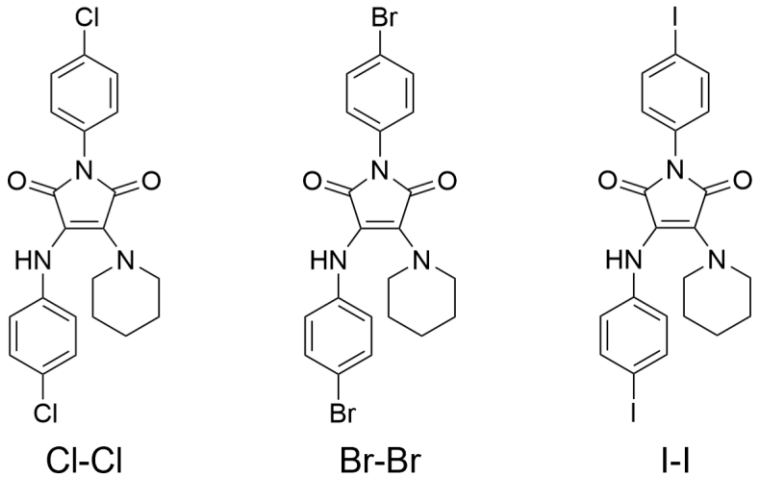


Figure 4.2 Each chemical structure synthesized in this Chapter.

In this synthetic design, N-Phenylmaleimide is utilized as the host molecule, with halogenated aniline attached to the nitrogen atom and the double bond of maleimide. This approach is guided by two main considerations. Firstly, halogens are introduced to increase the likelihood of intersystem crossing. Secondly, N-Phenylmaleimide was chosen due to its structural similarity to the compound being designed. Additionally, N-Phenylmaleimide has a melting point of 80°C and crystallizes easily, which simplifies the doping process (Fig 4.2). All the obtained compounds were characterized by $^{1}H$ NMR, $^{13}C$ NMR, high-resolution mass spectrometry, and single-crystal X-ray diffraction (supporting information).

## 4.3 Results and Discussion

### 4.3.1 photophysical properties

#### Investigation of UV-vis absorption and fluorescent spectra

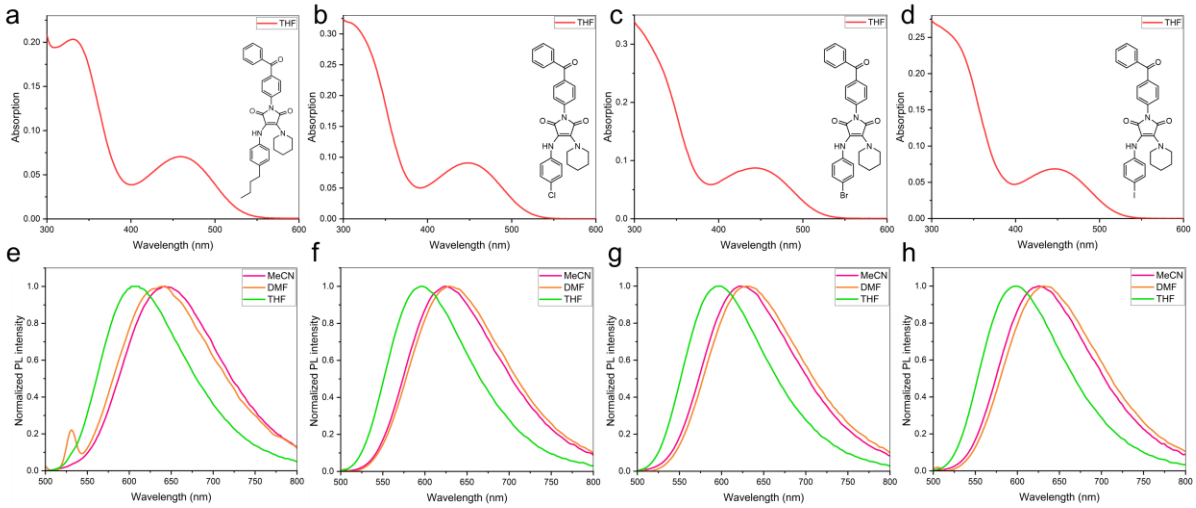


Figure 4.3 (a, e) UV-vis and FL spectra of BPO-Butyl; (b, f) UV-vis and FL spectra of BPO-Cl; (c, g) UV-vis and FL spectra of BPO-Br; (d, h) UV-vis and FL spectra of BPO-I. The UV-vis spectra was measured in THF, 1 μg/ml, FL spectra was measured in THF, MeCN and DMF, 1 μg/ml, Ex = 450nm.

Table 4.1 The summary of the photophysical properties.

| Solvent | Compound | $\lambda_{abs}$ (nm) | $\lambda_{ex}$ (nm) | $\lambda_{em}$ (nm) | $\Delta\lambda$ ($\lambda_{em}$ - $\lambda_{ex}$) | Φ (%) |
|---|---|---|---|---|---|---|
| MeCN | BPO-Butyl | 287, 465 | 467 | 639 | 175 | 6.1 |
| | BPO-Cl | 290, 456 | 458 | 629 | 166 | 4.8 |
| | BPO-Br | 290, 453 | 455 | 631 | 167 | 2.8 |
| | BPO-I | 290, 456 | 457 | 631 | 168 | 1.4 |
| DMF | BPO-Butyl | 290, 461 | 464 | 642 | 175 | 0.7 |
| | BPO-Cl | 289, 445 | 446 | 624 | 183 | 0.5 |
| | BPO-Br | 290, 436 | 439 | 622 | 192 | 0.3 |
| | BPO-I | 290, 440 | 443 | 625 | 188 | 0.09 |
| THF | BPO-Butyl | 290, 459 | 461 | 606 | 145 | 17.8 |
| | BPO-Cl | 293, 451 | 452 | 596 | 144 | 12.1 |
| | BPO-Br | 293, 442 | 445 | 598 | 153 | 10.7 |
| | BPO-I | 294, 447 | 449 | 599 | 150 | 9.1 |

Figures 4.3 (a, b, c, d) show that all molecules exhibit two absorption peaks, located around 290 nm and 450 nm. The absorption peak near 290 nm is attributed to the π→π* transition resulting from the conjugation between the benzene ring and the maleimide ring, while the peak at 450 nm arises from the extended conjugation due to diamine substitution, which induces intramolecular charge transfer (ICT).[165,224] Additionally, Figures 4.3 (e, f, g, h) indicate that the emission wavelengths of all molecules exhibit solvent dependency, with the emission wavelengths red-shifting as solvent polarity increases. For example, the emission wavelength of BPO-Butyl in DMF is red-shifted by 36 nm compared to that in THF. This redshift is caused by the TICT effect, where increased solvent polarity enhances charge transfer interactions between the fluorophore and solvent molecules, lowering the excited-state energy level and leading to a red shift in the emission wavelength. Moreover, Table 4.1 shows that the quantum yield decreases as solvent polarity increases. For instance, the quantum yield of BPO-Butyl drops from 17.8% in THF to 0.7% in DMF. This decrease is also attributed to the TICT effect, which enhances non-radiative decay pathways.[142]

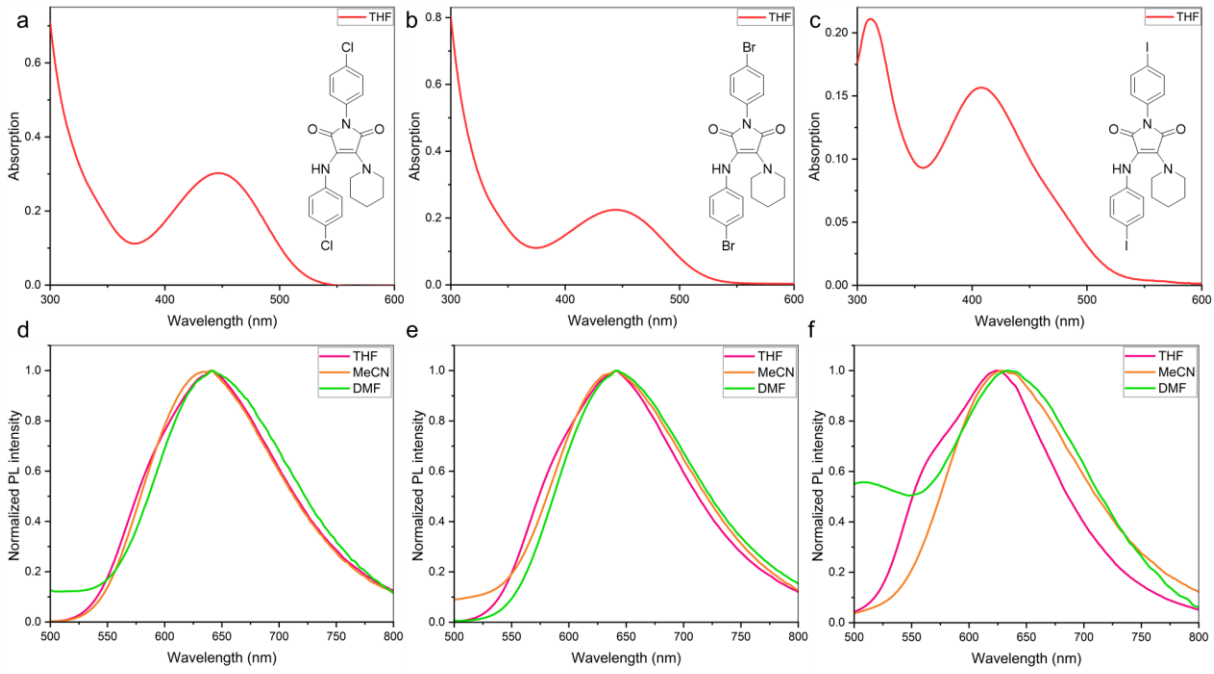


Figure 4.4 (a, d) UV-vis and FL spectra of Cl-Cl; (b, e) UV-vis and FL spectra of Br-Br; (c, f) UV-vis and FL spectra of I-I. The UV-vis spectra was measured in THF, 1 μg/ml, FL spectra was measured in THF, MeCN and DMF, 1 μg/ml, Ex = 450nm.

Table 4.2 The summary of the photophysical properties.

| Solvent | Compound | $\lambda_{abs}$ (nm) | $\lambda_{ex}$ (nm) | $\lambda_{em}$ (nm) | $\Delta\lambda$ ($\lambda_{em}$ - $\lambda_{ex}$) | Φ (%) |
|---|---|---|---|---|---|---|
| THF | Cl-Cl | 291, 447 | 450 | 624 | 174 | 20.6 |
| | Br-Br | 292, 444 | 448 | 625 | 177 | 17.3 |
| | I-I | 317, 409 | 412 | 622 | 210 | 16.5 |
| MeCN | Cl-Cl | 291, 435 | 440 | 636 | 196 | 7.4 |
| | Br-Br | 292, 443 | 445 | 626 | 181 | 3.1 |
| | I-I | 317, 412 | 416 | 637 | 221 | 1.8 |
| DMF | Cl-Cl | 292, 446 | 451 | 638 | 195 | 1.7 |
| | Br-Br | 293, 444 | 447 | 627 | 180 | 0.81 |
| | I-I | 290, 408 | 410 | 641 | 231 | 0.07 |

Figures 4.4 (a, b, c) show that all molecules exhibit two absorption peaks, located around 290 nm and 450 nm. The absorption peak near 290 nm is attributed to the π→π* transition resulting from the conjugation between the benzene ring and the maleimide ring, while the peak near 450 nm arises from the extended conjugation due to diamine substitution, which induces intramolecular charge transfer. This is consistent with the previous experimental results. Additionally, Figures 4.4 (d, e, f) indicate that the emission wavelengths of all molecules do not exhibit solvent dependency, as no significant shifts in emission wavelength are observed across solvents of different polarities. Based on this, we propose the following hypotheses: considering the presence of two halogen atoms in the molecules, the photophysical properties are predominantly influenced by the locally excited (LE) state, which overrides the TICT effect.[225-227] The electronegativity and inductive effects of halogen atoms facilitate the formation of the LE state. The LE state represents the initial state of a molecule in its excited state, and through internal twisting and geometric reconfiguration, the molecule may transition to the TICT state. However, the presence of halogen atoms restricts molecular twisting in the excited state, thereby preventing the transition to the TICT state and favouring the LE state instead. Moreover, the impact of solvent polarity on the LE state is minimal, as the electron distribution in the LE state is relatively stable and uniform, preventing significant solvent reorganization effects in polar environments.[141,228-230]

**Investigation of Phosphorescence property in low-temperature condition**

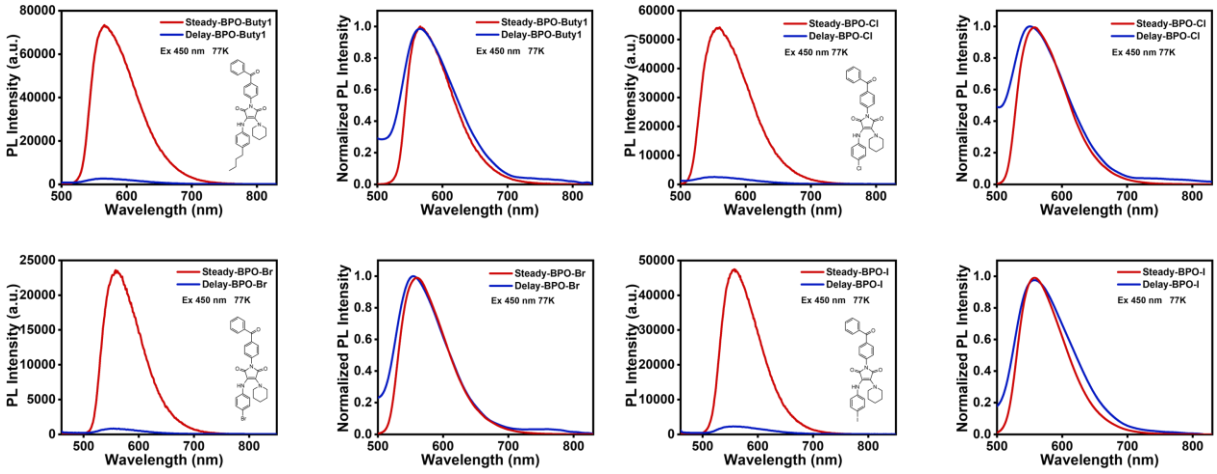


Figure 4.5 Steady and delay fluorescent spectra (red line represents the steady spectra, blue line represents the delay spectra) (the concentration is 1 $\times 10^{-5}$ M in 2-Methyl-THF, 77K, delay time: 0.05ms).

Phosphorescence was initially measured at 77K in 2-methyl-THF (Fig 4.5). Under low-temperature conditions, the frozen solution restricted intramolecular rotation, facilitating intersystem crossing. The phosphorescence spectra at 77K showed that each molecule exhibited phosphorescence with the same wavelength as fluorescence, suggesting a minimal energy difference between the triplet state ($T_1$) and the singlet state ($S_1$). If these energy levels are nearly identical, the photons emitted during fluorescence and phosphorescence can have very similar or even identical wavelengths. Additionally, if intersystem crossing (the transition from $S_1$ to $T_1$) is highly efficient and rapid, the molecule might emit from the triplet state almost immediately after excitation, making the observed emission wavelength appear similar to fluorescence. Furthermore, at low temperatures, non-radiative losses are minimized, and the relaxation processes between the singlet and triplet states might not differ significantly, resulting in very close emission wavelengths.

The same phenomenon was observed for the halo-phenyl-based maleimide derivatives, where the phosphorescence wavelength matched the fluorescence wavelength (Fig 4.6). This indicates that both benzophenone-based and halo-phenyl-based maleimide derivatives exhibit similar phosphorescence properties under low-temperature conditions.

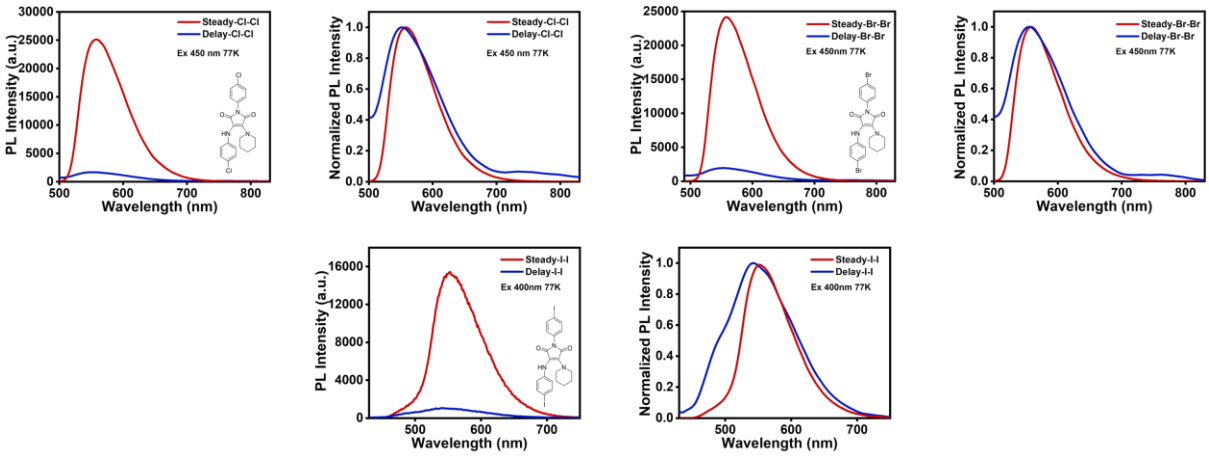


Figure 4.6 Steady and delay fluorescent spectra (the concentration is 1 $\times 10^{-5}$ M in 2-Methyl-THF, 77K, delay time: 0.05ms).

**Investigation of phosphorescence properties using a small molecule-small molecule host-guest doping strategy**

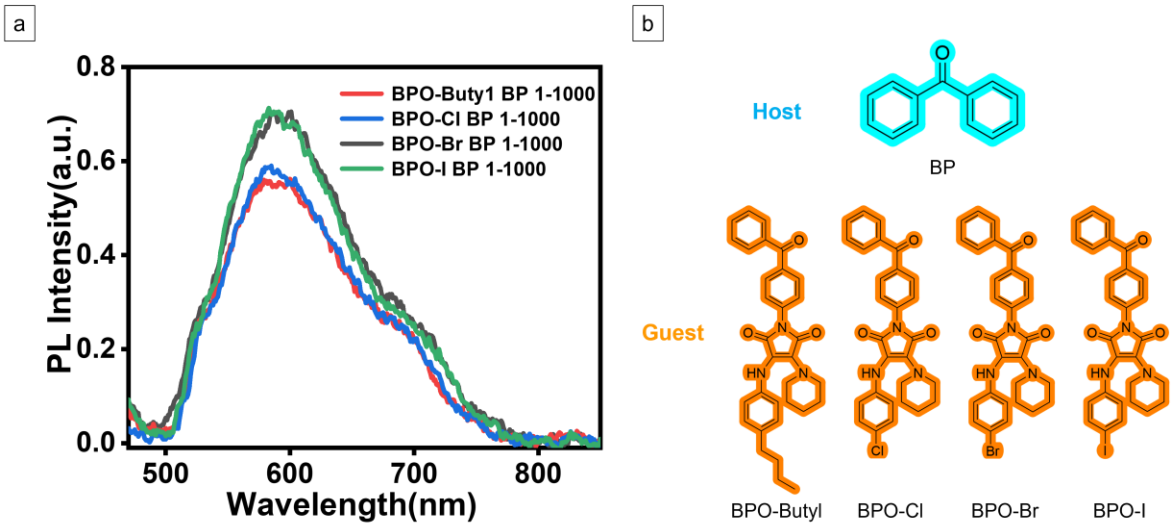


Figure 4.7 (a) Phosphorescence spectra via host-guest doping strategy, the molar doping ratio of the host to guest is 1000:1 (host: 1000, guest: 1). The excitation wavelength is 450 nm, with a slit width of 10 × 10. (b) Host molecule, named BP. Each guest molecule is named BPO-Butyl, BPO-Cl, BPO-Br, and BPO-I, respectively.

The phosphorescence properties of benzophenone-based maleimide derivatives were measured using a host-guest doping strategy (Figure 4.7). Based on previous experience, the optimal host-guest molar dopant ratio is 1000:1 (host: 1000, guest: 1). Excessive doping levels can cause the ISC pathways of multiple guest molecules to overlap, leading to collisions between excitons during the ISC process. These collisions result in energy dissipation, which in turn prevents excitons from transitioning from the singlet to the triplet state.[120] The host molecules

embed the guest molecules in their crystal lattice, restricting their movement and increasing the intersystem crossing probability. When the doping ratio of guest molecules increases, phosphorescence is not observed due to the reduced confinement ability of the host molecules. However, phosphorescence spectra showed that after doping with host molecules, each guest molecule did not emit phosphorescence. This unexpected result may be due to the guest molecule being too large to be fully embedded by the host molecule. As a result, the host molecule's lattice cannot completely restrict the intramolecular vibration and rotation of the guest molecule, causing excitons to decay via non-radiative transitions, thus preventing phosphorescence from occurring.

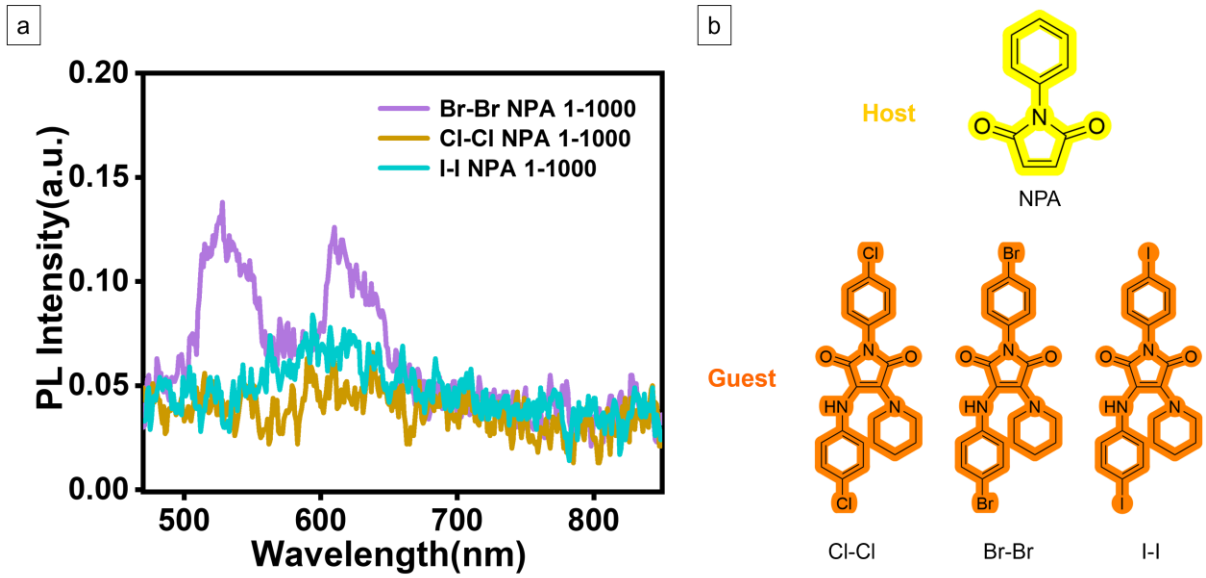


Figure 4.8 (a) Phosphorescence spectra via host-guest doping strategy, the molar doping ratio of the host to guest is 1000:1 (host: 1000, guest: 1). The excitation wavelength is 450 nm, with a slit width of 10 × 10. (b) Host molecule, named NPA. Each guest molecule is named Cl-Cl, Br-Br, and I-I, respectively.

The phosphorescence properties of halo-phenyl-based maleimide derivatives were measured using the same method (Fig 4.8). The phosphorescence spectra showed that similar to the benzophenone-based maleimide derivatives, each guest molecule did not exhibit phosphorescence after being doped with the host molecule. This indicates that the host molecule failed to fully restrict the intramolecular vibration and rotation of the guest molecule.

**Investigation of phosphorescence properties using a polymer-small molecule host-guest doping strategy**

Since room-temperature phosphorescence properties were not observed when small molecules

were used as doping hosts, we speculated that this was due to their inability to effectively immobilize the guest molecules. To address this, we chose polymers as the doping host. Currently, commonly used polymer matrices include polystyrene (PS), polyvinyl alcohol (PVA), and polymethyl methacrylate (PMMA).[113,120] However, based on our experience, PS has a significant drawback. Due to its high rigidity, PS films exhibit numerous voids that can store oxygen. This oxygen reacts with triplet excitons, consuming them and preventing sufficient triplet excitons from returning to the ground state to produce phosphorescence. Moreover, although PVA is widely used as a polymer matrix, its hydroxyl groups form intermolecular hydrogen bonds with the carbonyl groups of imide rings. These hydrogen bonds significantly affect the photophysical properties. Therefore, after comprehensive consideration, we decided to use PMMA as the polymer matrix. PMMA can effectively embed small guest molecules, restrict their motion, and thereby increase the probability of intersystem crossing.

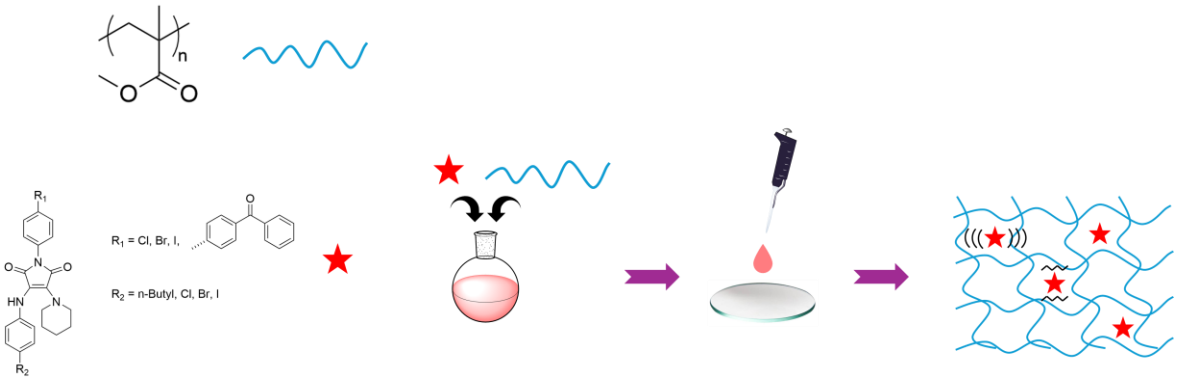


Figure 4.9 Illustration of the strategy of the host-guest doping.

Dissolve PMMA and the small-molecule fluorophore separately in anhydrous acetone, then combine them in a round-bottom flask. Stir the mixture continuously while purging with nitrogen overnight to ensure that the small molecules fully embed into the polymer chains. Next, drop the mixed solution onto a glass dish and allow it to evaporate naturally. Once the solution has evaporated, place the dish in a vacuum oven at room temperature for 24 hours to ensure complete evaporation. Finally, used the prepared film for subsequent testing (Fig 4.9).

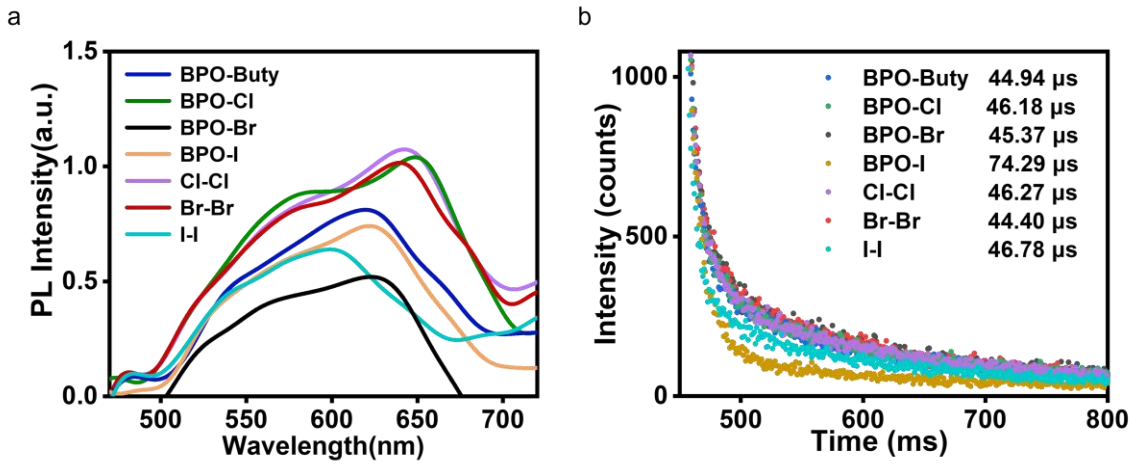


Figure 4.10 (a) Phosphorescence spectra of the PMMA (Mn = 35000 Da)-maleimide fluorophores doping (the doping ratio is 1000:1); (b) Phosphorescence lifetime.

As mentioned above, PMMA was selected as the dopant matrix. In this study, we used PMMA with a number-average molecular weight of 35,000 Da, and the molar doping ratio of polymer to small molecule (host: guest) was 1000:1. This choice was mainly based on the following considerations: based on our experience, PMMA with a lower molecular weight does not have sufficient capability to effectively immobilise the guest molecules. Conversely, PMMA with a higher molecular weight presents issues with solubility and film formation. After several trials, PMMA with a molecular weight of 35,000 showed the most satisfactory results. The doping ratio was also chosen based on experience. A too-low doping ratio cannot effectively restrict the motion of guest molecules, while a too-high doping ratio results in insufficient phosphorescence intensity or no phosphorescence at all due to the low concentration of guest molecules. Therefore, after trials, we found that a doping ratio of 1000:1 is the most ideal.

The phosphorescence spectra indicated that doping with PMMA increased the phosphorescence intensity compared to doping with small molecules, suggesting that PMMA is an effective matrix for achieving room-temperature phosphorescence (RTP). The emission wavelength of each molecule was approximately 600 nm, exhibiting a slight redshift compared to low-temperature conditions. Among the molecules studied, Cl-Cl showed the strongest emission intensity, while BPO-Br exhibited the weakest. Additionally, the phosphorescence lifetimes of all molecules were very short, only at the nanosecond level, indicating that triplet excitons are primarily quenched through non-radiative pathways. There is also the possibility of triplet excitons returning to the singlet state (Fig 4.10).

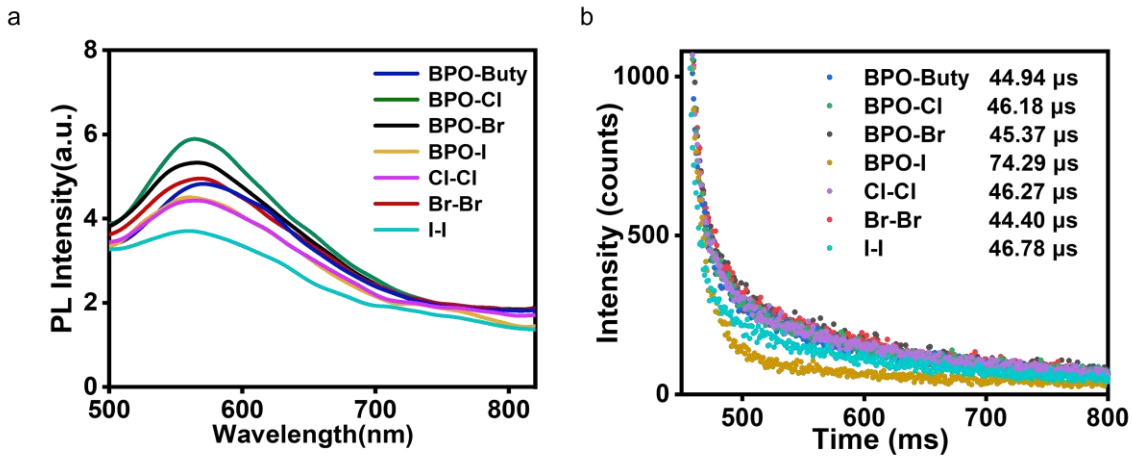


Figure 4.11 Each data was recorded after irradiating by a handheld UV torch (365nm) for 3 min. (a) Phosphorescence spectra of the PMMA (Mn = 35000)-maleimide fluorophores doping (the doping ratio is 1000:1); (b) Phosphorescence lifetime.

Although using a polymer as the dopant matrix can achieve RTP, the phosphorescence intensity was relatively low. We hypothesised that this was due to the unavoidable presence of oxygen within the polymer film, which consumes triplet excitons and thereby reduces phosphorescence intensity. To address this issue, we first irradiated the sample under UV (365nm) light for 3 minutes to consume the oxygen in the film, followed by phosphorescence spectroscopy testing.

The new phosphorescence spectra indicated a significant increase in phosphorescence intensity after eliminating the influence of oxygen. Additionally, the emission wavelengths of each molecule were more concentrated around 580 nm. The luminescence intensity had also changed, with BPO-Cl showing the highest intensity and I-I the weakest. However, the phosphorescence lifetime remained unchanged (Fig 4.11).

### 4.3.2 Single-crystal analysis

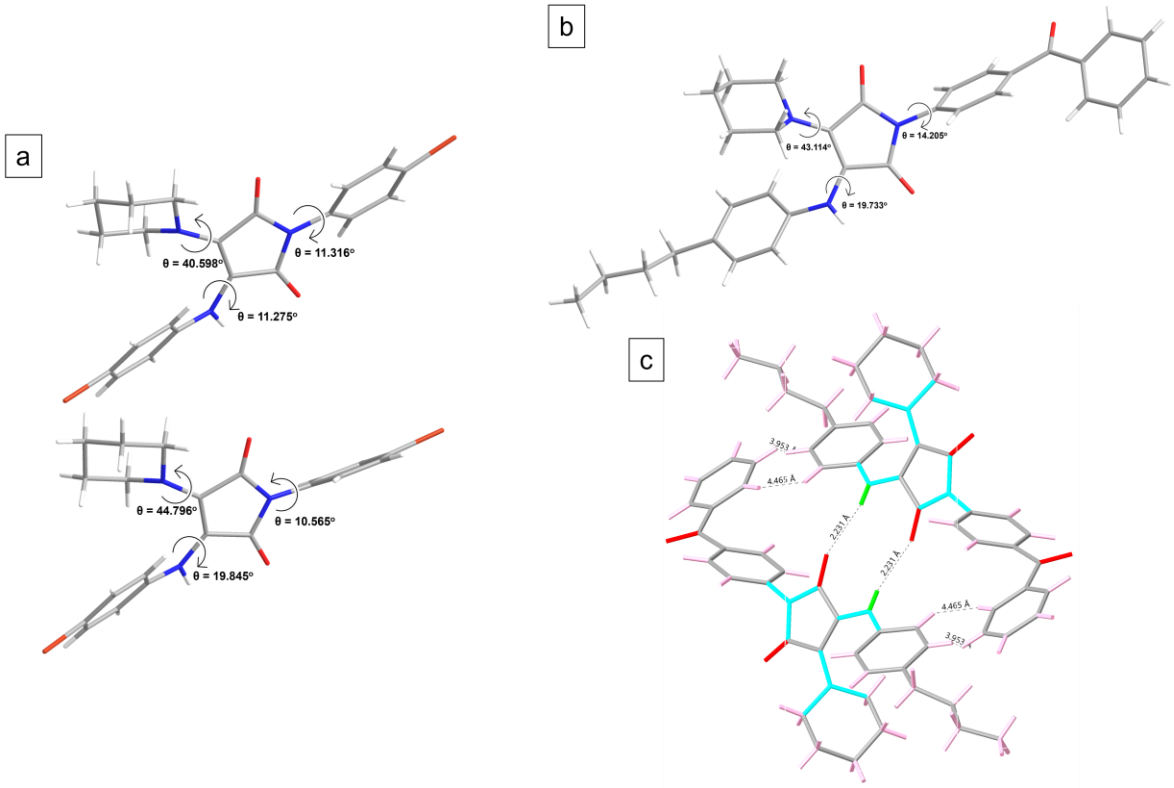


Figure 4.12 (a) Single-crystal structure of Br-Br; (b) Single-crystal structure of BPO-B; (c) molecular packing pattern of BPO-B.

Using solvent evaporation in chloroform and n-hexane, we successfully obtained the single-crystal structures of BPO-B, Br-Br, and I-I. Despite various attempts, we were unable to obtain single crystals for the other structures, as they exhibited issues with polycrystallinity or disorder. Additionally, the molecular packing diagrams for Br-Br and I-I could not be resolved, likely due to the formation of cross-linked network structures through multiple hydrogen bonds, π-π interactions, and lone pair hybridization between halogen atoms and surrounding heteroatoms. As the single-crystal structures of Br-Br and I-I are similar, we chose BPO-B and Br-Br as examples to analyse the impact of single-crystal structure on phosphorescence emission (details in SI). Figure 4.12 (a) shows that Br-Br exhibits two distinct degrees of torsion in its single-crystal structure. The torsional angles between the p-bromophenyl group and the maleimide ring are 11.316° and 10.565°, respectively. These relatively small torsional angles may be due to the lower electron cloud density of the bromophenyl group, which reduces repulsion in this region, thereby eliminating the need for larger rotations to stabilize the molecule. Additionally, the presence of halogen atoms may further restrict phenyl ring rotation. The torsional angles between the piperidine group and the maleimide ring are 40.598° and 44.796°, which we

attribute to the lack of significant intermolecular packing and interactions in this region, allowing the piperidine group to rotate freely. The torsional angles between the p-bromophenyl group and the maleimide ring at the double bond are 11.275° and 19.845°. These torsional angles help prevent planar stacking in the aggregated state, effectively inhibiting intermolecular π-π interactions and thereby reducing non-radiative decay pathways in the solid state. The torsional angles observed in Figure 4.12 (b) are similar to those in Figure 4.12 (a). Furthermore, Figure 4.12 (b) shows that the torsional angle between the benzophenone group and the maleimide ring is 14.205°. Given that no significant intermolecular hydrogen bonds are present in this region (C-H···H-C distances of 3.953 Å and 4.465 Å, both exceeding the maximum hydrogen bond length of 2.9 Å), we hypothesize that this torsional angle is primarily due to the steric hindrance imposed by the bulky benzophenone group, necessitating a certain degree of torsion to stabilize the molecule. Additionally, figure 4.3.10 (c) reveals an intermolecular N-H···O=C hydrogen bond at 2.231 Å in BPO-B, which helps restrict molecular motion in solution, reducing non-radiative decay pathways. Based on the single-crystal structures and the phosphorescence spectra, we propose potential reasons for the observed similarity in emission wavelengths between fluorescence and phosphorescence, as well as the relatively weak phosphorescence intensity: First, considering the intramolecular torsional angles, even when the molecules are fixed through freezing or doping, the inevitable torsion within the molecules leads to relatively loose molecular packing. As a result, when excitons transition from the singlet to the triplet state via intersystem crossing, most excitons are likely dissipated through intramolecular rotation, significantly reducing phosphorescence intensity. Additionally, intramolecular torsion facilitates spatial separation between specific occupied and unoccupied molecular orbitals, reducing the energy gap between the singlet and triplet states, thereby increasing intersystem crossing rates and resulting in phosphorescence emission wavelengths that are close to those of fluorescence.[112,231,232]

### 4.3.3 Theoretical analysis

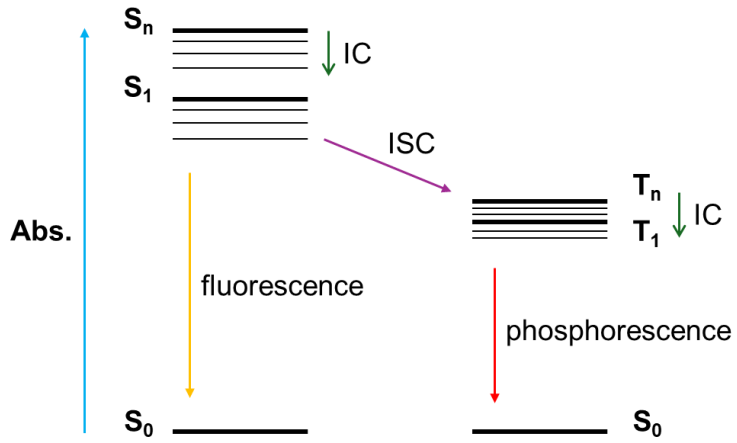


Figure 4.13 Proposed luminescence mechanism between fluorescence and phosphorescence.

Figure 4.13 depicts the luminescence mechanism of phosphorescence. When a molecule absorbs a photon, an exciton undergoes a transition from the ground state to the excited state ($S_n$). Subsequently, it undergoes internal conversion to the first excited state ($S_1$). When the exciton is in the first excited state, it reaches the triplet excited state ($T_n$) through intersystem crossing. Then, it further undergoes internal conversion to the first triplet state ($T_1$) and finally decays to the ground state through radiative transition, releasing energy in the form of phosphorescence. Generally, due to the energy consumption during intersystem crossing, the triplet state energy level is lower than the singlet state energy level. Therefore, the emission wavelength of phosphorescence is longer than that of fluorescence. However, if the energy-level difference between $S_1$ and $T_n$ is smaller and the intersystem crossing rate is relatively large, the emission wavelengths of phosphorescence and fluorescence will approach each other infinitely. According to the formula $k_{\mathrm{ISC}} = \frac{2\pi}{\hbar}|\langle S_1|H_{\mathrm{SOC}}|T_1\rangle|^2 \cdot \rho(\Delta E) \cdot FC$ (where $H_{SOC}$ is the spin-orbit coupling Hamiltonian, $\rho(\Delta E)$ is the density of states, usually related to the energy gap ($\Delta E = E(S_1) - E(T_n)$) , and FC (Franck-Condon factor) represents the overlap of vibrational wave functions), and combined with the energy-gap law formula $k_{\mathrm{ISC}} \propto \frac{\zeta^2}{\Delta E^2 + \Gamma^2}$ , the formula $k_{\mathrm{ISC}} \propto \frac{\zeta^2}{\Delta E^2} \cdot e^{-\beta \Delta E}$ can be obtained. From this formula, it can be seen that the energy-level difference ($\Delta E$) between the singlet state and the triplet state is inversely proportional to the intersystem crossing rate ($K_{ISC}$) and also inversely proportional to the SOC constant ($\zeta$). That is, the smaller the energy-level difference, the larger $K_{ISC}$ and the larger the SOC constant.

Table 4.3 Summarized ΔE, SOC constant and the intersystem crossing rate.

| Name | ΔE (eV) | SOC constant ζ ($cm^{-1}$) | $K_{ISC}$ ($S^{-1}$) |
|---|---|---|---|
| Cl-Cl | $S_1 \rightarrow T_3$ = 0.21 | 33.24 | $1.51\times10^8$ |
| | $S_1 \rightarrow T_2$ = 0.13 | 58.83 | $4.33\times10^8$ |
| | $S_1 \rightarrow T_1$ = 0.06 | 104.64 | $1.02\times10^9$ |
| Br-Br | $S_1 \rightarrow T_3$ = 0.21 | 33.18 | $1.46\times10^8$ |
| | $S_1 \rightarrow T_2$ = 0.13 | 57.97 | $4.19\times10^8$ |
| | $S_1 \rightarrow T_1$ = 0.07 | 104.52 | $8.89\times10^8$ |
| I-I | $S_1 \rightarrow T_3$ = 0.20 | 32.77 | $1.53\times10^8$ |
| | $S_1 \rightarrow T_2$ = 0.14 | 59.23 | $4.08\times10^8$ |
| | $S_1 \rightarrow T_1$ = 0.06 | 105.19 | $1.03\times10^9$ |
| BPO-B | $S_1 \rightarrow T_3$ = 0.23 | 36.18 | $1.63\times10^8$ |
| | $S_1 \rightarrow T_2$ = 0.16 | 60.52 | $4.55\times10^8$ |
| | $S_1 \rightarrow T_1$ = 0.07 | 107.81 | $1.43\times10^9$ |
| BPO-Cl | $S_1 \rightarrow T_3$ = 0.22 | 35.11 | $1.65\times10^8$ |
| | $S_1 \rightarrow T_2$ = 0.16 | 58.48 | $4.47\times10^8$ |
| | $S_1 \rightarrow T_1$ = 0.07 | 106.92 | $1.38\times10^9$ |
| BPO-Br | $S_1 \rightarrow T_3$ = 0.21 | 35.54 | $1.70\times10^8$ |
| | $S_1 \rightarrow T_2$ = 0.18 | 50.12 | $4.61\times10^8$ |
| | $S_1 \rightarrow T_1$ = 0.06 | 105.59 | $1.62\times10^9$ |
| BPO-I | $S_1 \rightarrow T_3$ = 0.21 | 37.09 | $1.66\times10^8$ |
| | $S_1 \rightarrow T_2$ = 0.17 | 49.58 | $4.82\times10^8$ |
| | $S_1 \rightarrow T_1$ = 0.07 | 107.22 | $1.70\times10^9$ |

To gain a more in-depth understanding of the phosphorescence luminescence mechanism of each molecule, it is essential to explore the relationship between the singlet state and the triplet state. Firstly, in the vacuum state, molecular optimizations of each molecule in the ground state, the first singlet excited state, and the first triplet excited state were carried out using density functional theory at the level of the cam-B3LYP functional and the 6-31G*(d, p) basis set. Subsequently, the energy-level differences between the first singlet excited state and different triplet excited states of each molecule were calculated using time-dependent DFT and Multiwfn

at the same level.[233] Finally, the SOC constants and intersystem crossing rates between the singlet state and the triplet state of each molecule were calculated using the ORCA program package at the TD-PBE0/6 - 311G (d, p) level.[234] As shown in Table 4.3, the results of the energy-level differences between the three triplet states and the first excited state of all molecules indicate that the energy-level differences gradually decrease from $T_3$ to $T_1$. Taking the Cl-Cl molecule as an example, the energy-level difference in $S_1 \rightarrow T_3$ is 0.21 eV, 0.13 eV in $S_1 \rightarrow T_2$, and only 0.06 eV in $S_1 \rightarrow T_1$, suggesting that the energy levels between the triplet states are very close, and the calculation results among different molecules are quite similar. For instance, the differences in different energy levels of the Br-Br molecule are 0.21, 0.13, and 0.07 respectively, and those of the BPO-Cl molecule are 0.22, 0.16, and 0.07 respectively. In addition, the SOC constants and intersystem crossing rates of each molecule also increase as the triplet-state energy levels decrease. For the Cl-Cl molecule, in $S_1 \rightarrow T_3$, the SOC constant is 33.24 $cm^{-1}$ and the rate is$1.51 \times 10^8$, in $S_1 \rightarrow T_2$, they are 58.83 $cm^{-1}$ and $4.33 \times 10^8$ respectively, and in $S_1 \rightarrow T_1$, they increase to 104.64 and $1.02 \times 10^9$ respectively. The calculation results among different molecules are relatively close. These calculation results demonstrate that the energy levels between the triplet state and the singlet state are very close. Therefore, the emission wavelengths ($\lambda_{max}$) of phosphorescence and fluorescence are relatively close, which is consistent with the above-mentioned experimental results. Moreover, the large SOC constants and intersystem crossing rates indicate that excitons can easily and rapidly cross from the singlet state to the triplet state through intersystem crossing. This may be due to the heavy-atom effect of the halogen atoms in the molecules. That is, the attraction of the atomic nucleus to the outer-layer electrons is enhanced, and the movement speed of the electrons is accelerated, which strengthens the coupling between the electron spin and orbital motion, thus being conducive to increasing the SOC constant. In addition, halogen atoms make the transition of electrons in the molecule between different spin states easier, thereby promoting the intersystem crossing process and increasing the intersystem crossing rate.

## 4.5 Conclusion

In this study, we successfully designed and synthesized a series of maleimide-based derivatives by integrating benzophenone and halogenated aniline moieties to explore their potential for room-temperature phosphorescence through host-guest doping strategies. Our systematic investigation into their photophysical properties across various solvents revealed distinct solvent-dependent behaviours, particularly the influence of intramolecular charge transfer and twisted intramolecular charge transfer effects on emission characteristics. Low-temperature

phosphorescence measurements at 77K indicated that all synthesized compounds exhibited phosphorescence, with emission wavelengths closely mirroring those of fluorescence, suggesting minimal energy gaps between the singlet and triplet states and supporting the occurrence of rapid intersystem crossing under these conditions. Despite rigorous efforts to achieve RTP using both small molecule and polymer-based host matrices, the results showed that neither benzophenone-based nor halo-phenyl-based maleimide derivatives exhibited significant RTP under ambient conditions. This was attributed to the inability of the host matrices to adequately immobilize the guest molecules, allowing non-radiative decay pathways to dominate. Single-crystal structural analyses further revealed that intramolecular torsion and relatively loose molecular packing contributed to the weak phosphorescence intensity and the similarity in emission wavelengths between fluorescence and phosphorescence. Theoretical calculations supported these findings, highlighting small energy gaps between excited states as a fundamental reason for the close emission characteristics.

## 4.6 Supplementary information

### 4.6.1 Materials

2,3-Dichloromaleic anhydride (97%), 4-Aminobenzophenone (98%), 4-butylaniline (97%), 4-chloroaniline (98%), 4-bromoaniline (97%), 4-iodoaniline (98%), Piperidine (99%) were purchased from Merck (UK) and utilized as received without further purification. All solvents were purchased from Merck (UK) or Thermo Fisher Scientific (UK) and utilized as received without further purification. Dimethyl sulfoxide-d6 (DMSO-d6), used for nuclear magnetic resonance (NMR) measurement, was purchased from Thermo Fisher Scientific (UK).

### 4.6.2 Instrumentations

1. NMR spectroscopy: NMR spectra were recorded on a Bruker Avance 300, a Bruker Avance III HD 400 or a Bruker Avance III HD 500 spectrometer at 298K and 300, 400 and 500 MHz, respectively. Shifts are quoted in δ in parts per million and quoted relative to the internal standard trimethylsilane (TMS).

2. High-Resolution Mass Spectra (HR-MS) were obtained by using Bruker UHR-Q-ToF MaXis spectrometer with electrospray ionization.

3. UV-vis spectroscopy was performed on Evolution 350 UV-vis spectrophotometer equipped with Xenon Flash Lamp light source and Dual Matched Silicon Photodiodes detector. Quartz cells (170 – 2000 nm) from Hellma with two polished sides were used for examining the absorption spectral data by using Thermo INSIGHT-2 v.10.0.30319.1 software.

4. Fluorescence spectral data in various solvents and solid state were obtained with an Edinburgh Instruments FS5 Spectrofluorometer, Phosphorescence was measured by Edinburgh Instruments FLS1000 Spectrofluorometer. Photoluminescence measurements (for solution) were performed in a conventional quartz cuvette (light path 10 mm) on a Cary Eclipse equipped with a Cary single-cuvette peltier accessory. 77K delay spectra were measured on Edinburgh Instruments Fluorescence Spectrometer (FLS900).

5. X-ray analysis data were collected on Agilent Technologies SuperNova single crystal X-ray diffractometer with dual wavelength microfocus X-ray sources (Mo and Cu) and an Atlas detector. The system is complemented by an Oxford Cryosystems Cryostream to collect data at temperatures as low as 100 K. The structures were solved by direct methods and refined anisotropically by the least-squares procedure implemented in the SHELX program system.

## 4.6.3 Synthetic methods

1. synthesis of halo-based single-substitution maleimide derivatives

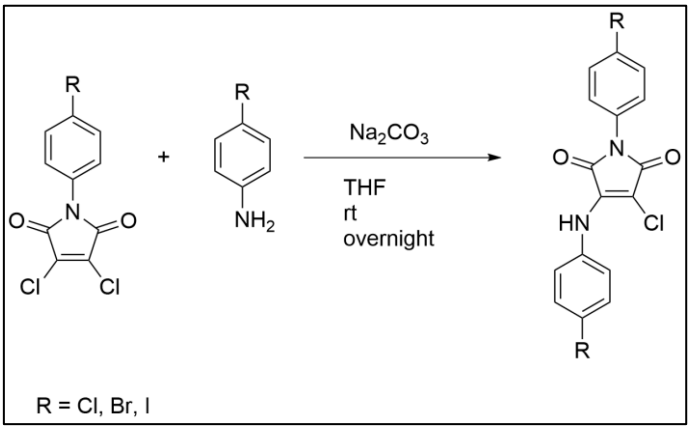


Scheme 1 Synthesis of halo-based single-substitution maleimide derivatives.

The reactants (Cl-M-DC, Br-M-DC, I-M-DC) (1 eq.) were dissolved in THF, followed by the addition of anhydrous sodium carbonate ($Na_2CO_3$) (2.5 eq.). Subsequently, 4-chloroaniline(or 4-bromoaniline, or 4-iodoaniline) (1.5 eq.) was added into the mixture. The mixture was then stirred at room temperature overnight. Upon completion of the reaction, the solids were filtered out, and the solution was evaporated under reduced pressure. The residual solid was washed with methanol, yielding the final yellow products, each with an approximate yield of 90%.

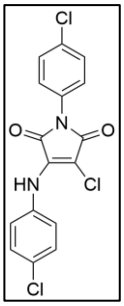


**$^1$H NMR (400 MHz, DMSO-d6, 25°C, TMS) δ (ppm)**: 10.06 (s, 1H), 7.59 (dd, J = 8.0, 0.4 Hz, 2H), 7.45 (m, 4H), 7.24 (dd, J = 6.6, 0.8 Hz, 2H).

**$^{13}$C NMR (101 MHz, DMSO-d6) δ (ppm):** 166.32, 164.65, 138.76, 136.30, 132.60, 130.96, 129.67, 129.63, 129.41, 129.17, 128.78, 128.72, 125.87, 94.04, 40.63, 40.42, 40.21, 40.05, 40.00, 39.79, 39.58, 39.37.

**HRMS**: m/z: calculated for $[C_{16}H_9Cl_3N_2O_2]^-$: 365.9730, found: 365.9721.

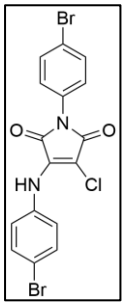


**$^1$H NMR (400 MHz, DMSO-d6, 25°C, TMS) δ (ppm)**: 10.05 (s, 1H), 7.74 (d, J = 6.7 Hz2H), 7.58 (d, J = 4.7 Hz, 2H), 7.37 (d, J = 6.7 Hz, 2H), 7.17 (d, J = 4.6Hz, 2H).

**$^{13}$C NMR (101 MHz, DMSO-d6) δ (ppm):** 166.25, 164.60, 162.40, 138.69, 136.74, 133.27, 132.62, 132.36, 131.63, 131.40, 130.79, 129.43, 129.06, 126.16, 121.99, 121.02, 117.77, 94.23, 40.63, 40.42, 40.26, 40.21, 40.00, 39.79, 39.59, 39.37.

**HRMS**: m/z: calculated for $[C_{16}H_9Br_2ClN_2O_2]^-$: 453.8719, found: 453.8726.

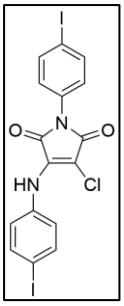

**$^{1}$H NMR (400 MHz, DMSO-d6, 25°C, TMS) δ (ppm)**: 10.03 (s, 1H), 7.89 (dd, J = 6.7, 4.2 Hz, 2H), 7.73 (dd, J = 6.8 Hz, 2H), 7.21 (dd, J = 6.7, 4.2 Hz, 2H), 7.03 (d, J = 6.8 Hz, 2H).

**$^{13}$C NMR (101 MHz, DMSO-d6) δ (ppm):** 166.22, 164.59, 162.37, 138.57, 138.47, 138.21, 137.44, 137.19, 133.26, 131.86, 131.26, 129.42, 129.11, 126.30, 95.10, 94.28, 93.95, 89.99, 40.63, 40.42, 40.27, 40.21, 40.06, 40.01, 39.80, 39.59, 39.38.

**HRMS**: m/z: calculated for $[C_{16}H_9I_2ClN_2O_2]^-$: 549.8442, found: 549.8457.

2. synthesis of halo-based maleimide fluorophores

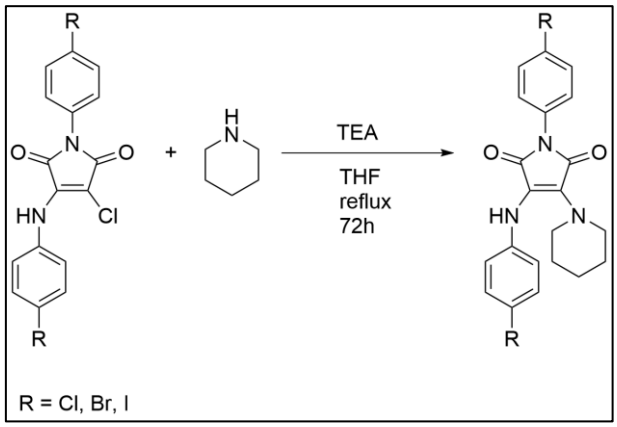


Scheme 2 synthesis of halo-based maleimide fluorophores

The reactant from Step 2 (1 eq.) was dissolved in THF, followed by sequential additions of piperidine (5 eq.) and triethylamine (NEt3) (5 eq.). This mixture was refluxed for 72 hours. Upon the reaction's completion, the solution was cooled and then filtered. The filtrate was evaporated under reduced pressure, leaving a solid residue. This residue was washed with methanol, resulting in the isolation of the final product, which was either orange or red, with each compound yielding approximately 70%.

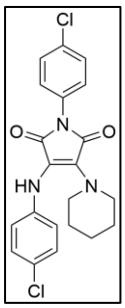

**$^{1}$H NMR (400 MHz, DMSO-d6, 25°C, TMS) δ (ppm)**: 7.86 (s, 1H), 7.53 (d, J = 6.6 Hz, 2H), 7.39 (d, J = 4.6 Hz, 2H), 7.21 (d, J = 6.9 Hz, 2H), 6.79 (d, J = 4.7 Hz, 2H), 3.47 (t, J = 5.3Hz, 4H), 1.50-1.43 (dd, 24.9, 5.6 Hz, 6H).

**$^{13}$C NMR (101 MHz, DMSO) δ (ppm):** 168.03, 166.34, 143.83, 134.78, 131.76, 131.37, 129.14, 128.90, 128.58, 122.42, 117.16, 108.95, 48.59, 40.68, 40.63, 40.42, 40.27, 40.21, 40.01, 39.80, 39.59, 39.38, 26.23, 24.00.

**HRMS**: m/z: calculated for $[C_{21}H_{19}Cl_2N_3O_2]^-$: 415.0854, found: 415.0861.

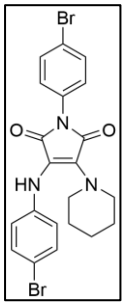

**$^{1}$H NMR (400 MHz, DMSO-d6, 25°C, TMS) δ (ppm)**: 7.85 (s, 1H), 7.66 (d, J = 8.8Hz, 2H), 7.33 (d, J = 7.0Hz, 2H), 6.75 (d, J = 6.8Hz 2H), 3.48 (t, J = 5.3Hz, 4H), 1.49-1.44 (ddd, J = 23.8, 7.5, 4.1 Hz, 6H).

**$^{13}$C NMR (101 MHz, DMSO-d6) δ (ppm):** 167.96, 166.23, 144.40, 135.25, 132.08, 131.80, 131.76, 128.90, 120.14, 117.58, 109.95, 108.52, 48.58, 40.63, 40.42, 40.26, 40.22, 40.01, 39.80, 39.59, 39.38, 26.25, 24.00.

**HRMS**: m/z: calculated for $[C_{21}H_{19}Br_2N_3O_2]^-$: 502.9844, found: 502.9841.

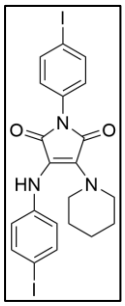

**$^{1}$H NMR (400 MHz, DMSO-d6, 25°C, TMS) δ (ppm)**: 7.82 (m, 3H), 7.46 (d, J = 8.8Hz, 2H), 7.16 (dd, J = 7.1, 7.1Hz, 2H), 6.63 (d, J = 8.8Hz, 2H), 3.48 (t, J = 5.2Hz, 4H), 1.53-1.40 (m, 6H).

**$^{13}$C NMR (101 MHz, DMSO-d6) δ (ppm):** 167.93, 166.16, 165.21, 164.15, 145.04, 142.76, 138.05, 137.93, 137.54, 135.59, 132.26, 131.91, 129.37, 128.98, 118.08, 108.17, 40.64, 40.43, 40.27, 40.22, 40.06, 40.01, 39.80, 39.38, 26.82, 24.00.

**HRMS**: m/z: calculated for $[C_{21}H_{19}I_2N_3O_2]^-$: 598.9567, found: 598.9561.

3. synthesis of Benzophenone-based maleimide substitution

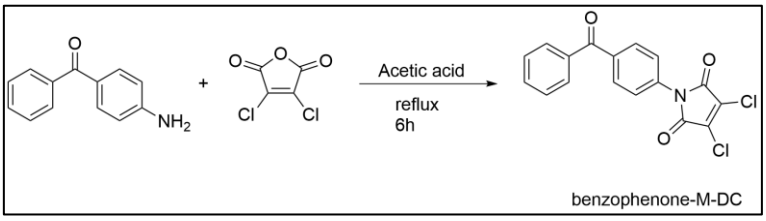


Scheme 3 Synthesis of Benzophenone-based maleimide substitution.

In a one-neck round-bottom flask, 2,3-dichloromaleic anhydride (1 eq.) was dissolved in acetic acid, followed by the addition of 4-Aminobenzophenone (1 eq.). The resulting mixture was refluxed for 6 hours. Upon completion of the reaction, the solution was cooled to room temperature, inducing the precipitation of the product. The precipitate was then filtered and washed with methanol, yielding a light yellow solid. The yield of each compound was approximately 95%.

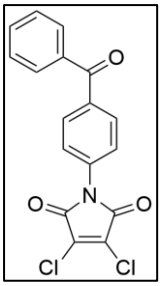

**$^{1}$H NMR (400 MHz, DMSO-d6, 25°C, TMS) δ (ppm)**: 7.79 (dd, J = 1.6, 1.6 Hz, 2H), 7.70 (d, J = 5.5 Hz, 2H), 7.48 (d, J = 6.5Hz, 3H), 7.40 (d, J = 5.5 2H).

**$^{13}$C NMR (101 MHz, THF-d8) δ (ppm):** 193.98, 161.40, 137.46, 136.89, 134.83, 133.25, 132.20, 130.38, 129.70, 128.18, 125.27, 66.87, 66.79, 66.65, 66.56, 66.43, 66.21, 66.00, 24.88, 24.75, 24.67, 24.55, 24.47, 24.35, 24.15, 23.95.

**HRMS**: m/z: calculated for $[C_{17}H_9Cl_2NO_3]^-$: 344.9959, found: 344.9951.

4. synthesis of Benzophenone-based single substitution maleimide derivatives

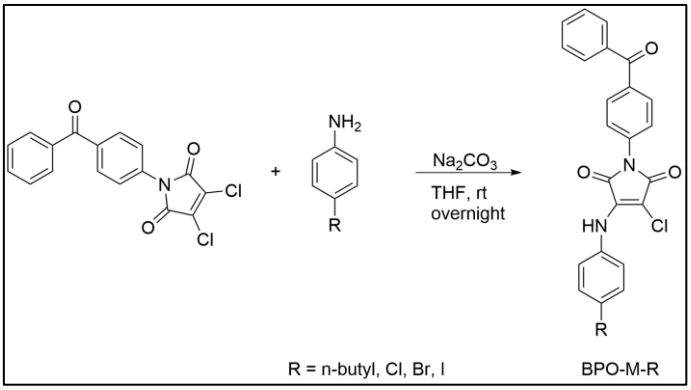


Scheme 4 Synthesis of Benzophenone-based single substitution maleimide derivatives.

The reactants BPO-M-DC (1 eq.) were dissolved in THF, followed by the addition of anhydrous sodium carbonate ($Na_2CO_3$) (2.5 eq.). Subsequently, 4-Butylaniline (4-chloroaniline, 4-bromoaniline, or 4-iodoaniline) (1.5 eq.) was added into the mixture. The mixture was then stirred at room temperature overnight. Upon completion of the reaction, the solids were filtered out, and the solution was evaporated under reduced pressure. The residual solid was washed with methanol, yielding the final yellow products, each with an approximate yield of 90%.

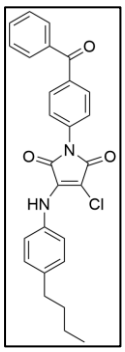

**$^{1}$H NMR (400 MHz, DMSO-d6, 25°C, TMS) δ (ppm)**: 10.12 (s, 1H), 7.88 (d, J = 6.8 Hz, 2H), 7.79 (d, J = 6.0 Hz, 2H), 7.70 (dd, J = 7.48Hz, 7.48Hz, 2H), 7.63 (m, 3H), 7.46 (d, J = 8.5 Hz, 2H), 7.25 (d, J = 8.5 Hz, 2H), 2.58 (t, 14.8Hz, 2H), 1.56 (m, 2H), 1.32 (m, 2H), 0.91 (t, J = 7.3Hz, 3H).

**$^{13}$C NMR (101 MHz, DMSO-d6) δ (ppm):** 195.45, 166.36, 164.60, 140.09, 139.23, 137.34, 136.03, 135.87, 134.67, 133.28, 130.76, 130.13, 129.11, 128.52, 126.37, 124.63, 92.20, 67.49, 40.63, 40.42, 40.26, 40.21, 40.00, 39.79, 39.58, 39.38, 34.78, 33.57, 25.60, 22.24, 14.27.

**HRMS**: m/z: calculated for $[C_{27}H_{23}ClN_2O_3]^-$: 458.1397, found: 458.1391.

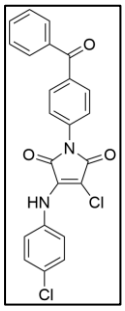

**$^{1}$H NMR (400 MHz, DMSO-d6, 25°C, TMS) δ (ppm)**: 10.12 (s, 1H), 7.88 (d, J = 7.8Hz, 2H), 7.79 (d, J = 6.9 Hz 2H), 7.70 (dd, J = 7.4, 7.4Hz, 2H), 7.63 (dd, J = 12.3, 8.1 Hz, 3H), 7.46 (d, J = 8.7Hz, 2H), 7.25 (d, J = 8.7Hz, 2H).

**$^{13}$C NMR (101 MHz, DMSO-d6) δ (ppm):** 195.44, 166.18, 164.56, 138.89, 137.32, 136.27, 136.10, 135.77, 133.29, 130.79, 130.13, 129.71, 129.11, 128.73, 126.37, 125.95, 124.48, 94.24, 67.49, 40.63, 40.42, 40.21, 40.00, 39.79, 39.58, 39.37, 25.60.

**HRMS**: m/z: calculated for $[C_{23}H_{14}ClN_2O_3]^-$: 436.0381, found: 436.0378.

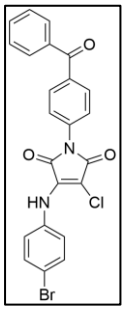

**$^{1}$H NMR (400 MHz, DMSO-d6, 25°C, TMS) δ (ppm)**: 10.11 (s, 1H), 7.88 (dd, J = 7.7, 8.6Hz, 2H), 7.79 (d, J = 7.1Hz, 2H), 7.72 (dd, J = 7.8, 0.8Hz, 1H), 7.61 (m, 6H), 7.19 (d, J = 7.8Hz, 2H).

**$^{13}$C NMR (101 MHz, DMSO-d6) δ (ppm):** 195.45, 166.17, 164.57, 162.38, 138.80, 137.32, 137.17, 137.00, 136.71, 136.11, 135.77, 135.03, 133.40, 133.29, 131.64, 130.91, 130.79, 130.18, 130.14, 129.14, 129.12, 126.94, 126.39, 126.24, 117.85, 94.42, 40.63, 40.42, 40.26, 40.21, 40.00, 39.79, 39.58, 39.38.

**HRMS**: m/z: calculated for $[C_{23}H_{14}BrClN_2O_3]^-$: 479.9876, found: 479.9871.

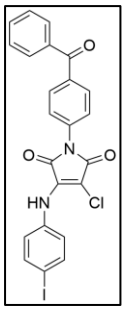

**$^{1}$H NMR (400 MHz, DMSO-d6, 25°C, TMS) δ (ppm)**: 10.10 (s, 1H), 7.87 (d, J = 7.9Hz, 2H), 7.78 (dd, J = 7.8, 7.8Hz, 2H), 7.74 (m, 5H), 7.60 (d, J = 7.9Hz, 2H), 7.04 (d, J = 7.9Hz, 2H).

**$^{13}$C NMR (101 MHz, DMSO-d6) δ (ppm):** 195.45, 166.16, 164.58, 138.69, 138.39, 137.46, 137.32, 137.16, 136.11, 135.77, 133.29, 130.78, 130.14, 129.12, 127.41, 126.39, 126.38, 124.41, 94.47, 90.11, 40.42, 40.21, 40.01, 39.80, 39.59, 39.38.

**HRMS**: m/z: calculated for $[C_{23}H_{14}IClN_2O_3]^-$: 527.9738, found: 527.9742.

5. synthesis of Benzophenone-based maleimide fluorophores

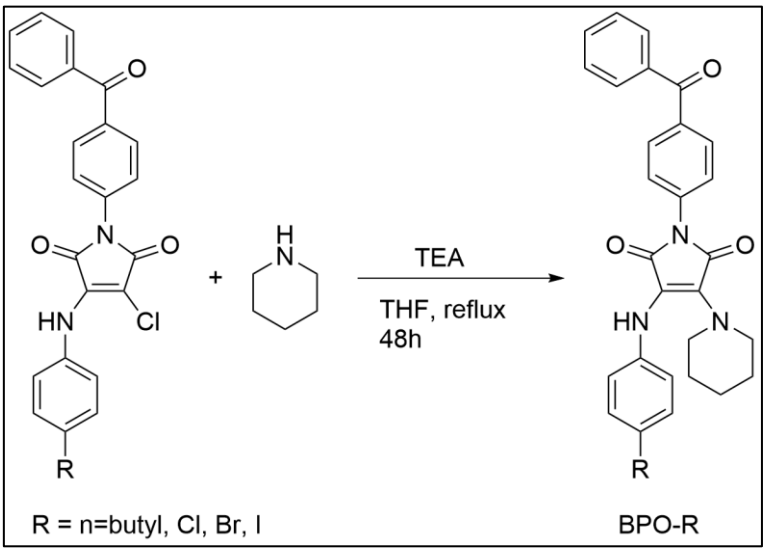


Scheme 5 Synthesis of Benzophenone-based maleimide fluorophores.

The reactant from Step 2 (1 eq.) was dissolved in THF, followed by sequential additions of piperidine (5 eq.) and triethylamine (NEt3) (5 eq.). This mixture was refluxed for 72 hours. Upon the reaction's completion, the solution was cooled and then filtered. The filtrate was evaporated under reduced pressure, leaving a solid residue. This residue was washed with methanol, resulting in the isolation of the final product, which was either orange or red, with each compound yielding approximately 70%.

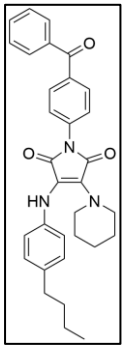

**$^{1}$H NMR (400 MHz, DMSO-d6, 25°C, TMS) δ (ppm)**: 7.88 (s, 1H), 7.83 (d, J = 2.0Hz, 2H), 7.77 (d, J = 7.1Hz, 2H), 7.71 (dd, J = 4.1, 4.1Hz, 1H), 7.58 (td, J = 6.9, 1.3 Hz, 4H), 7.02 (d, J = 8.5Hz, 2H), 6.76 (d, J = 8.5Hz, 2H), 3.35 (m, 4H), 2.48 (d, 2H), 1.41 (m, 10H), 0.88 (t, J = 7.3Hz, 3H).

**$^{13}$C NMR (101 MHz, $CDCl_3$) δ (ppm):** 195.77, 167.97, 166.98, 139.08, 137.59, 136.03, 135.85, 135.28, 132.42, 130.80, 130.02, 128.87, 128.32, 126.92, 124.63, 117.68, 113.77, 77.37, 77.05, 76.73, 48.99, 46.43, 34.88, 33.86, 29.71, 26.01, 25.66, 24.04, 22.26, 13.98.

**HRMS**: m/z: calculated for $[C_{32}H_{33}N_3O_3]^-$: 507.2522, found: 507.2531.

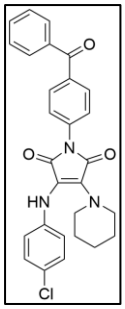

**$^{1}$H NMR (400 MHz, DMSO-d6, 25°C, TMS) δ (ppm)**: 7.94 (s, 1H), 7.84 (d, J = 8.6Hz, 2H), 7.77 (d, J = 6.7Hz, 2H), 7.58 (m, 4H), 7.22 (d, J = 8.0Hz, 2H), 6.82 (d, J = 8.0Hz, 2H), 3.47 (t, J = 5.2Hz, 4H), 1.49 (m, 6H).

**$^{13}$C NMR (101 MHz, $CDCl_3$) δ (ppm):** 195.74, 167.87, 166.38, 140.91, 137.51, 135.62, 135.52, 132.48, 130.81, 130.02, 129.74, 129.02, 128.34, 125.88, 124.76, 117.96, 110.74, 77.35, 77.03, 76.72, 48.82, 29.70, 26.23, 23.98.

**HRMS**: m/z: calculated for $[C_{28}H_{24}ClN_3O_3]^-$: 485.1506, found: 485.1521.

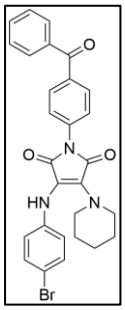

**$^{1}$H NMR (400 MHz, DMSO-d6, 25°C, TMS) δ (ppm)**: 7.90 (s, 1H), 7.84 (d, J = 8.1Hz, 2H), 7.76 (d, J = 7.5Hz, 4H), 7.58 (dd, J = 7.1, 7.1Hz, 3H), 7.33 (d, J = 9.0 Hz, 2H), 6.77 (d, J = 9.0 Hz, 2H), 3.49 (t, J = 5.2Hz 4H), 1.48 (m, 6H).

**$^{13}$C NMR (101 MHz, $CDCl_3$) δ (ppm):** 195.73, 167.84, 166.32, 141.54, 137.51, 135.60, 135.53, 132.48, 131.94, 130.81, 130.78, 130.64, 130.10, 130.02, 128.34, 125.29, 125.01, 124.77, 118.28, 113.13, 110.33, 77.35, 77.03, 76.71, 67.99, 49.89, 49.74, 48.80, 26.81, 26.48, 26.25, 25.62, 24.20, 24.09, 23.98.

**HRMS**: m/z: calculated for $[C_{28}H_{24}BrN_3O_3]^-$: 529.1001, found: 529.1013.

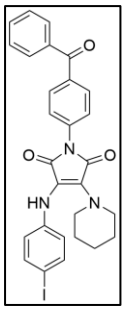

**$^{1}$H NMR (400 MHz, DMSO-d6, 25°C, TMS) δ (ppm)**: 8.01 (s, 1H), 7.82 (d, J = 8.4Hz, 2H), 7.77 (d, J = 7.7 Hz, 2H), 7.58 (m, 5H), 7.47 (d, J = 8.6Hz, 2H), 6.65 (d, J = 8.6Hz, 2H), 3.50 (t, J = 5.4 Hz, 4H), 1.46 (m, 6H).

**$^{13}$C NMR (101 MHz, $CDCl_3$) δ (ppm):** 195.73, 167.84, 166.26, 142.40, 138.09, 138.03, 137.84, 137.51, 135.59, 135.54, 132.48, 130.80, 130.50, 130.02, 128.34, 127.25, 124.78, 123.97, 118.67, 109.90, 82.79, 77.35, 77.03, 76.72, 67.98, 48.79, 46.78, 26.28, 26.20, 25.62, 24.52, 23.98.

**HRMS**: m/z: calculated for $[C_{28}H_{24}IN_3O_3]^-$: 577.0862, found: 577.0871.

## 4.6.4 UV-vis and FL spectra

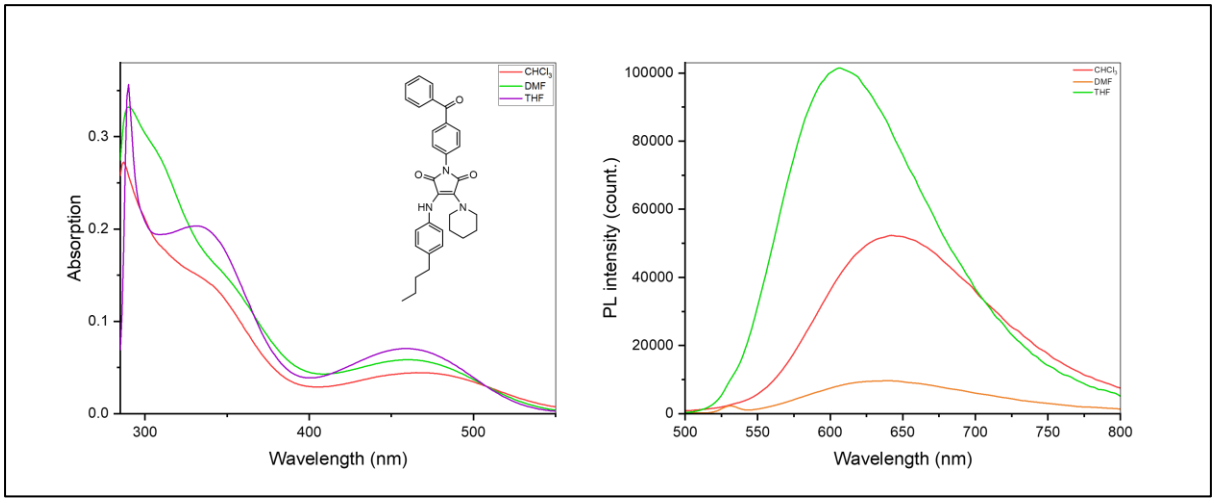


Figure 1 UV-vis and FL spectra in various solvents. ([c] = 0.01mg/ml)

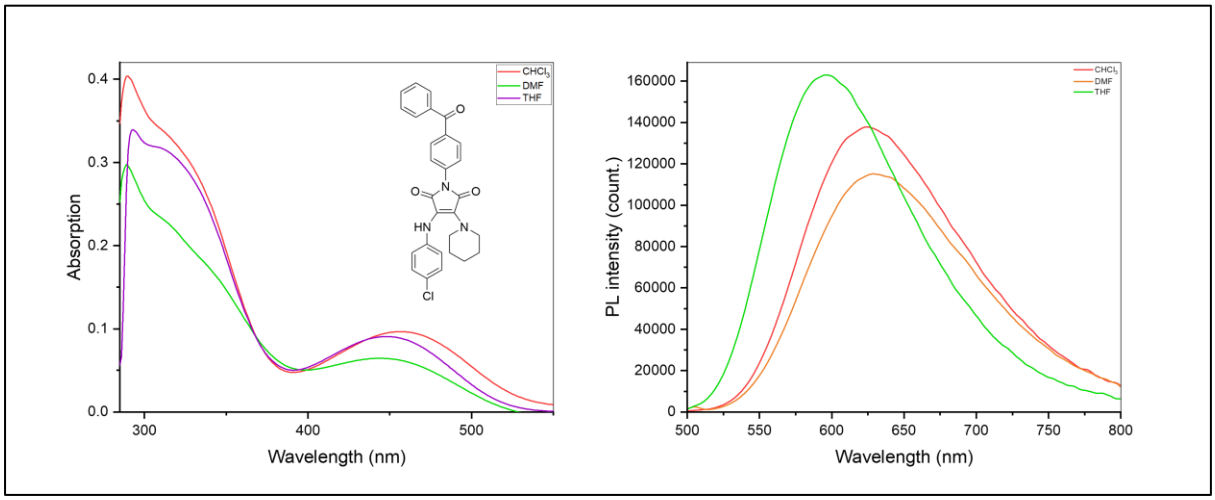


Figure 2 UV-vis and FL spectra in various solvents. ([c] = 0.01mg/ml).

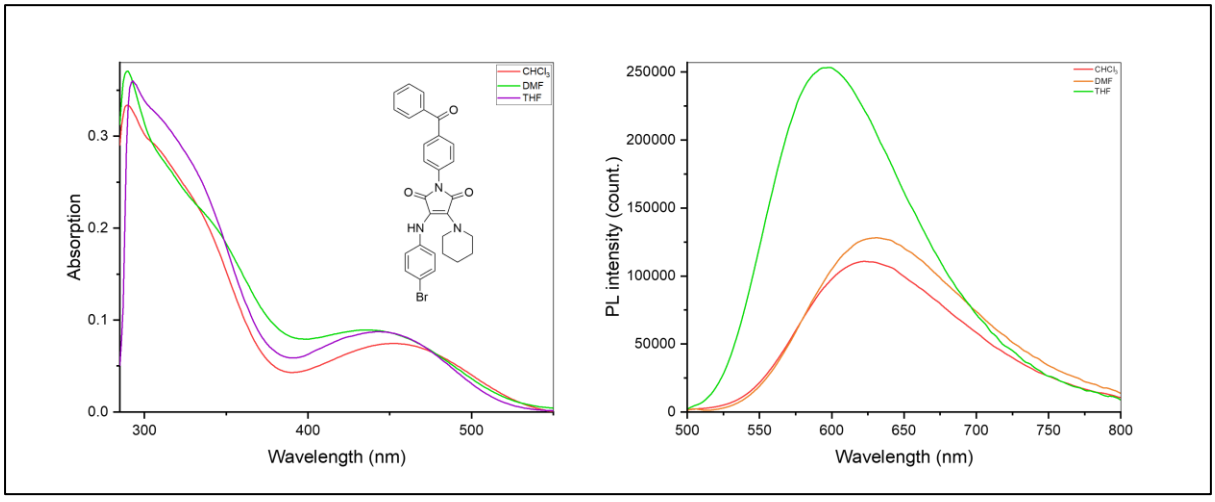

Figure 3 UV-vis and FL spectra in various solvents. ([c] = 0.01mg/ml).

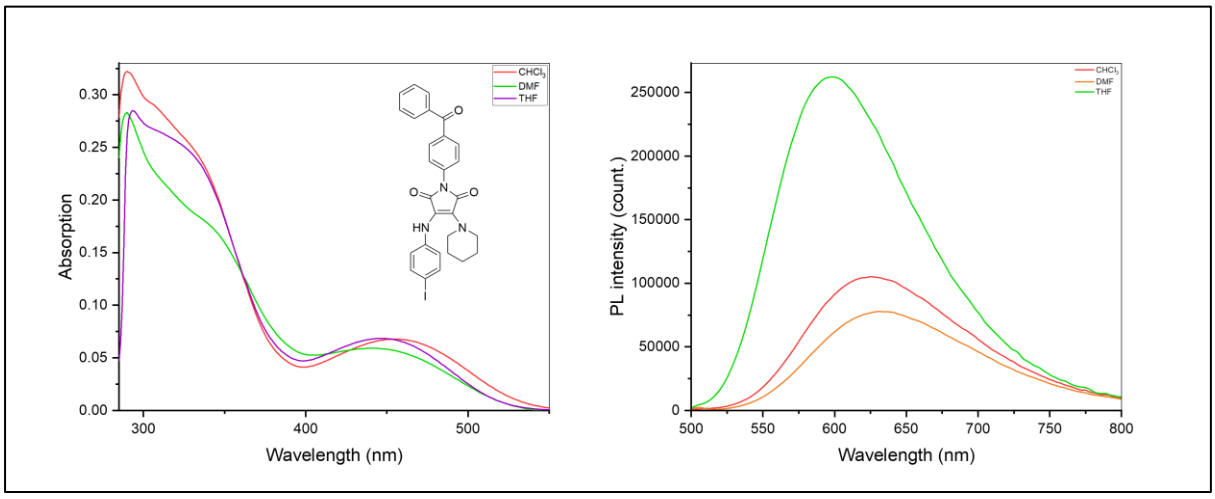


Figure 4 UV-vis and FL spectra in various solvents. ([c] = 0.01mg/ml).

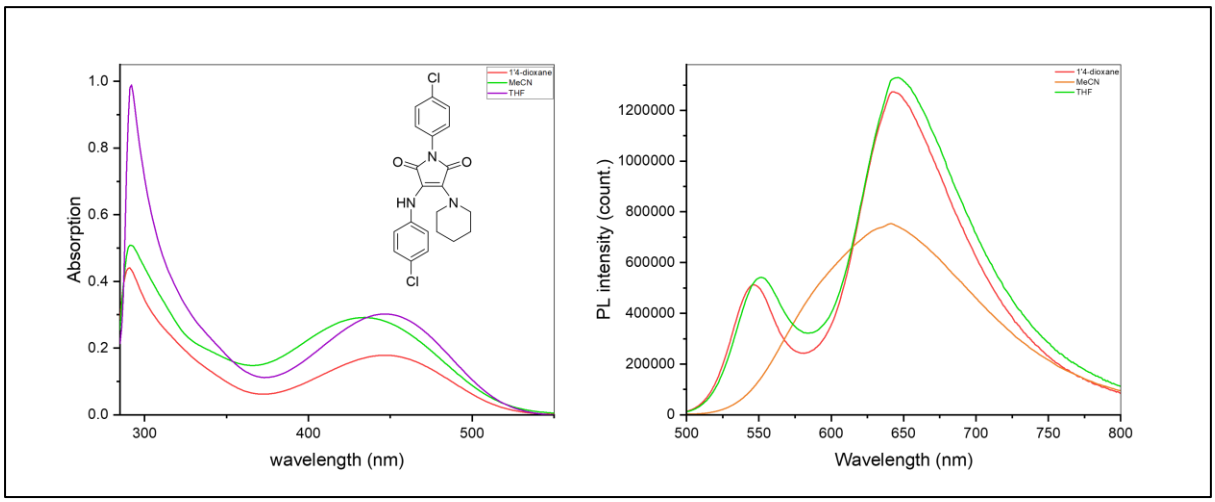


Figure 5 UV-vis and FL spectra in various solvents. ([c] = 0.01mg/ml).

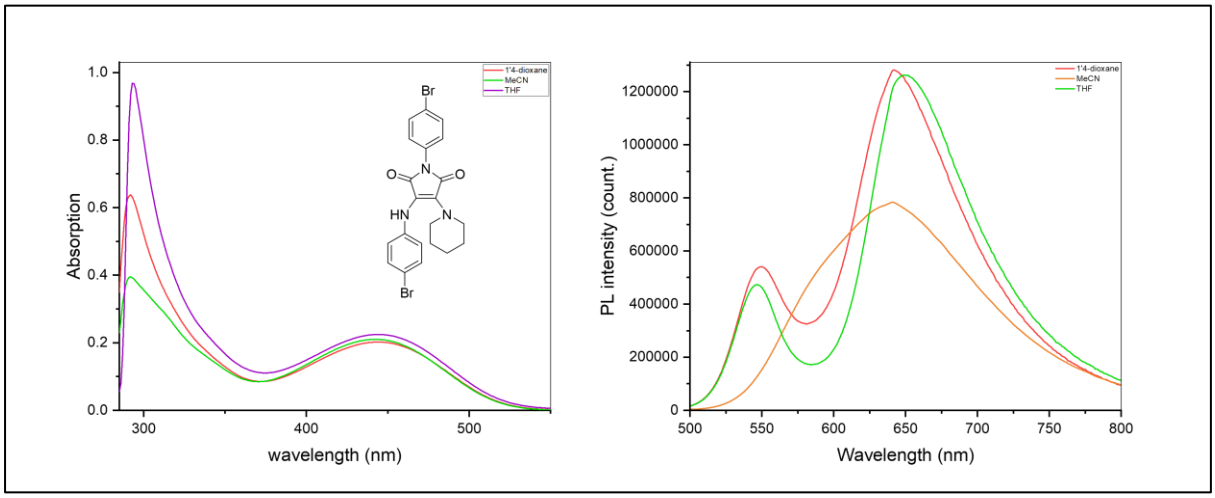

Figure 6 UV-vis and FL spectra in various solvents. ([c] = 0.01mg/ml).

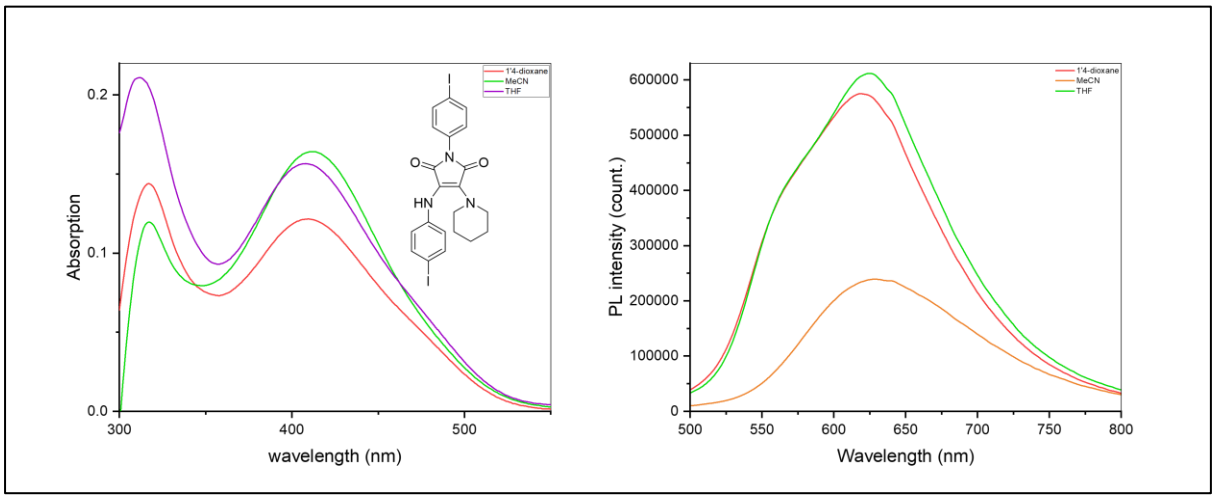


Figure 7 UV-vis and FL spectra in various solvents. ([c] = 0.01mg/ml).

**Phosphorescence spectra in low-temperature conditions**

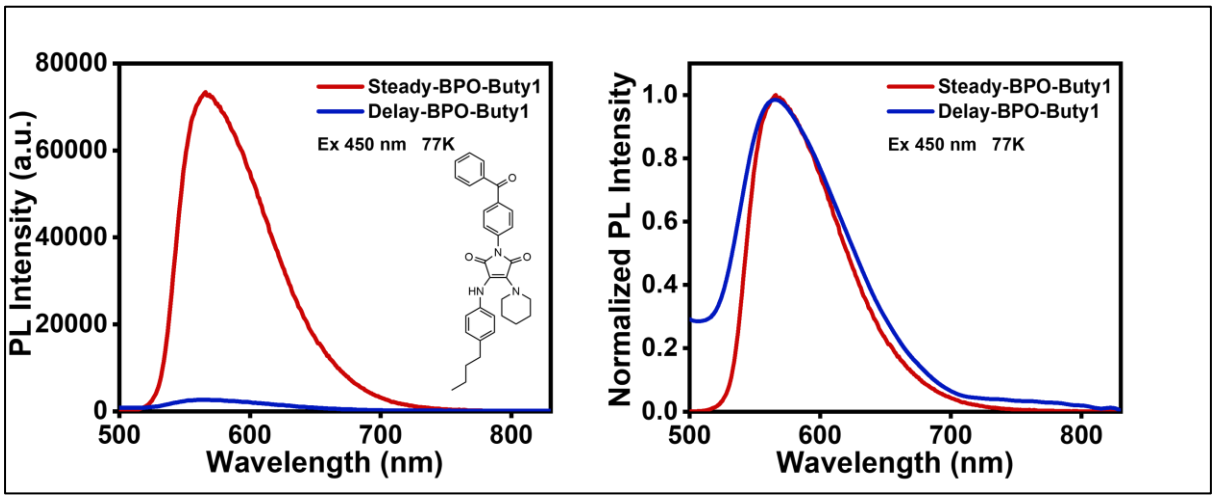


Figure 8 Phosphorescence spectra. (2-Methy-THF, $1\times10^{-5}$M, Ex = 450nm 77K).

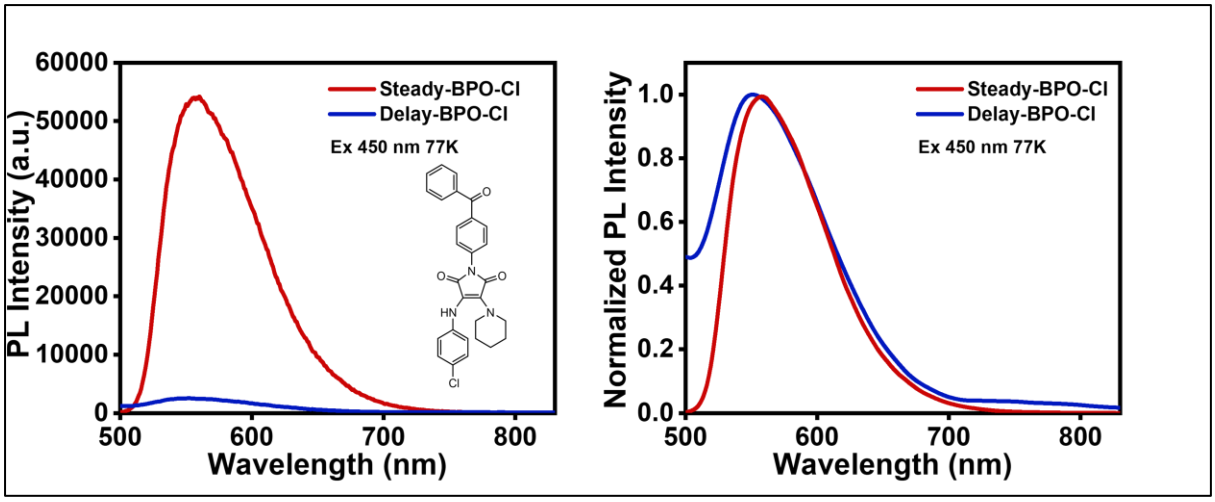


Figure 9 Phosphorescence spectra. (2-Methy-THF, $1\times10^{-5}$M, Ex = 450nm 77K).

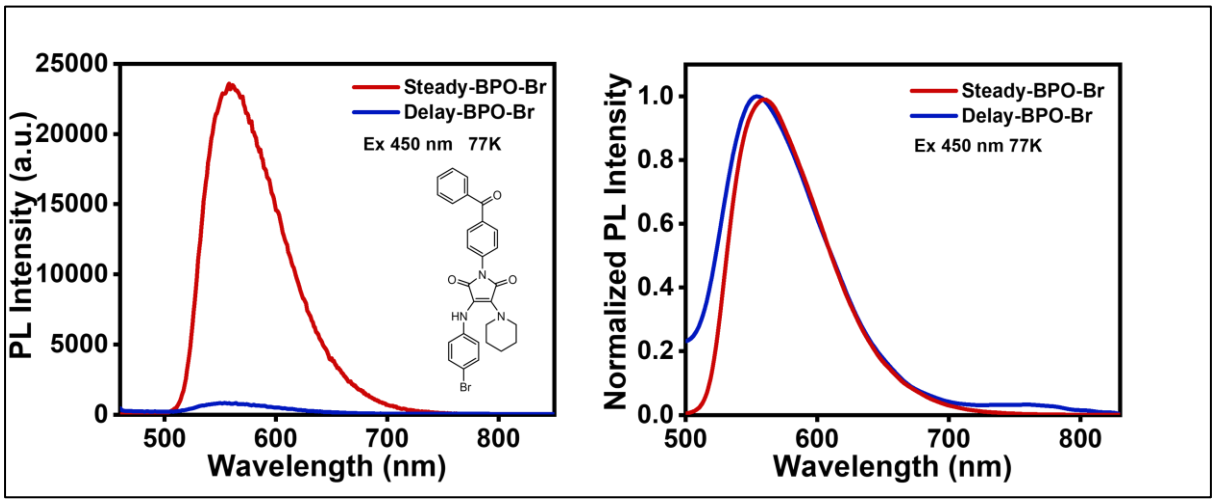


Figure 10 Phosphorescence spectra. (2-Methy-THF, $1\times10^{-5}$M, Ex = 450nm 77K).

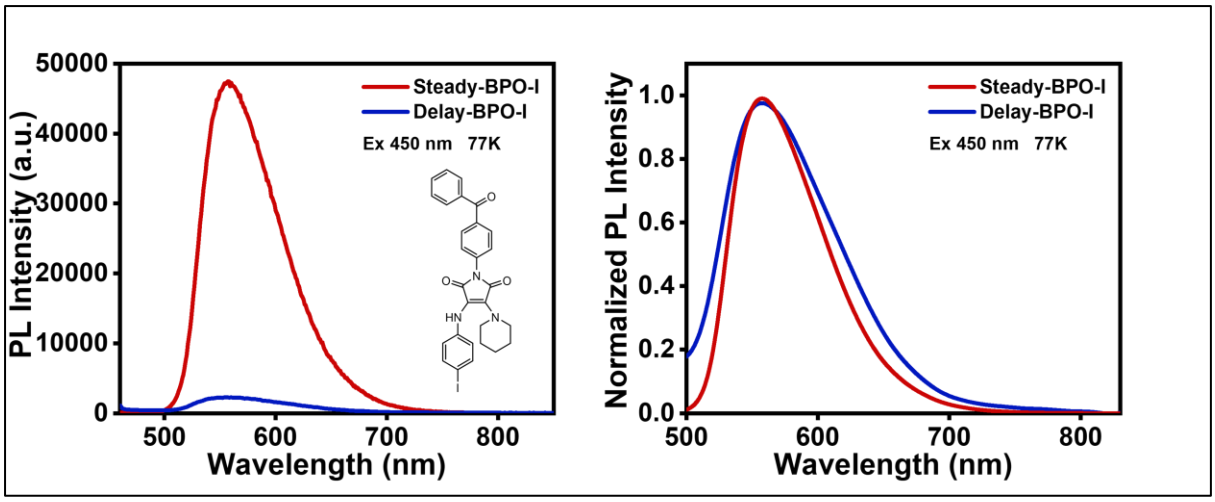


Figure 11 Phosphorescence spectra. (2-Methy-THF, $1\times10^{-5}$M, Ex = 450nm 77K).

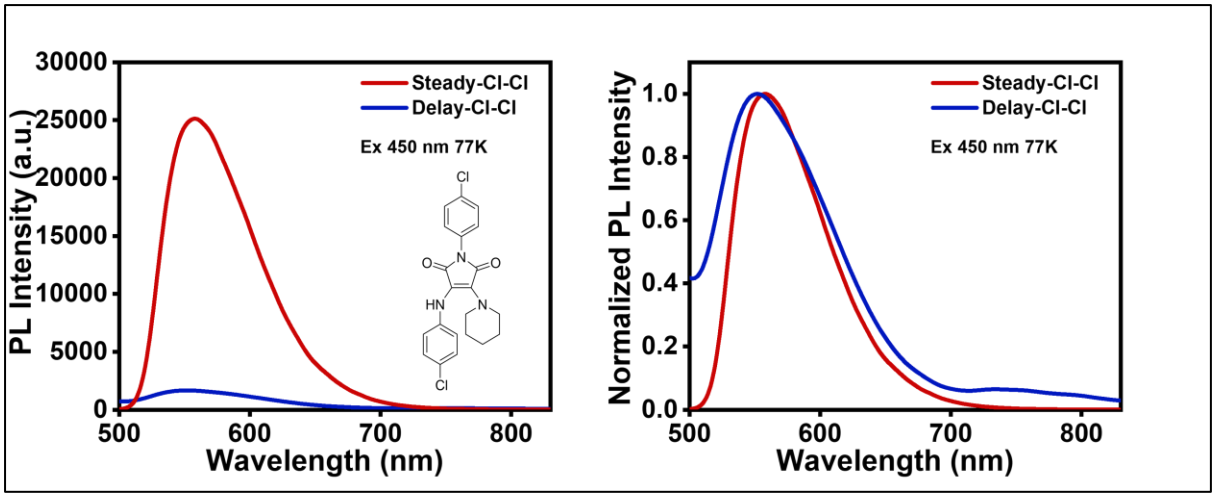


Figure 12 Phosphorescence spectra. (2-Methy-THF, $1\times10^{-5}$M, Ex = 450nm 77K).

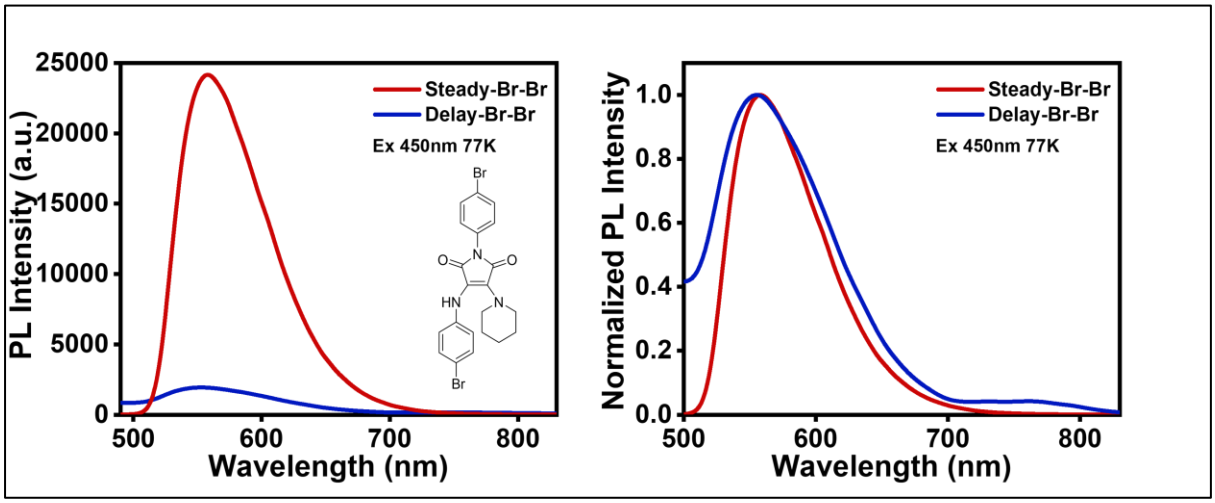


Figure 13 Phosphorescence spectra. (2-Methy-THF, $1\times10^{-5}$M, Ex = 450nm 77K).

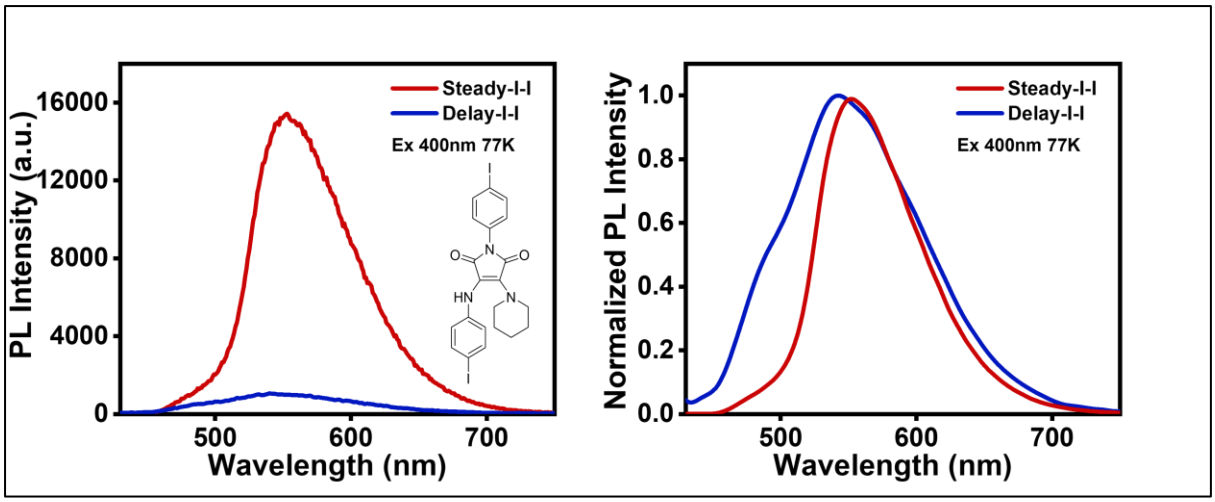


Figure 14 Phosphorescence spectra. (2-Methy-THF, $1\times10^{-5}$M, Ex = 450nm 77K).

**Phosphorescence spectra via host-guest doping (small – small molecule)**

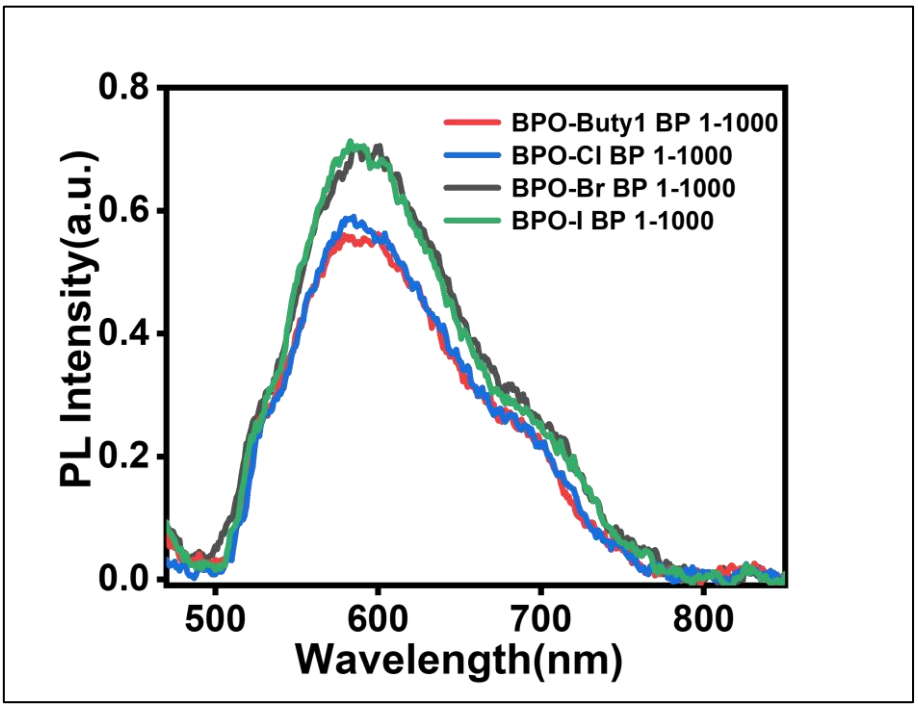


Figure 15 Phosphorescence spectra of Benzophenone-based maleimide fluorophores (MF). (the doping ratio was BPO: MF = 1000:1, Ex = 450nm).

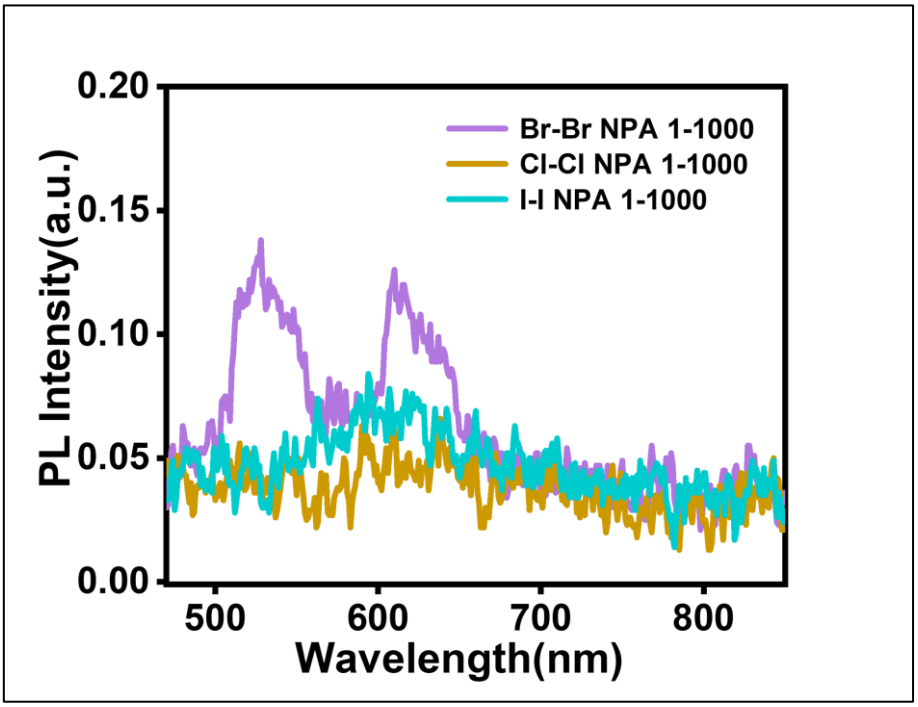


Figure 15 Phosphorescence spectra of halo-based maleimide fluorophores (MF). (the doping ratio was NPA: MF = 1000:1, Ex = 450nm).

**Phosphorescence spectra via host-guest doping (polymer – small molecule)**

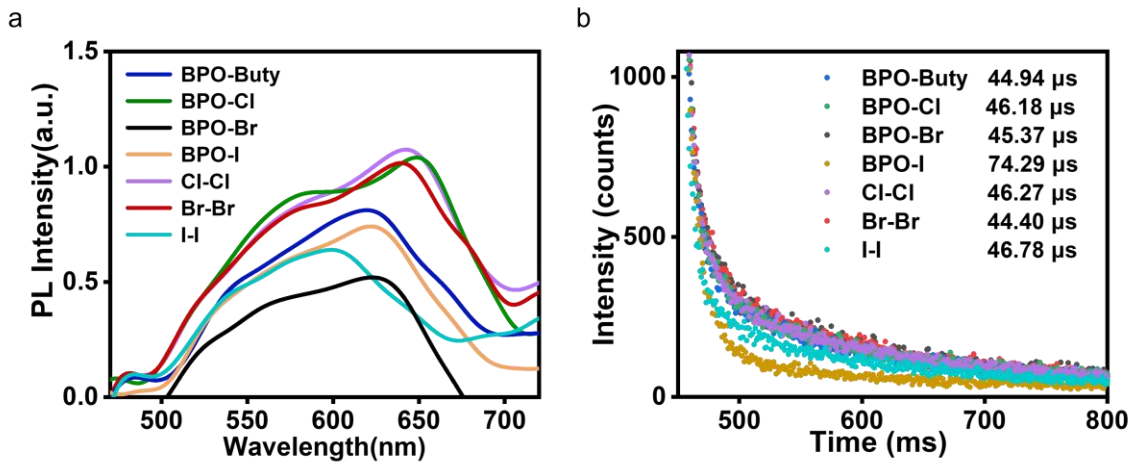


Figure 16 (a) Phosphorescence spectra of each maleimide fluorophore (MF). (the doping ratio was PMMA (Mn = 35000): MF = 1000:1, Ex = 450nm). (b) Phosphorescence lifetime.

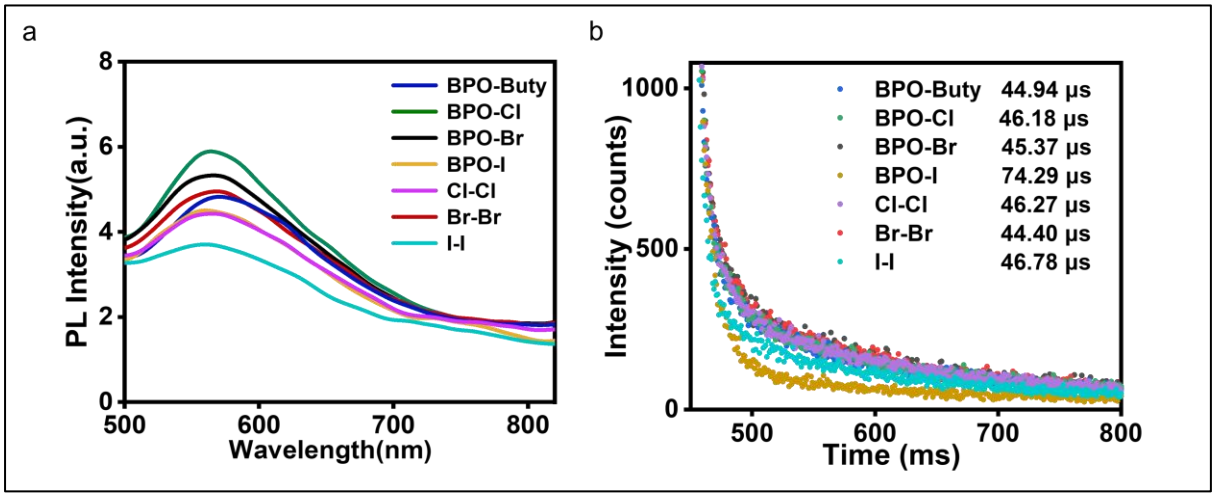


Figure 17 (a) Phosphorescence spectra of each maleimide fluorophore (MF), the data was recorded after irradiating by UV (365nm) for 3 min. (the doping ratio was PMMA (Mn = 35000): MF = 1000:1, Ex = 450nm). (b) Phosphorescence lifetime.

## 4.6.5 Nuclear magnetic resonance spectroscopy

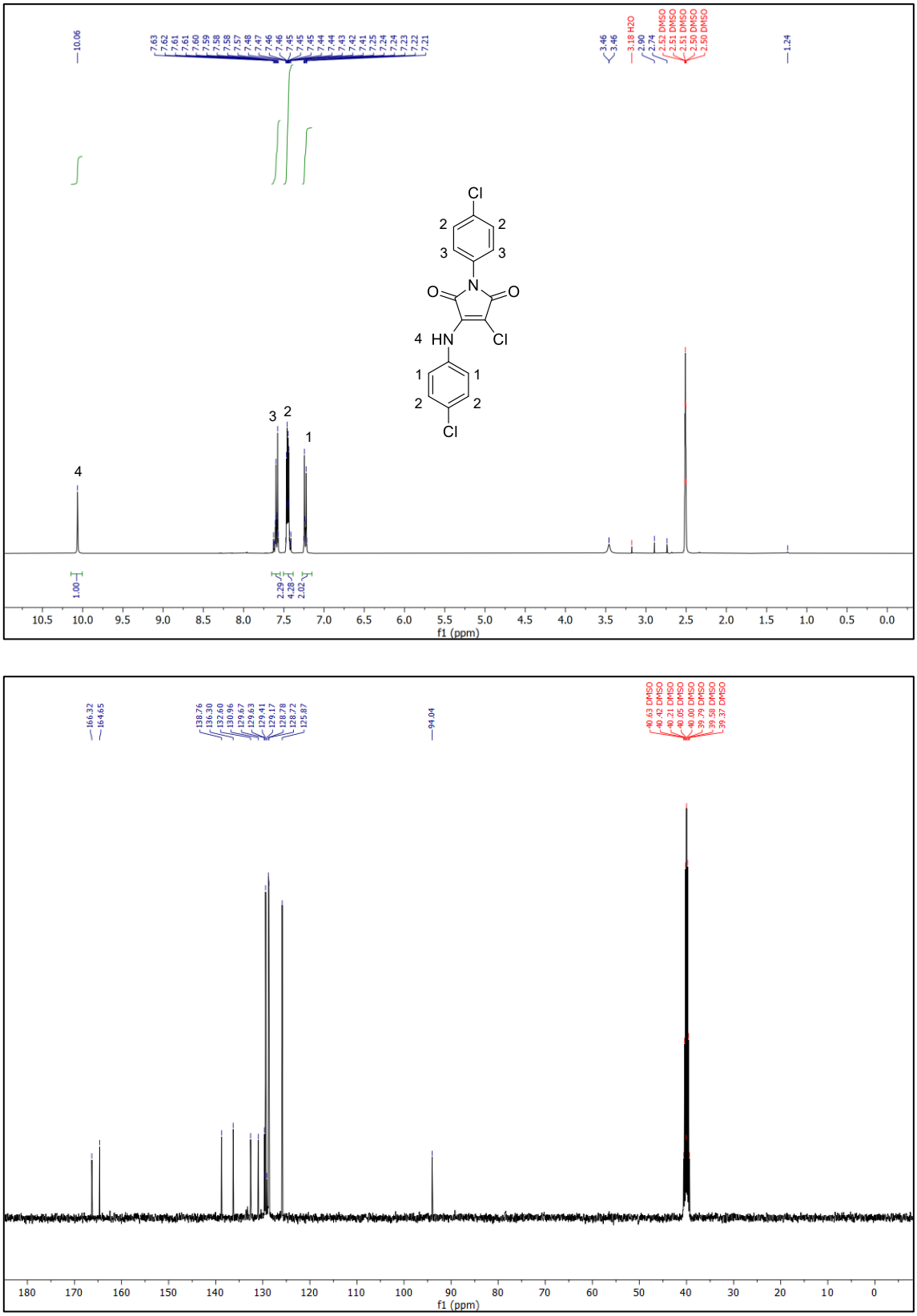


Figure 18 $^{1}H$ and $^{13}C$ NMR spectra (DMSO-d6, 400MHz).

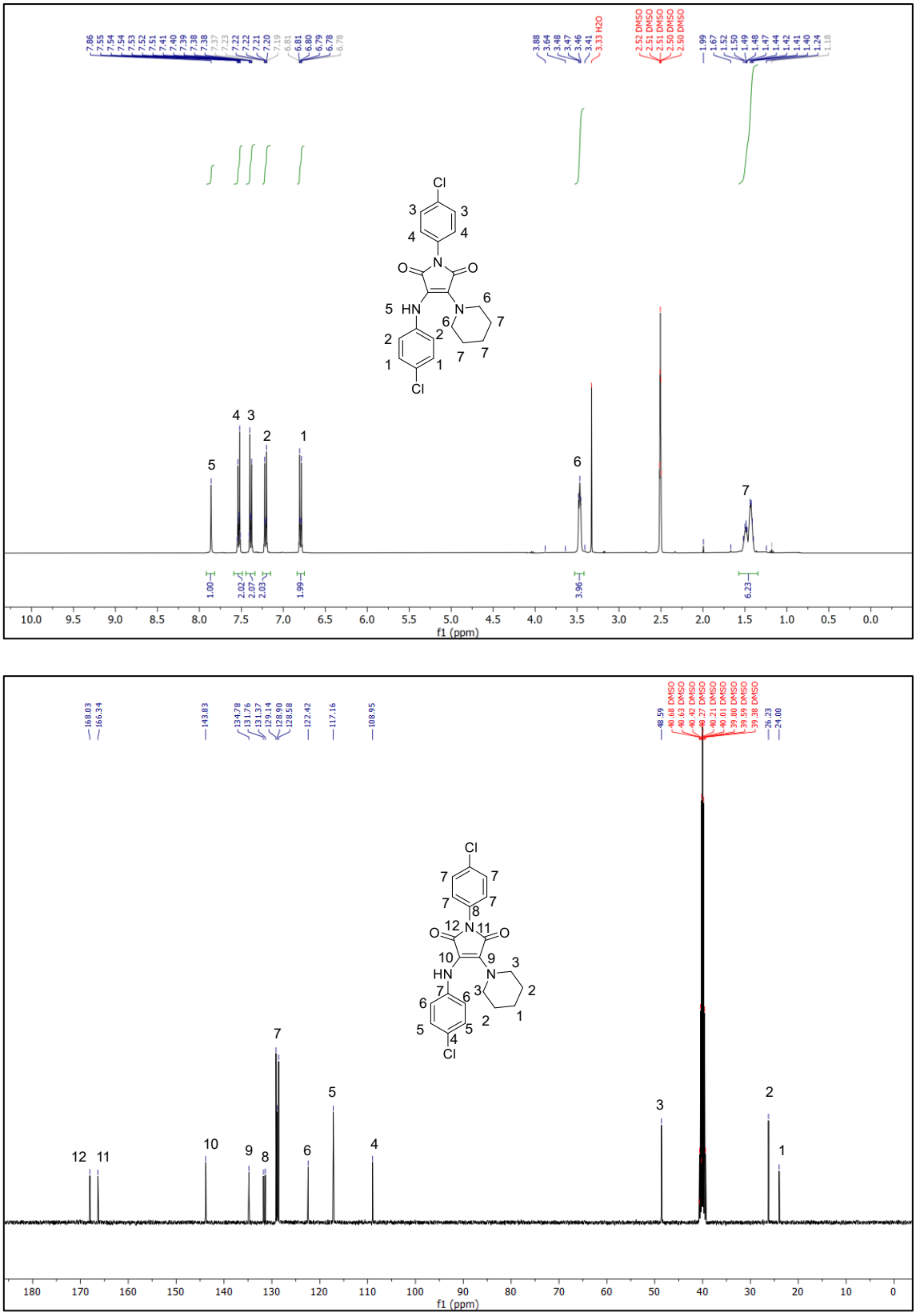


Figure 19 $^{1}H$ and $^{13}C$ NMR spectra (DMSO-d6, 400MHz).

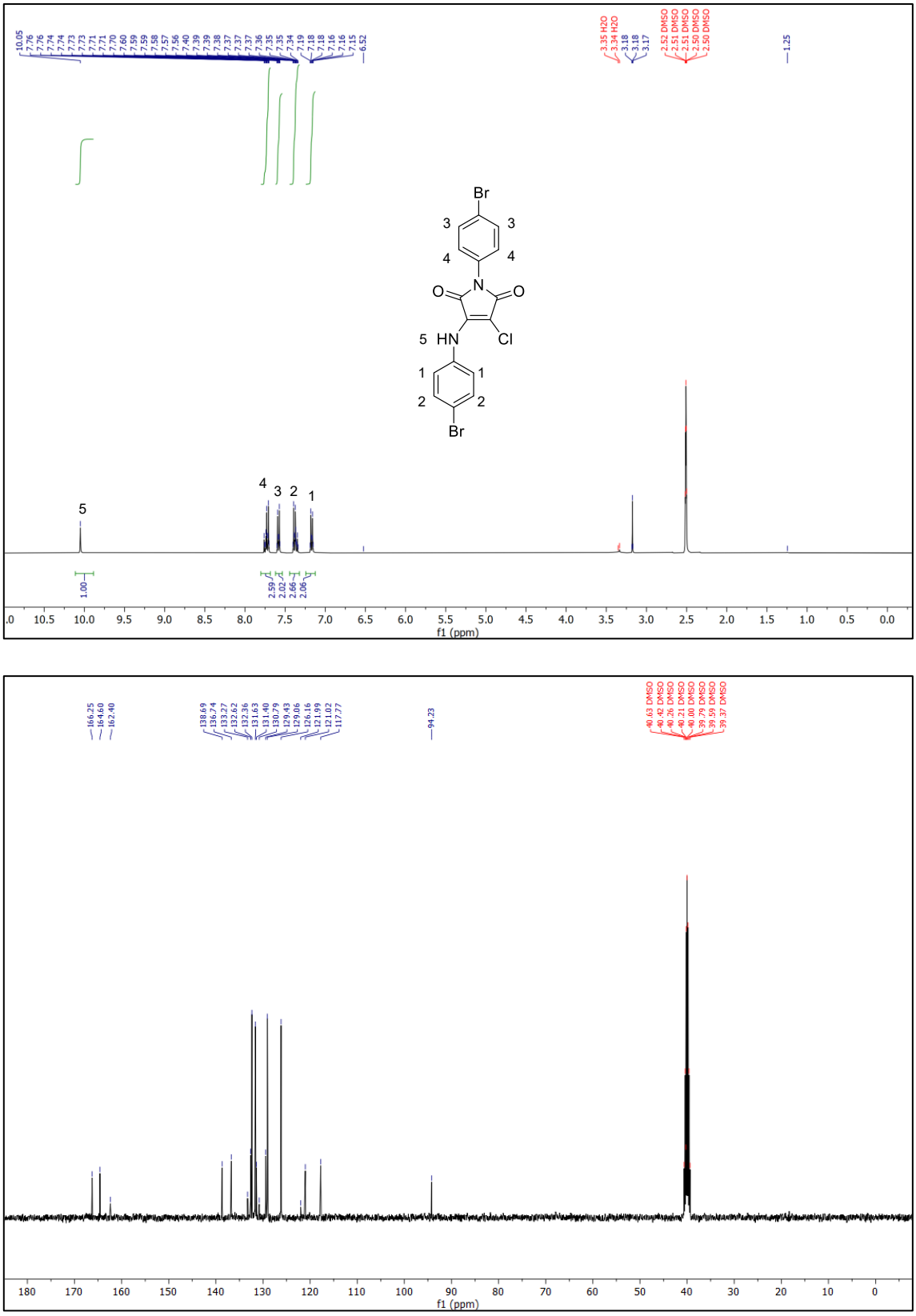


Figure 20 $^{1}H$ and $^{13}C$ NMR spectra (DMSO-d6, 400MHz).

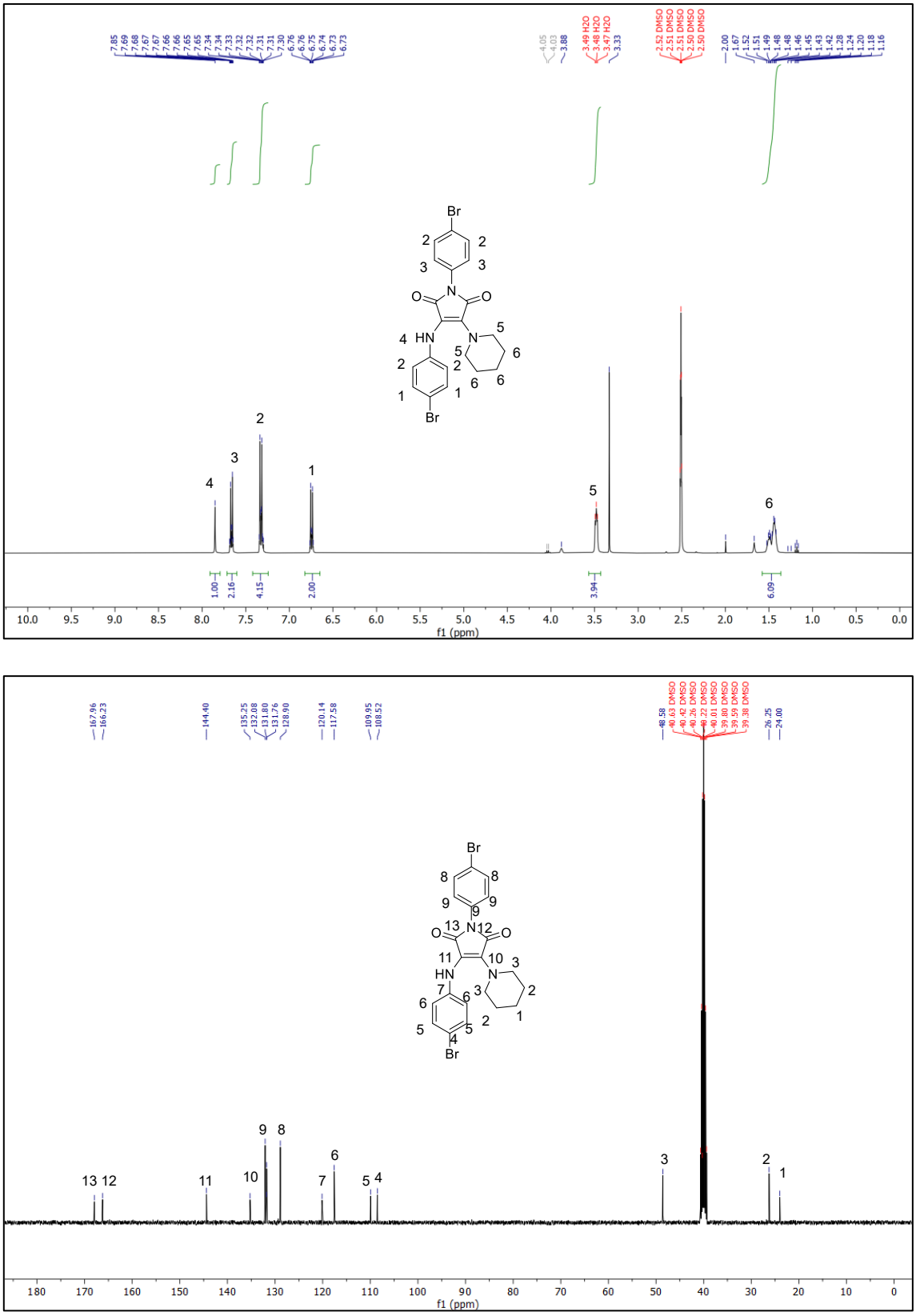


Figure 21 $^{1}H$ and $^{13}C$ NMR spectra (DMSO-d6, 400MHz).

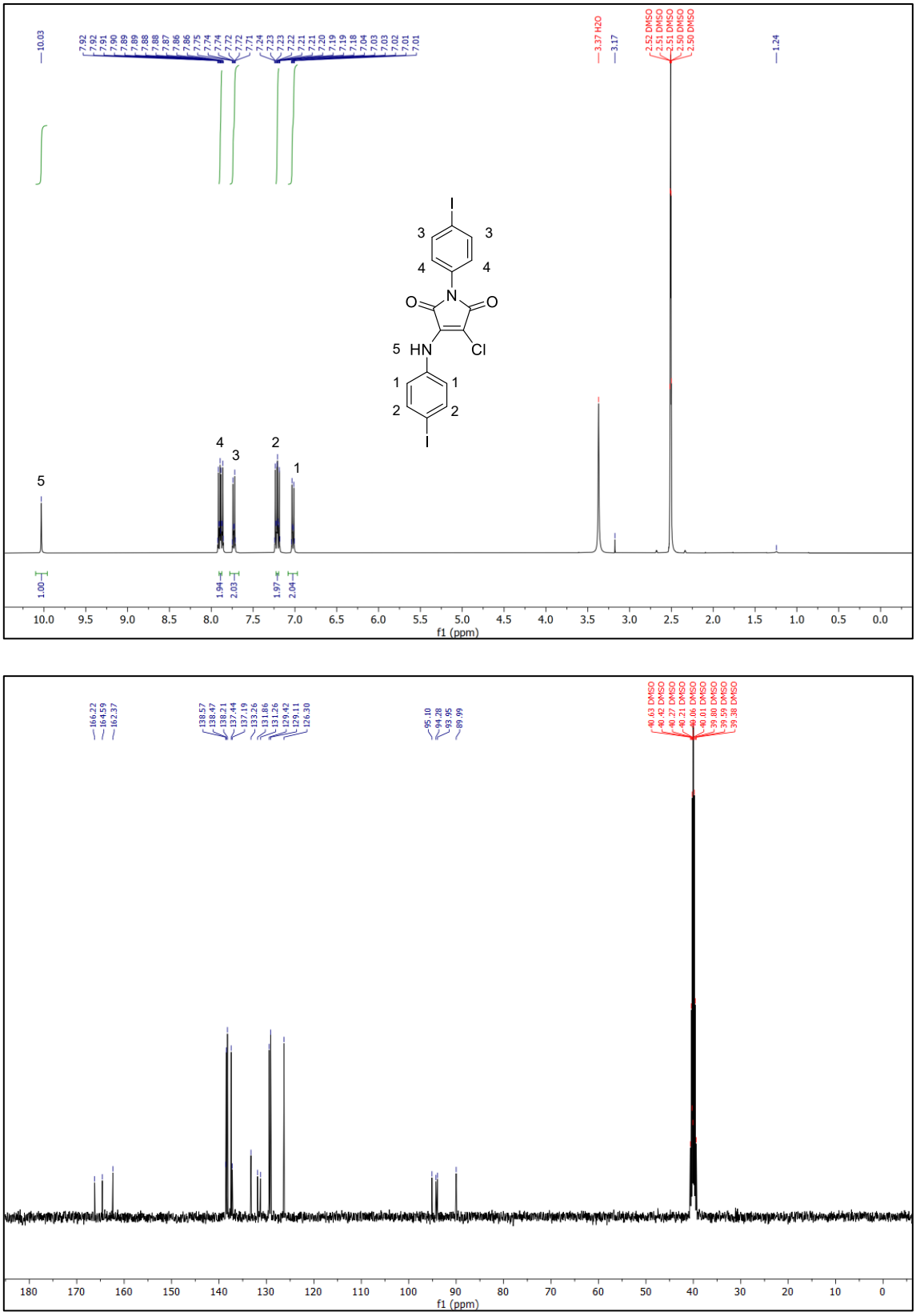


Figure 22 $^{1}H$ and $^{13}C$ NMR spectra (DMSO-d6, 400MHz).

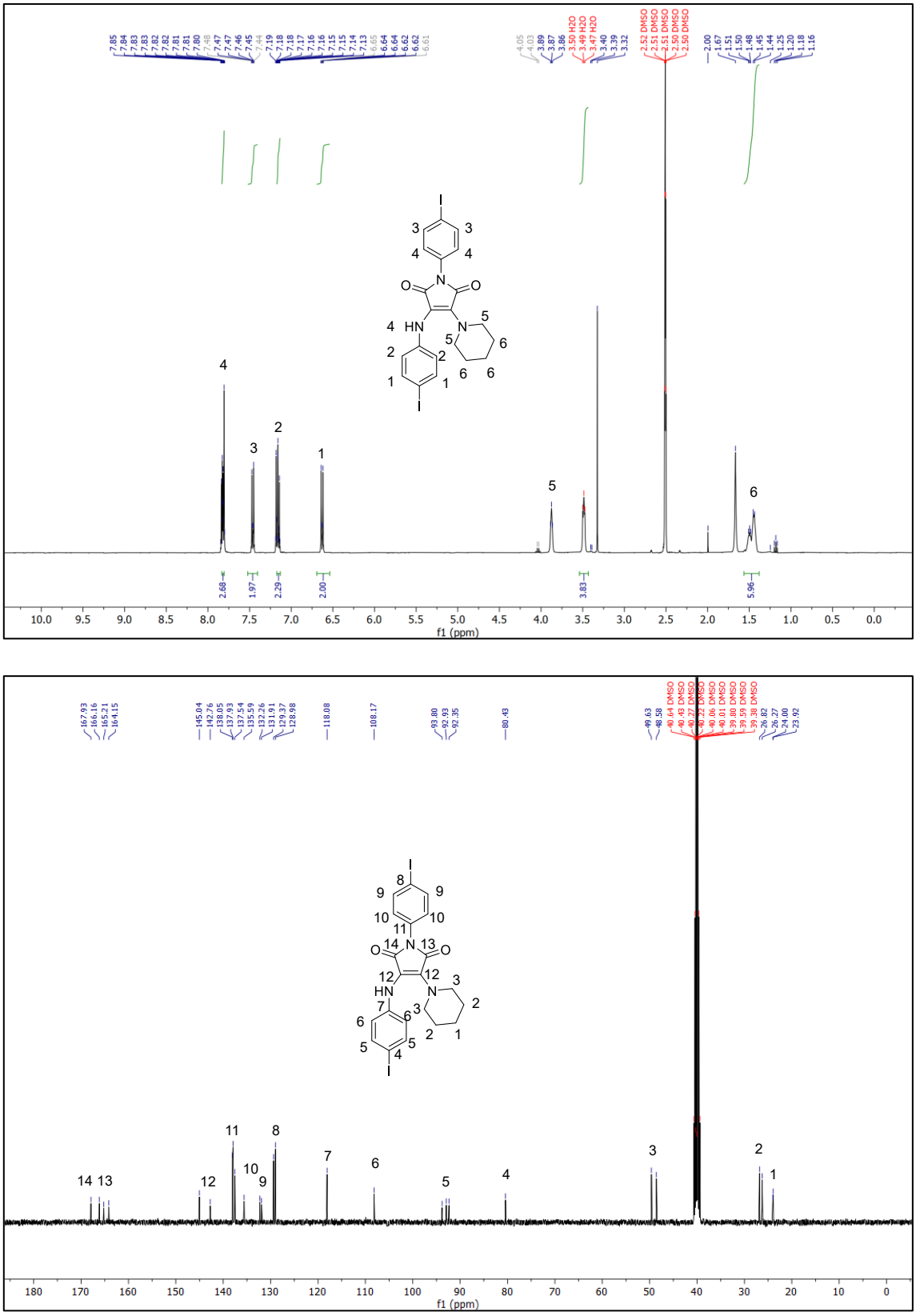


Figure 23 $^{1}H$ and $^{13}C$ NMR spectra (DMSO-d6, 400MHz).

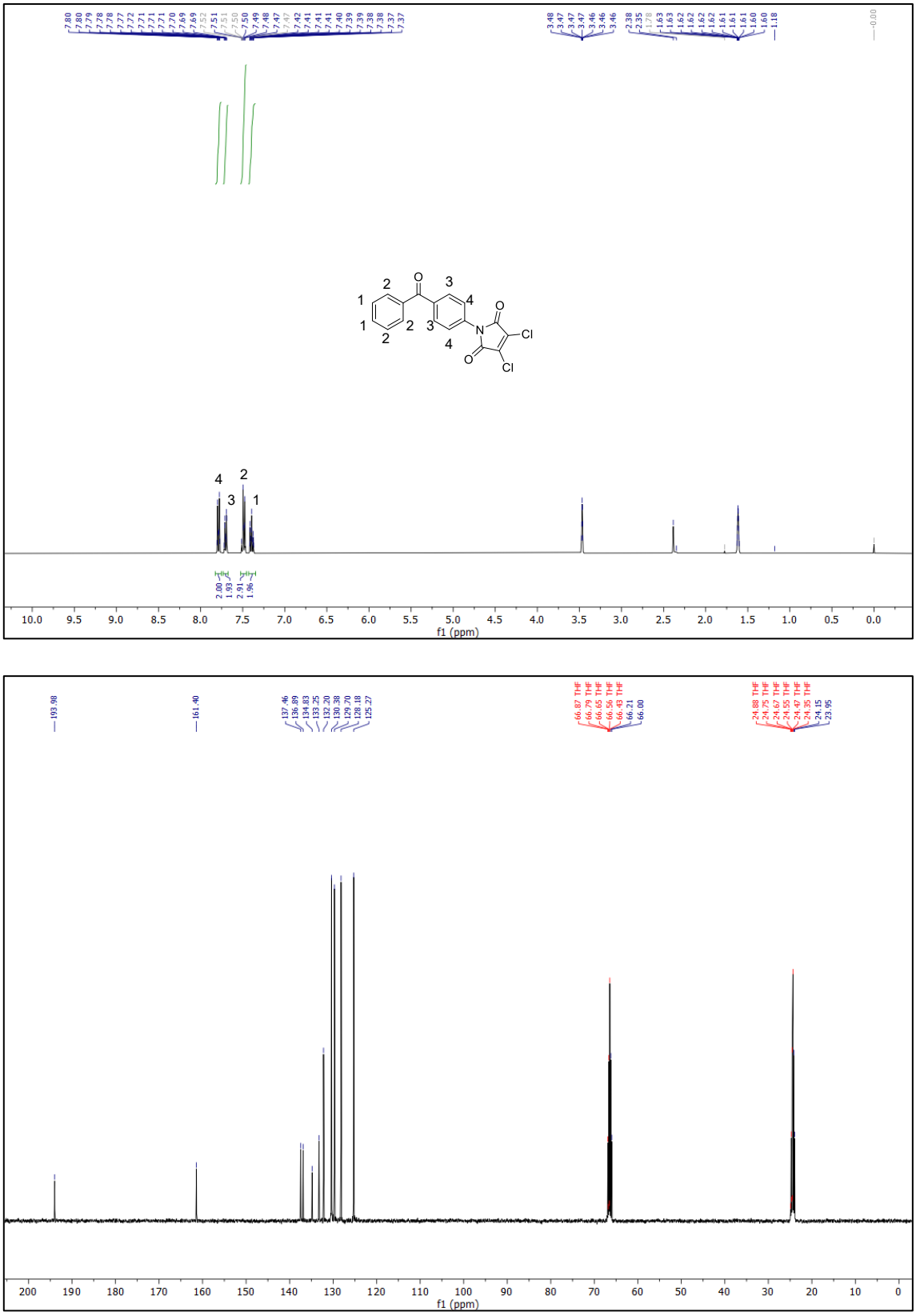


Figure 24 $^{1}H$ and $^{13}C$ NMR spectra (DMSO-d6, 400MHz).

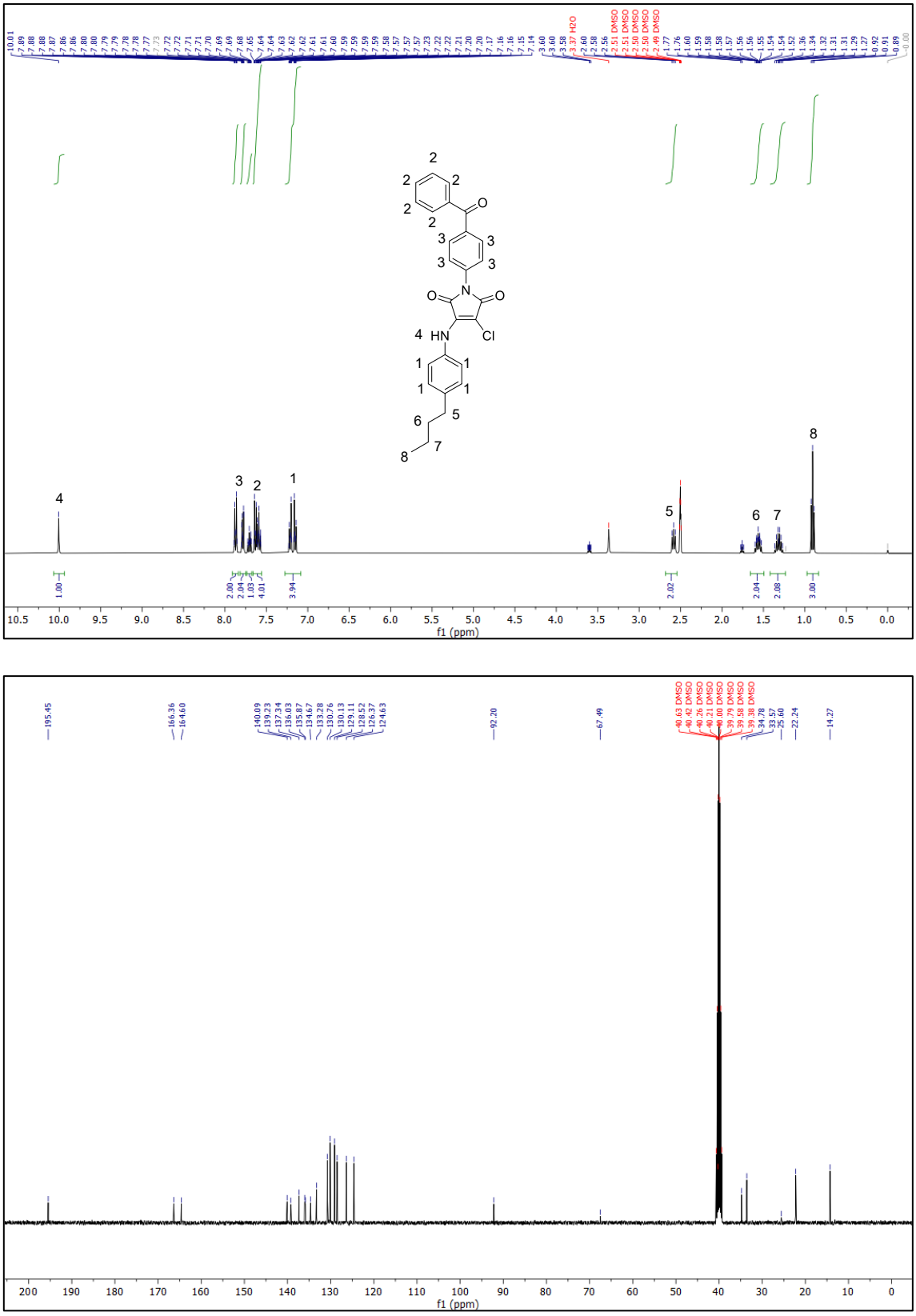


Figure 25 $^{1}H$ and $^{13}C$ NMR spectra (DMSO-d6, 400MHz).

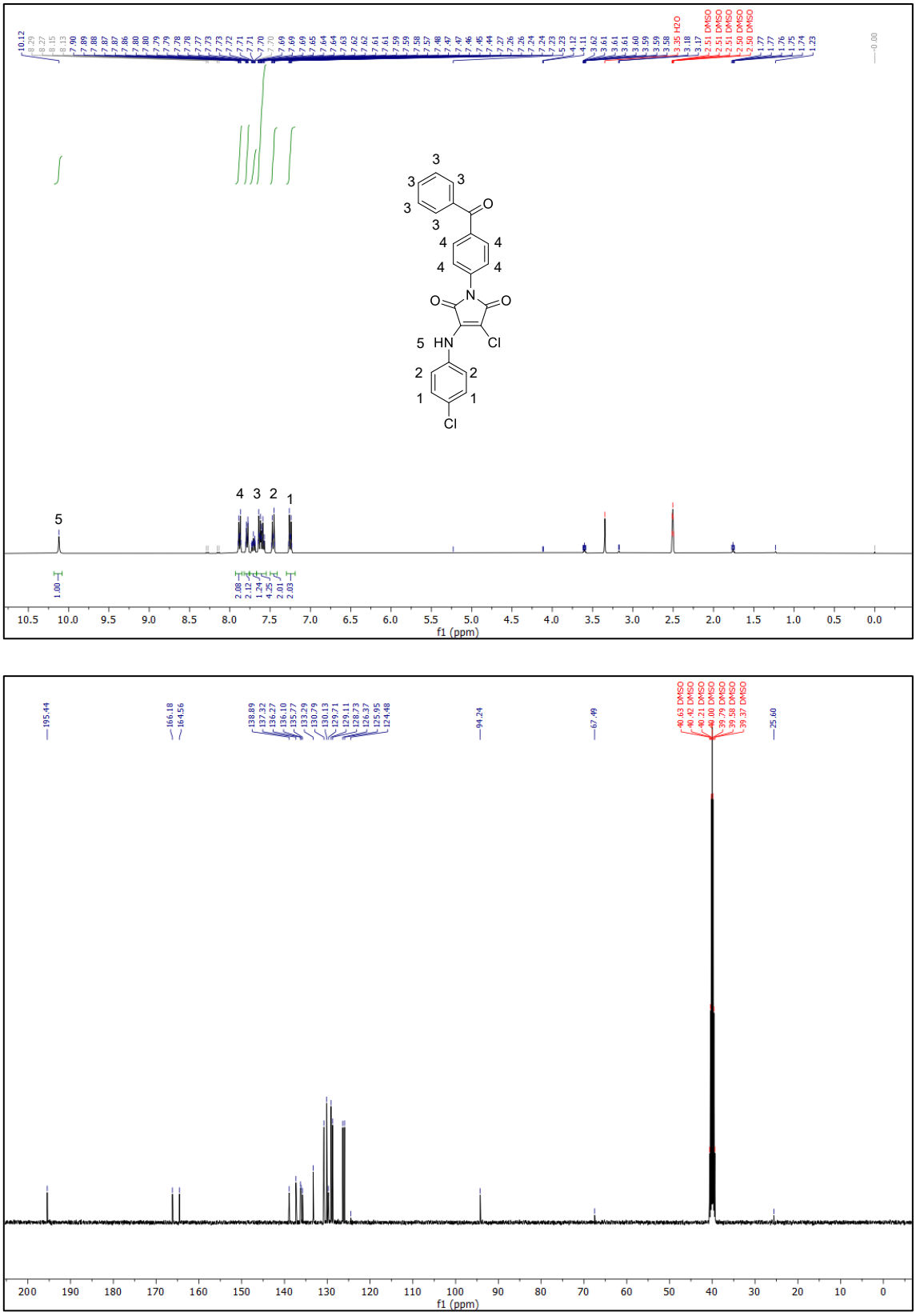


Figure 26 $^{1}H$ and $^{13}C$ NMR spectra (DMSO-d6, 400MHz).

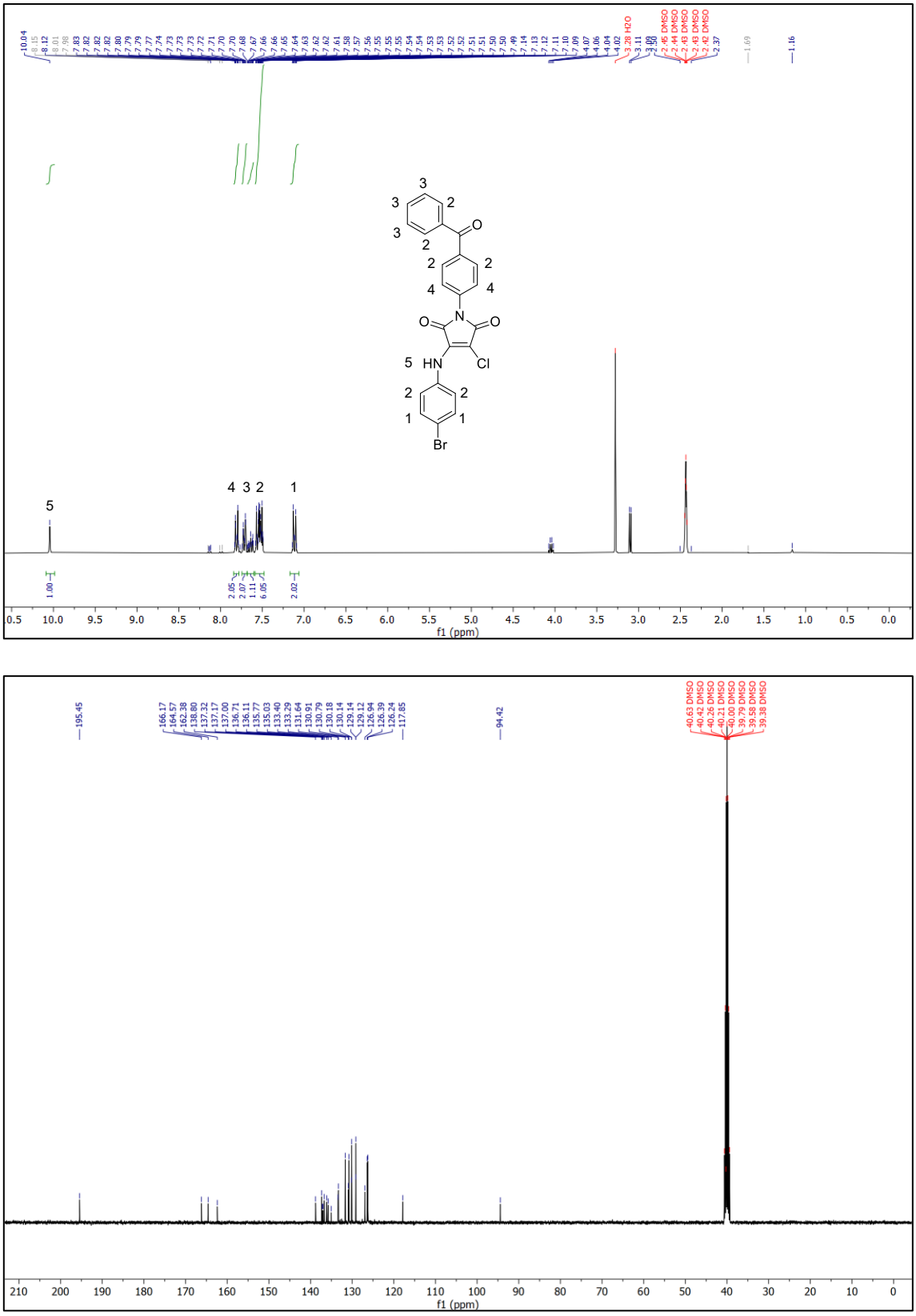


Figure 27 $^{1}H$ and $^{13}C$ NMR spectra (DMSO-d6, 400MHz).

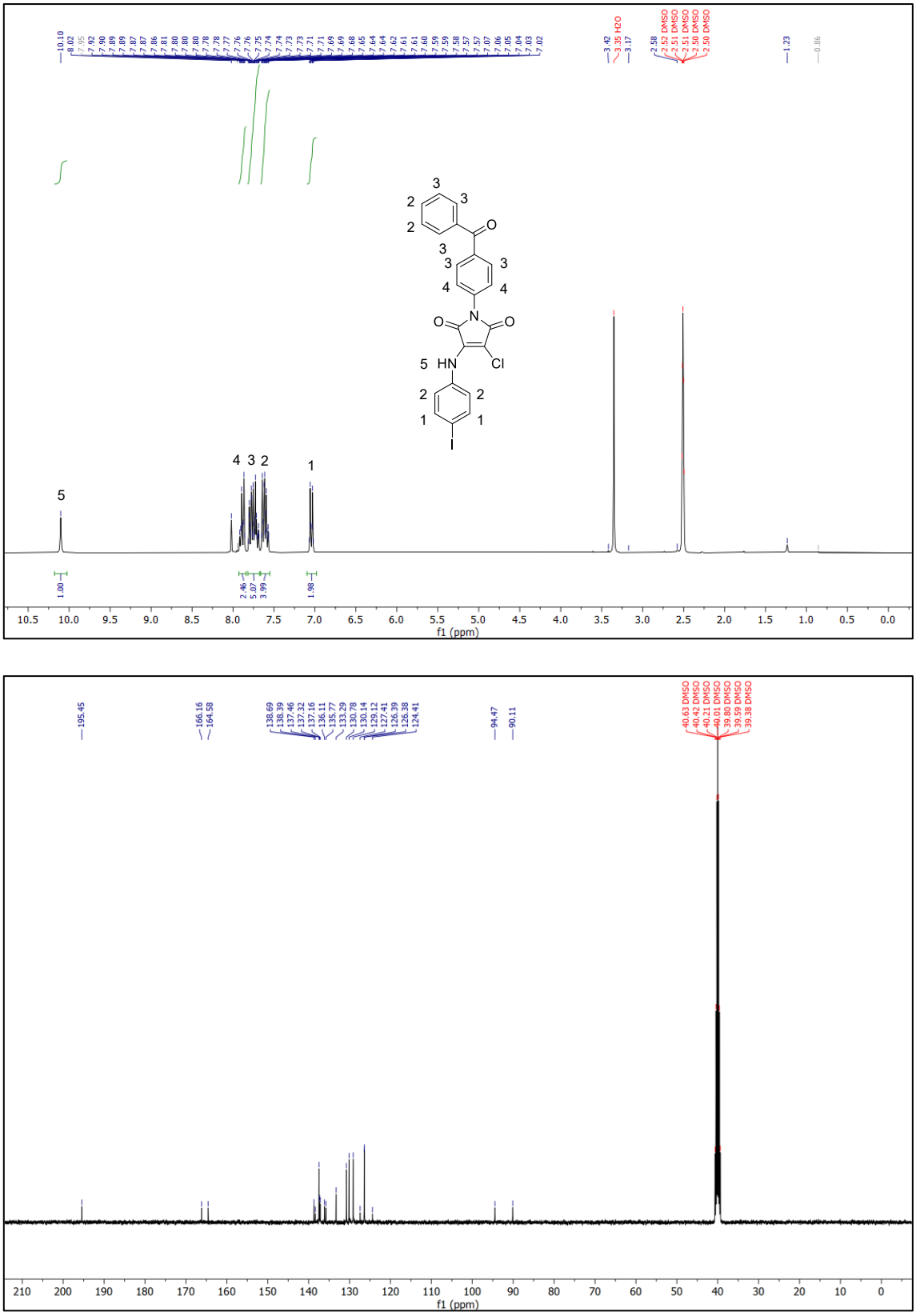


Figure 28 $^{1}H$ and $^{13}C$ NMR spectra (DMSO-d6, 400MHz).

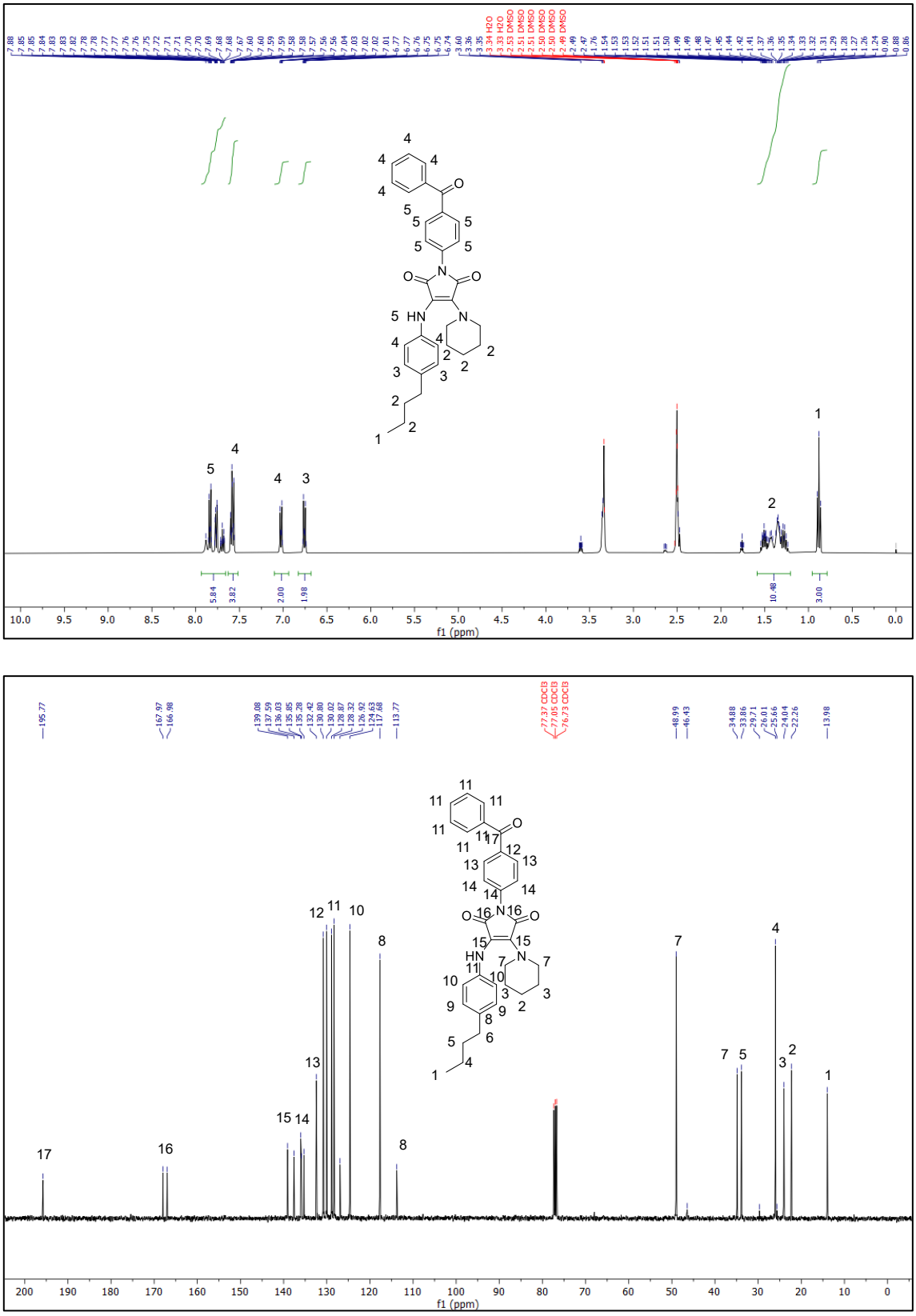

Figure 29 $^{1}H$ and $^{13}C$ NMR spectra (DMSO-d6, 400MHz).

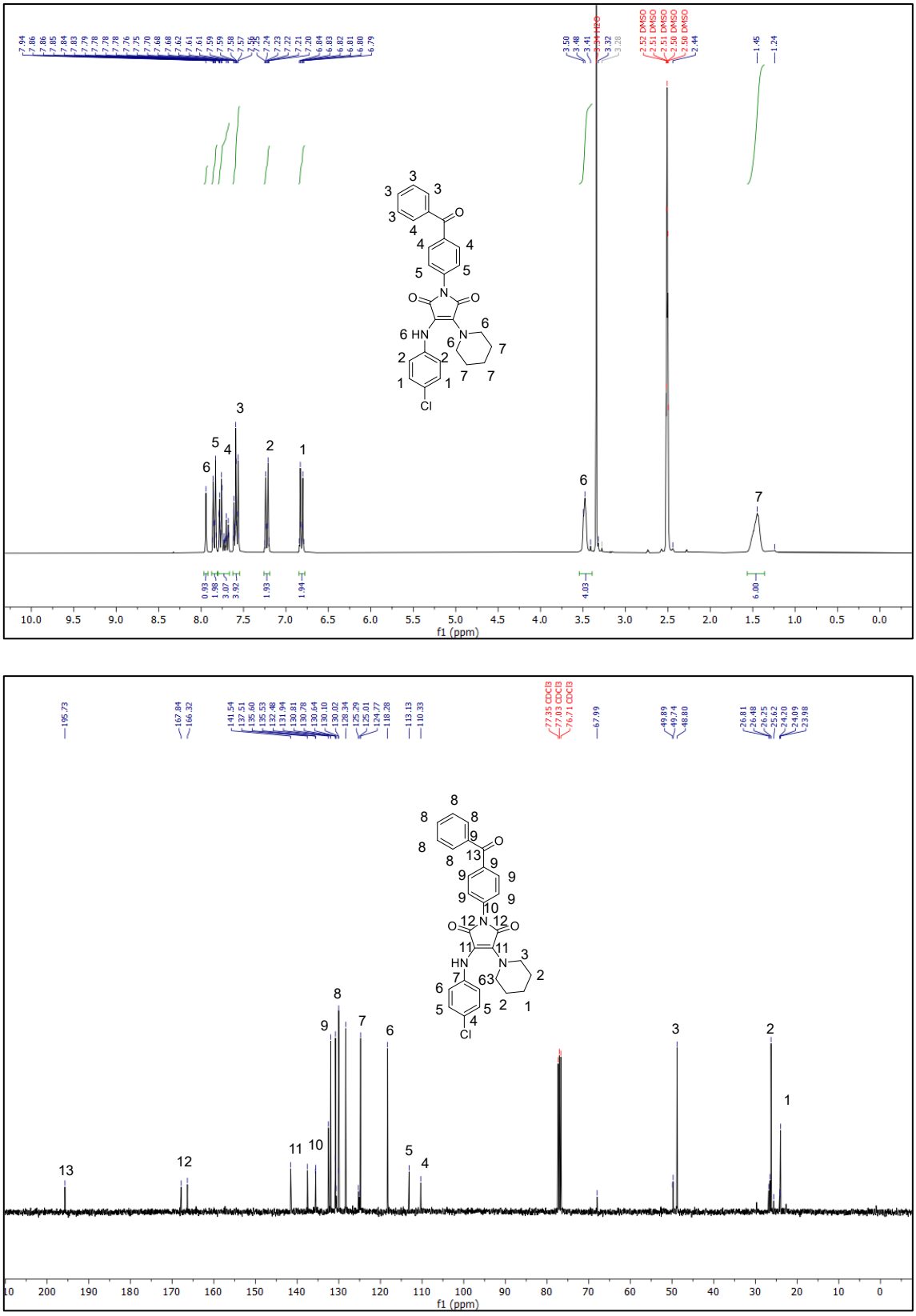


Figure 30 $^{1}H$ and $^{13}C$ NMR spectra (DMSO-d6, 400MHz).

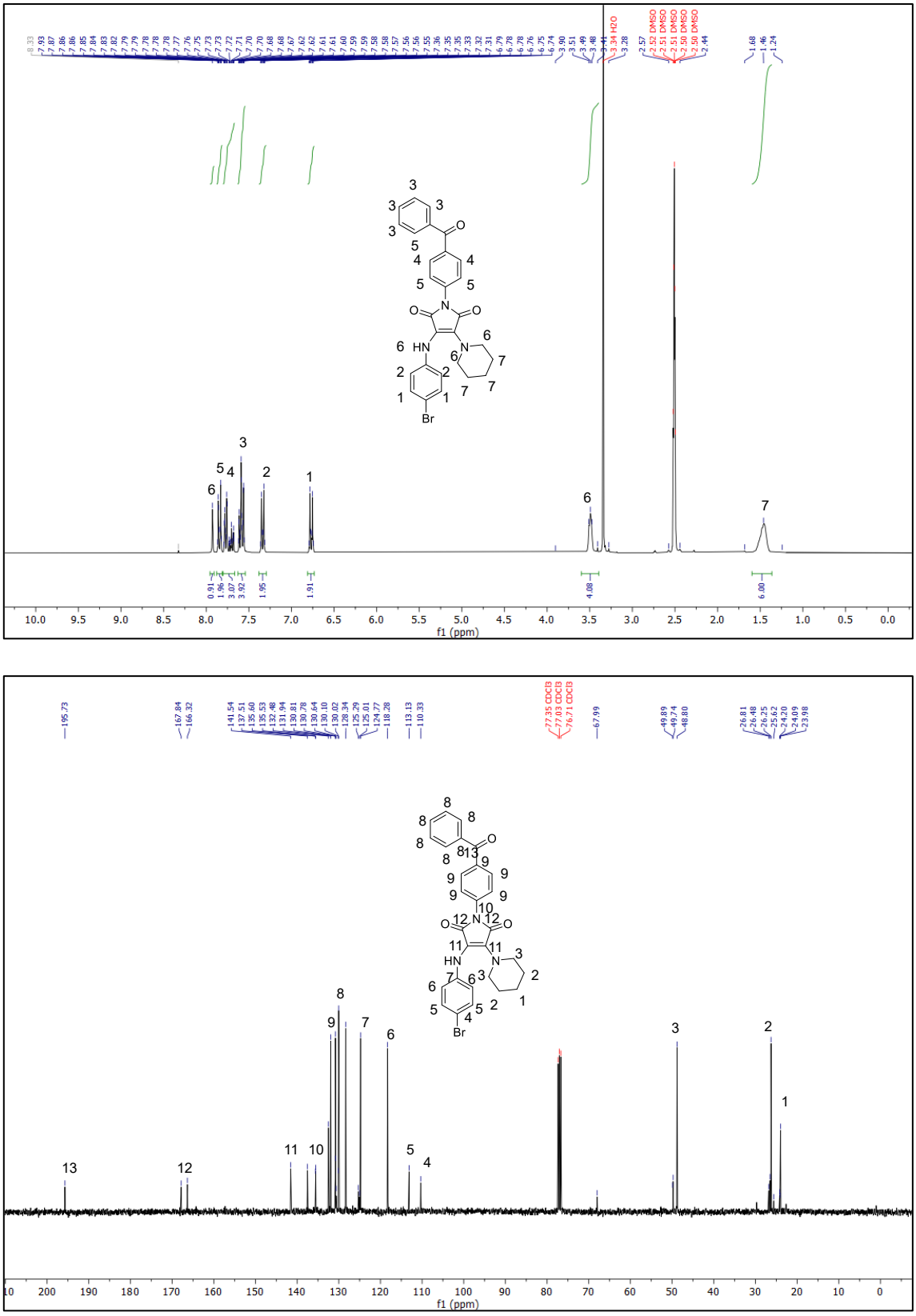


Figure 31 $^{1}H$ and $^{13}C$ NMR spectra (DMSO-d6, 400MHz).

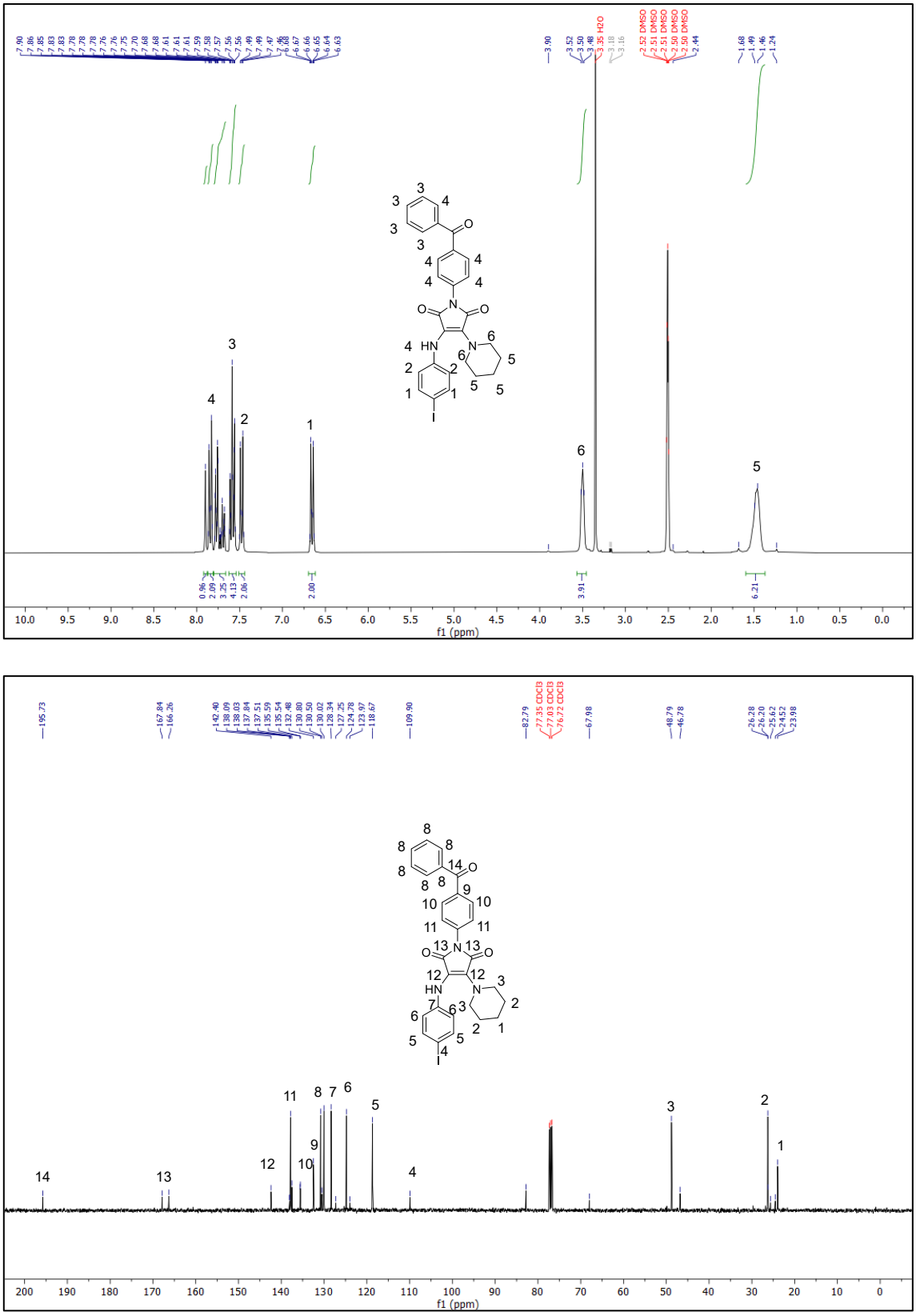

Figure 32 $^{1}H$ and $^{13}C$ NMR spectra (DMSO-d6, 400MHz).

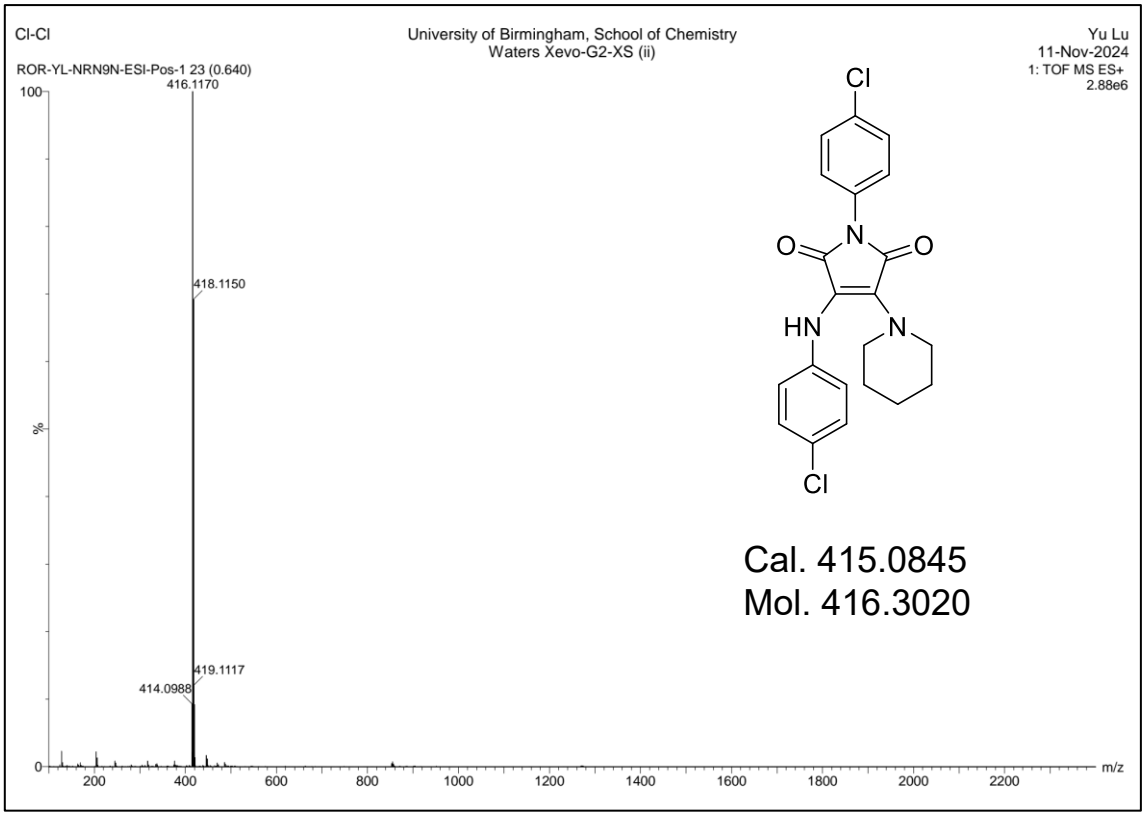
Cl-Cl
University of Birmingham, School of Chemistry
Waters Xevo-G2-XS (ii)
Yu Lu
11-Nov-2024
1: TOF MS ES+
2.88e6
ROR-YL-NRN9N-ESI-Pos-1 23 (0.640)
416.1170
418.1150
419.1117
414.0988
100
%
0
200
400
600
800
1000
1200
1400
1600
1800
2000
2200
m/z
Cl
N
O
O
HN
N
Cl
Cal. 415.0845
Mol. 416.3020

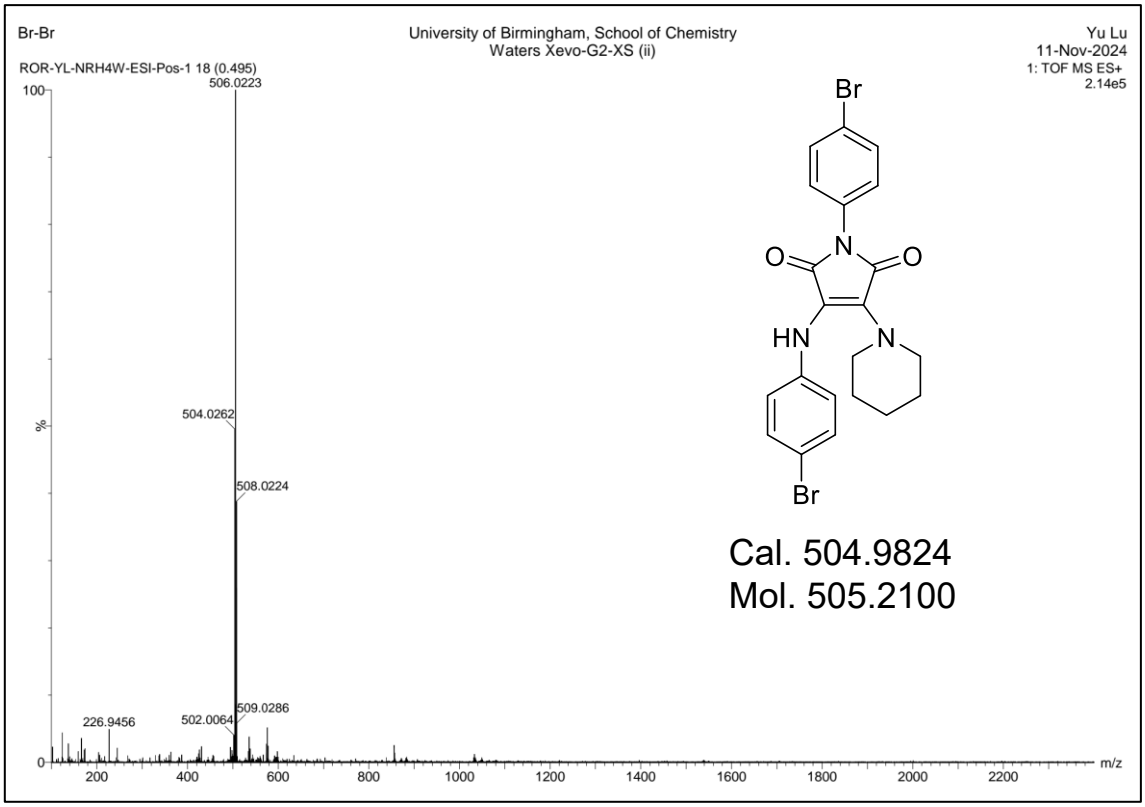
Br-Br
University of Birmingham, School of Chemistry
Waters Xevo-G2-XS (ii)
Yu Lu
11-Nov-2024
1: TOF MS ES+
2.14e5
ROR-YL-NRH4W-ESI-Pos-1 18 (0.495)
506.0223
504.0262
508.0224
509.0286
502.0064
226.9456
100
%
0
200
400
600
800
1000
1200
1400
1600
1800
2000
2200
m/z
Br
N
O
O
HN
N
Br
Cal. 504.9824
Mol. 505.2100

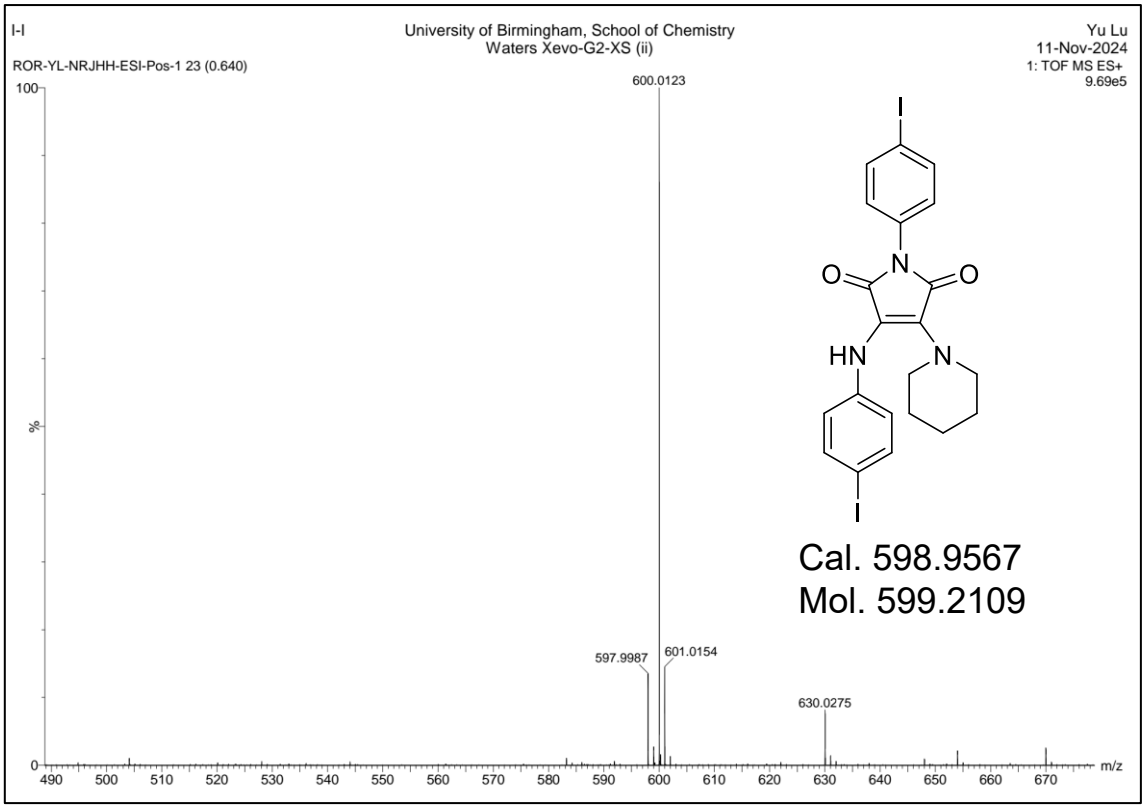
I-I
University of Birmingham, School of Chemistry
Waters Xevo-G2-XS (ii)
Yu Lu
11-Nov-2024
1: TOF MS ES+
9.69e5
ROR-YL-NRJHH-ESI-Pos-1 23 (0.640)
100
%
0
600.0123
597.9987
601.0154
630.0275
490 500 510 520 530 540 550 560 570 580 590 600 610 620 630 640 650 660 670
m/z
I
O
N
O
HN
N
I
Cal. 598.9567
Mol. 599.2109

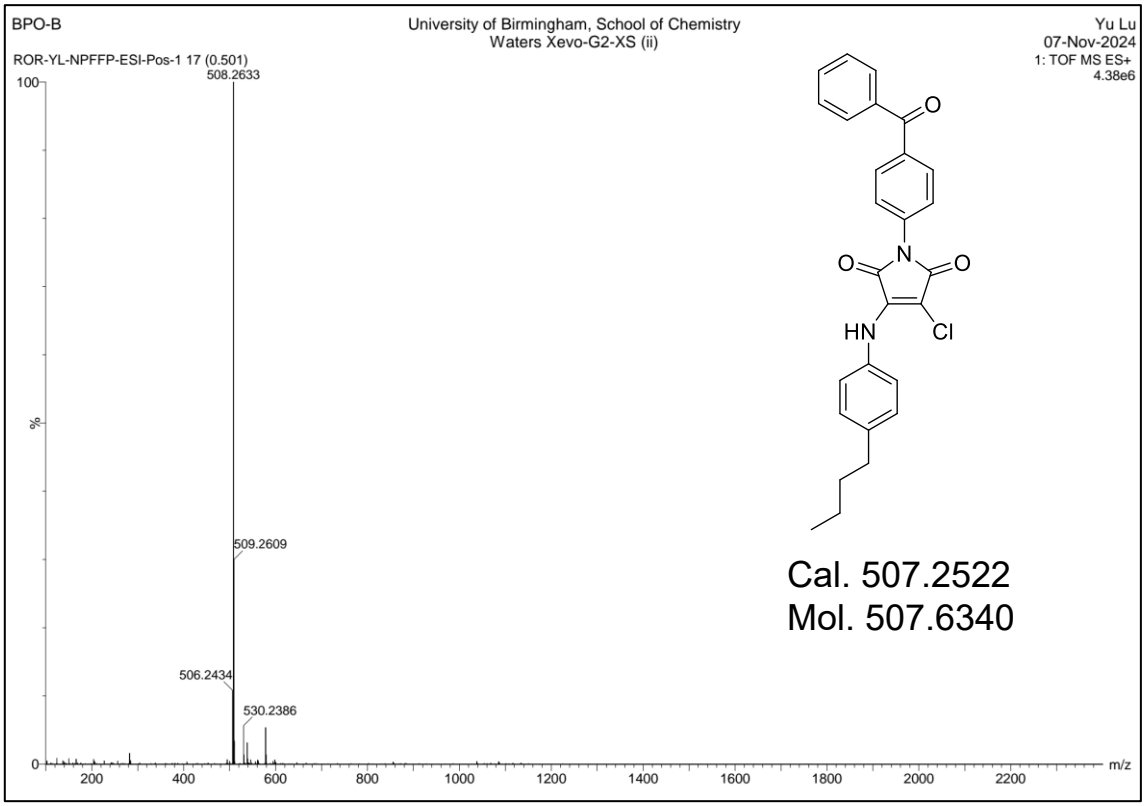
BPO-B
University of Birmingham, School of Chemistry
Waters Xevo-G2-XS (ii)
Yu Lu
07-Nov-2024
1: TOF MS ES+
4.38e6
ROR-YL-NPFFP-ESI-Pos-1 17 (0.501)
100
%
0
508.2633
509.2609
506.2434
530.2386
200 400 600 800 1000 1200 1400 1600 1800 2000 2200
m/z
O
O
N
O
HN
Cl
Cal. 507.2522
Mol. 507.6340

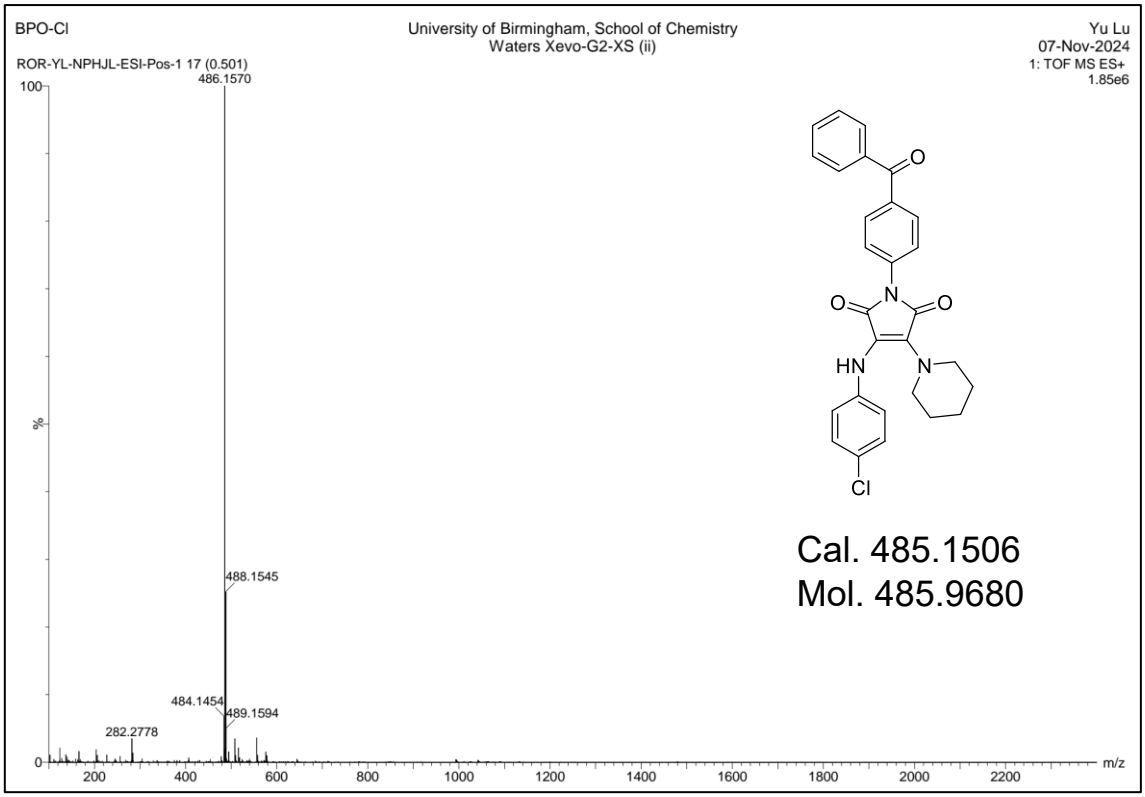
BPO-Cl
University of Birmingham, School of Chemistry
Waters Xevo-G2-XS (ii)
Yu Lu
07-Nov-2024
1: TOF MS ES+
1.85e6
ROR-YL-NPHJL-ESI-Pos-1 17 (0.501)
486.1570
488.1545
484.1454
489.1594
282.2778
Cal. 485.1506
Mol. 485.9680
m/z

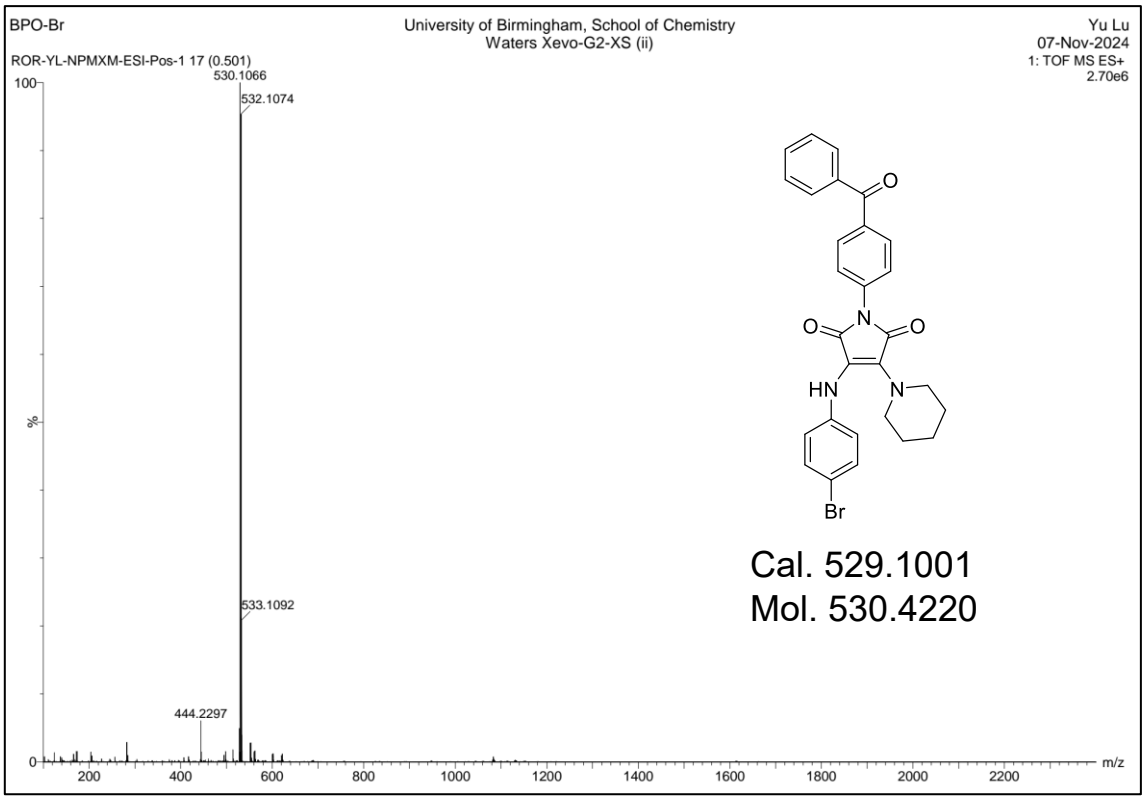
BPO-Br
University of Birmingham, School of Chemistry
Waters Xevo-G2-XS (ii)
Yu Lu
07-Nov-2024
1: TOF MS ES+
2.70e6
ROR-YL-NPMXM-ESI-Pos-1 17 (0.501)
530.1066
532.1074
533.1092
444.2297
Cal. 529.1001
Mol. 530.4220
m/z

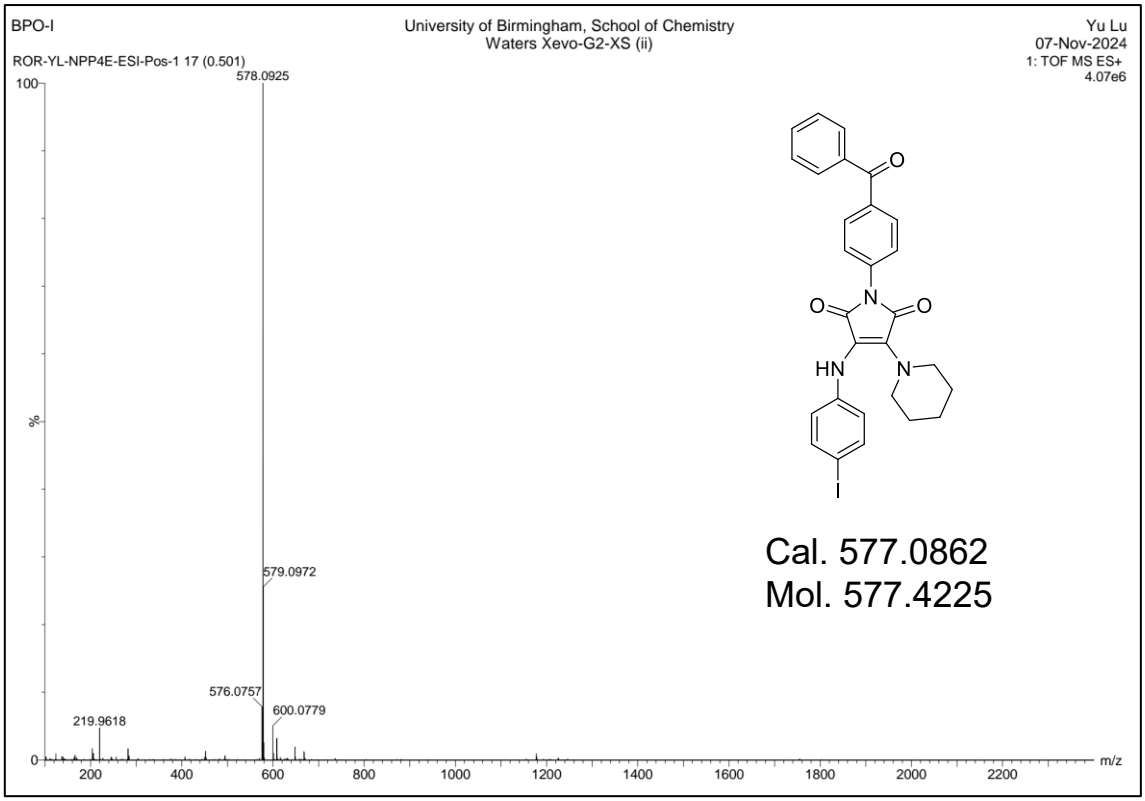


## 4.6.6 Single-crystal data

### Cl-Cl

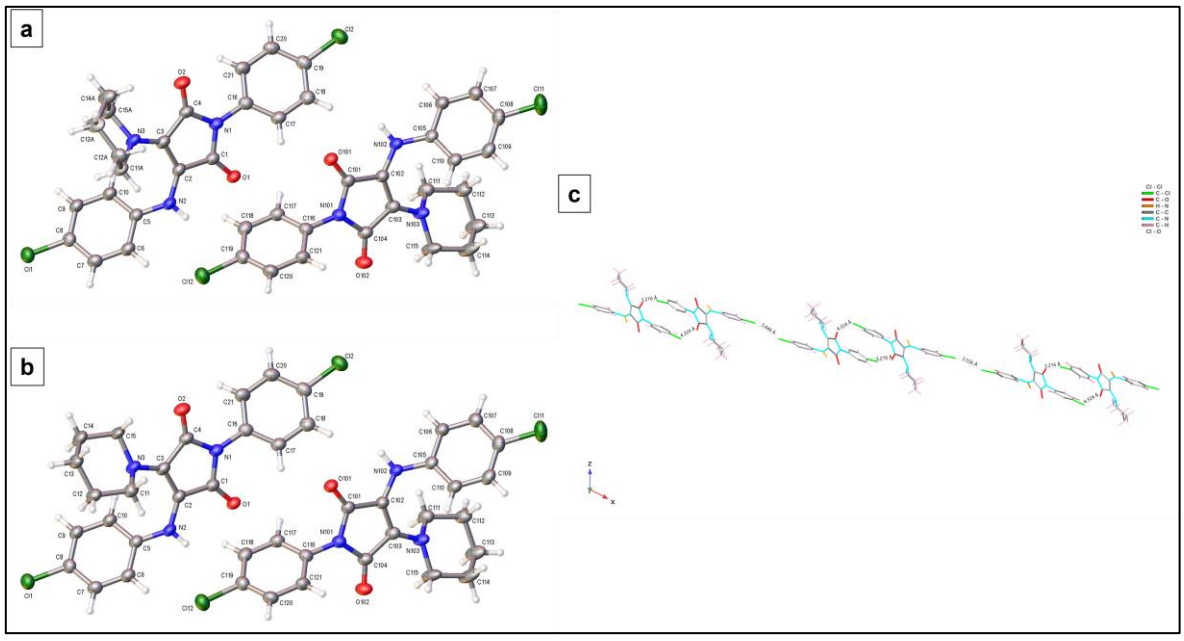


Figure 33 (a) Minor disorder component; (b) Major disorder component; (c) molecular packing pattern.

Crystal data and structure refinement for Cl-Cl.

| | |
|---|---|
| Identification code | Cl-Cl |
| Empirical formula | C21H19Cl2N3O2 |
| Formula weight | 416.29 |
| Temperature/K | 99.99(10) |
| Crystal system | monoclinic |
| Space group | C2/c |
| a/Å | 37.1320(11) |
| b/Å | 6.49640(10) |
| c/Å | 35.9137(11) |
| α/° | 90 |
| β/° | 117.859(4) |
| γ/° | 90 |
| Volume/Å3 | 7659.2(4) |
| Z | 16 |
| ρcalcg/cm3 | 1.444 |
| μ/mm-1 | 3.239 |
| F(000) | 3456.0 |
| Crystal size/mm3 | 0.25 × 0.03 × 0.02 |
| Radiation | Cu Kα (λ = 1.54184) |
| 2Θ range for data collection/° | 5.654 to 157.546 |
| Index ranges | -46 ⩽ h ⩽ 45, -7 ⩽ k ⩽ 4, -45 ⩽ l ⩽ 42 |
| Reflections collected | 32350 |
| Independent reflections | 7929 [Rint = 0.0706, Rsigma = 0.0510] |
| Data/restraints/parameters | 7929/27/559 |

Goodness-of-fit on F2 1.039

Final R indexes [I>=2σ (I)] R1 = 0.0577, wR2 = 0.1491

Final R indexes [all data] R1 = 0.0702, wR2 = 0.1593

Largest diff. peak/hole / e Å-3 0.46/-0.56

**Br-Br**

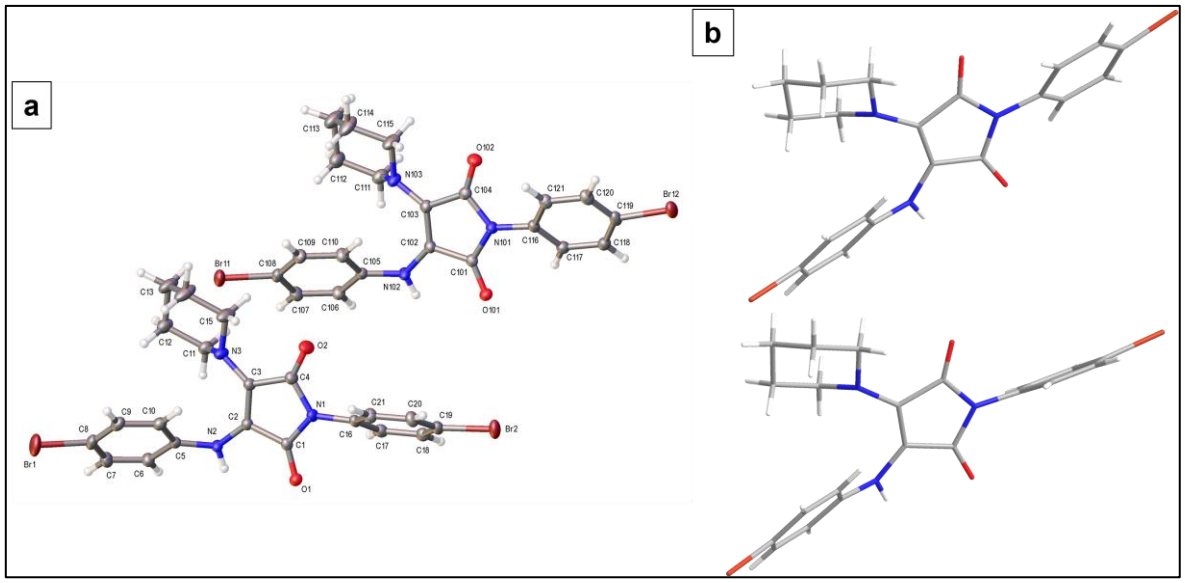


Figure 34 (a) single-crystal structure with atom number; (b) single-crystal structure.

Crystal data and structure refinement for Br-Br.

Identification code Br-Br

Empirical formula C21H19N3O2Br2

Formula weight 505.21

Temperature/K 150.00(10)

Crystal system monoclinic

Space group C2/c

a/Å 37.9119(9)

b/Å 6.48980(10)

c/Å 36.0446(8)

α/° 90

β/° 117.147(3)

γ/° 90

Volume/Å3 7891.5(3)

Z 16

ρcalcg/cm3 1.701

μ/mm-1 5.399

F(000) 4032.0

Crystal size/mm3 0.21 × 0.145 × 0.024

Radiation Cu Kα (λ = 1.54184)

2Θ range for data collection/° 9.18 to 145.574

Index ranges -46 ⩽ h ⩽ 46, -8 ⩽ k ⩽ 8, -44 ⩽ l ⩽ 38

Reflections collected 41188

Independent reflections 7755 [Rint = 0.0295, Rsigma = 0.0171]

Data/restraints/parameters 7755/0/513

Goodness-of-fit on F2 1.026

Final R indexes [I>=2σ (I)] R1 = 0.0268, wR2 = 0.0672

Final R indexes [all data] R1 = 0.0299, wR2 = 0.0695

Largest diff. peak/hole / e Å-3 0.52/-0.48

**I-I**

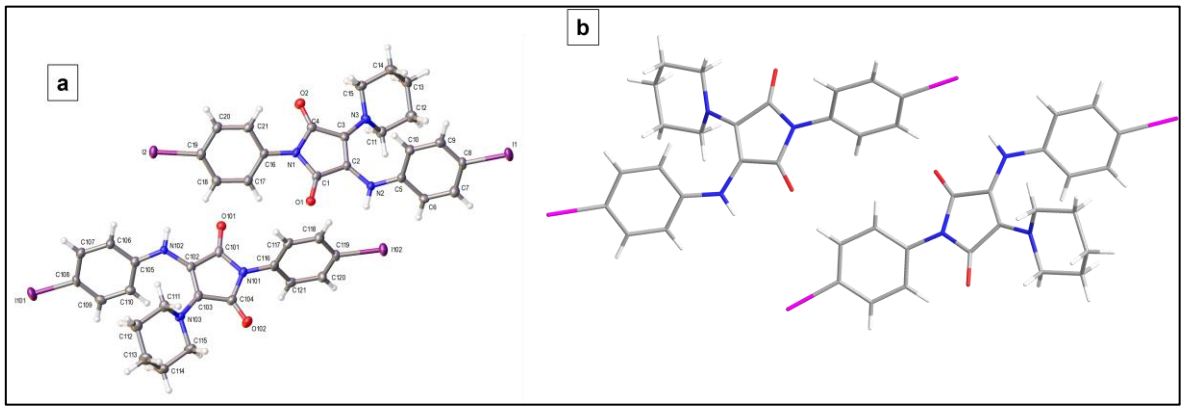


Figure 35 (a) single-crystal structure with atom number; (b) single-crystal structure.

Crystal data and structure refinement for I-I.

| | |
|---|---|
| Identification code | I-I |
| Empirical formula | C21H19N3O2I2 |
| Formula weight | 599.19 |
| Temperature/K | 100.00(10) |
| Crystal system | monoclinic |
| Space group | C2/c |
| a/Å | 38.9806(6) |
| b/Å | 6.45420(10) |
| c/Å | 36.2418(6) |
| α/° | 90 |
| β/° | 115.661(2) |
| γ/° | 90 |
| Volume/Å3 | 8218.7(3) |
| Z | 16 |
| ρcalcg/cm3 | 1.937 |
| μ/mm-1 | 24.223 |

F(000) 4608.0

Crystal size/mm3 0.073 × 0.063 × 0.043

Radiation Cu Kα (λ = 1.54184)

2Θ range for data collection/° 8.846 to 144.252

Index ranges -42 ⩽ h ⩽ 48, -7 ⩽ k ⩽ 7, -44 ⩽ l ⩽ 44

Reflections collected 44420

Independent reflections 8021 [Rint = 0.1056, Rsigma = 0.0607]

Data/restraints/parameters 8021/1/511

Goodness-of-fit on F2 0.952

Final R indexes [I>=2σ (I)] R1 = 0.0338, wR2 = 0.0718

Final R indexes [all data] R1 = 0.0455, wR2 = 0.0762

Largest diff. peak/hole / e Å-3 1.05/-0.64

**BPO-B**

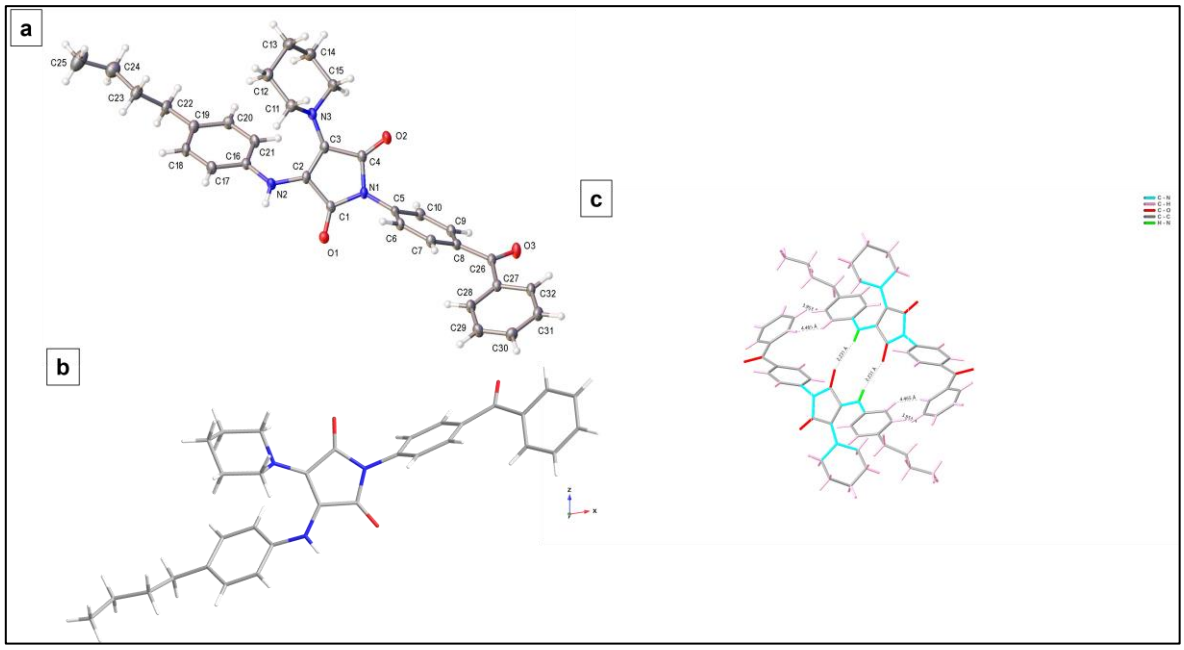


Figure 36 (a) single-crystal structure with atom number; (b) single-crystal structure; (c) molecular packing pattern.

Crystal data and structure refinement for BPO-B.

| | |
|---|---|
| Identification code | BPO-B |
| Empirical formula | C32H33N3O3 |
| Formula weight | 507.61 |
| Temperature/K | 99.99(10) |
| Crystal system | triclinic |
| Space group | P-1 |
| a/Å | 6.30750(10) |
| b/Å | 13.1874(3) |
| c/Å | 16.4271(7) |
| α/° | 77.841(3) |
| β/° | 80.846(2) |
| γ/° | 88.299(2) |
| Volume/Å3 | 1318.72(7) |
| Z | 2 |
| ρcalcg/cm3 | 1.278 |
| μ/mm-1 | 0.657 |
| F(000) | 540.0 |
| Crystal size/mm3 | 0.193 × 0.09 × 0.035 |
| Radiation | Cu Kα (λ = 1.54184) |
| 2Θ range for data collection/° | 5.572 to 136.494 |
| Index ranges | -4 ⩽ h ⩽ 7, -15 ⩽ k ⩽ 15, -19 ⩽ l ⩽ 19 |
| Reflections collected | 22298 |
| Independent reflections | 4811 [Rint = 0.0402, Rsigma = 0.0309] |
| Data/restraints/parameters | 4811/0/348 |

Goodness-of-fit on F2 1.091

Final R indexes [I>=2σ (I)] R1 = 0.0872, wR2 = 0.2334

Final R indexes [all data] R1 = 0.0911, wR2 = 0.2362

Largest diff. peak/hole / e Å-3 0.78/-0.35

# Chapter 5 Conclusions and Future Work

This thesis focuses on the luminescence mechanism and molecular structural characteristics of maleimide-based fluorophores, with the aim of enhancing the theoretical understanding, developing novel maleimide-based fluorophores, and exploring their applications. A series of studies have been conducted, leading to notable progress in this field:

In summary, this thesis designs and synthesizes a series of functionalized fluorophores based on the molecular structure characteristics and luminescence mechanism of maleimide. The study not only reveals the application potential of maleimide molecules in the field of fluorescence but also provides new research ideas for the development of fluorescent materials. In Chapter 2, by introducing halogenated anilines (Cl, Br, I) and 4-n-butylaniline into different sites of the imide ring, fluorophores with dual-state emission properties were successfully prepared. Combined with single-crystal structure analysis and theoretical calculations, the mechanism of this molecular design was deeply explored, thereby proposing a universal design strategy for dual-state emission molecules. Chapter 3 reports for the first time the design and synthesis of photochromic maleimide fluorophores: starting from azophenyl derivatives, after verifying their photochromic properties, the universality of this molecular design strategy was confirmed by introducing different photoresponsive groups. This study highlights the application value of the maleimide skeleton in constructing photochromic molecules, providing important references for the design of photoresponsive materials. In Chapter 4, the room-temperature phosphorescence properties of maleimide molecules were systematically investigated for the first time through host-guest doping strategies of small-molecule-small-molecule and polymer-small-molecule systems, and the phosphorescence mechanism was elucidated by theoretical calculations. This work provides pioneering guidance for the design of maleimide-based RTP molecules and adds new candidate molecular systems to the field of room-temperature phosphorescence.

While significant progress has been made in the theoretical investigation and functional development of maleimide-based fluorophores, many challenges remain. For instance, there are currently no reports on the fabrication of maleimide-based fluorophores with solid-state photoresponsive properties. In our studies, all observed photoresponsive behaviors occurred only in dilute solutions, primarily due to tight intermolecular packing. Therefore, developing maleimide-based fluorophores that exhibit photochromic behaviour in the aggregated state will be a challenging yet highly significant endeavour. Additionally, constructing maleimide derivatives

with near-infrared room-temperature phosphorescence (NIR RTP) also presents both opportunities and challenges. Our research indicates that restricting intermolecular motion and controlling intermolecular charge transfer are key to achieving NIR RTP, yet current efforts have not fully succeeded in this area. Thus, overcoming the inherent limitations of maleimide-based fluorophores through innovative molecular design to achieve long-lifetime, high-quantum yield NIR RTP compounds remains a challenging but crucial task.

# References

(1) Feng, G.; Zhang, G.-Q.; Ding, D. Design of superior phototheranostic agents guided by Jablonski diagrams. *Chemical Society Reviews* **2020**, *49* (22), 8179-8234.

(2) Del Valle, J. C.; Catalán, J. Kasha's rule: a reappraisal. *Physical chemistry chemical physics* **2019**, *21* (19), 10061-10069.

(3) Kitai, A. *Luminescent materials and applications*; John Wiley & Sons, 2008.

(4) Blasse, G. The physics of new luminescent materials. *Materials chemistry and physics* **1987**, *16* (3-4), 201-236.

(5) Ha, J. M.; Hur, S. H.; Pathak, A.; Jeong, J.-E.; Woo, H. Y. Recent advances in organic luminescent materials with narrowband emission. *NPG Asia Materials* **2021**, *13* (1), 53.

(6) Ramírez-Barroso, S.; Romeo-Gella, F.; Fernández-García, J. M.; Feng, S.; Martínez-Fernández, L.; García-Fresnadillo, D.; Corral, I.; Martín, N.; Wannemacher, R. Curved Nanographenes: Multiple Emission, Thermally Activated Delayed Fluorescence, and Non-Radiative Decay. *Advanced Materials* **2023**, *35* (38), 2212064.

(7) Zhang, T.; Xiao, Y.; Wang, H.; Kong, S.; Huang, R.; Ka-Man Au, V.; Yu, T.; Huang, W. Highly Twisted Thermally Activated Delayed Fluorescence (TADF) Molecules and Their Applications in Organic Light-Emitting Diodes (OLEDs). *Angewandte Chemie* **2023**, *135* (39), e202301896.

(8) Valiev, R. R.; Nasibullin, R. T.; Cherepanov, V. N.; Kurtsevich, A.; Sundholm, D.; Kurten, T. Fast estimation of the internal conversion rate constant in photophysical applications. *Physical Chemistry Chemical Physics* **2021**, *23* (11), 6344-6348.

(9) Valiev, R. R.; Cherepanov, V. N.; Baryshnikov, G. V.; Sundholm, D. First-principles method for calculating the rate constants of internal-conversion and intersystem-crossing transitions. *Physical Chemistry Chemical Physics* **2018**, *20* (9), 6121-6133.

(10) Bagchi, B.; Oxtoby, D. W.; Fleming, G. R. Theory of the time development of the Stokes shift in polar media. *Chemical physics* **1984**, *86* (3), 257-267.

(11) Ren, T.-B.; Xu, W.; Zhang, W.; Zhang, X.-X.; Wang, Z.-Y.; Xiang, Z.; Yuan, L.; Zhang, X.-B. A general method to increase stokes shift by introducing alternating vibronic structures. *Journal of the American Chemical Society* **2018**, *140* (24), 7716-7722.

(12) Iwai, R.; Suzuki, S.; Sasaki, S.; Sairi, A. S.; Igawa, K.; Suenobu, T.; Morokuma, K.; Konishi, G. i. Bridged stilbenes: AIEgens designed via a simple strategy to control the non-radiative decay pathway. *Angewandte Chemie* **2020**, *132* (26), 10653-10660.

(13) Dai, L.; Zhang, Q.; Ma, Q.; Lin, W. Emerging near infrared fluorophore: Dicyanoisophorone-based small-molecule fluorescent probes with large stokes shifts for bioimaging. *Coordination Chemistry Reviews* **2023**, *489*, 215193.
(14) Mieczkowski, M.; Steinmetzger, C.; Bessi, I.; Lenz, A.-K.; Schmiedel, A.; Holzapfel, M.; Lambert, C.; Pena, V.; Höbartner, C. Large Stokes shift fluorescence activation in an RNA aptamer by intermolecular proton transfer to guanine. *Nature Communications* **2021**, *12* (1), 3549.
(15) Zhang, J.; Peng, Y.; Li, Y.; Wang, N.; Chai, Y.; Qin, C.; Wang, X.; Liu, S.; Zhou, Y.; Zhang, X. Development of a near-infrared fluorescent probe with large Stokes shift for carboxylesterases detection and its application in living systems. *Dyes and Pigments* **2022**, *198*, 109993.
(16) Wong, K.-L.; Bünzli, J.-C. G.; Tanner, P. A. Quantum yield and brightness. *Journal of Luminescence* **2020**, *224*, 117256.
(17) Ishida, H.; Tobita, S.; Hasegawa, Y.; Katoh, R.; Nozaki, K. Recent advances in instrumentation for absolute emission quantum yield measurements. *Coordination chemistry reviews* **2010**, *254* (21-22), 2449-2458.
(18) Sem, S.; Jenatsch, S.; Stavrou, K.; Danos, A.; Monkman, A. P.; Ruhstaller, B. Determining non-radiative decay rates in TADF compounds using coupled transient and steady state optical data. *Journal of Materials Chemistry C* **2022**, *10* (12), 4878-4885.
(19) Senden, T.; Rabouw, F. T.; Meijerink, A. Photonic effects on the radiative decay rate and luminescence quantum yield of doped nanocrystals. *ACS nano* **2015**, *9* (2), 1801-1808.
(20) Würth, C.; Grabolle, M.; Pauli, J.; Spieles, M.; Resch-Genger, U. Comparison of methods and achievable uncertainties for the relative and absolute measurement of photoluminescence quantum yields. *Analytical chemistry* **2011**, *83* (9), 3431-3439.
(21) Weber, G.; Teale, F. Determination of the absolute quantum yield of fluorescent solutions. *Transactions of the Faraday Society* **1957**, *53*, 646-655.
(22) Würth, C.; Grabolle, M.; Pauli, J.; Spieles, M.; Resch-Genger, U. Relative and absolute determination of fluorescence quantum yields of transparent samples. *Nature protocols* **2013**, *8* (8), 1535-1550.
(23) Birks, J. Fluorescence quantum yield measurements. *Journal of research of the National Bureau of Standards. Section A, Physics and chemistry* **1976**, *80* (3), 389.
(24) Crosby, G. A.; Demas, J. N. Measurement of photoluminescence quantum yields. Review. *The Journal of Physical Chemistry* **1971**, *75* (8), 991-1024.
(25) Lakowicz, J. R.; Lakowicz, J. R. Measurement of fluorescence lifetimes. *Principles of fluorescence spectroscopy* **1983**, 51-93.

(26) Berezin, M. Y.; Achilefu, S. Fluorescence lifetime measurements and biological imaging. *Chemical reviews* **2010**, *110* (5), 2641-2684.
(27) Becker, W. Fluorescence lifetime imaging–techniques and applications. *Journal of microscopy* **2012**, *247* (2), 119-136.
(28) Ma, X.; Sun, R.; Cheng, J.; Liu, J.; Gou, F.; Xiang, H.; Zhou, X. Fluorescence aggregation-caused quenching versus aggregation-induced emission: a visual teaching technology for undergraduate chemistry students. *Journal of Chemical Education* **2016**, *93* (2), 345-350.
(29) Yuan, W. Z.; Lu, P.; Chen, S.; Lam, J. W.; Wang, Z.; Liu, Y.; Kwok, H. S.; Ma, Y.; Tang, B. Z. Changing the behavior of chromophores from aggregation-caused quenching to aggregation-induced emission: development of highly efficient light emitters in the solid state. *Advanced materials* **2010**, *22* (19), 2159-2163.
(30) Luo, J.; Xie, Z.; Lam, J. W.; Cheng, L.; Chen, H.; Qiu, C.; Kwok, H. S.; Zhan, X.; Liu, Y.; Zhu, D. Aggregation-induced emission of 1-methyl-1, 2, 3, 4, 5-pentaphenylsilole. *Chemical communications* **2001**, (18), 1740-1741.
(31) Mei, J.; Leung, N. L.; Kwok, R. T.; Lam, J. W.; Tang, B. Z. Aggregation-induced emission: together we shine, united we soar! *Chemical reviews* **2015**, *115* (21), 11718-11940.
(32) Mei, J.; Hong, Y.; Lam, J. W.; Qin, A.; Tang, Y.; Tang, B. Z. Aggregation-induced emission: the whole is more brilliant than the parts. *Advanced materials* **2014**, *26* (31), 5429-5479.
(33) Belmonte-Vázquez, J. L.; Amador-Sánchez, Y. A.; Rodríguez-Cortés, L. A.; Rodríguez-Molina, B. Dual-State Emission (DSE) in Organic Fluorophores: Design and Applications. *Chemistry of Materials* **2021**, *33* (18), 7160-7184. DOI: 10.1021/acs.chemmater.1c02460.
(34) Liu, Y.; Zhang, Y.; Wu, X.; Lan, Q.; Chen, C.; Liu, S.; Chi, Z.; Jiang, L.; Chen, X.; Xu, J. Deep-blue luminescent compound that emits efficiently both in solution and solid state with considerable blue-shift upon aggregation. *Journal of Materials Chemistry C* **2014**, *2* (6), 1068-1075.
(35) Zhang, X.; Zhou, Y.; Wang, M.; Chen, Y.; Zhou, Y.; Gao, W.; Liu, M.; Huang, X.; Wu, H. Metal-Free Facile Synthesis of Multisubstituted 1-Aminoisoquinoline Derivatives with Dual-State Emissions. *Chemistry–An Asian Journal* **2020**, *15* (11), 1692-1700.
(36) Dai, W.; Liu, P.; Guo, S.; Liu, Z.; Wang, M.; Shi, J.; Tong, B.; Liu, T.; Cai, Z.; Dong, Y. Triphenylquinoline (TPQ)-Based dual-state emissive probe for cell imaging in multicellular tumor spheroids. *ACS Applied Bio Materials* **2019**, *2* (8), 3686-3692.
(37) Wu, H.; Chen, Z.; Chi, W.; Bindra, A. K.; Gu, L.; Qian, C.; Wu, B.; Yue, B.; Liu, G.; Yang, G. Structural engineering of luminogens with high emission efficiency both in solution and in the solid state. *Angewandte Chemie International Edition* **2019**, *58* (33), 11419-11423.

(38) Xu, Y.; Ren, L.; Dang, D.; Zhi, Y.; Wang, X.; Meng, L. A Strategy of "Self-Isolated Enhanced Emission" to Achieve Highly Emissive Dual-State Emission for Organic Luminescent Materials. *Chemistry–A European Journal* **2018**, *24* (41), 10383-10389.
(39) Dang, D.; Wang, X.; Wang, D.; Yang, Z.; Hao, D.; Xu, Y.; Zhang, S.; Meng, L. Fluorescent organic nanoparticles constructed by a facile "self-isolation enhanced emission" strategy for cell imaging. *ACS Applied Nano Materials* **2018**, *1* (5), 2324-2331.
(40) Belmonte-Vázquez, J. L.; Hernández-Morales, E. A.; Hernández, F.; García-González, M. C.; Miranda, L. D.; Crespo-Otero, R.; Rodríguez-Molina, B. Asymmetric Dual-State Emitters Featuring Thiazole Acceptors. *European Journal of Organic Chemistry* **2022**, *2022* (35), e202200372.
(41) Jian, N.; Qu, K.; Gu, H.; Zou, L.; Liu, X.; Hu, F.; Xu, J.; Yu, Y.; Lu, B. Highly fluorescent triazolopyridine–thiophene D–A–D oligomers for efficient pH sensing both in solution and in the solid state. *Physical Chemistry Chemical Physics* **2019**, *21* (13), 7174-7182.
(42) Gopikrishna, P.; Iyer, P. K. Monosubstituted dibenzofulvene-based luminogens: aggregation-induced emission enhancement and dual-state emission. *The Journal of Physical Chemistry C* **2016**, *120* (46), 26556-26568.
(43) Zeng, C.; Yang, T.; Wang, Z.; Chen, K.; Ge, Q.; Peng, W.; Zhang, J.; Liu, J.; Zhang, T.; Sun, M. Functional-group-regulated stimuli-responsive banana-shaped α-cyanostilbene derivatives: Dual-state emission, AIEE, acidochromism and their applications in anti-counterfeiting, fingerprint recognition and OLEDs. *Journal of Luminescence* **2024**, *269*, 120452.
(44) Ouyang, C.; Li, Y.; Rees, T. W.; Liao, X.; Jia, J.; Chen, Y.; Zhang, X.; Ji, L.; Chao, H. Supramolecular Assembly of An Organoplatinum (II) Complex with Ratiometric Dual Emission for Two-Photon Bioimaging. *Angewandte Chemie* **2021**, *133* (8), 4196-4203.
(45) Li, J.; Zhao, X.; Gong, X. Rational Design of Dual-Mode Emitting Carbon Dots to Exploit the Synergistic Effect of Matrices for High-Efficiency WLEDs and Anti-Counterfeiting. *Advanced Optical Materials* **2024**, *12* (7), 2302297.
(46) Xia, G.; Si, L.; Wang, H. Dual-state emission: the compatible art of substantial rigidity and twisting conformation within a single molecule. *Materials Today Chemistry* **2023**, *30*. DOI: 10.1016/j.mtchem.2023.101596.
(47) Su, M.; Song, Y. Printable smart materials and devices: strategies and applications. *Chemical reviews* **2021**, *122* (5), 5144-5164.
(48) Bahl, S.; Nagar, H.; Singh, I.; Sehgal, S. Smart materials types, properties and applications: A review. *Materials Today: Proceedings* **2020**, *28*, 1302-1306.

(49) Musarurwa, H.; Tavengwa, N. T. Stimuli-responsive polymers and their applications in separation science. *Reactive and Functional Polymers* **2022**, *175*, 105282.
(50) Shu, T.; Hu, L.; Shen, Q.; Jiang, L.; Zhang, Q.; Serpe, M. J. Stimuli-responsive polymer-based systems for diagnostic applications. *Journal of Materials Chemistry B* **2020**, *8* (32), 7042-7061.
(51) Wang, X.; Shan, M.; Zhang, S.; Chen, X.; Liu, W.; Chen, J.; Liu, X. Stimuli-Responsive antibacterial materials: molecular structures, design principles, and biomedical applications. *Advanced Science* **2022**, *9* (13), 2104843.
(52) Zhang, Q.; Zhang, Y.; Wan, Y.; Carvalho, W.; Hu, L.; Serpe, M. J. Stimuli-responsive polymers for sensing and reacting to environmental conditions. *Progress in Polymer Science* **2021**, *116*, 101386.
(53) Haldar, R.; Heinke, L.; Wöll, C. Advanced photoresponsive materials using the metal–organic framework approach. *Advanced Materials* **2020**, *32* (20), 1905227.
(54) Luo, W.; Wang, G. Photo-responsive fluorescent materials with aggregation-induced emission characteristics. *Advanced Optical Materials* **2020**, *8* (24), 2001362.
(55) Xu, F.; Feringa, B. L. Photoresponsive Supramolecular Polymers: From Light-Controlled Small Molecules to Smart Materials. *Advanced Materials* **2023**, *35* (10), 2204413.
(56) Żmija, J.; Małachowski, M. New organic photochromic materials and selected applications. *Journal of Achievements in Materials and Manufacturing Engeneering* **2010**, *41*, 48-56.
(57) Nakatani, K.; Piard, J.; Yu, P.; Métivier, R. Introduction: organic photochromic molecules. *Photochromic materials: preparation, properties and applications* **2016**, 1-45.
(58) Crano, J. C.; Guglielmetti, R. J. *Organic photochromic and thermochromic compounds: volume 2: physicochemical studies, biological applications, and thermochromism*; Springer, 2002.
(59) Zhao, W.; Carreira, E. M. Solid-phase synthesis of photochromic spiropyrans. *Organic letters* **2005**, *7* (8), 1609-1612.
(60) Masson, J.-F.; Hartmann, T.; Dürr, H.; Booksh, K. S. Solid-phase synthesis and photochromic switching of a polymeric photochromic layer on a gold surface. *Optical Materials* **2004**, *27* (3), 435-439.
(61) Zhang, J.; He, B.; Hu, Y.; Alam, P.; Zhang, H.; Lam, J. W.; Tang, B. Z. Stimuli-Responsive AIEgens. *Advanced Materials* **2021**, *33* (32), 2008071.
(62) Wang, J.; Zhang, L.; Li, Z. Aggregation-Induced Emission Luminogens with Photoresponsive Behaviors for Biomedical Applications. *Advanced Healthcare Materials* **2021**, *10* (24), 2101169.

(63) Zhang, M.; Zhang, J.; Alam, P.; Li, W.; Lam, J. W.; Jia, G.; Tang, B. Z. Hydrazone-based AIEgens with photofluorochromic ability for rewritable, intensity-variable, and high-resolution photopattern. *Advanced Functional Materials* **2023**, *33* (12), 2213927.
(64) Delaire, J. A.; Nakatani, K. Linear and nonlinear optical properties of photochromic molecules and materials. *Chemical Reviews* **2000**, *100* (5), 1817-1846.
(65) Zhang, J.; Zou, Q.; Tian, H. Photochromic materials: more than meets the eye. *Advanced Materials* **2013**, *25* (3), 378-399.
(66) Fihey, A.; Perrier, A.; Browne, W. R.; Jacquemin, D. Multiphotochromic molecular systems. *Chemical Society Reviews* **2015**, *44* (11), 3719-3759.
(67) Wang, X.; Yu, H.; Yang, R.; Li, B.; Wang, M.; Xu, B.; Tian, W. Fluorescence Switching and Photoisomerization of a Spiropyran Molecular Photoswitch through Confined Spaces Regulation in Crystals. *The Journal of Physical Chemistry Letters* **2024**, *15*, 4224-4228.
(68) Lin, S.; Gutierrez-Cuevas, K. G.; Zhang, X.; Guo, J.; Li, Q. Fluorescent photochromic α-cyanodiarylethene molecular switches: an emerging and promising class of functional diarylethene. *Advanced Functional Materials* **2021**, *31* (7), 2007957.
(69) Ouyang, G.; Bialas, D.; Würthner, F. Reversible fluorescence modulation through the photoisomerization of an azobenzene-bridged perylene bisimide cyclophane. *Organic Chemistry Frontiers* **2021**, *8* (7), 1424-1430.
(70) Kondo, M. Photomechanical materials driven by photoisomerization or photodimerization. *Polymer Journal* **2020**, *52* (9), 1027-1034.
(71) Gonzalez, A.; Kengmana, E.; Fonseca, M.; Han, G. Solid-state photoswitching molecules: structural design for isomerization in condensed phase. *Materials Today Advances* **2020**, *6*, 100058.
(72) Fujino, T.; Arzhantsev, S. Y.; Tahara, T. Femtosecond time-resolved fluorescence study of photoisomerization of trans-azobenzene. *The Journal of Physical Chemistry A* **2001**, *105* (35), 8123-8129.
(73) Huang, Y.; Zhang, G.; Zhao, R.; Zhang, D. Tetraphenylethene-Based cis/trans Isomers for Targeted Fluorescence Sensing and Biomedical Applications. *Chemistry–A European Journal* **2023**, *29* (30), e202300539.
(74) Eiring, P.; McLaughlin, R.; Matikonda, S. S.; Han, Z.; Grabenhorst, L.; Helmerich, D. A.; Meub, M.; Beliu, G.; Luciano, M.; Bandi, V. Targetable Conformationally Restricted Cyanines Enable Photon-Count-Limited Applications. *Angewandte Chemie International Edition* **2021**, *60* (51), 26685-26693.

(75) He, X.; Wei, P. Recent advances in tunable solid-state emission based on α-cyanodiarylethenes: from molecular packing regulation to functional development. *Chemical Society Reviews* **2024**.
(76) Yu, H.; Wu, W.; Zhao, H.; Chen, K.; Li, S.; Tan, M.; Wang, T.; Huang, X.; Wang, N.; Hao, H. Cyanostyrene derivative with multi-stimuli responsive properties: Multicolor-and high-color-contrast switching in response to force, heat and light. *Dyes and Pigments* **2023**, *220*, 111727.
(77) Zhao, Q.; He, J.; Yang, W.; Zhang, H.; Lin, L.; Jin, F.; Zhan, Y. Aggregation-induced emission characteristics and distinct fluorescent responses to external pressure stimuli based on dumbbell D-π-A-π-D cyanostyrene derivatives. *Tetrahedron* **2020**, *76* (50), 131675.
(78) Xue, J.; Tang, F.; Wang, C.; Yang, J.; Ding, A. Tuning Electronic Structures of Carbazole-Cyanostyrene Molecules to Achieve Dual-State Emission for Trace Water Analysis, Picric Acid Sensing, and Reversible Mechanofluorochromism. *ChemPhotoChem* **2022**, *6* (12), e202200184.
(79) Konig, N. F.; Mutruc, D.; Hecht, S. Accelerated Discovery of alpha-Cyanodiarylethene Photoswitches. *J Am Chem Soc* **2021**, *143* (24), 9162-9168. DOI: 10.1021/jacs.1c03631.
(80) Wang, Y.-L.; Fan, C.; Xin, B.; Zhang, J.-P.; Luo, T.; Chen, Z.-Q.; Zhou, Q.-Y.; Yu, Q.; Li, X.-N.; Huang, Z.-L. AIE-based super-resolution imaging probes for β-amyloid plaques in mouse brains. *Materials Chemistry Frontiers* **2018**, *2* (8), 1554-1562.
(81) Jiang, Q.; Ruan, H.; Wang, T.; Zhang, Y.; Qiu, Y.; Wang, H.; Liao, Y.; Xie, X. Extending conjugation of linear cyanostilbene derivatives via a pyridine moiety for multi-stimuli-responsive fluorescence organogels. *Langmuir* **2023**, *39* (31), 10904-10912.
(82) Li, N.; Liang, Y.; Liu, X.; Liang, G.; Zhang, Q.; Zhang, R.; Gao, H.; Xiao, Y. Positional isomerism mediated the self-assembly and optical properties of amphiphilic cyanostyrene-based mesogens. *Journal of Luminescence* **2023**, *258*, 119810.
(83) Zhang, Y.; Li, H.; Zhang, G.; Xu, X.; Kong, L.; Tao, X.; Tian, Y.; Yang, J. Aggregation-induced emission enhancement and mechanofluorochromic properties of α-cyanostilbene functionalized tetraphenyl imidazole derivatives. *Journal of Materials Chemistry C* **2016**, *4* (14), 2971-2978.
(84) Tonga, M. Regulation of aggregation-induced emission color of α-cyanostilbene luminogens through donor engineering of amino derivatives. *Tetrahedron Letters* **2021**, *69*, 152972.
(85) Ding, Z.; Zhang, Y.; Gao, Y.; Yang, B.; Jiang, S. Tunable morphologies and emission of photosensitive supramolecular self-assemblies through positional and trans–cis isomerization. *Nanoscale* **2020**, *12* (3), 2071-2080.
(86) Gulino, A.; Lupo, F.; Condorelli, G. G.; Fragalà, M. E.; Amato, M. E.; Scarlata, G. Reversible photoswitching of stimuli-responsive Si (100) surfaces engineered with an assembled 1-cyano-1-

phenyl-2-[4′-(10-undecenyloxy) phenyl]-ethylene monolayer. *Journal of Materials Chemistry* **2008**, *18* (41), 5011-5018.

(87) Chung, J. W.; Yoon, S.-J.; An, B.-K.; Park, S. Y. High-contrast on/off fluorescence switching via reversible E–Z isomerization of diphenylstilbene containing the α-cyanostilbenic moiety. *The Journal of Physical Chemistry C* **2013**, *117* (21), 11285-11291.

(88) Chung, J. W.; You, Y.; Huh, H. S.; An, B.-K.; Yoon, S.-J.; Kim, S. H.; Lee, S. W.; Park, S. Y. Shear-and UV-induced fluorescence switching in stilbenic π-dimer crystals powered by reversible [2+ 2] cycloaddition. *Journal of the American Chemical Society* **2009**, *131* (23), 8163-8172.

(89) Wei, P.; Zhang, J.-X.; Zhao, Z.; Chen, Y.; He, X.; Chen, M.; Gong, J.; Sung, H. H.-Y.; Williams, I. D.; Lam, J. W. Multiple yet controllable photoswitching in a single AIEgen system. *Journal of the American Chemical Society* **2018**, *140* (5), 1966-1975.

(90) Mu, B.; Hao, X.; Luo, X.; Yang, Z.; Lu, H.; Tian, W. Bioinspired polymeric supramolecular columns as efficient yet controllable artificial light-harvesting platform. *Nature Communications* **2024**, *15* (1), 903.

(91) Dong, Y.; Wu, H.; Liu, J.; Zheng, S.; Liang, B.; Zhang, C.; Ling, Y.; Wu, X.; Chen, J.; Yu, X. Multicolor Photochemical Printing Inside Polymer Matrices for Advanced Photonic Anticounterfeiting. *Advanced Materials* **2024**, 2401294.

(92) Hartley, G. S. The cis-form of azobenzene. *Nature* **1937**, *140* (3537), 281-281.

(93) Bandara, H. D.; Burdette, S. C. Photoisomerization in different classes of azobenzene. *Chemical Society Reviews* **2012**, *41* (5), 1809-1825.

(94) Forber, C. L.; Kelusky, E. C.; Bunce, N. J.; Zerner, M. C. Electronic spectra of cis-and trans-azobenzenes: consequences of ortho substitution. *Journal of the American Chemical Society* **1985**, *107* (21), 5884-5890.

(95) Zimmerman, G.; Chow, L.-Y.; Paik, U.-J. The photochemical isomerization of azobenzene1. *Journal of the American Chemical Society* **1958**, *80* (14), 3528-3531.

(96) Rau, H.; Lueddecke, E. On the rotation-inversion controversy on photoisomerization of azobenzenes. Experimental proof of inversion. *Journal of the American Chemical Society* **1982**, *104* (6), 1616-1620.

(97) Crecca, C. R.; Roitberg, A. E. Theoretical study of the isomerization mechanism of azobenzene and disubstituted azobenzene derivatives. *The Journal of Physical Chemistry A* **2006**, *110* (26), 8188-8203.

(98) Cheng, H. B.; Zhang, S.; Qi, J.; Liang, X. J.; Yoon, J. Advances in application of azobenzene as a trigger in biomedicine: Molecular design and spontaneous assembly. *Advanced Materials* **2021**, *33* (26), 2007290.

(99) Baby, A.; Abinaya, S.; John, A. M.; Jose, S. P.; Balakrishnan, S. P. Photoresponse and electrochemical behaviour of azobenzene anchored graphene oxide for energy storage application. *Materials Chemistry and Physics* **2023**, *301*, 127592.
(100) Waldeck, D. H. Photoisomerization dynamics of stilbenes. *Chemical Reviews* **1991**, *91* (3), 415-436.
(101) Görner, H.; Kuhn, H. J. Cis-trans photoisomerization of stilbenes and stilbene-like molecules. *Advances in photochemistry* **1994**, *19*, 1-117.
(102) Xu, F.; Sheng, J.; Stindt, C. N.; Crespi, S.; Danowski, W.; Hilbers, M. F.; Buma, W. J.; Feringa, B. L. All-visible-light-driven stiff-stilbene photoswitches. *Chemical Science* **2024**.
(103) Villarón, D.; Wezenberg, S. J. Stiff-stilbene photoswitches: from fundamental studies to emergent applications. *Angewandte Chemie* **2020**, *132* (32), 13292-13302.
(104) Julian, M. Mechanism of photodimerization in single crystals of anthracene. *Acta Crystallographica Section A: Crystal Physics, Diffraction, Theoretical and General Crystallography* **1973**, *29* (2), 116-120.
(105) Bunker, C. E.; Rollins, H. W.; Gord, J. R.; Sun, Y.-P. Efficient photodimerization reaction of anthracene in supercritical carbon dioxide. *The Journal of Organic Chemistry* **1997**, *62* (21), 7324-7329.
(106) Fritzsche. Ueber die festen Kohlenwasserstoffe des Steinkohlentheers. *Journal für praktische Chemie* **1867**, *101* (1), 333-343.
(107) Greene, F. D.; Misrock, S. L.; Wolfe Jr, J. R. The structure of anthracene photodimers. *Journal of the American Chemical Society* **1955**, *77* (14), 3852-3855.
(108) Günay, K. A.; Ceccato, T. L.; Silver, J. S.; Bannister, K. L.; Bednarski, O. J.; Leinwand, L. A.; Anseth, K. S. PEG–anthracene hydrogels as an on-demand stiffening matrix to study Mechanobiology. *Angewandte Chemie International Edition* **2019**, *58* (29), 9912-9916.
(109) Li, C.; Liu, J.; Qiu, X.; Yang, X.; Huang, X.; Zhang, X. Photoswitchable and Reversible Fluorescent Eutectogels for Conformal Information Encryption. *Angewandte Chemie* **2023**, e202313971.
(110) Lewis, G. N.; Kasha, M. Phosphorescence and the triplet state. *Journal of the American Chemical Society* **1944**, *66* (12), 2100-2116.
(111) Itoh, T. Fluorescence and phosphorescence from higher excited states of organic molecules. *Chemical reviews* **2012**, *112* (8), 4541-4568.
(112) Zhao, W.; He, Z.; Tang, B. Z. Room-temperature phosphorescence from organic aggregates. *Nature Reviews Materials* **2020**, *5* (12), 869-885.

(113) Guo, J.; Yang, C.; Zhao, Y. Long-lived organic room-temperature phosphorescence from amorphous polymer systems. *Accounts of chemical research* **2022**, *55* (8), 1160-1170.
(114) Yin, G.; Huo, G.; Qi, M.; Liu, D.; Li, L.; Zhou, J.; Le, X.; Wang, Y.; Chen, T. Precisely Coordination-Modulated Ultralong Organic Phosphorescence Enables Biomimetic Fluorescence-Afterglow Dual-Modal Information Encryption. *Advanced Functional Materials* **2024**, *34* (12), 2310043.
(115) Zhu, H.; Badia-Dominguez, I.; Shi, B.; Li, Q.; Wei, P.; Xing, H.; Ruiz Delgado, M. C.; Huang, F. Cyclization-promoted ultralong low-temperature phosphorescence via boosting intersystem crossing. *Journal of the American Chemical Society* **2021**, *143* (4), 2164-2169.
(116) Wang, W.; Zhang, Y.; Jin, W. J. Halogen bonding in room-temperature phosphorescent materials. *Coordination Chemistry Reviews* **2020**, *404*, 213107.
(117) Mandal, S.; Durairaj, P.; Kommula, B.; Sarkar, S.; Bhattacharyya, S. Switching between fluorescence and room temperature phosphorescence in Carbon Dots: key role of Heteroatom functionalities. *The Journal of Physical Chemistry C* **2023**, *127* (5), 2430-2439.
(118) Hamzehpoor, E.; Perepichka, D. F. Crystal engineering of room temperature phosphorescence in organic solids. *Angewandte Chemie* **2020**, *132* (25), 10063-10067.
(119) Liu, H.; Bian, Z.; Cheng, Q.; Lan, L.; Wang, Y.; Zhang, H. Controllably realizing elastic/plastic bending based on a room-temperature phosphorescent waveguiding organic crystal. *Chemical science* **2019**, *10* (1), 227-232.
(120) Tian, Y.; Yang, J.; Liu, Z.; Gao, M.; Li, X.; Che, W.; Fang, M.; Li, Z. Multistage stimulus-responsive room temperature phosphorescence based on host–guest doping systems. *Angewandte Chemie International Edition* **2021**, *60* (37), 20259-20263.
(121) Xia, Y.; Zhu, C.; Cao, F.; Shen, Y.; Ouyang, M.; Zhang, Y. Host–Guest Doping in Flexible Organic Crystals for Room-Temperature Phosphorescence. *Angewandte Chemie* **2023**, *135* (8), e202217547.
(122) Gao, H.; Ma, X. Recent progress on pure organic room temperature phosphorescent polymers. *Aggregate* **2021**, *2* (4), e38.
(123) Zheng, H.; Zhang, Z.; Cai, S.; An, Z.; Huang, W. Enhancing Purely Organic Room Temperature Phosphorescence via Supramolecular Self-Assembly. *Advanced Materials* **2024**, 2311922.
(124) Deng, Y.; Li, P.; Li, J.; Sun, D.; Li, H. Color-Tunable Aqueous Room-Temperature Phosphorescence Supramolecular Assembly. *ACS Appl Mater Interfaces* **2021**, *13* (12), 14407-14416. DOI: 10.1021/acsami.1c01174 From NLM PubMed-not-MEDLINE.

(125) Iredale, R. J.; Ward, C.; Hamerton, I. Modern advances in bismaleimide resin technology: A 21st century perspective on the chemistry of addition polyimides. *Progress in Polymer Science* **2017**, *69*, 1-21. DOI: 10.1016/j.progpolymsci.2016.12.002.

(126) Evsyukov, S.; Pohlmann, T.; ter Wiel, M. Modern approaches to the processing of bismaleimide resins. *Polymer* **2020**, *20*.

(127) Renault, K.; Fredy, J. W.; Renard, P. Y.; Sabot, C. Covalent Modification of Biomolecules through Maleimide-Based Labeling Strategies. *Bioconjug Chem* **2018**, *29* (8), 2497-2513. DOI: 10.1021/acs.bioconjchem.8b00252 From NLM Medline.

(128) Yeh, H.-C.; Wu, W.-C.; Chen, C.-T. The colourful fluorescence from readily-synthesised 3, 4-diaryl-substituted maleimide fluorophores. *Chemical communications* **2003**, (3), 404-405.

(129) Imoto, H.; Fujii, R.; Naka, K. 3, 4-Diaminomaleimide Dyes–Simple Luminophores with Efficient Orange-Red Emission in the Solid State. *European Journal of Organic Chemistry* **2018**, *2018* (6), 837-843.

(130) Robin, M. P.; Wilson, P.; Mabire, A. B.; Kiviaho, J. K.; Raymond, J. E.; Haddleton, D. M.; O'Reilly, R. K. Conjugation-induced fluorescent labeling of proteins and polymers using dithiomaleimides. *Journal of the American Chemical Society* **2013**, *135* (8), 2875-2878.

(131) Mabire, A. B.; Robin, M. P.; Quan, W.-D.; Willcock, H.; Stavros, V. G.; O'Reilly, R. K. Aminomaleimide fluorophores: a simple functional group with bright, solvent dependent emission. *Chemical Communications* **2015**, *51* (47), 9733-9736.

(132) Xie, Y.; Husband, J. T.; Torrent-Sucarrat, M.; Yang, H.; Liu, W.; O'Reilly, R. K. Rational design of substituted maleimide dyes with tunable fluorescence and solvafluorochromism. *Chemical Communications* **2018**, *54* (27), 3339-3342.

(133) Xie, Y.; Arno, M. C.; Husband, J. T.; Torrent-Sucarrat, M.; O'Reilly, R. K. Manipulating the fluorescence lifetime at the sub-cellular scale via photo-switchable barcoding. *Nature communications* **2020**, *11* (1), 2460.

(134) Zhou, P.; Liu, J.; Yang, S.; Chen, J.; Han, K.; He, G. The invalidity of the photo-induced electron transfer mechanism for fluorescein derivatives. *Physical Chemistry Chemical Physics* **2012**, *14* (43), 15191-15198.

(135) Pan, J.; Du, J.; Hu, Q.; Liu, Y.; Zhang, X.; Li, X.; Zhou, D.; Yao, Q.; Long, S.; Fan, J. Photo-Induced Electron Transfer-Triggered Structure Deformation Promoting Near-Infrared Photothermal Conversion for Tumor Therapy. *Advanced Healthcare Materials* **2023**, *12* (27), 2301091.

(136) Yuan, W. Z.; Gong, Y.; Chen, S.; Shen, X. Y.; Lam, J. W.; Lu, P.; Lu, Y.; Wang, Z.; Hu, R.; Xie, N. Efficient solid emitters with aggregation-induced emission and intramolecular charge

transfer characteristics: molecular design, synthesis, photophysical behaviors, and OLED application. *Chemistry of Materials* **2012**, *24* (8), 1518-1528.
(137) Ahn, M.; Kim, M., Ji; Cho, D. W.; Wee, K.-R. Electron push–pull effects on intramolecular charge transfer in perylene-based donor–acceptor compounds. *The Journal of Organic Chemistry* **2020**, *86* (1), 403-413.
(138) Gedeck, P.; Schneider, S. Numerical self-consistent reaction field study of the excited-state properties of p-(dimethylamino)-benzonitrile derivatives. *Journal of Photochemistry and Photobiology A: Chemistry* **1999**, *121* (1), 7-15.
(139) Robinson, D. W.; Long, C. A. Quadratic hyperpolarizability of 4-(dimethylamino) benzonitrile in solvents of differing polarity. *The Journal of Physical Chemistry* **1993**, *97* (29), 7540-7542.
(140) Grabowski, Z. R.; Rotkiewicz, K.; Rettig, W. Structural changes accompanying intramolecular electron transfer: focus on twisted intramolecular charge-transfer states and structures. *Chemical reviews* **2003**, *103* (10), 3899-4032.
(141) Sasaki, S.; Drummen, G. P.; Konishi, G.-i. Recent advances in twisted intramolecular charge transfer (TICT) fluorescence and related phenomena in materials chemistry. *Journal of Materials Chemistry C* **2016**, *4* (14), 2731-2743.
(142) Wang, C.; Chi, W.; Qiao, Q.; Tan, D.; Xu, Z.; Liu, X. Twisted intramolecular charge transfer (TICT) and twists beyond TICT: From mechanisms to rational designs of bright and sensitive fluorophores. *Chemical Society Reviews* **2021**, *50* (22), 12656-12678.
(143) Yoshihara, T.; Druzhinin, S. I.; Zachariasse, K. A. Fast intramolecular charge transfer with a planar rigidized electron donor/acceptor molecule. *Journal of the American Chemical Society* **2004**, *126* (27), 8535-8539.
(144) Zhong, C. The driving forces for twisted or planar intramolecular charge transfer. *Physical Chemistry Chemical Physics* **2015**, *17* (14), 9248-9257.
(145) Grabowski, Z.; Dobkowski, J. Twisted intramolecular charge transfer (TICT) excited states: energy and molecular structure. *Pure and Applied Chemistry* **1983**, *55* (2), 245-252.
(146) Hanaoka, K.; Iwaki, S.; Yagi, K.; Myochin, T.; Ikeno, T.; Ohno, H.; Sasaki, E.; Komatsu, T.; Ueno, T.; Uchigashima, M. General design strategy to precisely control the emission of fluorophores via a twisted intramolecular charge transfer (TICT) process. *Journal of the American Chemical Society* **2022**, *144* (43), 19778-19790.
(147) Husband, J. T.; Xie, Y.; Wilks, T. R.; Male, L.; Torrent-Sucarrat, M.; Stavros, V. G.; O'Reilly, R. K. Rigidochromism by imide functionalisation of an aminomaleimide fluorophore. *Chemical Science* **2021**, *12* (31), 10550-10557.

(148) Faul, M. M.; Winneroski, L. L.; Krumrich, C. A. A new one step synthesis of maleimides by condensation of glyoxylate esters with acetamides. *Tetrahedron letters* **1999**, *40* (6), 1109-1112.
(149) Lauer, M. H.; Drekener, R. L.; Correia, C. R. D.; Gehlen, M. H. Fluorescence from bisaryl-substituted maleimide derivatives. *Photochemical & Photobiological Sciences* **2014**, *13*, 859-866.
(150) Ol'shevskaya, V. A.; Alpatova, V. M.; Radchenko, A. S.; Ramonova, A. A.; Petrova, A. S.; Tatarskiy, V. V.; Zaitsev, A. V.; Kononova, E. G.; Ikonnikov, N. S.; Kostyukov, A. A. β-Maleimide substituted meso-arylporphyrins: Synthesis, transformations, physico-chemical and antitumor properties. *Dyes and Pigments* **2019**, *171*, 107760.
(151) Patil, N. S.; Deshmukh, G. B.; Patil, S. V.; Bholay, A. D.; Gaikwad, N. D. Synthesis and biological evaluation of novel N-aryl maleimide derivatives clubbed with α-hydroxyphosphonates. *European journal of medicinal chemistry* **2014**, *83*, 490-497.
(152) Chen, Y.; Tsao, K.; De Francesco, E.; Keillor, J. W. Ring substituent effects on the thiol addition and hydrolysis reactions of N-arylmaleimides. *The Journal of Organic Chemistry* **2015**, *80* (24), 12182-12192.
(153) Zheng, R.; Mei, X.; Lin, Z.; Zhao, Y.; Yao, H.; Lv, W.; Ling, Q. Strong CIE activity, multi-stimuli-responsive fluorescence and data storage application of new diphenyl maleimide derivatives. *Journal of Materials Chemistry C* **2015**, *3* (39), 10242-10248.
(154) Zhu, B.-y.; Han, L.; Li, Y.-J.; Gao, J.-r.; Ye, Q. The AIEE properties and solid state fluorescence of 3-indolyl-4-indazolyl maleimide compounds: Synthesis and fluorescence characteristics. *Tetrahedron* **2017**, *73* (12), 1602-1610.
(155) Xie, H.-d.; Ho, L. A.; Truelove, M. S.; Corry, B.; Stewart, S. G. Fluorescent triphenyl substituted maleimide derivatives: synthesis, spectroscopy and quantum chemical calculations. *Journal of fluorescence* **2010**, *20*, 1077-1085.
(156) Ma, Z.; Qiu, S.; Chen, H.-C.; Zhang, D.; Lu, Y.-L.; Chen, X.-L. Maleimide structure: a promising scaffold for the development of antimicrobial agents. *Journal of Asian Natural Products Research* **2022**, *24* (1), 1-14.
(157) Shen, P.; Guo, Y.; Wei, J.; Zhao, H.; Zhai, H.; Zhao, Y. Straightforward synthesis of succinimide-fused pyrrolizidines by a three-component reaction of α-diketone, amino acid, and maleimide. *Synthesis* **2021**, *53* (07), 1262-1270.
(158) Gui, R.; Jin, H.; Bu, X.; Fu, Y.; Wang, Z.; Liu, Q. Recent advances in dual-emission ratiometric fluorescence probes for chemo/biosensing and bioimaging of biomarkers. *Coordination Chemistry Reviews* **2019**, *383*, 82-103.

(159) Yu, F.; Zhao, H.; Li, Y.; Xia, G.; Wang, H. D–A-Type fluorophores with efficient dual-state emission for imaging at ultralow concentration. *Materials Chemistry Frontiers* **2022**, *6* (2), 155-162.

(160) Li, C.; Liang, J.; Liang, B.; Li, Z.; Cheng, Z.; Yang, G.; Wang, Y. An organic emitter displaying dual emissions and efficient delayed fluorescence white OLEDs. *Advanced Optical Materials* **2019**, *7* (10), 1801667.

(161) Kang, S.; Jung, H.; Lee, H.; Park, S.; Kim, J.; Park, J. Highly efficient dual-core derivatives with EQEs as high as 8.38% at high brightness for OLED blue emitters. *Journal of Materials Chemistry C* **2019**, *7* (46), 14709-14716.

(162) Sun, J.; Mei, H.; Wang, S.; Gao, F. Two-photon semiconducting polymer dots with dual-emission for ratiometric fluorescent sensing and bioimaging of tyrosinase activity. *Analytical Chemistry* **2016**, *88* (14), 7372-7377.

(163) Eberlin, L. S.; Haddad, R.; Neto, R. C. S.; Cosso, R. G.; Maia, D. R.; Maldaner, A. O.; Zacca, J. J.; Sanvido, G. B.; Romão, W.; Vaz, B. G. Instantaneous chemical profiles of banknotes by ambient mass spectrometry. *Analyst* **2010**, *135* (10), 2533-2539.

(164) Zhu, Q.; Ye, Z.; Yang, W.; Cai, X.; Tang, B. Z. One-Pot Synthesis and Structure–Property Relationship of Aminomaleimides: Fluorescence Efficiencies in Monomers and Aggregates Easily Tuned by Switch of Aryl and Alkyl. *The Journal of Organic Chemistry* **2017**, *82* (2), 1096-1104.

(165) Huang, Y.; Zheng, X.; Huang, L.; Ling, Q.; Lin, Z. Highly efficient and tunable dual-state emission from diarylmaleimide derivatives in both solution and solid states for sensing and lighting. *Dyes and Pigments* **2024**, *222*, 111875.

(166) Pervez, M.; Pearce, A. K.; Husband, J. T.; Male, L.; Torrent-Sucarrat, M.; O'Reilly, R. K. Enhancing Dual-State Emission in Maleimide Fluorophores through Fluorocarbon Functionalisation. *Chemistry – A European Journal* **2022**, *28* (58). DOI: 10.1002/chem.202201877.

(167) Chen, H.; Huang, H.; Huang, X.; Clifford, J. N.; Forneli, A.; Palomares, E.; Zheng, X.; Zheng, L.; Wang, X.; Shen, P. High molar extinction coefficient branchlike organic dyes containing di (p-tolyl) phenylamine donor for dye-sensitized solar cells applications. *The Journal of Physical Chemistry C* **2010**, *114* (7), 3280-3286.

(168) Yoon, W. S.; Kim, D. W.; Park, J.-M.; Cho, I.; Kwon, O. K.; Whang, D. R.; Kim, J. H.; Park, J.-H.; Park, S. Y. A novel bis-lactam acceptor with outstanding molar extinction coefficient and structural planarity for donor–acceptor type conjugated polymer. *Macromolecules* **2016**, *49* (22), 8489-8497.

(169) Namuangruk, S.; Fukuda, R.; Ehara, M.; Meeprasert, J.; Khanasa, T.; Morada, S.; Kaewin, T.; Jungsuttiwong, S.; Sudyoadsuk, T.; Promarak, V. D–D− π–A-Type organic dyes for dye-sensitized solar cells with a potential for direct electron injection and a high extinction coefficient: synthesis, characterization, and theoretical investigation. *The Journal of Physical Chemistry C* **2012**, *116* (49), 25653-25663.

(170) Zeng, W.; Gong, S.; Zhong, C.; Yang, C. Prediction of oscillator strength and transition dipole moments with the nuclear ensemble approach for thermally activated delayed fluorescence emitters. *The Journal of Physical Chemistry C* **2019**, *123* (15), 10081-10086.

(171) Gong, J.; Han, J.; Liu, Q.; Ren, X.; Wei, P.; Yang, L.; Zhang, Y.; Liu, J.; Dong, Y.; Wang, Y. An ideal platform of light-emitting materials from phenothiazine: facile preparation, tunable red/NIR fluorescence, bent geometry-promoted AIE behaviour and selective lipid-droplet (LD) tracking ability. *Journal of Materials Chemistry C* **2019**, *7* (14), 4185-4190.

(172) Luo, J.; Guo, S.; Chen, F.; Jiang, B.; Wei, L.; Gong, Y.; Zhang, B.; Liu, Y.; Wei, C.; Tang, B. Z. Rational design strategies for nonconventional luminogens with efficient and tunable emission in dilute solution. *Chemical Engineering Journal* **2023**, *454*, 140469.

(173) Wang, X.; Yang, X.; Jiang, G.; Hu, Z.; Liao, T.; Wang, G.; Zhang, X.; He, X.; Zhang, J.; Zhang, J. Unlocking the NIR-II AIEgen for High Brightness through Intramolecular Electrostatic Locking. *Angewandte Chemie International Edition* **2024**, e202404142.

(174) He, B.; Luo, W.; Hu, S.; Chen, B.; Zhen, S.; Nie, H.; Zhao, Z.; Tang, B. Z. Synthesis and photophysical properties of new through-space conjugated luminogens constructed by folded tetraphenylethene. *Journal of Materials Chemistry C* **2017**, *5* (47), 12553-12560.

(175) Yu, L.; Liao, H.; Wu, H.; Li, W.; Zhu, Q. Through-bond/space conjugated nonaromatic dihydrobenzoquinolines: Luminogens with simple synthesis method, strong aggregation-induced emission and emissive excimers. *Dyes and Pigments* **2022**, *205*, 110543.

(176) Lide, D. R. *CRC handbook of chemistry and physics*; CRC press, 2004.

(177) Li, C.; Hou, M.; Dong, H.; Liu, R. Theoretical insights into photoinduced excited-state behaviors for the novel CHPPhl fluorophore: Effects of solvent polarity. *Journal of the Chinese Chemical Society* **2024**, *71* (2), 120-127.

(178) Belay, A.; Libnedengel, E.; Kim, H. K.; Hwang, Y. H. Effects of solvent polarity on the absorption and fluorescence spectra of chlorogenic acid and caffeic acid compounds: determination of the dipole moments. *Luminescence* **2016**, *31* (1), 118-126.

(179) Yin, G.; Li, Y.; Li, S.; Xu, B.; Yang, Q.; Zhang, Y.; Zhao, J.; Cao, X. Hexaphenylbenzene based push-pull fluorophores displaying intriguing polarity-dependent fluorescence behavior, AIE (E) characteristics and mega-large Stokes shifts. *Dyes and Pigments* **2022**, *198*, 110013.

(180) Kubin, R. F.; Fletcher, A. N. Fluorescence quantum yields of some rhodamine dyes. *Journal of Luminescence* **1982**, *27* (4), 455-462.
(181) Zhang, X.-F.; Zhang, Y.; Liu, L. Fluorescence lifetimes and quantum yields of ten rhodamine derivatives: Structural effect on emission mechanism in different solvents. *Journal of luminescence* **2014**, *145*, 448-453.
(182) Wang, Z.; Yu, L.; Wang, Y.; Wang, C.; Mu, Q.; Liu, X.; Yu, M.; Wang, K. N.; Yao, G.; Yu, Z. Dynamic adjust of non-radiative and radiative attenuation of AIE molecules reinforces NIR-II imaging mediated photothermal therapy and immunotherapy. *Advanced Science* **2022**, *9* (8), 2104793.
(183) Suzuki, S.; Sasaki, S.; Sairi, A. S.; Iwai, R.; Tang, B. Z.; Konishi, G. i. Principles of aggregation-induced emission: design of deactivation pathways for advanced AIEgens and applications. *Angewandte Chemie International Edition* **2020**, *59* (25), 9856-9867.
(184) Liu, W.; Wang, Y.; Ge, G.; Ma, L. Exploration the inherent mechanism of polymorphism and mechanochromism based on isomerism and AIE theory. *Dyes and Pigments* **2019**, *171*, 107663.
(185) Yang, W.; Liu, C.; Lu, S.; Du, J.; Gao, Q.; Zhang, R.; Liu, Y.; Yang, C. AIE-active smart cyanostyrene luminogens: polymorphism-dependent multicolor mechanochromism. *Journal of Materials Chemistry C* **2018**, *6* (2), 290-298.
(186) Cai, M.; Gao, Z.; Zhou, X.; Wang, X.; Chen, S.; Zhao, Y.; Qian, Y.; Shi, N.; Mi, B.; Xie, L. A small change in molecular structure, a big difference in the AIEE mechanism. *Physical Chemistry Chemical Physics* **2012**, *14* (15), 5289-5296.
(187) Yan, D.; Wu, Q.; Wang, D.; Tang, B. Z. Innovative synthetic procedures for luminogens showing aggregation-induced emission. *Angewandte Chemie International Edition* **2021**, *60* (29), 15724-15742.
(188) Würthner, F. Aggregation-induced emission (AIE): a historical perspective. *Angewandte Chemie International Edition* **2020**, *59* (34), 14192-14196.
(189) Zhang, J.; Zhang, H.; Lam, J. W.; Tang, B. Z. Restriction of intramolecular motion (RIM): investigating AIE mechanism from experimental and theoretical studies. *Chemical Research in Chinese Universities* **2021**, *37*, 1-15.
(190) Jerca, F. A.; Jerca, V. V.; Hoogenboom, R. Advances and opportunities in the exciting world of azobenzenes. *Nat Rev Chem* **2022**, *6* (1), 51-69. DOI: 10.1038/s41570-021-00334-w From NLM PubMed-not-MEDLINE.
(191) Leistner, A. L.; Pianowski, Z. L. Smart photochromic materials triggered with visible light. *European Journal of Organic Chemistry* **2022**, *2022* (19), e202101271.

(192) Sacherer, M.; Hampel, F.; Dube, H. Diaryl-hemiindigos as visible light, pH, and heat responsive four-state switches and application in photochromic transparent polymers. *Nature Communications* **2023**, *14* (1), 4382.
(193) Podlesný, J.; Jelínková, V.; Pytela, O.; Klikar, M.; Bureš, F. Acceptor-induced photoisomerization in small thienothiophene push-pull chromophores. *Dyes and Pigments* **2020**, *179*, 108398.
(194) Park, J. M.; Jung, C. Y.; Jang, W.-D.; Jaung, J. Y. Effect of donor-π-acceptor structure on photochromism of dithienylethene-based dyes. *Dyes and Pigments* **2020**, *177*, 108315.
(195) Georgiev, A.; Bubev, E.; Dimov, D.; Yancheva, D.; Zhivkov, I.; Krajčovič, J.; Vala, M.; Weiter, M.; Machkova, M. Synthesis, structure, spectral properties and DFT quantum chemical calculations of 4-aminoazobenzene dyes. Effect of intramolecular hydrogen bonding on photoisomerization. *Spectrochimica Acta Part A: Molecular and Biomolecular Spectroscopy* **2017**, *175*, 76-91.
(196) Wang, L.; Xu, J.; Zhou, H.; Yi, C.; Xu, W. Cis–trans isomerization mechanism of 4-aminoazobenzene in the S0 and S1 states: A CASSCF and DFT study. *Journal of Photochemistry and Photobiology A: Chemistry* **2009**, *205* (2-3), 104-108.
(197) Yang, Z.; Guo, Y.; Ai, S.-L.; Wang, S.-X.; Zhang, J.-Z.; Zhang, Y.-X.; Zou, Q.-C.; Wang, H.-X. Rational design and facile preparation of maleimide-based functional materials for imaging and optoelectronic applications. *Materials Chemistry Frontiers* **2019**, *3* (4), 571-578.
(198) Nevesely, T.; Wienhold, M.; Molloy, J. J.; Gilmour, R. Advances in the E→ Z isomerization of alkenes using small molecule photocatalysts. *Chemical reviews* **2021**, *122* (2), 2650-2694.
(199) Jhun, B. H.; Yi, S. Y.; Jeong, D.; Cho, J.; Park, S. Y.; You, Y. Aggregation of an n–π* molecule induces fluorescence turn-on. *The Journal of Physical Chemistry C* **2017**, *121* (21), 11907-11914.
(200) Imato, K.; Sasaki, A.; Ishii, A.; Hino, T.; Kaneda, N.; Ohira, K.; Imae, I.; Ooyama, Y. Sterically hindered stiff-stilbene photoswitch offers large motions, 90% two-way photoisomerization, and high thermal stability. *The Journal of Organic Chemistry* **2022**, *87* (23), 15762-15770.
(201) Xu, F.; Sheng, J.; Stindt, C. N.; Crespi, S.; Danowski, W.; Hilbers, M. F.; Buma, W. J.; Feringa, B. L. All-visible-light-driven stiff-stilbene photoswitches. *Chemical Science* **2024**, *15* (18), 6763-6769.
(202) Liu, G.; Leng, J.; Zhou, Q.; Deng, Z.; Shi, L.; Fan, C.; Xu, X.; Song, M.-P. Fluorescence photoswitch of stiff-stilbene derivatives for anti-counterfeiting. *Dyes and Pigments* **2022**, *203*, 110361.

(203) Rafique, S.; Irshad, H.; Majeed, S.; Rubab, R.; Imran, M.; Khan, A. M.; Shahzad, S. A. AIEE active stilbene based fluorescent sensor with red-shifted emission for vapor phase detection of nitrobenzene and moisture sensing. *Journal of Photochemistry and Photobiology A: Chemistry* **2023**, *437*, 114459.

(204) Sun, P.; Shi, Z.; Sima, W.; Tang, X.; Yuan, T.; Yang, M.; Xu, H.; Li, Z. A UV-responsive mechanically robust insulating polymer that achieves intrinsic self-healing of electrical tree damage based on reversible anthracene photodimerization. *Journal of Materials Chemistry C* **2023**, *11* (41), 14217-14225.

(205) Nehmeh, B.; Haydous, F.; Akoury, E. Mass calibrants for positive chemical ionization-high resolution mass spectrometry (CI-HRMS) for the identification of unknown compounds using accurate mass measurements. *RSC advances* **2023**, *13* (20), 14001-14009.

(206) Zastrow, L.; Speer, K.; Schwind, K.-H.; Jira, W. A sensitive GC–HRMS method for the simultaneous determination of parent and oxygenated polycyclic aromatic hydrocarbons in barbecued meat and meat substitutes. *Food Chemistry* **2021**, *365*, 130625.

(207) Hirata, S. Recent advances in materials with room-temperature phosphorescence: photophysics for triplet exciton stabilization. *Advanced Optical Materials* **2017**, *5* (17), 1700116.

(208) Peng, Q.; Ma, H.; Shuai, Z. Theory of long-lived room-temperature phosphorescence in organic aggregates. *Accounts of Chemical Research* **2020**, *54* (4), 940-949.

(209) Shao, W.; Kim, J. Metal-free organic phosphors toward fast and efficient room-temperature phosphorescence. *Accounts of Chemical Research* **2022**, *55* (11), 1573-1585.

(210) Zhuang, F. D.; Sun, Z. H.; Yao, Z. F.; Chen, Q. R.; Huang, Z.; Yang, J. H.; Wang, J. Y.; Pei, J. BN-Embedded Tetrabenzopentacene: A Pentacene Derivative with Improved Stability. *Angewandte Chemie International Edition* **2019**, *58* (31), 10708-10712.

(211) Omoto, K.; Nakae, T.; Nishio, M.; Yamanoi, Y.; Kasai, H.; Nishibori, E.; Mashimo, T.; Seki, T.; Ito, H.; Nakamura, K. Thermosalience in macrocycle-based soft crystals via anisotropic deformation of disilanyl architecture. *Journal of the American Chemical Society* **2020**, *142* (29), 12651-12657.

(212) She, P.; Yu, Y.; Qin, Y.; Zhang, Y.; Li, F.; Ma, Y.; Liu, S.; Huang, W.; Zhao, Q. Controlling organic room temperature phosphorescence through external heavy-atom effect for white light emission and luminescence printing. *Advanced Optical Materials* **2020**, *8* (4), 1901437.

(213) Wei, J.; Liang, B.; Duan, R.; Cheng, Z.; Li, C.; Zhou, T.; Yi, Y.; Wang, Y. Induction of strong long-lived room-temperature phosphorescence of N-phenyl-2-naphthylamine molecules by confinement in a crystalline dibromobiphenyl matrix. *Angewandte Chemie International Edition* **2016**, *55* (50), 15589-15593.

(214) Yan, X.; Peng, H.; Xiang, Y.; Wang, J.; Yu, L.; Tao, Y.; Li, H.; Huang, W.; Chen, R. Recent advances on host–guest material systems toward organic room temperature phosphorescence. *Small* **2022**, *18* (1), 2104073.
(215) Lei, Y.; Dai, W.; Tian, Y.; Yang, J.; Li, P.; Shi, J.; Tong, B.; Cai, Z.; Dong, Y. Revealing insight into long-lived room-temperature phosphorescence of host–guest systems. *The journal of physical chemistry letters* **2019**, *10* (20), 6019-6025.
(216) Ji, M.; Ma, X. Recent progress with the application of organic room-temperature phosphorescent materials. *Industrial Chemistry & Materials* **2023**, *1* (4), 582-594.
(217) Zhi, J.; Zhou, Q.; Shi, H.; An, Z.; Huang, W. Organic room temperature phosphorescence materials for biomedical applications. *Chemistry–An Asian Journal* **2020**, *15* (7), 947-957.
(218) Yang, J.; Fang, M.; Li, Z. Stimulus-responsive room temperature phosphorescence materials: internal mechanism, design strategy, and potential application. *Accounts of Materials Research* **2021**, *2* (8), 644-654.
(219) Xu, X.; Yan, B. Recent advances in room temperature phosphorescence materials: design strategies, internal mechanisms and intelligent optical applications. *Physical Chemistry Chemical Physics* **2023**, *25* (3), 1457-1475.
(220) Zhu, T.; Yang, T.; Zhang, Q.; Yuan, W. Z. Clustering and halogen effects enabled red/near-infrared room temperature phosphorescence from aliphatic cyclic imides. *Nature communications* **2022**, *13* (1), 2658.
(221) Liu, X.; Dai, W.; Qian, J.; Lei, Y.; Liu, M.; Cai, Z.; Huang, X.; Wu, H.; Dong, Y. Pure room temperature phosphorescence emission of an organic host–guest doped system with a quantum efficiency of 64%. *Journal of Materials Chemistry C* **2021**, *9* (10), 3391-3395.
(222) Guo, Y.; Wang, Y.; Gao, Y.; Zhang, J.; Wang, C.; Zhao, G. Host-guest doping induced excited state energy transfer for efficient room temperature phosphorescence emission. *Journal of Industrial and Engineering Chemistry* **2023**, *120*, 140-146.
(223) Wang, D.; Xie, Y.; Wu, X.; Lei, Y.; Zhou, Y.; Cai, Z.; Liu, M.; Wu, H.; Huang, X.; Dong, Y. Excitation-dependent triplet–singlet intensity from organic host–guest materials: tunable color, white-light emission, and room-temperature phosphorescence. *The Journal of Physical Chemistry Letters* **2021**, *12* (7), 1814-1821.
(224) Guo, Y.; Yao, L.; Luo, L.; Wang, H.-X.; Yang, Z.; Wang, Z.; Ai, S.-L.; Zhang, Y.; Zou, Q.-C.; Zhang, H.-L. Alkylaminomaleimide fluorophores: synthesis via air oxidation and emission modulation by twisted intramolecular charge transfer. *Organic Chemistry Frontiers* **2021**, *8* (2), 239-248.

(225) Song, H.; Wang, K.; Kuang, Z.; Zhao, Y. S.; Guo, Q.; Xia, A. Solvent modulated excited state processes of push–pull molecule with hybridized local excitation and intramolecular charge transfer character. *Physical Chemistry Chemical Physics* **2019**, *21* (7), 3894-3902.
(226) Gao, Y.; Zhang, S.; Pan, Y.; Yao, L.; Liu, H.; Guo, Y.; Gu, Q.; Yang, B.; Ma, Y. Hybridization and de-hybridization between the locally-excited (LE) state and the charge-transfer (CT) state: a combined experimental and theoretical study. *Physical Chemistry Chemical Physics* **2016**, *18* (35), 24176-24184.
(227) Wang, C.; Qiao, Q.; Chi, W.; Chen, J.; Liu, W.; Tan, D.; McKechnie, S.; Lyu, D.; Jiang, X. F.; Zhou, W. Quantitative design of bright fluorophores and AIEgens by the accurate prediction of twisted intramolecular charge transfer (TICT). *Angewandte Chemie* **2020**, *132* (25), 10246-10258.
(228) Thiagarajan, V.; Selvaraju, C.; Malar, E. P.; Ramamurthy, P. A novel fluorophore with dual fluorescence: Local excited state and photoinduced electron-transfer-promoted charge-transfer State. *ChemPhysChem* **2004**, *5* (8), 1200-1209.
(229) Xiao, F.; Liu, X.; Lin, K.; Zhou, Y.; Gao, W.; Lei, Y.; Liu, M.; Huang, X.; Wu, H. Pyranone–arylbenzene molecules controlled by the competition of local excited state and twisted intramolecular charge-transfer state: dual-state emission, polymorphism, and mechanofluorochromism. *The Journal of Physical Chemistry C* **2021**, *125* (30), 16792-16802.
(230) Kundu, A.; Karthikeyan, S.; Sagara, Y.; Moon, D.; Anthony, S. P. Temperature-controlled locally excited and twisted intramolecular charge-transfer state-dependent fluorescence switching in triphenylamine–benzothiazole derivatives. *ACS omega* **2019**, *4* (3), 5147-5154.
(231) Lin, Z.; Kabe, R.; Wang, K.; Adachi, C. Influence of energy gap between charge-transfer and locally excited states on organic long persistence luminescence. *Nature communications* **2020**, *11* (1), 191.
(232) Dang, Q.; Jiang, Y.; Wang, J.; Wang, J.; Zhang, Q.; Zhang, M.; Luo, S.; Xie, Y.; Pu, K.; Li, Q. Room-temperature phosphorescence resonance energy transfer for construction of near-infrared afterglow imaging agents. *Advanced Materials* **2020**, *32* (52), 2006752.
(233) Lu, T.; Chen, F. Multiwfn: A multifunctional wavefunction analyzer. *Journal of computational chemistry* **2012**, *33* (5), 580-592.
(234) Neese, F.; Wennmohs, F.; Becker, U.; Riplinger, C. The ORCA quantum chemistry program package. *The Journal of chemical physics* **2020**, *152* (22).